

**THERMO-ACOUSTIC COUPLING
AND DYNAMIC RESPONSE OF A PREMIXED
METHANE-AIR FLAME**

Thesis by
Steven L. Palm

In Partial Fulfillment of the Requirements for the degree
of
Doctor of Philosophy

Caltech

CALIFORNIA INSTITUTE OF TECHNOLOGY
Pasadena, California

2017
(Defended May 8th, 2017)

© 2017

Steven L. Palm

ORCID: 0000-0003-3095-0368

DEDICATION

In loving memory of and with profound gratitude to
my parents:

George Donald Palm
(March 25, 1923 – October 15, 2000)

Wilhelmina (Micki) Ellen Palm
(March 3, 1924 – April 26, 2001)

Members of the Greatest Generation
Veterans of World War II



You lived a humble life, giving so much of yourselves to so many others,
especially to me.

All my love and appreciation goes to you.

FOREWORD

When I began this journey in the fall of 1996, no one could have convinced me that it would take so many years to complete. After all, I had finished my Caltech BS in 1991 and MS in 1993, worked for three years as an engineer, and just married my beloved Linda after dating her through the whole stretch. As they say, the future was our oyster... or so it seemed. Unbeknownst to us, tragedies and challenges loomed over the horizon, just out of sight. Only the nagging worry of my parents' health took up residence in a basement corner of my mind.

The whole of the story is far too involved to recount in detail here. In short, my parents passed (six months apart) and I was forced to take a leave in order to handle the estate, which was in disarray. In the meantime research funding for my project evaporated. These and other complications left no easy path for a return to the institute. In a bold (and, albeit, foolish) move, I decided to complete my research on my own by founding a company (Aerofluidics, LLC) and building a laboratory. After all, how hard could it be?

It suffices to say that the last decade and a half has been quite a learning experience. Certainly not just in the aspects of this research, but in the areas of business, finance, manufacturing, fabrication, construction, contract law, and others. My parents always warned me how demoralizing and expensive the “school of hard-knocks” could be. I know what they meant.

It has also been a period of tremendous emotional and spiritual growth for both my wife and me. We have experienced the joys of childbirth and parenthood along with the agony that came with the death of two of our children, Heather and Matthew. We have struggled financially, living as minimalists, while I gainfully worked just enough to cover our expenses. The balance of the time was spent building a facility, designing and fabricating equipment, repairing instruments,

scouring for parts, negotiating deals with vendors, writing software and finally, lastly, doing research.

It seems as if calamities arose at every turn, both at home and in the lab. Indeed, they appeared at a rate that defied all logic. Although numerous issues arose, it was serious child-related health problems that marked the focal-point at home. On the business front, poorly negotiated deals, as well as strong-arm tactics and blatant subterfuge by others all took their toll. My own ignorance and lack of experience resulted in the need to relocate the laboratory facility twice. Component failures in the lab only added to the consternation and expense.

Through all of this my wife stood by my side. Her love and support were unwavering. Instead of harming our relationship the trials only served to draw us closer. With each onslaught, we fortified and comforted each other. As this journey draws to a close, I can confidently say that we are emerging on the other side as a stronger and more fulfilled family.

ACKNOWLEDGEMENTS

The completion of this thesis has been a long and arduous trek. There is no doubt that its realization is not through my efforts alone, but also through the support and encouragement of many others. I would first and foremost like to express my deepest gratitude to my advisor, Dr. Fred Culick. His guidance and support, as well as his near-infinite patience and understanding have been indispensable over the years. In addition, I have deeply valued his friendship and personal advice. Thank you.

Next, I would like to thank my family. My wife, Linda, has been unwavering in her faith, love and emotional fortitude. Our children, Rachel, Sarah, Aaron and Jacob have provided love and encouragement, and displayed understanding beyond their years. My sister Sharon and her husband John, as well as my sister Lisa and her husband Chuck have stood by me and provided their emotional support. Likewise, my wife's parents, Allan and Sue Dunbar, along with her grandparents, Paul and Marge Phillips, have supported us both through their love and encouragement, as well as through their financial assistance.

I would also like to acknowledge many of my friends and colleagues. Certainly many of them have helped me along the way, more than I can list here. Please know that my appreciation goes out to all of you. Nevertheless, a few require special recognition. A great thanks goes to my close friend and research colleague, Winston Pun. While still at Caltech, Winston and I shared an office and worked together developing the initial techniques used in this research. We spent many hours working in the lab together, and I have greatly appreciated his help, advice and encouragement over the years.

I would also like to express my profound thanks and appreciation to my dear friend and colleague, David LeCren. Dave and I met at Alturdyne in the early 1990s and worked together for

many years thereafter. His help and support on this project has been indispensable. He has been there for me every time I've asked for his assistance, whether it was for manual labor such as building laboratory walls, pulling cable, and running plumbing, or simply for his technical expertise and advice. Dave was instrumental to my achievement.

Another dear friend who deserves recognition is Scott Dolim. Scott and I were roommates and became good friends during our undergraduate years at Caltech in the late 1980s. Since then, Scott and I have maintained a brotherly friendship that has lasted for decades. As a fantastically talented software engineer, he has helped me greatly with his programming advice and assistance over the years. Additionally, his help in maintaining the network of Linux servers I used for data management in this research was crucial. Thank you very much, Scott.

Yet another individual who has been critical in my success is my close friend Sheng Wu. Sheng is a well-known non-linear optical expert and is renowned in the field. His technical assistance and encouragement (or flat-out insistence) was pivotal in steering me away from a dye-laser approach and toward developing the ring-cavity optical parametric oscillator that was used for UV laser-light generation. He also provided the nonlinear optical crystals as well as many of the other optics for the system at greatly reduced cost. My great appreciation goes to him.

Thanks also go to other work associates who have provided assistance and encouragement along the way. These include Ted Andreas, Chris Cooper, Gary Jones, Katie Jones, Brian Root, Troy Sherrillo, Carole Turpin, and Mark Wheelus. Thank you, all.

Further, I would like to express my gratitude to the OEMs and vendors that provided hardware or services for this research through special arrangements. Included in these is Andor Technology plc, which manufactured the ICCD camera that was used during the PLIF experiments. Tom Greis of Andor was instrumental in arranging the initial acquisition of the camera while Chris Campillo later facilitated its repair when the photo-intensifier failed.

Finally, I would like to deeply thank my parents. As a late-life child, I had the benefit of being raised by members of the Greatest Generation. Having grown up during the Great Depression and being veterans of WWII, my parents instilled in me a world view and an outlook on life that few of my classmates shared. They led by example, raising me to understand the value of truth, love, ethics, hard work, frugality, and a man's word. They were not wealthy, but were rich in spirit, loving each other and their children very much. They sacrificed a great many things, including their retirement, to ensure that I would have the opportunity for a life better than theirs. As the dusk of their lives set into night, I promised each of them that I would finish this thesis. It took much longer than I had planned, but as you taught me Mom and Dad, I have kept my word. Thank you so much for making this possible.

ABSTRACT

The work herein generally applies to the problem of combustion instability. Combustion instabilities first arose in engineering practice in the 1940s when they were experienced during the development of solid and liquid propellant rocket engines. Later, similar problems arose in gas turbine combustors and afterburners. However, the earliest technical case of the phenomenon dates back to Rijke in 1859 with his “singing” tube.

The presented work focuses on the study of a simple, stagnation plane stabilized, laminar, flat-flame burner. In particular the dynamic response of the burner is examined under excitation by a driven acoustic field. After characterization of the burner’s operational range, the response of the system is measured from 20 Hz to nearly 2000 Hz over the span of operating parameters using an optically filtered PMT and lens combination. A library of the collected and reduced data is generated.

A deeper investigation of the burner dynamics at a given reference operating condition is performed using phase-resolved PLIF. Fluctuations in the spatial distributions of the LIF signals for several target species (OH , CH , CH_2O) under acoustic forcing are measured. In addition, visualization of the unsteady reactant flow using precision acetone seeding and PLIF at 277 nm is performed. Subsequent cinematographic sequences are produced along with spatially resolved plots of the combustion response function and the forced Rayleigh index for numerous drive frequencies. A library of the collected and reduced data is assembled.

Analysis of the collected data reveals two principal mechanisms contributing to the unsteady response of the flame. Structure development in (and subsequent convention along) the unsteady shear layer of the laminar jet dominates the response at the outer reaches of the flame. The inner region of the flame is driven largely by the Helmholtz response of the burner nozzle

cavity. These two operations mutually contribute to produce the general shape of the combustion response curve. Ultimately, the data is used to construct a simplified model for the combustion response function. The model is enhanced with two additional revisions guided by the improved understanding of the mechanisms involved.

The document ends with numerous appendices describing, in detail, the equipment used, much of which was fabricated specifically for this work. These appendices, in combination with information presented in the chapters, provide substantial detail regarding the experimental configuration and operating conditions. Great effort was made to provide the necessary information to allow replication of the experiments as well as to support future modeling endeavors as a validation dataset.

TABLE OF CONTENTS

Dedication.....	iii
Foreword.....	iv
Acknowledgements.....	vi
Abstract.....	ix
Table of Contents.....	xi
List of Figures.....	xiv
List of Tables.....	xxx
Chapter I: Introduction.....	1
1.1 Introduction to Combustion Instabilities	1
1.2 A Conceptual Model and Rayleigh's Criterion	3
1.3 Previous Work	5
1.4 Objectives	12
Chapter II: Experimental Equipment.....	15
2.1 Overview.....	15
2.2 Acoustic Forcing Chamber	16
2.3 Stagnation-Plane Flat-Flame Burner.....	18
2.4 Laser Source	22
2.5 Light-Gathering Equipment	23
2.6 Data Acquisition System.....	25
Chapter III: Experimental Work Using Chemiluminescence	29
3.1 Overview and Motivation.....	29
3.2 Experimental Setup	30
3.3 Test Envelope	32
3.4 Experimental Results.....	34
3.4.1 The Combustion Response Function	34
3.4.2 Combustion Response Variation with Free Parameters	39
3.4.3 Role of the Transport Delay	44
3.4.4 Phase Branches	48
3.4.5 The Forced Rayliegh Index	50
3.4.6 Phase Branch Bifurcation Revisited	60
Chapter IV: Experimental Work Using PLIF.....	62
4.1 Overview.....	62
4.2 PLIF Motivation	63
4.3 LIF Theory.....	65
4.3.1 Electronic Spectroscopy	66
4.3.2 Collisional Quenching	69
4.4 Laser, Delivery Optics and Imaging System.....	71
4.4.1 Laser Light Source.....	71
4.4.2 Delivery and Sheet-Forming Optics	71
4.4.3 Imaging System	74
4.4.4 Laser Sheet Intensity Profilometer.....	75
4.5 General Data Collection Procedure.....	77
4.6 First-Pass Data Reduction	79
4.6.1 Data Merging	80

4.6.2 Background Image Generation	80
4.6.3 Image Phase Averaging.....	81
4.6.4 Report Generation.....	82
4.6.5 Image Data Output.....	83
4.7 OH PLIF Results	83
4.7.1 OH Excitation Regime	85
4.7.2 Correction for Spatial and Temporal Variation in Excitation	86
4.7.3 Reduced OH PLIF Data	90
4.8 CH PLIF Results.....	105
4.8.1 Reduced CH PLIF Data.....	107
4.9 CH ₂ O PLIF Results	118
4.9.1 Reduced CH ₂ O PLIF Data	120
4.10 Combined OH-CH ₂ O PLIF Results	131
4.10.1 Resulting Combined OH-CH ₂ O PLIF Data.....	132
4.11 Image Chemiluminescence Results	142
4.11.1 Reduced Image Chemiluminescence Data	143
4.12 Acetone PLIF Results.....	153
4.12.1 Resulting Acetone PLIF Data	154
Chapter V: Burner Modeling	160
5.1 Motivation for Modeling.....	160
5.2 Transfer Function Fitting.....	161
5.3 A Revised Transfer Function	168
5.4 Transfer Function – Revision 2.....	176
Chapter VI: Concluding Remarks.....	182
6.1 Summary	182
6.2 Future Work.....	187
Appendix A: Spatial Averaging in Simple Thermoacoustic Systems	190
A.1 Introduction.....	190
A.2 The Rijke Tube	191
A.2.1 Rijke Tube Exact Solution.....	191
A.2.2 Rijke Tube Solution by Spatial Averaging	201
A.3 A Closed-Open Tube	209
A.3.1 Closed-Open Tube Exact Solution.....	211
A.3.2 Dowling's Solution by Modal Expansion.....	212
A.3.3 Closed-Open System Spatial Averaging Solution - Corrected	216
Appendix B: A Stagnation Plane Stabilized Flat-Flame Burner	222
B.1 Overview	222
B.2 Nozzle Design.....	222
B.3 Stagnation Body	229
B.4 Burner Assembly	232
B.5 Fuel/Air Feed System	234
B.6 Burner Operational Range and Characteristics.....	239
Appendix C: Acetone Seeding System	242
C.1 Overview	242
C.2 Seeder Design	242
C.3 Seeder Operation.....	246
Appendix D: Acoustic Forcing Chamber Magnitude and Phase Calibration.....	248
D.1 Description and Necessity	248
D.2 Calibration Method.....	249

D.3 Resulting Calibration.....	251
D.4 Verification Through Simulated Response Testing.....	252
Appendix E: Laser Sources – Design, Fabrication and Performance	257
E.1 Introduction and Overview	257
E.2 Nd:YAG Laser Design.....	259
E.2.1 Optical Layout.....	261
E.3 Optical Parametric Oscillator (OPO).....	267
E.3.1 OPO Theory	267
E.3.2 OPO Design.....	271
E.3.2.1 Oscillator Cavity (Circulator)	271
E.3.2.2 Generation of 350-390 nm Output.....	276
E.3.2.3 Generation of 282 nm Output	279
E.3.2.4 Generation of 226 nm Output	281
E.3.3 OPO Control Software	283
E.3.4 OPO Wavelength Calibration.....	285
Appendix F: Custom Instrumentation – The AFC-100	288
F.1 Motivation and Overview	288
F.2 Base Instrument - Acoustic Forcing Controller.....	290
F.2.1 Digital Controller.....	292
F.2.2 Input Signal Conditioning	293
F.2.3 Signal Selection and Amplification	293
F.2.4 Measurement Stage	294
F.2.5 Oscillator Section	294
F.2.6 Amplitude Control Section	295
F.2.7 Power Supply.....	295
F.3 AFC-100-EX1 – Phase Targeter Expansion	296
F.3.1 Pressure Signal Conditioning and Conversion	298
F.3.2 Data Collection Timing and Storage	301
F.3.3 Laser and Camera Timing Control	303
F.3.4 Laser Energy and Timing Measurement.....	304
F.3.5 Data Retrieval and Storage.....	305
F.4 AFC-100-EX2 – Input Filter Expansion	306
F.4.1 High-Pass Filter Network.....	309
F.4.2 Low-Pass Filter Network	312
F.4.3 Bump Filter.....	313
F.5 AFC-100 Commands and Functions	313
Appendix G: Library of Bulk Chemiluminescence Data	318
G.1 Overview.....	318
G.2 Presented Data	319
Appendix H: Library of Spatially Resolved Experimental Data	385
H.1 Overview.....	385
H.2 Presented Data	386
H.2.1 OH PLIF Experimental Data.....	394
H.2.2 CH PLIF Experimental Data	413
H.2.3 CH ₂ O PLIF Experimental Data.....	435
H.2.4 OH-CH ₂ O PLIF Data.....	457
H.2.5 Chemiluminescence Experimental Data	476
H.2.6 Acetone PLIF Experimental Data	495
References	510

LIST OF FIGURES

Figure 1-1: Effect of equivalence ratio on NO _x production.....	2
Figure 1-2: Feedback coupling between fluctuating pressure and heat release	3
Figure 2-1: General schematic of the experimental apparatus	16
Figure 2-2: Acoustic forcing chamber.....	17
Figure 2-3: Flat-flame burner assembly	20
Figure 2-4: Flat-flame burner nozzle.....	20
Figure 2-5: Intensifier photocathode performance on Andor iStar ICCD camera.....	24
Figure 2-6: Data acquisition general system diagram.....	26
Figure 2-7: The AFC-100 acoustic forcing controller	27
Figure 3-1: General schematic of the experimental apparatus for performing phase-resolved chemiluminescence experiments	30
Figure 3-2: Burner operational envelope shown with transition boundaries	33
Figure 3-3: Burner operational envelope with the nozzle exit velocity normalized by the flame ingestion limit.....	34
Figure 3-4: Combustion response function plotted for the flat-flame burner operating on premixed methane and air with an equivalence ratio of 0.85 and a nozzle exit velocity ratio of 4.0	36
Figure 3-5: Amplitude portion of the combustion response function as seen in Figure 3-4 plotted in parallel with the fluctuating pressure seen within the larger portion of the burner nozzle cavity	37
Figure 3-6: Phase portion of the combustion response function as seen in Figure 3-4.....	38
Figure 3-7: Amplitude portion of the combustion response function for a nozzle for a nozzle exit velocity ratio of 4.0 and equivalence ratios from 0.75 to 0.90.....	40

Figure 3-8: Amplitude portion of the combustion response function for an equivalence ratio of 0.85 and for nozzle exit velocity ratios (V_R) varying from 3.5 to 6.5	41
Figure 3-9: Combustion response curves (magnitude and phase) for four test cases with nearly identical nozzle exit velocities (range 205 cm/s to 210 cm/s)	42
Figure 3-10: Combustion response data from experimental cases shown in Figure 3-7 plotted against Strouhal number	43
Figure 3-11: Combustion response data from experimental cases shown in Figure 3-8 plotted against Strouhal number	43
Figure 3-12: Plots of the transport time delay versus the nozzle exit velocity as determined by curve-fitting the combustion response phase curve in the sub-transitional region	46
Figure 3-13: Plot of the measured transition frequency versus the nozzle exit velocity	47
Figure 3-14: Plot of the final (accumulated) phase of the combustion response function at high frequencies (1800 to 2000 Hz) versus the nozzle exit velocity	49
Figure 3-15: Plot of the combustion response function for two identical experimental runs with response bifurcation shown	50
Figure 3-16: Forced Rayleigh index, R_f , for test case with equivalence ratio of 0.85 and a nozzle exit velocity ratio of 4.0 – linear scale	53
Figure 3-17: Forced Rayleigh index, R_f , for test case with equivalence ratio of 0.85 and a nozzle exit velocity ratio of 4.0 – logarithmic scale	54
Figure 3-18: Forced Rayleigh index, R_f , for a nozzle exit velocity ratio of 4.0 and equivalence ratios from 0.75 to 0.90	54
Figure 3-19: Forced Rayleigh index, R_f , for an equivalence ratio of 0.85 and for nozzle exit velocity ratios, V_R , varying from 3.5 to 6.5	55
Figure 3-20: Interpolated contour level-set showing the peak positive (driving) forced Rayleigh index observed over the burner operating envelope	57

Figure 3-21: Interpolated contour level-set showing the frequency (in Hertz) of the peak positive (driving) forced Rayleigh index observed over the burner operating envelope	57
Figure 3-22: Interpolated contour level-set showing the peak negative (damping) forced Rayleigh index observed over the burner operating envelope	58
Figure 3-23: Interpolated contour level-set showing the frequency (in Hertz) of the peak negative (damping) forced Rayleigh index observed over the burner operating envelope	58
Figure 3-24: Scatter plot of the extrema of the forced Rayleigh index for all experimental test conditions	59
Figure 3-25: Forced Rayleigh index, R_f , for parametrically identical test runs 86 and 116	60
Figure 4-1: Simplified Jablonski diagram	66
Figure 4-2: Photo of optical “bridge” with orange optical guard installed	72
Figure 4-3: Layout of optical elements on the bridge	73
Figure 4-4: Laser sheet profilometer tool	76
Figure 4-5: Phase-averaging procedure for PLIF or chemiluminescence images	82
Figure 4-6: LIF excitation spectra of OH radicals around 283 nm as simulated by LIFBase 2.1.1	84
Figure 4-7: Fluorescence intensity of OH radicals in a steady flame versus laser shot energy	85
Figure 4-8: OH PLIF image of flame under steady conditions	90
Figure 4-9: Phase resolved OH PLIF images for acoustic forcing at 55 Hz	91
Figure 4-10: Resulting waveforms from the 55 Hz OH PLIF experiment	93
Figure 4-11: Combustion response function - points computed from OH PLIF data superimposed on the curves computed from the bulk chemiluminescence experiments	96
Figure 4-12: Forced Rayleigh index - points computed from OH PLIF data superimposed on the curves computed from the bulk chemiluminescence experiments	96

Figure 4-13: Spatially resolved combustion response function produced from OH PLIF data	100
Figure 4-14: Spatially resolved forced Rayleigh index produced from OH PLIF data	102
Figure 4-15: LIF excitation spectra of CH (B-X) around 390 nm as simulated by LIFBase 2.1.1	106
Figure 4-16: Fluorescence intensity of CH radicals in a steady flame versus laser shot energy	106
Figure 4-17: CH PLIF image of flame under steady conditions	108
Figure 4-18: Phase resolved CH PLIF images for acoustic forcing at 55 Hz	109
Figure 4-19: Combustion response function - points computed from CH PLIF data superimposed on the curves computed from the bulk chemiluminescence experiments	111
Figure 4-20: Forced Rayleigh index - points computed from CH PLIF data superimposed on the curves computed from the bulk chemiluminescence experiments	111
Figure 4-21: Spatially resolved combustion response function produced from CH PLIF data	113
Figure 4-22: Spatially resolved forced Rayleigh index produced from CH PLIF data	115
Figure 4-23: CH ₂ O PLIF image of flame under steady conditions	121
Figure 4-24: Phase resolved CH ₂ O PLIF images for acoustic forcing at 55 Hz	122
Figure 4-25: Combustion response function - points computed from CH ₂ O PLIF data superimposed on the curves computed from the bulk chemiluminescence experiments	123
Figure 4-26: Forced Rayleigh index - points computed from CH ₂ O PLIF data superimposed on the curves computed from the bulk chemiluminescence experiments	123
Figure 4-27: Spatially resolved combustion response function produced from CH ₂ O PLIF data	126
Figure 4-28: Spatially resolved forced Rayleigh index produced from CH ₂ O PLIF data	128

Figure 4-29: Combined OH-CH ₂ O PLIF image of flame under steady conditions	133
Figure 4-30: Phase resolved OH-CH ₂ O (combined) PLIF images for acoustic forcing at 55 Hz.....	134
Figure 4-31: Combustion response function - points computed from the combined OH-CH ₂ O PLIF data superimposed on the curves computed from the bulk chemiluminescence experiments.....	136
Figure 4-32: Forced Rayleigh index - points computed from the combined OH-CH ₂ O PLIF data superimposed on the curves computed from the bulk chemiluminescence experiments.....	136
Figure 4-33: Spatially resolved combustion response function produced from OH-CH ₂ O PLIF combination data	138
Figure 4-34: Spatially resolved forced Rayleigh index produced from OH-CH ₂ O PLIF combination data	140
Figure 4-35: Chemiluminescence image of flame under steady conditions	144
Figure 4-36: Phase resolved chemiluminescence images for acoustic forcing at 55 Hz	146
Figure 4-37: Combustion response function - points computed from the image chemiluminescence data superimposed on the curves computed from the bulk chemiluminescence experiments.....	147
Figure 4-38: Forced Rayleigh index - points computed from the image chemiluminescence data (shown as crosshairs) superimposed on the curves computed from the bulk chemiluminescence experiments	147
Figure 4-39: Spatially resolved combustion response function produced from chemiluminescence data	149
Figure 4-40: Spatially resolved forced Rayleigh index produced from chemiluminescence data	151
Figure 4-41: Acetone PLIF image of seeded reactant flow under steady conditions	155
Figure 4-42: Phase resolved acetone PLIF images for acoustic forcing at 55 Hz	156
Figure 4-43: Acetone PLIF images for the acoustically forced cases showing resulting shear layer structures	157

Figure 4-44: Shear layer structure position (height) versus time.....	158
Figure 5-1: Combustion response function plotted for the flat-flame burner operating on premixed methane and air with an equivalence ratio of 0.85 and a nozzle exit velocity ratio of 4.0.....	162
Figure 5-2: Plot of combustion response transfer function model, $G_5(s)$, versus experimental data for the reference burner test condition – magnitude	165
Figure 5-3: Plot of combustion response transfer function model, $G_5(s)$, versus experimental data for the reference burner test condition – phase	166
Figure 5-4: Plot of combustion response transfer function model, $G_6(s)$, versus experimental data for the reference burner test condition – phase	167
Figure 5-5: Block diagram of reformulated transfer function model $G_9(s)$	170
Figure 5-6: Plots for the combustion response model functions $G_{7a}(s)$ and $G_8(s)$	173
Figure 5-7: Plot of the revised model, $G_9(s)$, for the combustion response transfer function versus experimental data for the reference burner test condition – magnitude	174
Figure 5-8: Plot of the revised model, $G_9(s)$, for the combustion response transfer function versus experimental data for the reference burner test condition – phase	175
Figure 5-9: Block diagram of 2 nd revision transfer function model $H_2(s)$	176
Figure 5-10: Plots for the model function $G_{10}(s)$ – peaking function	177
Figure 5-11: Magnitude corrector curve for generating $f(\omega)$	179
Figure 5-12: Plot of 2 nd revision model, $H_2(s)$, for the combustion response transfer function versus experimental data for the reference test case – magnitude	180
Figure 5-13: Plot of 2 nd revision model, $H_2(s)$, for the combustion response transfer function versus experimental data for the reference test case – phase	181
Figure A-1: Horizontal Rijke tube apparatus used by Matveev et. al.	192
Figure A-2: Simplified cross-section of Rijke tube used by Matveev et. al.....	192

Figure A-3: Plots of exact solution of Rijke tube as given by equation (A-29a).	200
Figure A-4: Plots of the spatial averaging and exact solutions of the Rijke tube.	208
Figure A-5: Acoustically closed-open cavity with heater.....	210
Figure A-6: Solutions by Dowling (1995) for the closed-open system.....	215
Figure A-7: Plots of the spatial averaging and exact solutions of the closed-open system.	221
Figure B-1: Manufacturing drawing for 14 mm burner nozzle.....	224
Figure B-2: Assembly of 14 mm nozzle components.	226
Figure B-3: Configuration of Pitot probe used to measure the jet velocity profile at the exit of the contraction.....	228
Figure B-4: Measured velocity profiles at exit of aerodynamic contraction with $D_{exit} = 14$ mm.	228
Figure B-5: Upgraded stagnation body with water cooling and fabricated from stainless steel.....	231
Figure B-6: Simplified burner assembly.....	232
Figure B-7: Upper end of completed burner and entire burner assembly as installed in the test chamber.....	233
Figure B-8: Plumbing and instrumentation diagram for the experimental burner fuel/air feed system.	235
Figure B-9: Fuel/air mixing panel and mixing system control electronics.....	238
Figure B-10: Operational envelope of the stagnation plane flat-flame burner with 14 mm diameter nozzle.	239
Figure B-11: Principal operating modes of the burner within the region of sustainable operation.....	240
Figure B-12: Burner operational envelope shown with transition boundaries.	241
Figure C-1: Acetone seeding panel installed on the side of the experiment table.	244
Figure C-2: Plumbing and instrumentation diagram for the acetone seeding system.....	245
Figure D-1: Probe microphone assembly and assembly installed in the chamber test section.....	250

Figure D-2: Magnitude and phase calibration plots for the acoustic forcing chamber	251
Figure D-3: Single-line schematic of experimental setup used in chemiluminescence experiments	252
Figure D-4: Single-line schematic for acoustic calibration setup.....	253
Figure D-5: Microphone filter network for verifying acoustic calibration as well as system software and hardware	254
Figure D-6: Computed magnitude and phase responses of the microphone filter networks.	255
Figure D-7: Measured magnitude responses overlaid on computed transfer functions.....	255
Figure D-8: Measured phase responses overlaid on computed transfer functions.....	256
Figure E-1: Laser source general system diagram.....	258
Figure E-2: Nd:YAG laser and power supply used as the principal light source in the phase-resolved PLIF experiments.....	260
Figure E-3: Nd:YAG laser optical layout and component description.....	262
Figure E-4: Oscillator cavity output coupler reflectivity profile.....	263
Figure E-5: Redesigned Nd:YAG laser oscillator cavity and resulting oscillator output burn (near-field).....	266
Figure E-6: Energy level diagrams for three different cases of frequency conversion in nonlinear optical crystals	270
Figure E-7: Completed optical parametric oscillator (OPO)	272
Figure E-8: General layout of the optical parametric oscillator	273
Figure E-9: OPO ring cavity oscillator fabricated on a custom sub-plate	273
Figure E-10: Optical parametric oscillator configuration for generating 390 nm UV light for CH PLIF or 352 nm UV light for formaldehyde PLIF	277
Figure E-11: Optical parametric oscillator performance generating 390 nm output.....	278
Figure E-12: Optical parametric oscillator configuration for generating 283 nm UV light for OH PLIF	279

Figure E-13: Optical parametric oscillator performance generating 283 nm output.....	280
Figure E-14: Optical parametric oscillator configuration for generating 226 nm UV light for NO PLIF	282
Figure E-15: Screenshot of the OPO control and interface software.....	284
Figure E-16: Typical neon optogalvanic spectrum recorded during OPO calibration scan.....	287
Figure F-1: First version of the AFC-100 acoustic forcing controller.....	290
Figure F-2: Block diagram of the base system of the AFC-100 acoustic forcing controller.....	291
Figure F-3: EX1 phase targeter expansion board installed in the AFC-100 instrument.....	298
Figure F-4: Block diagram of the board level structure of the AFC-100-EX1 phase targeter expansion.....	299
Figure F-5: Block diagram of the logic implemented in the phase targeter CPLD.....	300
Figure F-6: EX2 input filter board installed in the AFC-100 instrument	307
Figure F-7: Block diagram of the EX2 input filter expansion board.....	308
Figure F-8: Best effort 2nd order Chebyshev high-pass filter	310
Figure F-9: Magnitude and phase responses of the two filter blocks, $G_1(s)$ and $G_2(s)$	311
Figure F-10: Magnitude and phase of the high-pass filter block	312
Figure G-1: Measured combustion response for $\varphi = 0.675$ and $V_R = 2.0$	323
Figure G-2: Measured combustion response for $\varphi = 0.700$ and $V_R = 2.0$	324
Figure G-3: Measured combustion response for $\varphi = 0.700$ and $V_R = 2.5$	325
Figure G-4: Measured combustion response for $\varphi = 0.725$ and $V_R = 2.0$	326
Figure G-5: Measured combustion response for $\varphi = 0.725$ and $V_R = 2.5$	327
Figure G-6: Measured combustion response for $\varphi = 0.725$ and $V_R = 3.0$	328
Figure G-7: Measured combustion response for $\varphi = 0.750$ and $V_R = 2.0$	329
Figure G-8: Measured combustion response for $\varphi = 0.750$ and $V_R = 2.5$	330
Figure G-9: Measured combustion response for $\varphi = 0.750$ and $V_R = 3.0$	331
Figure G-10: Measured combustion response for $\varphi = 0.750$ and $V_R = 3.5$	332

Figure G-11:	Measured combustion response for $\varphi = 0.750$ and $V_R = 4.0$	333
Figure G-12:	Measured combustion response for $\varphi = 0.775$ and $V_R = 2.5$	334
Figure G-13:	Measured combustion response for $\varphi = 0.775$ and $V_R = 3.0$	335
Figure G-14:	Measured combustion response for $\varphi = 0.775$ and $V_R = 3.5$	336
Figure G-15:	Measured combustion response for $\varphi = 0.775$ and $V_R = 4.0$	337
Figure G-16:	Measured combustion response for $\varphi = 0.775$ and $V_R = 4.5$	338
Figure G-17:	Measured combustion response for $\varphi = 0.800$ and $V_R = 3.0$	339
Figure G-18:	Measured combustion response for $\varphi = 0.800$ and $V_R = 3.5$	340
Figure G-19:	Measured combustion response for $\varphi = 0.800$ and $V_R = 4.0$	341
Figure G-20:	Measured combustion response for $\varphi = 0.800$ and $V_R = 4.5$	342
Figure G-21:	Measured combustion response for $\varphi = 0.800$ and $V_R = 5.0$	343
Figure G-22:	Measured combustion response for $\varphi = 0.825$ and $V_R = 3.0$	344
Figure G-23:	Measured combustion response for $\varphi = 0.825$ and $V_R = 3.5$	345
Figure G-24:	Measured combustion response for $\varphi = 0.825$ and $V_R = 4.0$	346
Figure G-25:	Measured combustion response for $\varphi = 0.825$ and $V_R = 4.5$	347
Figure G-26:	Measured combustion response for $\varphi = 0.825$ and $V_R = 5.0$	348
Figure G-27:	Measured combustion response for $\varphi = 0.825$ and $V_R = 5.5$	349
Figure G-28:	Measured combustion response for $\varphi = 0.825$ and $V_R = 6.0$	350
Figure G-29:	Measured combustion response for $\varphi = 0.850$ and $V_R = 3.5$	351
Figure G-30:	Measured combustion response for $\varphi = 0.850$ and $V_R = 4.0$	352
Figure G-31:	Measured combustion response for $\varphi = 0.850$ and $V_R = 4.5$	353
Figure G-32:	Measured combustion response for $\varphi = 0.850$ and $V_R = 5.0$	354
Figure G-33:	Measured combustion response for $\varphi = 0.850$ and $V_R = 5.5$	355
Figure G-34:	Measured combustion response for $\varphi = 0.850$ and $V_R = 6.0$	356
Figure G-35:	Measured combustion response for $\varphi = 0.850$ and $V_R = 6.5$	357
Figure G-36:	Measured combustion response for $\varphi = 0.875$ and $V_R = 3.5$	358
Figure G-37:	Measured combustion response for $\varphi = 0.875$ and $V_R = 4.0$	359
Figure G-38:	Measured combustion response for $\varphi = 0.875$ and $V_R = 4.5$	360
Figure G-39:	Measured combustion response for $\varphi = 0.875$ and $V_R = 5.0$	361
Figure G-40:	Measured combustion response for $\varphi = 0.875$ and $V_R = 5.5$	362
Figure G-41:	Measured combustion response for $\varphi = 0.875$ and $V_R = 6.0$	363

Figure G-42:	Measured combustion response for $\varphi = 0.875$ and $V_R = 6.5$	364
Figure G-43:	Measured combustion response for $\varphi = 0.875$ and $V_R = 7.0$	365
Figure G-44:	Measured combustion response for $\varphi = 0.900$ and $V_R = 4.0$	366
Figure G-45:	Measured combustion response for $\varphi = 0.900$ and $V_R = 4.5$	367
Figure G-46:	Measured combustion response for $\varphi = 0.900$ and $V_R = 5.0$	368
Figure G-47:	Measured combustion response for $\varphi = 0.900$ and $V_R = 5.5$	369
Figure G-48:	Measured combustion response for $\varphi = 0.900$ and $V_R = 6.0$	370
Figure G-49:	Measured combustion response for $\varphi = 0.900$ and $V_R = 6.5$	371
Figure G-50:	Measured combustion response for $\varphi = 0.925$ and $V_R = 4.0$	372
Figure G-51:	Measured combustion response for $\varphi = 0.925$ and $V_R = 4.5$	373
Figure G-52:	Measured combustion response for $\varphi = 0.925$ and $V_R = 5.0$	374
Figure G-53:	Measured combustion response for $\varphi = 0.925$ and $V_R = 5.5$	375
Figure G-54:	Measured combustion response for $\varphi = 0.925$ and $V_R = 6.0$	376
Figure G-55:	Measured combustion response for $\varphi = 0.950$ and $V_R = 4.5$	377
Figure G-56:	Measured combustion response for $\varphi = 0.950$ and $V_R = 5.0$	378
Figure G-57:	Measured combustion response for $\varphi = 0.950$ and $V_R = 5.5$	379
Figure G-58:	Measured combustion response for $\varphi = 0.975$ and $V_R = 4.5$	380
Figure G-59:	Measured combustion response for $\varphi = 0.975$ and $V_R = 5.0$	381
Figure G-60:	Measured combustion response for $\varphi = 0.975$ and $V_R = 5.5$	382
Figure G-61:	Measured combustion response for $\varphi = 1.000$ and $V_R = 5.0$	383
Figure G-62:	Measured combustion response for $\varphi = 1.000$ and $V_R = 5.5$	384
Figure H-1:	OH PLIF image of flame under steady conditions	394
Figure H-2:	Resulting waveforms from the 55 Hz OH PLIF experiment.....	395
Figure H-3:	Resulting waveforms from the 75 Hz OH PLIF experiment.....	396
Figure H-4:	Resulting waveforms from the 100 Hz OH PLIF experiment.....	397
Figure H-5:	Resulting waveforms from the 150 Hz OH PLIF experiment.....	398
Figure H-6:	Resulting waveforms from the 220 Hz OH PLIF experiment.....	399
Figure H-7:	Resulting waveforms from the 265 Hz OH PLIF experiment.....	400
Figure H-8:	Resulting waveforms from the 375 Hz OH PLIF experiment.....	401
Figure H-9:	Phase-resolved OH PLIF images for acoustic forcing at 55 Hz	402

Figure H-10: Phase-resolved OH PLIF images for acoustic forcing at 75 Hz	404
Figure H-11: Phase-resolved OH PLIF images for acoustic forcing at 100 Hz	406
Figure H-12: Phase-resolved OH PLIF images for acoustic forcing at 150 Hz	408
Figure H-13: Spatially resolved combustion function produced from OH PLIF data	410
Figure H-14: Spatially resolved forced Rayleigh index produced from OH PLIF data	412
Figure H-15: CH PLIF image of flame under steady conditions	413
Figure H-16: Resulting waveforms from the 55 Hz CH PLIF experiment	414
Figure H-17: Resulting waveforms from the 75 Hz CH PLIF experiment	415
Figure H-18: Resulting waveforms from the 100 Hz CH PLIF experiment	416
Figure H-19: Resulting waveforms from the 150 Hz CH PLIF experiment	417
Figure H-20: Resulting waveforms from the 220 Hz CH PLIF experiment	418
Figure H-21: Resulting waveforms from the 240 Hz CH PLIF experiment	419
Figure H-22: Resulting waveforms from the 243 Hz CH PLIF experiment	420
Figure H-23: Resulting waveforms from the 265 Hz CH PLIF experiment	421
Figure H-24: Resulting waveforms from the 375 Hz CH PLIF experiment	422
Figure H-25: Phase-resolved CH PLIF images for acoustic forcing at 55 Hz	423
Figure H-26: Phase resolved CH PLIF images for acoustic forcing at 75 Hz	425
Figure H-27: Phase resolved CH PLIF images for acoustic forcing at 100 Hz	427
Figure H-28: Phase resolved CH PLIF images for acoustic forcing at 150 Hz	429
Figure H-29: Spatially resolved combustion function produced from OH PLIF data	431
Figure H-30: Spatially resolved forced Rayleigh index produced from OH PLIF data	433
Figure H-31: CH ₂ O PLIF image of flame under steady conditions	435

Figure H-32: Resulting waveforms from the 55 Hz CH ₂ O PLIF experiment.....	436
Figure H-33: Resulting waveforms from the 75 Hz CH ₂ O PLIF experiment.....	437
Figure H-34: Resulting waveforms from the 100 Hz CH ₂ O PLIF experiment.....	438
Figure H-35: Resulting waveforms from the 150 Hz CH ₂ O PLIF experiment.....	439
Figure H-36: Resulting waveforms from the 220 Hz CH ₂ O PLIF experiment.....	440
Figure H-37: Resulting waveforms from the 240 Hz CH ₂ O PLIF experiment.....	441
Figure H-38: Resulting waveforms from the 243 Hz CH ₂ O PLIF experiment.....	442
Figure H-39: Resulting waveforms from the 265 Hz CH ₂ O PLIF experiment.....	443
Figure H-40: Resulting waveforms from the 375 Hz CH ₂ O PLIF experiment.....	444
Figure H-41: Phase resolved CH ₂ O PLIF images for acoustic forcing at 55 Hz	445
Figure H-42: Phase resolved CH ₂ O PLIF images for acoustic forcing at 75 Hz	447
Figure H-43: Phase resolved CH ₂ O PLIF images for acoustic forcing at 100 Hz	449
Figure H-44: Phase resolved CH ₂ O PLIF images for acoustic forcing at 150 Hz	451
Figure H-45: Spatially resolved combustion function produced from CH ₂ O PLIF data	453
Figure H-46: Spatially resolved forced Rayleigh index produced from CH ₂ O PLIF data	455
Figure H-47: Combined OH-CH ₂ O PLIF image of flame under steady conditions	457

Figure H-48: Resulting waveforms from the 55 Hz OH-CH ₂ O PLIF combination.....	458
Figure H-49: Resulting waveforms from the 75 Hz OH-CH ₂ O PLIF combination.....	459
Figure H-50: Resulting waveforms from the 100 Hz OH-CH ₂ O PLIF combination.....	460
Figure H-51: Resulting waveforms from the 150 Hz OH-CH ₂ O PLIF combination.....	461
Figure H-52: Resulting waveforms from the 220 Hz OH-CH ₂ O PLIF combination.....	462
Figure H-53: Resulting waveforms from the 265 Hz OH-CH ₂ O PLIF combination.....	463
Figure H-54: Resulting waveforms from the 375 Hz OH-CH ₂ O PLIF combination.....	464
Figure H-55: Phase resolved OH-CH ₂ O PLIF combination images for acoustic forcing at 55 Hz	465
Figure H-56: Phase resolved OH-CH ₂ O PLIF combination images for acoustic forcing at 75 Hz	467
Figure H-57: Phase resolved OH-CH ₂ O PLIF combination images for acoustic forcing at 100 Hz	469
Figure H-58: Phase resolved OH-CH ₂ O PLIF combination images for acoustic forcing at 150 Hz	471
Figure H-59: Spatially resolved combustion function produced from OH-CH ₂ O PLIF combination data	473
Figure H-60: Spatially resolved forced Rayleigh index produced from OH-CH ₂ O PLIF combination data	475
Figure H-61: Chemiluminescence image of flame under steady conditions	476
Figure H-62: Resulting waveforms from the 55 Hz chemiluminescence experiment.....	477
Figure H-63: Resulting waveforms from the 75 Hz chemiluminescence experiment.....	478
Figure H-64: Resulting waveforms from the 100 Hz chemiluminescence experiment.....	479

Figure H-65: Resulting waveforms from the 150 Hz chemiluminescence experiment.....	480
Figure H-66: Resulting waveforms from the 220 Hz chemiluminescence experiment.....	481
Figure H-67: Resulting waveforms from the 265 Hz chemiluminescence experiment.....	482
Figure H-68: Resulting waveforms from the 375 Hz chemiluminescence experiment.....	483
Figure H-69: Phase resolved chemiluminescence images for acoustic forcing at 55 Hz.....	484
Figure H-70: Phase resolved chemiluminescence images for acoustic forcing at 75 Hz.....	486
Figure H-71: Phase resolved chemiluminescence images for acoustic forcing at 100 Hz.....	488
Figure H-72: Phase resolved chemiluminescence images for acoustic forcing at 150 Hz.....	490
Figure H-73: Spatially resolved combustion function produced from chemiluminescence data	492
Figure H-74: Spatially resolved forced Rayleigh index produced from chemiluminescence data	494
Figure H-75: Acetone PLIF image of seeded flame under steady conditions	495
Figure H-76: Phase resolved acetone PLIF images for acoustic forcing at 55 Hz	496
Figure H-77: Phase resolved acetone PLIF images for acoustic forcing at 75 Hz	498
Figure H-78: Phase resolved acetone PLIF images for acoustic forcing at 100 Hz	500
Figure H-79: Phase resolved acetone PLIF images for acoustic forcing at 150 Hz	502
Figure H-80: Phase resolved acetone PLIF images for acoustic forcing at 220 Hz	504

Figure H-81: Phase resolved acetone PLIF images for acoustic forcing	
at 265 Hz	506
Figure H-82: Phase resolved acetone PLIF images for acoustic forcing	
at 375 Hz	508

LIST OF TABLES

Table 1-1: Previous work in oscillating flames related to investigation of combustion dynamics	7
Table 3-1: Chemiluminescence test cases for which the nozzle exit velocity lies between 205 cm/s and 210 cm/s	42
Table 4-1: Harmonic content of the measured acoustic and intensity fields for the 55 Hz PLIF case	93
Table 4-2: Global unsteady combustion responses as discerned using OH PLIF for the seven prescribed base drive frequencies	94
Table 4-3: Global unsteady combustion responses as discerned using CH PLIF for all nine prescribed drive frequencies	110
Table 4-4: Global unsteady combustion responses as discerned using CH ₂ O PLIF for all nine prescribed drive frequencies	121
Table 4-5: Global unsteady combustion responses as discerned using the combined OH-CH ₂ O PLIF data for the seven base drive frequencies	135
Table 4-6: Global unsteady combustion responses as discerned using the chemiluminescence data for the seven base drive frequencies	145
Table 5-1: Optimized parameters for the trial transfer function, $G_5(s)$	165
Table 5-2: Optimized parameters for the revised transfer function, $G_9(s)$	165
Table 5-3: Optimized parameters for the trial transfer function, $G_{10}(s)$	177
Table E-1: Specifications for the four OPO cavity mirrors as well as the output separator M209	274
Table E-2: List of observable neon I electrical transitions used in wavelength calibration of the OPO	286
Table F-1: AFC-100 command-line-interface (CLI) command set	315
Table G-1: Parameters held constant during bulk chemiluminescence experiments	318

Table G-2: Index of burner operating conditions and corresponding figures with bulk response function plots.....	321
Table H-1: Parameters held constant during PLIF and image chemiluminescence experiments	385
Table H-2: Index of Tables appearing in appendix H	389
Table H-3: Index of Figures appearing in appendix H.....	390
Table H-4: Values of the global (bulk) combustion response function	393
Table H-5: Values of the global (bulk) forced Rayleigh index (Rf)	393
Table H-6: Global (bulk) harmonic content of the 55 Hz OH PLIF case.....	395
Table H-7: Global (bulk) harmonic content of the 75 Hz OH PLIF case.....	396
Table H-8: Global (bulk) harmonic content of the 100 Hz OH PLIF case.....	397
Table H-9: Global (bulk) harmonic content of the 150 Hz OH PLIF case.....	398
Table H-10: Global (bulk) harmonic content of the 220 Hz OH PLIF case.....	399
Table H-11: Global (bulk) harmonic content of the 265 Hz OH PLIF case.....	400
Table H-12: Global (bulk) harmonic content of the 375 Hz OH PLIF case.....	401
Table H-13: Global (bulk) harmonic content of the 55 Hz CH PLIF case	414
Table H-14: Global (bulk) harmonic content of the 75 Hz CH PLIF case	415
Table H-15: Global (bulk) harmonic content of the 100 Hz CH PLIF case	416
Table H-16: Global (bulk) harmonic content of the 150 Hz CH PLIF case	417
Table H-17: Global (bulk) harmonic content of the 220 Hz CH PLIF case	418
Table H-18: Global (bulk) harmonic content of the 240 Hz CH PLIF case	419
Table H-19: Global (bulk) harmonic content of the 243 Hz CH PLIF case	420
Table H-20: Global (bulk) harmonic content of the 265 Hz CH PLIF case	421
Table H-21: Global (bulk) harmonic content of the 375 Hz CH PLIF case	422
Table H-22: Global (bulk) harmonic content of the 55 Hz CH ₂ O PLIF case.....	436
Table H-23: Global (bulk) harmonic content of the 75 Hz CH ₂ O PLIF case.....	437
Table H-24: Global (bulk) harmonic content of the 100 Hz CH ₂ O PLIF case.....	438
Table H-25: Global (bulk) harmonic content of the 150 Hz CH ₂ O PLIF case.....	439

Table H-26: Global (bulk) harmonic content of the 220 Hz CH ₂ O	
PLIF case.....	440
Table H-27: Global (bulk) harmonic content of the 240 Hz CH ₂ O	
PLIF case.....	441
Table H-28: Global (bulk) harmonic content of the 243 Hz CH ₂ O	
PLIF case.....	442
Table H-29: Global (bulk) harmonic content of the 265 Hz CH ₂ O	
PLIF case.....	443
Table H-30: Global (bulk) harmonic content of the 375 Hz CH ₂ O	
PLIF case.....	444
Table H-31: Global (bulk) harmonic content of the combined 55 Hz	
OH-CH ₂ O PLIF case.....	458
Table H-32: Global (bulk) harmonic content of the combined 75 Hz	
OH-CH ₂ O PLIF case.....	459
Table H-33: Global (bulk) harmonic content of the combined 100 Hz	
OH-CH ₂ O PLIF case.....	460
Table H-34: Global (bulk) harmonic content of the combined 150 Hz	
OH-CH ₂ O PLIF case.....	461
Table H-35: Global (bulk) harmonic content of the combined 220 Hz	
OH-CH ₂ O PLIF case.....	462
Table H-36: Global (bulk) harmonic content of the combined 265 Hz	
OH-CH ₂ O PLIF case.....	463
Table H-37: Global (bulk) harmonic content of the combined 375 Hz	
OH-CH ₂ O PLIF case.....	464
Table H-38: Global (bulk) harmonic content of the 55 Hz image	
chemiluminescence case.....	477
Table H-39: Global (bulk) harmonic content of the 75 Hz image	
chemiluminescence case.....	478
Table H-40: Global (bulk) harmonic content of the 100 Hz image	
chemiluminescence case.....	479
Table H-41: Global (bulk) harmonic content of the 150 Hz image	
chemiluminescence case.....	480

Table H-42: Global (bulk) harmonic content of the 220 Hz image	
chemiluminescence case	481
Table H-43: Global (bulk) harmonic content of the 265 Hz image	
chemiluminescence case	482
Table H-44: Global (bulk) harmonic content of the 375 Hz image	
chemiluminescence case	483

Chap ter 1

INTRODUCTION

1.1 Introduction to Combustion Instabilities

Millennia have passed since man first used fire as a source of heat, and yet to this day, at the dawn of the 21st century, mankind's primary source of energy is still through the combustion of organic fuels. Currently, combustion of natural gas, coal and crude oil, as well as their derivatives, constitute more than eighty percent of the energy consumed in the world. Aside from the fuel that is used for direct heating applications, virtually all of the remaining balance is consumed in order to produce mechanical energy. This is seen in small-scale systems such as the cars we drive and the gasoline-powered gardening tools we use. It is also seen in large-scale systems such as giant steam or direct-fired gas turbine engines that produce hundreds of mechanical megawatts per machine. In most cases, these prime movers are used to drive generators, producing electricity for our businesses and homes.

In recent decades, serious concerns have arisen over the production of pollutants and greenhouse gasses, and their possible impact on the environment. In 1970, the Clean Air Act was passed, and regulators such as the Environmental Protection Agency (EPA) began limiting the level of emissions allowed from fuel burning equipment. The principal emissions monitored were carbon monoxide, nitrogen oxides, sulfur dioxide, volatile organic compounds (VOCs), particulate matter and lead. In the three decades that followed, significant reductions were made in all of these categories except for nitrogen oxides. Reduction of NOx proved vexing due to the stability of the molecules involved as well as the chemistry. In the past twenty years, the EPA has responded by progressively tightening the rules governing NOx emissions. In addition, the concern over global climate change has increased attention on greenhouse gases such as CO₂. These regulatory

changes, compounded by higher fuel costs due to increased world demand, have driven engine manufacturers to produce cleaner burning systems with higher thermal efficiencies.

Unfortunately, these gains come with a caveat. In continuous combustion systems like those seen in gas turbine engines, most major engine manufacturers have resorted to some form of lean, premixed combustion to reduce the generation of oxides of nitrogen. Under typical operating conditions in these engines, the Zeldovich or thermal NO_x mechanism dominates. By using lean, premixed fuel/air mixtures in these combustors, local reaction zone temperatures are kept low resulting in greatly reduced NO_x production, as seen in Figure 1-1.

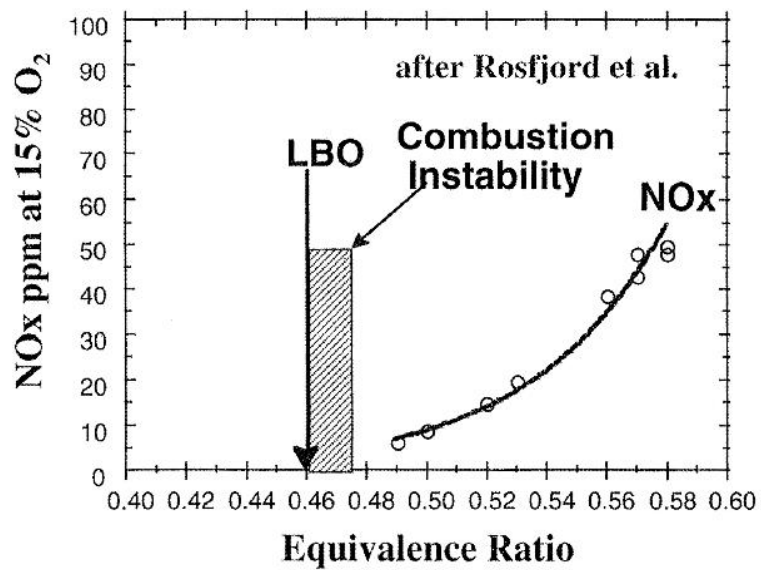


Figure 1-1: Effect of equivalence ratio on NO_x production (from Rosfjord 1995)

However, operating near the lean blowout limit (LBO) greatly increases the likelihood of encountering combustion instabilities. Increasing combustor pressures to improve engine thermal efficiency further exacerbates the instability problem.

Combustion instabilities are characterized by large amplitude, self-sustained pressure oscillations within the combustor. They were first encountered and seriously examined in liquid and solid propellant rocket engines beginning in the 1940s. They later became problematic in other systems such as gas turbine engines as power densities in those devices increased. In very high power density systems such as liquid propellant rocket engines, fluctuating pressure fields can disrupt boundary layer coolant and increase heat transfer rates resulting in catastrophic failure. In gas turbine systems, the effects are typically more benign, yet still problematic. Usually mechanical vibrations occur leading to fatigue and component failure. However, a significant increase in pollutant production is also common under oscillating conditions, thus defeating the primary advantage of operating in the LBO region.

1.2 A Conceptual Model and Rayleigh's Criterion

In many cases, the presence of an oscillating pressure field along with an unsteady heat release suggests that there exists a feedback loop as shown in Figure 1-2. Here, q' is the fluctuating part of the heat release, while p' represents the fluctuating part of the local pressure.

The *combustor dynamics* describe how a varying heat input to the system produces a fluctuating pressure component. This is typically governed by the equation of state and by the acoustic behavior of the combustor, both of which can be calculated with reasonable accuracy.

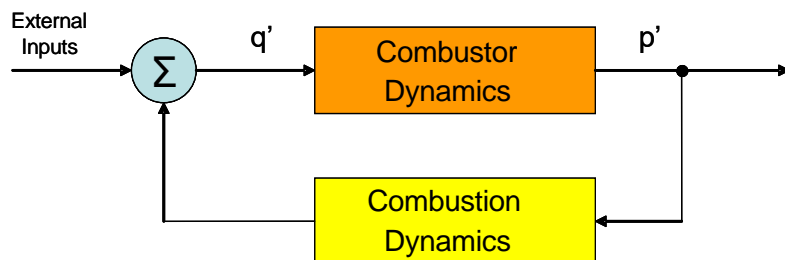


Figure 1-2: Feedback coupling between fluctuating pressure and heat release (Pun, Palm, Culick, 2000)

The *combustion dynamics* describe how the fluctuating pressure field couples back to generate a time varying heat release. This component of the system behavior is not nearly as well understood and encompasses many more factors. These include (but are not limited to) the local large and small-scale fluid mechanics (including unmixedness), chemical kinetics, and issues related to feed system coupling.

It was in 1878 that Lord Rayleigh first formulated his criterion for heat-driven pressure oscillations. He stated, “If heat be given to the air at the moment of greatest condensation, or be taken from it at the moment of greatest rarefaction, the vibration is encouraged. On the other hand, if heat be given at the moment of greatest rarefaction, or abstracted at the moment of greatest condensation, the vibration is discouraged.” This has become known as Rayleigh’s criterion for thermoacoustic instability. Since this observation numerous individuals have developed analytic representations of the phenomenon. Most notable is the work by Culick (1976, 1987, 1997) which explored and honed the formulation over two decades.

In its basic form, Rayleigh’s criterion can be summarized in the following relation:

$$(1-1) \quad \Delta E = \frac{(\gamma - 1)}{\gamma \bar{p}} \int_V dV \int_t^{t+\tau} p'(\bar{x}, t) \dot{Q}'(\bar{x}, t) dt .$$

Here, $p'(\bar{x}, t)$ is the varying portion of the pressure field and $\dot{Q}'(\bar{x}, t)$ is the varying portion of the heat release. The energy added to the system over one cycle is then given by ΔE . In some cases, ΔE or its product with certain constants is called the Rayleigh index. It can be seen that if $p'(\bar{x}, t)$ and $\dot{Q}'(\bar{x}, t)$ are appropriately in phase then energy is fed into the system and the Rayleigh index is positive. This result implies that the feedback loop illustrated in Figure 1-2 produces self-induced driving of the system. If the energy put into the system exceeds the losses, instability will occur. However, if the phase of $p'(\bar{x}, t)$ and $\dot{Q}'(\bar{x}, t)$ are such that ΔE is negative, then oscillations result in energy being removed from the system. In this case the system is self-damping.

The Rayleigh index will be revisited in chapters 3 and 4 where it is used in conjunction with the collected experimental data to explore the stability behavior of the tested flat-flame burner.

1.3 Previous Work

Notable progress has been made in understanding the fundamental contributors to the combustion dynamic response. A large portion of the work has focused on the effects of unmixedness as driven by the acoustic field. Shih et al. (1996) performed experiments to evaluate the contribution of unmixedness to unstable combustion. Indeed, it was found that fluctuations in fuel distribution resulting in localized variations in equivalence ratio were a strong driver for combustion instability. Later, simulations performed by Lieuwen et al. (1998) also showed a strong coupling between combustor oscillations and resulting variations in mixture fractions. Around the same time, Anderson et al. (1998) and Torger et al. (1998) performed experiments assessing the coupling between an applied acoustic field and fuel injectors under cold-flow conditions.

Work by Cohen et al. (2001, 2003) then investigated modulating the fuel flow in a combustor to actively control the unmixedness. It was shown that substantial control authority was achievable using this method and that the coupling mechanism between the fluctuating heat release and the modulated fuel was strongly related to the mixing process. Similar (although not so dramatic) results had been observed years earlier by Zsak (1993) and Kendrick (1995) in an experimental dump combustor. Further work by Hardalupas et al. (2002) and Demare et al. (2004) focused on acoustic actuation of reactant inlet streams in order to enhance mixing and combustion. The method was also used to approach issues related to flame attachment and combustor flame-out. Other work in acoustically enhanced combustion had been performed by Cadou et al. (1991) and Cadou (1996) on a double-ledge dump combustor. Cadou also found enhanced combustion in some regimes when the system was driven near resonance.

Somewhat related work was performed by Richards et. al. (1998, 2005). This research focused on passive techniques for control of combustion instabilities. Among other things, Richards investigated transport delays in premixed or jet-mixed systems. The result was the development of the τ - f product method for relating frequencies with positive Rayleigh index to the convection transport time delay from the fuel injector to the flame stabilization point. This has proved to be remarkably powerful in real industrial applications and has been used successfully by various large gas turbine engine manufacturers.

Overall, however, most work has focused directly on combustion dynamics. Many techniques have certainly been employed. From the standpoint of system identification, one novel method in particular is worth highlighting. Work by Seywert and Culick (1999), and Seywert (2001) involved the passive identification of the net combustion response in a system by the measurement of noise intrinsic to the combustor operation. The technique is based on Burg's method (also known as the maximum entropy method) and can provide a level of system identification in situations where only pressure data are available.

Nonetheless, a great deal of experimental work has focused on direct examination of the combustion dynamics of various systems by observing, in some fashion, the relation between the unsteady heat release and the fluctuating portion of the pressure or velocity field. Most of these methods fall into two distinct categories: those using chemiluminescence to infer the heat release rate and those using laser induced fluorescence (LIF). These, in turn, can be divided, into two sub-categories: Those experiments in which the combustion system was naturally unstable and those in which the system was acoustically forced. Table 1-1 shows the resulting matrix of this work. Frequencies at which observations were made, whether naturally occurring or forced, are shown.

Much of the early chemiluminescence work used photomultiplier tubes (PMT) to observe the luminescence signal. In experiments by Sterling (1991), Chen et al. (1993) and Kappei et al. (2000), a slit was incorporated to provide some level of spatial resolution. Typically, the slit was

	Chemiluminescence	PLIF
Naturally Unsteady	<ul style="list-style-type: none"> • Poinsot et al. (1987) (440-590 Hz) • Sterling and Zukoski (1991) (188 Hz) • Kendrick (1995) (188 Hz) • Broda et al. (1998) (1750 Hz) • Kendrick et al. (1999) (235 Hz, 355 Hz) • Venkataraman et al. (1999) (490 Hz) • Kappei et al. (2000) (370-460 Hz) • Lee et al. (2000) (1750 Hz) 	<ul style="list-style-type: none"> • Cadou et al. (1991) (43 Hz) • Shih et al. (1996) (400 Hz) • Cadou et al. (1998) (328 Hz) • Kopp-Vaughan et al. (2009) (158 Hz) • Boxx et al. (2010) (308 Hz) • Steinberg et al. (2010) (308 Hz) • Caux-Brisebois et al. (2014) (289-418 Hz)
Acoustic Forcing	<ul style="list-style-type: none"> • Chen et al. (1993) (300 Hz, 400 Hz) • Durox et al. (2002) (Up to 400 Hz) • Pun et al. (2002) (< 60 Hz) • Kulsheimer et al. (2002) (< 350 Hz) • Schuller et al. (2003) (Up to 400 Hz) • Kim et al. (2010) (100-400 Hz) • Shin et al. (2011) (250 Hz) 	<ul style="list-style-type: none"> • Cadou et al. (1998) (360 Hz, 420 Hz) • Pun et al. (2000, 2001, 2003) (22-55 Hz) • Santhanam et al. (2002) (200 Hz) • Balachandran et al. (2005) (40-310 Hz) • Kang (2006) (22-400 Hz) • Bellows et al. (2007) (130 Hz, 410 Hz) • Thumuluru et al. (2009) (130 Hz, 270 Hz) • Kim et al. (2009) (514 Hz) • Yilmaz et al. (2010) (85 Hz, 125 Hz, 222 Hz) • Coats et al. (2010) (200-1200 Hz)

Table 1-1: Previous work in oscillating flames related to investigation of combustion dynamics.

oriented to provide resolution in the streamwise direction. Experiments by others, however, used 2-D imaging systems (historically CCD based) to obtain spatially-resolved luminescence signals. This includes work by Kendrick (1995), Broda et al. (1998), Kendrick et al. (1999), Venkataraman et al. (1999), Pun (2001, 2002), Schuller (2003) and Kang (2006), among others. In recent years, high speed CMOS imagers with and without coupled intensifiers have grown in availability and popularity. In many cases, this allows direct observation of the unsteady behavior without resorting to phase-locking.

The work using chemiluminescence listed in Table 1-1 spans a range of combustor types. Experiments by Sterling et al. (1991) and Kendrick (1995) involved a single-ledge dump combustor that exhibited a natural instability at 188 Hz. Experimental research by Chen et al. (1993) incorporated premixed flames and utilized the same equipment used by Sankar et al. (1990). These experiments were specifically designed to simulate combustion of solid rocket propellants and utilized only two forcing frequencies. Work by Durox et al. (2002) and Schuller et al. (2003) involved acoustic forcing of a flame at frequencies up to 400 Hz. However, the flame was operated in an open field (versus a drive chamber) and the CH^* luminescence response data collected contained only magnitude information. Research by Pun et. al. (2002) examined a single element, jet-mixed burner operating on landfill surrogate gas. The burner was forced at frequencies from 22 to 55 Hz and phase resolved chemiluminescence image data were collected. Kim et al. (2010) applied inlet forcing to a premixed gas turbine combustor at frequencies from 100 Hz to 400 Hz. Both bulk and image CH^* chemiluminescence data were collected and flame transfer functions were computed.

In contrast to CH^* chemiluminescence, others have chosen to use OH^* chemiluminescence as a measure of heat release rate. Lee et al. (2000) examined a naturally unstable, premixed combustor with inlet swirl. OH PLIF was used for flame visualization; however, OH^* luminescence was used as the unsteady heat release metric. Steinberg et al. (2010) imaged OH^* chemiluminescence in an unstable, dual-swirl combustor oscillating at 308 Hz. Kulsheimer et al. (2002) performed experiments on a premixed, swirl-stabilized burner. The reactant mixture was modulated at frequencies up to 350 Hz and with amplitudes up to 70% of the mean flow. Imaging of OH^* luminescence was used as a measure of the dynamic response.

One fundamental disadvantage with the chemiluminescence measurement technique is the lack of depth of field resolution. Generally speaking, measured fluorescence is integrated over the depth of the flame. This difficulty is essentially eliminated by the use of planar laser induced

fluorescence (PLIF). Here, fluorescence is restricted to the plane of the laser sheet, which is coincident with the object plane of the imaging lens. Additionally, this spectroscopic method allows selected chemical species to be stimulated into fluorescence by optical pumping at specific wavelengths, typically in the ultraviolet. The first documented demonstration of PLIF of OH radicals in a flame was performed by Dyer and Crosley in 1982. Since then, the technique has been improved and refined with technical advances in lasers, optical coatings and intensified imaging systems being major contributors.

PLIF measurements have been used as a locator of the reaction zone and as a metric for heat release in numerous combustion experiments. Bergthorson (2005) used CH PLIF in experiments on a stagnation burner under steady conditions to measure the reaction zone location, thickness and CH concentration profile. CH PLIF was used by Coats et al. (2010) to estimate flame front area as a measure of heat release rate in an acoustically-forced, lean premixed, multi-port laminar burner. Cadou et al. (1991), Shih et al. (1996), Pun et al. (2000, 2001 and 2003), Ratner et al. (2002), Kang (2006) and Yilmaz et al. (2010) used OH PLIF as a direct measure of heat release in unsteady (naturally unstable and forced) experiments. OH PLIF was also used in naturally unstable combustion experiments by Kopp-Vaughan et al. (2009), Boxx et al. (2010), Steinberg et al. (2010) and Caux-Brisebois et al. (2014), as well as inlet-driven, unsteady experiments by Santhanam et al. (2002), Bellows et al. (2007), Thumuluru et al. (2009) and Kim et al. (2009); in these cases, PLIF data were used for flame visualization and/or flame surface area estimation. Heat release rates (where determined) were either measured by collection of CH^* or OH^* chemiluminescence or estimated from the computed flame sheet area. PLIF signal intensity itself was not used as a heat release rate metric.

Paul et al. (1998) demonstrated the use of OH PLIF in combination with CH_2O PLIF to produce an improved measure of the heat release rate. This combination was later used by Balachandran et al. (2005) to evaluate unsteady heat release in an inlet-driven, turbulent, premixed

burner. Additionally, Cadou et al. (1998) used nitric oxide seeding and NO PLIF to measure the temperature field within a double-ledge dump combustor. Ratner et al. (2003) used NO PLIF in experiments on an acoustically forced combustor to measure the unsteady production of nitric oxide.

Much of the experimental work performed on unsteady combustion in gas phase systems has revolved around specific combustors and usually ones that are naturally unstable. This may, in part, be the result of desperation. It is not surprising that attention (and consequently, money) is focused on commercial combustors that exhibit an instability problem and are pacing a delivery schedule. (Managers can be quite sensitive to this.) Such work (generally speaking) concentrates either on a specific problem inherent to a particular combustor, or on the generalized, large-scale behavior of the examined systems in order to generate some global insight into their dynamics.

Regardless, these experiments have helped to improve general understanding of the combustion instability phenomena, and have also served to validate experimental techniques such as those used by numerous researchers including Pun et al, Ratner et al. and Kang. Nonetheless, little experimental work has focused specifically on fundamentally simple burners and examining the combustion dynamics therein. Most of the burners or combustors involved in previous research have been complex in nature, involving various levels of unmixedness (in premixed systems) and any combination of turbulent flows, recirculation, swirl, and so on. With such systems and with incomplete information about the fields involved (pressure, temperature, velocity, reactant concentrations, etc.) it is difficult to arrive at definite conclusions about some fundamental mechanisms.

Great strides have been made in recent years in the development of high speed imaging systems (intensified CMOS units in particular) and pulse-burst Nd:YAG lasers (Jiang et al. 2010; Den Hartog et al. 2010). These systems allow short cinematographic sequences to be captured in various laser-based imaging techniques. This allows detailed investigation of flame evolution in

systems that do not exhibit strict periodic behavior. Nonetheless, to this point the investigative power of these systems has yet to be fully leveraged.

Finally, one would be remiss in not mentioning work in this research area accomplished through numerical means. A great deal of simulation work has focused on response characterization of complex, gas-turbine derived combustors. Examples include work by Roux et al. (2005), Selle et al. (2006), and Huber and Polifke (2009). The combustion systems simulated in these cases were turbulent and employed some level of inlet swirl. Roux and Selle used large eddy simulation (LES) in their numerical methods while Huber and Polifke used a commercial CFD package to execute unsteady Reynolds-averaged, Navier-Stokes (URANS) simulations.

Nonetheless, other numerical work has focused on acoustically driven behavior in simpler systems. Single-element, turbulent, bluff-body stabilized burners have been explored by Armitage et al. (2006), Han and Morgens (2015), and Han, Yang and Mao (2016). Various numerical codes were used, employing both URANS and LES. In all unsteady cases, inlet velocity forcing was applied.

Finally, there are numerical simulations of acoustically forced laminar flames. These have the greatest relevance to the work at hand. Most of this work involves the study of one of two types of flames: the inverted ‘V’ flame with a central rod, and the Bunsen style flame. Inverted ‘V’ flames have been studied by Kaufmann, Nicoud and Poinsot (2002), and Birbaud et. al. (2008). Acoustically driven Bunsen style flames have been simulated by Truffin and Poinsot (2005), Duchaine (2012), and Silva et al. (2015). Both styles of flames were simulated by Schuller, Durox and Candel (2003), where the results were then compared against previously analytically generated transfer functions. The simulation codes employed were typically compressible DNS Navier-Stokes solvers, with the most notable one being AVBP developed jointly by CERFACS and IFP.

1.4 Objectives

Despite the aforementioned efforts, notably less experimental attention has been given to directly examining the dynamics and coupling mechanisms at a fundamental level in simple, laminar, premixed flames. At the outset of this work (many years ago), some researchers claimed that little coupling would be observed in such burners. Others proposed that the combustion response would be “flat” and uninteresting. The presented work (along with work by others in the interim) challenges these notions. Past investigation has likely been limited by the fact that great care must be taken in the experiments to obtain reasonable signal-to-noise ratios, and to ensure that the results are not contaminated by other spurious sources.

As such, it is the focus of this work to examine the thermo-acoustic coupling in a simple premixed methane/air flame under acoustically forced conditions. This is accomplished by examination of a stagnation-plane-stabilized flat-flame burner inside of a chamber that applies an acoustic field. By careful characterization of the acoustic behavior of the chamber, it is possible to decouple the combustion response components from the acoustic characteristics of the experimental apparatus.

The goal of the work at hand is not simply to gain insight into the fundamental mechanisms through experimental investigation, but also to generate a database of information that can be used to create and/or validate models as well as verify results from numerical simulations. By transitioning the experimental focus to a simple, approachable and well-understood burner much of the uncertainty surrounding the experimental conditions can be eliminated. It is this ancillary information (intrinsic parameters, initial and boundary conditions, etc.) in conjunction with the collected experimental data that are essential for correctly discerning the fundamental mechanisms involved in the combustion dynamics, as well as providing a complete and accurate dataset necessary for constructing models or validating numerical simulations.

The research work presented in this thesis is divided into three major sections. Chapter 2 describes the experimental equipment used and the manner in which it was configured. This chapter is merely an overview, providing only enough detail to enable the reader to understand its uses in the experiments described in the following chapters. Much of the equipment used was custom designed and built specifically for this research and the full body of information on its construction is daunting. If it so interests the reader, greater detail on the design, fabrication and calibration of this hardware can be found in appendices B through F.

The next section constitutes the experimental work which is covered in chapters 3 and 4. Chapter 3 presents the initial work on the flat-flame burner, characterizing its global combustion response function using a PMT. Data collection runs were made over much of the operating range of the burner. The motivation for this was two-fold; first it was to gain a sense of the burner's general response over a wide range of operating conditions. Secondly, it was to find regions of interest within this operational envelope that would be the focus of later PLIF experiments.

Chapter 4 follows with the aforementioned PLIF experiments, along with supplementary 2-D image chemiluminescence measurements. The data collected from the spatially resolved chemiluminescence and planar laser-induced fluorescence experiments are used as trial measures of the heat release within the flame. Fluoresced species in the PLIF work include OH, CH and CH₂O. Additionally, PLIF of acetone seeded into the burner reactant supply is used to visualize the flow of premixed fuel and air as it leaves the burner nozzle and enters the reaction zone. A selected burner operating point is investigated using these methods under steady conditions and at several acoustic drive frequencies. The spatially and phase-resolved data are reduced and results are shown.

The third major section is contained in chapter 5. This covers modeling of the response observed in the selected reference case. As a start, a simple model is generated by fitting a transfer function to the collected combustion response data. After this, two consecutive revisions are made

to this model based on observations from both the bulk chemiluminescence measurements and the PLIF imaging. These observations, and the guidance they provide to updating the model, generate important insight into the mechanisms involved in producing the net combustion response of the burner.

Chapter 6 concludes the thesis by providing a summary of the work done and the results obtained. It also provides a critique of the presented material and suggestions for future investigations into the phenomena.

C h a p t e r 2

EXPERIMENTAL EQUIPMENT

2.1 Overview

As stated earlier, the objective of the work at hand is to improve the fundamental understanding of the coupling between a fluctuating pressure field and the heat release in a relatively simple premixed flame. Indeed, the principal focus is to investigate the coupling between an applied fluctuating pressure and the resulting varying heat release as produced by various mechanisms. Attempts have been made to minimize any feed system coupling; nonetheless, contributions from the Helmholtz resonance of the burner are necessarily intrinsic, and are considered.

In order to take the desired measurements, an experimental apparatus was designed and constructed from scratch. Many system components were either highly customized or completely novel in their design. A schematic overview of the apparatus is shown in Figure 2.1. Overall, the setup consists of five major components:

- a) The acoustic forcing chamber and drive cross,
- b) The experimental flat-flame burner and fuel feed system,
- c) The laser light source for the PLIF experiments,
- d) The light collection and detection system,
- e) The data acquisition system.

General descriptions of these components along with their interconnections and uses are given in the following sections. Details of their designs, features and capabilities are presented in the appendices.

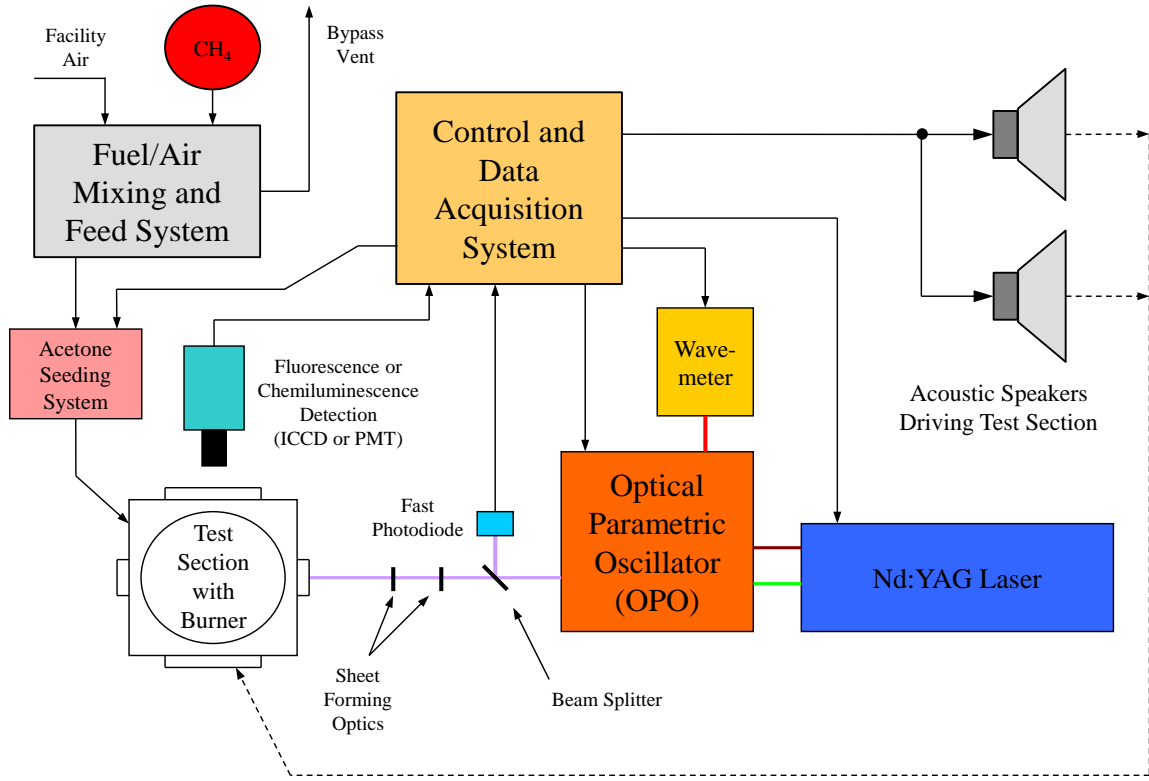


Figure 2-1: General schematic of the experimental apparatus. During chemiluminescence experiments the laser system is not used.

2.2 Acoustic Forcing Chamber

The focal point of the setup is the acoustic forcing chamber. The chamber is similar to that used by Pun et al, Ratner et al, and Kang in previous work and is shown in the picture and sketch presented in Figure 2-2. It consists of four major subcomponents: the base, the test section, the extension tubes, and the drive cross. All sections interlock using a common set of circular tongue-and-groove registers. With the exception of the test section, all components are circular in cross-section and have a standard internal diameter of 31.8 cm. The test section is regular-octagonal in cross section and has an internal minor diameter equal to that of the other components.

The test section is fitted with registers on each of the four radially facing sides to allow for installation of 6.35 mm thick fused silica windows. This allows optical access for both the laser sheet in PLIF experiments as well as for viewing the fluorescence or chemiluminescence signal

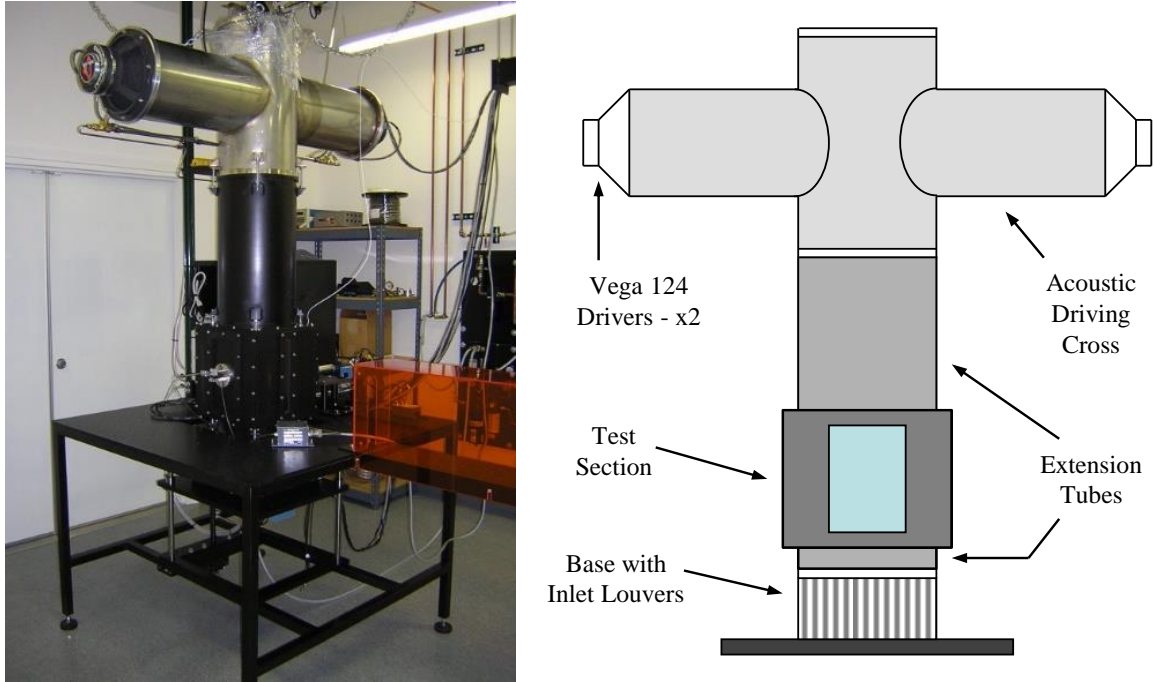


Figure 2-2: Acoustic forcing chamber. The chamber allows the imposition of a standing acoustic wave on the burner element. This allows the element to be exposed to an externally generated fluctuating pressure field.

with an ICCD or PMT. The windows are retained using screw mounted flanges with gaskets. Black anodized aluminum blanks can be substituted for the windows in the event that individual ports are not needed. This reduces the possibility of contamination from stray light. The test section is also fitted with pressure transducers for measuring the varying part of the pressure during an experiment. The location of these transducers will be discussed in Section 2.3.

The base module sits below the test section and is mated to it using a short, 8.9 cm extension tube. The base provides the interface that ties the acoustic forcing chamber to the experiment support table. A removable bottom plug in the base unit provides feed-thrus for the instrumentation lines as well as for the plumbing related to the burner fuel/air feed and the closed-loop cooling water connections. Additionally, adjustable louvers are provided in the base section to support burners that require naturally convected air.

A 61 cm inch extension tube connects to the top of the test section and extends upward to the acoustic drive cross. The acoustic drive cross is used to couple two 12 inch Cerwin-Vega drivers to the chamber. The drivers are Vega 124 series subwoofers and are capable of 400 watts RMS continuous, and 800 watts RMS peak, per device. Film cooling rings are installed between each driver and its mating flange on the cross. These rings inject air in front of the speaker cones to prevent them from being damaged due to the heat convected from the test burner. These are only required when running larger burners and were not used in the present work. The entire assembly is held together using short stud sections of 3/8"-16 threaded rods in conjunction with appropriate nuts and washers. These tie between interconnection brackets located on each section. This can be seen in the photograph in Figure 2-2.

When operated, the drivers establish a standing wave within the chamber. Under typical conditions, the chamber acts as an open-closed system, with the closed condition being satisfied by a base-plate in the test section just below the burner. The frequency of operation is primarily limited by the height from the plate to the point of stabilization of the flame. This distance must be much shorter than the wavelength of interest to ensure that the flame is located away from the first acoustic node. Given that this condition is satisfied, the chamber is capable of operation from 20 to 2000 Hertz, both these limits being set by the drivers. At the low end, the drivers have insufficient throw to couple acoustic energy into the chamber at a usable level. The high end is limited by the frequency response of the drivers themselves.

2.3 Stagnation-Plane Flat-Flame Burner

The burner used in the present work is a stagnation-plane-stabilized flat-flame burner. Here, a laminar jet of premixed fuel/air with a top-hat velocity profile is directed normal to a planar surface. The flame stabilizes between the nozzle exit and the stagnation plane. Depending on the

operating conditions, the flame either attaches itself to the nozzle exit as a Bunsen flame, or establishes itself as a flat flame in free space.

This burner configuration has been used by Vagelopoulos and Egolfopoulos (1998) as well as Bergthorson and Dimotakis (2005) in experiments to determine laminar flame speed. By operating near the transition point between the attached and detached conditions, the flame strain rate is near zero, and laminar flame speeds can be measured.

The burner for the present work was chosen to be similar to that used by Vagelopoulos et al. (1998). The nozzle exit diameter is 14 mm and the height of the stagnation body above the nozzle is 21 mm or 1.5 D. Figure 2-3 shows schematic of the burner assembly as well as a picture of the unit removed from the test section (but still attached to the base plug.) Figure 2-4 shows a sectional view of the nozzle assembly.

The nozzle is constructed from four components forming three distinct chambers. These chambers are separated by two sintered bronze disks, each with a thickness of 2.3 mm and with an average pore size of 30 μm . These disks act both as linear restrictors as well as flow distributors. Premixed methane and air enter the bottom chamber through an integral, precision needle valve and then through a diffuser plug which redirects the flow radially. The differential pressure across the needle valve is kept sufficiently high to maintain choked conditions, thus ensuring there is no feed system coupling in the measured response.

The flow then passes through the first sintered disk and into the middle chamber. The restriction in this disk encourages the flow to distribute itself across it evenly. The flow emerges from the first disk and then passes into the second sintered restrictor. Again the presented pressure drop helps to further balance the flow so that the resulting velocity profile on the upper side of the second disk is uniform. A pressure tap present in the second chamber allows the differential pressure between it and test section (atmosphere) to be measured using a Datametrics Barocel. Due to the small size of the pores in the sintered disk the resulting Reynolds number is very low (10 or

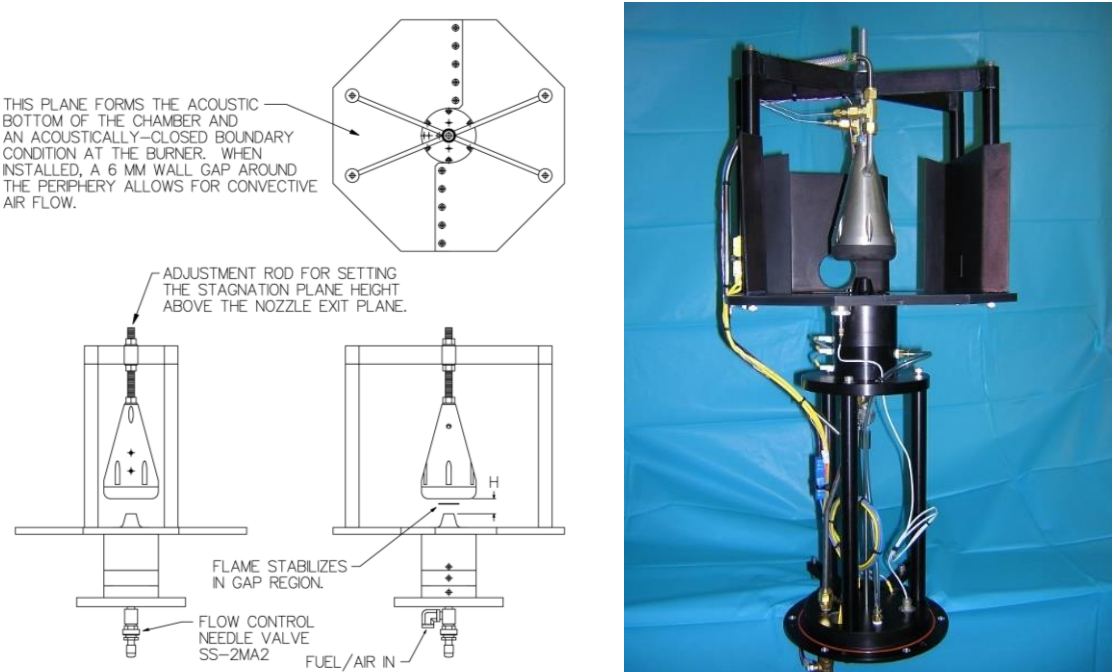


Figure 2-3: Flat-flame burner assembly. (Left) Simplified three-view showing the nozzle, stagnation body and stagnation body support structure. (Right) Photo of burner assembly along with chamber base-plug and interconnecting support rods. Stagnation body height, H , is shown as 21 mm. This corresponds to an $H/D = 1.5$, which is the value used for all experiments.

SECTION A-A

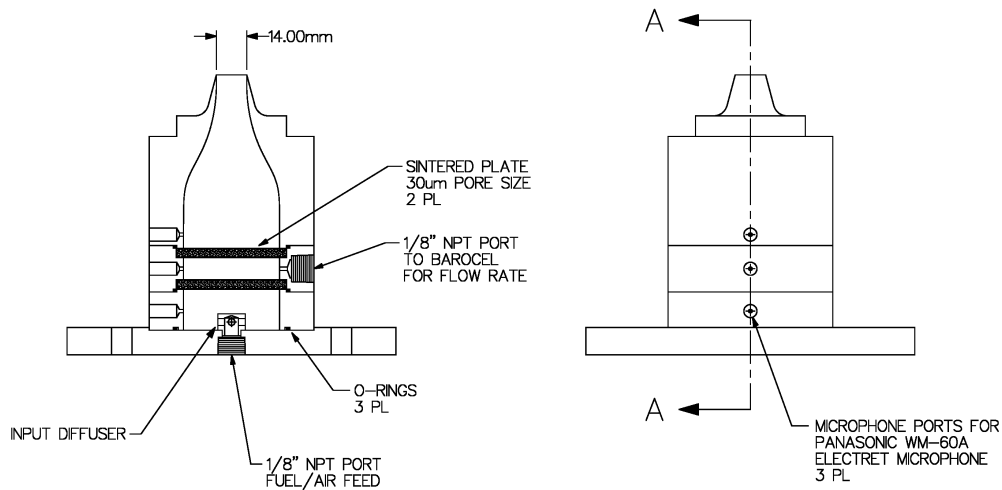


Figure 2-4: Flat-flame burner nozzle. Outline view is shown on right while sectional view is shown on left.

less). Consequently, the restriction acts very similar to a laminar flow element. The measured value is used to compute fuel/air flow rate and the corresponding nozzle exit velocity based on the current conditions (equivalence ratio and temperature) and calibration data.

The flow then enters the upper section of the nozzle assembly which contains the aerodynamic contraction. This contraction was designed using the method outlined by Chmielewski (1974) in order to produce an exit velocity that is near top-hat in profile. A contraction area ratio of 10 was chosen along with an L/D of 1.75 resulting in a nozzle with a cavity L_c/D_c on the order of unity.

Each of the three cavity sections in the nozzle assembly contains small ports for 6 mm diameter, integral, cartridge microphones (Panasonic WM-60A). These microphones are used to measure the amplitude and mode shape of the pressure field coupled into the nozzle from the acoustic forcing. Indeed, this data is an essential part of understanding the different contributions resulting in the p' to q' coupling.

Once the flow leaves the nozzle it impinges against the planar stagnation body. This body is fabricated in two parts from 304 CRES and is water cooled. The lower portion of the body is black-oxide conversion coated to minimize light scattering during PLIF experiments. Type K thermocouples measure the inlet and exit water temperatures and an internal RdF heat flux patch measures (approximately) the heat flux through the face. The burner heat flux was estimated over its predicted operating range and the thickness of the body material between the stagnation face and the cooling water cavity was chosen to guarantee that the surface temperature would always remain above 100 °C. This, in turn, ensured that condensation would not collect on the face during operation.

The diameter of the planar section of the stagnation body is 5.7 cm, corresponding to just over four times the nozzle exit diameter. For all presented experiments, the distance from the nozzle exit to the stagnation plane is 21 mm which is equal to 1.5 nozzle exit diameters.

The combustible mixture is fed to the burner from the fuel mixing and feed panel. The panel mixes filtered and dried facility air with UHP (ultra-high purity) bottled methane and delivers it to the burner. The methane flow is controlled in an open-loop fashion by a manual flow controller. Its flow rate is measured using a thermal mass flow meter. This measurement, in turn, is used to closed-loop control the flow rate of the air using a thermal mass flow controller. The closed-loop controller operates to target a specific equivalence ratio. The two component streams are passed through a pair of mixers before moving on to the distribution manifold and ultimately to a ported relief valve. This valve regulates the operating pressure of the manifold to 206.7 kPaG, dumping any excess fuel/air mixture overboard to an outside vent. Premixed fuel/air is then tapped from this manifold and directed to the burner. The flow rate to the burner is independently controlled by the needle valve incorporated in its base.

By using the bypass regulation scheme as described (versus direct flow control), the control of the fuel/air equivalence ratio and the flow rate to the burner are effectively decoupled. This allows for far more accurate control of each of these parameters, as well as much improved long term operational stability. Details of the design and construction of both the burner and the fuel feed system are presented in appendix B.

2.4 Laser Source

The laser source used for planar laser induced fluorescence (PLIF) experiments is a custom Nd:YAG pumped optical parametric oscillator (OPO). Initially, the YAG laser was a rebuilt and modified Quantel YG-581. However, the base performance of the Quantel laser was poor and, over time, sections of the laser were reengineered and replaced. By the time meaningful experiments were being performed the entire optical bed of the laser had been reconfigured. The new laser design incorporated an EO Q-switched unstable resonator with two stages of amplification. An intracavity etalon was used to improve line width. Ultimately, the Nd:YAG laser

output was increased to a total of 2 Joules per pulse at 1064 nm (10 Hz) and in excess of 1 Joule per pulse at 532 nm. Details of this upgrade can be found in appendix E.

An OPO for UV light generation was custom built and is of a totally unique design. The device incorporates a ring-cavity oscillator with intracavity harmonic generation. It is capable of producing output wavelengths for LIF of a variety of species. These include 226 nm for NO, 277-282 nm for acetone and OH, 352 nm for CH₂O and 390 nm for CH. Output pulse energies vary depending on configuration and wavelength, but in general range from a couple of millijoules up to 20 millijoules per pulse at 390 nm. Long-term tuning stability is typically better than ± 20 pm for the centerline wavelength at the cavity fundamental. The linewidth at the cavity fundamental is on the order of 3 cm⁻¹. Details of the OPO development and resulting performance can be found in appendix E.

2.5 Light-Gathering Equipment

Light detection in the experiments was accomplished using two different sensors. For the non-imaging chemiluminescence experiments, an eight element Electron Tubes Ltd. photomultiplier tube (model 9125B) was used exclusively. This tube was selected for its high gain and relatively constant sensitivity between 400 and 500 nm. It was used in conjunction with an ETL QL30FP1 enclosure and PS1800/5 power supply module. Custom adapters were machined to interface the PMT enclosure to a standard bayonet (F-mount) lens and also to allow insertion of standard 25.4 mm diameter optical filters between the lens and tube. For all the experiments presented, the PMT was coupled to a Nikon Nikkor 50 mm f/1.2 lens with a Semrock FF01-447/60-25 optical band-pass filter installed.

For imaging an Andor iStar DH712-18F-03 ICCD (Intensified CCD) camera (S/N ICCD-3056) was used. This device incorporates a 512x512 pixel E2V focal plane (24 μ m square pixels) as well as a DEP photo-intensifier for light amplification and gating. The intensifier uses a type II

photocathode which is sensitive from the deep UV up through the visible spectra. Figure 2-5 shows graphs of the photocathode sensitivity and quantum efficiency as a function of wavelength. The maximum read-out rate is 1 MSPS. With CCD timing signals included, this results in a maximum frame rate of 3.2 frames per second. Through pixel binning or the use of image sub-windows it is possible to achieve frame rates of 10 Hz, matching the laser firing rate. However, for the experiments presented, only sub-windows were employed and the resulting frame was 5 Hz.

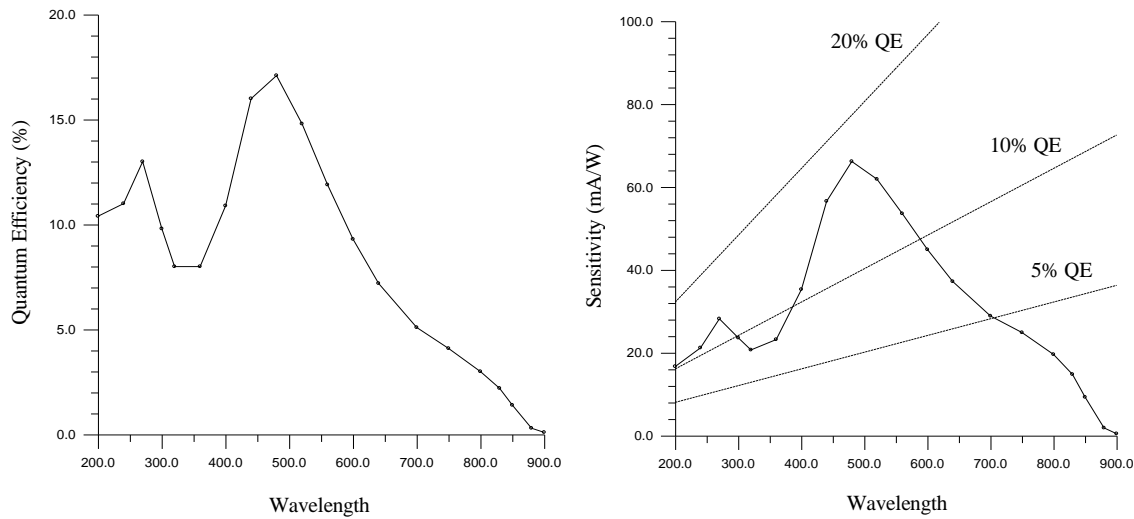


Figure 2-5: Intensifier photocathode performance on the Andor iStar ICCD camera. Sensitivity and quantum efficiency shown as a function of wavelength.

The camera includes adapters to accept either C-mount or F-mount lenses. In addition, mounts were machined to allow 25.4 mm diameter filters to be installed between the lens and the photocathode. For all experiments involving fluorescence at wavelengths shorter than 390 nm, the camera was mated to a Cerco 2085 UV lens fabricated by EADS-Sodern. This lens has a focal length of 94 mm and aperture number of f/4.1. For experiments involving CH and CH₂O PLIF where fluorescence is at wavelengths above 390 nm, the same Nikkor 50 mm lens was used as in the chemiluminescence experiments.

2.6 Data Acquisition System

The data acquisition system consists of several interconnected components. Figure 2-6 presents a general system diagram, showing the components and their interconnections. Select components are used depending on the type of experiment being performed and there are no cases where all components are used simultaneously.

The focal point of the data collection system is a PC that serves as the master controller. This computer runs a custom software package (OPO v125) that orchestrates the entire experiment. It communicates through RS-232 serial interfaces with the AFC-100, the EG&G dual-phase lock-in analyzer, the optical parametric oscillator, and the acetone seeding system. It also incorporates a Measurement Computing DAS-08 card which provides digital I/O for interfacing with the Andor ICCD controller, as well as analog inputs for recording slowly changing or DC signals. The software interface provides extensive control of the OPO including features for general tuning, wavelength scans, and crystal peaking. It also incorporates a comprehensive interface to the AFC-100. Built-in routines provide features such as automated combustion response scans using the AFC-100, PMT and lock-in analyzer. The software also features an internal scripting language that allows the operator to write scripts that run experiments fully autonomously. This was deemed advantageous since many of the experiments are long and arduous.

The workhorse of the data collection system is the AFC-100 (acoustic forcing controller). This is a custom instrument that was engineered and built entirely from scratch. It was designed to solve many of the issues uncovered with the experimental technique when it was initially developed by Pun and Palm in the late 1990s. A detailed description of its construction, capabilities and the problems that it solved is covered in appendix F. Photos of the instrument can be seen in Figure 2-7. Its primary functions include:

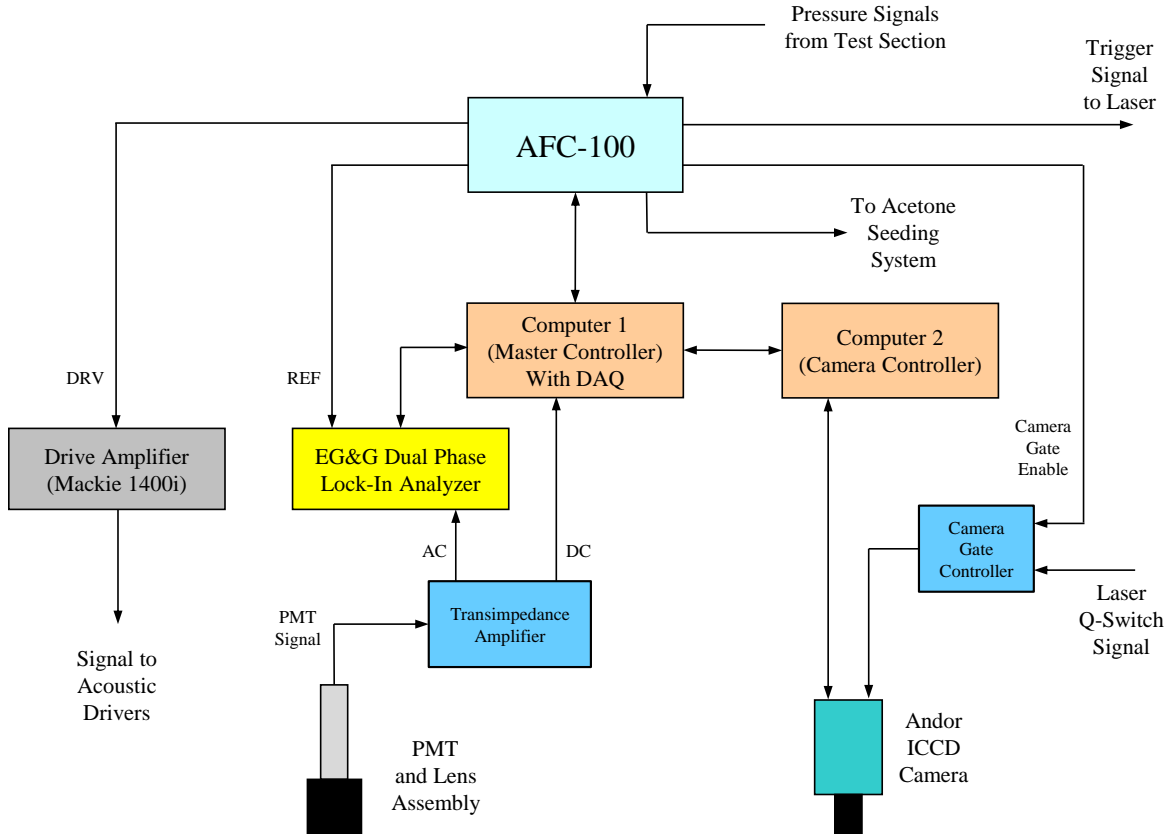


Figure 2-6: Data acquisition general system diagram. PMT and ICCD camera systems are used independently depending on the experiments being performed.

- Pressure Sensor Signal Multiplexing and Conditioning – The AFC-100 provides eight inputs for piezoelectric pressure transducers or electret microphones. Each input has an independent DC current source to power the transducer. The eight inputs are buffered and then fed to two signal multiplexers. The output of each multiplexer constitutes one of the signal channels that is selectively conditioned/amplified, analyzed and recorded.
- Acoustic Drive Control – The instrument closed-loop controls the frequency and amplitude of the standing wave in the chamber using feedback from strategically located pressure transducers in the test section. The feedback transducer must be multiplexed to channel 1.
- Laser Timing Control (Phase Targeter) – A laser trigger signal is generated by the unit to initiate each laser shot. In targeting mode, the laser shot timing is jittered in order to collect

PLIF images at specific acoustic phase angles while still maintaining an average laser firing rate of 10 Hz.

- d) ICCD Enable Control (Camera Gate Enable) – The CGE signal is generated by the laser timing system and the “skip” register. Setting the skip register to a value other than zero inhibits the camera gate signal and data collection every N shots where N is the skip register value. This grants the ICCD the required read-out time when that time exceeds the time between laser shots.
- e) Waveform Collection – During data collection, the instrument samples and records sections of waveforms from each of the two channels. These sections or windows encompass the instant of the image collecting laser shot. Along with this, a “bit pointer” is recorded indicating the sample at which the laser shot occurred. The recoded waveform data provides 14 bit resolution and the laser shot information provides better than one degree phase accuracy.



Figure 2-7: The AFC-100 acoustic forcing controller. The instrument was custom engineered and built to solve many of the difficulties previously discovered in the experimental technique. Details of its design and resulting features can be found in appendix F.

Lastly, an EG&G model 5206 dual-phase lock-in analyzer is used to process the signal from the photomultiplier tube during the bulk chemiluminescence experiments. Because of the periodic nature of the signal being measured, the lock-in analyzer provides exceptional sensitivity and a dynamic range that spans six decades. With the dual lock-in feature, the unit provides both amplitude and phase information on the measured signal.

The photomultiplier is coupled to the lock-in analyzer through a transimpedance amplifier. This device serves two functions. First, it performs the conversion from the current signal provided by the PMT to the voltage signal required by the lock-in analyzer. The second function is to split the AC and DC components of the signal and provide them on separate output connectors. By design, the crossover frequency from AC to DC is chosen to be at 0.5 Hz. Although the impedance looking into the amplifier input is 50 ohms, the actual transimpedance between the input and the outputs is $100\text{ k}\Omega$ for the AC channel and $20\text{ k}\Omega$ for the DC channel. The signal from the AC channel is directed to the lock-in analyzer while the signal from the DC channel is fed to one of the inputs on the DAS-08 for logging of the average chemiluminescence signal.

C h a p t e r 3

EXPERIMENTAL WORK USING CHEMILUMINESCENCE

3.1 Overview and Motivation

The ultimate goal of the work at hand is to explore the dynamic behavior of the presented flat-flame burner under an oscillating pressure field in order to gain a better understanding of the fundamental mechanisms involved in the p' to q' coupling. Although the desire is to explore these dynamics using PLIF (planar laser induced fluorescence), practicality restricts these experiments to a limited number of test cases. Indeed, the parameter space generated by the operational envelope of the burner (as experimentally determined and presented in appendix B) is quite large. Individual PLIF experiments to characterize behavior at one burner operating point and one acoustic drive frequency take nearly three hours. Consequently, the hope of exploring the entire parameter space in this manner vanishes and it becomes necessary to find a method to narrow the region of focus.

As a solution, the first collection of experiments used simpler and much faster bulk chemiluminescence measurements. A photomultiplier tube and lens assembly was used to gather the bulk luminescence signal from the flame during acoustic forcing. Processing of the PMT signal was performed with a highly selective dual-phase lock-in analyzer. The experiments were fully automated, producing response functions (magnitude and phase) for frequencies from 20 Hz to nearly 2000 Hz. Experiments were performed for 62 different burner operating conditions, spanning equivalence ratio and burner nozzle exit velocity. The result was a map depicting the combustion response landscape, which not only provided insight needed for narrowing the scope of the PLIF experiments, but is also quite informational and intriguing on its own.

3.2 Experimental Setup

Figure 3-1 shows a block diagram for the chemiluminescence experiments. In these experiments, the laser is not used and light is collected passively from the flame using a photomultiplier tube and lens assembly. In other regards, the configuration is similar to those used by the phase-resolved PLIF experiments.

The master control computer runs the experiment, sending commands to, and requesting data from both the AFC-100 and the lock-in analyzer. The AFC-100 generates the acoustic drive

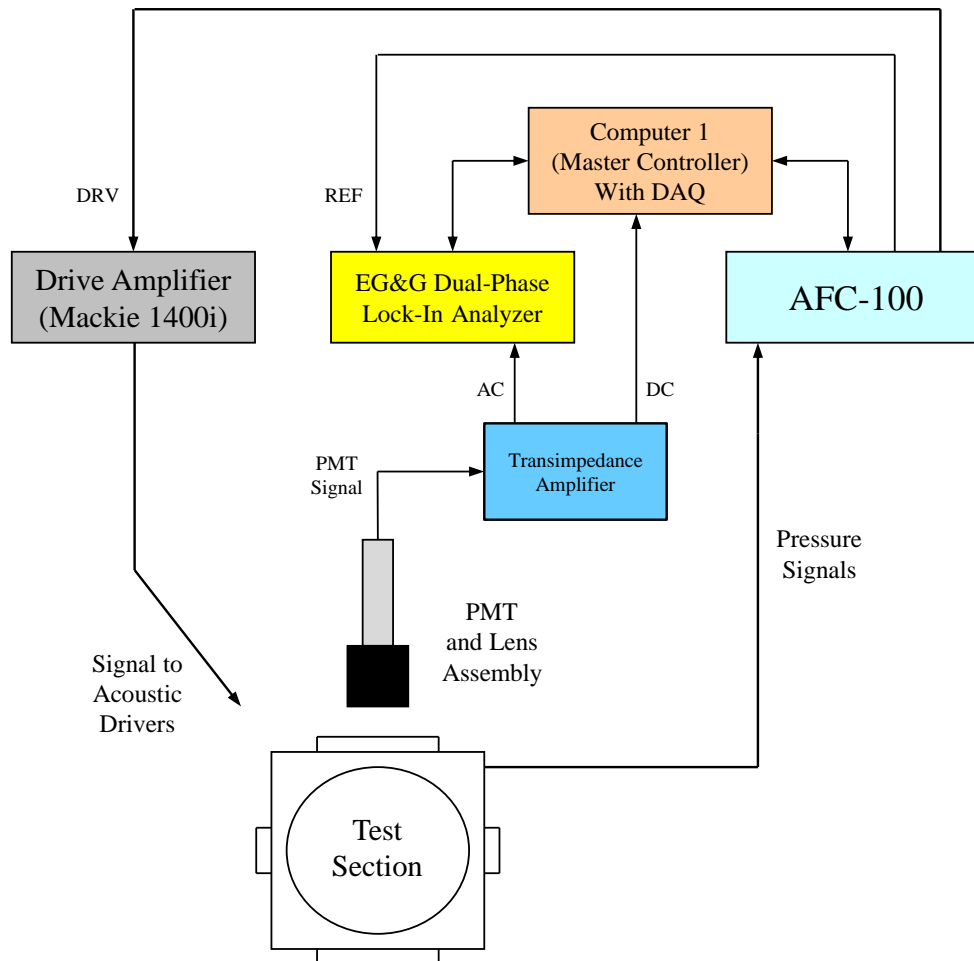


Figure 3-1: General schematic of the experimental apparatus for performing phase-resolved chemiluminescence experiments. The laser system is not used.

signal that is amplified by the Mackie 1400i power amplifier and then fed to the acoustic drivers on the test chamber. The varying pressure in the test section is measured by two PCB 106B50 piezoelectric pressure transducers and relayed back to the AFC-100. The signal from one of the transducers is band-pass notch-filtered around the drive frequency and used to closed-loop control the amplitude of the acoustic forcing. Additionally, the AFC-100 performs on-line fast-Fourier transforms on both input signals and relays the results to the control computer for storage. The FFT data along with the chamber calibration data (covered in appendix D) is used to determine the phase of the acoustic drive in relation to the reference signal provided to the lock-in analyzer by the AFC-100.

Light from the chemiluminescence of the flame is collected with the PMT and lens combination. No slit or aperture is used, and light is gathered from the entire flame. A Semrock FF01-447/60-25 optical bandpass filter (417-477nm), installed between the lens and PMT, is used to pass only the CH^* and CO_2^* chemiluminescence signals of interest. The current signal from the PMT is passed to a transimpedance amplifier where it is split into its AC and DC components. The DC component is measured directly by a DAS-08 data acquisition board and recorded for later use as a measure of the average heat release. The AC signal is directed to the EG&G 5206 dual-phase lock-in analyzer to measure its amplitude and phase in relation to the reference drive signal. The master controller collects this data and records it for later post processing.

The master control computer marches the drive frequency from a specified start frequency to a specified stop frequency. The number of steps is also prescribed along with the selection of linear or logarithmic step spacing. Based on calibration data, drive frequency points may be automatically jogged to an adjacent frequency if the target wavelength lies in a region for which the chamber has poor characteristics. At each step, the system pauses to allow the closed-loop controlled drive amplitude to settle to its target value. After this, the lock-in analyzer is automatically adjusted to the optimal input range and then instructed to collect data by the

computer. At the same time the computer issues a command to the AFC-100 to perform a signal FFT. Both data packets are then collected and stored for later processing in order to produce the combustion response for that frequency.

3.3 The Test Envelope

Chemiluminescence experiments were performed on the flat-flame burner described earlier and in appendix B. The burner was operated on premixed ultra-high purity methane (99.97%) and dry air. The stagnation body height above the nozzle exit plane remained fixed at 21 mm ($H/D = 1.5$) for all experiments. The burner equivalence ratio and nozzle exit velocity were the varied parameters.

Figure 3-2 is a duplicate of Figure B-12, showing the experimentally determined operating envelope of the burner. The laminar flame speed as computed by Cantera using the GRI-Mech 3.0 kinetics model is shown for reference as a dotted curve near the bottom. The upper-most and lower-most solid curves define the operating boundaries of the burner. At nozzle exit velocities above the upper solid curve, the flame blows out. For exit velocities below the lower solid curve, the flame is ingested by the burner nozzle.

The solid curves shown within this operating range define boundaries of operating behavior. Hysteresis was found when traversing these boundaries and, consequently, two curves are shown for each transition. The details of the burner operation around these curves are presented in appendix B. For all the chemiluminescence and PLIF experiments performed, the burner operating conditions were chosen to be in the flat-flame regime, above the upper hysteresis band.

Before choosing the conditions with which to populate the test matrix, the vertical axis of Figure 3-2 was normalized by the lower curve defining the minimum operating nozzle exit velocity. Figure 3-3 shows the resulting plot. The cross-hairs on the graph represent operating points at which chemiluminescence experiments were performed. The points are on an evenly spaced grid

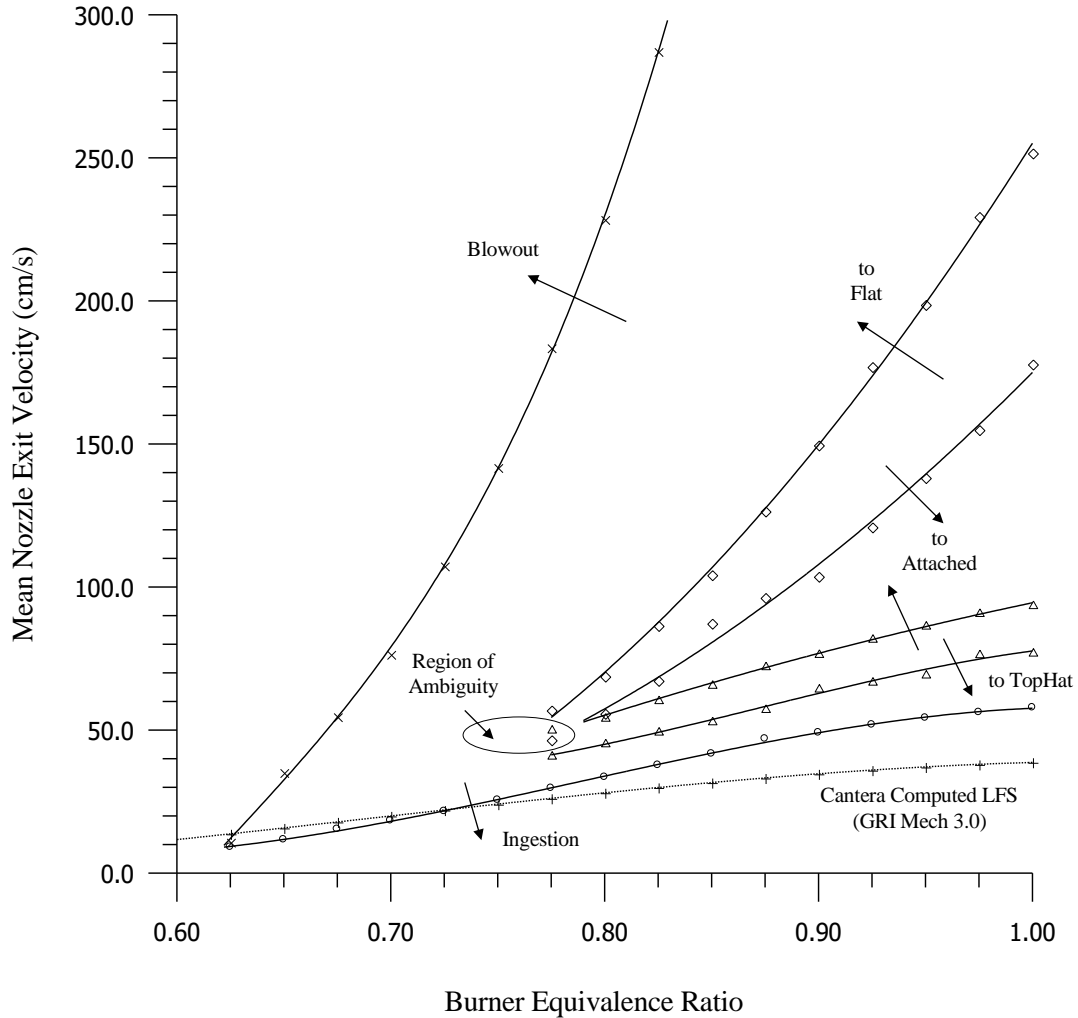


Figure 3-2: Burner operational envelope shown with transition boundaries. Transitions between operating modes exhibit hysteresis. Two lines are shown for each mode (branch) pair – one for each transition direction.

with step sizes in equivalence ratio being 0.25 and step sizes in dimensionless nozzle exit velocity being 0.5. A total of 62 operating conditions were chosen, all lying within the flat-flame operating regime. The curtailing of points in the upper-right corner of the graph was the result of insufficient flow capability from the fuel/air feed system. The acoustic drive level was held constant at 110.8 dB (SPL) for all bulk chemiluminescence experiments.

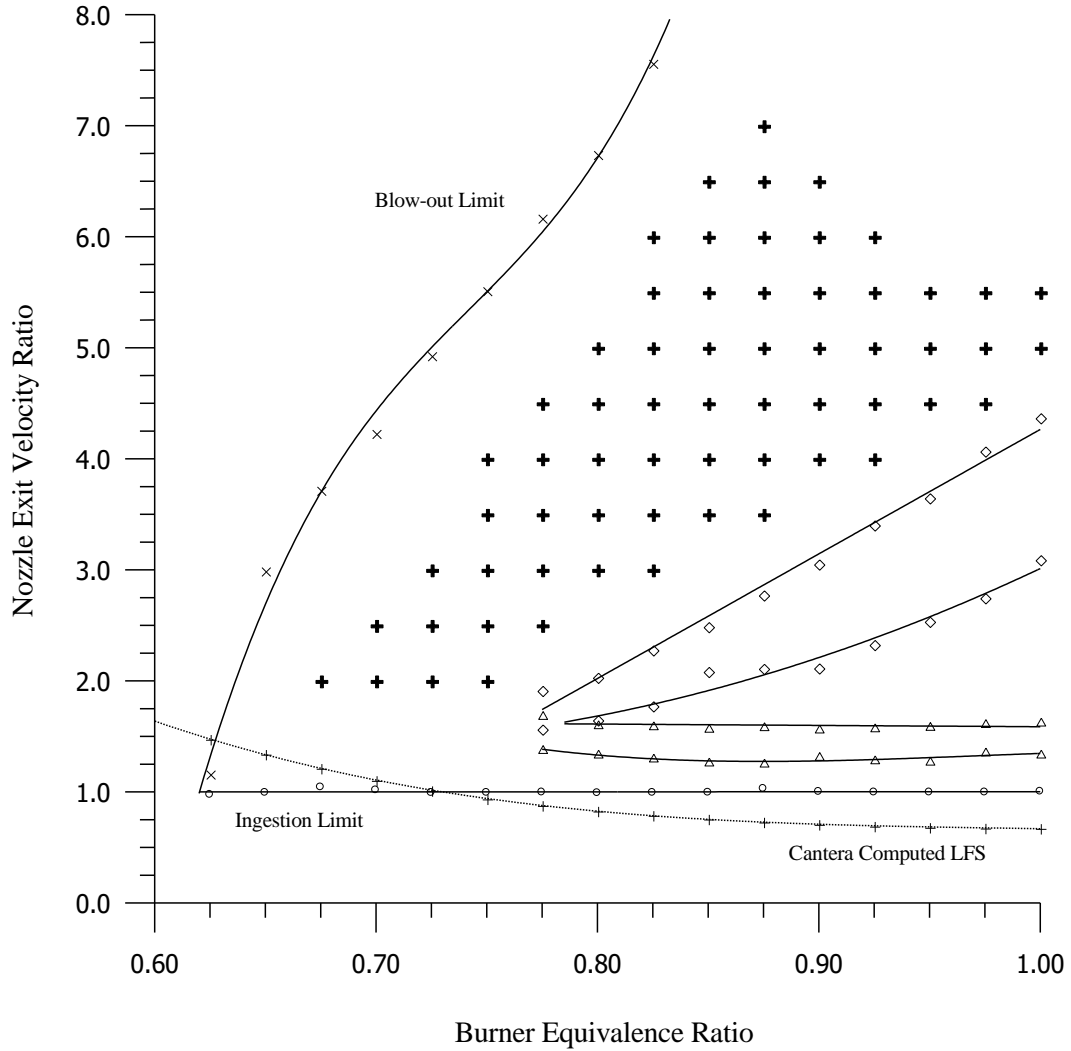


Figure 3-3: Burner operational envelope with the nozzle exit velocity normalized by the flame ingestion limit (i.e. lower operating boundary). Cross-hairs indicate operating points at which chemiluminescence experiments were performed.

3.4 Experimental Results

3.4.1 The Combustion Response Function

The collected data was post processed to produce Bode plots of the combustion response function. Here, the combustion response function is defined as:

$$(3-1) \quad H(s) = \frac{\bar{p}}{p'(s)} \frac{q'(s)}{\bar{q}} \quad ; \quad s = i\omega.$$

In this relation, \bar{p} and \bar{q} are the average values of the pressure and heat release rate, respectively.

The fluctuating values of the pressure and heat release are represented by $p'(s)$ and $q'(s)$, which are complex valued. For the chemiluminescence experiments presented, the heat release rate is assumed to be approximately proportional to the intensity measured by the optically filtered PMT such that:

$$(3-2) \quad \frac{q'(s)}{\bar{q}} \simeq \frac{I'(s)}{\bar{I}(s)},$$

where I is the optical intensity. Owing to effects such a collisional quenching and reabsorption it is known that, in general, $q(s) \neq \alpha I(s)$, $\alpha = \text{const}$; however, it is conjectured that for moderate heat release rates (on average) and where fluctuations are small, $|q'(s)| \ll \bar{q}(s)$, that equation (3-2) holds approximately. Given this, the combustion response function can be rewritten as:

$$(3-3) \quad H(s) = \frac{\bar{p}}{p'(s)} \frac{I'(s)}{\bar{I}(s)} ; \quad s = i\omega.$$

The plots generated from the experimental data display the magnitude and phase of this function from 20 Hz to nearly 2000 Hz. Negative phase values represent an unsteady heat release that lags the unsteady pressure. Figure 3-4 shows a representative plot for the test case with an equivalence ratio of 0.85 and a nozzle exit velocity ratio on 4.0.

For the case shown, several features of interest can be noted. The combustion response magnitude peaks around 60 Hz and remains near the peak up to nearly 100 Hz. Ripples can be seen in the ascending side of the magnitude between 20 Hz and 40 Hz. In addition, ripples in the amplitude are also noticeable on the descending side of the amplitude curve between 100 Hz and 160 Hz. A notch in the amplitude response is present at 243 Hz with a corresponding jump in the phase. To the right of this, a broad peak is seen in the amplitude between 250 Hz and 500 Hz. This portion of the response corresponds with the Helmholtz resonance of the burner nozzle and cavity.

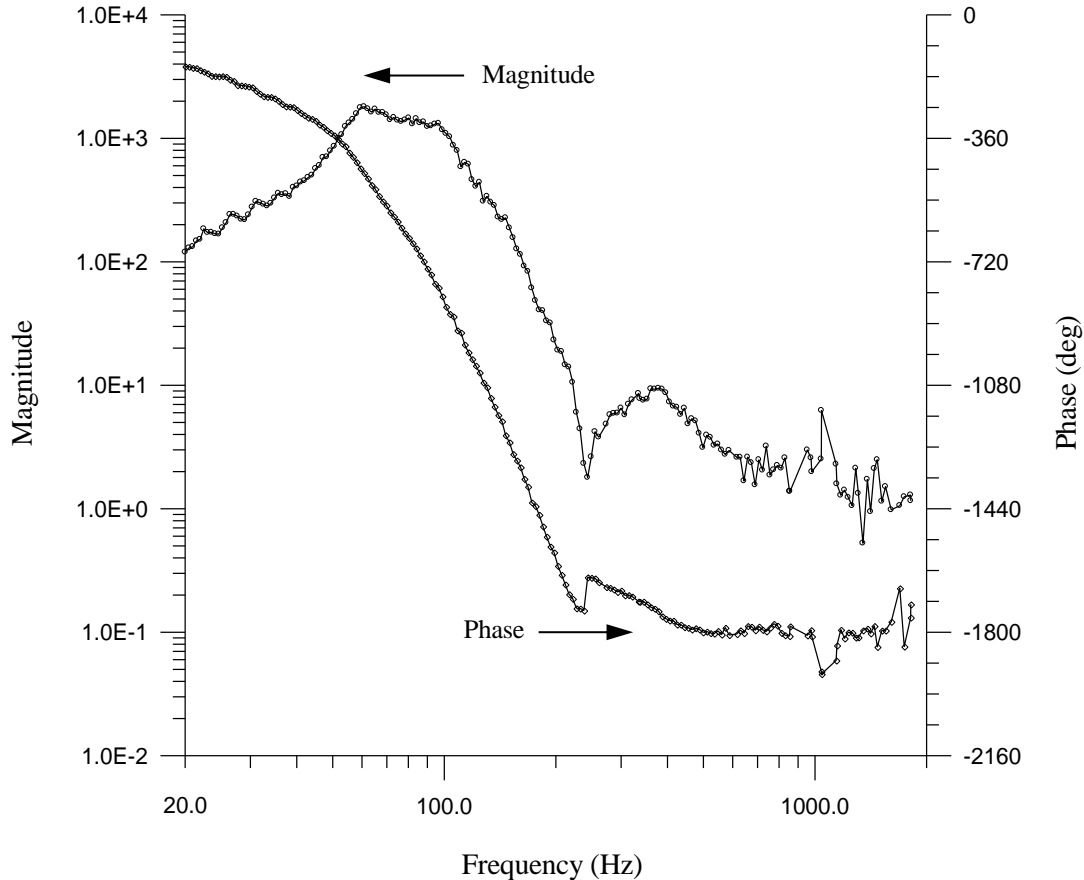


Figure 3-4: Combustion response function plotted for the flat-flame burner operating on premixed methane and air with an equivalence ratio of 0.85 and a nozzle exit velocity ratio of 4.0. Both magnitude and phase are presented. Negative phase corresponds to the fluctuating heat release lagging the fluctuating pressure.

This can be seen in Figure 3-5 where the same peak is present in the signal from the internal nozzle microphone. This microphone is located in the side of the aerodynamic contraction near the bottom, just above the upper sintered disk. The plot of the microphone signal is on a logarithmic vertical axis; however, its scale is arbitrary and the curve is shown simply for comparison to the combustion response amplitude plot. Beyond this point, the combustion response appears to decay towards the noise floor.

The phase of the combustion response function rolls off smoothly from 20 Hz to 200 Hz. As the notch in the response is approached, the phase jumps in the positive (leading) direction.

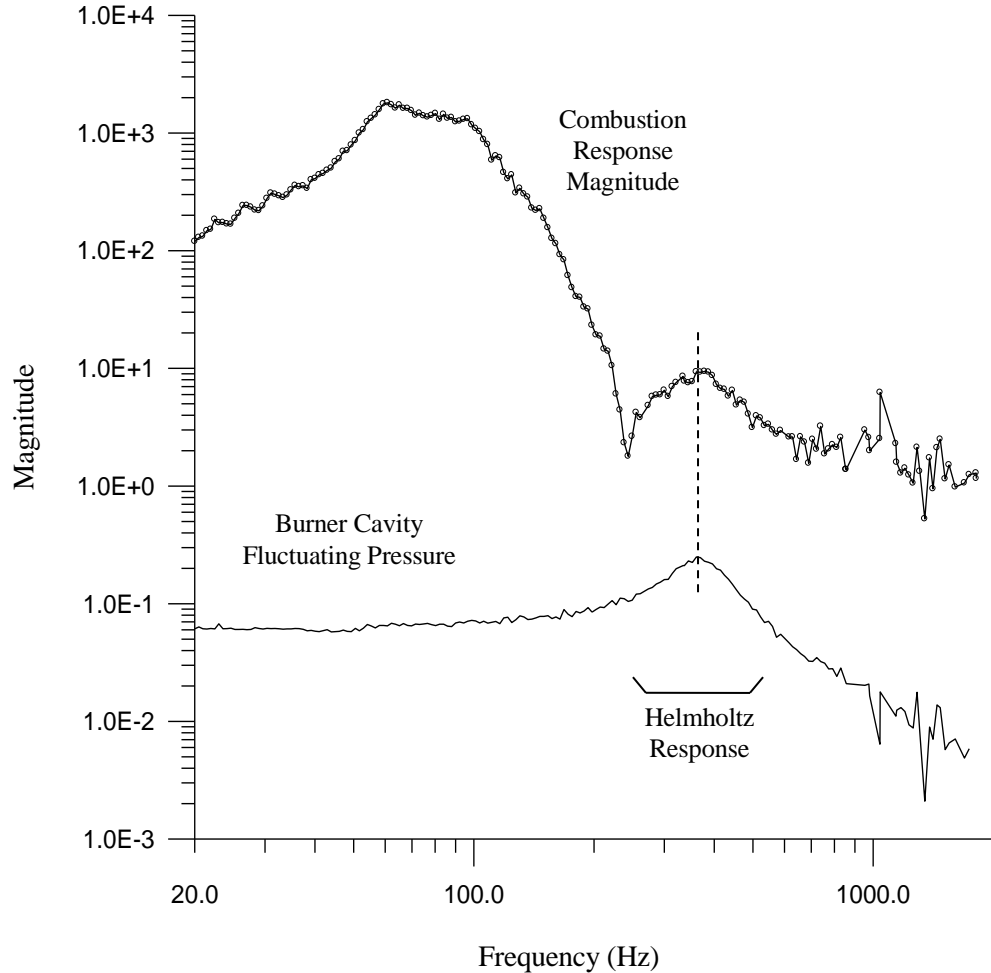


Figure 3-5: Amplitude portion of the combustion response function as seen in Figure 3-4 plotted in parallel with the fluctuating pressure seen within the larger portion of the burner nozzle cavity. The peak in the combustion response function centered around 375 Hz corresponds to the Helmholtz resonance of the burner nozzle and cavity.

Beyond this (after the Helmholtz resonance range has been passed) the response settles into being in phase with the fluctuating pressure. It is quickly noticed that the phase behavior between 20 Hz and 200 Hz looks suspiciously like a transport delay. It is known that for “real” physical systems the phase must approach a multiple of 90° at zero frequency. Given this constraint, linear fits were produced by the least-squares method to the low frequency phase data for all datasets, and the intercept at the origin was determined in each case. These fits unequivocally indicated that the chemiluminescence response at zero frequency is in-phase with the varying pressure. With this

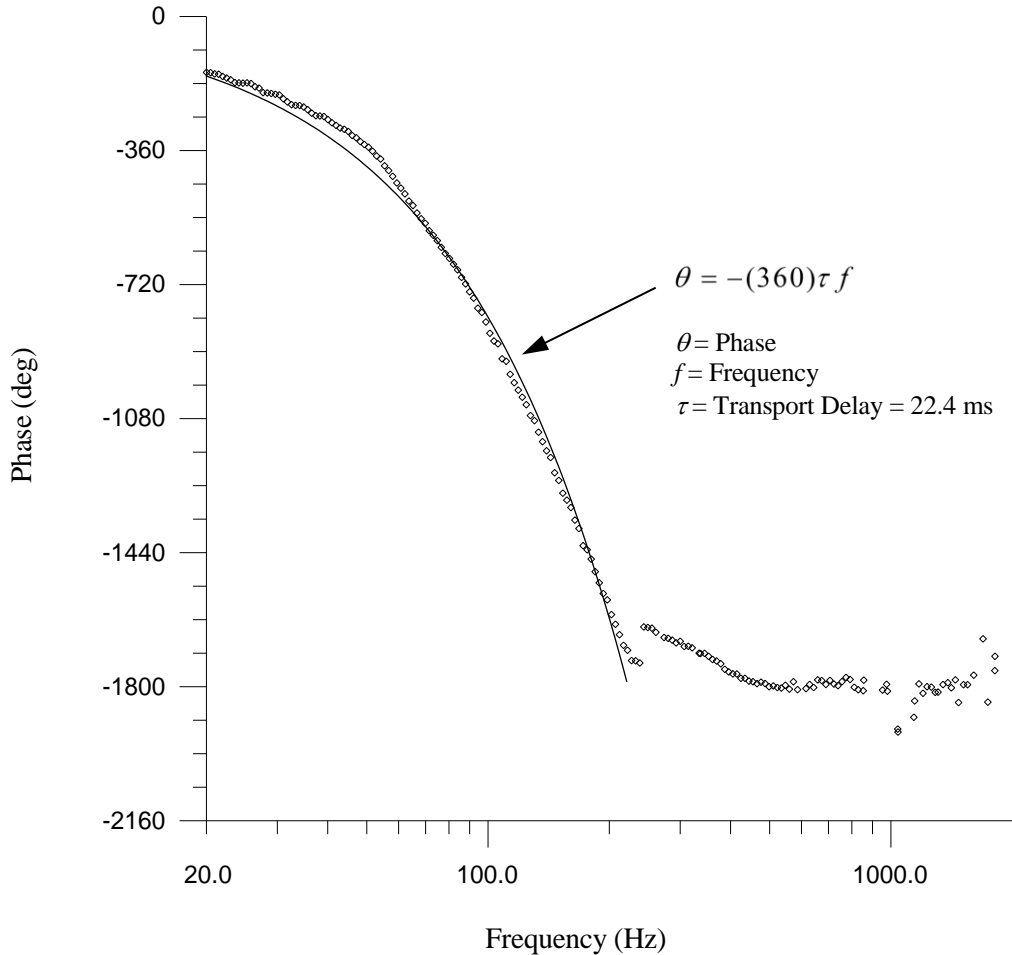


Figure 3-6: Phase portion of the combustion response function as seen in Figure 3-4. Solid curve corresponds to the phase behavior of a 22.4 ms time or transport delay. Curve generated by least-squares fit to data points from 20 Hz to 222 Hz.

information in hand, the pertinent phase data for the experiment under review was fit again, but with the constraint that the phase be equal to zero at the origin. The result was an estimated transport delay of 22.4 ms. This can be seen in Figure 3-6.

As was alluded to above, all of the collected chemiluminescence data exhibits transport delay phase behavior at low frequencies. At some distinct frequency the system's phase behavior changes abruptly. In the case presented in Figure 3-6, this occurs at 222 Hz. This location is dubbed the "transition frequency." The frequency range below the transition point is called the sub- or pre-transitional region. For frequencies above the transition point (called the post-transition

region) the system phase changes are typically small and remain within one phase-wrap. Eventually the phase equilibrates to the in-phase condition at the highest frequencies.

3.4.2 Combustion Response Variation with Free Parameters

Given the definition of the combustion response function, it is now possible to examine how this function varies with the free parameters, namely the nozzle exit velocity ratio and the burner equivalence ratio. As a starting point, a fixed value of 4.0 is selected for the nozzle exit velocity ratio, this being in the middle of the operating range. The combustion response is then plotted for four values of equivalence ratio ranging from 0.75 to 0.90. This plot is shown in Figure 3-7.

As can be seen, the general behavior of the magnitude response is the same across the presented range of equivalence ratios. Nonetheless, the peak is seen to shift toward higher frequencies, as well as increase in amplitude slightly, as the equivalence ratio is increased. In addition, the location of the transition frequency also shifts to the right with increasing equivalence ratio. Notches at the transition exhibit variation in depth. After passing this transition, the curves roughly coincide, passing through the Helmholtz response and then leveling-out as the highest test frequencies are approached.

Next, a fixed equivalence ratio of 0.85 is chosen and the nozzle exit velocity ratio is varied from 3.5 to 6.5. These plots are shown in Figure 3-8. Once again, the response functions are similar in nature, but with their peaks shifting from lower frequency to higher frequency as the velocity ratio increases. Deep notches appear in the responses for the cases with $V_R = 4.5$ and 6.5 , but are essentially absent in the other two traces. Beyond the transition points, the curves return to being approximately coincident.

Upon examination of the operating parameters of the test cases, it is noticed that the frequency shift in the response peak appears to track with the actual nozzle exit velocity (and not

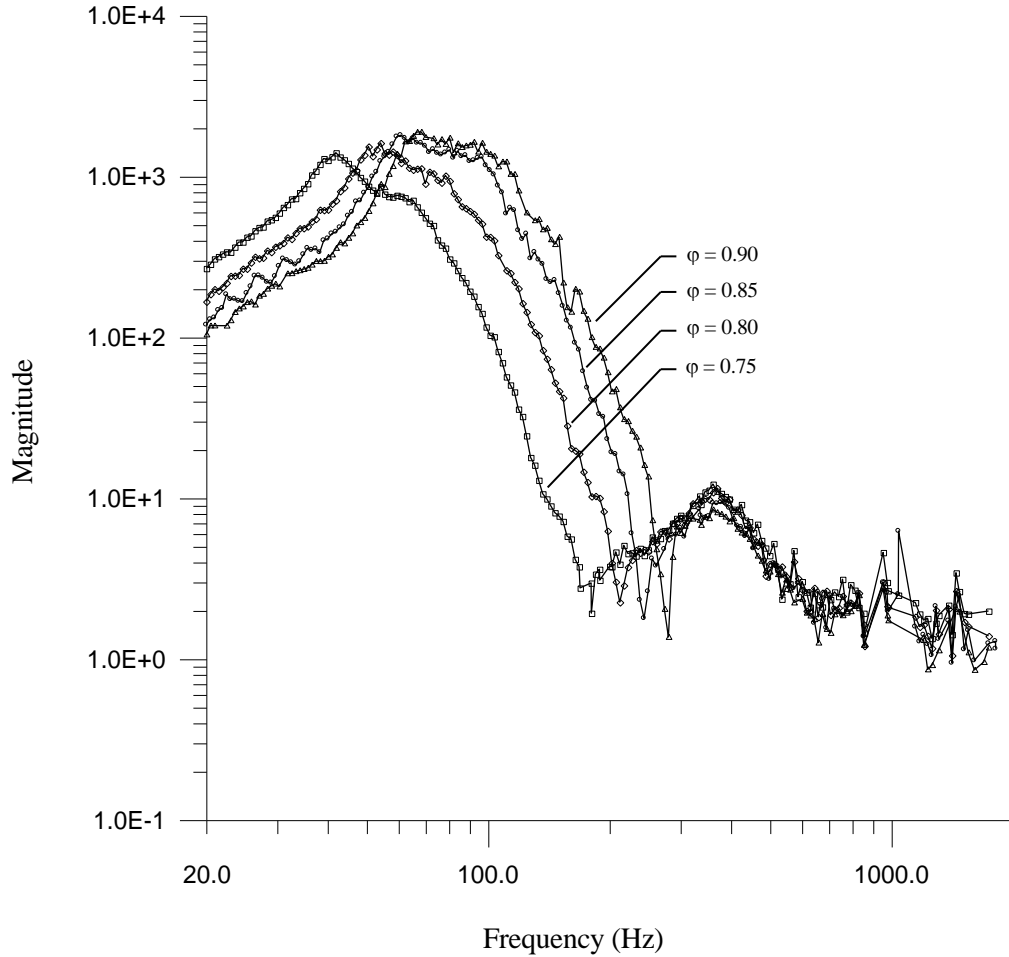


Figure 3-7: Amplitude portion of the combustion response function for a nozzle exit velocity ratio of 4.0 and equivalence ratios from 0.75 to 0.90.

with the non-dimensionalized velocity or velocity ratio, V_R). This is consistent with the earlier suspicion regarding the pre-transitional phase response appearing to be that of a time or transport delay. If it is assumed the flame stabilization height is relatively insensitive to the changes in equivalence ratio and nozzle exit velocity for flat-flame operation far from the attached condition, then the distance from the nozzle exit plane to the flame is approximately constant. In this case, the transport delay is inversely proportional to the nozzle exit velocity. If this is, indeed, the critical parameter then operation of the burner at constant exit velocity but different equivalence ratios should produce response curves with similarly located peak response frequencies. To test this, four individual data sets with nearly identical exit velocities are pulled from the test matrix

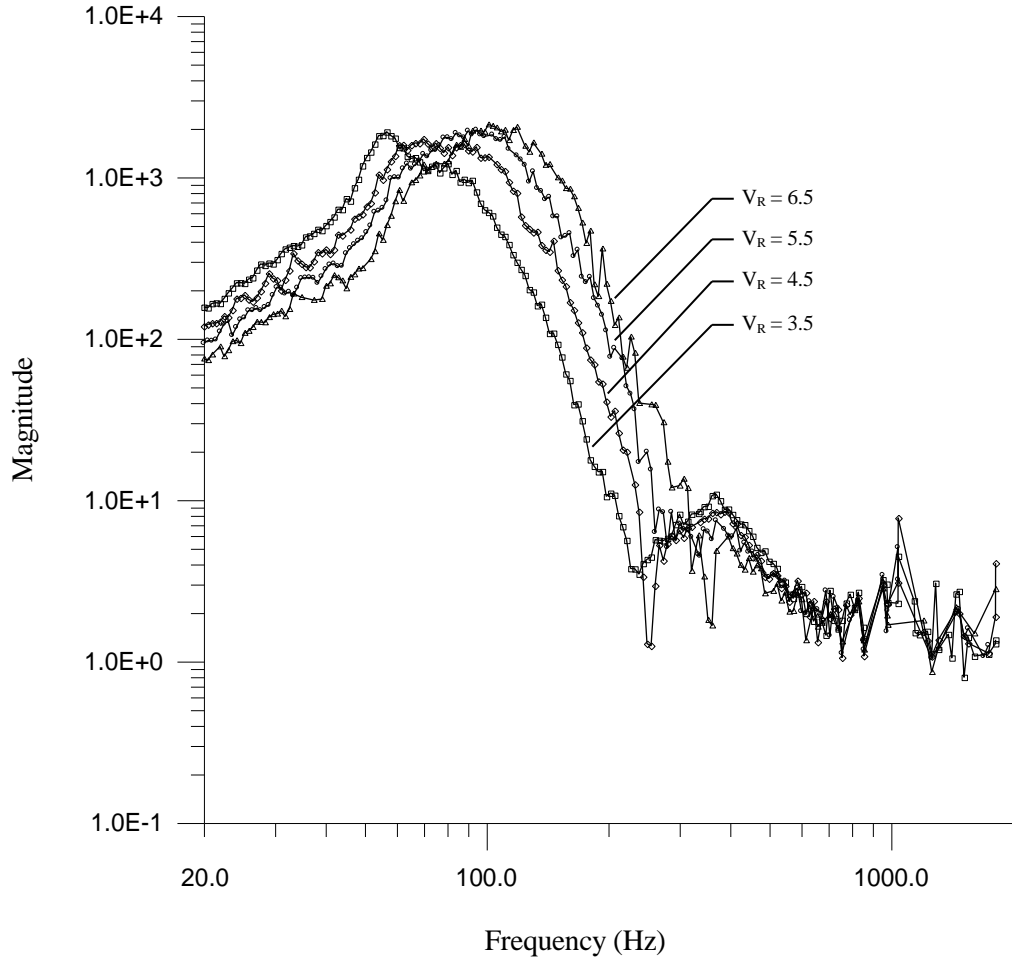


Figure 3-8: Amplitude portion of the combustion response function for an equivalence ratio of 0.85 and for nozzle exit velocity ratios (V_R) varying from 3.5 to 6.5.

and plotted. The cases selected are presented in Table 3-1 while the plots are shown in Figure 3-9. As can be seen, the curves for both the magnitude and phase portions of the response are nearly identical across the different test cases. This adds credibility to the notion that the transport time to the reaction zone plays a key role in the combustion response.

In examining the plots in Figure 3-9, it is also noticed that the behavior around the transition is benign; the phase curves show very little upset in the transition region and the amplitude plots are devoid of any deep notches. This is in contrast to other response functions that were measured such as the one presented in Figure 3-4. A more detailed look and subsequent explanation is presented in chapter 5.

Trace Number	Equivalence Ratio (φ)	Exit Velocity Ratio (V_R)	Exit Velocity (cm/s)	Data Set Number
I	0.825	5.5	208.9	110
II	0.850	5.0	209.6	70
III	0.875	4.5	205.4	76
IV	0.925	4.0	208.1	88

Table 3-1: Test cases for which the nozzle exit velocity lies between 205 cm/s and 210 cm/s. Magnitude and phase response curves for these four cases are plotted in Figure 3-9.

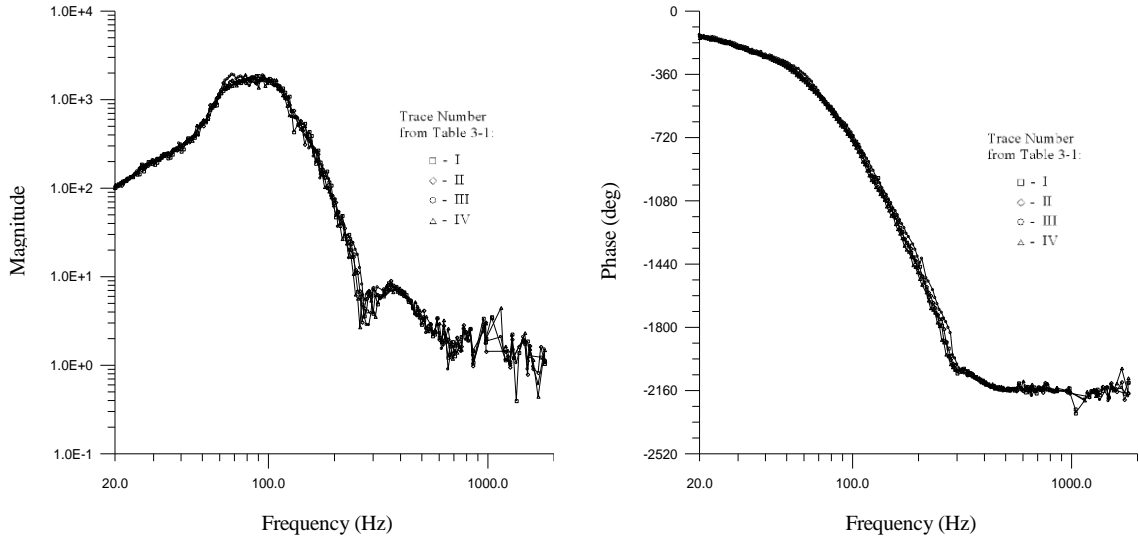


Figure 3-9: Combustion response curves (magnitude and phase) for four test cases with nearly identical nozzle exit velocities (range 205 cm/s to 210 cm/s). Basic forms of the curves are essentially coincident.

Given that a “free” jet is involved and that the above data collapsed well for matching jet velocity, it is prudent to reexamine the data from Figures 3-7 and 3-8 by plotting them again, however, this time with the horizontal axis prescribed as the Strouhal number based on the nozzle exit diameter. Figure 3-10 presents the data for a varying equivalence ratio spanning from 0.75 to 0.90, and a fixed velocity ratio of 4.0. Figure 3-11 plots the data for a fixed equivalence ratio of 0.85 but a varying nozzle velocity ratio spanning from 3.5 to 6.5. As can be seen, the magnitude

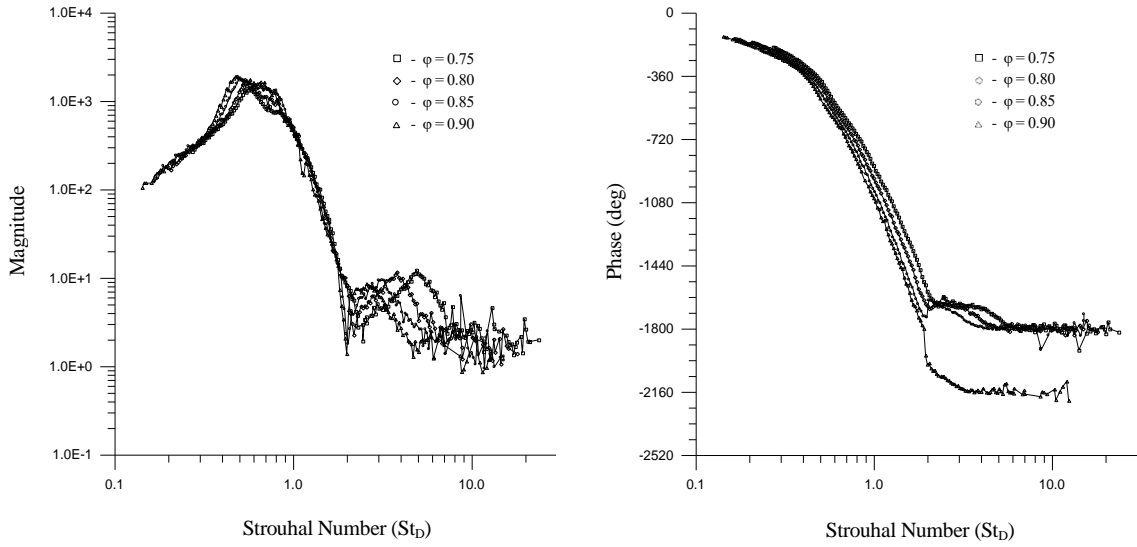


Figure 3-10: Combustion response data from experimental cases shown in Figure 3-7 now plotted against Strouhal number on the horizontal axis.

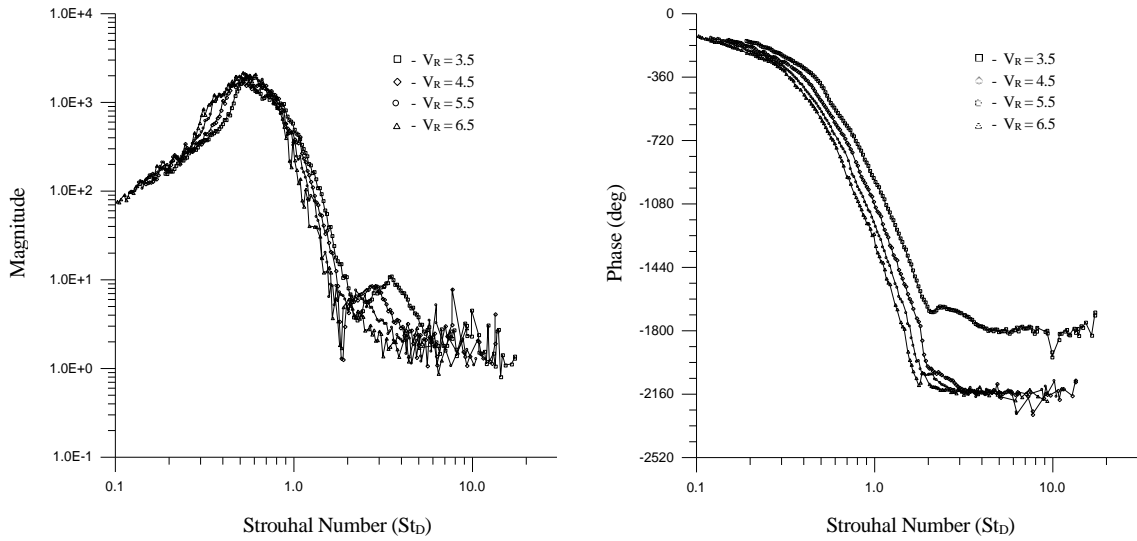


Figure 3-11: Combustion response data from experimental cases shown in Figure 3-8 now plotted against Strouhal number on the horizontal axis.

data in the sub-transitional region collapse well when plotted against the Strouhal number. The peak of the response appears to be located close to $St_D = 0.5$. Variation still exists in the phase

data, as shown. This behavior hints that the combustion response at low frequencies is possibly driven by an instability in the jet shear layer. This will be further explored in chapter 4.

3.4.3 Role of the Transport Delay

To further investigate the transport-delay behavior of the combustion response curves in the pre-transitional region, it is of interest to plot the measured time delay for each test case against the corresponding nozzle exit velocity. As before, the time delay is computed using a least-squares best fit to phase data in the pre-transitional region. Individual crosshairs are used to indicate results for each of the 62 test cases. These results are shown Figure 3-12.

To compare these with an estimate of the fuel/air transit time from the nozzle exit plane to the reaction zone, a simple potential flow model for the flow field is introduced. As a very rough approximation, cold-flow is examined with no jump condition included for the flame. For inviscid, axisymmetric stagnation flow the stream function and resulting axial velocity can be shown to be:

$$(3-4a,b) \quad \psi = -ar^2 z \quad \text{and} \quad u_z = -2az$$

where the origin is on the stagnation plane. It is now easy to solve for the axial position as a function of time:

$$(3-5) \quad \frac{dz}{dt} + 2az = 0 \quad \Rightarrow \quad z = z_0 e^{-2a(t-t_0)}.$$

Setting the initial position coordinate $z_0 = L$ (where L is the distance from the stagnation plane to the nozzle exit plane) at time $t = 0$ implies $t_0 = 0$. Furthermore, knowing the nozzle exit velocity, $-V_j$, provides a solution for the last free parameter:

$$(3-6) \quad a = \frac{1}{2} \frac{V_j}{L}.$$

The resulting position equation is:

$$(3-7) \quad z = L \exp\left(-\frac{V_j t}{L}\right).$$

This equation can then be inverted to produce a relation for the transit time to a given flame position:

$$(3-8) \quad \tau_d = \frac{L}{V_j} \ln\left(\frac{z_f}{L}\right).$$

A value for z_f must now be determined. Clearly the flame location will change with variation of the operating parameters; nonetheless, for simplicity, a fixed value is chosen for illustrative purposes. For the test case presented in Figure 3-5, the flame location is approximately 16 mm above the nozzle exit plane, or 5 mm below the stagnation body. Using this value produces the resulting dashed traces in Figure 3-12.

As an alternate approximation, a fixed flame speed can be taken in lieu of a fixed flame position. Combining equations (3-4b) and (3-6) yields a relation for the flame speed given the flame equilibrium location:

$$(3-9) \quad S_F = \frac{z_f V_j}{L}.$$

The flame speed is then computed using the flame position and jet velocity from the test case mentioned above. With this parameter fixed, equation (3-9) is now combined with equation (3-7) to produce:

$$(3-10) \quad \tau_d = \frac{L}{V_j} \ln\left(\frac{V_j}{S_F}\right).$$

This relation is plotted in Figure 3-12 as the dash-dotted curve.

Neither model produces good results. The fixed flame position model generates a curve that underestimates the transport delay for jet velocities greater than 100 cm/s while overestimating the delay for jet velocities less than 100 cm/s. The fixed-flame-speed model underestimates the

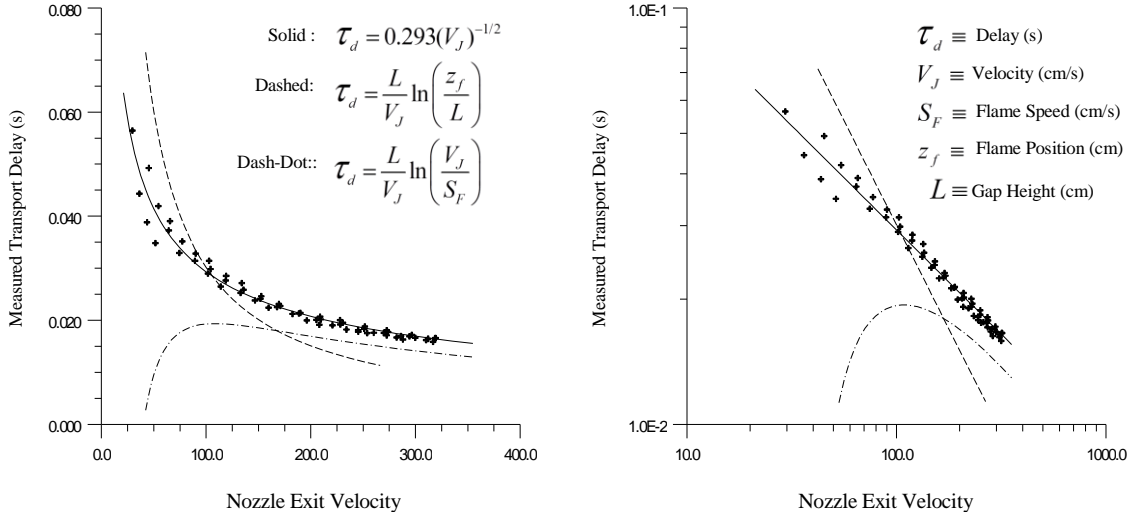


Figure 3-12: Plots of the transport time delay versus the nozzle exit velocity as determined by curve-fitting the combustion response phase curve in the sub-transitional region. Crosshairs indicate individual data point. The solid curve indicates a power-law fit given in wequation (3-11). The dashed curve shows the result of the fixed flame location transport delay model given in equation (3-8). The dotted curve shows the result of the fixed flame speed transport delay model given in equation (3-10). The left plot shows the data on linear scales while the right plot uses logarithmic axes.

transport delay for all jet velocities. Visual inspection of the experimental data points plotted on logarithmic axes indicates power-law behavior. The exponent to the power law appears to be very close to $-1/2$. For this exponent, a least-squares minimization fit for the data is given by:

$$(3-11) \quad \tau_d = 0.293(V_J)^{-1/2}.$$

Here the transport delay, τ_d , is in seconds and the jet velocity, V_J , is in cm/s. This result is shown as the solid curve in Figure 3-12.

The shortfall in the transport delay estimates for the reference test condition suggests that the transport mechanism involved has an effective velocity that is slower than the core jet velocity. This, in addition to the collapse of the combustion response data plotted against Strouhal number earlier, reinforces the notion that it is shear layer structures at the outer boundary of the jet that are convecting variations in mass flow or equivalence ratio into the reaction zone.

Another parameter of interest is the transition frequency. As mentioned earlier, it is defined by the frequency at which the transport-delay behavior ends. The transition (at a minimum) is marked by an abrupt change in slope of the phase curve. It is also commonly accompanied by a jump in phase. Additionally, the magnitude response frequently exhibits a notch at the same location. These behaviors can be seen in Figure 3-4 at approximately 222 Hz.

Figure 3-13 shows a plot of the measured transition frequency versus the nozzle exit velocity. Only the solid-diamond data points were used in determining the linear fit that is

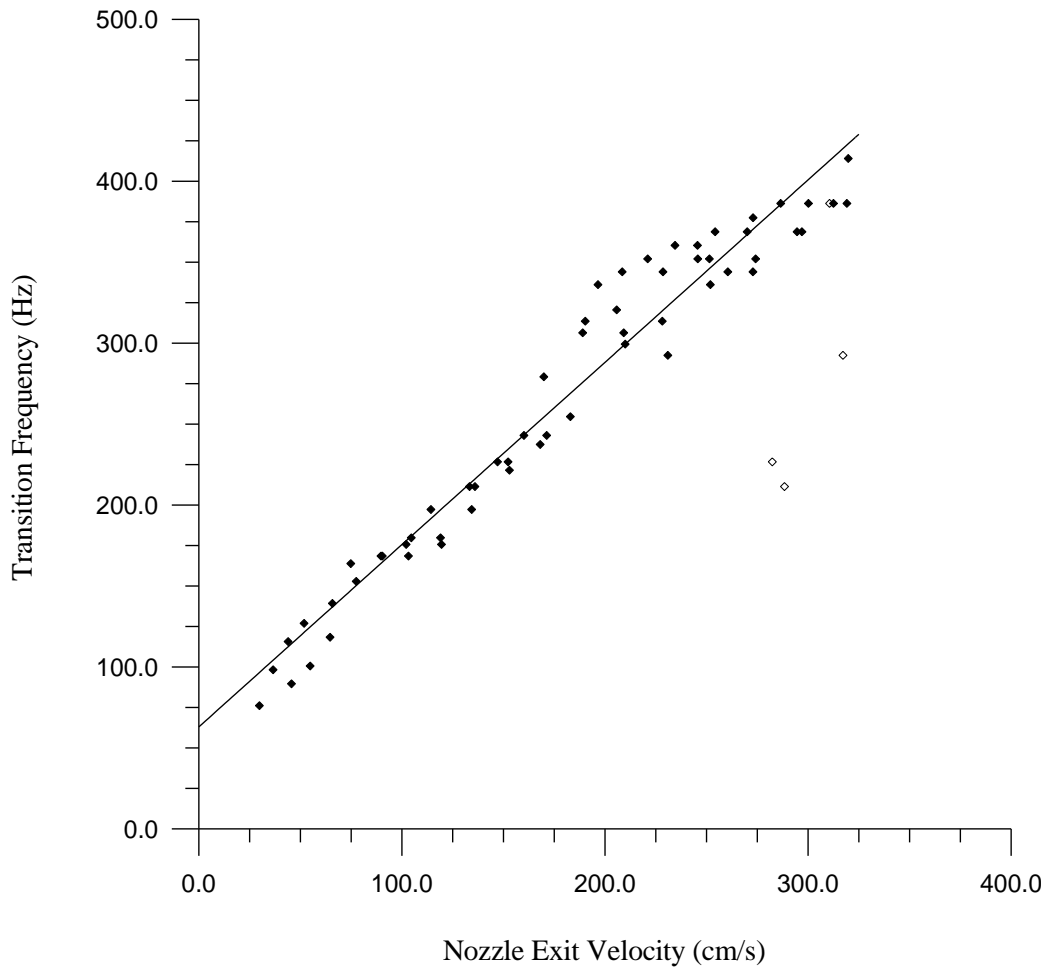


Figure 3-13: Plot of the measured transition frequency versus the nozzle exit velocity. Diamonds indicate the collected data points. The solid line corresponds to a least-squares linear fit to the data shown as solid diamonds. Open diamonds indicate transition points for test cases where the combustion response exhibited non-standard behavior.

presented. The open-diamonds represent data points from test cases that exhibited unusual (and interesting) behavior. These cases are covered in section 3.4.4. The given linear fit has an intercept of 63 Hz at zero exit velocity, and has a slope of 1.13 Hz/(cm/s) or 1.13 cyc/cm. The inverse of this slope produces a characteristic wavelength, $\lambda_c = 0.88$ cm. Alternatively, this can be expressed as a characteristic Strouhal number based on nozzle exit diameter: $St_D = 1.58$.

3.4.4 Phase Branches

In the pre-transitional region, the phase is seen to wrap numerous times as the frequency increases. At high frequencies, the experiments all show a response that is in-phase with the fluctuating pressure. Consequently, the combustion response function has a phase that is an integer multiple of 360 degrees; however, the experiments do not all end on the same phase branch at high frequencies. Figure 3-14 demonstrates this by showing the final (accumulated) phase for all the test cases versus the nozzle exit velocity.

Despite some overlap being seen, it is apparent that the trend in accumulated phase is of increasing wrap number with increasing nozzle exit velocity. Four test cases violate this behavior and are shown as open diamonds. These are the same test cases presented as open diamonds in Figure 3-13. These outliers were somewhat perplexing and warranted further investigation.

After sifting through supplemental data that duplicated many of the runs presented here, it was discovered that a few of the test conditions exhibited bifurcated behavior in the combustion response. These are the cases represented by the open diamonds. Figure 3-15 shows one of these cases. For the two experiments shown the burner equivalence ratio is 0.9 and the nozzle exit velocity 294 cm/s ($V_R = 6.0$). All other operating parameters are typical.

It can be seen that, with the exception of a notch location, both test cases match well in the magnitude response. It is in the phase response that noticeable separation is observed beyond the bifurcation frequency of 238 Hz. After reaching this frequency, dataset 86 continues to follow the

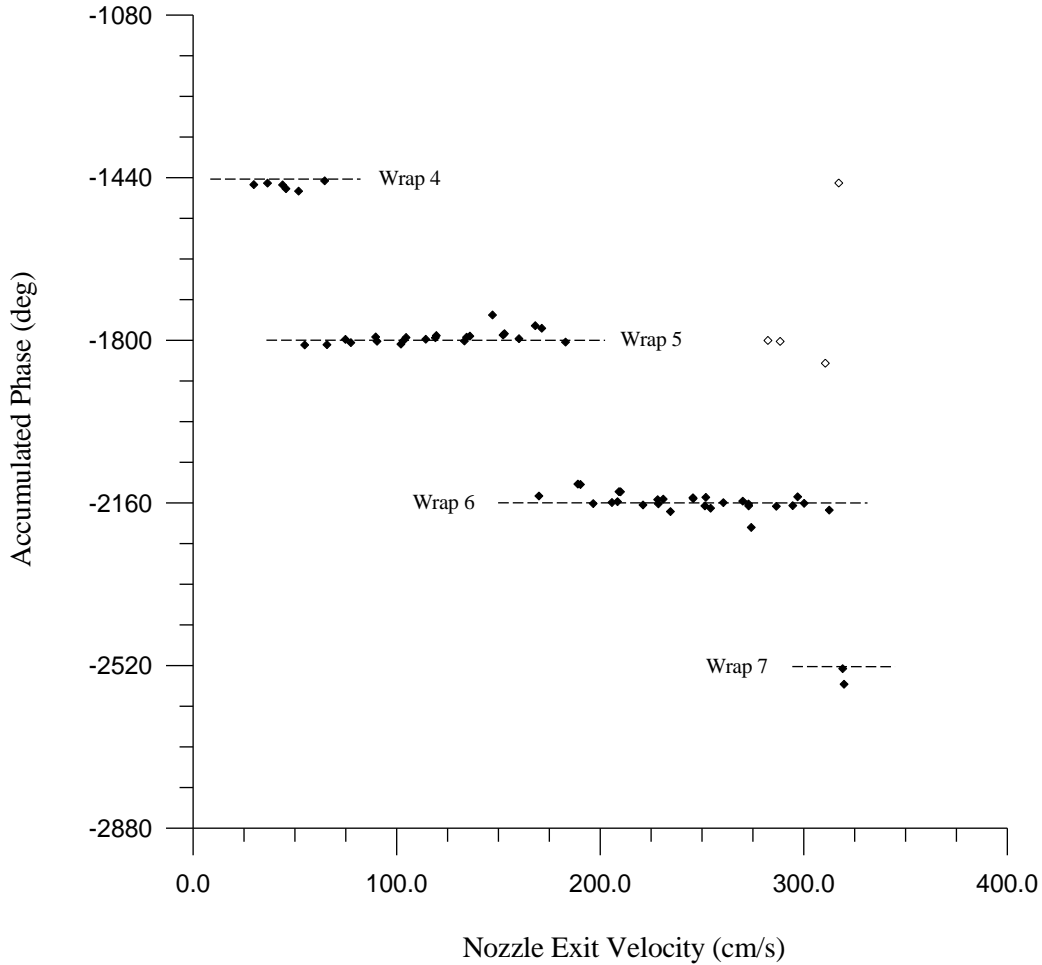


Figure 3-14: Plot of the final (accumulated) phase of the combustion response function at high frequencies (1800 to 2000 Hz) versus the nozzle exit velocity. At high frequencies, the heat release is seen to be in phase with the fluctuating pressure; however, the total accumulated phase falls on different branches. Open diamonds correspond to the same test cases with non-standard behavior as seen in Figure 3-11.

transport-delay phase trajectory up to approximately 350 Hz. After this the accumulated phase settles to -2160 degrees which is an integer wrap number of 6. In contrast, dataset 116 ceases to plunge in phase at the bifurcation point and instead oscillates in phase up to roughly 350 Hz. The peak-to-peak amplitude of this oscillation is approximately 240 degrees. Beyond this, its phase settles to -1440 degrees which corresponds to an integer wrap number of 4.

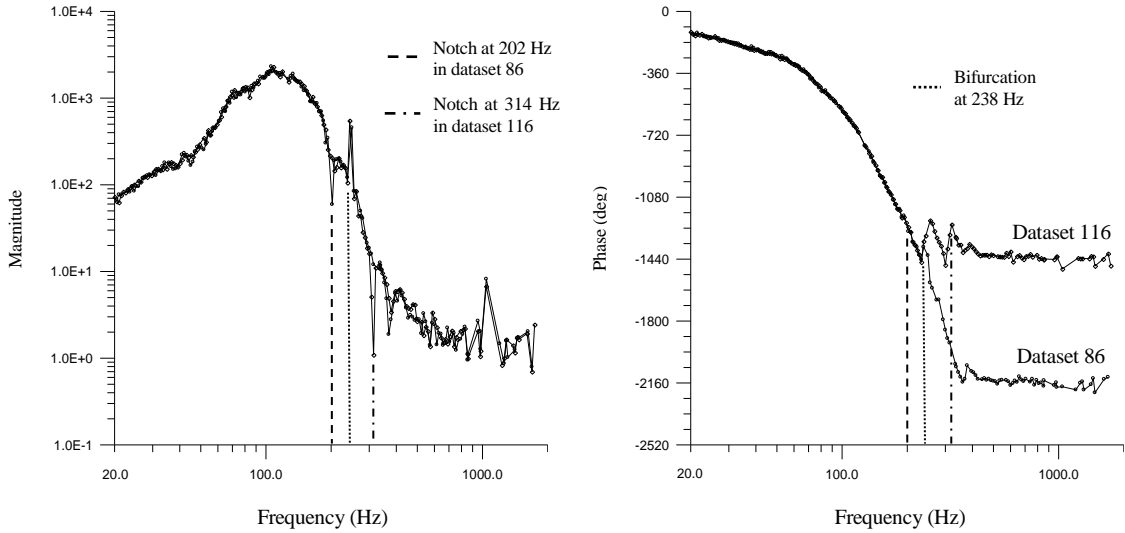


Figure 3-15: Plot of the combustion response function for two identical experimental runs. The bifurcation in the response phase occurs at approximately 238 Hz. The experimental burner was operated at an equivalence ratio of 0.9 with a nozzle exit velocity of 294 cm/s.

Interestingly, both datasets exhibit a strong, narrow peak in their magnitude response at the bifurcation location. For dataset 86, a deep, narrow notch in the amplitude response is seen at 202 Hz, which is not present in the magnitude for dataset 116. Despite the notch, there is no phase upset at this location. Similarly, dataset 116 shows an amplitude notch at 314 Hz that is not present in dataset 86. This notch is aligned with one of the peaks of the phase oscillations that were experienced.

3.4.5 The Forced Rayleigh Index

In chapter 1, the formulation of Rayleigh's Criterion as derived by Culick (1976, 1987, 1997) was presented in equation (1-1). It is repeated here for convenience.

$$(3-12) \quad \Delta E = \frac{(\gamma-1)}{\gamma \bar{p}} \int dV \int_t^{t+\tau} p'(\bar{x}, t) Q'(\bar{x}, t) dt .$$

Once again, $p'(\bar{x}, t)$ is the varying portion of the pressure field and $Q'(\bar{x}, t)$ is the varying portion of the heat release. The energy added to the system over one cycle is then given by ΔE . For

positive ΔE the closed-loop system is self-driving (although not necessarily unstable), and for negative ΔE the closed-loop system is self-damping.

In 2000, Pun, Palm and Culick proposed the forced Rayleigh index for acoustically forced systems:

$$(3-13) \quad R_f = \int_0^1 \frac{p'(\xi)q'(\xi)}{(p')_{rms} \bar{q}} d\xi.$$

Here, variable substitutions have been made so that the fluctuating pressure and heat release are $p'(\xi)$ and $q'(\xi)$ respectively. The new argument, ξ , spans from 0 to 1, constituting a full cycle of the acoustic forcing. The pressure value $(p')_{rms}$, appearing in the denominator, is the root-mean-square value of the fluctuating pressure component.

The selection of this relation for the forced Rayleigh index is arguably a poor choice as it eliminates any dependence on average system pressure. On closer examination it also becomes apparent that the relation produces an index that is not independent of the forcing amplitude in the linear regime as is desired. Consequently, a reevaluation of the forced Rayleigh index is warranted.

A relation, in the spirit of equation (3-13), is desired that is properly normalized such that it produces a dimensionless index that is independent of the forcing amplitude. The exploration begins by assuming forms for the acoustic forcing and the response of the heat release:

$$(3-14) \quad p'(\omega, t) = \sqrt{2} \frac{(p')_{rms}}{\bar{p}} \bar{p} \cos(\omega t),$$

$$(3-15) \quad q'(\omega, t) = \sqrt{2} \frac{(p')_{rms}}{\bar{p}} \bar{q} Q(\omega) \cos(\omega t + \vartheta(\omega)).$$

Here, as before, \bar{p} and \bar{q} are the average pressure in the test section and the average intensity or heat release rate in the examined flame region, respectively. And, again, the quantity $(p')_{rms}$ is

the root-mean-square value of the fluctuating portion of the pressure. The group $\sqrt{2} \frac{(p')_{rms}}{\bar{p}}$ is

the amplitude multiplier for the acoustic forcing. Experimentally, efforts are made to hold this value constant. Nonetheless, for the following analysis it can be allowed to vary with ω for the sake of generality.

Similarly, $Q(\omega)$ is the amplitude multiplier in the heat release equation while $\vartheta(\omega)$ is the phase offset between the fluctuating pressure and heat release. Indeed, the quantities $Q(\omega)$ and $\vartheta(\omega)$ are just the magnitude and phase components of the combustion response function which have already been produced from the collected data.

Multiplying (3-14) and (3-15) and then integrating over a single cycle of the forcing gives:

$$(3-16) \quad R_f \sim \frac{(p')_{rms}^2}{\bar{p}} \bar{q} Q(\omega) \frac{2}{\tau} \int_t^{t+\tau} \cos(\omega t) \cos(\omega t + \vartheta(\omega)) dt.$$

Using $\omega = \frac{2\pi}{\tau}$ and substituting $\xi = \frac{t}{\tau}$ gives:

$$(3-17) \quad R_f \sim 2 \frac{(p')_{rms}^2}{\bar{p}} \bar{q} Q(\omega) \int_0^1 \cos(2\pi\xi) \cos(2\pi\xi + \vartheta(\omega)) d\xi.$$

It quickly becomes apparent (by inspection) that the proper normalizing factor is:

$$(3-18) \quad \alpha_N = \frac{\bar{p}}{(p')_{rms}^2 \bar{q}}.$$

So that the appropriate forced Rayleigh index becomes:

$$(3-19) \quad R_f = \frac{\bar{p}}{(p')_{rms}^2 \bar{q}} \int_0^1 p'(\xi) q'(\xi) d\xi.$$

Applying the normalizing factor to equation (3-17) produces:

$$(3-20) \quad R_f = 2 Q(\omega) \int_0^1 \cos(2\pi\xi) \cos(2\pi\xi + \vartheta(\omega)) d\xi$$

and solving the integral produces the beautifully simple relation:

$$(3-21) \quad R_f = Q(\omega) \cos(\vartheta(\omega)).$$

As mentioned earlier, the two parameters involved have already been computed in determining the combustion response function. As a result, the generation of the forced Rayleigh index from the experimental data collected becomes a triviality.

Figure 3-16 shows the forced Rayleigh index for the test case presented in Figure 3-4. In this run, the burner equivalence ratio was 0.85 and the nozzle exit velocity ratio was 4.0. As can be seen, the strong combustion response at low frequencies in combination with the ever-increasing phase lag generated by the transport-delay-like behavior results in strong, oscillatory behavior of the Rayleigh Index between 40 Hz and 200 Hz. The data is shown again in Figure 3-17 where the amplitude axes are chosen to be logarithmic to enhance the detail at small amplitudes. In this

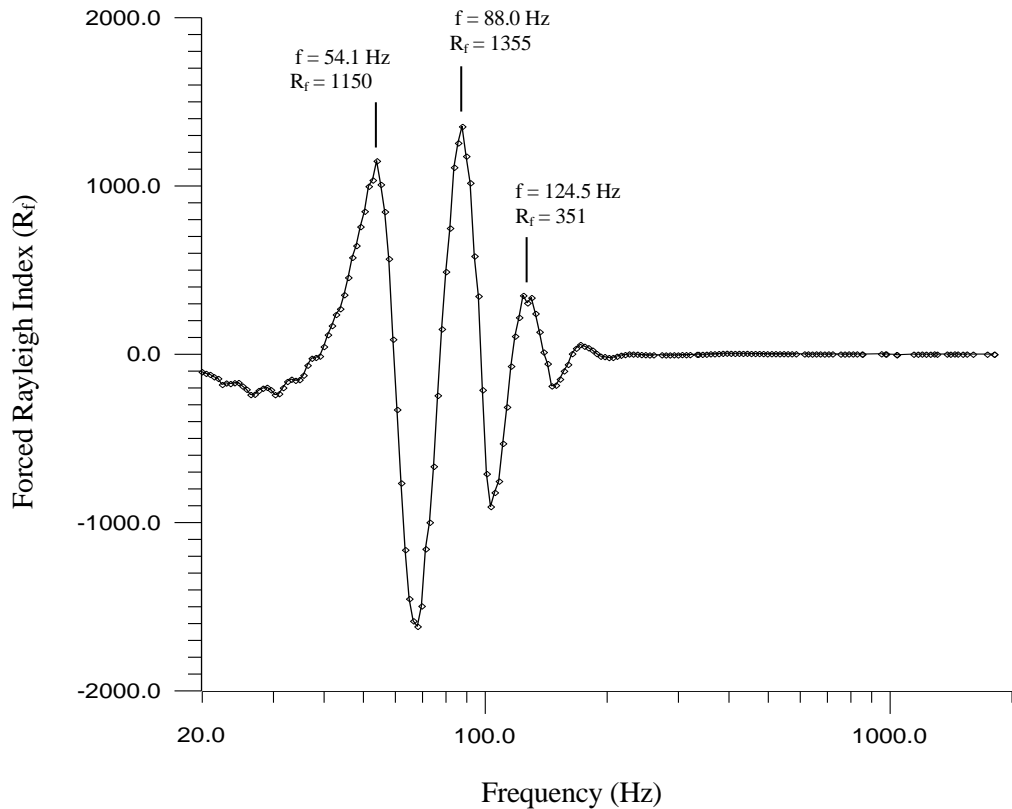


Figure 3-16: Forced Rayleigh index, R_f , for test case with equivalence ratio of 0.85 and a nozzle exit velocity ratio of 4.0. Strong driving bands (i.e. large, positive Rayleigh Index) lie from 40 to 60 Hz, 78 to 97 Hz, and 118 to 140 Hz.

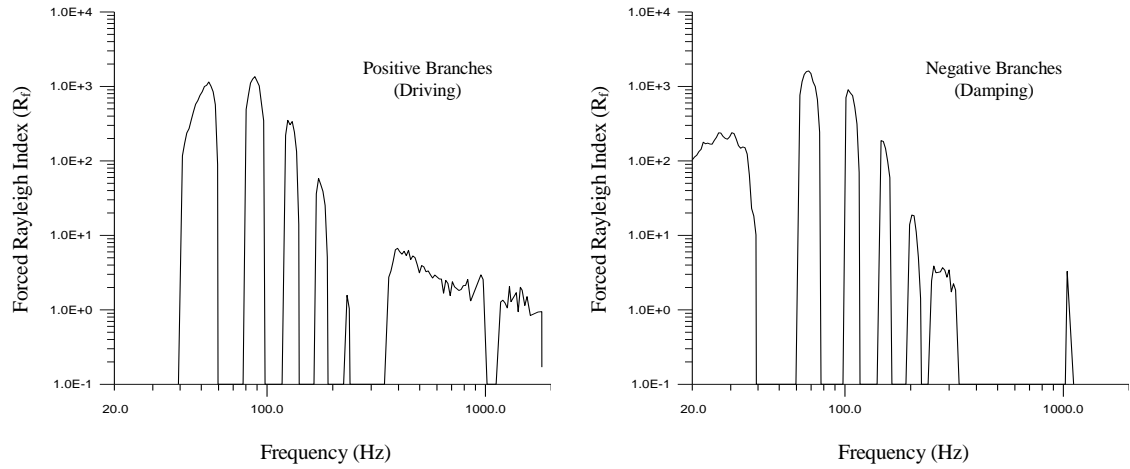


Figure 3-17: Forced Rayleigh index, R_f , for test case with equivalence ratio of 0.85 and a nozzle exit velocity ratio of 4.0. Results are shown with logarithmic amplitude axes and with positive and negative branches presented on separate graphs.

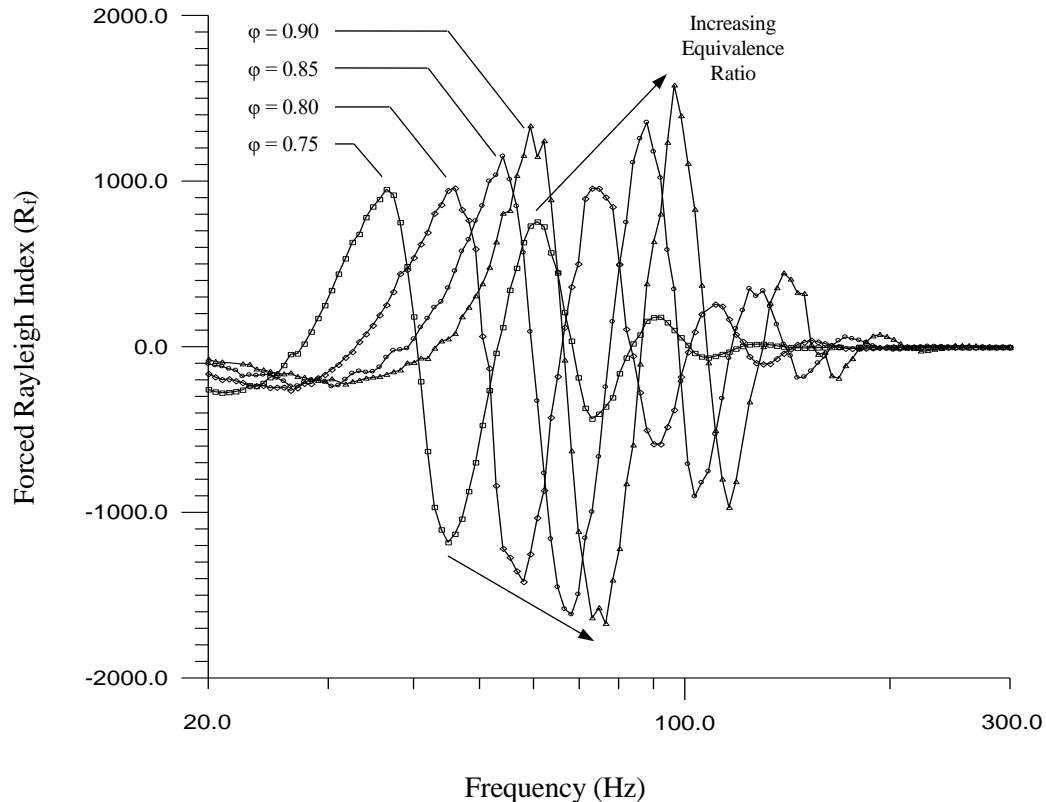


Figure 3-18: Forced Rayleigh index, R_f , for a nozzle exit velocity ratio of 4.0 and equivalence ratios from 0.75 to 0.90.

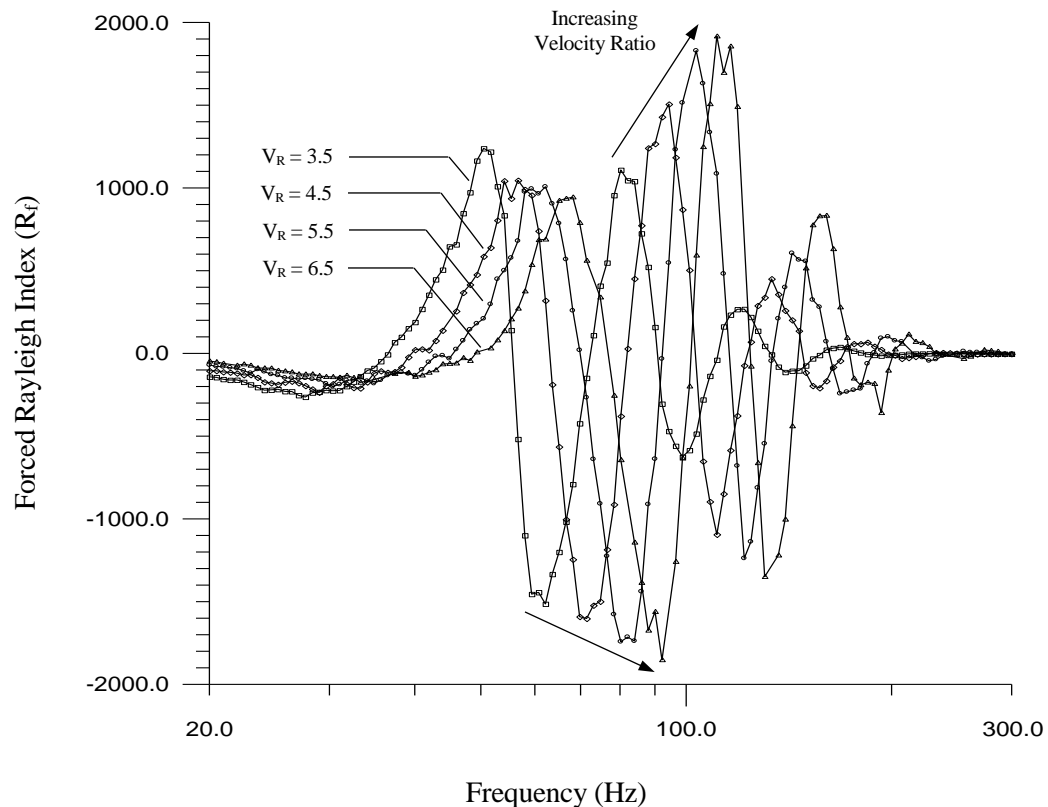


Figure 3-19: Forced Rayleigh index, R_f , for an equivalence ratio of 0.85 and for nozzle exit velocity ratios, V_R , varying from 3.5 to 6.5.

presentation, the positive and negative branches of the forced Rayleigh index have been separated onto adjacent plots.

It is now possible to generate plots in the same vein as Figures 3-7 and 3-8, this time revealing the variation in forced Rayleigh index versus burner equivalence ratio and nozzle exit velocity ratio. These graphs are shown in Figures 3-18 and 3-19. Note that the horizontal axes of the graphs have been truncated at 300 Hz and stretched accordingly to improve visibility of the features present at lower frequencies.

As expected for the previously presented data, both Figures 3-18 and 3-19 show the Rayleigh Index curves shifting to the right for increasing equivalence ratio, as well as increasing

nozzle exit velocity ratio. In general, they also display increasing peak magnitudes with increased equivalence ratio and exit velocity ratio.

To examine these features more closely, Figures 3-20 through 3-23 are presented. The datasets for the entire tested operating regime of the burner were processed to discern the magnitude and location of the extrema of the forced Rayleigh index for each test condition. Figure 3-20 shows level-set contours indicating the peak positive (driving) value of R_f observed as a function the burner equivalence ratio, φ , and the nozzle exit velocity ratio, V_R . Cross-hairs on the plot mark the actual locations of the experimental data points. The companion plot in Figure 3-21 indicates the frequency (in Hertz) at which these R_f peaks are observed. As an example, for the operating condition at $\varphi = 0.90$ and $V_R = 5.0$, Figure 3-20 shows that the peak forced Rayleigh index observed is approximately 1700. Figure 3-21 then indicates that this peak R_f value is observed at a drive frequency of approximately 110 Hertz.

In a similar fashion, Figures 3-22 presents the level-set contours for the peak negative (damping) values of the forced Rayleigh index over the operating range. The companion plot indicating the drive frequency at these minima is shown in Figure 3-23. Trending behavior in the two cases is similar and is, in general, consistent with the discussion above; the magnitude of the extrema tends to grow with increasing equivalence ratio, and increasing nozzle exit velocity ratio. Furthermore, the frequencies at which these extrema occur tend to increase, likewise, with these parameters.

As an aside, it is interesting to plot the Rayleigh Index extrema presented above on a scatterplot showing their position as a function of the frequency at which the peak value occurs versus the magnitude of the peak. This data is presented in Figure 3-24.

For low nozzle exit velocity ratios (corresponding to $V_R = 2.0$ and $V_R = 2.5$) the extrema appear to lie on their own independent branches. These can be seen as the dotted lines in the figure. (Note that these are linear fits and only appear curved due to the logarithmic frequency

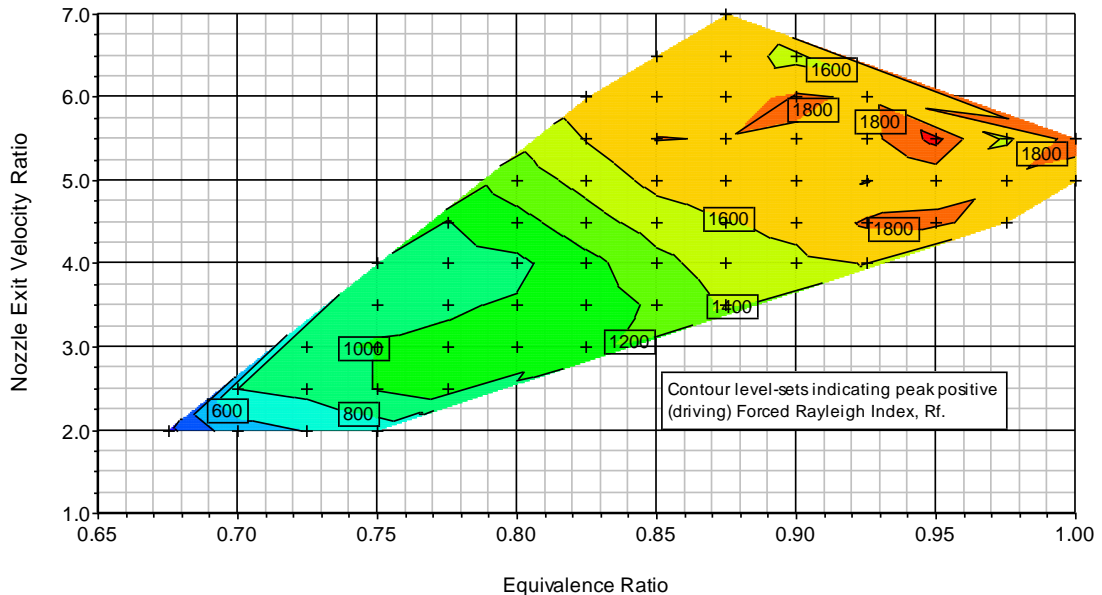


Figure 3-20: Interpolated contour level-set showing the peak positive (driving) forced Rayleigh index observed over the burner operating envelope. Cross-hairs indicate the locations of experimental data points.

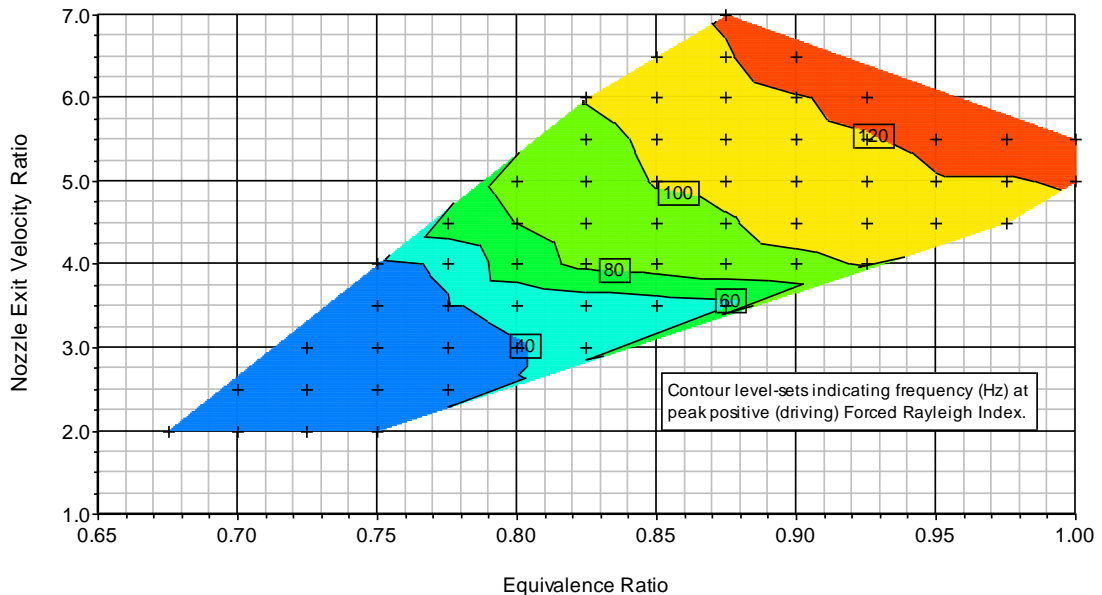


Figure 3-21: Interpolated contour level-set showing the frequency (in Hertz) of the peak positive (driving) forced Rayleigh index observed over the burner operating envelope. Cross-hairs indicate the locations of the experimental data points.

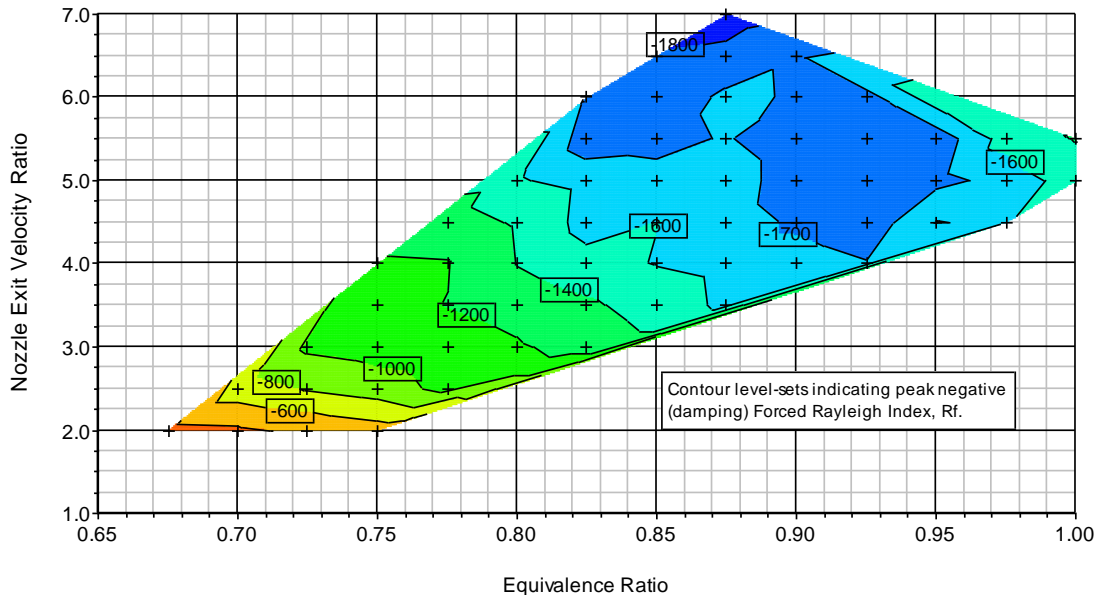


Figure 3-22: Interpolated contour level-set showing the peak negative (damping) forced Rayleigh index observed over the burner operating envelope. Cross-hairs indicate the locations of experimental data points.

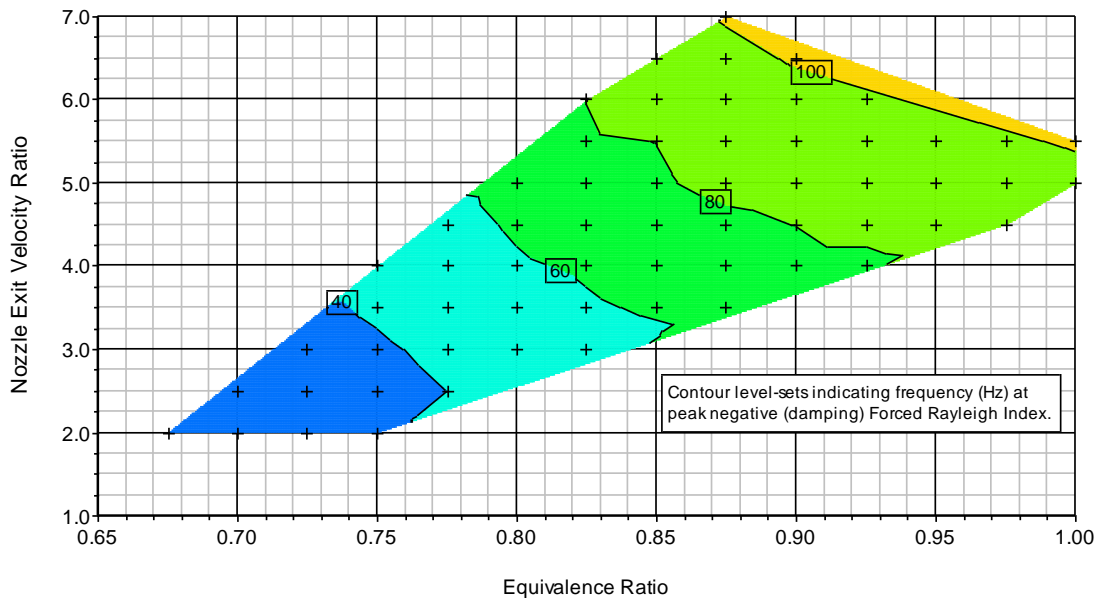


Figure 3-23: Interpolated contour level-set showing the frequency (in Hertz) of the peak negative (damping) forced Rayleigh index observed over the burner operating envelope. Cross-hairs indicate the locations of the experimental data points.

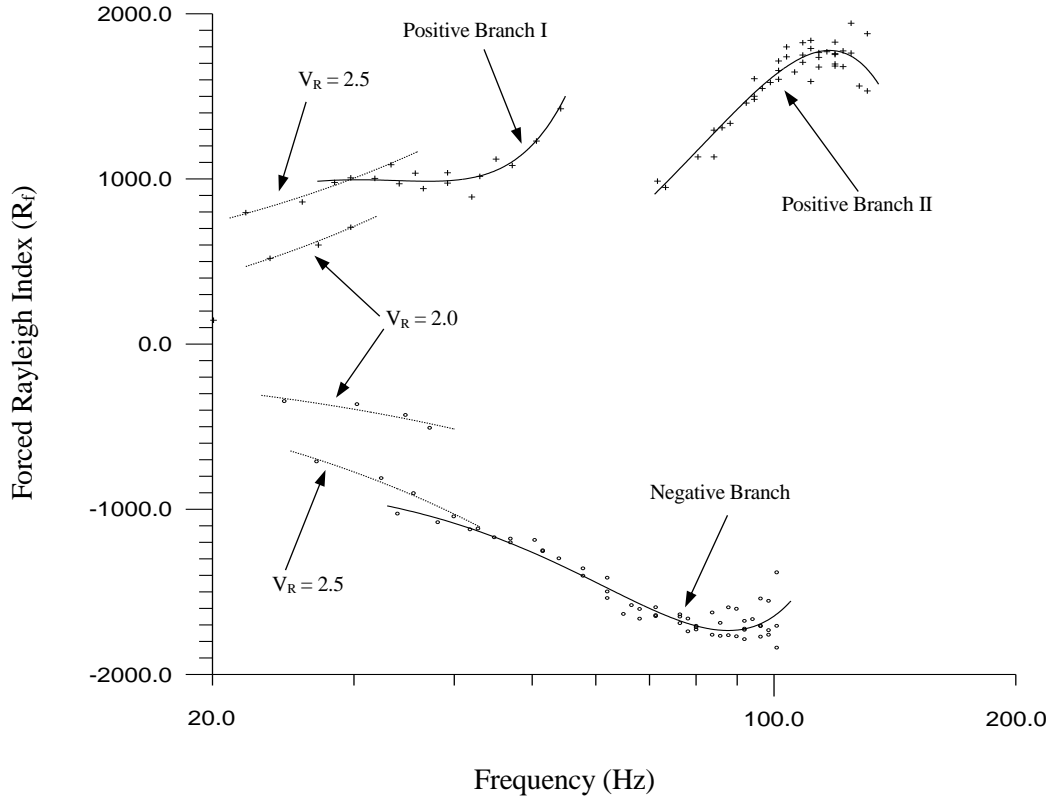


Figure 3-24: Scatter plot of the extrema of the forced Rayleigh index for all experimental test conditions. These are plotted as extrema location (frequency) versus extrema magnitude. Both positive and negative branches are shown.

axis.) However, for all higher velocity ratios, the data points appear to collapse into collective branches. A single “continuous” negative branch appears near the bottom of the plot. The term “negative” is used to identify this as the branch formed by the peak negative (damping) values of the forced Rayleigh index. At the top of the plot, two distinct positive branches are present. There is a very noticeable gap between the end of the first positive branch and the beginning of the second positive branch. This gap in frequency spans 54.1 to 71.4 Hertz. The R_f magnitude of the last data point in the first positive branch is approximately 1430 while the magnitude of the first data point in the second branch is approximately 990.

The reason for this discontinuity is unclear and requires further investigation. However, the resulting implication is this: for the given burner configuration, there is a band of frequencies

lying between 54 and 71 Hertz for which the burner has no maximum sensitivity, regardless of operating condition (i.e. equivalence ratio and nozzle exit velocity ratio.)

3.4.6 Phase Branch Bifurcation Revisited

With the forced Rayleigh index in hand, it is now possible to reexamine the two datasets presented in Figure 3-15. With the Rayleigh Index plotted for both test cases 86 and 116 on the same graph, a surprising realization is made. This can be seen in Figure 3-25. Inspection reveals that the forced Rayleigh index for both datasets is essentially coincident, both before and after the bifurcation, despite the dramatic difference in phase trajectories. Only in the vicinity of the bifurcation is an upset seen. At the phase bifurcation location (around 238 Hz), R_f for the two dataset suddenly diverge. They reach a peak separation at a frequency of approximately 245 Hz, with the R_f for dataset 86 taking a strong positive value while the R_f for dataset 116 obtains a strong negative value. The total separation in Rayleigh Index at this location is approximately 870. Within 10 Hz of this separation, the two indices collapse back to being nearly identical, and maintain that relationship all the way to the high frequency drive limit. This is in spite of the fact that dataset 116 exhibits oscillatory phase behavior for approximately 150 Hz after the upset, while dataset 86 shows an ever-increasing phase lag over the same period.

The mechanism behind this unusual behavior is yet unknown. The fact that both experimental runs produce an upset (albeit with opposite sign) at this particular location lends credibility to the notion that this is a real physical phenomenon versus an instrumentation malfunction. Further investigation is warranted, first using the chemiluminescence system with high resolution frequency scans in the region of interest. Depending on what is observed, it may then be desirable to engage in the use of phase resolved PLIF to provide spatially resolved data that can shed insight into the mechanisms involved.

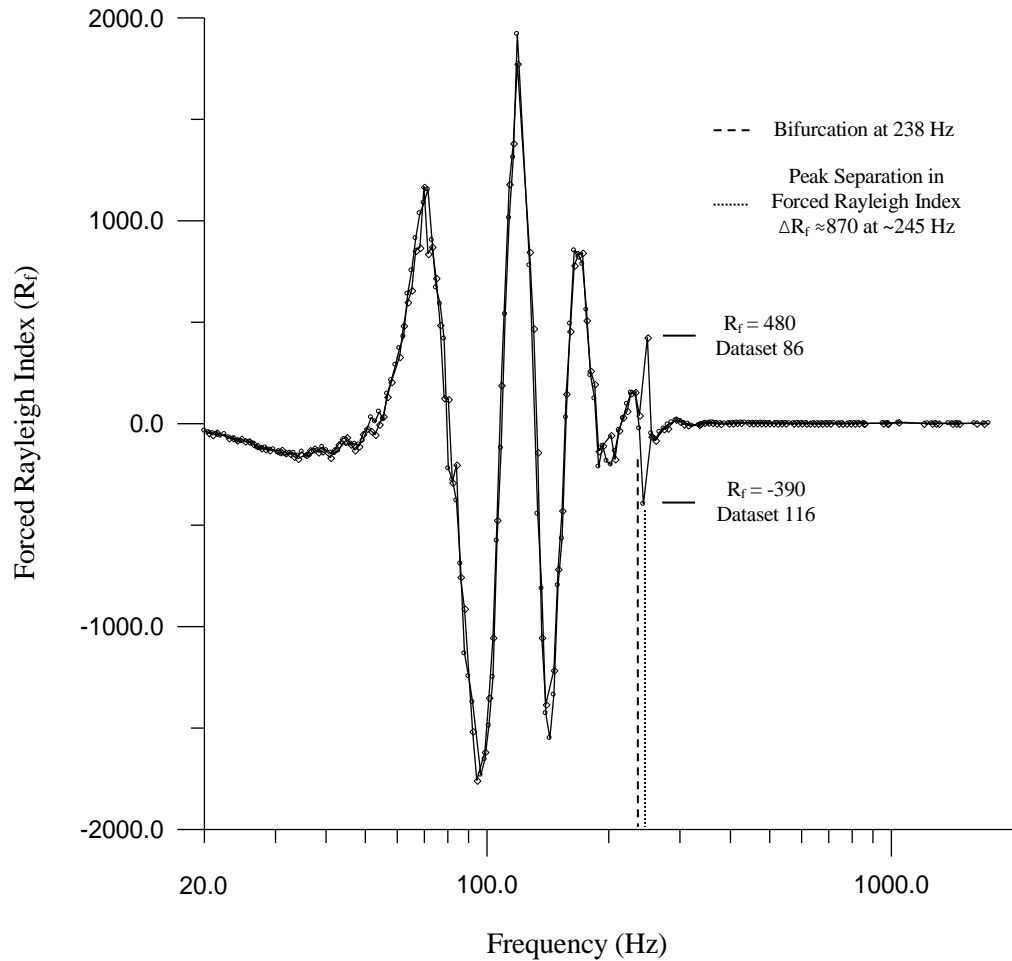


Figure 3-25: forced Rayleigh index, R_f , for parametrically identical test runs 86 and 116. R_f for both runs appear to be essentially coincident, both before and after the bifurcation seen in Figure 3-15. Only an upset is seen in the vicinity of the bifurcation where the Forced Rayleigh Indices for the two cases take opposite polarity.

C h a p t e r 4

SPATIALLY RESOLVED EXPERIMENTAL WORK: PLIF AND IMAGE CHEMILUMINESCENCE

4.1 Overview

With bulk chemiluminescence experiments completed and the resulting data reviewed, it is now possible to step forward by selecting a particular burner-operating condition of interest and exploring its behavior using spatially resolved techniques. In the present chapter, a single operating condition for the experimental burner is chosen, and PLIF (Planar Laser Induced Fluorescence), as well as imaged chemiluminescence, is used to explore the p' to q' coupling mechanisms. The chosen condition corresponds to a nozzle exit velocity ratio (V_R) of 4.0 and an equivalence ratio (ϕ) of 0.85. This operating point is the same as used in the experiment represented by the example plots presented in Figure 3-4 of chapter 3. All other operating parameters are typical, with the exception of the acoustic drive amplitude which is held constant at 13.79 Pa RMS (equivalent to 116.8 dB SPL), a level that is twice the RMS pressure used in the bulk chemiluminescence experiments.

Imaging experiments are run at either seven or nine distinct acoustic drive frequencies. The seven base frequencies are: 55 Hz, 75 Hz, 100 Hz, 150 Hz, 220 Hz, 265 Hz, and 375 Hz. In addition, two of the image groups also included drive frequencies of 240 Hz and 243 Hz. The drive frequencies were selected after examination of the combustion response plot for the chosen burner operating condition. The first four frequencies were selected to span the range where the combustion response magnitude is near its maximum, but where different phases of the response are seen. All four of these frequencies lie in the pre-transitional region.

The next two drive frequencies were chosen to bracket the transition zone occurring at approximately 243 Hz. This is the location where the time-delay-like behavior of the combustion response gives way to the Helmholtz response of the burner nozzle, and then ultimately to the high frequency in-phase response of the system. The goal of closely bracketing this transition is to elicit some understanding of the mechanism (or mechanisms) involved in the conversion. In the test case examined, the transition is accompanied by a notch in magnitude and an upset in phase that exceeds 90 degrees.

The last base drive frequency (375 Hz) is centered on the Helmholtz response of the burner nozzle. This data is collected simply for comparative purposes and also to examine a case where feed-system modulation is likely to be the dominant mechanism.

The additional two drive frequencies of the 240 Hz and 243 Hz were added to the test matrix near the end of the experimental work. After analyzing some of the collected PLIF data, it was realized that it may be possible to observe coupling behavior in the notch portion of the combustion response function, despite the low global magnitude of the function in that frequency range. Only the datasets for CH and CH₂O contain data for these two supplemental drive frequencies.

4.2 PLIF Motivation

Laser measurement techniques such as LIF (laser induced fluorescence), Rayleigh and Mie scattering, Raman spectroscopy, LIBS (laser induced breakdown spectroscopy), LITA (laser induced thermal acoustics) and others have converged into a powerful diagnostic arsenal in the past two and a half decades. One of the principle advantages of these methods is that they are non-invasive and, to varying degrees, remote. As a result, they are well suited to combustion systems where obtaining accurate measurements can be difficult (if not impossible) by more traditional means.

A technique related to LIF, called planar laser induced fluorescence (PLIF) was chosen to be the principal method used for the presented work. Unlike LIF, which produces a fluorescence signal for a point or line volume, PLIF allows a 2-D data field (or image) to be obtained. In this case, a UV beam from the laser source is formed into a thin sheet using cylindrical optics. The sheet is then passed through the combustion region under investigation, exciting specific electro-vibronic modes in the targeted molecular radicals. Some of the radicals in the excited state fluoresce, producing a signal that can be imaged by an intensified CCD camera positioned at right angles to the laser sheet. These images provide information related to spatial and temporal distribution of the fluoresced species.

The spatial resolution of such a system is on the order of the projected camera pixel area multiplied by the laser sheet thickness. In the system used for the presented work this is on the order of $100\text{um} \times 100\text{um} \times 250\text{um} = 2.5 \times 10^{-12} \text{ m}^3$ for the integrated volume per pixel. In addition to tight spatial resolution, PLIF also provides superior temporal resolution. The ICCD cameras used in these systems employ a gated intensifier tube with a photocathode transition time on the order of a few nanoseconds. Typical fluorescence lifetimes of the measured species are on the order of tens of nanoseconds. Therefore, in relation to the unsteady phenomena being measured in combustion instabilities (which have frequencies in the acoustic range), the images captured by the PLIF system are essentially instantaneous and devoid of any motion blur.

This is in stark contrast to the more common technique of imaging passive chemiluminescence of CH^* and CO_2^* . Passive imaging suffers from two major difficulties. The first is that the selectivity over the depth of field is poor. All the light captured by the camera lens in the solid-angle field of view is deposited on the focal plane somewhere, even if it is out of focus.

As such, the chemiluminescence is integrated over the depth of the flame but is not projected on the focal plane properly (except for that light which originated at the corresponding object plane.) In recent years, computational post-processing techniques have been applied in an

attempt to correct this problem; the most notable of these being the use of Abel deconvolution (Smith et. al., 2001) This has shown marked success in many cases. Nonetheless, it does not address the second major drawback of passive imaging which is the loss in temporal resolution. Compared to the PLIF imaging, the integration times required for passive chemiluminescence imaging in a combustion system can be orders of magnitude longer. Typical chemiluminescence integration times can be on the order of 10us to 100us versus 100ns seen in PLIF imaging. With such long integration periods, motion blur becomes an issue and feature detail can be lost.

In addition to the PLIF data collected, a set of experimental runs using chemiluminescence imaging were also performed on the experimental combustor at the previously indicated test conditions. These results will be compared with both the PLIF results as well as the bulk chemiluminescence measurements.

4.3 LIF Theory

In principle, laser induced fluorescence measurements involve a three-step process. The first step is to excite the radical or species of interest. This is typically accomplished using a tunable, pulsed UV laser. The laser wavelength is tuned to a target absorption line corresponding to a particular electronic transition in the species being probed. The second step is fluorescence where some fraction of the molecules or radicals will return to the ground state energy by emitting a photon. Not all excited species' members follow this pathway as there are other competing mechanisms that will be discussed in the next section. The third and final step is detection. This involves collecting and measuring the fluorescence photons, typically with a photo-multiplier tube (PMT) or an intensified CCD camera.

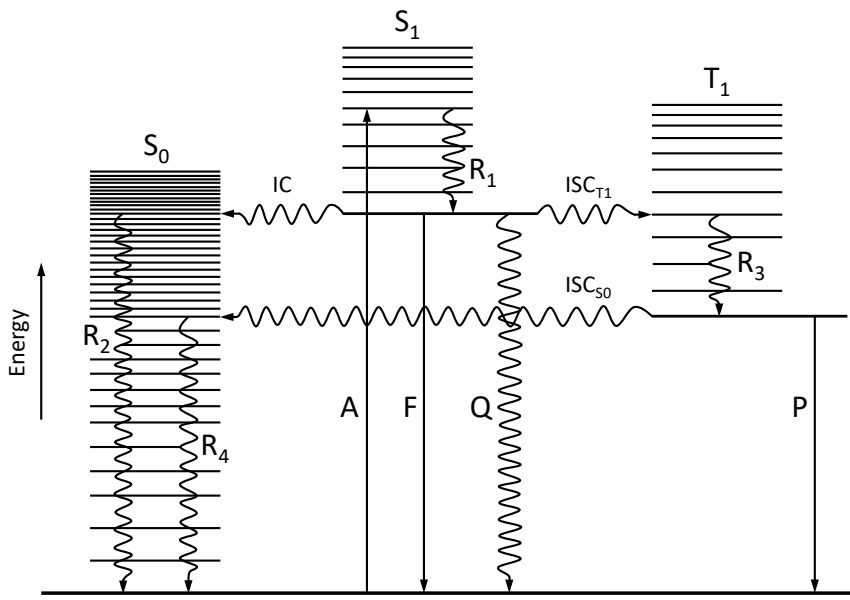


Figure 4-1: Simplified Jablonski diagram illustrating the possible electronic processes in a molecule or radical after absorption of a photon. Note that only the first excited state is shown.

4.3.1 Electronic Spectroscopy

The absorption and fluorescent emission of energy by the target species constitutes the basis of the technique and requires the greatest explanation. Figure 4-1 shows the Jablonski diagram which illustrates the possible electronic processes in a diatomic molecule following the absorption of a photon (Bertolucci and Harris, 1989).

The diagram shows three electronic states; these are S_0 which is the singlet ground state, S_1 which is the first singlet excited state, and T_1 which is the first triplet excited state. The solid, darker lines at the bottom of each state indicate the ground vibrational mode for that state. Parallel lines stacking upward mark progressively higher vibrational modes. The straight-lined arrows indicate a transition that involves the absorption or emission of a photon. Wavy-lined arrows indicate energy transfers or losses that don't involve a photon.

In the application of LIF, a pulsed UV laser is tuned to a specifically chosen absorption line of the target species. An incident photon that is absorbed transfers this complex from the S_0

state to the S_1 state. This is shown as the arrow labelled 'A' in the Jablonski diagram. Typically, this transition does not involve the electron transferring to the S_1 ground vibrational mode. Instead, a transfer to a higher vibrational mode may be favored depending on the overlap of wave-functions (known as the Franck-Condon factor). This is actually advantageous in LIF for reasons that will become clear.

Once in the excited state, the species quickly experiences vibrational relaxation. This occurs when collisions with surrounding neighbors convert vibrational energy into heat. In the process, the complex's state decays to the lowest vibrational mode for S_1 . This is seen as the wavy arrow R_1 in Figure 4-1. The lifetime of this relaxation is typically 10^{-15} to 10^{-9} seconds.

From the ground vibrational state of S_1 several competing paths become available. The desired path is fluorescence which is shown as the straight-line arrow marked 'F'. Transition from the vibrational ground state of S_1 to a low order vibrational state of S_0 produces a photon with lower energy than that used in the initial excitation. Furthermore, the photon emission has no directional preference. The shift in wavelength allows collection of this light using band-pass or long-pass filters to block contamination from the shorter wavelength laser source. The omnidirectional nature of the emission allows the detector to be placed at right angles to the source, facilitating PLIF imaging.

Unfortunately fluorescence is not the only path that can be taken. Competing with this are other paths created by internal conversion (IC), intersystem crossing (ISC) and direct quenching (Q) mechanisms. These, as a group, are usually classified as collisional quenching. Internal conversion is a process by which an electron in the ground vibrational state of S_1 can move laterally across the energy diagram to a higher vibration mode of the S_0 electronic ground state. This is seen as the wavy arrow labelled IC in the Jablonski diagram. Once in this configuration, the associated vibrational energy is quickly dissipated through collisional relaxation as represented by R_2 .

Another possibility is for conversion from a singlet to a triplet state. This is considered an intersystem crossing and is represented by the wavy arrow labelled ISC in Figure 4-1. Here, not only does a lateral move on the Jablonski diagram occur, but the involved electron flips spin, putting itself in a triply degenerate spin state (i.e. spin multiplicity). Once this happens, fluorescence can no longer occur since it is now spin-forbidden. Photon generation can still occur, but the process is slow, requiring time scales on the order of 10^4 to 10^2 seconds. This is referred to as phosphorescence and is designated as ‘P’ in Figure 4-1.

Finally, a direct quenching pathway is available through mechanisms like Förster or Dexter transfers. In this case, molecular collisions with surrounding neighbors directly extract the excited state energy and return the system to the electronic ground state. This is illustrated as the arrow “Q” in the Jablonski diagram.

Rates of collisional quenching are difficult to predict and are direct functions of the surrounding species populations. This becomes problematic when attempting to make quantitative measurements of species concentrations using LIF since knowledge of the collisional partners and their concentrations, as well as the local temperature and pressure, is required. This is discussed in more detail below.

Allen, McManus and Sonnenfroh (1995a) proposed that the LIF fluorescence signal can be approximated using a two-level steady state model given by the equation:

$$(4-1) \quad S_f = \eta \left(\frac{\Omega}{4\pi} \right) V_c I_v \left[\frac{A_{eff}}{A + Q(\chi_p, P, T)} \right] \chi_j P_t \sum_i \left[f_{B,i}(T) B_i g_i(v, P, T) \right],$$

where the following terms are defined:

η	=	quantum efficiency of the detector
Ω	=	collection optics solid angle
V_c	=	collection volume of one "detector pixel"
I_v	=	excitation source spectral fluence
A_{eff}	=	effective Einstein coefficient of spontaneous emission
A	=	Einstein coefficient for spontaneous emission
$Q(\chi_p, P, T)$	=	electronic quenching rate
χ_j	=	mole fraction of measured specie j in measurement volume
P_t	=	total gas pressure
B_i	=	Einstein coefficient for stimulated emission for transition i
$g_i(v, P, T)$	=	overlap integral (convolution of absorption line and laser lineshape)
$f_{B,i}(T)$	=	Boltzmann fraction of absorbing specie in state i.

The beauty of equation (4-1) is that it shows a relation between the fluorescence intensity that is linearly proportional to the mole fraction of the species of interest within the probe volume. This elicits the hope that quantitative measurements can be made given the proper corrections for competing quenching processes.

4.3.2 Collisional Quenching

Accounting for collisional quenching in PLIF measurements of combustion systems has proved arduous, to say the least. In some lucky cases (such as LIF of acetone), no corrections are needed since variations in the quenching rate are dwarfed by dominant conversion processes. The result is a very low, yet very consistent quantum yield that provides a linear relation between the acetone concentration and the fluorescence (Lozano et. al., 1992).

For the less fortunate cases, numerous models for quenching corrections have been produced, the most notable ones being from Paul et. al. Specifically, Paul et. al. (1994) have produced models for correcting both OH and NO LIF which show good agreement with others' empirical correlations. These models define the quenching rate as

$$(4-2) \quad Q = \langle v_j \rangle \langle \langle \sigma(\chi_i, T) \rangle \rangle \frac{P}{k_B T},$$

where

$$(4-3) \quad \langle v_j \rangle = \left(\frac{8}{\pi} \frac{k_B T}{m_j} \right)^{1/2}$$

and the total electronic quenching cross-section is given by

$$(4-4) \quad \langle \langle \sigma(\chi_j, T) \rangle \rangle = \sum_i \chi_i \left(1 + \frac{m_j}{m_i} \right)^{1/2} \langle \langle \sigma_i(T) \rangle \rangle.$$

Nonetheless, these models still require knowledge of the temperature, pressure and species concentration in the probed volume.

An alternative method to modelling is to directly infer the quenching rate by direct measurement of the fluorescence decay rate. This technique has been demonstrated by Kollner and Monkhouse (1995), as well as Cadou (1996). Typical decay times are on the order of just a few nanoseconds. As a result, an extremely fast detector and data collection system are required. In addition the setup must exhibit extremely low jitter in its time-base. This has typically been achieved using photomultiplier tubes and associated electronics, with the unfortunate restriction that only point measurements can be taken. Although an ICCD could be used to generate 2D images, the current technology does not exist to obtain the needed readout rates. For experiments that are steady or exhibit strict periodic behavior, multiple independent imaging shots can be collected to form the fluorescence decay database needed; however, great attention is required to insure proper timing.

For the unsteady combustion work at hand it is assumed (albeit dubiously) that the temporal variations in the collisional quenching rates are small. Since the measurements involve the ratio of varying fluorescence signals over their average, it is then supposed that the errors induced into this

ratio due to the above variations will also be small. Consequently, no attempt is made to correct for collisional quenching.

4.4 Laser, Delivery Optics and Imaging System

4.4.1 Laser Light Source

The PLIF experiments use a custom-designed laser system as the source for UV tunable laser light. The system incorporates a home-brew short-pulse Nd:YAG laser constructed on the bed of an old Quantel YG581. This laser employs an unstable resonator and two stages of amplification. The laser operates at 10 Hz with a typical pulse duration of 8 to 10 ns and with a maximum output pulse energy of 2 Joules at 1064 nm. Frequency doubling with a KTP SHG produces in excess of 1 Joule at 532 nm.

The YAG laser pumps a totally novel and custom-built, tunable, ring-cavity optical parametric oscillator (OPO). The OPO incorporates intra-cavity doubling and mixing allowing a wide range of UV output wavelengths to be produced. These include 226 nm for NO PLIF, 277 nm and 283 nm for acetone and OH PLIF, 352 nm for CH₂O PLIF, and 390 nm for CH PLIF. Details of the design, construction and capabilities of both the YAG laser and the OPO can be found in appendix E.

4.4.2 Delivery and Sheet-Forming Optics

UV light is directed out of the OPO by a right-angle prism followed by a Pellin-Broca prism which not only produces a second 90° turn but also provides wavelength selectivity. The second turn directs the beam down a long structure called “the bridge” and toward the test section. The bridge contains all the optics associated with forming the laser sheet. Figure 4-2 shows a photograph of the bridge while Figure 4-3 provides a drawing of the layout of the optical elements.

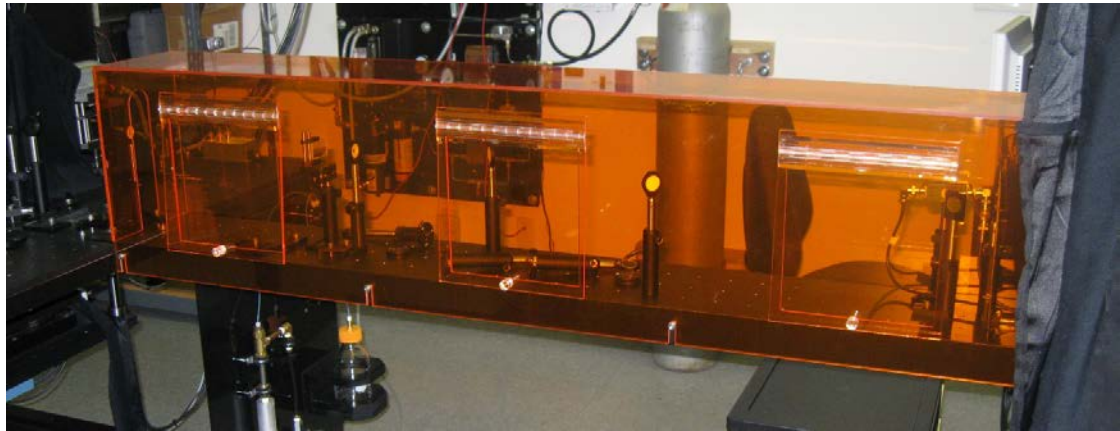


Figure 4-2: Photograph of “the bridge” with orange acrylic optical guard installed. The bridge contains the laser pulse measurement photodiode, as well as apertures and sheet-forming optics. Beam path is from right to left.

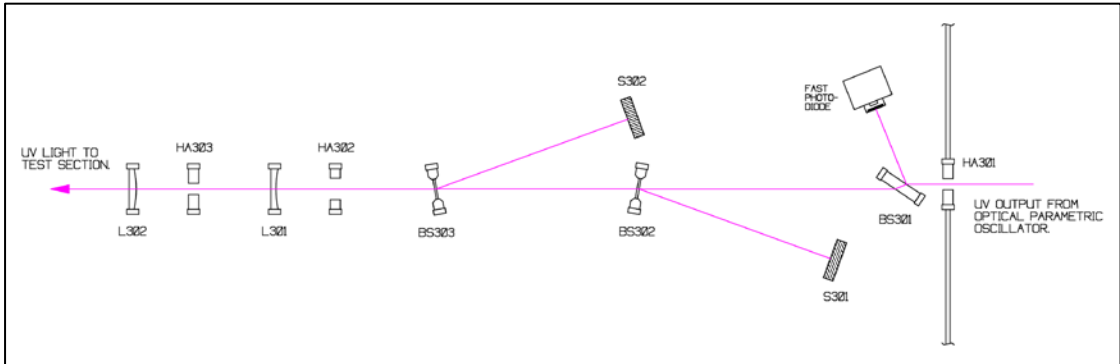


Figure 4-3: Layout of optical elements on the bridge. Beam path is from right to left. Beam splitters BS302 and BS303 are on magnetic kinematic mounts and are removable. Note that the drawing is not to scale.

In the layout above, the beam path is from right to left. The beam exiting the harmonic separator of the OPO passes through aperture HA301. This is a white PTFE disk 25.4 mm in diameter and 6 mm thick, containing a 7.5 mm round hole through the center. The disk is mounted in a Thor Labs FMP1 fixed optic mount. (The same type of mount is also used for beam-splitter BS301, apertures HA302 and HA303, and beam stops S301 and S302.) A section of black poster-board is used to continue the stop beyond the edges of the mount. The poster-board section is rectangular, being 200 mm wide and 280 mm tall and containing a hole coincident with the location

of HA301. The hard-aperture along with its poster-board accessory allows the desired UV laser beam to pass while blocking all other harmonics separated by the Pellin-Broca prism.

After leaving the aperture, the UV beam passes through beam-splitter BS301. This beam-splitter is simply an uncoated fused-silica window (Edmund Optics P/N 43-424) rotated near the Brewster angle. A small amount of the laser energy is reflected from the surface and into the photodiode assembly. The remaining light passes through the optic. The photodiode energy detector is a custom built assembly fabricated around a fast photodiode purchased from Thor Labs (P/N FDS010). A 10 mm diameter, ground fused silica optical diffuser (Edmund Optics P/N 49-155) is mounted on the assembly just in front of the photodiode to help spatially balance the light being measured. The photodiode is properly reverse biased in order to achieve the specified 1 ns response time and is terminated to a 50 Ohm output. A 50 Ohm coaxial cable feeds this signal directly back to the AFC-100 instrument. The AFC-100 not only uses this signal for measurement of laser shot timing, but also to measure and record the energy of each shot.

After leaving BS301, the UV beam travels down the bridge where it may encounter two optional beam-splitters, BS302 and BS303. These elements are mounted on internally-threaded, fixed optics holders (Thor Labs P/N LMR1), which are attached to magnetically-secured kinematic bases (Thor Labs P/N SB1). As such, they can be installed and removed as needed. These beam-splitters are used to strongly attenuate the laser sheet passing into the test section without changing its lateral position or intensity distribution. This is required when taking measurements of the laser sheet intensity profile for image post-processing. (Further details of this procedure are discussed in section 4.4.4) The beam-splitters are manufactured by CVI Laser Optics (P/Ns UVDA-266-1.00-10 and UVDA-266-1.50-10). Under normal PLIF imaging conditions, BS302 and BS303 are removed.

Finally, the laser enters the sheet-forming section. The beam first passes through aperture HA302. This aperture is not circular, but instead is a horizontal slot with full-radius ends. The

element is fabricated from a white PTFE disk, 25.4 mm in diameter and 6.0 mm thick. The machined slot height is 7.0 mm and the length along the centerline is 19.5 mm. This crops any out-of-position rays in the vertical direction. After clearing the HA302, the beam passes through L301, a plano-concave cylindrical lens with focal length -500.0 mm (Thor Labs P/N LK4989-UV). This lens is mounted using a kinematic platform mount (Thor Labs P/N's CH1A and KM100B) and is oriented to expand the beam in the vertical direction.

The vertically expanding beam is then passed through another slot aperture, HA303. This aperture is identical to HA302 with the exception that the slot is oriented vertically, blocking any out-of-position rays in the horizontal direction. After clearing HA303, the beam passes through L302, a plano-convex cylindrical lens with focal length +500.0 mm (Thor Labs P/N LJ4147-UV). The lens is mounted similarly to L302, but with a slightly larger mount (Thor Labs P/N's CH2B and KM100B). It is oriented to compress the beam in the horizontal direction, forming a thin sheet.

After leaving the bridge, and just prior to entering the test section, a final pair of independently adjustable aperture plates are used to trim the laser sheet to the correct height. The plates are adjusted such that the top of the laser sheet slightly grazes the bottom of the burner stagnation body, and the bottom of the laser sheet clears the top of the burner nozzle.

4.4.3 Imaging System

The imaging system used to resolve PLIF emissions or image chemiluminescence employs an Andor Technologies iStar ICCD camera, model number DH712-18F-03 (S/N ICCD-3056). The camera incorporates a 512x512 pixel E2V focal plane as well as a DEP photo-intensifier for light amplification and gating. Details of the imager are presented in chapter 2.

Two different lenses are used in conjunction with the ICCD. For CH and CH₂O PLIF, as well as chemiluminescence imaging, a Nikon Nikkor 50 mm f/1.2 lens is used. This was possible since the signature photons emitted in these experiments are near or within the visible wavelength

range. For the experiments with emissions at shorter wavelengths (OH and acetone PLIF) a Cerco 2085 UV lens is used. This lens has a focal length of 94 mm and an aperture number of f/4.1. Custom spacers and a filter mount were fabricated for use with the Andor F-mount lens adapter. The spacers make it possible to realize identical object-to-image ratios for both lenses. The filter mount allows 25.4 mm diameter circular filters to be installed in front of the intensifier photocathode, thus providing wavelength selectivity for the collected emissions.

In the experimental setup, the ICCD camera is mounted at right angles to the incoming laser sheet. From the imaging point of view, the laser sheet is approaching from left to right. Efforts were made to configure each camera and lens pair such that a single focal-plane pixel corresponds to a 100 μm unit square in real object space.

4.4.4 Laser Sheet Intensity Profilometer

When processing the data from the PLIF experiments, it is necessary to correct for the spatial variation in intensity over the laser sheet. The UV laser beam passes through the plano-concave lens (L301) on the bridge and begins expanding in the vertical direction. Since the laser beam does not have uniform intensity in the radial direction (but something closer to Gaussian), the laser sheet also has a spatial intensity distribution. Of greatest concern is the variation in the vertical direction. The system can be modelled as rays emanating from the virtual focus of L301. By knowing the intensity along a somewhat vertical path (i.e. a path that is not close to being parallel with the light rays), it is possible to use ray-tracing to infer the pump intensity over the entire field covered by the laser sheet.

To accomplish the measurement of intensity along a vertical path, a simple profilometer tool was constructed. Photographs of this tool are shown in Figure 4-4. The body of the tool is designed to attach to the side of the test section in place of the port-hole cover. A pair of 6.35 mm diameter push-pull rods allow small beam-stops to be moved in and out of the laser sheet path.

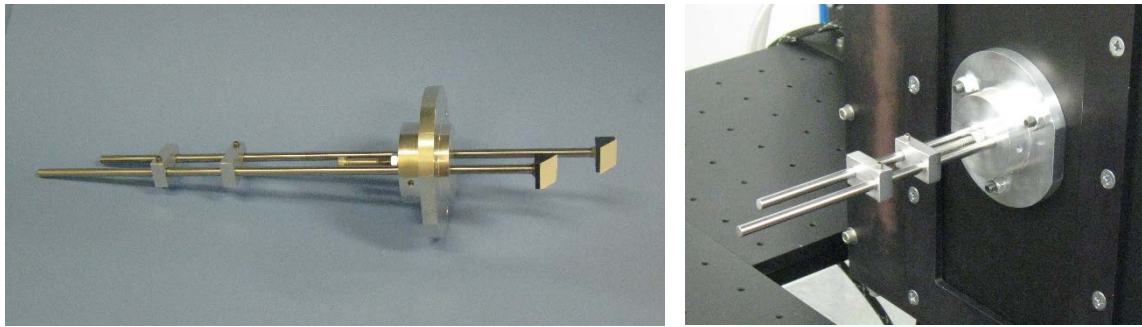


Figure 4-4: Left – laser sheet profilometer tool with rear beam-stop partially deployed and front beam-stop retracted. Right – profilometer tool installed in chamber test section.

Integral mechanical guides and stops prevent the rods from rotating and also set the proper depth of the beam-stops when fully engaged, resulting in good positioning repeatability. The faces of the beam-stops are mitered at 45° and covered with white fluorescent card stock. The height and position of the beam-stops is such that they graze the bottom of the burner stagnation-body, and clear the top of the burner nozzle by approximately 1 mm.

When taking a laser sheet profile reading, the UV beam is heavily attenuated by inserting beam-splitters BS302 and BS303 on the bridge. Additionally, the ICCD camera gain is set to minimum. The profilometer beam-stop that is farthest from the sheet forming optics is inserted first. From the camera's point of view, the incident laser sheet forms a line on the fluorescent card that appears to the right of the burner nozzle, near the right most edge of the image. The ICCD then takes a group of images of this intensity distribution (typically 200 images). Afterward, the second profilometer beam-stop is inserted. The camera sees this as a new vertical line to the left of the burner nozzle, with the previous line on the right vanishing due to the blockage. Again, another group of images are taken (typically 200). These images along with the ray-tracing routines in the data processing software are used to generate the desired laser sheet intensity map. The map data is then used by other subroutines for image corrections.

It should be noted that the profilometer tool is not left installed during normal experimental runs. It is only installed for laser sheet profile measurements and then promptly removed. Laser sheet profile measurements are taken at the beginning and end of every experimental run.

4.5 General Data Collection Procedure

As discussed in chapter 2, the entire experiment execution and data collection process is orchestrated by the master controller PC that runs the OPOv125 software. The actual operational sequence is dictated by script files that run under this software. Prior to script execution, numerous preparatory operations need to be performed. These include the following:

- 1) Laser Preparation
 - a) Configure OPO for desired wavelength band.
 - b) Warm up Nd:YAG laser and OPO.
 - c) Load calibration tables for OPO and tune to desired wavelength. Verify wavelength with Burleigh wavemeter.
- 2) Burner Preparation
 - a) Warm up fuel/air system control electronics.
 - b) Check air system filters and change desiccant load.
 - c) Open reactant feed valves. Adjust desired equivalence ratio on controller.
 - d) Open burner feed valve and adjust needle-valve for desired burner flow rate.
 - e) Light burner.
- 3) ICCD Camera Preparation
 - a) Run the Andor iStar software and load the setup file.
 - b) Configure free parameters not stored in the setup file (TE cooler temperature, and starting dataset number).
 - c) Verify fluorescence imaging and focus.

- d) Load and start the AndorBASIC program that controls the operation of the camera and communicates with the AFC-100.
- 4) Data Acquisition System Preparation
 - a) Warm up all instruments.
 - b) Run through AFC-100 setup parameter checklist.
 - c) Calibrate the photodiode energy monitor.
 - d) Run the AFC-100 routine to calibrate the acoustic drive phase offset.

Once all preparatory steps are completed and the experiment is ready to begin, execution of the associated experiment script file is started in the OPO software. A typical script file sequences an experiment through the following steps:

- 1) Set up the data collection and transfer configuration within the AFC-100, including the phase bin precession rate.
- 2) Collect background images with no laser sheet present, and without the burner operating.
(Collect 2 sets of 200 images = 400 total).
- 3) Collect background images with laser sheet present, but without the burner operating.
(Collect 2 sets of 200 images = 400 total).
- 4) Collect laser sheet profile images with profilometer. Capture 200 images with the right (far) beam-stop engaged. Capture 200 images with the left (near) beam-stop engaged.
- 5) Signal the operator to remove the profilometer, light the experimental burner and then leave the laboratory. Enter into fully autonomous mode.
- 6) After warm-up period, collect steady PLIF images with no acoustic forcing. (Collect 2 sets of 200 images = 400 total).

- 7) Bring acoustic forcing up to the desired drive level. Wait for amplitude controller to equilibrate. Engage the phase-targeter with automatic phase-angle precession enabled. (15° automatic precession is typical).
- 8) Begin collecting acoustically forced PLIF data. Capture 200 images per data group. Repeat group capture process 48 times, collecting a total of 9600 images.
- 9) Ramp the acoustic drive amplitude back down to no output.
- 10) Collect more steady PLIF images with no acoustic forcing. (Collect 2 sets of 200 images = 400 total).
- 11) Transmit signal to belt-pager requesting the operator to return to the laboratory.
- 12) Signal the operator to extinguish the burner and install the profilometer.
- 13) Collect more laser sheet profile images with profilometer. Capture 200 images with the right (far) beam-stop engaged. Capture 200 images with the left (near) beam-stop engaged.
- 14) Signal the operator that the experiment is finished.

It should be noted that all references to captured image groups in the above list also include the capturing of corresponding datasets from the AFC-100. These datasets include the acoustic waveforms, laser shot timing and laser shot energy associated with each image.

4.6 First-Pass Data Reduction

Image and data reduction is performed by an image processing program written specifically for this purpose. This program, called PLIF_II, is written entirely in GNU C (gcc) and runs under Linux. The program handles both the Andor .sif files and the data files from the AFC-100 directly. From these it produces its own native files (.spif) with all the related data internally linked.

The PLIF_II program provides a semi-interactive interface allowing the user to run individual commands to perform specific data manipulation or reduction operations. However, the most powerful use of the program is through its interpreted scripting language. This allows the crafting of complicated data reduction sequences that may take quite some time to execute. These scripts can then be started and left to run unattended.

The scripts that are constructed can vary quite a bit in structure depending on the goal of the given script file. Nonetheless, the core procedures in the process are typically the same. The following sections describe the functions of the most common of these procedures.

4.6.1 Data Merging

The data merging process combines the image files collected from the Andor ICCD camera and the data files generated by the OPO software (from the data collected by the AFC-100). An .sif image file and the corresponding .dat data file are loaded and then combined into a native format record called SPIF (Standard PLIF Image File). The resulting group is then written out to a file with the .spif extension. It is these files that are used during all of the following data processing.

4.6.2 Background Image Generation

A background image is created in order to correct the data images for errors associated with intrinsic camera offsets such as CCD dark charge and CCD amplifier offset error, as well as for stray (yet relatively constant) light sources in the field of view such as laser sheet scattering and radiosity effects.

The background image is generated by loading images from selected data files and averaging them together. The images used are those where the laser sheet is present, but the burner is not operating. Images can be selected from multiple source files. Typically 400 images are used

in the average. The background frame is then stored in a special background frame register for later application.

4.6.3 Image Phase Averaging

With the collected data and given tools, it is now possible to exploit the periodic nature of the acoustic forcing and the corresponding periodic response of the flame through the data reduction process. The first step in this process is assigning the number of phase bins that will be used. If phase targeting was used in the data collection process, then the number of bins selected should produce the same phase spacing as was used in targeting. For the current experimental work, phase targeting with 15° spacing was used. This corresponds to the selection of 24 phase bins.

Next, each image of the specified dataset is loaded and the acoustic data for that image is processed by FFT. The phase information from the FFT is used to locate the rising-edge zero crossing of the fundamental mode. This is labelled as the zero-degree point. Then the phase location of the laser shot is identified within the dataset. The difference of these locations is taken (modulo 360°) and the result is used to choose the appropriate phase bin. This procedure is shown schematically in Figure 4-5 for the case of eight phase bins. Prior to averaging the image into the prescribed bin, corrections (if needed) are applied for variations in total laser energy and for the “intensity and species concentration to fluorescence” function. These are handled on a case-by-case basis based on the species being fluoresced, and are discussed in the following sections. As mentioned earlier, due to the relative (ratiometric) use of the collected measurements, no attempt to correct for collisional quenching is made.

Depending on the processing steps used, the background image generated above may be applied on an image-by-image basis during the phase averaging process. Otherwise, once all the

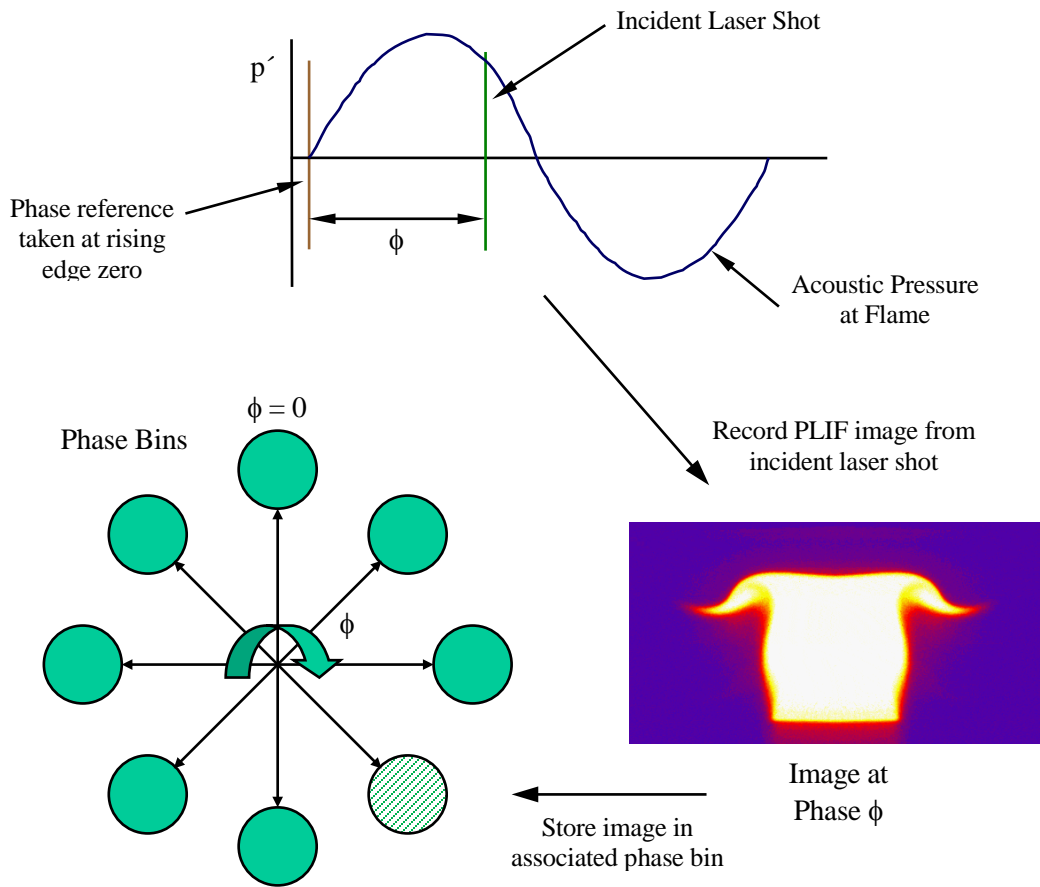


Figure 4-5: Phase-averaging procedure for PLIF or chemiluminescence images. The phase location at the time of the laser shot is determined and the image is averaged into the appropriate phase bin.

images from dataset files have been processed and averaged into their appropriate phase bins, the background frame is subtracted from each bin.

In the experiments presented a total of 9600 data images are taken per experiment for phase averaging. This corresponds to 400 images averaged per phase bin.

4.6.4 Report Generation

After the base reduction of the data is completed a detailed report can be generated. The report contains results from the phase-averaging process including spectral data for both the acoustic forcing, as well as for the response as seen in the varying fluorescence. The region of the

image field over which the fluorescence is integrated to generate this response scalar is called the interrogation window. This is a rectangular region and is defined by the operator.

From this data, the global combustion response and global forced Rayleigh index are both computed. These are presented in their “raw” format (for the planar image, as is) as well as properly spatially integrated (over radius) to give the true global results for the given axisymmetric case. Two lists of time-versus-magnitude ordered pairs are also output in the report file corresponding to the acoustic and fluorescence waveforms. Finally, certain statistical data is also recorded in the report file for validation of the reduction process.

4.6.5 Image Data Output

Another built-in command provides the ability to output frame data to image files for manipulation or plotting outside of the PLIF_II software. Images stored in frame registers (or any of the phase bins) can be output as individual .gif (graphics interchange format) files or as text data files in (x,y,z) triplet format for plotting purposes. If the .gif file option is chosen, the user has the ability to define the color map used.

Additionally, the phase bins can be output as a group into an animated .gif file. This allows the visualization of the unsteady response seen in the fluorescence. Again, the color map used is selected by the user.

4.7 OH PLIF Results

The first set of data to be presented is for OH PLIF. PLIF of the OH radical in flames has been prevalent for many years due to its accessibility and high signal-to-noise ratio. For the given experiments, excitation of the A-X(1,0) band near 283 nm was chosen. In particular, a group of overlapping Q-branch lines at 282.93 nm (λ -air) was selected. This is shown in Figure 4-6. This set of lines exhibits a strong LIF response as well as very good temperature stability. The penalty

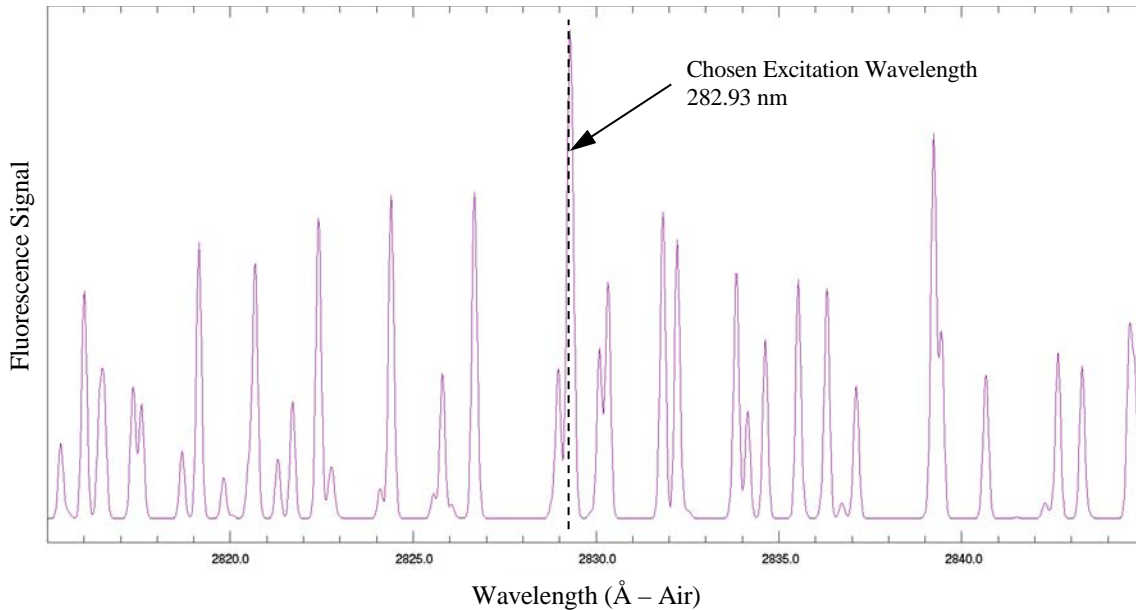


Figure 4-6: LIF excitation spectra of OH radicals around 283 nm as simulated by LIFBase 2.1.1. Pressure is 1 atm and temperature is 1500K. The chosen pump wavelength is shown at 282.93 nm (λ -air) and overlaps several Q-branch lines. Very little temperature variation is seen in the fluorescence.

paid here is that the absorption of the laser sheet as it transverses the flame is not negligible.

Corrections for this are made in the data reduction process as will be described later.

The OPO output energy at 283 nm was limited to approximately 10 mJ. During normal operation, the pulse energy averaged approximately 7.5 mJ at the entry window to the test section. Wavelength stability of the OPO was good over the duration of each experiment. Maximum variation in mean output wavelength was typically within ± 4 pm or about ± 0.5 cm^{-1} . This is significantly smaller than the linewidth of the OPO output.

Image collection was performed with the Andor ICCD camera coupled to the Cerco UV lens. A 3 mm thick WG305 Schott glass filter was installed in front of the intensifier to minimize interference from scattered 283 nm light.

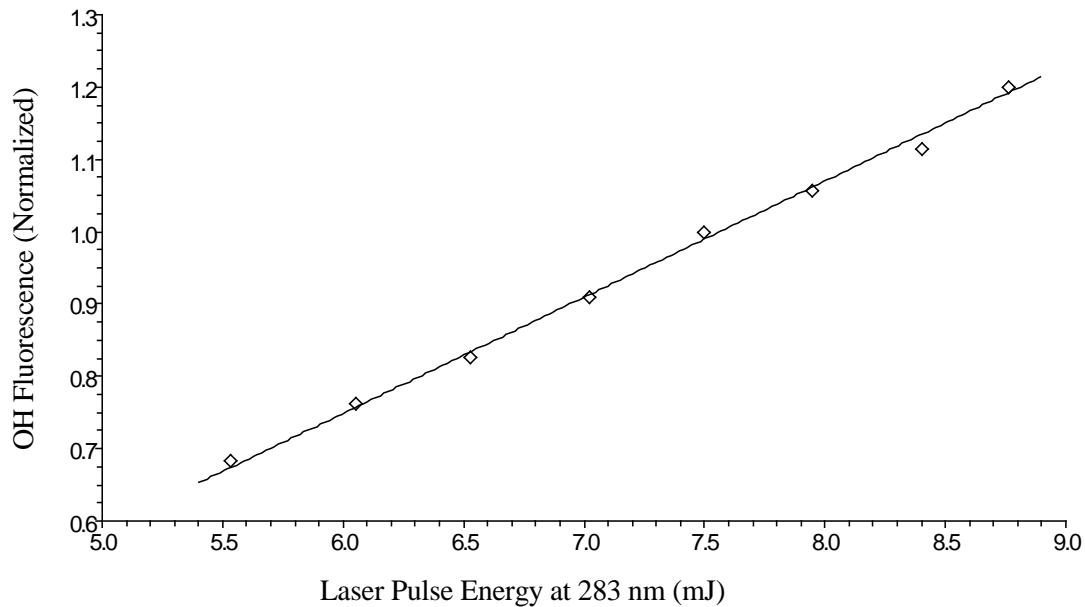


Figure 4-7: Fluorescence intensity of OH radicals in a steady flame versus laser shot energy. Diamond symbols specify resultant measurements at different energies. A solid line shows the least-squares linear fit to the data.

4.7.1 OH Excitation Regime

Given these modest pulse energies in combination with the OPO linewidth, it is necessary to investigate the OH fluorescence response as a function of laser pulse energy to determine the excitation regime (linear, saturated or other) in which the experiment is operating. Steady-state data (no acoustic forcing) from each experiment was analyzed by sorting the fluorescence images as a function of laser shot energy. The natural shot-to-shot variation of the laser pulse energy was used and no externally prescribed energy variation was necessary. The images were sorted (and averaged) into energy bins with 0.5 mJ spacing. The average image fluorescence (in regions of different vertical position, as well as over the whole flame) was used as the resultant for each bin. Figure 4-7 shows a typical result. At the given linewidth and excitation energy fluence, the OH fluorescence response was found to be in the linear regime. Diamonds in the plot correspond to results from individual energy bins. The solid line is the least-squares linear fit to this data. This

information is used by the data reduction software to correct for shot-to-shot variations in energy as well as variable intensity distribution over the laser sheet.

4.7.2 Correction for Spatial and Temporal Variation in Excitation

There are three principal adjustments applied during the data reduction process to correct for variations in laser sheet intensity. Two of these three require the accurate determination of the location (in relation to the image frame) of the virtual focus of the plano-concave lens (L301) that expands the laser beam in the vertical direction. This information is needed in order to perform virtual ray-tracing during these corrections.

The horizontal distance between the virtual focus and burner centerline has been accurately measured by mechanical means and determined to be 1484 mm. On the other hand, the height offset is slightly more difficult to determine. With great care, mechanical measurements can be made. However, as an alternative, a real ray-tracing method was chosen. In this technique, the attenuated laser sheet is allowed to pass through the sheet forming optics and into the test section. Just prior to entering the test section, the upper and lower edges of the laser sheet are slightly clipped by an iris (effectively knife edges on top and bottom). The profile of the laser sheet is then measured using the homemade profilometer described earlier. The corresponding end points of the two generated lines then define rays that pass back through the focal center. These end points are located algorithmically with an intensity-center-finding method which produces results down to a fraction of a pixel. Since the ‘x’ coordinate of the focal center is already known, the ‘y’ coordinate is determined by finding the intercept of one or both of these rays at the plane specified by the given ‘x’ coordinate. The accuracy and repeatability of the method is surprisingly good. Clipped laser sheet profile measurements are taken at the beginning of every experimental run in order to verify the sheet focal center location for that group of data.

With the virtual focus location in hand it is possible to proceed with the aforementioned intensity corrections. The first correction is simply for the shot-to-shot energy variation from the laser. This is applied to each collected frame after background subtraction has been performed. It is accomplished by multiplying each pixel in the image by $\left(\frac{I_0}{f(E)} \right)$ where $f(E)$ is the relation between measured intensity versus the laser shot energy and I_0 is a fixed reference intensity. The function $f(E)$ was determined in Figure 4-7 and found to be linear for the given OH PLIF experiments at the prescribed laser wavelength, linewidth and sheet energy fluence. This particular correction is typically applied during the phase averaging process.

After the entire dataset has been phase averaged, the remaining corrections are applied. The first of these is to correct for the spatial (vertical) variation in the laser sheet intensity. As covered in section 4.4.4, a simple profilometer was constructed to measure the laser sheet vertical intensity distribution. Using the images collected from the profilometer experiments and by tracing virtual rays through the generated lines back toward the virtual focus of L301, a correction frame is created that provides a local laser intensity multiplier at each pixel of interest. Intrinsic to this generation method is also the correction for the $(1/r)$ drop in the sheet intensity as the distance from L301 increases. Once this frame is generated, its reciprocal (element by element) is simply multiplied by each image frame.

Finally, the last correction is applied to adjust for the laser sheet absorption as it passes through the flame. In many cases where the absorbing species are sparse or where the absorption cross section is small, no correction of this type is required. However for the given case with the chosen OH Q-branch line, the laser absorption is not negligible and, in fact, can be a several percent over the width of the flame. To correct for this a Beer's Law approach is taken. Beer's Law states that

$$(4-5) \quad A = \varepsilon \ell c ,$$

where ε is the extinction coefficient, ℓ is the path length, c is the species concentration, and A is the resulting molar absorptivity. In terms of initial and final intensities, this can be written as

$$(4-6) \quad \log_{10} \left(\frac{I_f}{I_0} \right) = -\varepsilon \ell c .$$

This can now be applied to the field of view by discretizing over the image space with a length scale on the order of the pixel size. The equation becomes

$$(4-7) \quad \log_{10} \left(\frac{I_n}{I_0} \right) = -\varepsilon \ell \left[\frac{1}{2} c_n + \sum_{i=0}^{n-1} c_i \right] .$$

Here, the subscripts correspond to the coordinate in the horizontal direction with the origin being at the left side of the frame (the side from which the laser sheet approaches). For the given problem, the unit of measure of length is taken to be one pixel. As such, for a horizontal ray, $\ell = 1$. For non-horizontal rays, $\ell = \sqrt{1+m^2}$, where m is the slope of the ray. Now, equation (4-7) becomes

$$(4-8) \quad \log_{10} \left(\frac{I_n}{I_0} \right) = -\varepsilon (1+m^2)^{1/2} \left[\frac{1}{2} c_n + \sum_{i=0}^{n-1} c_i \right] .$$

Finally, based on the linear fluorescence behavior seen in section 4.7.1, it is assumed that species concentration can be related to local laser intensity and fluorescence by

$$(4-9) \quad S_n \propto I_n c_n ,$$

where S_n is the measured fluorescence.

The parameters of interest are now non-dimensionalized in the following way:

$$(4-10) \quad I_n^* = \frac{I_n}{I_0} ; \quad S_n^* = \frac{S_n}{\tilde{S}} ; \quad c_n^* = \frac{c_n}{\tilde{c}} .$$

I_0 is then chosen to be unity at the left edge of the image frame, and \tilde{S} and \tilde{c} are chosen such that

$$(4-11) \quad S_n^* = I_n^* c_n^* .$$

Substituting (4-10) and (4-11) into (4-8) gives

$$(4-12) \quad \log_{10} S_n^* - \log_{10} c_n^* = -\varepsilon^\dagger (1+m^2)^{\frac{1}{2}} \left[\frac{1}{2} c_n^* + \sum_{i=0}^{n-1} c_i^* \right],$$

where ε^\dagger is the modified extinction coefficient, $\varepsilon^\dagger = \tilde{c}\varepsilon$. By inspection, it can be seen that if $\varepsilon = 0$ then $S_n^* = c_n^*$ which is the degenerate result when no absorption is present. The equation can be rearranged:

$$(4-13) \quad \log_{10} c_n^* - \frac{\varepsilon^\dagger}{2} (1+m^2)^{\frac{1}{2}} c_n^* = \log_{10} S_n^* + \varepsilon^\dagger (1+m^2)^{\frac{1}{2}} \sum_{i=0}^{n-1} c_i^*.$$

In this form, the equation can be solved for all n by marching (breadth-first) from the left side of the frame toward the right, and iteratively solving for c_n at each pixel location. For the algorithm developed, the c_i 's are linearly interpolated between pixels along rays cast back through the virtual focus of L301. For a given “input” fluorescence field, S_n^* , the corrected image is output as c_n^* .

The only remaining unknown in equation (4-13) is the modified extinction coefficient, ε^\dagger . This is computed by taking advantage of the symmetry of the flame under examination. A line of symmetry exists down the axial centerline of the burner. The PLIF image to the left of the centerline should be the mirror image of the PLIF image to the right of the centerline after full correction. Using a group of steady-state images from the dataset being processed, an iterative approach is used to balance the resulting c_n^* 's within a prescribed interrogation window (and its mirror image) by adjusting ε^\dagger . Once this value is determined, the solution method given above can be used on image frames that have had the first two intensity correction methods already applied. As with the laser sheet intensity profile correction, this Beer’s Law correction is typically applied to the binned images after all phase averaging has been completed. This operation constitutes the final correction process.

4.7.3 Reduced OH PLIF Data

OH PLIF experiments were performed for the seven base drive frequencies mentioned in the overview. The resulting reduced data is presented in its entirety in appendix H. Figure 4-8 shows an OH PLIF image of the flame under steady-state conditions (no acoustic forcing). The horizontal axis represents the radius from the centerline of the burner, and the vertical axis represents the height above the nozzle exit plane. The stagnation body height is at $z = 21$ mm, which is shown as the top line of the graph frame. The data presented is, in reality, only for the left side of the flame and has been mirrored across the centerline of the burner to complete the visual appearance. The intensity scale presented has been normalized around the maximum intensity in the image.

Figure 4-9 shows typical results for the corrected, phase resolved images. The presented image phase angles are in degrees past the rising edge zero-crossing of the local unsteady pressure. As such, the image at 90° corresponds to the point of maximum pressure and the image at 270° corresponds to the point of minimum pressure. Although data were collected at 15° phase increments, only 30° steps are shown in the figure.

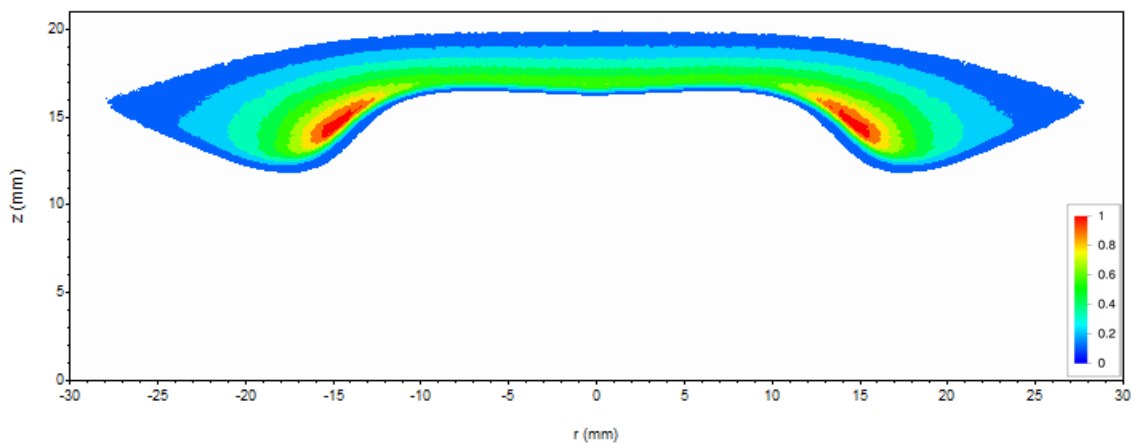


Figure 4-8: OH PLIF image of experimental burner flame under steady conditions (no acoustic forcing). Collected data appears on the left, and is mirrored across the centerline for a visual representation of entire flame. $\phi = 0.85$, $V_R = 4.0$

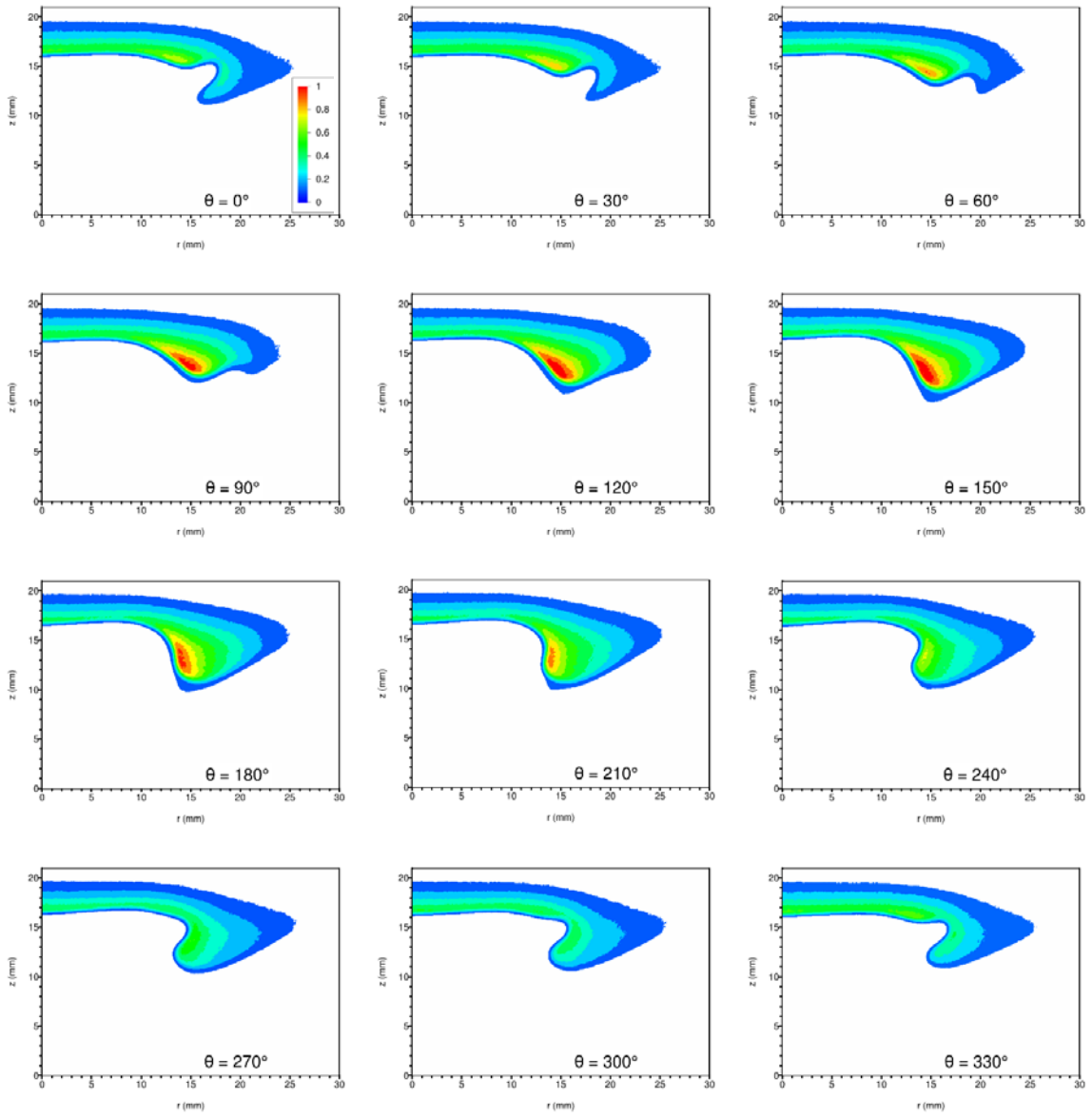


Figure 4-9: Phase resolved OH PLIF images for acoustic forcing at 55 Hz. The horizontal axis is the radius (mm) from the centerline of the burner. The vertical axis is the distance (mm) above the nozzle exit plane. Phase angle $\theta = 0^\circ$ corresponds to the rising-edge zero crossing of the local unsteady pressure. Data from experiment 652. Burner operating parameters are: $\varphi = 0.85$, $V_R = 4.0$.

The intensity of the 24 images was (individually) integrated over the full height and from the centerline outward. Volume integration was performed, incorporating the 'r' dependence for the axisymmetric nature of the flame. Waveform results for the 55 Hz case presented in Figure 4-9 are shown in Figure 4-10. The solid curve represents the measured pressure field while the dashed curve is the intensity signal generated from the PLIF data. Diamond symbols indicate the individual data points produced from each of the phase bins; a periodic cubic spline is used for the intervening curve. Both the pressure and intensity data shown in the graph are normalized by their peak values.

Table 4-1 shows the spectral content (as computed by FFT) of the two waveforms in Figure 4-10. All magnitude values have been normalized by the magnitude of the corresponding first mode. Phases are all in reference to the acoustic first mode. The sign convention is such that negative phases are leading and positive phases are lagging. Note that this is the opposite convention from that used in the bulk chemiluminescence experiments.

If it is posited (in a way similar to that in chapter 3) that the OH LIF intensity is related to the heat release such that

$$(4-14) \quad \frac{q'(s)}{\bar{q}} \simeq \frac{I'(s)}{\bar{I}(s)},$$

then it is possible to determine the global combustion response function, $H(s)$ and the global forced Rayleigh index, R_f . Restating equation (3-3), the combustion response function can be computed by

$$(4-15) \quad H(s) = \frac{\bar{p}}{p'(s)} \frac{I'(s)}{\bar{I}(s)} ; \quad s = i\omega.$$

Furthermore, the forced Rayleigh index can be computed by equation (3-21) which is repeated here:

$$(4-16) \quad R_f = Q(\omega) \cos(\vartheta(\omega)),$$

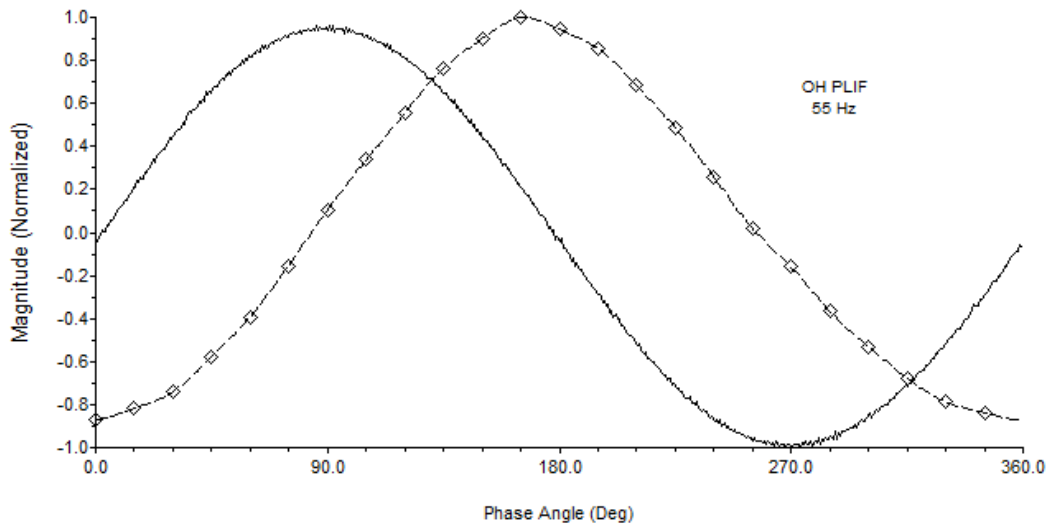


Figure 4-10: Resulting waveforms from the 55 Hz OH PLIF experiment (Experiment 652). The solid curve shows the measured acoustic waveform with the rising-edge zero-crossing marking the zero degree point. Diamonds represent total (fully integrated) intensity data points computed from the phase bins. The dashed curve is a periodic cubic spline fit to this data. Signals are normalized by their maximum values.

Mode	Pressure (p')		Intensity (I')	
	Mag	Phase	Mag	Phase
1	1.0000	0.0	1.0000	81.6
2	0.0107	87.6	0.0715	-137.2
3	0.0037	107.2	0.0150	85.8
4	0.0017	69.8	0.0061	-112.4
5	0.0007	164.7	0.0054	-34.2
6	0.0004	168.6	0.0058	147.1
7	0.0003	-151.6	0.0010	25.7
8	0.0004	-110.2	0.0022	-96.1
9	0.0003	-30.1	0.0013	-52.3
10	0.0003	1.4	0.0072	94.2
11	0.0003	5.7	0.0032	-15.7

Table 4-1: Harmonic content of the measured acoustic and intensity fields for the 55 Hz PLIF case. The measured intensity is total (fully integrated). Magnitudes are normalized by the first mode values. All phases are in reference to the phase of the first acoustic mode. Sign convention is such that negative phases are leading while positive phases are lagging.

where $Q(\omega)$ is the magnitude part of $H(s)$ and $\vartheta(\omega)$ is the phase part of $H(s)$. For the 55 Hz OH PLIF case, these relations produce:

$$|H(s)|_{55Hz} = 1068 \quad \angle H(s)|_{55Hz} = 81.3^\circ \quad (I' \text{ lags } p')$$

and

$$R_f|_{55Hz} = 160.8.$$

It can be seen that the magnitude of the combustion response function is much greater than unity, indicating that the system has substantial gain at 55 Hz (assuming the OH LIF signal is a suitable indicator for the heat release rate). At this frequency the phase of I' lags p' by more than 80° . The resulting global forced Rayleigh index is positive but relatively small considering the magnitude of $H(s)$. Consequently, the system has a weak-to-moderate self-driving characteristic at this frequency.

Given the presented methodology, it is now possible to compute the global combustion response function and the global forced Rayleigh index for OH PLIF test cases at all seven drive frequencies. The results are presented in Table 4-2.

Drive Frequency (Hz)	Combustion Response, H(s)		Forced Rayleigh Index, R _f
	Mag	Phase	
55	1048	81.6	154
75	880	-58.2	464
100	376	170.7	-371
150	57.1	-154.7	-51.6
220	25.4	-22.7	23.4
265	46.4	-136.6	-33.7
375	24.4	-147.1	-20.5

Table 4-2: Global unsteady combustion responses as discerned using OH PLIF for the seven prescribed base drive frequencies. Positive phases correspond to the heat release lagging the pressure.

For comparison purposes, this data can now be superimposed on the graphs presented in chapter 3 (Figures 3-4 and 3-16) showing the combustion response function and the forced Rayleigh index for the given burner operating condition as determined by the bulk chemiluminescence measurements. The combustion response is presented in Figure 4-11. In the magnitude plot, the OH data points at lower frequencies are seen to follow the same trend as the chemiluminescence data despite having lower values. However, for frequency points at 220 Hz and above the OH PLIF data appears to substantially over emphasize the response in comparison to the baseline data. In contrast, the phase data points for OH appear to track more closely with the chemiluminescence baseline. The OH PLIF-generated phase consistently lags the baseline phase by 40° to 60° for the first five data points spanning from 55 Hz to 220 Hz. For the sixth OH data point, the phase matches the baseline within a few degrees. For the seventh OH data point, the phase remains relatively constant while the chemiluminescence data descends by 75°. It is possible that the attenuated magnitude values (seen at 150 Hz and less) as well as the retarded phase may be attributable to the long lifetime of the OH radical at elevated temperatures; OH tends to persist and convect with the combustion products.

Figure 4-12 shows the resulting forced Rayleigh index data points produced from the combustion response data according to equation (4-16). Agreement is poor in this chart. Not only are the discrepancies in magnitude values (as seen in Figure 4-11) reflected in this plot but, more critically, the offsets in phase produce widely varying results. Examining the data point for 75 Hz, it is seen that the magnitude for R_f is nearly the same as that for the baseline case; however; due to the phase shift, the cosine function in equation (4-16) has actually alternated sign. Therefore, the OH data produces a large positive forced Rayleigh index at 75 Hz while the baseline chemiluminescence data produces an equally large but negative forced Rayleigh index.

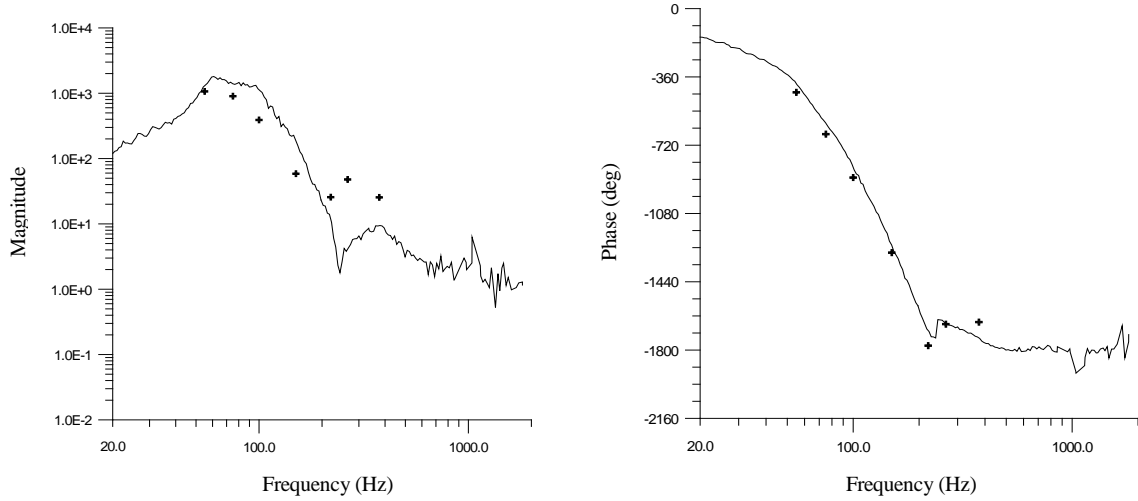


Figure 4-11: Combustion response function - points computed from OH PLIF data (shown as crosshairs) superimposed on the curves computed from the bulk chemiluminescence experiments. Phase data points were placed on the appropriate branch for closest proximity to the curve.

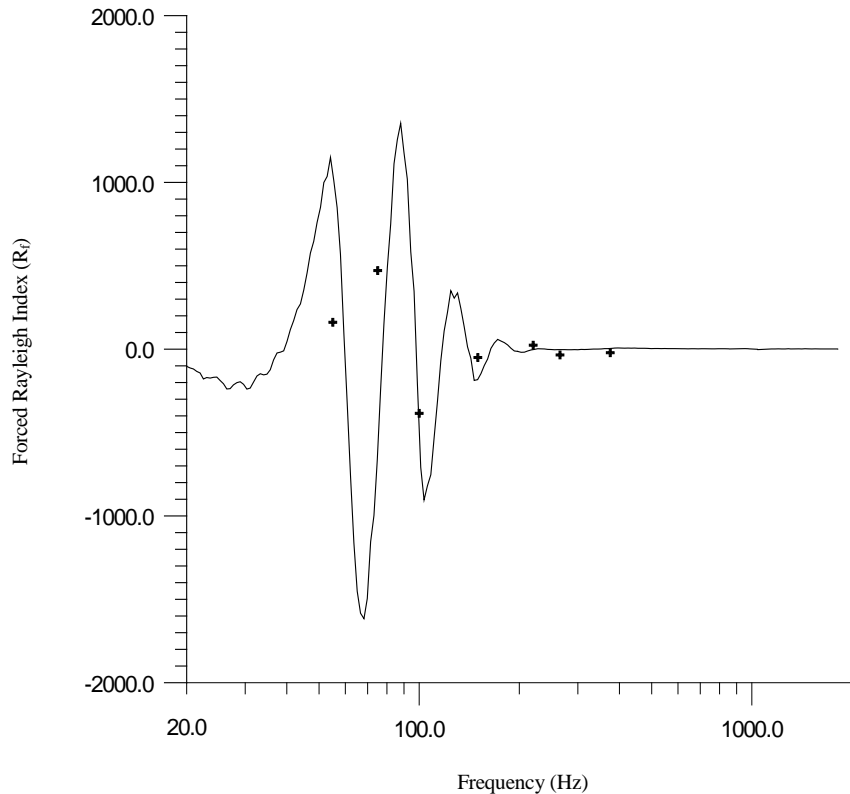


Figure 4-12: Forced Rayleigh index - points computed from OH PLIF data (shown as crosshairs) superimposed on the curves computed from the bulk chemiluminescence experiments.

Given that the collected PLIF fluorescence data are not mere point measurements, but are full 2-D images, it is now possible to define the spatially (or pixel) resolved combustion response function, as well as the spatially (or pixel) resolved forced Rayleigh index. Implicit in the original definition of the combustion response function given in equation (3-3) was the understanding that I' was a total (integrated) value over the whole flame. This was for the global result. More formally, this can be written

$$(4-17) \quad H(s) = \frac{\bar{p}}{p'(s)} \frac{1}{\bar{I}(s)} \int_V I'(s, V) dV ; \quad s = i\omega.$$

The volume integral can be rewritten taking advantage of the axisymmetric nature of the burner. This gives

$$(4-18) \quad H(s) = \frac{\bar{p}}{p'(s)} \frac{2\pi}{\bar{I}(s)} \int_0^R \int_0^Z I'(s, r, z) r dr dz.$$

This relation can be discretized in order to accommodate the collected, pixelated image data:

$$(4-19) \quad H(s) = \frac{\bar{p}}{p'(s)} \frac{2\pi}{\bar{I}(s)} \sum_{k=1}^{Z_{size}} \sum_{j=1}^{R_{size}} I'_{pix}(s, j, k) r_j \Delta r \Delta z,$$

where the temporally averaged fluorescence intensity is:

$$(4-20) \quad \bar{I}(s) = 2\pi \sum_{k=1}^{Z_{size}} \sum_{j=1}^{R_{size}} \bar{I}_{pix}(s, j, k) r_j \Delta r \Delta z.$$

In these relations, j and k are the pixel indices into the images being reduced. One should also take notice that although $\bar{I}_{pix}(s, j, k)$ has a complex argument 's', the resultant of the function (and consequently $\bar{I}(s)$) is purely real, contributing no phase component.

For the spatially resolved combustion response function, the sums along with the r dependence are removed:

$$(4-21) \quad \begin{aligned} H_{pix}(s, j, k) &= \frac{\bar{p}}{p'(s)} \frac{1}{\bar{I}_p(s)} I'_{pix}(s, j, k) \Delta r \Delta z, \\ \bar{I}_p(s) &= \sum_{k=1}^{Z_{size}} \sum_{j=1}^{R_{size}} \bar{I}_{pix}(s, j, k) \Delta r \Delta z. \end{aligned}$$

These are now “planar” values, seen as a transverse slice through the flame. The equations no longer takes account of the axisymmetric nature of the flame by integrating over the volume. This produces more natural looking images as it eliminates the strong radial gradient in intensity that would otherwise appear. From here, the magnitude or phase portion of the combustion response function can now be plotted pixel by pixel. It should be noted that since these are planar values, $H(s)$ is not simply the sum of the $H_{pix}(s, j, k)$ values. Instead, the reconstruction involves reintroducing the radial dependence of the volume:

$$(4-22) \quad H(s) = 2\pi \frac{\bar{I}_p(s)}{\bar{I}(s)} \sum_{k=1}^{Z_{size}} \sum_{j=1}^{R_{size}} r_j H_{pix}(s, j, k),$$

Given the relations above, the forced Rayleigh index can also be presented in a spatially resolved way. First, the pixel-resolved response function can be split into its magnitude and phase parts:

$$(4-23) \quad Q_{pix}(\omega, j, k) = |H_{pix}(s, j, k)| \quad \text{and} \quad \vartheta_{pix}(\omega, j, k) = \angle H_{pix}(s, j, k).$$

These can then be inserted into equation (4-16) to give

$$(4-24) \quad R_{f-pix}(j, k) = Q_{pix}(\omega, j, k) \cos(\vartheta_{pix}(\omega, j, k)).$$

As with the combustion response, the resulting spatially resolved forced Rayleigh index is also planar in nature. Without much effort it can be shown that the equation is, in reality, just

$$(4-25) \quad R_{f-pix}(j, k) = \operatorname{Re}(H_{pix}(s, j, k)).$$

The spatially resolved functions shown in equations (4-21) and (4-24) can now be used to generate plots given the OH PLIF data for each of the seven base drive frequencies. Figure 4-13

shows the combustion response function for each of these frequencies, with the magnitude data appearing in the left column and the phase data appearing in the right column. The spatially resolved forced Rayleigh index images are shown in Figure 4-14.

Despite the sizable regions where OH is seen to be present and to persist in Figure 4-9, the resulting spatially resolved combustion response function and forced Rayleigh index show relatively small regions of activity generated by the acoustic forcing. The largest regions of activity are seen at the two lowest drive frequencies (55 Hz and 75 Hz). These are the two frequencies that are closest to the peak excitation frequency of the shear layer instability intrinsic to the laminar jet emitted by the burner nozzle. (See acetone PLIF data in section 4.12). It is also where the global combustion response function is near its maximum. In these cases, the active region appears as a tadpole shape with the head near the edge of the flame and the tail reaching back to the burner centerline. The “head” portion is generated by the periodic disturbances or structures travelling along the shear layer toward the reaction zone. This is more easily seen in the acetone PLIF images presented later in the chapter. The thinner “tail” region, on the other hand, appears to be produced by modulation in the reactant flow resulting in unsteady production of OH radicals. Interestingly, the tail in these response images appears as a single band, implying that the reaction zone near the centerline is not moving vertically in relation to the acoustic forcing. However, this is not the case, as will be shown in later images. Here, the appearance of a single band is probably an artifact of the long persistence of OH at elevated temperatures.

Although the size and shape, as well as the magnitudes, of these regions are similar between the 55 Hz and 75 Hz cases, there is a dramatic difference in their corresponding phases. For the 55 Hz case, the head portion of the region has a phase that lags the pressure field by 45° to 135° while the tail portion leads the pressure by 45° to 90° . However, by increasing the drive frequency to 75 Hz, the phase behaviors of the two regions appear to swap. The tail now lags the pressure by 90° to 180° while the head principally leads the pressure by 45° to 90° . This exchange of behavior can

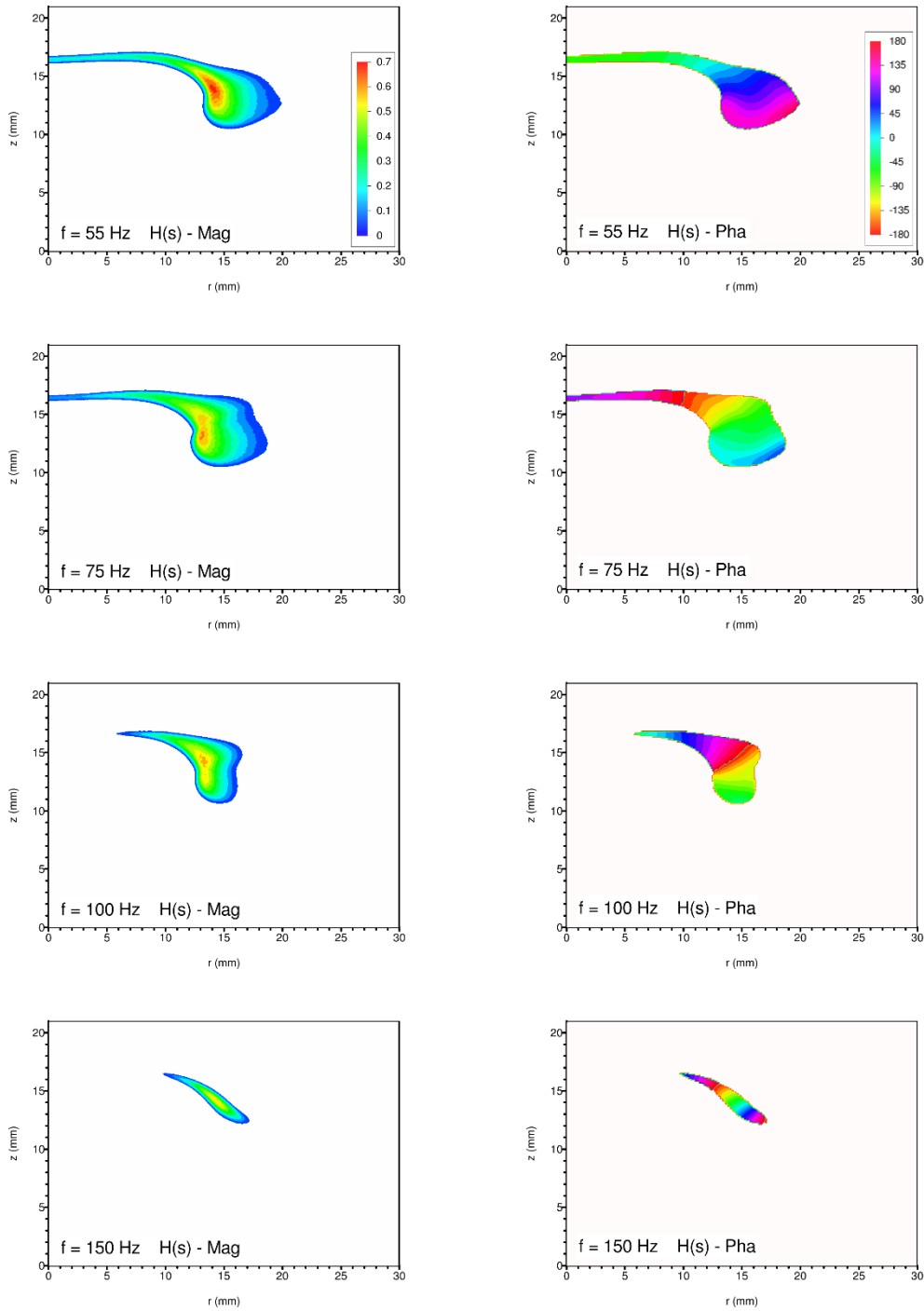


Figure 4-13: Spatially resolved combustion response function produced from OH PLIF data. Magnitude plots appear in the left column while phase plots are shown on the right. Note that positive phase values correspond to I' lagging P' . The coordinate system origin is along the burner centerline at the nozzle exit plane. Data for all seven drive frequencies are shown. (See next page.)

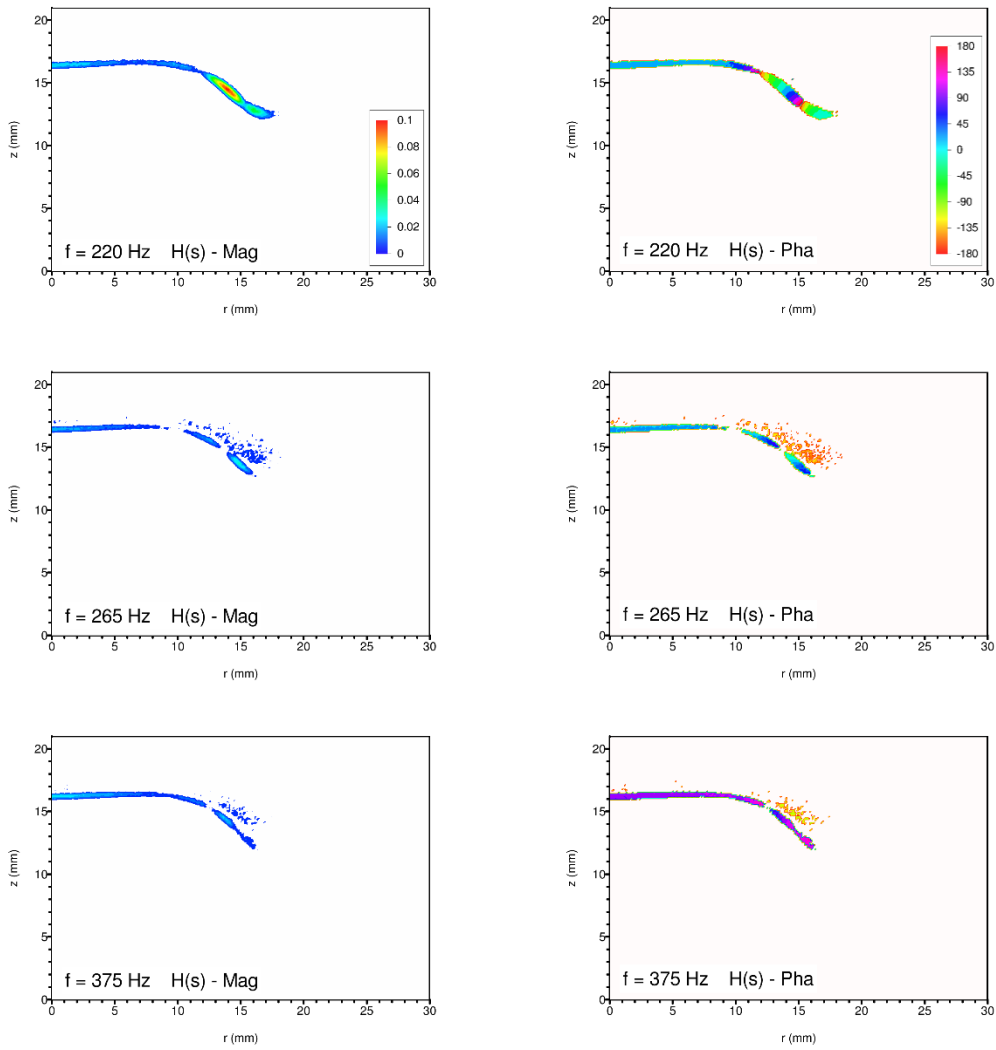


Figure 4-13 (cont.): Spatially resolved combustion response function produced from OH PLIF data. Magnitude plots appear in the left column while phase plots are shown on the right. Data for all seven drive frequencies are shown. (See previous page.) Note the change in magnitude scale versus the plots for 150 Hz and lower.

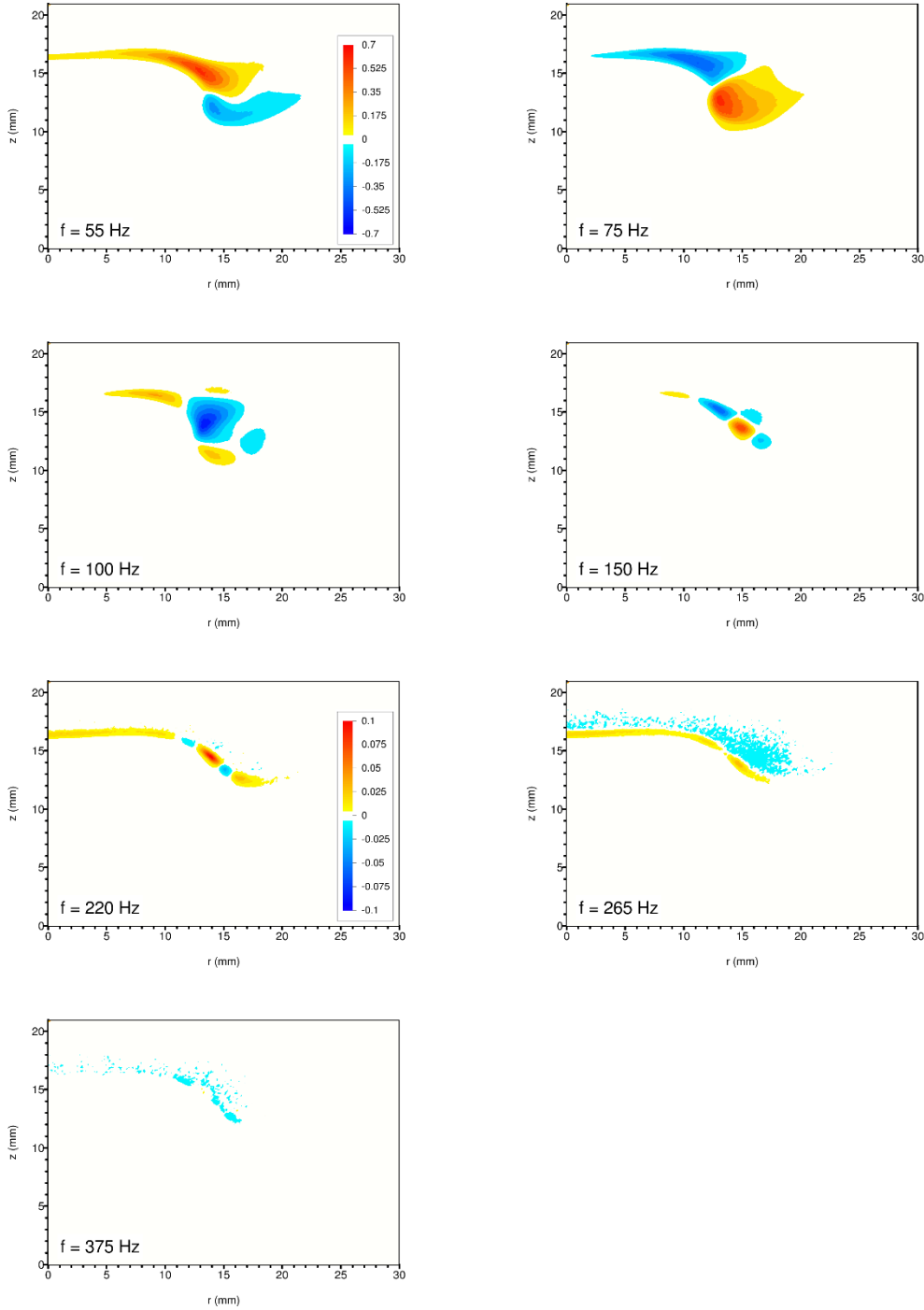


Figure 4-14: Spatially resolved forced Rayleigh index produced from OH PLIF data. Data for all seven drive frequencies are shown. Plots for the four lower frequencies use the top magnitude legend. Plots for the three higher frequencies use the bottom magnitude legend.

be more clearly seen in the two corresponding forced Rayleigh index images shown in Figure 4-14. In these plots, yellow-red zones show regions where the intensity fluctuations have an in-phase component with regard to the pressure field, and are consequently “driving” in nature. In contrast, the blue zones correspond to regions where the intensity has an out-of-phase component with regard to the pressure field, resulting in damping behavior. At 55 Hz, the tail and upper portion of the head display a driving characteristic while the lower portion of the head exhibits a damping characteristic. For the 75 Hz case these color attributes are reversed. One may estimate by inspection that, in both these cases, the yellow-red regions appear to be larger in area than the blue regions, resulting in net global driving characteristics. This is confirmed by revisiting the global Forced Rayleigh Indices listed in Table 4-2.

Examining the 100 Hz and 150 Hz cases, it can be seen that the regions of activity become progressively smaller, but still maintain the same single-peak topography. They contain a single maxima located in their region interiors with a negative gradient radiating outward in all directions. In addition, the phase behaviors also appear similar (visually) to the previous two cases. The phase of the response progresses smoothly as a path is traced through the active region from smaller r and larger z to larger r and smaller z . Unlike the previous cases, however, the phase distribution in the 100 Hz and 150 Hz cases is seen to span a larger range, making a complete wrap or more. The consequences of this can be seen in the associated forced Rayleigh index diagrams where more than two lobes now appear. The R_f plot for the 100 Hz driving frequency now shows three major lobes (and two minor lobes) while the 150 Hz plot shows four major lobes (and one minor lobe). As one might expect, the major lobes alternate in sign (driving versus damping) along the path described above.

For the three highest frequency cases (220 Hz, 265 Hz and 375 Hz), the response magnitudes become quite small. Consequently, the magnitude legend as well as the appearance threshold in the plots have been altered to improve visibility of the active regions. In addition, the

flame motions that are seen appear quite small; ripples or displacements in the flame are on the order of one to a few reaction zone thicknesses. In the images, the active regions appear as thin features, resembling the shape of the steady state flame. At 220 Hz, a noticeable maxima still occurs in the combustion response image near the outer edge of the flame, but within the area of negative curvature. In the two higher frequency plots, this maxima gives way to a more constant magnitude distribution, albeit with the active region now broken into multiple islands. The phase for the 220 Hz case still exhibits a smooth progression as a path is walked from an inner radius outward. In the flat-flame region this phase is nearly constant and in phase with the pressure. However, as the outer boundary is approached, the phase begins to lag, eventually making almost two complete wraps as the outer edge of the active region is reached. In contrast, the phases of the active regions in the two highest frequency cases are relatively constant throughout. In the 265 Hz case, the response is essentially in-phase, with phase angles spanning from -45° to $+45^\circ$. At the 375 Hz drive condition, the response phase shifts to lagging the pressure by approximately 90° to 120° . This shift seems consistent with expectation given the burner nozzle's Helmholtz response.

In addition to the description above, another interesting phenomenon is also noticed in the 265 Hz and 375 Hz cases, principally in the combustion response function plots. Near the outer edge of the flame and just above the principle active regions, there appears a distribution or "cloud" of points. These points only appear in the two highest frequency cases and are not present in the other images. In the magnitude response plots these points have values that are similar to the larger active regions. The phase plots, on the other hand, show a striking difference. While the main active regions show responses that are either in phase or lagging, the point clouds exhibit leading phase. Upon close examination, each tiny region (i.e. point) is surrounded by a thin red outline corresponding to a phase of 180° . This is indicative of dilatation of the points in response to the fluctuating pressure field. At low pressure the point sizes are larger and encompass their associated boundaries, providing a stronger signal along them. When the pressure is high, each

point compresses resulting in a lower signal being present on the boundary. This out-of-phase relationship produces the characteristic red (180°) outline. As mentioned above, the phase indicated within the interior of these points leads the pressure field substantially. In the 265 Hz case, the collective cloud phase appears to be around -120° while in the 375 Hz case the phase shift appears closer to -90°. It is not clear what these point clouds represent; however, it is interesting that they only appear in the post-transitional frequency range.

4.8 CH PLIF Results

This section presents data from the CH PLIF experiments. Unlike OH PLIF, laser induced fluorescence of the CH radical presents a much greater challenge. CH radicals appear in much smaller concentrations than OH in hydrocarbon flames. Furthermore, the fluorescent quantum yield of CH is also smaller than that of OH under typical conditions. The result is a much lower signal-to-noise ratio.

In order to obtain as much signal as possible, excitation of the $Q_1(7)$ transition in the B-X(0,0) band was chosen. This transition is near 390.18 nm (λ-air) and produces good fluorescent yield as has been well proven by others (Carter et. al. 1998; Sutton and Driscoll 2003; Bergthorson 2005). The spectral line chosen can be seen in Figure 4-15.

The OPO output energy in the 390 nm configuration was limited to approximately 16 mJ. Experiments were performed with an average energy of approximately 12 mJ. OPO stability around the target wavelength was found to be satisfactory with a maximum variation during steady operation of about ± 10 pm ($\sim \pm 0.7$ cm $^{-1}$). As was the case with operation in the 283 nm region, this variation is smaller than the linewidth of the output.

Image collection was performed with the Andor ICCD camera coupled to the Nikon 50 mm lens. A Semrock FF01-447/60-25 optical band-pass filter was installed in front of the intensifier to pass only the CH fluorescence while blocking scattered excitation light.

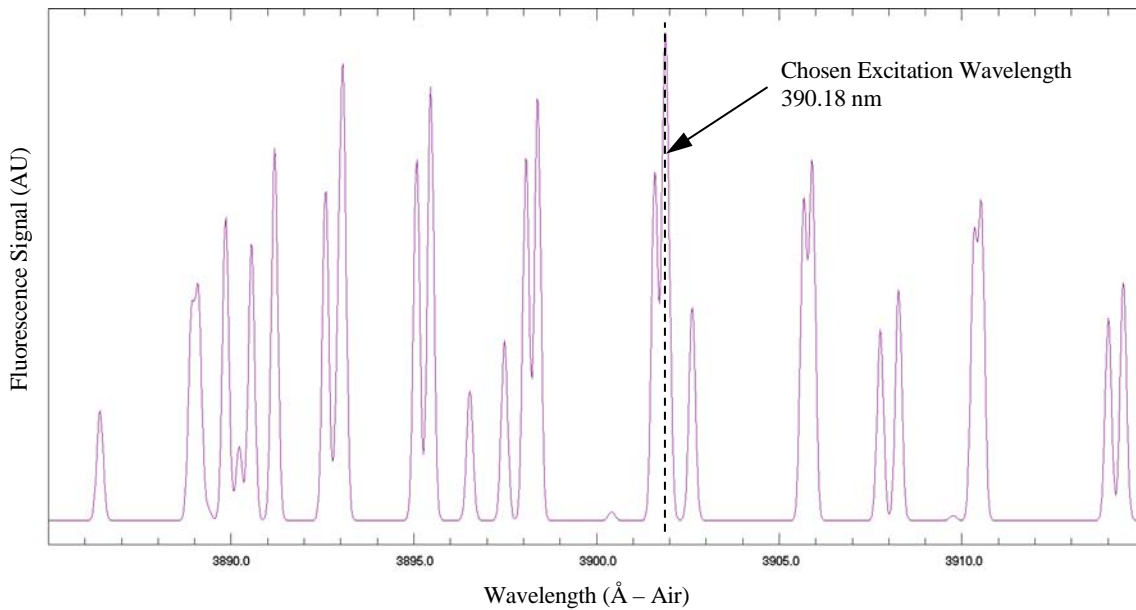


Figure 4-15: LIF excitation spectra of CH (B-X) around 390 nm as simulated by LIFBase 2.1.1. Pressure is 1 atm and temperature is 1500K. The chosen line shown at 390.18 nm (λ_{air}) corresponds to the $Q_1(7)$ transition of the B-X(0,0) band and exhibits good quantum yield when pumped.

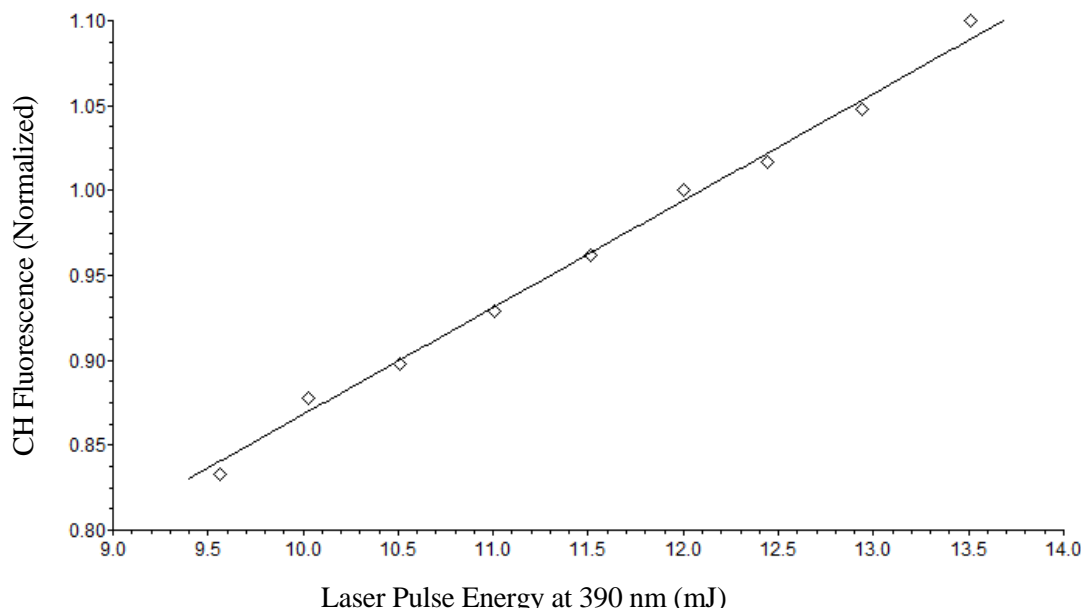


Figure 4-16: Fluorescence intensity of CH radicals in a steady flame versus laser shot energy. Diamond symbols specify resultant measurements at different energies. A solid line shows the least-squares linear fit to the data.

The CH excitation and fluorescence behavior was investigated using the same method as described for OH in section 4.7.1. The fluorescence response was found to be in the linear regime for the given laser sheet energy fluence and OPO output linewidth. Figure 4-16 shows one of the response plots generated during this evaluation.

Post processing operations for the CH PLIF images included corrections for shot-to-shot variations in the laser output energy as well as corrections for spatial variation of intensity in the laser sheet. However, unlike the OH PLIF case, the CH species concentration as well as its absorption cross section at the target wavelength were both small enough to make absorption correction (as described in section 4.7.2) unnecessary.

4.8.1 Reduced CH PLIF Data

CH PLIF experiments were performed for the seven base drive frequencies mentioned in the overview. In addition, two more drive frequencies were added to the CH test matrix after processing some of the previously collected data. These two frequencies (240 Hz and 243 Hz) were added in order to explore the behavior in the notch seen in the combustion response function for the given test case. As a result, a total of nine experimental drive frequencies were used. The reduced CH data is presented in its entirety in appendix H. Figure 4-17 shows a sample CH PLIF image of the flame under steady-state conditions (no acoustic forcing). As before, the horizontal axis represents the radius from the centerline of the burner, and the vertical axis represents the height above the nozzle exit plane. The stagnation body height is at $z = 21$ mm, which is shown as the top line of the graph frame. Also, as before, the data has been mirrored across the centerline of the burner to complete the visual appearance. The intensity scale presented has been normalized around the maximum intensity in the image.

Figure 4-18 shows typical results for the corrected, phase resolved CH PLIF images. The images shown are for the 55 Hz acoustic drive frequency experiment. The phase angles shown

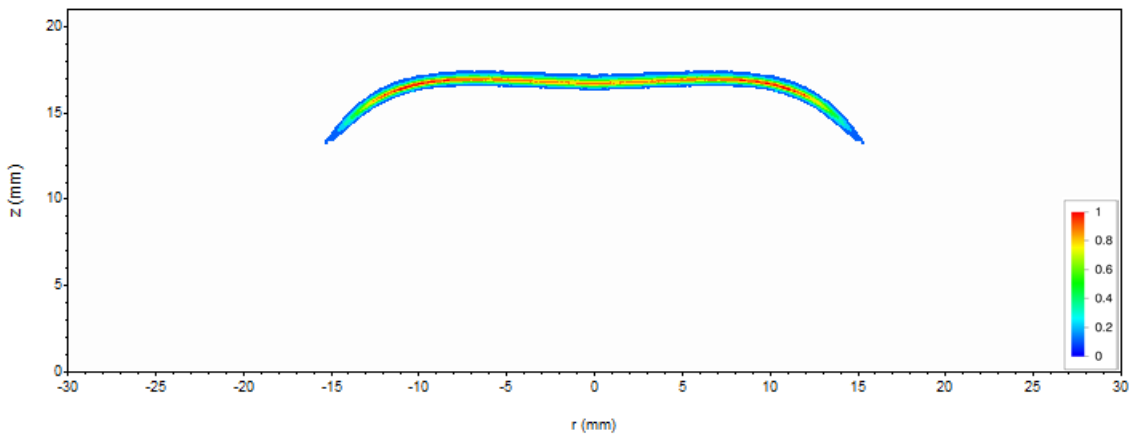


Figure 4-17: CH PLIF image of experimental burner flame under steady conditions (no acoustic forcing). Collected data appears on the left, and is mirrored across the centerline for a visual representation of the entire flame. $\varphi = 0.85$, $V_R = 4.0$

indicate the angle in degrees past the rising edge zero-crossing of the local unsteady pressure. The image at 90° corresponds to the point of maximum pressure while the image at 270° corresponds to the point of minimum pressure. Although only 12 images are shown in Figure 4-18 (each spaced 30° apart), the phase-resolved images presented in appendix H are indexed on 15° spacing (i.e. 24 images per drive frequency).

As was done previously, the intensities of the 24 images for each drive frequency case were fully integrated (including the r dependence) and then processed by FFT in order to generate the global combustion response and forced Rayleigh index for the nine acoustic drive frequencies. The results are shown in Table 4-3.

These data points can then be plotted on the graphs for the global combustion response function and the global forced Rayleigh index that were generated by bulk chemiluminescence measurements for the relevant test condition in chapter 3. These are shown in Figures 4-19 and 4-20.

Agreement between the CH PLIF experiments and bulk chemiluminescence is similar if not slightly better than the results shown in the OH PLIF comparison. The trend in the magnitude

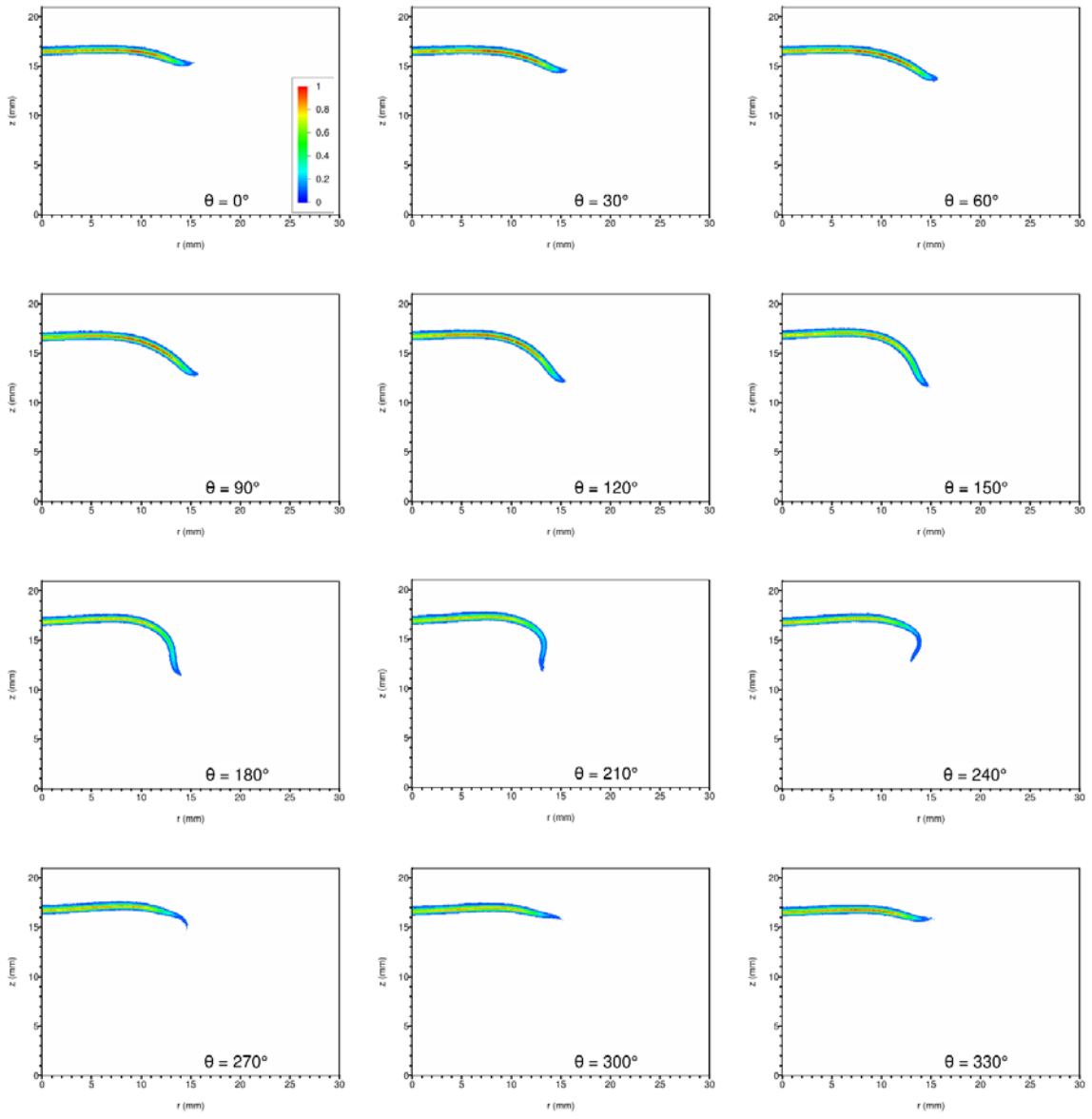


Figure 4-18: Phase resolved CH PLIF images for acoustic forcing at 55 Hz. The horizontal axis is the radius (mm) from the centerline of the burner. The vertical axis is the distance (mm) above the nozzle exit plane. Phase angle $\theta = 0^\circ$ corresponds to the rising-edge zero crossing of the local unsteady pressure. Data from experiment 696. Burner operating parameters are: $\varphi = 0.85$, $V_R = 4.0$

Drive Frequency (Hz)	Combustion Response, H(s)		Forced Rayleigh Index, R _f
	Mag	Phase	
55	1575	-1.7	1575
75	1393	-150.0	-1207
100	1908	64.9	810
150	282	101.9	-58.0
220	13.9	-12.4	13.6
240	36.4	157.7	-33.7
243	41.7	-131.7	-27.8
265	57.4	-179.5	-57.4
375	88.7	123.8	-49.3

Table 4-3: Global unsteady combustion responses as discerned using CH PLIF for all nine prescribed drive frequencies. Positive phases correspond to the heat release lagging the pressure.

of the CH PLIF combustion response is similar to that of the chemiluminescence data; however, unlike the OH PLIF data examined previously, the CH PLIF data consistently overestimates the magnitude of the response. The overestimation is not large until drive frequencies over 220 Hz are reached. Above 220 Hz, the CH PLIF data points for the combustion response magnitude still follow a contour that is similar in shape to that of the chemiluminescence curve, but the values of these points are a full order of magnitude higher than those generated by bulk chemiluminescence. This large difference is similar to that seen in the OH PLIF results presented in section 4.7.3.

By examining the phase plot in Figure 4-19, a definite agreement in trend can be seen between the CH PLIF data and the chemiluminescence curve for the pre-transitional region of the response. Unlike the OH data (which also agreed well in trend for this region), the CH PLIF data produces phase points that lead the reference trace rather than lag. The expected phase step at the transition point can clearly be seen in the PLIF data, although the values show marked disagreement from the reference curve. At the 375 Hz drive frequency, the CH PLIF data shows a large phase error (almost 180°) in comparison to the reference trace. This type of error at the highest drive frequency was also seen in the OH PLIF results, although the offset in that case was only about half as large.

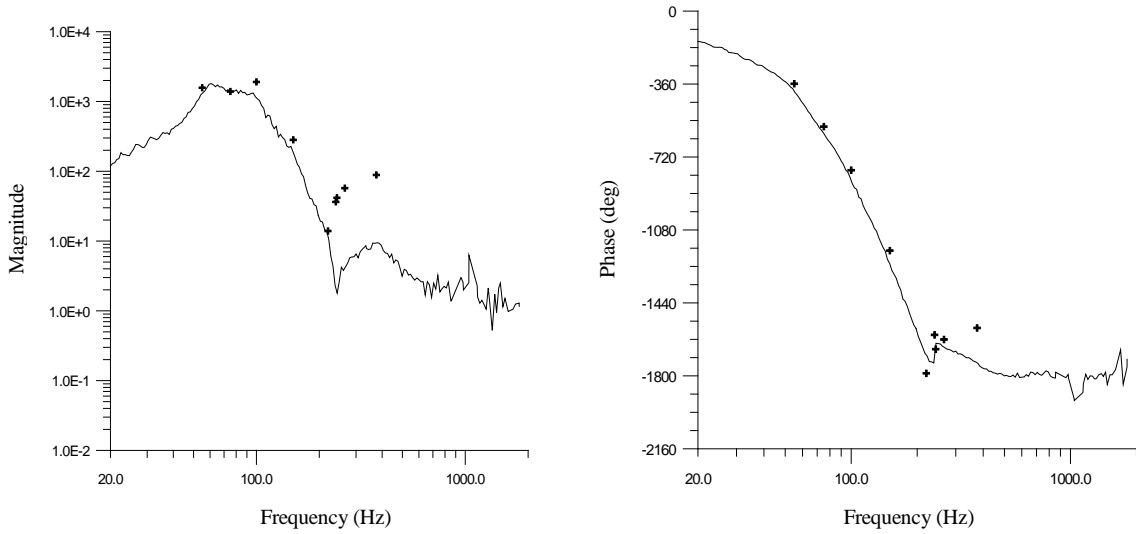


Figure 4-19: Combustion response function - points computed from CH PLIF data (shown as crosshairs) superimposed on the curves computed from the bulk chemiluminescence experiments. Phase data points were placed on the appropriate branch for closest proximity to the curve. Here, negative phases correspond to I' lagging p' .

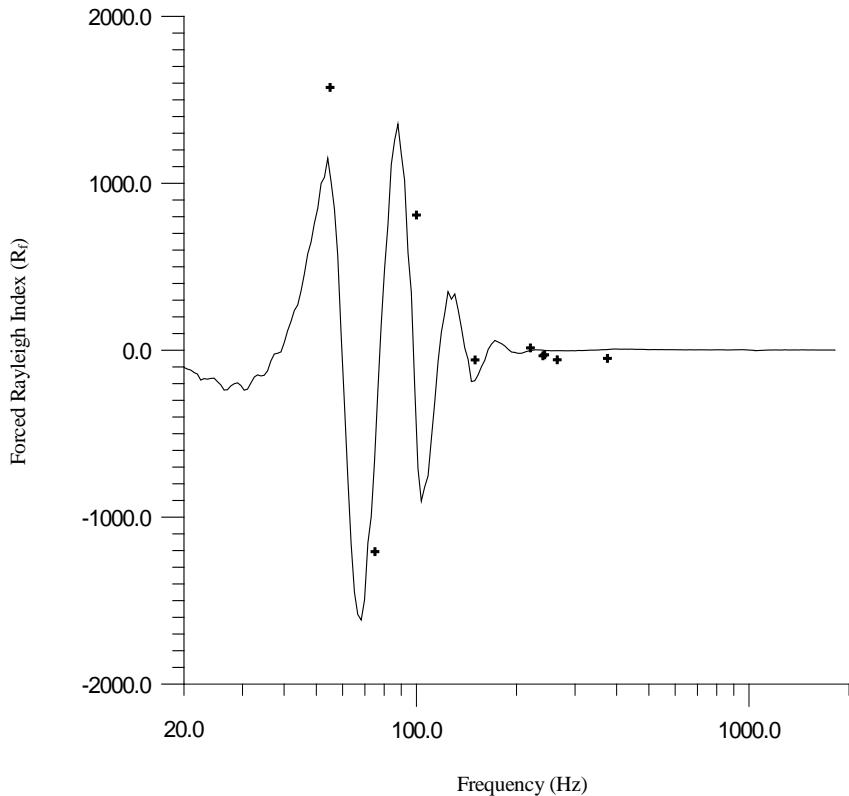


Figure 4-20: Forced Rayleigh index - points computed from CH PLIF data (shown as crosshairs) superimposed on the curves computed from the bulk chemiluminescence experiments.

Figure 4-20 shows the previously generated forced Rayleigh index graph, but this time with the CH PLIF generated data superimposed on it. Although agreement between CH PLIF data points and the baseline bulk chemiluminescence data is arguably better than that seen in the OH PLIF comparison, the results are still poor. Again, the combination of variations in both the magnitude and phase between the methods for evaluating the heat release produce widely varying values of the forced Rayleigh index.

The spatially resolved functions produced from the CH PLIF data can be seen in Figures 4-21 and 4-22. The spatially resolved combustion response function is shown in the first figure. The magnitude response plots for each drive frequency are shown on the left-hand side of the page and their corresponding phase plots are shown on the right. With the addition of the two supplemental drive frequencies (240 Hz and 243 Hz), the plots are now distributed over three pages. The magnitude plots now show a distinct pattern that was not visible in the spatially resolved OH PLIF data. All these plots from the lowest to the highest drive frequency show two distinct bands spaced apart from each other in the vertical direction. This feature is produced by the vertical movement of the flame (in response to the acoustic forcing) in combination with the very short lifetime of the CH radicals in the flame.

For the lower frequency cases (150 Hz and down) the spacing near the centerline of the flame is much smaller than that seen at the outer edge. As mentioned earlier the acoustic forcing at lower frequencies excites a shear layer instability in the jet of reactants heading into the flame. Structures from this instability pass into the reaction zone at these outer radii producing the larger displacements and features seen in the plots. Although structurally different, the reversal in phase seen between the 55 Hz and 75 Hz cases in the OH PLIF data is also seen here in the CH PLIF data. In the CH combustion response phase plot for 55 Hz, the upper band shows a lagging response (I' lagging p') ranging from 110° to 180° , while the lower band shows a response that is in-phase to leading p' by as much as 60° . However, for the 75 Hz case, the phase behavior of the bands is

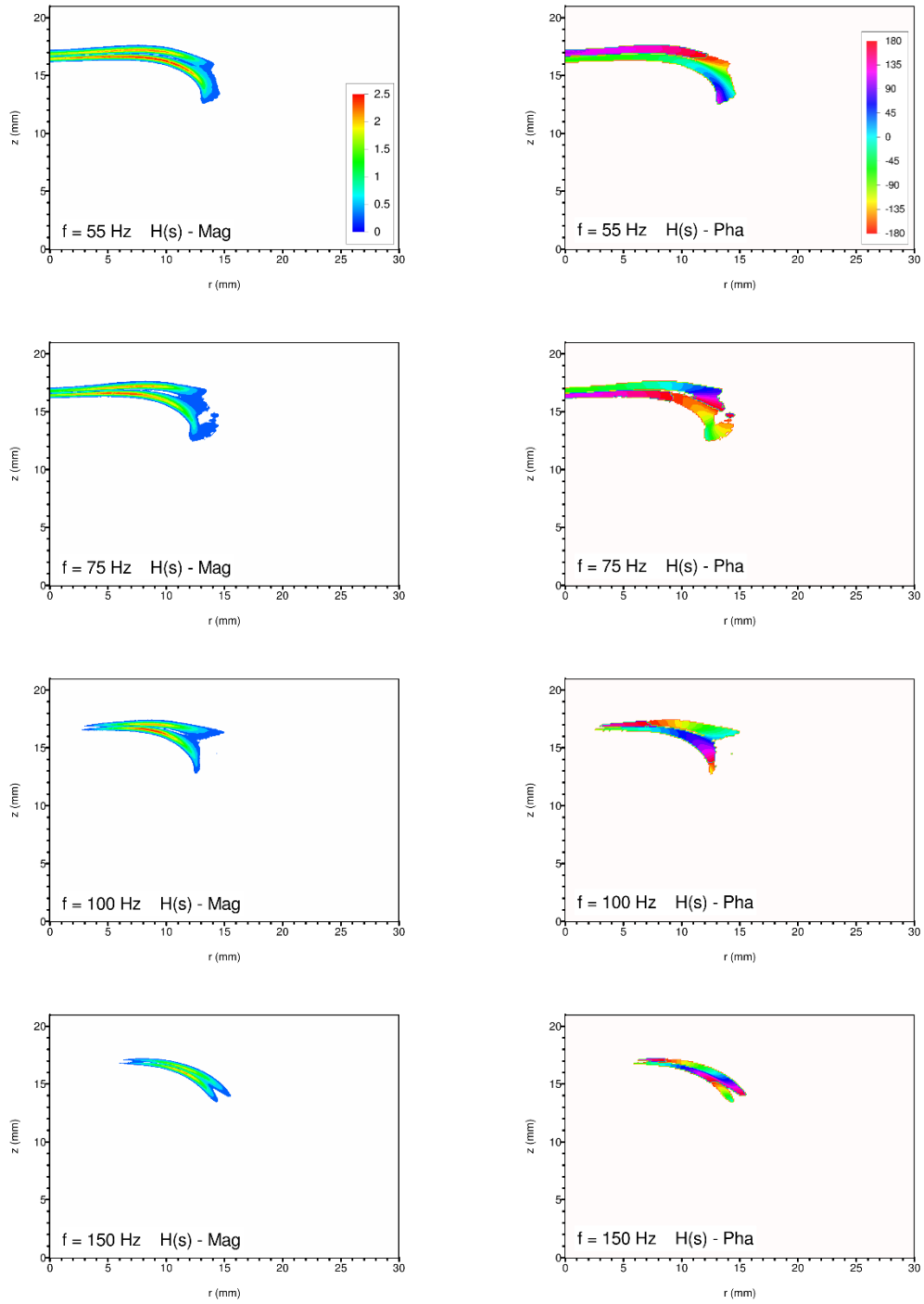


Figure 4-21: Spatially resolved combustion response function produced from CH PLIF data. Magnitude plots appear in the left column while phase plots are shown on the right. Note that positive phase values correspond to I' lagging P' . The coordinate system origin is along the burner centerline at the nozzle exit plane. Data for all nine drive frequencies are shown. (See next two pages.)

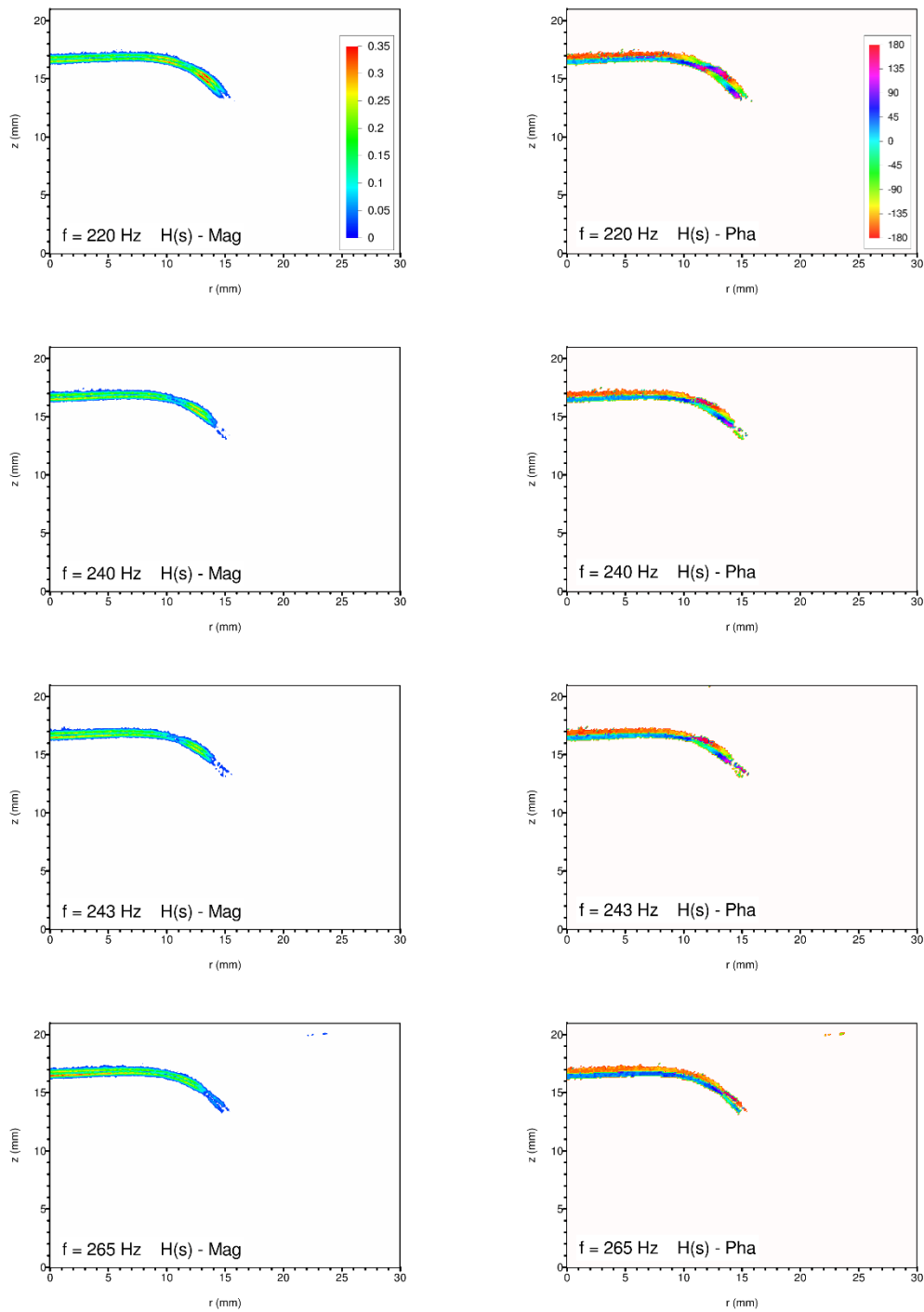


Figure 4-21 (cont): Spatially resolved combustion response function produced from CH PLIF data. Magnitude plots appear in the left column while phase plots are shown on the right. Data for all nine drive frequencies are shown. (See previous and next page.) Note the change in magnitude scale versus the plots for 150 Hz and lower.

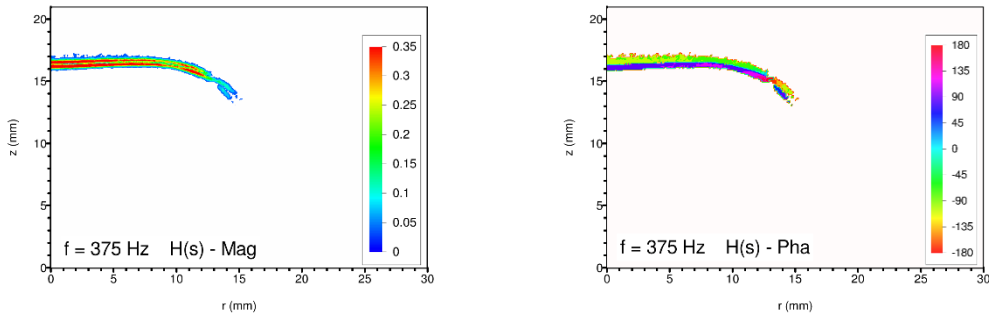


Figure 4-21 (cont.): Spatially resolved combustion response function produced from CH PLIF data. Magnitude plots appear in the left column while phase plots are shown on the right. Data for all nine drive frequencies are shown. (See previous page.) Note the change in magnitude scale versus the plots for 150 Hz and lower.

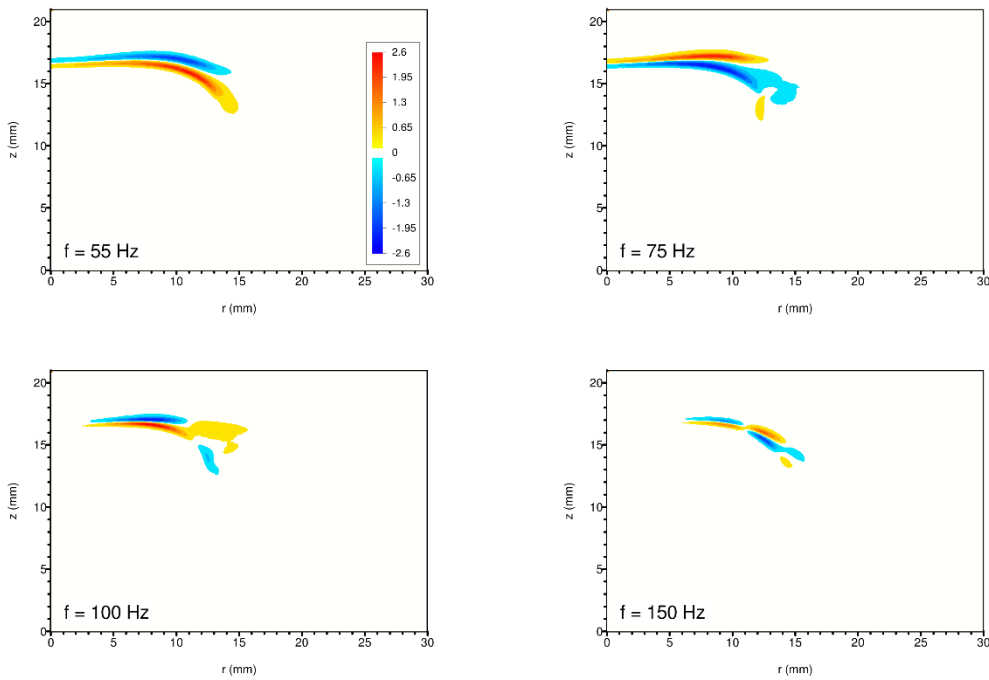


Figure 4-22: Spatially resolved forced Rayleigh index plots produced from CH PLIF data. Data for all nine drive frequencies are shown. (See next page.) Note the difference between the magnitude legends for the lower four drive frequencies and the upper five drive frequencies.

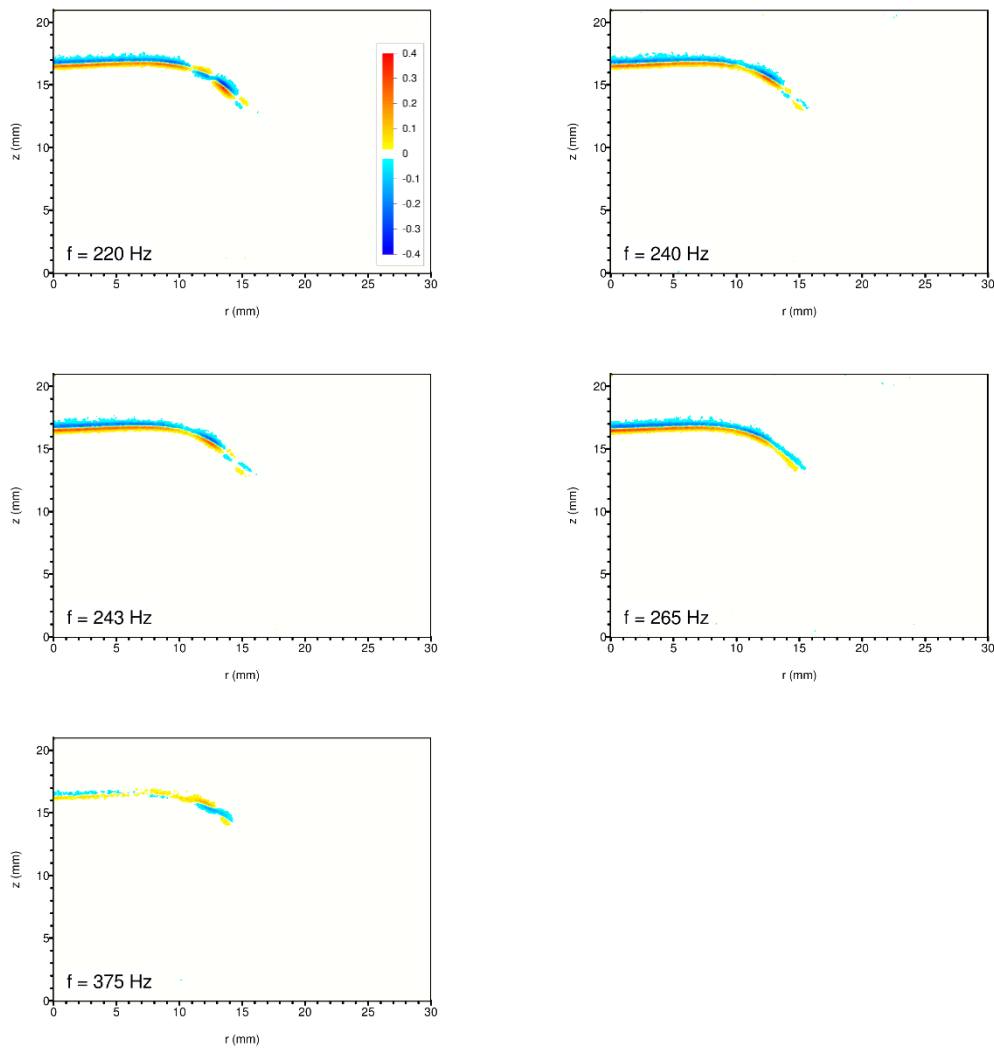


Figure 4-22 (cont.): Spatially resolved forced Rayleigh index plots produced from CH PLIF data. Data for all nine drive frequencies are shown. (See previous page.) Note the difference between the magnitude legends for the lower four drive frequencies and the upper five drive frequencies.

reversed; the upper band is now in-phase with p' while the lower band exhibits predominantly an out-of-phase characteristic.

At higher drive frequencies (above 150 Hz) the combustion response magnitudes are greatly diminished, requiring a revision to the legend used in Figure 4-21. In these plots, the two bands previously described have now positioned themselves directly adjacent to each other over their entire lengths. Their magnitudes also appear essentially identical to each other. However, the differences are noticeable in the phase plots. For the four test cases from 220 Hz up to 265 Hz, the phase behavior from the burner centerline out to a radius of approximately 10 mm appears constant and well behaved. In this region, the upper band appears out of phase with p' while the lower band is in phase with p' . Again, this is the signature of a vertical displacement (modulation) of the flame in response to the fluctuating pressure. Near the outer edge of the flame, the larger structures mentioned earlier have attenuated into small ripples. This results in an alternating pattern of phase along the two bands as the outer edge of the flame is approached. The pattern gives an appearance that might be described as two pieces of colored rope twisted together. This appearance persists through to the 375 Hz drive case. However, for this highest frequency case, the color of the phase bands closer to the burner centerline indicate a shift to leading by 90° on the top band, and lagging by 90° on the bottom band – a result that may be expected due to the Helmholtz resonance of the burner nozzle. It is also noticed in the left-hand plot for the 375 Hz case that the magnitude of the bands are significantly larger than those seen in the previous four cases.

The spatially resolved forced Rayleigh index plots for the CH PLIF experiments are shown in Figure 4-22. Again, the banded appearance is present as was seen in the associated combustion response function plots. At 55 Hz and 75 Hz, the band pairs have opposite signs, with one driving and one damping. Although the banded representation is structurally different to the “head and tail” configuration seen in the OH PLIF data, the reversal of the signs of the regions as the frequency

increases from 55 to 75 Hz is similar. Visually examining the first of these two images, one may come to the conclusion that for the 55 Hz experiment, the yellow-red driving region is more pronounced than the damping blue region. Then, examining the second image for the 75 Hz experiment, it may appear that the blue damping region is larger in area than the yellow-red driving region. These two observations would imply that at 55 Hz the CH PLIF generated global forced Rayleigh index is positive while for the 75 Hz case, it is negative. This is, in fact, correct as can be seen in the results in Table 4-3. For all the higher frequency drive cases, the band pairs are seen to cross over each other in the twisted rope formation described earlier. Additionally, in all these cases (100 Hz and above), the behavior of the reaction zone at small radii is such that the yellow-red band (driving) appears on the bottom while the blue band (damping) appears on the top. It is only the 75 Hz case that reverses this.

At forcing frequencies of 220 Hz and higher, the amplitudes of the forced Rayleigh index drop dramatically, similar to the drop seen in the combustion response function. As such, the scales for the last five plots in Figure 4-22 use a revised legend. In the plots from 220 Hz to 265 Hz, all the variability appears at radii greater than 10 mm. This is where the crossover behavior is seen. For the 240 Hz and 243 Hz experiments, the forced Rayleigh index fades to nearly zero at radii beyond 13.5 mm. Interestingly, the crossover behavior seems to vanish at 265 Hz where the two bands parallel each other closely with no twists. At the highest drive frequency of 375 Hz, the twisted rope appearance returns; however, the signal at small radii (less than 10 mm) in this case essentially vanishes as the band phases shift to roughly $\pm 90^\circ$.

4.9 CH₂O PLIF Results

Formaldehyde PLIF experiments were also performed and the results are presented in this section. It was not intended to use CH₂O PLIF observations as a stand-alone indicator of heat release; rather, the data was collected to use in conjunction with the previously gathered OH PLIF

data to estimate the spatially resolved heat release using the method described by Paul and Najm (1998). This method is presented and discussed in section 4.10. Nevertheless, given its availability, the formaldehyde data is presented and reviewed using the same methodology applied in the previous OH and CH PLIF sections. Both the combustion response function and forced Rayleigh index results are presented, if for no other reason than as an instructive comparison.

It was originally planned to excite CH₂O at a favorable transition around 352 nm using the custom built OPO. Unfortunately, this would require the OPO cavity fundamental to operate at 704 nm which was out of range of the existing cavity mirrors. Instead, the formaldehyde molecules were excited directly with the tripled output of the Nd:YAG at 355 nm. This excites rotational transitions within the $\tilde{A}^1A_2 - \tilde{X}^1A_1 4^1_0$ absorption band as described by Harrington and Smyth (1993). Absorption at this wavelength is poor; however, given enough pulse energy, good signal-to-noise ratios can be achieved. In this case, average pulse energies around 100 mJ were used and the fluorescence signal was found to be strong. Furthermore, by varying the laser pulse energy and integrating the resulting fluorescence, it was found (as in the previous cases) that the fluorescent response was linear for the given laser sheet height (~20 mm) and the full range of laser energies available.

Image collection was, again, performed with the Andor ICCD camera coupled to the Nikon 50 mm lens. However, this time a Semrock FF01-417/60-25 optical band-pass filter was installed in front of the intensifier. This passed the CH₂O fluorescence while blocking scattered excitation light at 355 nm.

Once again, the post-processing operations on the collected images included corrections for shot-to-shot variations in the laser output energy as well as corrections for spatial variation of intensity in the laser sheet. As with the CH PLIF case, no corrections were needed for absorption

of the laser. Since coupling of the 355 nm laser energy to the transitions of interest is so weak, the reduction in laser energy due to absorption is negligible.

4.9.1 Reduced CH₂O PLIF Data

CH₂O PLIF experiments were performed for all nine defined drive frequencies. (The seven base drive frequencies plus the two supplemental drive frequencies.) The reduced CH₂O data is presented in its entirety in appendix H. Figure 4-23 shows a sample CH₂O PLIF image of the flame under steady-state conditions (no acoustic forcing). As before, the horizontal axis represents the radius from the centerline of the burner, and the vertical axis represents the height above the nozzle exit plane. The stagnation body height is at $z = 21$ mm, which is shown as the top line of the graph frame. Also, as before, the data has been mirrored across the centerline of the burner to complete the visual appearance. The intensity scale presented has been normalized around the maximum intensity in the image.

Examining the steady image presented in Figure 4-23, it quickly becomes apparent that using formaldehyde PLIF as an independent indicator of the global or spatially resolved heat release rate is an unwise choice. The reason is that formaldehyde has an indefinite lifetime at low temperatures when it is not surrounded by an active radical pool. This can be seen by the “wings” appearing on either side of the flame in the image above. Here, CH₂O has escaped the edge of the flame and has entered the cooler, air-dominated surroundings where it persists. This type of residual adds an unknown, variable (during unsteady conditions), and frequently large contribution to the PLIF signal that is not directly related to the heat release rate.

Figure 4-24 shows typical results for the corrected, phase resolved CH₂O PLIF images. The presented images are for the 55 Hz acoustic drive frequency experiment. Only 12 of the 24 generated images are displayed. The phase angles shown follow the same conventions as described previously.

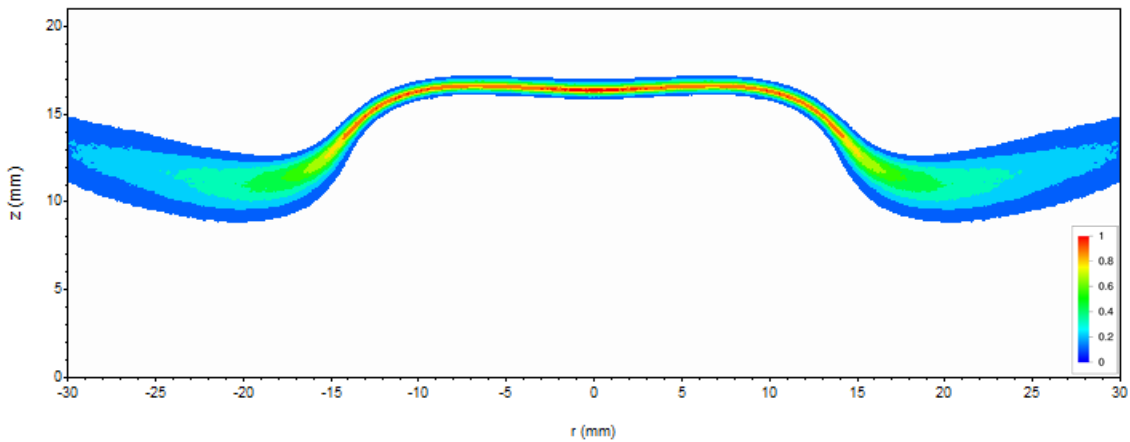


Figure 4-23: CH_2O PLIF image of experimental burner flame under steady conditions (no acoustic forcing). Collected data appears on the left, and is mirrored across the centerline for a visual representation of entire flame. $\varphi = 0.85$, $V_R = 4.0$

As was done before, the intensities of the 24 images for each drive frequency case were fully integrated (including the r dependence) and then processed by FFT in order to generate the global combustion response and forced Rayleigh index for the nine acoustic drive frequencies. The results are shown in Table 4-4.

Drive Frequency (Hz)	Combustion Response, $H(s)$		Forced Rayleigh Index, R_f
	Mag	Phase	
55	170	-41.9	127
75	125	131.6	-83.3
100	183	62.1	85.9
150	20.7	-51.6	12.8
220	6.72	1.5	6.72
240	27.6	-49.8	17.8
243	50.9	9.8	50.2
265	22.7	-28.0	20.0
375	57.0	75.8	14.0

Table 4-4: Global unsteady combustion responses as discerned using CH_2O PLIF for all nine prescribed drive frequencies. Positive phases correspond to the heat release lagging the pressure.

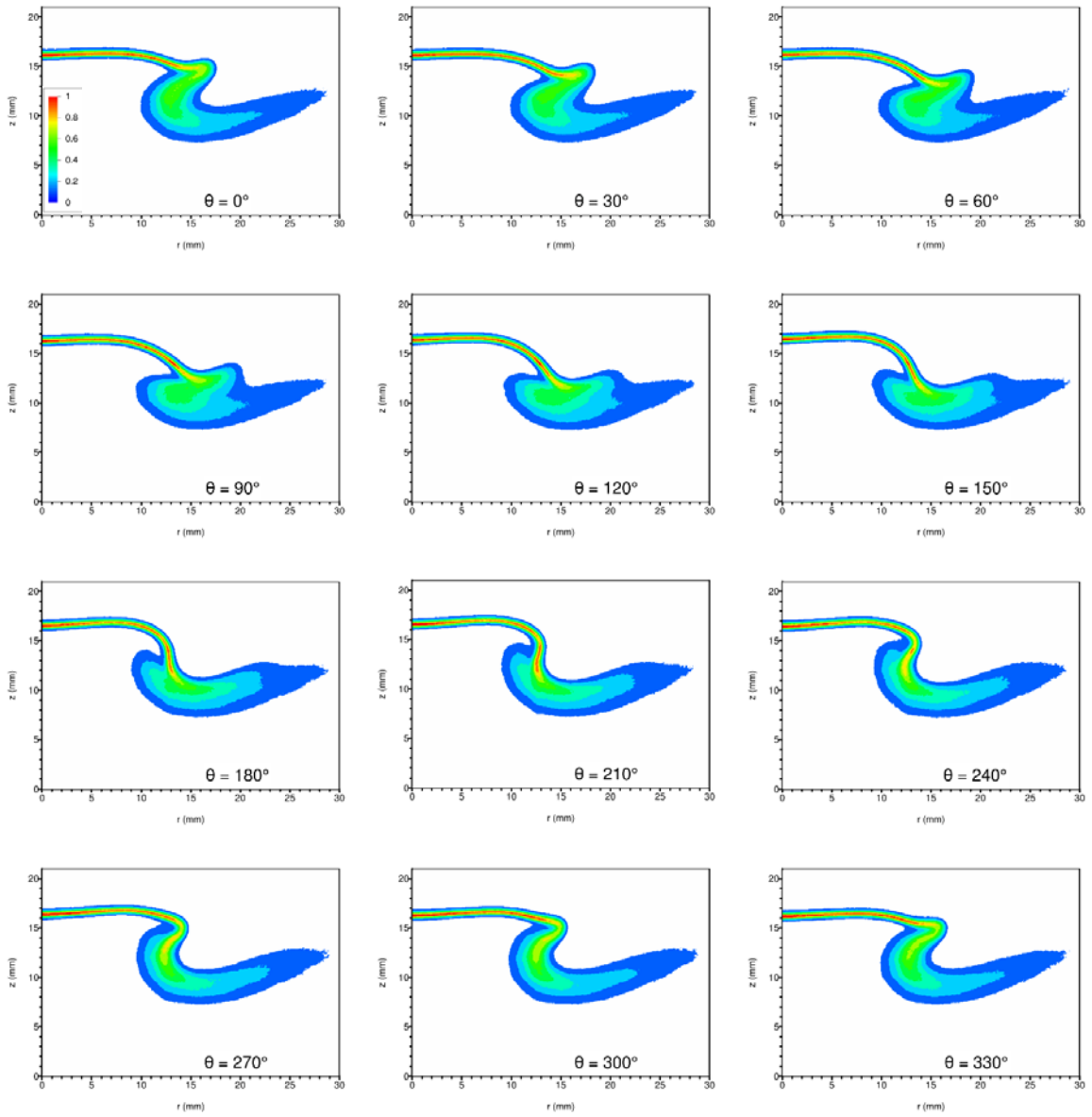


Figure 4-24: Phase resolved CH_2O PLIF images for acoustic forcing at 55 Hz. The horizontal axis is the radius (mm) from the centerline of the burner. The vertical axis is the distance (mm) above the nozzle exit plane. Phase angle $\theta = 0^\circ$ corresponds to the rising-edge zero crossing of the local unsteady pressure. Data from experiment 709. Burner operating parameters are: $\varphi = 0.85$, $V_R = 4.0$

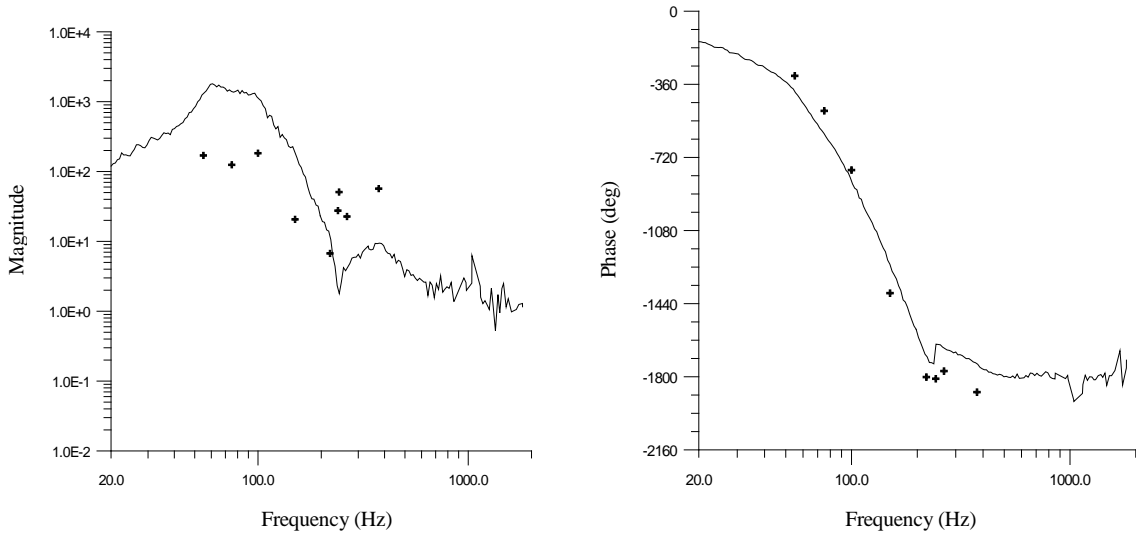


Figure 4-25: Combustion response function - points computed from CH₂O PLIF data (shown as crosshairs) superimposed on the curves computed from the bulk chemiluminescence experiments. Phase data points were placed on the appropriate branch for closest proximity to the curve. Here, negative phases correspond to I' lagging p' .

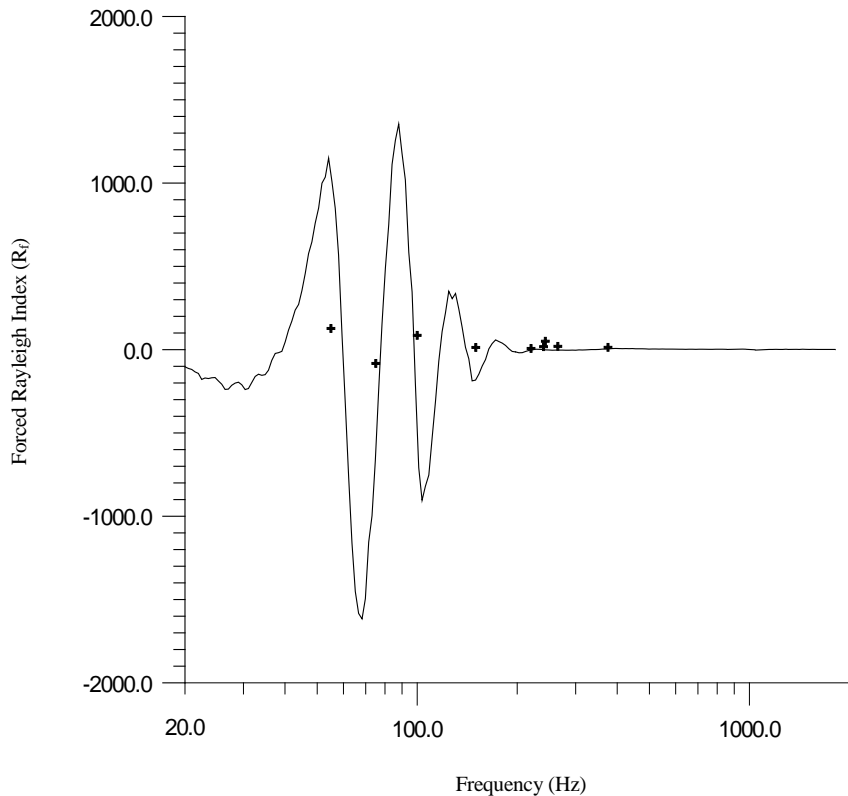


Figure 4-26: Forced Rayleigh index - points computed from CH₂O PLIF data (shown as crosshairs) superimposed on the curves computed from the bulk chemiluminescence experiments.

These data points can then be plotted on the graphs for the global combustion response function and the global forced Rayleigh index that were generated by bulk chemiluminescence measurements for the relevant test condition in chapter 3. These are shown in Figures 4-25 and 4-26.

As predicted, the formaldehyde data is in very poor agreement with the baseline bulk chemiluminescence data. Examining Figure 4-25, it can be seen that the global magnitudes for drive frequencies of 150 Hz and lower fall woefully short of the baseline values. For the cases where the drive frequency is 240 Hz or higher, the magnitudes overshoot the baseline data in a fashion similar to that seen in the previous cases. However, the CH_2O data points for these frequencies are noticeably erratic and exhibit less of a trend than was seen in the previous data.

Phase data in Figure 4-25 also shows substantial disagreement with the chemiluminescence baseline. Phase errors are large and occur in both directions; the low frequency data points tend to lead the baseline while higher frequency points tend to lag the baseline. Errors nearing 180° are present which hint at the possibility that some errors may actually be larger than shown but the corresponding data points have had the fortune of being placed on the incorrect branch during plotting.

Figure 4-26 repeats the forced Rayleigh index plot generated from the baseline bulk chemiluminescence data. This time, the CH_2O PLIF-generated forced Rayleigh index data points are displayed on the graph. Points representing 55 Hz and 150 Hz drive frequencies show large errors. The intervening points at 75 Hz and 100 Hz appear to be in fair agreement with the chemiluminescence data; however, this is merely a coincidence as incorrect magnitudes and phases have conspired together to produce nearly correct results. Data points at 240 Hz and higher have Forced Rayleigh Indices that are small, being comparable to the baseline; however, this (again) is not necessarily for the correct reasons.

The spatially resolved functions produced by using the CH₂O PLIF data as an indicator of heat release are shown in the next two figures. Figure 4-27 presents the spatially resolved combustion response function plots for each drive frequency with the magnitude images appearing on the left and the phase images appearing on the right. These plots show a banded appearance (with two bands) similar to what was seen in the CH PLIF images. As with the previous case, vertically displaced bands are observed for locations at smaller radii ($r < 10$ mm). This is seen to be true throughout the drive frequency range. For drive frequencies of 150 Hz and lower, however, the bands in the CH₂O data take on a “head and tail” appearance similar to what was seen in the OH PLIF data; for the upper bands, prominent lobes appear at larger radii. Indeed, these bands bear a striking resemblance to their counterparts seen in the OH PLIF images. The lower bands, on the other hand, display much smaller lobes which are typically nestled under and to the inside of their larger associates. Visual inspection of the images reveal that the features with the largest magnitudes appear in the 75 Hz plot versus the 55 Hz plot as was the case in the OH data.

While some commonality in features was noted between the CH₂O PLIF images and the corresponding OH PLIF data, an interesting parallel is also seen in the phase behavior between the formaldehyde PLIF images and their counterparts in the CH PLIF data. In examining the right-hand plots in Figure 4-27, the phases seen in the “tail” portions of the formaldehyde PLIF data appear relatively constant in the horizontal regions as a path is traced along each band from small radius to large radius. Furthermore, the phases shown in these “tail” regions are virtually identical to those presented in the corresponding CH PLIF images. Focusing on the low frequency cases (150 Hz and lower), the phase of each “tail” in the upper bands transitions smoothly into their respective “heads,” similar to what was seen in the OH PLIF data; no phase discontinuities appear. However, for the lower bands in these four cases, the phase transitions between the “tail” and “head” can be steep, bordering on discontinuous. Despite these aggressive transitions, the variation in phase over the whole area of each “head” is typically less than one complete phase wrap.

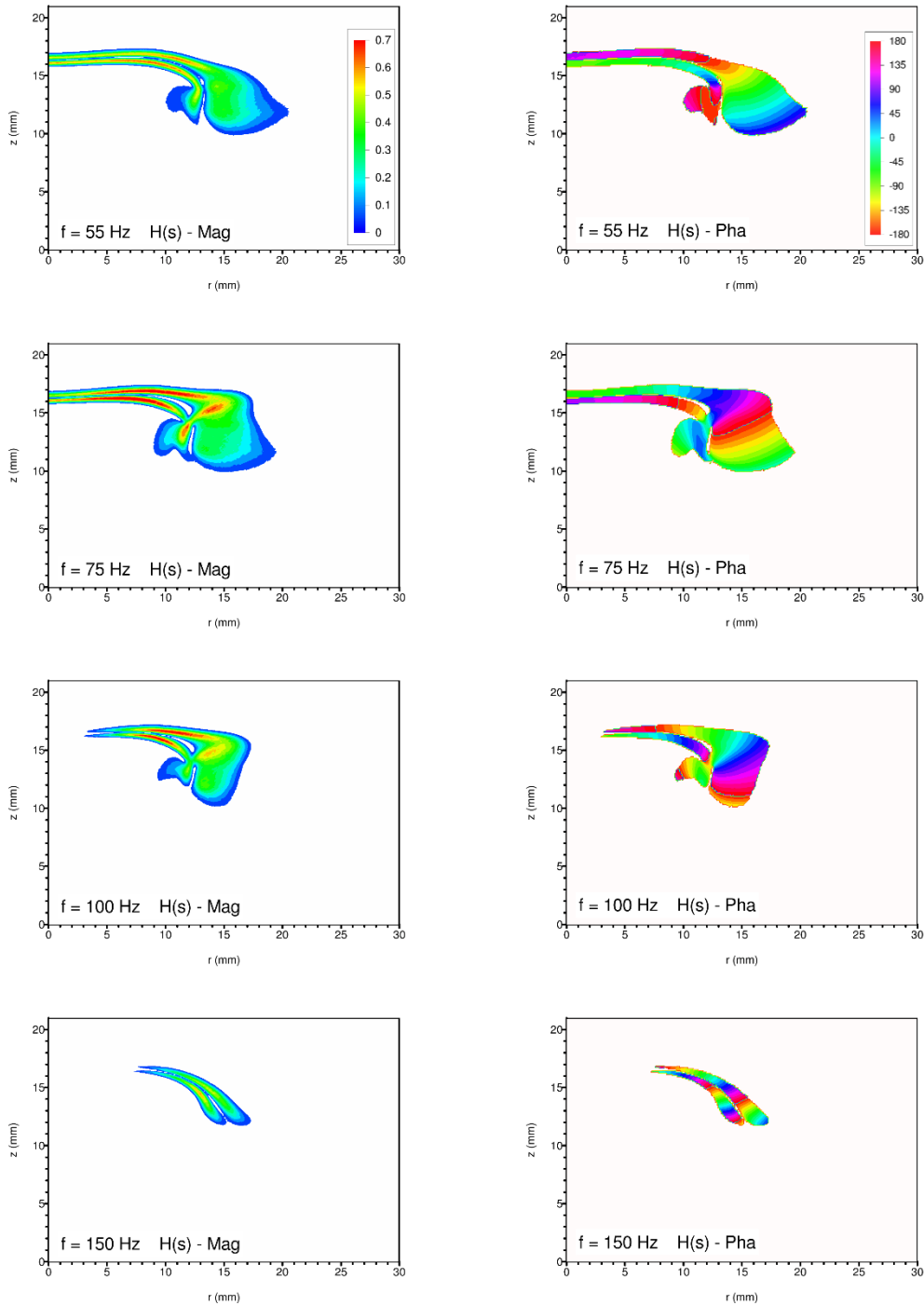


Figure 4-27: Spatially resolved combustion response function produced from CH_2O PLIF data. Magnitude plots appear in the left column while phase plots are shown on the right. Note that positive phase values correspond to I' lagging p' . The coordinate system origin is along the burner centerline at the nozzle exit plane. Data for all nine drive frequencies are shown. (See next two pages.)

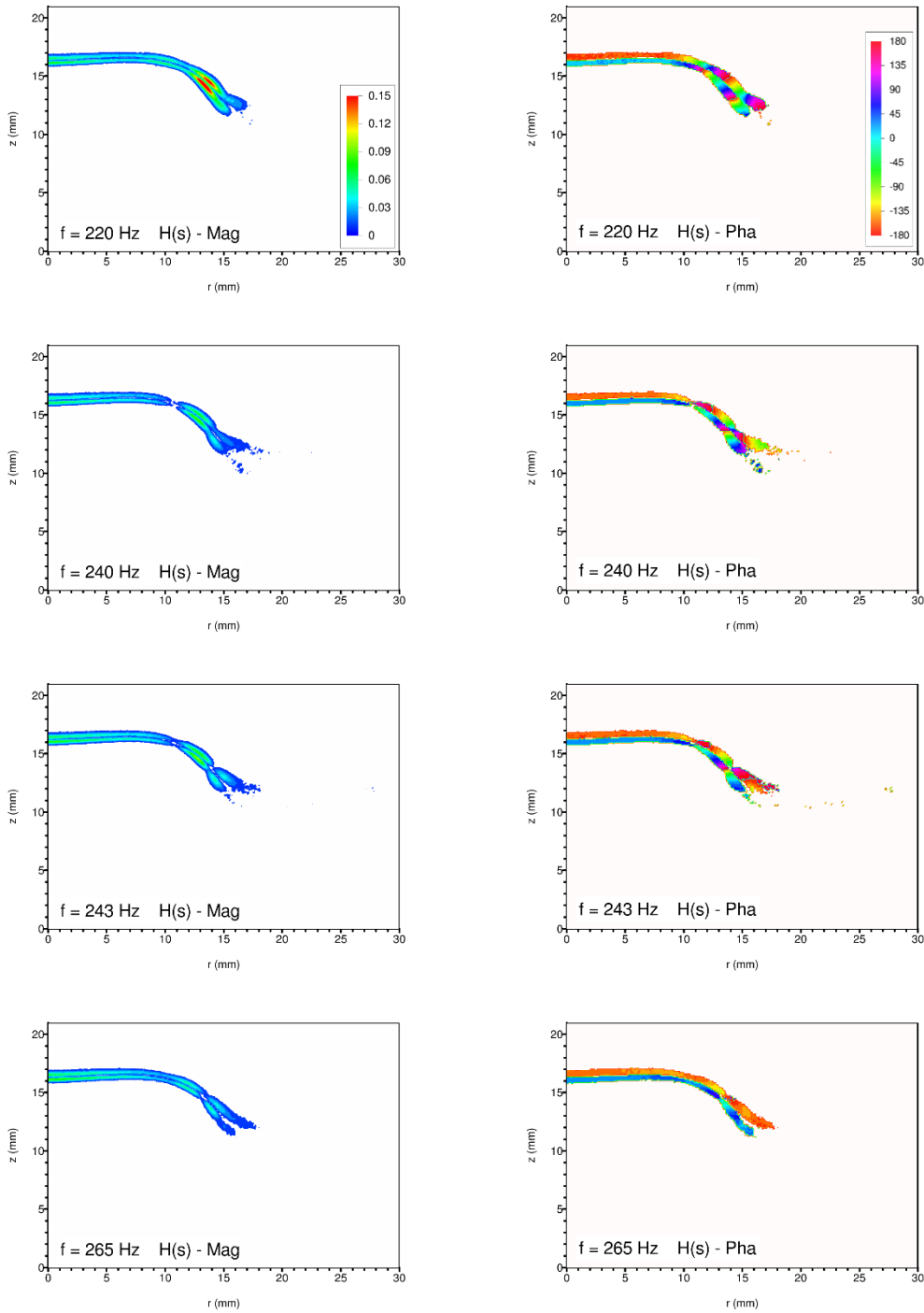


Figure 4-27 (cont): Spatially resolved combustion response function produced from CH_2O PLIF data. Magnitude plots appear in the left column while phase plots are shown on the right. Data for all nine drive frequencies are shown. (See previous and next page.) Note the change in magnitude scale versus the plots for 150 Hz and lower.

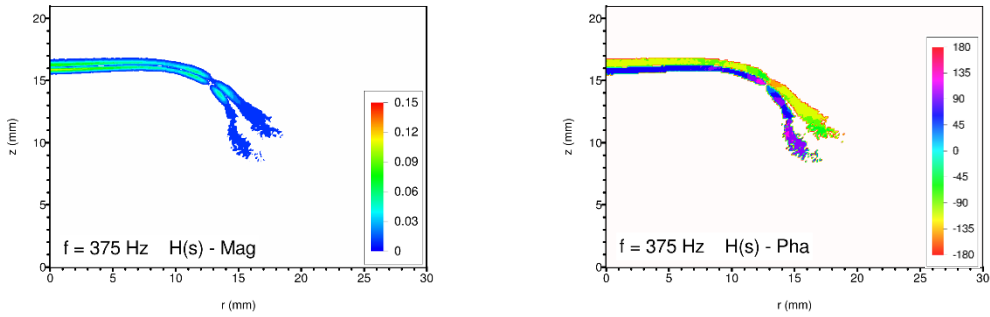


Figure 4-27 (cont.): Spatially resolved combustion response function produced from CH_2O PLIF data. Magnitude plots appear in the left column while phase plots are shown on the right. Data for all nine drive frequencies are shown. (See previous two pages.) Note the change in magnitude scale versus the plots for 150 Hz and lower.

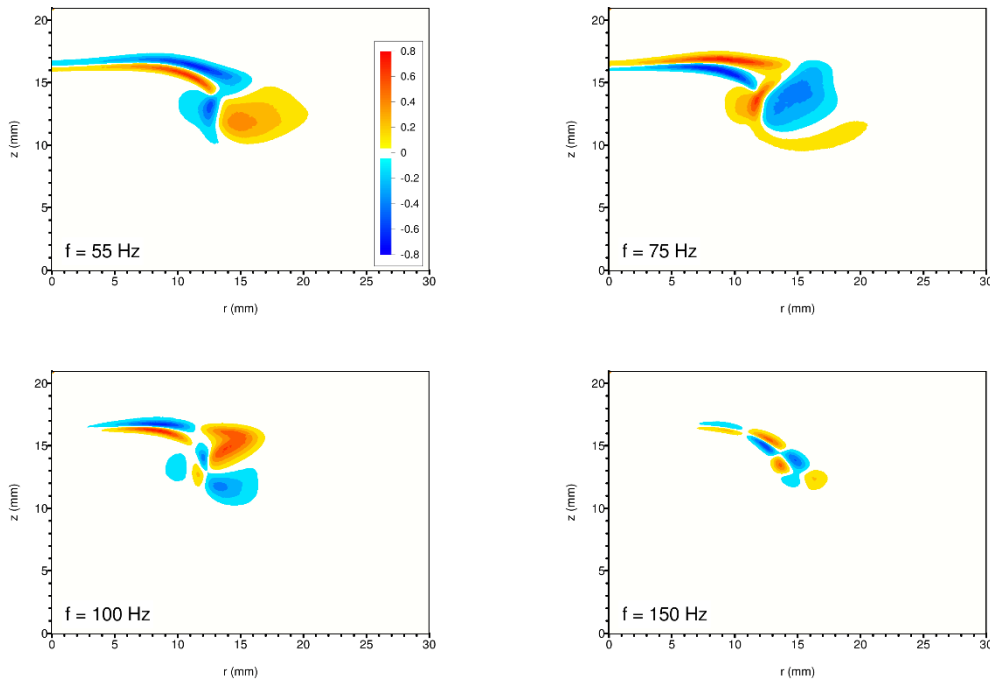


Figure 4-28: Spatially resolved forced Rayleigh index produced from CH_2O PLIF data. Data for all nine drive frequencies are shown. (See next page.) Note the difference between the magnitude legends for the lower four drive frequencies and the upper five drive frequencies.

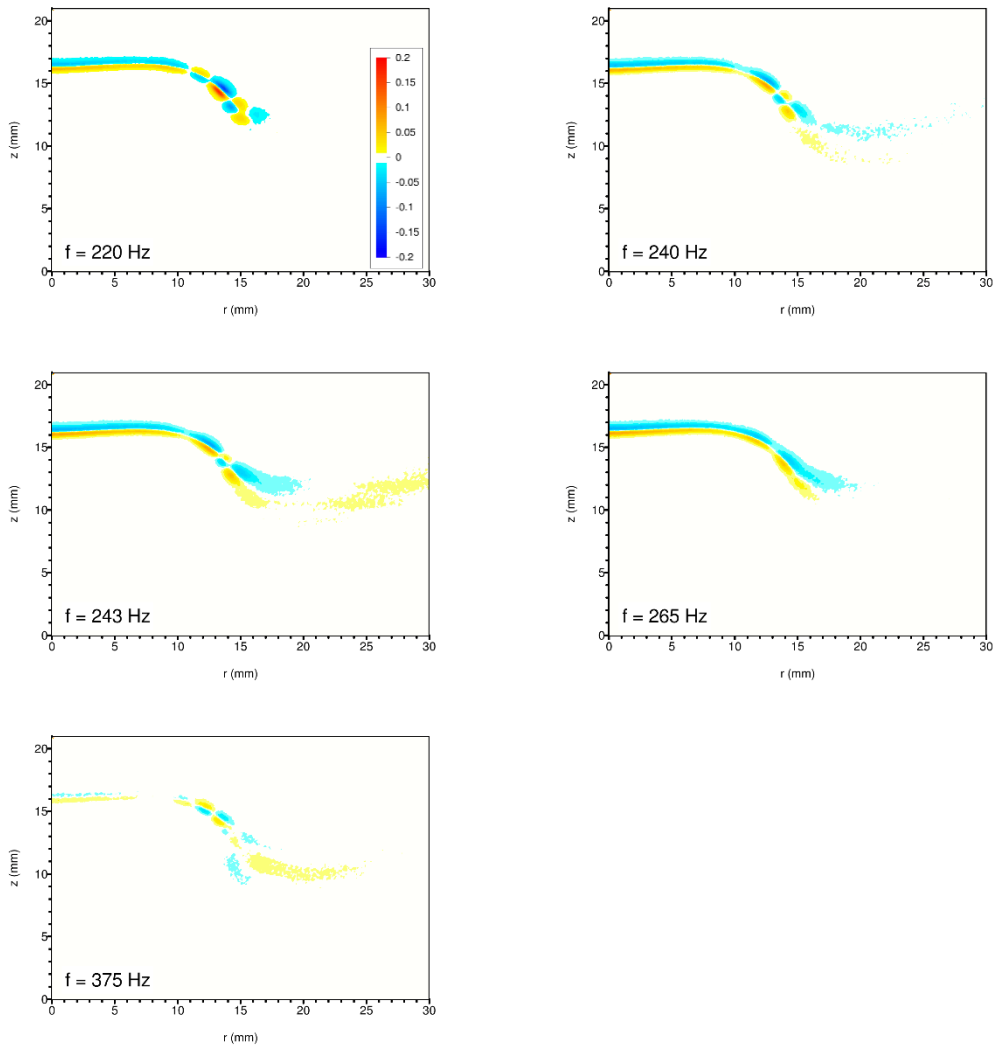


Figure 4-28 (cont.): Spatially resolved forced Rayleigh index produced from CH_2O PLIF data. Data for all nine drive frequencies are shown. (See previous page.) Note the difference between the magnitude legends for the lower four drive frequencies and the upper five drive frequencies.

For the higher drive frequency plots (220 Hz and greater), the similarities in both magnitude and phase between the CH_2O PLIF data and the CH PLIF data are striking. Although the bands in the CH_2O images appear slightly thicker than those seen in the CH PLIF images, the distributions of magnitude and phase between the two cases (for each specific drive frequency) are almost identical up to a radial coordinate of approximately 14 mm. Around this radial position, the bands of the CH PLIF images terminate while the bands in the CH_2O PLIF continue for up to 3 more millimeters. It is this short area of extension that holds the greatest difference between the two data sets (CH and CH_2O PLIF) displayed in the higher frequency regime combustion response function plots. In this extended region, the upper and lower bands in the formaldehyde PLIF generated images diverge slightly and begin taking on a speckled appearance as they dissipate. Despite this, the progression of phase along these ends is smooth.

Figure 4-28 displays the frames corresponding to the CH_2O PLIF spatially resolved forced Rayleigh index for each of the acoustic drive frequencies. Once again, the size of the features in these images is somewhat akin to what was seen in the associated OH PLIF plots, while the double-banded nature is similar to what was displayed in the corresponding CH PLIF images. As observed in the previous CH data, the portions of the bands nearer to the burner centerline run virtually parallel to each other and have opposite sign. Additionally, at all drive frequencies except 75 Hz, the upper band is damping (negative sign) while the lower band is driving (positive sign). For the 75 Hz case, these signs are reversed. In the 55 Hz and 75 Hz images, the region at the outer radii of the flame ($r \approx 10$ to 20 mm) is dominated by activity generated by the shear layer structures reaching the reaction zone. The lower band is seen to terminate, allowing a bridge from the upper band to sneak through and form a lobe below the lower band. Beyond this gap, a large lobe forms to the right with a sign that is the same as the lower band. At a drive frequency of 100 Hz, the structure of the response becomes far more complicated. In this case, both bands terminate at approximately the same radial position ($r \approx 12$ mm). Beyond this point a host of five lobes appear,

two larger in size and three being small. The largest of these lobes is positive in sign while its counterpart is negative. By visual estimation, it appears there is more area covered in yellow-red zones within the image than there is covered in blue zones. This is consistent with the positive global forced Rayleigh index computed earlier and shown in Table 4-4.

As the drive frequency passes 150 Hz, the spatially resolved forced Rayleigh index develops the alternating lobe pattern observed earlier in the corresponding CH PLIF data. As discussed earlier, this sequence of lobes is generated by a continuous progression of the phase (along the band lines) for multiple wraps. The pattern is roughly centered on the path line that defines the reaction zone. Eight lobes are visible in the 150 Hz acoustic drive case, although three of the blue (damping) zones are not completely independent, but instead show narrow connections to each other. The peak number of lobes is seen at a drive frequency of 220 Hz. Counting the two bands that run back to the burner centerline, the total number of visible lobes is ten. Beyond this frequency, the number of lobes begins to decrease and varying levels of diffuse streaks (driving and/or damping) are seen to the right of the edge of the flame. At 265 Hz, the alternations vanish indicating that, in this case, the phase is relatively constant moving along each band. At 375 Hz, a string of lobes reappears at the outer edge of the flame, while the response near the center (small radius) portion of the flame nearly vanishes due to the phase shift generated by the burner nozzle's Helmholtz response.

4.10 Combined OH-CH₂O PLIF Results

This section uses the previously collected OH PLIF and CH₂O PLIF data to generate an estimate for the global and spatially resolved heat release rate within the flame. As proposed by Paul and Najm (1998), the procedure simply involves taking the pixel-by-pixel product of the two PLIF images assuming the intensities within the images have a linear relationship to the species concentrations. This approach is founded on three suppositions:

- 1) There is a strong correlation between the concentration of formyl radicals (HCO) and the local heat release rate in premixed flames.
- 2) The product of the concentrations of OH and CH₂O are directly proportional to the reaction rate of: CH₂O + OH → H₂O + HCO
- 3) The rate of the reaction listed above is good estimate for the total production rate of HCO and hence for the heat release rate.

Experiments employing this method were performed by Fayoux et. al. (2005) using a premixed, counterflow burner under steady conditions. The results were compared with numerical simulations and found to be in good agreement.

In the presented case, both the CH₂O and OH PLIF data were processed by the usual methods. The fully processed (corrected) image data were then normalized by the sensible maximum pixel value found in their associated drive frequency groups. The normalized images (CH₂O and OH) for each phase angle were then multiplied together, pixel by pixel. The resulting combined image sets (phase-resolved) were then further processed by the normal means to produce the desired output data, including the combustion response function and forced Rayleigh index plots.

4.10.1 Resulting Combined OH-CH₂O PLIF Data

It was only possible to generate combined results for the seven base acoustic drive frequencies. This was limited by the available OH PLIF datasets which were only collected for the seven base drive frequencies. The reduced OH-CH₂O data is presented in its entirety in appendix H. Figure 4-29 shows a sample of a combined OH-CH₂O PLIF image of the flame under steady-state conditions (no acoustic forcing). All the image particulars are the same as the previous steady state images. The horizontal axis represents the radius from the centerline of the burner, and the vertical axis represents the height above the nozzle exit plane. The stagnation body height is at

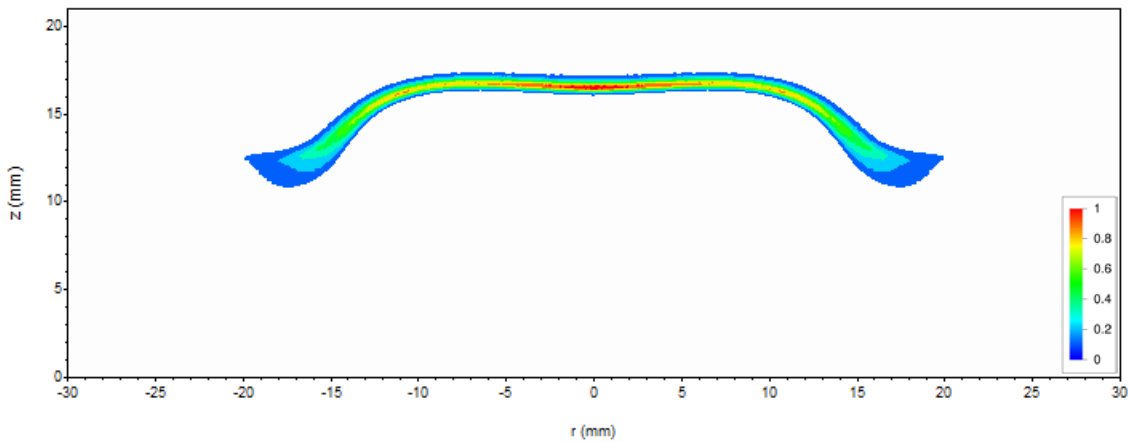


Figure 4-29: Combined OH-CH₂O PLIF image of experimental burner flame under steady conditions (no acoustic forcing). Collected data appears on the left, and is mirrored across the centerline for a visual representation of the entire flame. $\varphi = 0.85$, $V_R = 4.0$.

$z = 21$ mm, which is shown as the top line of the graph frame. The data has been mirrored across the centerline of the burner to complete the visual appearance. The intensity scale presented has been normalized around the maximum intensity in the image.

Figure 4-30 shows typical results for the phase resolved OH-CH₂O (combined) PLIF images. The presented images are for the 55 Hz acoustic drive frequency data. Only 12 of the 24 generated images are displayed. The phase angles shown follow the same conventions as described previously.

Examining the phase resolved images reveals a suspicious feature. Focusing on the images from 180° to 330° , it can be seen that the maximum intensity portion of the flame sheet splits into two peaks. In the 270° and 300° phase images, the flame sheet actually appears to separate. This is highly suspect and may be a product of small positional or scaling errors in the combination of the PLIF images from the two species. Extraordinary care was taken to insure that all images were scaled and registered properly. During the experiments, the imaging system was adjusted so that one pixel equated to a 100um x 100um region in the image plane. Furthermore, during the data processing for this combined case, great care was taken to assure the mated images were registered

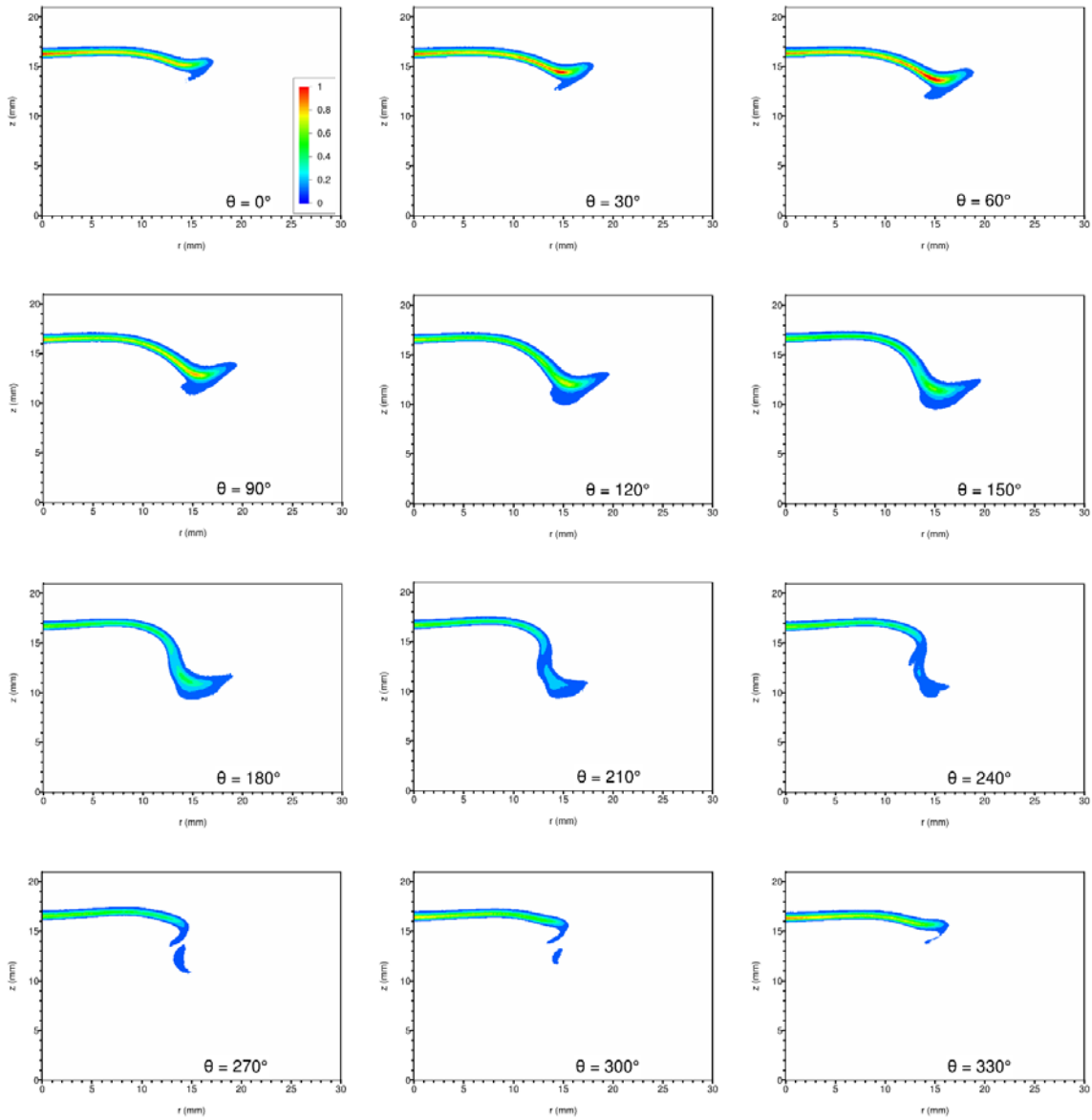


Figure 4-30: Phase-resolved OH-CH₂O (combined) PLIF images for acoustic forcing at 55 Hz. The horizontal axis is the radius (mm) from the centerline of the burner. The vertical axis is the distance (mm) above the nozzle exit plane. Phase angle $\theta = 0^\circ$ corresponds to the rising-edge zero crossing of the local unsteady pressure. Burner operating parameters are: $\varphi = 0.85$, $V_R = 4.0$.

Drive Frequency (Hz)	Combustion Response, H(s)		Forced Rayleigh Index, R _f
	Mag	Phase	
55	1306	16.4	1256
75	1142	-125.3	-660
100	626	99.2	-100
150	65.9	152.6	-58.5
220	44.5	-7.9	44.0
265	76.7	-156.5	-70.3
375	66.8	-125.6	-38.9

Table 4-5: Global unsteady combustion responses as discerned using the combined OH-CH₂O PLIF data for the seven base drive frequencies. Positive phases correspond to the heat release lagging the pressure.

to each other appropriately. Nonetheless, small errors in the procedure may have produced these unusual results. In any case, the data are presented (and further processed) with the awareness of this blemish.

Following the usual methodology, the intensities of the 24 images for each drive frequency case were fully integrated (including the *r* dependence) and then processed by FFT in order to generate the global combustion response and forced Rayleigh index for the seven acoustic drive frequencies. The results are shown in Table 4-5.

These data points can then be plotted on the graphs for the global combustion response function and the global forced Rayleigh index that were generated by bulk chemiluminescence measurements for the relevant test condition in chapter 3. These are shown in Figures 4-31 and 4-32.

Examining the data in the magnitude curve, a matching trend can be seen in the low frequency portion of the response. Similar to the OH data plotted in Figure 4-11, the magnitudes of the four lower frequency-combined OH-CH₂O data points fall under the chemiluminescence baseline curve. The size of this shortfall, however, is only about half of that seen in the OH data.

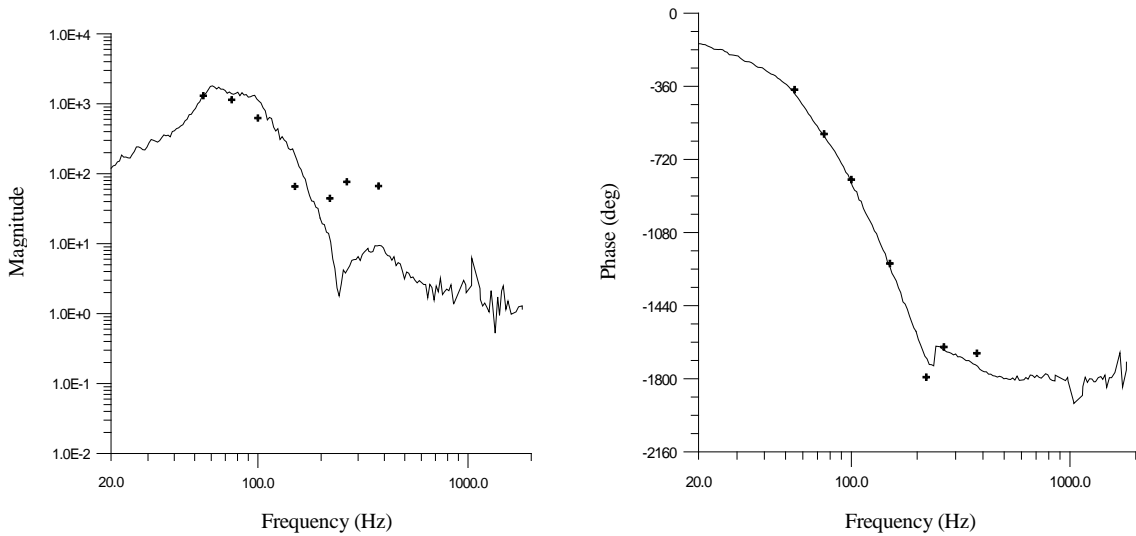


Figure 4-31: Combustion response function - points computed from the combined OH-CH₂O PLIF data (shown as crosshairs) superimposed on the curves computed from the bulk chemiluminescence experiments. Phase data points were placed on the appropriate branch for closest proximity to the curve. Here, negative phases correspond to I' lagging p' .

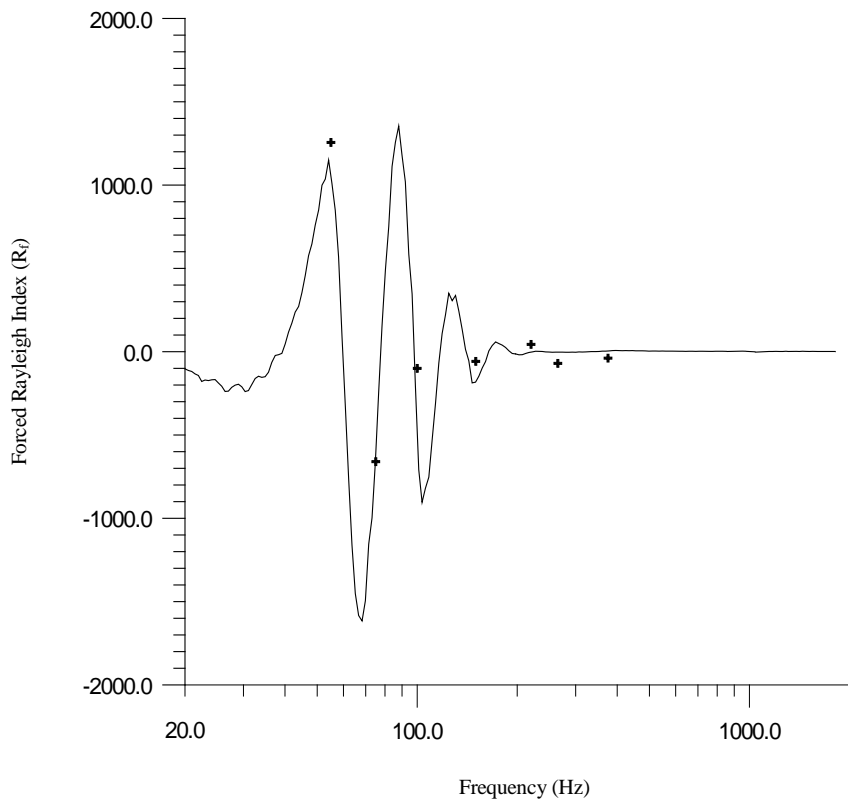


Figure 4-32: Forced Rayleigh index - points computed from the combined OH-CH₂O PLIF data (shown as crosshairs) superimposed on the curves computed from the bulk chemiluminescence experiments.

As was typical in the previously plotted data, the three higher frequency data points in the OH-CH₂O data show values significantly higher than the baseline curve.

Reviewing the phase plot, the four data points for the drive frequencies from 55 Hz to 150 Hz as well as the one for 265 Hz all show very good agreement with the chemiluminescence baseline. The remaining two higher frequency data points show some disagreement with the chemiluminescence curve; however, these errors are similar in magnitude to those seen in the CH PLIF data.

The forced Rayleigh index plot in Figure 4-32 shows the combined OH-CH₂O PLIF global data points overlaid on the baseline curve generated from the chemiluminescence data. Unlike the forced Rayleigh index plot for the previously reviewed species, this plot is in fair (if not good) agreement for the four lower drive frequencies. In fact, for the 75 Hz and 100 Hz data points, the agreement is very good. The three higher frequency data points show some scatter; this is similar to what was seen in the previously reviewed data.

The spatially resolved response functions generated from the combined OH-CH₂O data are presented next. The combustion response function plots are shown in Figure 4-33. Not surprisingly, these response images show larger regions of involvement at lower drive frequencies (150 Hz and less) and smaller regions at higher drive frequencies. The banded regions seen earlier in the formaldehyde images are still present in certain regions of each plot. For drive frequencies of 150 Hz and less, the banding can be seen in the responses for radii less than approximately 12 mm. For frequencies higher than this, the banding appears throughout, similar to the previous CH₂O combustion response data.

As previously seen, the low frequency combustion response plots for OH and CH₂O both exhibit the “head and tail” structure. In the case of formaldehyde, each band (upper and lower) has its own independent “head.” The lobes have clearly visible minima between them, and the phase

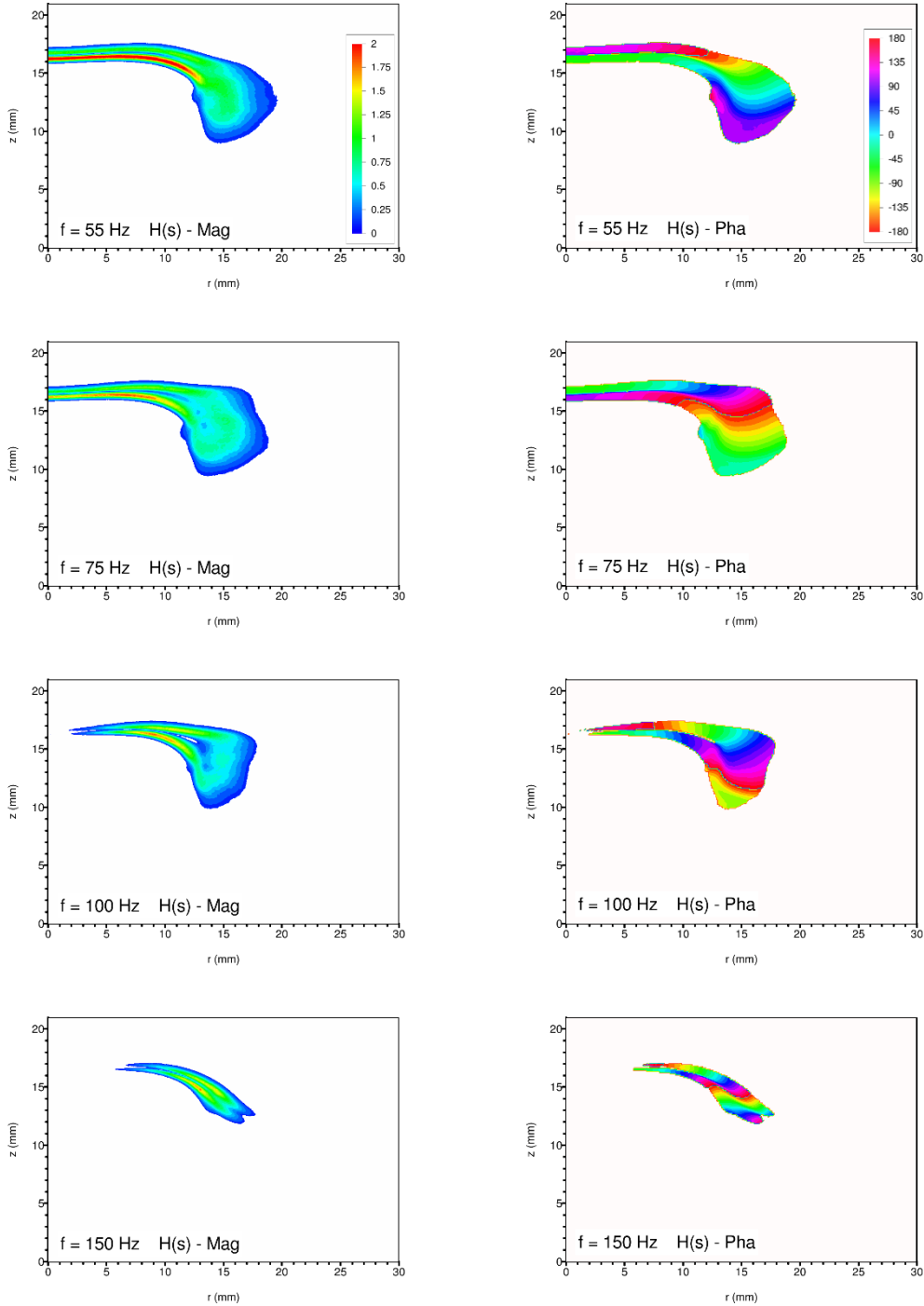


Figure 4-33: Spatially resolved combustion response function produced from OH-CH₂O PLIF combination data. Magnitude plots appear in the left column while phase plots are shown on the right. Note that positive phase values correspond to I' lagging p' . The coordinate system origin is along the burner centerline at the nozzle exit plane. Data for the seven base drive frequencies are shown. (See next page.)

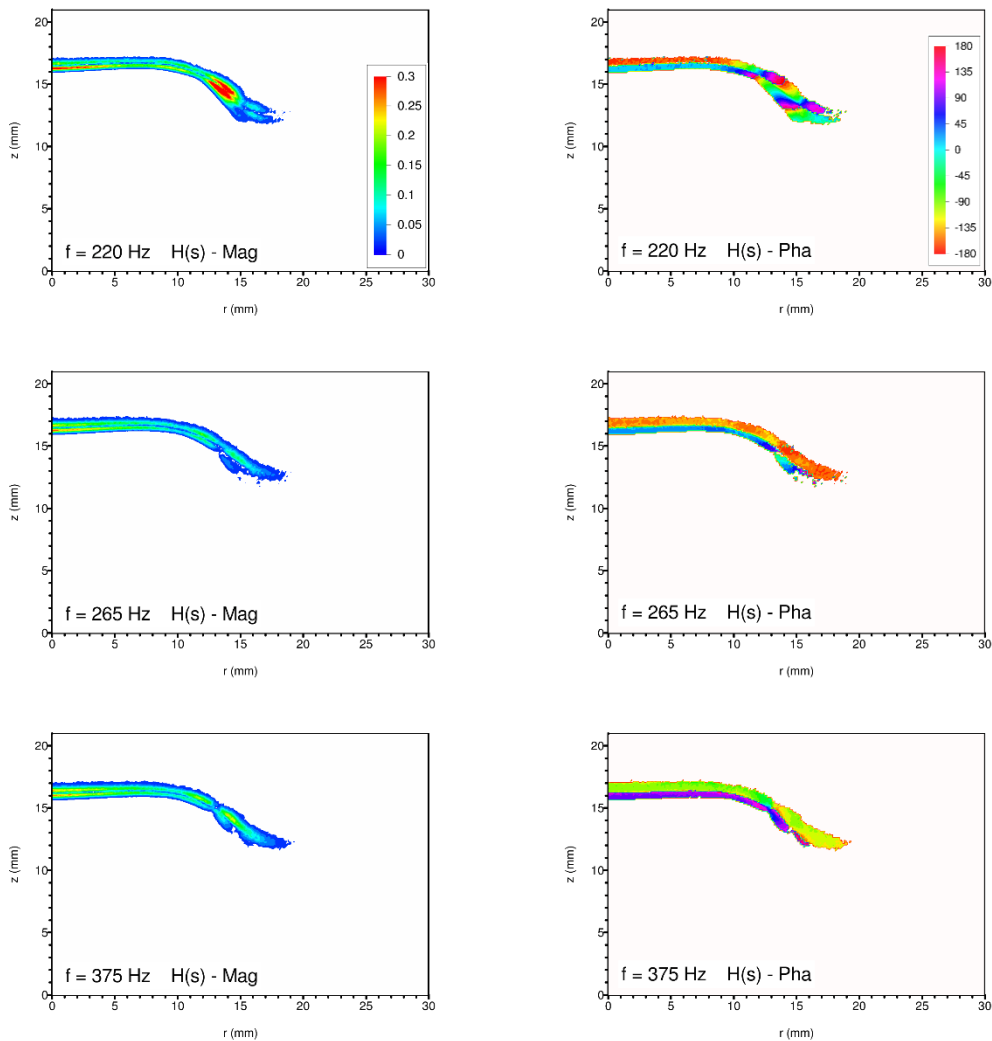


Figure 4-33 (cont): Spatially resolved combustion response function produced from OH-CH₂O PLIF combination data. Magnitude plots appear in the left column while phase plots are shown on the right. Data for the seven base drive frequencies are shown. (See previous page.) Note the change in magnitude scale versus the plots for 150 Hz and lower.

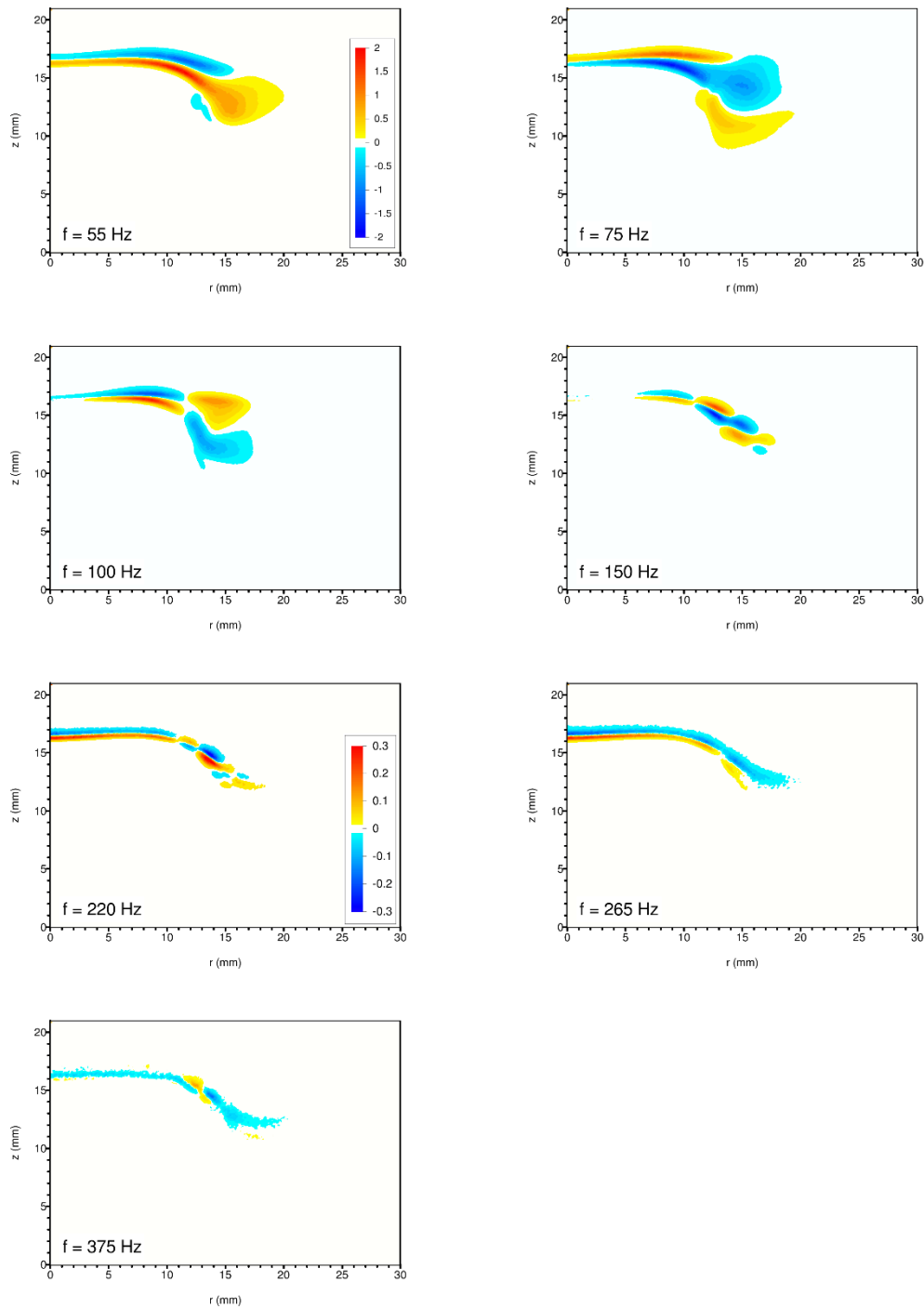


Figure 4-34: Spatially resolved forced Rayleigh index produced from OH-CH₂O PLIF combination. Data for the seven base drive frequencies are shown. Plots for the four lower frequencies use the top magnitude legend. Plots for the three higher frequencies use the bottom magnitude legend.

jumps across lobes at the points of closest distance are typically not small. However, for the corresponding test cases in the combined OH-CH₂O results, the two bands merge into a single “head” region. Although the phases in each band are very different (typically 180° apart), the phases blend together, continuously and smoothly within the “head” of the response zone.

For the 220 Hz to 375 Hz cases, the results are very similar in appearance to the associated images generated independently from the CH and CH₂O PLIF data. The thickness of the two bands at these drive frequencies is similar to that seen in the formaldehyde data. The phase behavior of the bands is relatively constant away from the edge of the flame (i.e. for $r < 10$ mm). For the 220 Hz and 265 Hz acoustic drive cases, the upper bands in the flame’s inner region are 180° out of phase with the oscillating pressure field while the lower bands are seen to be in phase. At the higher 375 Hz drive frequency, the phase shifts (as before) to the upper band leading the pressure by 90° and the lower band lagging the pressure by 90°.

Figure 4-34 shows the plots of the spatially resolved forced Rayleigh index for the combined OH-CH₂O data. Double banding is seen, once again, in the region away from the flame’s edge. The bands exhibit the same signs (polarities) as were seen in the CH and CH₂O forced Rayleigh index plots. In all the images except the 75 Hz case, the upper band has negative (damping) polarity while the lower band has positive (driving) polarity. For the 75 Hz case, this is reversed. Inspecting the 375 Hz drive case, the blue damping band is found to be dominant. Careful examination reveals a very faint yellow band below the blue band at small radii. Nonetheless, the total integrated magnitude of the yellow driving band is clearly much smaller than that of the damping blue band.

Focusing on the 55 Hz and the 75 Hz drive cases, a definite similarity exists with the corresponding plots from the formaldehyde PLIF data. Both 55 Hz plots have a damping upper band and a driving lower band, while the reverse is true for the 75 Hz plots. The main difference can be seen in the missing gap in the lower band for the combined data. In the CH₂O plots, the

lower band has a separation between its “head” and “tail,” allowing a narrow path of color to sneak through at the far end of the upper band down to a lower lobe. This is seen in both the 55 Hz and 75 Hz cases. However, in the OH-CH₂O images, the lower bands for these drive frequencies are continuous through to the “head” region.

In the 100 Hz image, the pattern has become far less complicated than the poly-lobed monstrosity seen in the formaldehyde images. In this case, the bands are seen with one pair of alternating lobes. As the drive frequency increases, the alternating lobe pattern develops, once again appearing as a “twisted rope.” This is seen in the forced Rayleigh index images for the 150 Hz and 220 Hz cases. At 265 Hz, the alternating lobes vanish and the two response bands appear nearly continuous over their whole lengths. Finally, at 375 Hz, the alternations return but are very faint. In this image, virtually all of the yellow-red driving color has disappeared. The image is dominated by a single, blue damping band. A single yellow stripe is seen twisting over the top of the blue band at a radius of approximately 13 mm. A few other faint hints of yellow appear in various locations, including below the blue band at the root of the flame. All of these are very weak.

4.11 Image Chemiluminescence Results

Along with the phase-resolved PLIF data that were taken to image OH, CH and CH₂O species, phase-resolved image chemiluminescence data were also collected. This was done for comparison purposes – to compare with both the species specific PLIF data as well as the bulk chemiluminescence data. Additionally, it was also collected to demonstrate the shortcomings of the image chemiluminescence technique.

The image chemiluminescence experiments were performed using virtually the same system configuration as that used for the PLIF experiments. The major exception is the elimination of the laser. Instead, the YAG laser trigger signal output from the AFC-100 was rerouted from the

laser controller to both the photodiode input on the AFC-100 as well as the trigger input on the camera gate controller. Afterward an automated phase offset calibration was performed to adjust for the change in signal timing.

The Andor iStar ICCD camera was used in conjunction with the Nikon Nikkor 50 mm f/1.2 macro lens for imaging. The Semrock FF01-447/60-25 optical band-pass filter was installed to block all but the CH^* and CO_2^* chemiluminescence emission. The f-stop aperture on the lens was opened to its maximum position of f/1.2 in order to collect as much light as possible. Even so, it was necessary to run the ICCD intensifier with a 10 μs gate width to achieve reasonable signal levels.

Processing of the image chemiluminescence data employed a subset of the same software routines as used in the previous PLIF data reduction. The obvious exclusions were the routines that performed corrections for variations in the laser pulse energy, laser sheet spatial distribution, and for laser absorption. The other significant difference was in the spatial integration used when calculating global values. In the PLIF reduction cases, spatial integrations included the r dependence to account for the axisymmetric nature of the flame. This was essential since the emission being collected originated within the thin laser sheet. However, for the image chemiluminescence case, the collected emissions were produced throughout the flame. Although most of the collected light was out of focus (especially at such a small aperture number), all the light still reached the focal plane (or so it was thought – this problem will be discussed later). Consequently, no modifier was needed in the global integration of the intensity.

4.11.1 Reduced Image Chemiluminescence Data

Chemiluminescence experiments were performed for the seven base drive frequencies. The reduced image chemiluminescence data is presented in its entirety in appendix H. Figure 4-35 shows a sample chemiluminescence image of the flame under steady-state conditions (no acoustic

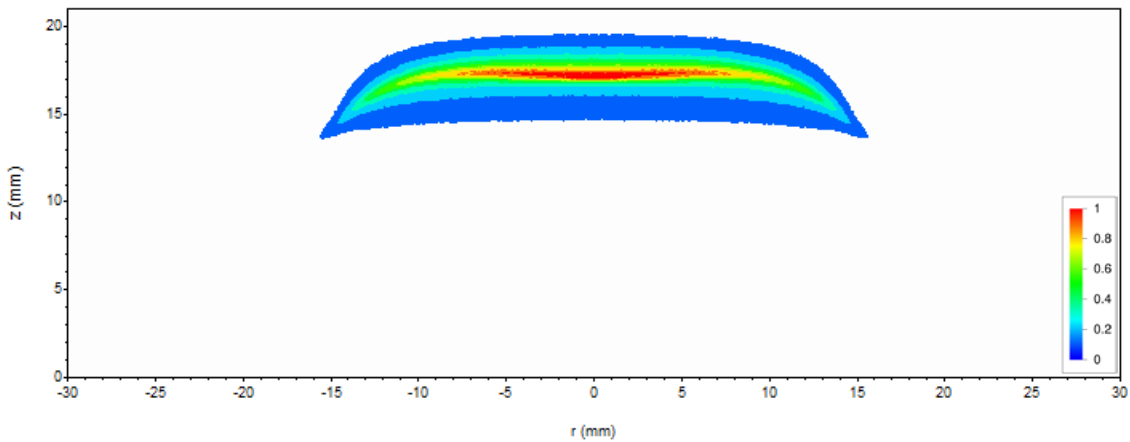


Figure 4-35: Chemiluminescence image of experimental burner flame under steady conditions (no acoustic forcing). Collected data appears on the left, and is mirrored across the centerline for a visual representation of entire flame. $\varphi = 0.85$, $V_R = 4.0$.

forcing). Again, the horizontal axis represents the radius from the centerline of the burner, and the vertical axis represents the height above the nozzle exit plane. The stagnation body height is at $z = 21$ mm, which is shown as the top line of the graph frame. The data has been mirrored across the centerline of the burner to complete the visual appearance. The intensity scale presented has been normalized around the maximum intensity in the image.

It is immediately obvious that the spatial resolution of the image is very poor. In comparison with the previously collected PLIF images, this frame provides very little detail. The vast amount of light collected that did not originate in the “object” plane of the lens has essentially washed away any meaningful features. The flame appears artificially thick, and a large amount of luminescence appears well below the location of the reaction zone.

What cannot be seen in the image due to the color scaling (but is nonetheless present in the data) is the background pedestal that has developed. The background value of the image has risen above the floor established by the ICCD camera. This is caused by the out-of-focus light being distributed all over the focal plane. As a result, any attempt to integrate the intensity to generate global values will require summation over the entire plane.

Drive Frequency (Hz)	Combustion Response, H(s)		Forced Rayleigh Index, R _f
	Mag	Phase	
55	1053	21.7	979
75	1181	-131.9	-788
100	768	80.1	132
150	134	119.9	-66.6
220	7.72	-150.3	-6.70
265	8.18	-133.5	-5.63
375	3.78	-76.1	0.91

Table 4-6: Global unsteady combustion responses as discerned using the chemiluminescence data for the seven base drive frequencies. Positive phases correspond to the heat release lagging the pressure.

Figure 4-36 shows typical results for the phase-resolved chemiluminescence images. The presented images are for the 55 Hz acoustic drive frequency experiment. Only 12 of the 24 generated images are displayed. The phase angles shown follow the same conventions as described previously.

Following the usual methodology, the intensities of the 24 images for each drive frequency case were fully integrated (as is) and then processed by FFT in order to generate the global combustion response and forced Rayleigh index for the seven acoustic drive frequencies. The results are shown in Table 4-6.

As done in the previous cases, the data points are then plotted on the graphs for the global combustion response function and the global forced Rayleigh index that were generated by bulk chemiluminescence measurements for the relevant test condition in chapter 3. These are shown in Figures 4-37 and 4-38.

Inspecting the combustion response data in Figure 4-37, the agreement between the image chemiluminescence data compared and the baseline bulk chemiluminescence data is good, as might

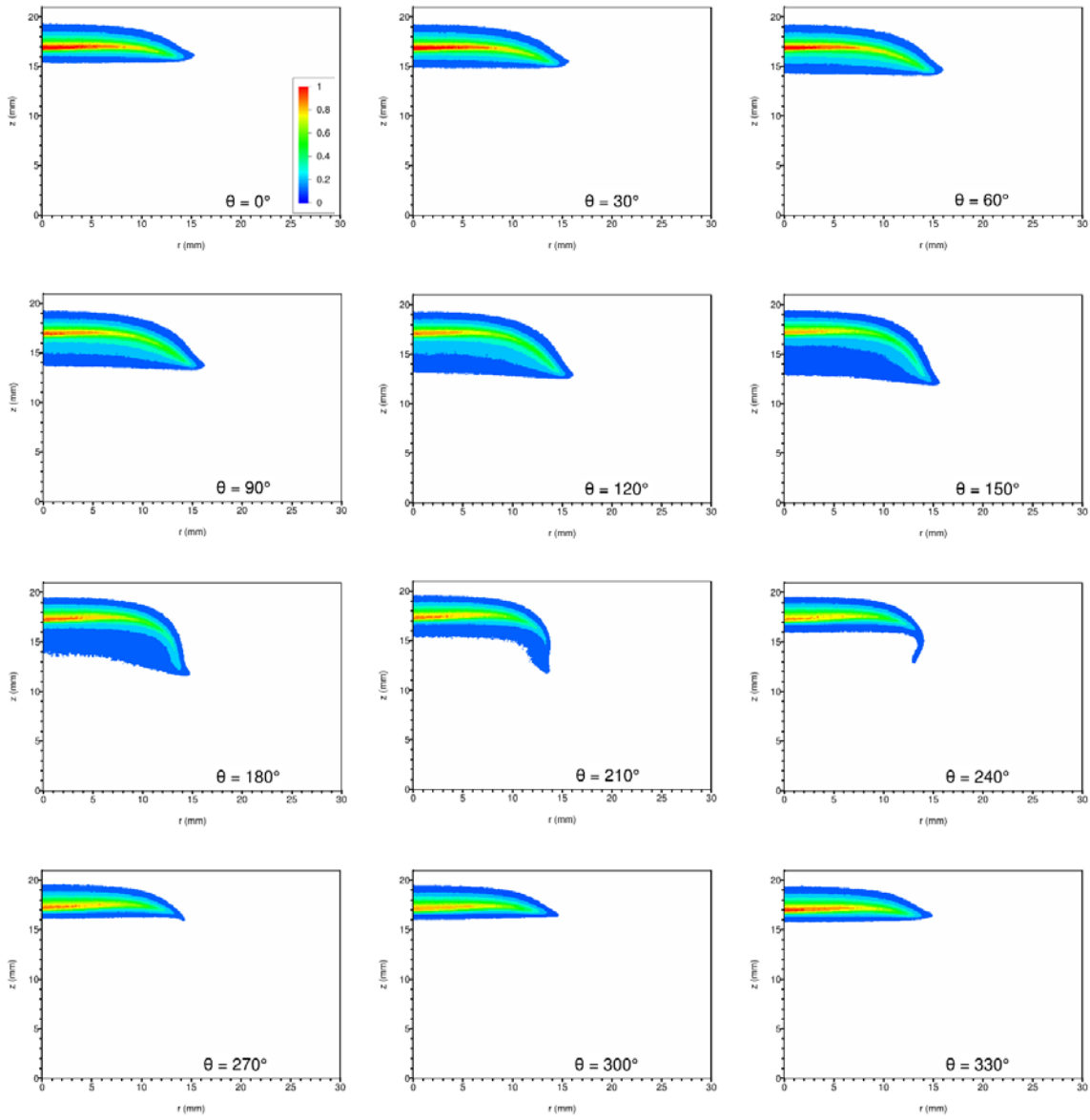


Figure 4-36: Phase-resolved chemiluminescence images for acoustic forcing at 55 Hz. The horizontal axis is the radius (mm) from the centerline of the burner. The vertical axis is the distance (mm) above the nozzle exit plane. Phase angle $\theta = 0^\circ$ corresponds to the rising-edge zero crossing of the local unsteady pressure. Burner operating parameters are: $\varphi = 0.85$, $V_R = 4.0$.

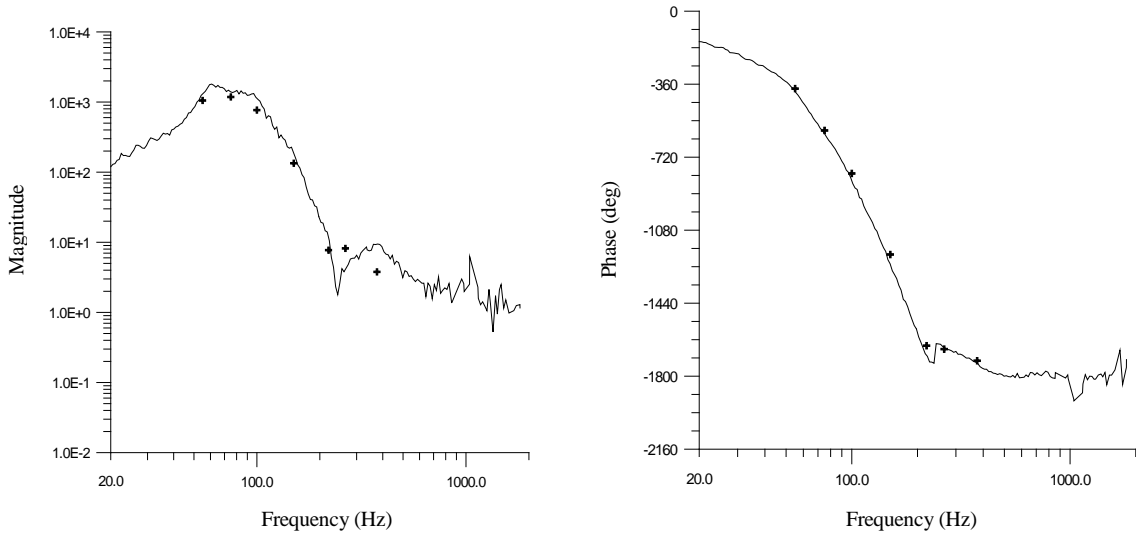


Figure 4-37: Combustion response function - points computed from the image chemiluminescence data (shown as crosshairs) superimposed on the curves computed from the bulk chemiluminescence experiments. Phase data points were placed on the appropriate branch for closest proximity to the curve. Here, negative phases correspond to I' lagging p' .

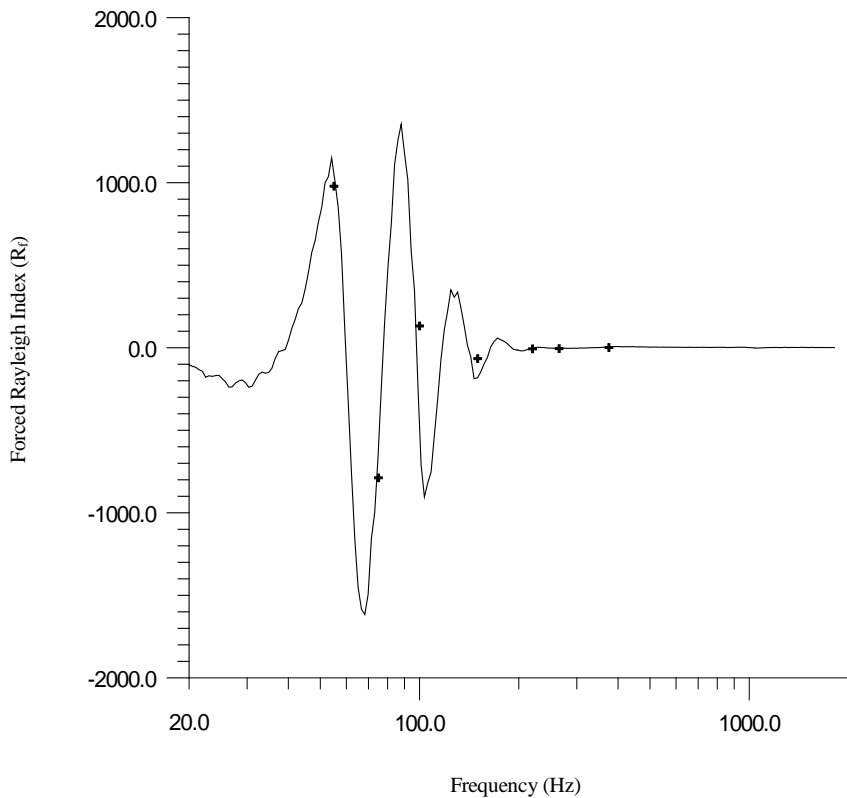


Figure 4-38: Forced Rayleigh index - points computed from the image chemiluminescence data (shown as crosshairs) superimposed on the curves computed from the bulk chemiluminescence experiments.

be expected. A small shortfall in the magnitude is seen in the four lowest frequency data points. Nonetheless, these results are noticeably better than those seen in any of the PLIF cases. For the two highest frequency data points, the magnitudes are (at least) in the correct order of magnitude.

Visual examination of the phase plot shows good agreement throughout. Looking closely at the rapidly descending portion of the phase trace where the first five data points lie, it appears that there may be a small frequency offset leading to the data points lying slightly to the right of the baseline curve. It is unclear if this is due to a set-point error or calibration issue in a parameter such as the burner flowrate, or if it is a bias generated by something more sinister – a problem in the image chemiluminescence setup itself that was only discovered after the data were reduced. (This is discussed below.)

Figure 4-38 shows the forced Rayleigh index plot produced from the bulk chemiluminescence data with the newly generated data points (image chemiluminescence) superimposed. Again, the agreement is good, despite the small frequency/phase offset mentioned above. As would be expected, the agreement in this case is superior to all the previously reviewed PLIF data cases.

The spatially resolved combustion response plots generated from the chemiluminescence image data are shown in the next two figures. Figure 4-39 presents the spatially resolved combustion response function. The magnitude and phase images are shown for all seven drive frequencies with the magnitude plots on the left and the phase plots on the right. Examination of these images reveals the disservice done by not having a cleanly defined image plane. The integration of luminescence over the entire depth of the flame, combined with the fact that most of this light is out of focus, produces images containing far less useful information compared to their earlier discussed counterparts. Some features can be resolved at higher drive frequencies (such as the banded behavior and the phase relation between the bands) but the resolution is generally poor.

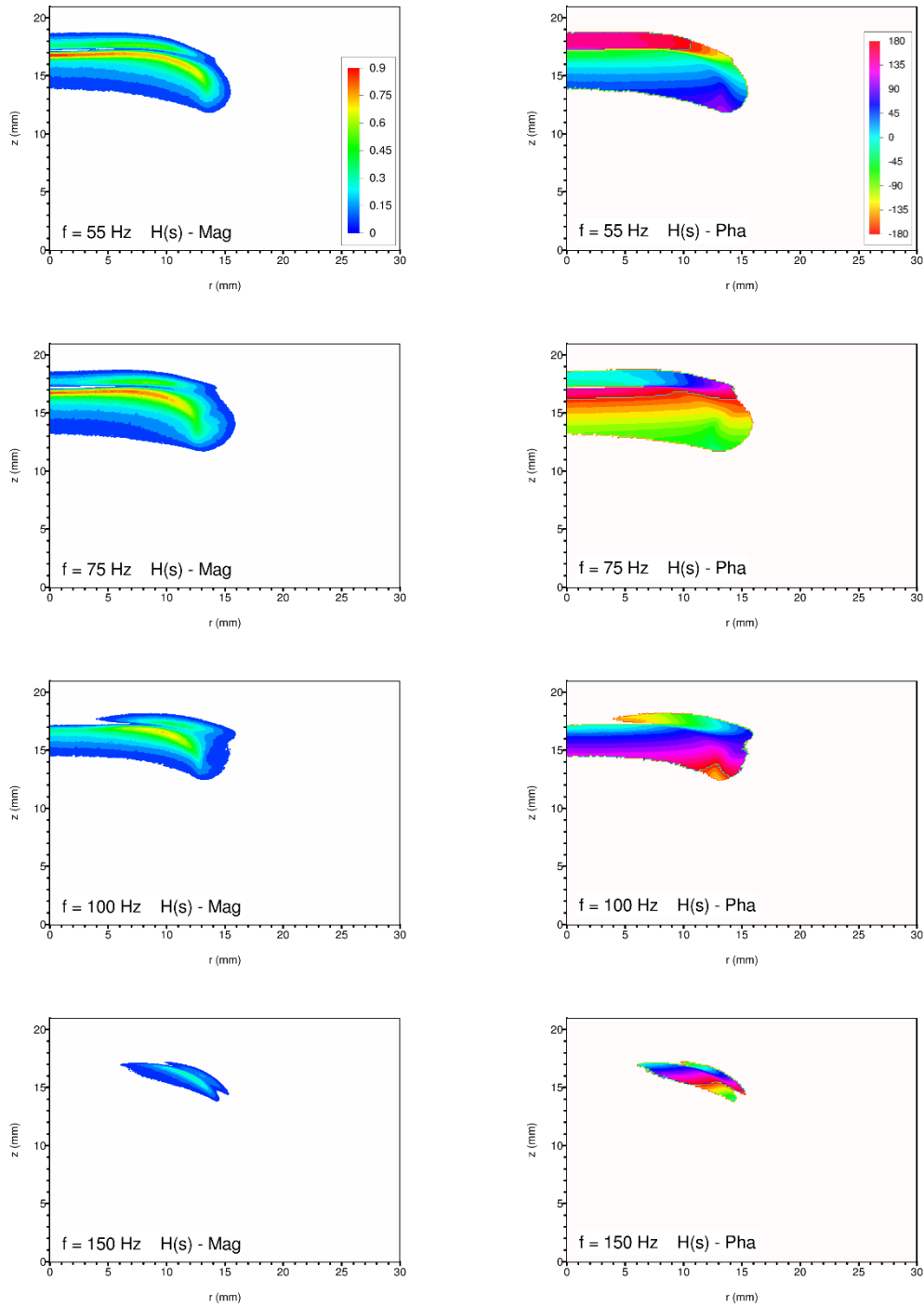


Figure 4-39: Spatially resolved combustion response function produced from chemiluminescence data. Magnitude plots appear in the left column while phase plots are shown on the right. Note that positive phase values correspond to I' lagging p' . The coordinate system origin is along the burner centerline at the nozzle exit plane. Data for the seven base drive frequencies are shown. (See next page.)

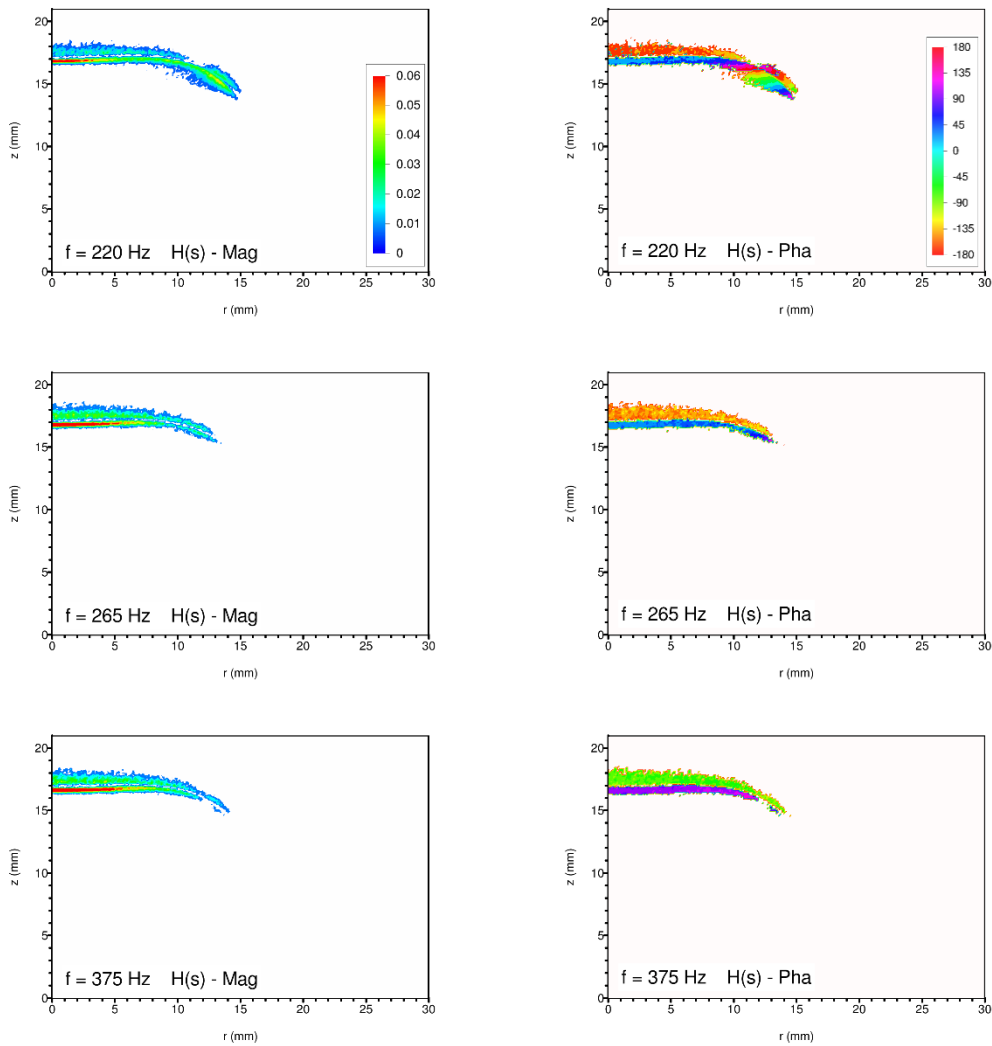


Figure 4-39 (cont.): Spatially resolved combustion response function produced from chemiluminescence data. Magnitude plots appear in the left column while phase plots are shown on the right. Data for the seven base drive frequencies are shown. (See previous page.) Note the change in magnitude scale versus the plots for 150 Hz and lower.

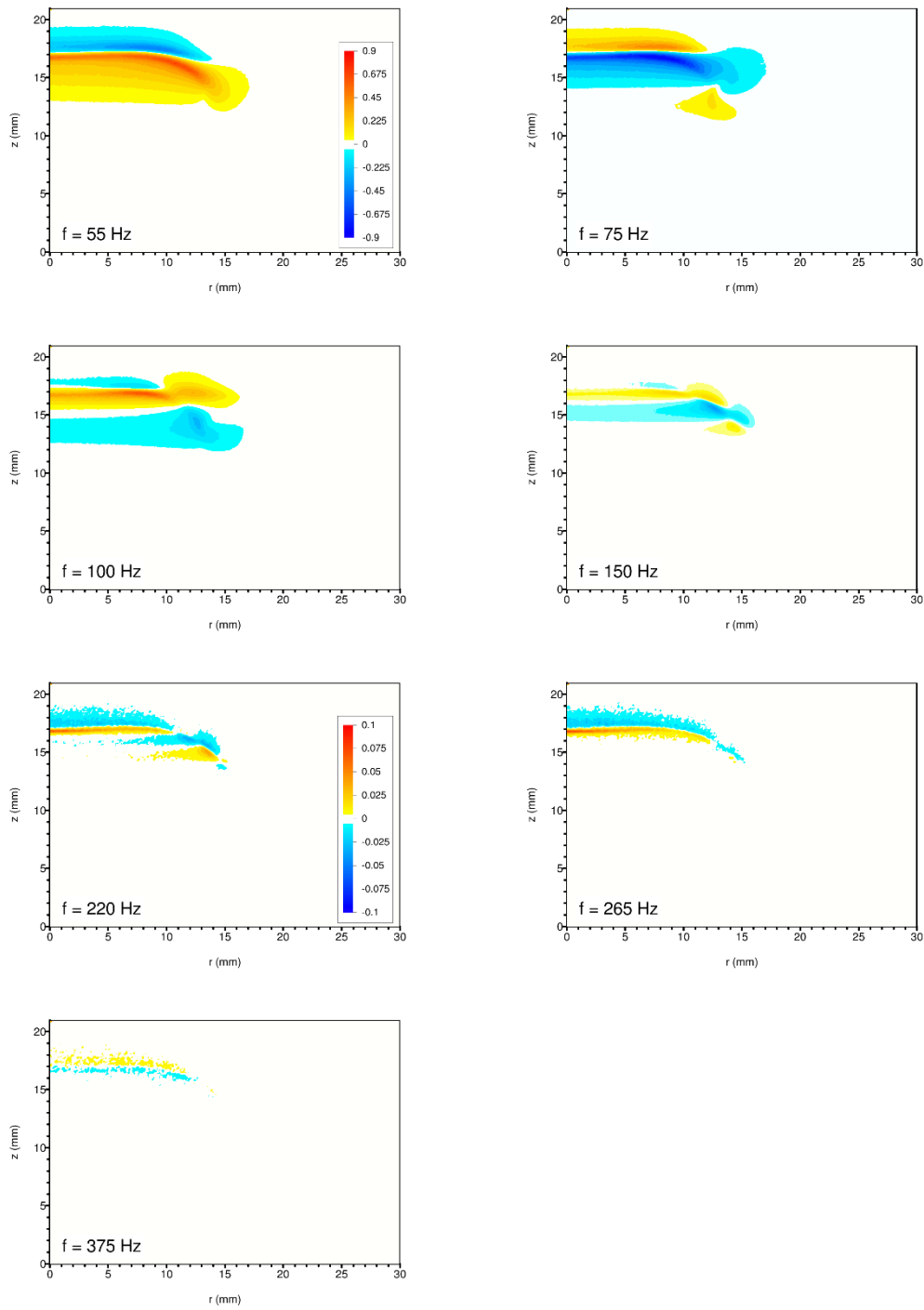


Figure 4-40: Spatially resolved forced Rayleigh index produced from chemiluminescence data. Data for the seven base drive frequencies are shown. Plots for the four lower frequencies use the top magnitude legend. Plots for the three higher frequencies use the bottom magnitude legend.

The corresponding forced Rayleigh index plots appear in Figure 4-40 and are seen to be equally obfuscated. In these images, all real detail is lost – washed away by the out-of-focus light. Large regions of yellow and light blue appear (indicating driving and damping zones) that are manifestations of the integration over depth. The small structures that can be discerned in the PLIF data are not seen at all. Together these conspire to make the data of minimal use.

As alluded to above, an additional problem was discovered with the image chemiluminescence technique – a problem that remained unknown until the experiments were complete and the data were being processed. The issue centers on the collection of the out-of-focus light. It was initially assumed, despite the fact that most of the luminescence from the flame was out of focus, that all the light would be captured on the focal plane of the ICCD camera. This was verified to be true in the bulk chemiluminescence experiments where the Nikon lens was coupled to a photomultiplier tube. However, in the bulk chemiluminescence case, the aperture number of the lens was set to f/4 resulting in a much smaller aperture area. This was possible due to the superior sensitivity and selectivity of the lock-in analyzer. Additionally, the photocathode on the PMT was larger in size than that of the ICCD photo-intensifier. As a consequence of these two differences, indeed, a majority of the luminescence collected by the lens was deposited on the active area of the PMT photocathode.

For image chemiluminescence, the situation was quite different. To achieve acceptable signal levels it was necessary to open the lens aperture to the full f/1.2 position. This resulted in greater signal, but also distributed the out-of-focus luminescence over a larger area. This was compounded by the smaller area of the intensifier photocathode (versus the PMT) which is only 12 mm x 12 mm. Finally, adding to the consternation was the fact that the flame image was (purposefully) off-center of the optical axis. The optical axis position was held constant through all experiments (PLIF and image chemiluminescence). It was positioned off-center in order to

provide visibility over a larger radial distance (on one side of the flame) while still maintaining the target resolution of 100 μm per pixel. The results of these combined issues were the following:

- 1) Some chemiluminescence signal was lost beyond the edge of the focal plane.
- 2) The loss of luminescence was not uniformly distributed over the field of view. Out-of-focus light originating near the optical axis was more likely to land on the focal plane than out-of-focus light originating at distances farther away from the optical axis.
- 3) Since the optical axis was not centered on the flame, the loss of light from the flame is not symmetric about the flame's centerline. Therefore, cropping the flame's image along the flame centerline does not necessarily result in a "half-flame" contribution to the fluorescence signal.

Ultimately, these results can lead to errors in the magnitudes and phases used to generate the response functions. It is quite possible that these account (at least in part) for the discrepancies seen previously between the bulk chemiluminescence data and image chemiluminescence data.

4.12 Acetone PLIF Results

The earliest acoustically forced PLIF experiments in the present setup quickly revealed strong unsteadiness at the outer edges of the flat flame. It was clear that some line of structures or shear-layer roll-up was being driven at the interface between the reactant jet and the surrounding quiescent air. To investigate this, acetone PLIF was performed to visualize the reactant jet travelling into the reaction zone. This was done purely to provide insight into the dynamic behavior of the jet and not to evaluate any particular combustion response.

Acetone was supplied to the reactant mixture by a precision metering premixer system that was controlled electronically through the OPO.EXE software. Details of this acetone seeding system can be found in appendix C. For all the acetone seeded experiments, the acetone seeding

rate was set to 0.25% by volume (molar) of the total reactant flowrate. The pre-seeding equivalence ratio, the acetone flow rate and the burner nozzle needle valve were all coordinated to provide the desired seeding volume fraction while also holding the heating rate (per unit mass) and nozzle exit velocity constant with respect to the established baseline case.

A pump wavelength of 277 nm was chosen to excite the acetone molecules. This wavelength is far from any excitable band for the OH in the flame, yet it provides good coupling to the broadband absorption of acetone between 250 nm and 300 nm. Fluorescence was collected using the iStar ICCD camera with the Cerco 2085 UV lens. A 3 mm thick WG305 optical filter was used in front of the intensifier photocathode to minimize contamination from scattered 277 nm laser light.

4.12.1 Resulting Acetone PLIF Data

Acetone PLIF experiments were performed for the seven base drive frequencies. The resulting processed data is presented in its entirety in appendix H. Figure 4-41 shows an acetone PLIF image of the flame under steady-state conditions (no acoustic forcing). The horizontal axis represents the radius from the centerline of the burner, and the vertical axis represents the height above the nozzle exit plane. The stagnation body height is at $z = 21$ mm, which is shown as the top line of the graph frame. The data has been mirrored across the centerline of the burner to complete the visual appearance. The intensity scale presented has been normalized around the maximum intensity in the image.

Figure 4-42 shows typical results for the phase-resolved acetone PLIF images. The presented images are for the 55 Hz acoustic drive frequency experiment. Only 12 of the 24 generated images are displayed. The phase angles shown follow the same conventions as described previously. The details of the phase-resolved images for all drive frequencies will not be covered here. Complete image data can be found in appendix H.

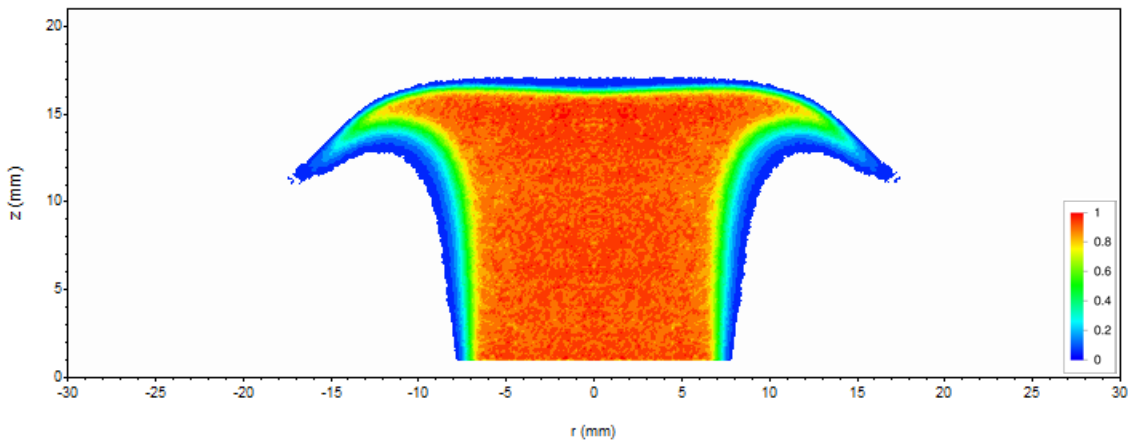


Figure 4-41: Acetone PLIF image of seeded reactant flow under steady conditions (no acoustic forcing). Collected data appears on the left, and is mirrored across the centerline for a visual representation of entire flame. Burner centerline is at $r = 0$. Position $z = 0$ corresponds to the nozzle exit plane.

Of specific interest are the observed shear layer structures and their corresponding convection speeds. Figure 4-43 presents a selected acetone PLIF image for each drive frequency. It can be seen from these images that structures are difficult to identify for some of the applied forcing frequencies. Structure tracking was performed for the 75 Hz and 150 Hz cases where visibility was favorable. The shear layer structure locations were recorded as a function of time. The vertical position of the structures (above the nozzle) was then plotted against time to visualize the trajectory, and to estimate the transport velocity and total delay. This plot is shown in Figure 4-44.

For the two cases shown, the transport velocity is seen to be 86 cm/s. This appears reasonable as the average jet velocity for this test case is 167 cm/s, or about twice the value. As the reaction zone is approached, the vertical velocity of the structures decreases while the horizontal velocity (not shown) increases. This roll-off in vertical velocity can be seen in the upper portion of Figure 4-44. Here, the two sets of data points in this region have been fit with 2nd-order polynomials purely for visualization purposes. The height of this structure deceleration region appears to scale with the structure size or wavelength. If it is assumed that a structure has “reached”

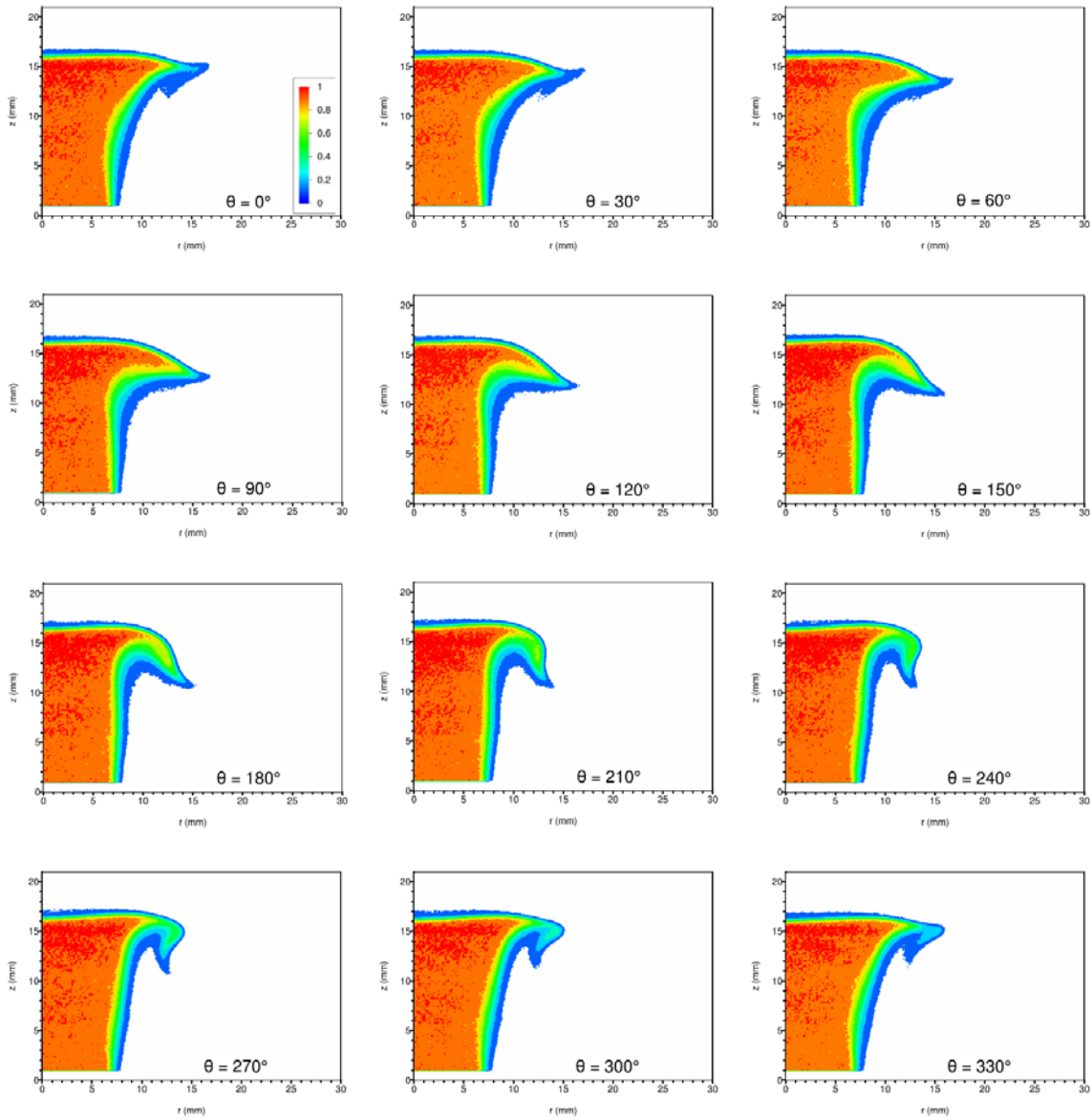


Figure 4-42: Phase-resolved acetone PLIF images for acoustic forcing at 55 Hz. The horizontal axis is the radius (mm) from the centerline of the burner. The vertical axis is the distance (mm) above the nozzle exit plane. Phase angle $\theta = 0^\circ$ corresponds to the rising-edge zero crossing of the local unsteady pressure. Burner operating parameters are: $\varphi = 0.85$, $V_R = 4.0$.

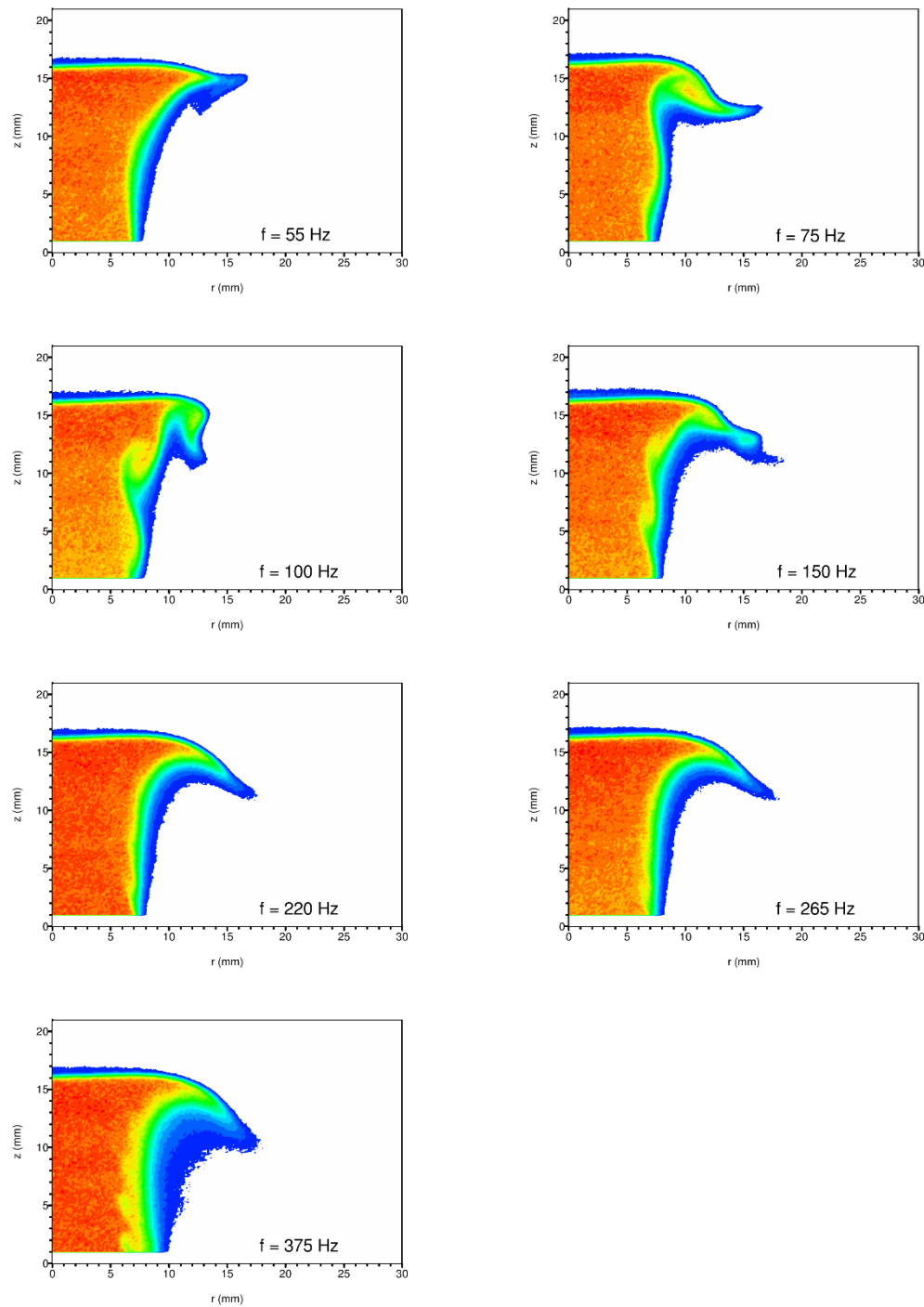


Figure 4-43: Acetone PLIF images for the acoustically forced cases showing resulting shear layer structures. Images for all seven base drive frequencies are presented. Images shown are for the 0° pressure phase angle (i.e. rising edge zero crossing of the fluctuating pressure).

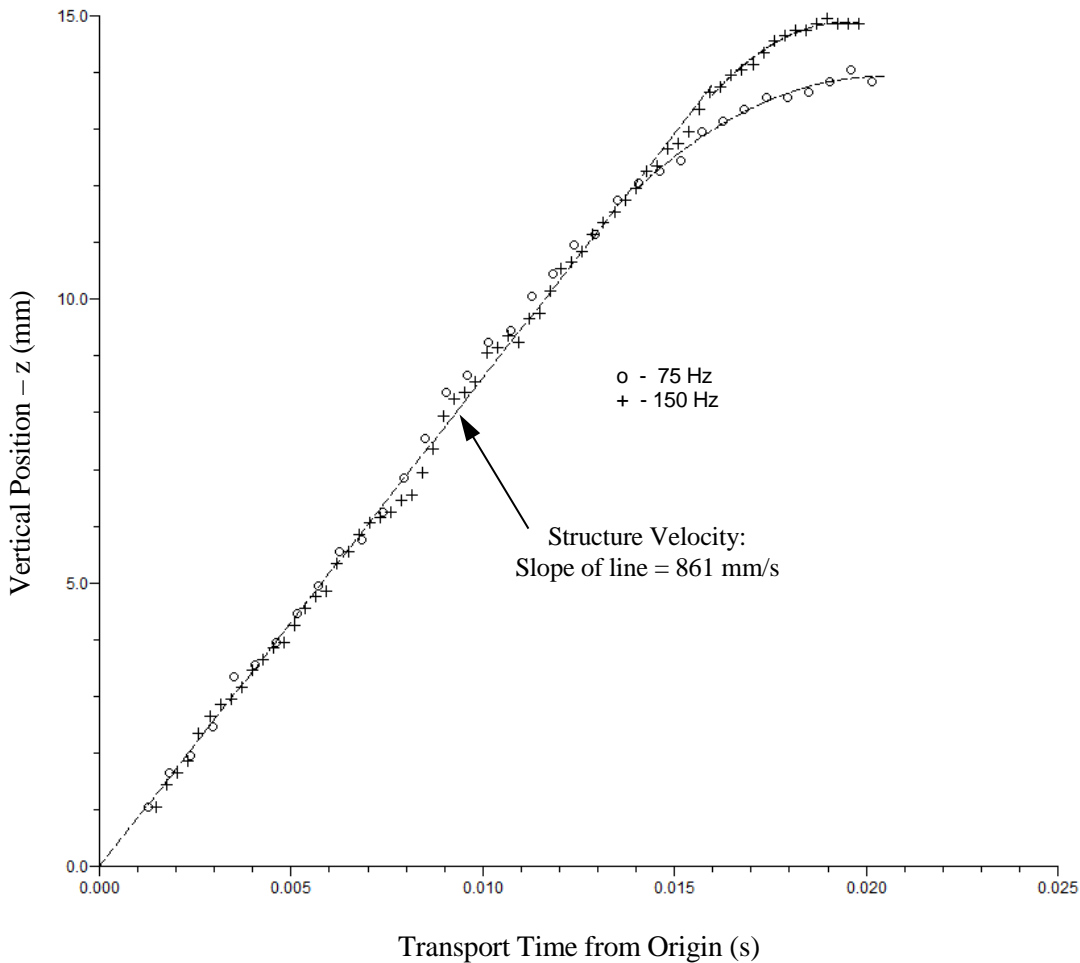


Figure 4-44: Shear layer structure position (height) versus time. The plot shows data from the 75 Hz and 150 Hz acetone PLIF experiments (Nos. 641 and 644, respectively). The vertical position origin is located at the burner nozzle exit plane. Time zero is taken such that the virtual structure location is at this exit plane.

the reaction zone where the slope of the vertical transport curve goes to zero, then the total transport time for the presented test case is about 20 ms. However, the argument may be made that the contact time is earlier than this, perhaps where the slope of the curve begins to change. This would produce transport times as low as 15 ms. In any case, these can then be compared with the transport delay curve deduced in chapter 3 from the bulk chemiluminescence phase response data. The power-law curve fit to that data was shown in equation (3-10) and is repeated here:

$$(4-26) \quad \tau_d = 0.293(V_J)^{-1/2},$$

Where V_J is in cm/s and τ_d is in seconds. Substituting $V_J = 167$ cm/s produces a time delay of 23 ms. This is close to the structure transport delay measured based on the zero-slope criteria.

Chapter 5

BURNER MODELING

5.1 Motivation for Modeling

The work at hand is fundamental in nature. It does not attempt to address the response of complex industrial or aerospace combustors to imposed acoustic fields. Indeed, it evaluates a simple laminar flat-flame burner. But the goal here is to grapple with the fundamental understanding of such a simple system. Modeling can be an important tool in such an endeavor.

These modeling efforts can be used to improve the understanding of the fundamental phenomenon involved in the coupling between the fluctuating pressure and velocity fields, and the resulting variation in the heat release rate. Producing models for this simple combustion system that are consistent with the collected data not only provides validation for the deduced mechanisms, but can also lead to further insights.

Furthermore, producing a reduced model involving chemical kinetics (using Cantera) where varying species concentrations can be extracted and compared with the collected PLIF data might be valuable in verifying (or discrediting) previous assumptions. By validating the model against the collected data, it may then be possible to directly evaluate the fluctuating heat release rate within the model and use that information to determine which PLIF species (or combination of species) is best suited as a heat release indicator.

Finally, modeling (at varying levels of complexity) can be generally useful when applied to engineering codes and calculations where direct computation of the phenomena is not possible or is unwarranted. The complexity of the model can be in step with the complexity or required accuracy of the computation at hand. The following sections look at a simplified model refined to various levels.

5.2. Transfer Function Fitting

The simplest model for the presented burner is generated by fitting a transfer function to the combustion response data examined in chapter 3. The combustion response of the burner assembly was experimentally found to be linear in amplitude for sound pressure levels up to at least 116.8 dB. However, as will be seen, the response does not satisfy the necessary conditions of a linear, time-invariant (LTI) system in general.

The combustion response transfer function for the reference burner operating condition ($\phi = 0.85$, $V_R = 4.0$) was originally shown in Figure 3-4 and is repeated here (with some additions) in Figure 5-1. Additional annotations on the plot highlight features of interest that were discussed earlier. The peak of the magnitude response is seen to begin around 60 Hz and continue (with a slight downward slope) up to 100 Hz. This appears to correspond to the peak receptivity of the reactant jet shear layer. As described by Davies, et. al. (1963), for a classical, free, laminar jet in an open half-space, the peak receptivity is seen to fall in a Strouhal number range from 0.42 to 0.48. In the presented case, the jet is constrained by the stagnation plane located at an $L/D = 1.5$ above the nozzle exit plane. Nonetheless, the maximum receptivity is seen to occur at a frequency of about 60 Hz, corresponding to a Strouhal number of

$$St = \frac{fD}{U} = \frac{(60 \text{ Hz})(14 \text{ mm})}{(1670 \text{ mm/s})} = 0.50.$$

At 100 Hz, where the peaked region ends, the associated Strouhal number is 0.84. The entirety of the pre-transitional region is marked by a roll-off in phase that is indicative of the transport delay of structures produced in the unsteady shear layer travelling from the nozzle exit to the reaction zone.

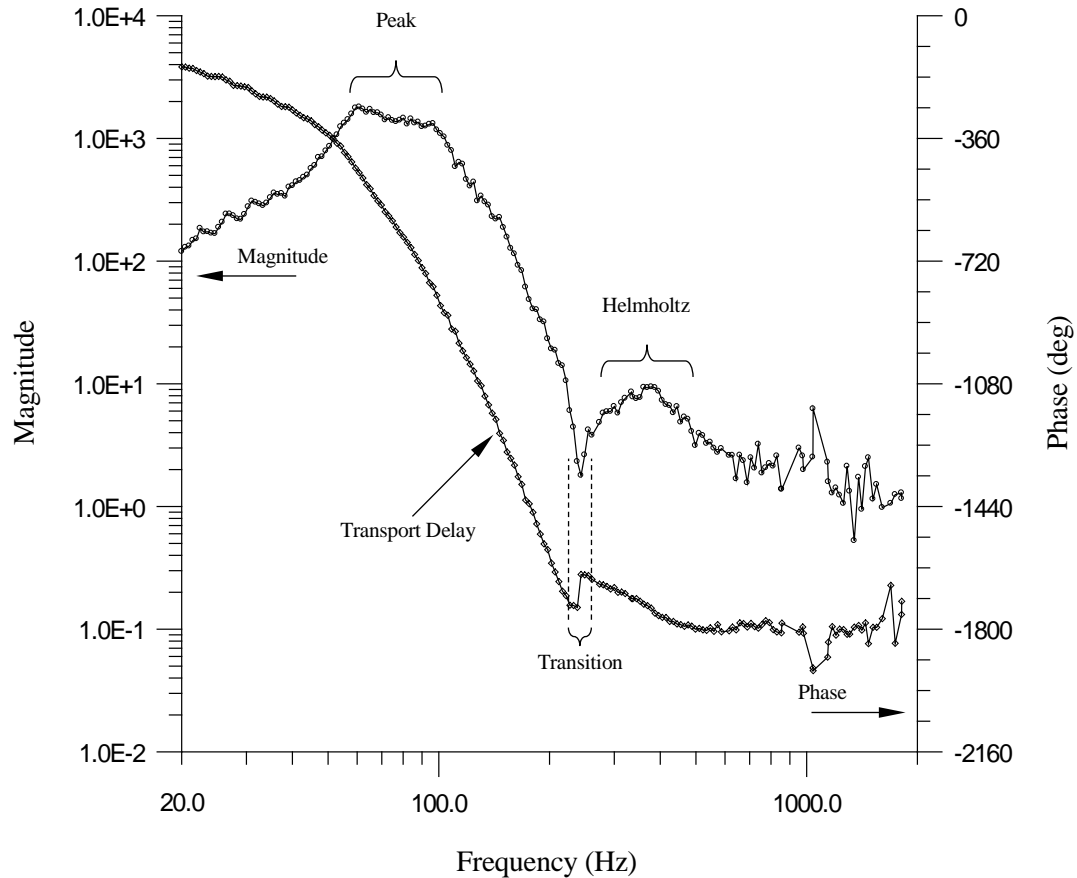


Figure 5-1: Combustion response function plotted for the flat-flame burner operating on premixed methane and air with an equivalence ratio of 0.85 and a nozzle exit velocity ratio of 4.0. Both magnitude and phase are presented along with notations identifying features of interest. Negative phase corresponds to the fluctuating heat release lagging the fluctuating pressure.

As was shown in chapter 3, an abrupt transition occurs where the character of the response changes dramatically. The transition is frequently marked with a notch in the magnitude response and an associated jump in the phase. For the reference case, the notch occurs at a drive frequency of approximately 240 Hz. Beyond the notch is the post-transitional region where the Helmholtz response of the burner cavity and nozzle is seen. This is centered at approximately 375 Hz.

Acknowledging the above features it is now possible to construct a simplified model transfer function for the described system. The process begins by predominantly (but not exclusively) focusing on the system magnitude response. The slope of the magnitude is upward at

low frequencies indicating improved coupling of the acoustic wave to the reactant flow and shear layer as the frequency is increased. Ripples are also seen in the response from 20 Hz to 40 Hz; however, these will not be addressed in the model. To generate the initial upward slope, at least one zero has to be located at the origin in the s-plane. This is problematic, however, since (as it was shown earlier in chapter 3) the combustion response tends toward the in-phase condition as the frequency goes to zero. A single zero at the origin (unfortunately) produces a $+90^\circ$ contribution. Therefore, to achieve the desired result a negated double zero must be used instead:

$$(5-1) \quad G_1(s) = -s^2. \quad (\text{initial upward slope})$$

As previously mentioned, the peak in receptivity of the shear layer appears between 60 Hz and 100 Hz. Four different approximations were tried for this portion of the response. These were a single complex pole pair, a double complex pole pair, a complex pole pair combined with a single real pole, and a complex pole pair combined with two real poles. The best agreement was found with the complex pole pair combined with a single real pole:

$$(5-2) \quad G_2(s) = \frac{1}{\left(\frac{s}{\omega_1} + 1\right)\left(\frac{s^2}{\omega_2^2} + \frac{s}{\omega_2 Q_2} + 1\right)}. \quad (\text{receptivity peak})$$

After this peak, a steep drop in amplitude is present, accompanied by a notch in the response and subsequent recovery to a lower amplitude level. This is observed to be characteristic of the transition portion of all responses, although varying notch depths are seen depending on the burner operating conditions. The shape of the response is highly reminiscent of a low-pass notch filter where the characteristic frequency of the complex zero pair is higher than the characteristic frequency of the complex pole pair. The transfer function appears as

$$(5-3) \quad G_3(s) = \frac{\left(\frac{s^2}{\omega_3^2} + \frac{s}{\omega_3 Q_3} + 1 \right)}{\left(\frac{s^2}{\omega_4^2} + \frac{s}{\omega_4 Q_4} + 1 \right)}. \quad (\text{low-pass notch})$$

Finally, at drive frequencies from 300 to 450 Hz, the Helmholtz resonant response of the burner cavity and nozzle is observed. This is modeled simply with a complex pole pair. The given transfer function is

$$(5-4) \quad G_4(s) = \frac{1}{\left(\frac{s^2}{\omega_5^2} + \frac{s}{\omega_5 Q_5} + 1 \right)}. \quad (\text{Helmholtz resonance})$$

Combining the above relations along with a global gain parameter (α) into single response transfer function gives

$$(5-5) \quad G_5(s) = \frac{-\alpha s^2 \left(\frac{s^2}{\omega_3^2} + \frac{s}{\omega_3 Q_3} + 1 \right)}{\left(\frac{s}{\omega_1} + 1 \right) \left(\frac{s^2}{\omega_2^2} + \frac{s}{\omega_2 Q_2} + 1 \right) \left(\frac{s^2}{\omega_4^2} + \frac{s}{\omega_4 Q_4} + 1 \right) \left(\frac{s^2}{\omega_5^2} + \frac{s}{\omega_5 Q_5} + 1 \right)}.$$

The values for the eleven free parameters in this transfer function now need to be determined. They are selected using a modified, least-squares fitting algorithm against the collected data presented in Figure 5-1. The least-squares metric is used in conjunction with a progressive Monte Carlo technique to approach an optimal solution. The parameters obtained are shown in Table 5-1.

The magnitude response of the resulting transfer function is plotted in Figure 5-2 for comparison with the experimental data. The model transfer function is seen to be in good agreement with the experimental results for the magnitude behavior. However, to this point, no special treatment has been made for the phase; in particular, the previously detected time delay has

Param	Value	Group
α	0.0106	Global Gain
ω_1	18.2 Hz (114 rad/s)	Receptivity
ω_2	65.2 Hz (410 rad/s)	
Q_2	2.70	Low-Pass Notch
ω_3	244 Hz (1533 rad/s)	
Q_3	16.0	
ω_4	109 Hz (683 rad/s)	
Q_4	2.36	Helmholtz Response
ω_6	371 Hz (2330 rad/s)	
Q_6	0.724	

Table 5-1: Optimized (fit) parameters for the trial transfer function, $G_5(s)$, presented as equation (5-5). Parameters were obtained using a modified least-squares metric in conjunction with a progressive Monte Carlo scheme.

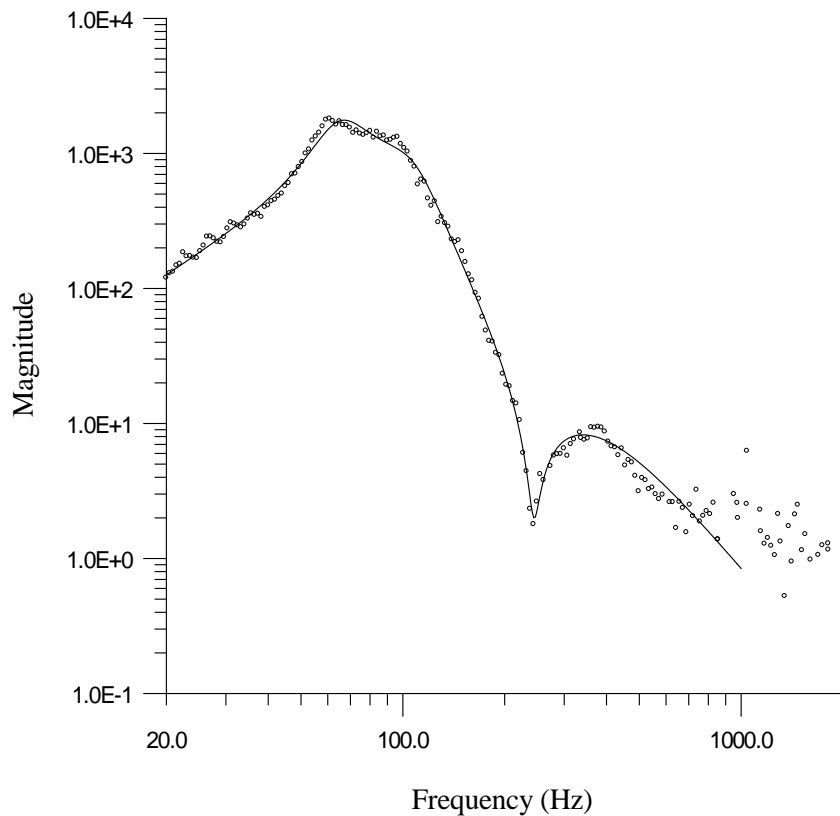


Figure 5-2: Combustion response transfer function model versus experimental data for the reference burner test condition with an equivalence ratio of 0.85 and a nozzle exit velocity ratio of 4.0. Plot shows the magnitude response only. The solid line represents the model prediction while the circles indicate individual data points from the experimental data.

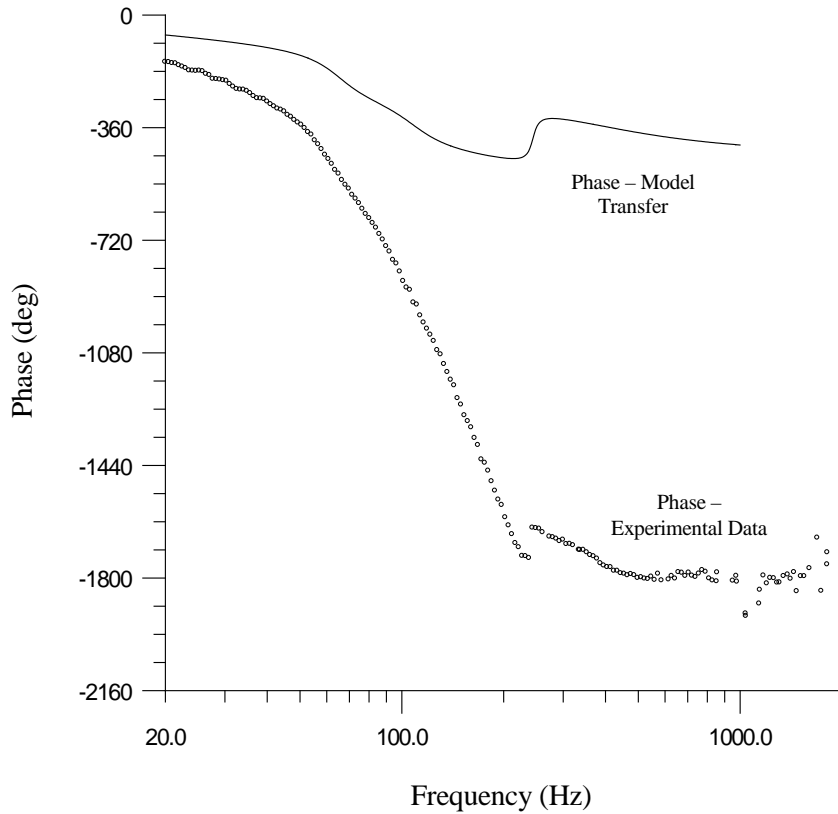


Figure 5-3: Combustion response transfer function model versus experimental data for the reference burner test condition with an equivalence ratio of 0.85 and a nozzle exit velocity ratio of 4.0. Plot shows the phase response. The solid line represents the model prediction while the circles indicate individual data points from the experimental data.

not been addressed. Figure 5-3 shows the phase response of the model transfer function, $G_5(s)$, in comparison with the collected experimental data. It can be seen that, without additional corrections, the phase response of $G_5(s)$ falls woefully short of aligning with the experimental results. In an attempt to correct this, the aforementioned time delay is added. The revised transfer function is shown as $G_6(s)$ below:

$$(5-6) \quad G_6(s) = \frac{-\alpha s^2 \left(\frac{s^2}{\omega_3^2} + \frac{s}{\omega_3 Q_3} + 1 \right) e^{-s\tau}}{\left(\frac{s}{\omega_1} + 1 \right) \left(\frac{s^2}{\omega_2^2} + \frac{s}{\omega_2 Q_2} + 1 \right) \left(\frac{s^2}{\omega_4^2} + \frac{s}{\omega_4 Q_4} + 1 \right) \left(\frac{s^2}{\omega_5^2} + \frac{s}{\omega_5 Q_5} + 1 \right)}.$$

Here, the additional parameter, τ , is the time (or transport) delay as described earlier. For the fixed parameters given in Table 5-1, the value for τ was optimized to produce the best least-squares fit with the phase data from 20 Hz to 220 Hz. The result was a time delay $\tau = 0.0148$ sec. The subsequent phase plot is shown in Figure 5-4.

There are two important things to note with this result. First is that the computed time delay is significantly smaller than the time delay that was estimated through analysis of the acetone PLIF images. Second is that, although the phase match between the model and the experimental data is quite good up to approximately 220 Hz, beyond this (as one might anticipate) the phases

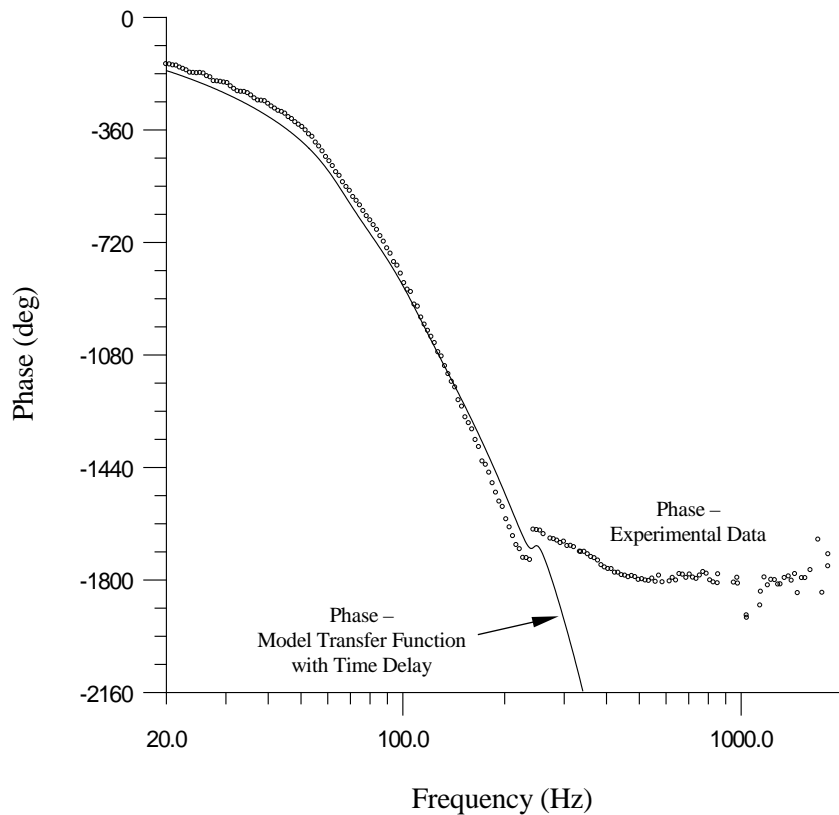


Figure 5-4: Combustion response transfer function model, $G_6(s)$, versus experimental data for the reference burner test condition with an equivalence ratio of 0.85 and a nozzle exit velocity ratio of 4.0. Plot shows the phase response. The solid line represents the model prediction with the time delay included. Circles indicate individual data points from the experimental data.

of the model and the experimental data diverge rapidly. The phase shown in the experimental data abruptly changes trajectory and levels off, heading toward -1800° . The model phase, on the other hand, continues rocketing toward greater and greater negative phases. Consequently, this first model is likely acceptable for cases where only the magnitude information is needed. The magnitude produced from the transfer function matches closely with the measured response through bulk chemiluminescence. However, if phase information is also required, the model's usefulness may be somewhat limited.

To arrive at a better solution, the model must be revisited. Rather than blindly fitting a transfer function to the observed data, a more clearly thought-out approach must be taken, applying what was learned through inspection of the PLIF data from chapter 4.

5.3 A Revised Transfer Function

To improve the combustion response model transfer function (for the given reference case), a more directed approach is taken by reviewing what was learned from the acoustically forced PLIF experiments. It had been noted earlier from the bulk chemiluminescence data that two distinct peaks exist in the response function. One peak is observed at low frequencies, with maximum values falling between 60 Hz and 100 Hz. The second peak appears at a substantially higher frequency, with the center near 375 Hz. It was quickly determined that the peak at higher frequency corresponded to the Helmholtz response of the burner cavity. This was readily seen in data from the built in microphones located within the burner nozzle assembly.

However, the mechanisms involved for the lower frequency response were less obvious. Nonetheless, after performing the PLIF and chemiluminescence imaging experiments, it became clear that the large response at low frequency was due to a driven instability in the laminar jet shear layer produced by the reactants emanating from the burner nozzle. These structures were clearly visualized in the series of cinematographic images taken with acetone PLIF. Surface waves were

observed in addition to shear layer roll-up for some ranges of drive frequencies. At high drive frequencies, near the point of Helmholtz resonance, periodic, radially inward jets of air were seen near the exit plane of the nozzle.

Development of structures in the reactant jet shear layer contributes to the varying heat release in two ways. The first is through variations in the spatial distribution of the principal reactants. As shear layer structures develop, the premixed methane and air tend to segregate into periodic regions of higher and lower concentration. As these regions are convected into the reaction zone, corresponding variations in the heat release rate are observed. The convection time of these structures from near the nozzle exit up to the reaction zone is responsible for the transport delay behavior seen in the combustion response data.

The second contribution comes from air entrainment in outer regions of the jet. The acetone PLIF images clearly show air being entrained in the shear layer structures when roll-up is present. In addition, at higher drive frequencies, air can be seen to be admitted to the flow near the nozzle exit plane through abrupt radial inflow. In both these cases, local addition of air to the reactant flow produces spatial variations in equivalence ratio. As these equivalence ratio variations are convected through the reaction zone, fluctuations in the heat release rate are produced.

In contrast to the heat release variations produced by convected disturbances, the fluctuations attributed to the acoustic resonance of the burner cavity appear to occur principally through direct modulation of the reactant flow. In this case, the reactant transport time is irrelevant. Velocity fluctuations seen at the burner nozzle exit are communicated to the reaction zone at the acoustic wave speed. Over the very small spatial scales present in the burner (on the order of 2 cm or less), this is essentially instantaneous. Fluctuations in the heat release rate are observed as the velocity of the premixed fuel and air passing through the reaction zone oscillates.

With these observations, it is possible to reformulate the transfer function model for the coupling between the varying pressure field and the resulting fluctuations in CH^* and CO_2^*

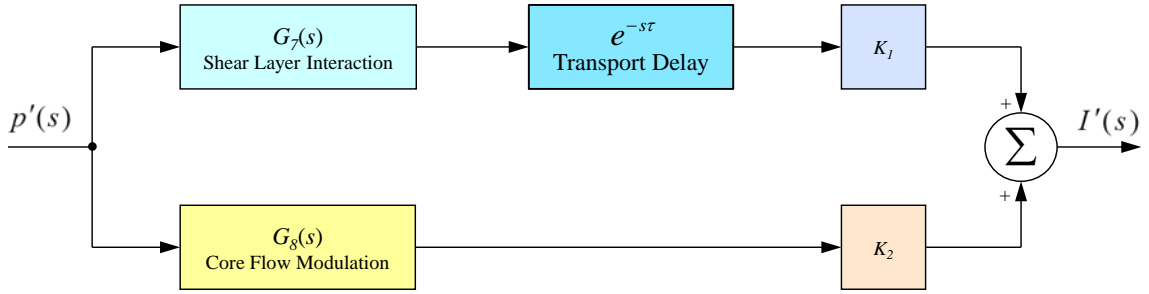


Figure 5-5: Reformulated transfer function model for the coupling between the fluctuating pressure field and the resulting variation in chemiluminescence intensity. Model is for the experimental burner at the previously prescribed test conditions. The group transfer function is designated as $G_9(s)$.

chemiluminescence. Suppose the transfer function is divided into two parts as shown in Figure 5-5. Here the contributions from the driven shear layer instability and the core flow modulation have been separated. The transfer function $G_7(s)$ (seen in the top leg) contains the response behavior associated with the unsteady shear layer. In line with this function is a time delay block containing the term $e^{-s\tau}$. As before, τ is the transport delay time for driven structures in the shear layer to reach the reaction zone.

The lower leg contains the transfer function $G_8(s)$. This term is responsible for the response generated by fluctuations in the core flow. As mentioned above, these fluctuations are communicated to the reaction zone at the acoustic wave speed. As such, no delay block is present in the lower path. K_1 and K_2 are matching constants to produce the desired chemiluminescence intensity variations. Going forward, it will be assumed that they are absorbed into the $G_7(s)$ and $G_8(s)$ transfer functions respectively.

Construction of $G_7(s)$ and $G_8(s)$ begin by examining the transfer function components used in the previous section. Functions $G_1(s)$ through $G_3(s)$ were responsible for producing the dominant response peak seen at low frequencies. Included in $G_3(s)$ was the complex zero pair associated with producing the deep notch seen at 244 Hz. This explicit generation of the notch is no longer needed,

as will be seen. Instead, additional poles are required to produce the steep magnitude roll-off observed between 100 Hz and 220 Hz. The resulting trial function for $G_7(s)$ is then

$$(5-7) \quad G_7(s) = \frac{-\alpha_1 s^2}{\left(\frac{s}{\omega_1} + 1\right) \left(\frac{s^2}{\omega_2^2} + \frac{s}{\omega_2 Q_2} + 1\right) \left(\frac{s^2}{\omega_3^2} + \frac{s}{\omega_3 Q_3} + 1\right) \dots \left(\frac{s^2}{\omega_6^2} + \frac{s}{\omega_6 Q_6} + 1\right)}.$$

If it is chosen to include the transport delay in this function, then it can be written as

$$(5-7a) \quad G_{7a}(s) = \frac{-\alpha_1 s^2 e^{-s\tau}}{\left(\frac{s}{\omega_1} + 1\right) \left(\frac{s^2}{\omega_2^2} + \frac{s}{\omega_2 Q_2} + 1\right) \left(\frac{s^2}{\omega_3^2} + \frac{s}{\omega_3 Q_3} + 1\right) \dots \left(\frac{s^2}{\omega_6^2} + \frac{s}{\omega_6 Q_6} + 1\right)}.$$

For producing the Helmholtz response at high frequency, $G_8(s)$ is taken to be analogous to $G_4(s)$.

In particular:

$$(5-8) \quad G_8(s) = \frac{-\alpha_2}{\left(\frac{s^2}{\omega_7^2} + \frac{s}{\omega_7 Q_7} + 1\right)}.$$

As shown in Figure 5-5, the sum of these two produces the desired function, $G_9(s)$. Using a similar progressive Monte Carlo scheme to the one described earlier, the free parameters were optimized for the best fit to the experimental data. The results are presented in Table 5-2.

Figure 5-6 shows the combustion response magnitude and phase plots of the resultant constituent transfer functions $G_{7a}(s)$ and $G_8(s)$. Examining the left-hand plot, it can be reasoned that the magnitude of the group transfer function $G_9(s)$ will be dominated by $G_{7a}(s)$ for low frequencies (< 200 Hz) and dominated by $G_8(s)$ for high frequencies (> 280 Hz). Likewise, the phase that dominates is determined by the magnitudes of these respective functions. Near crossover (where the magnitudes of the two functions are similar) the magnitude of the group function is determined by the phases of the two components being summed. If $G_{7a}(s)$ and $G_8(s)$ are in phase at this point, they constructively add to produce a rise in the magnitude plot. However, if they are

Param	Value
α_1	0.0106
α_2	6.00
τ	0.0112 s
ω_1	18.2 Hz (114 rad/s)
ω_2	65.2 Hz (410 rad/s)
Q_2	2.70
ω_3	69.2 Hz (435 rad/s)
Q_3	0.585
ω_4	99.1 Hz (623 rad/s)
Q_4	2.57
ω_5	148 Hz (930 rad/s)
Q_5	2.41
ω_6	218 Hz (1370 rad/s)
Q_6	2.73
ω_7	370 Hz (2330 rad/s)
Q_7	1.42

Table 5-2: Optimized (fit) parameters for the trial transfer function, $G_9(s)$, presented as Figure 5-5. Parameters were obtained using a modified least-squares metric in conjunction with a progressive Monte Carlo scheme.

out of phase, the combination is destructive and produces a sharp dip or notch in the response. This is true for the given test case as can be seen in the $G_9(s)$ magnitude plot shown in Figure 5-7. The notch is not as deep as the one present in the collected data; however, it demonstrates how two separate coupling mechanisms can collude to produce a null in the response.

The corresponding $G_9(s)$ phase plot is presented in Figure 5-8. This plot matches well with the experimental data and shows the jump in phase that occurs as the notch center is crossed. As one might deduce, the size of this jump is related to how far apart the phase vectors of the two constituent transfer functions are at the cross-over location; larger phase differences produce larger

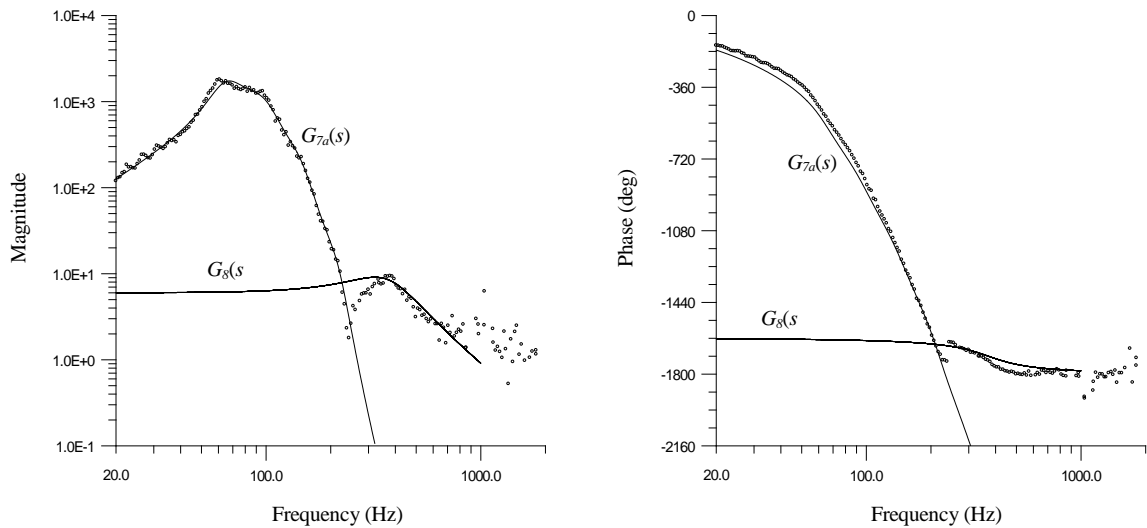


Figure 5-6: Plots for the combustion response model functions $G_{7a}(s)$ and $G_8(s)$. Magnitude plot appears on left while phase plot appears on right. Per convention, negative phase corresponds to I' lagging p' . Note that the phase plot for $G_8(s)$ has been moved to the correct phase branch to align it with the transition point.

jumps. It is also generally true, in the anti-phase condition, that larger phase differences produce deeper magnitude notches. The result is that for the system model transfer function, $G_9(s)$, deeper notches go hand in hand with larger phase jumps. This is seen to be true throughout the bulk chemiluminescence data presented in appendix G.

One disturbing discrepancy that remains is in the computed transport delay. In producing the phase fit, the optimization code finds the transport delay to only be $\tau = 0.0112$ seconds. This is in the range of the convection time for the core flow from the nozzle exit plane to the reaction zone; however, it is not consistent with the transport time of the shear layer structures as measured from the PLIF imagery. Addressing this requires another revision to the model.

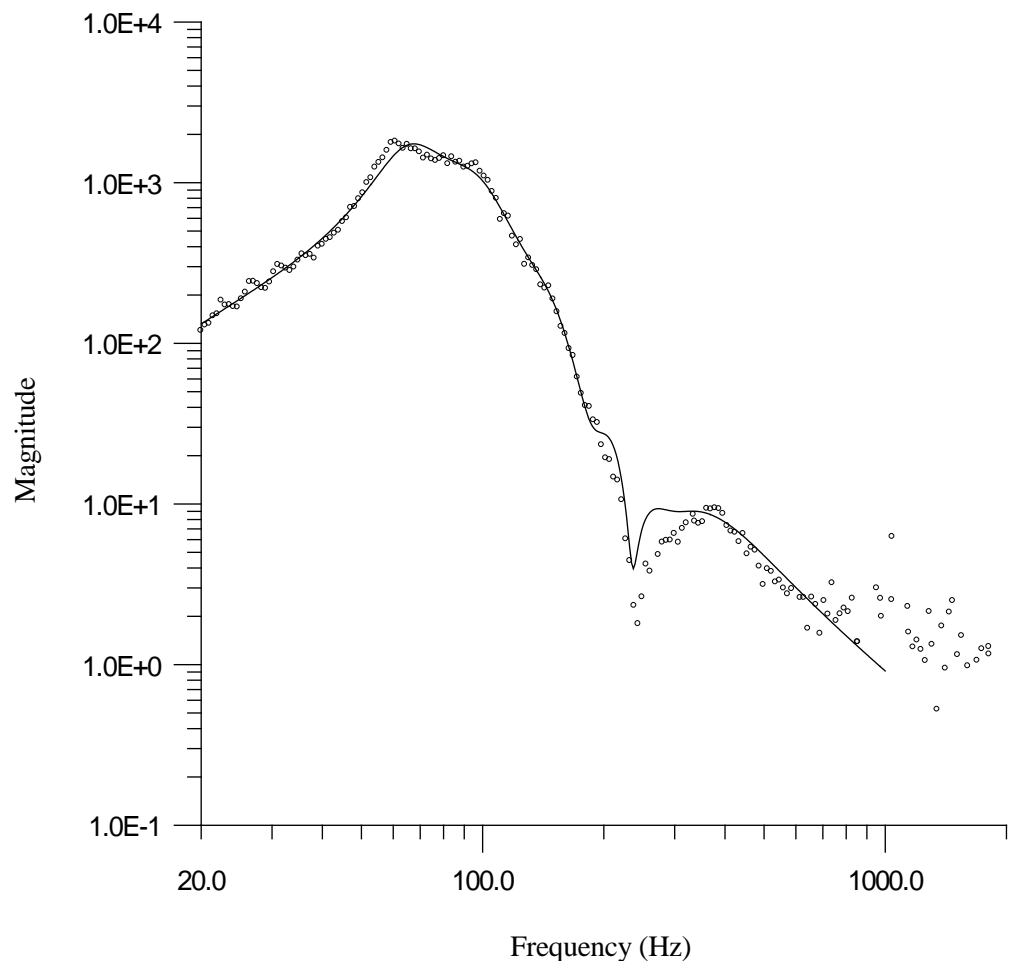


Figure 5-7: Revised model, $G_9(s)$, for the combustion response transfer function versus experimental data for the reference burner test condition with an equivalence ratio of 0.85 and a nozzle exit velocity ratio of 4.0. Plot shows the magnitude response. The solid line represents the model prediction while the circles indicate individual data points from the experimental data.

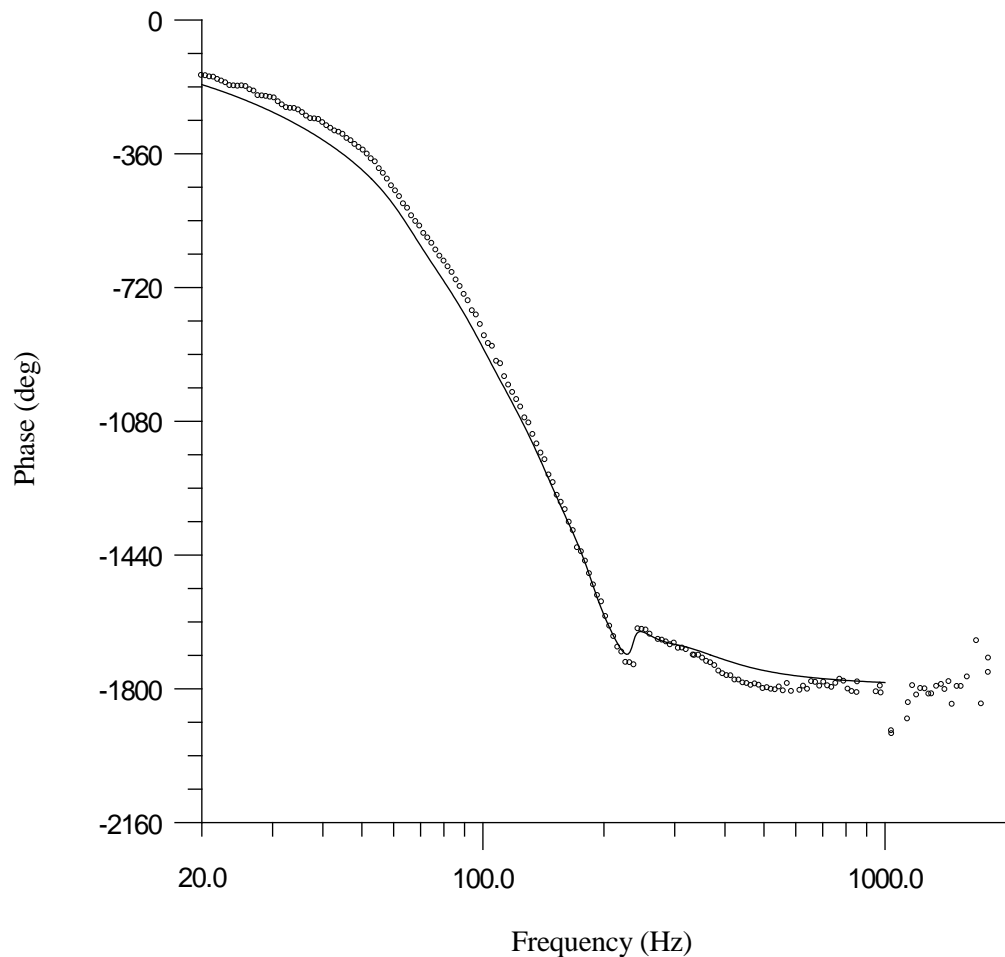


Figure 5-8: Revised model, $G_9(s)$, for the combustion response transfer function versus experimental data for the reference burner test condition with an equivalence ratio of 0.85 and a nozzle exit velocity ratio of 4.0. Plot shows the phase response. The solid line represents the model prediction while the circles indicate individual data points from the experimental data.

5.4 Transfer Function – Revision 2

So far, the presented model has been a linear one, satisfying the requirements of an LTI transfer function. With this model, however, a nagging discrepancy remains. The time constant in the transport delay term is inconsistent with the experimentally measured value using acetone PLIF. In order to bring this into alignment, it is necessary to reduce the phase lag introduced by the poles in $G_7(s)$ in order to allow the time delay term to supply the difference. However, for a linear, causal and stable system, this is not possible; $G_7(s)$ is already “minimum phase” and produces the minimum group delay for the given magnitude response. Any attempt to reduce the phase lag further (while maintaining the LTI nature) would result in a non-causal system.

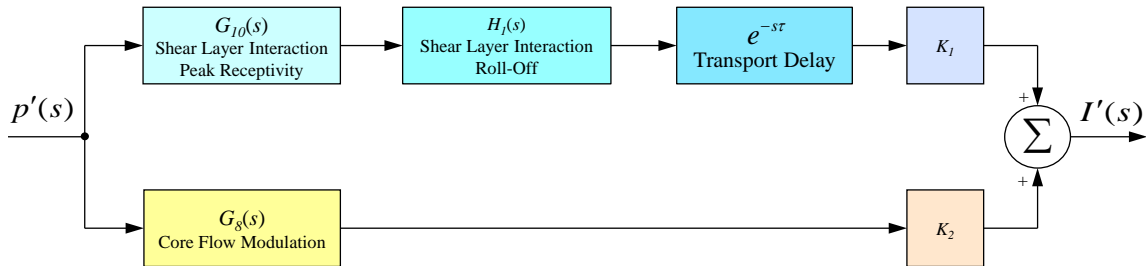


Figure 5-9: Further revised transfer function model for the coupling between the fluctuating pressure field and the resulting variation in chemiluminescence intensity. Block $G_7(s)$ has been split into two parts. $G_{10}(s)$ is LTI and contains the terms related to the peaking of the jet receptivity. $H_1(s)$ is a non-linear function that controls the receptivity roll-off while preserving phase. The resulting group transfer function is designated as $H_2(s)$.

Nonetheless, with this in mind, the group transfer function is modified again; however, this time in a way that violates its linearity. Figure 5-9 depicts the structure of this newly modified function, now designated $H_2(s)$. Compared with the last transfer function, $G_9(s)$ (shown in Figure 5-5), the new one has split $G_7(s)$ into two parts – an LTI part called $G_{10}(s)$ and the non-linear (heretical) part dubbed $H_1(s)$. $G_{10}(s)$ is simply the low frequency portion of $G_7(s)$. It incorporates the “peaking” part of the shear layer interaction. Specifically, it is taken as

$$(5-9) \quad G_{10}(s) = \frac{-\alpha_1 s^2}{\left(\frac{s}{\omega_1} + 1\right) \left(\frac{s^2}{\omega_2^2} + \frac{s}{\omega_2 Q_2} + 1\right) \left(\frac{s^2}{\omega_3^2} + \frac{s}{\omega_3 Q_3} + 1\right)}.$$

The scaling constant α_1 is taken to be the same as before; however, the remaining free parameters are re-optimized against the experimental data between 20 Hz and 1000 Hz. The results are shown in Table 5-3. Plots of the magnitude and phase behavior of the function are shown in Figure 5-10.

Param	Value
α_1	0.0106
ω_1	16.7 Hz (105 rad/s)
ω_2	63.2 Hz (397 rad/s)
Q_2	2.83
ω_3	113 Hz (710 rad/s)
Q_3	3.57

Table 5-3: Optimized (fit) parameters for the trial transfer function, $G_{10}(s)$, presented in equation 5-9. Parameters were obtained using a modified least-squares metric in conjunction with a progressive Monte Carlo scheme.

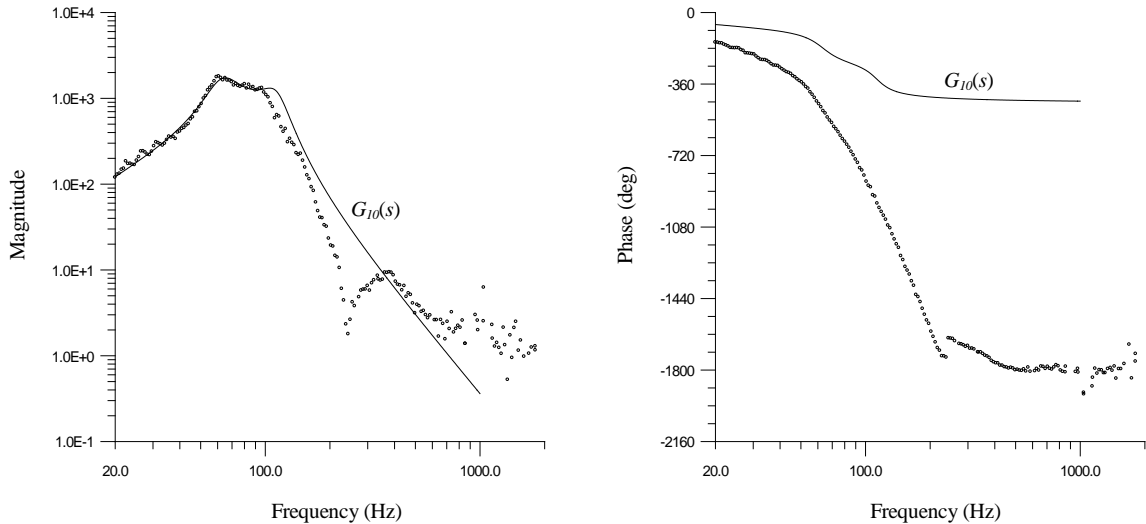


Figure 5-10: Plots for model function $G_{10}(s)$ (peaking function) as described in Figure 5-9. Magnitude plot appears on left while phase plot appears on right. Per convention, negative phase corresponds to I' lagging p' . The solid lines represent the model transfer function while the circles indicate individual data points from the experimental data.

With $G_{10}(s)$ defined, it is now possible to construct $H_1(s)$, albeit in a very ad-hoc way. $H_1(s)$ is taken such that

$$(5-10) \quad |H_1(s)| = f(\omega) \text{ where } \omega = |s| ; \quad \angle H_1(s) = 0.$$

Next, select a magnitude curve that fits the experimental data well between, say, 100 Hz and 200 Hz. For simplicity, the previously produced $|G_{7a}(s)|$ is chosen. Then:

$$(5-11) \quad |H_1(s)| = \frac{|G_{7a}(s)|}{|G_{10}(s)|}.$$

In an attempt to reduce complexity, $f(\omega)$ is constructed from piece-wise fits of the ratio given in equation (5-11). The resulting magnitude corrector is shown in Figure 5-11 and the corresponding fits are presented in equation (5-12).

For frequencies below 574 rad/s (91.3 Hz) the function returns unity. As such, the value of $G_{10}(s)$, which is correct for low frequency, is simply passed through. For the frequency range from 574 rad/s to 679 rad/sec (91.3 Hz to 108.0 Hz) a linear fit is employed. For the range from 679 rad/s to 1024 rad/s (108.0 Hz to 163.0 Hz) a fourth order polynomial is used to match the S shape in the function. Finally, for frequencies above 1024 rad/s (163.0 Hz) a decaying exponential is fit. The resulting magnitude and phase responses of the group transfer function, $H_2(s)$, are shown in Figures 5-12 and 5-13.

The agreement between the model and the collected data (for both magnitude and phase) is reasonable and similar to that seen in Figures 5-7 and 5-8. However, with the new model the transport delay time is now $\tau = 0.0162$ seconds. Although this is still short of the estimated structure transport time measured in Figure 4-44 (~20 ms), it is significantly closer to that value. Indeed, examining Figure 4-44, the 16.2 ms point lies beyond the break point where the vertical velocity is no longer constant and is instead dropping. Determination of the actual delay using this plot is somewhat subjective.

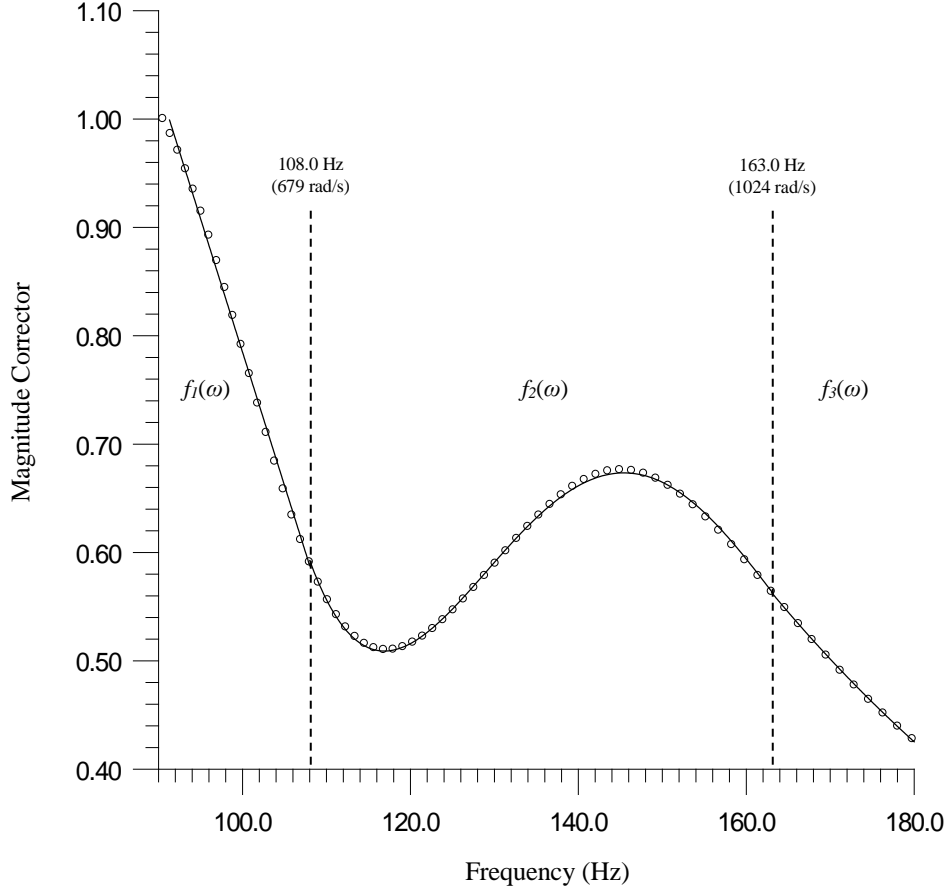


Figure 5-11: Magnitude corrector curve for generating $f(\omega)$ and ultimately $H_I(s)$. The reference points generated from equation 5-11 are curve-fit in a piecewise manner. The three segments are shown. ($\omega = 2\pi f$.)

$$(5-12) \quad f(\omega) = \begin{cases} 1 & \omega < 574 \text{ (rad/s)} \\ f_1(\omega) & 574 \leq \omega < 679 \\ f_2(\omega) & 679 \leq \omega < 1024 \\ f_3(\omega) & 1024 \leq \omega , \end{cases}$$

where:

$$\begin{aligned} f_1(\omega) &= (-3.9211 \times 10^{-3})\omega + 3.2484 \\ f_2(\omega) &= (1.5394 \times 10^{-10})\omega^4 + (-5.6545 \times 10^{-7})\omega^3 + (7.6825 \times 10^{-4})\omega^2 \\ &\quad + (-0.45740)\omega + 101.28 \\ f_3(\omega) &= (8.3279)e^{(-2.6302 \times 10^{-3})\omega} . \end{aligned}$$

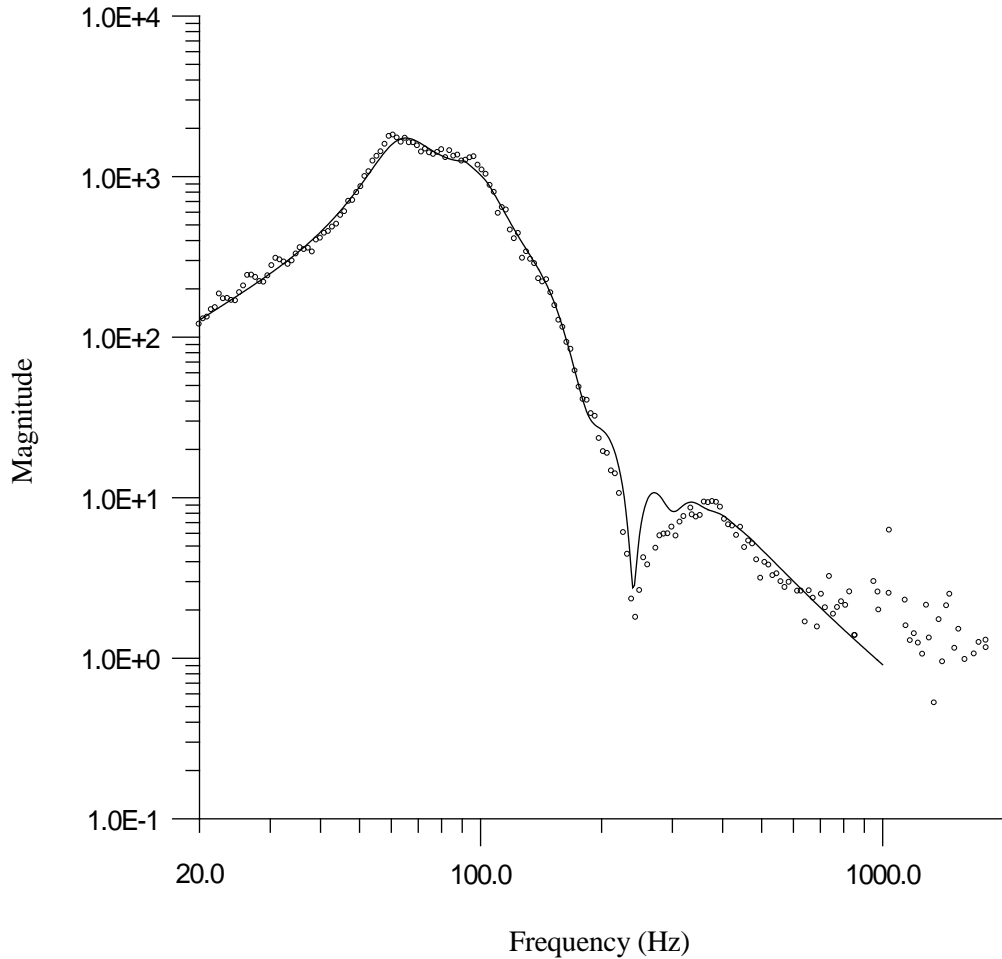


Figure 5-12: Further revised model, $H_2(s)$, for the combustion response transfer function versus experimental data for the reference test case. Plot shows the magnitude response. The solid line represents the model prediction while the circles indicate individual data points from the experimental data.

It is possible to remove more components (i.e. poles and zeros) from $G_{10}(s)$ to place into $H_1(s)$, thus reducing the phase contribution from $G_{10}(s)$ further. The extreme case was shown back in Figure 3-6, where the transport delay was computed blindly without considering any phase contribution from other transfer function components. Here the delay was found to be 22~23 ms. The important point to note is that it is not possible to construct an LTI transfer function that matches the experimental data in this case. To do so would result in a system that is non-causal or unstable. By necessity the linearity of the system must somehow be broken, perhaps as has been

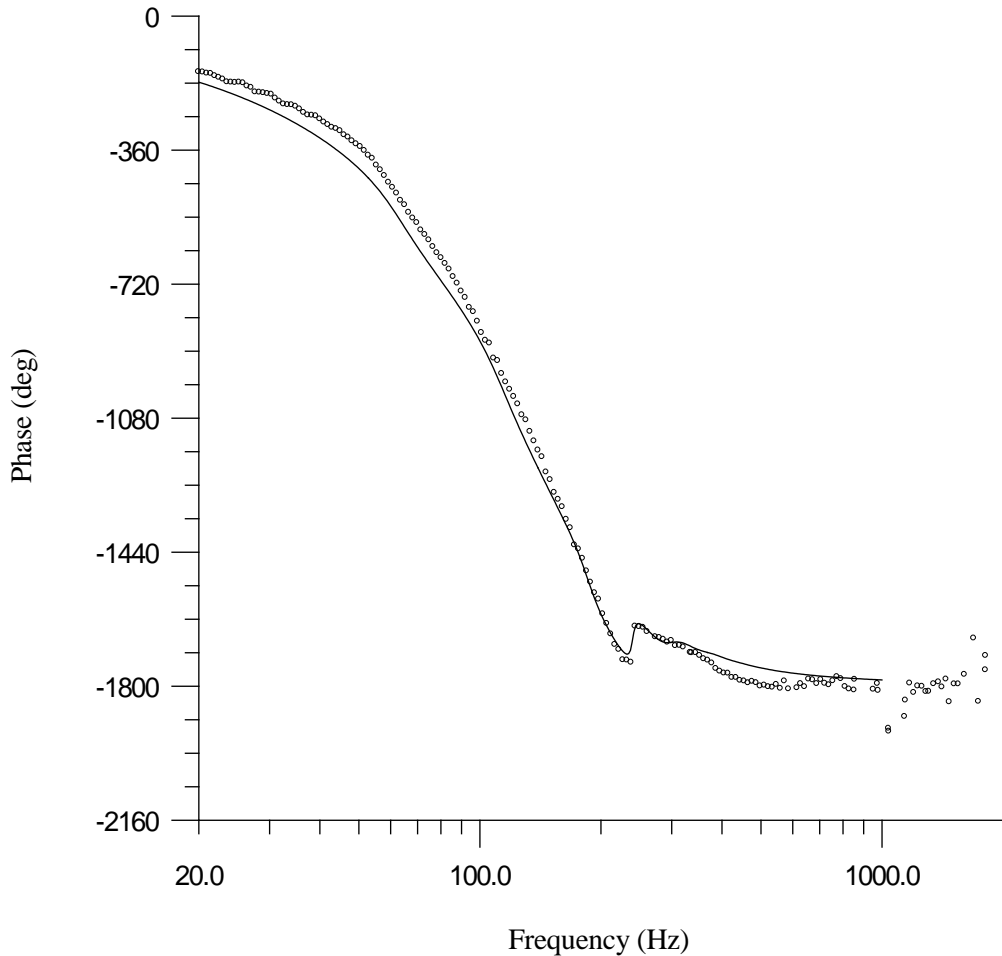


Figure 5-13: Further revised model, $H_2(s)$, for the combustion response transfer function versus experimental data for the reference test case. Plot shows the phase response. The solid line represents the model prediction while the circles indicate individual data points from the experimental data.

done in the last example above. As mentioned in chapter 3, early experiments indicated that the system is linear over varying (low) drive amplitudes for a single (monotone) drive frequency. However, no experiments were performed where the system was excited with two non-harmonic frequencies simultaneously (bi-tonal). It is suspected (based on observations of the driven shear layer) that it is under this type of superposition that the linearity will fail.

C h a p t e r 6

CONCLUDING REMARKS

6.1 Summary

The presented work centers on a dynamic response measurement technique for combustion originally pioneered by Pun, Palm and Culick in 2000. The method involves artificially acoustically forcing a burner or combustion system and measuring its dynamic response using phase-resolved planar laser induced fluorescence (PLIF). The material presented covers several facets of the method. These not only include experimental results and their interpretation, but also the development of custom equipment to support the technique.

The acoustic behavior of a simple, premixed, laminar, flat-flame burner is examined. Flame stabilization is achieved through impingement of the reactant jet against a stagnation plane. Most previous research using the acoustically-forced phase-resolved PLIF method has focused on turbulent combustion systems of low to moderate complexity. Such systems are certainly of interest; however, much simpler flames (as the one used in this work) are more suitable for evaluating the merits of the presented technique, while still being an interesting and enlightening specimen of study. Details of the burner used are found in appendix B.

An acoustic forcing chamber and drive system (similar to the one used in 2000) was fabricated for use in the experiments. The system was characterized for drive frequencies from 20 Hz to 2000 Hz. For most of this frequency range, sound pressure levels as high as 117 dB can be obtained. Details of the chamber characteristics can be found in appendix D.

A custom laser system was designed and built to support the experimental research. An Nd:YAG laser was constructed, employing an unstable resonator design and two stages of amplification. The nominal laser pulse rate is 10 Hz with pulse durations around 8-10 ns. Pulse

energies of 2 Joules at 1064 nm are achievable and energies in excess of 1 Joule per pulse at 532 nm are also possible using a KTP doubling crystal. The YAG laser is used to pump a ring-cavity optical parametric oscillator (OPO) uniquely designed and fabricated for this work. The OPO integrates harmonic generation directly within the ring cavity allowing it to produce tunable UV laser light as a principal output. Details of the laser system design and construction are discussed in appendix E.

A unique instrument was designed and fabricated to alleviate several difficulties that arose in the original experiments in 1999 and 2000. Among many other things, the unit (dubbed the AFC-100) coordinates and automates much of the experimental procedure. It provides amplitude control of the acoustic forcing, high-speed acoustic data collection around the window of image acquisition, laser shot timing and phase targeting, ICCD gate control and so on. Details on the design and capabilities of this instrument are given in appendix F.

With the necessary equipment in place, experimental investigation was begun. The operational range of the flat-flame burner was fully evaluated for a single mechanical configuration ($D_{nozzle} = 14$ mm, $L_{s-p} = 21$ mm) and operation on premixed methane and dry air. With the operational envelope determined, measurement of the global combustion response function from 20 Hz to nearly 2000 Hz was achieved using bulk chemiluminescence measurements from a PMT and lens combination. A total of 62 test conditions were explored.

The collected data were reduced and plots of the combustion response function magnitude and phase were generated. (These plots appear in appendix G.) Many interesting features were subsequently identified. The responses were found to have two fundamental regions along the frequency axis. The sub-transitional region (at low frequency) is dominated by a broad peak with a position that tracks with the Strouhal number based on jet exit diameter and velocity. The peak magnitude of the combustion response was found to be roughly between 1×10^3 and 3×10^3

regardless of the burner nozzle exit velocity or equivalence ratio. The “plateau” of the peak typically spans from $0.5 \leq St \leq 0.8$. Accompanying this magnitude crest is a phase response immediately reminiscent of a time delay. The phase lag is nearly linear with increasing frequency. Assuming no other contribution to phase, a least-squares fit to the phase data estimated a transport delay of approximately 22 ms.

The post-transitional region (at higher frequency) was typically marked by a smaller peak resulting from the Helmholtz response of the burner nozzle. The peak appears in most of the test cases – the exception being those at very high nozzle velocity ratios where the transition frequency overlaps the Helmholtz response. For all cases where the peak is present, its centerline frequency is approximately 375 Hz and its magnitude response is approximately 10.0, regardless of the operating parameters.

The transition frequency was found to have an approximately linear relationship with the nozzle exit velocity where the intercept at no-flow conditions was 63 Hz. The interface at the transition location (between the two regions) was commonly found to exhibit a notch in the magnitude response with a corresponding jump in phase. It was later discovered that this was a product of destructive interference between two competing physical processes.

Forced Rayleigh index plots were generated showing oscillatory swings between driving and damping character within the sub-transitional region as frequency is increased. Level-set plots for the entire data collection indicated that peak magnitudes of the forced Rayleigh index generally increased with increasing nozzle velocity ratio and with increasing equivalence ratio.

Phase branch bifurcations were observed in data for a few operating conditions, usually for high equivalence ratio and high velocity ratio test cases. All bifurcations occurred in the sub-transitional region. The plots were seen to exhibit a split in the phase trajectory concurrently with an upset in the magnitude trace. The phase paths ultimately terminated on separate phase branches.

The trigger for these events and the mechanisms involved are unclear. Careful analysis of the data and equipment has been unable to rule out a true physical phenomenon (versus issues with the experimental setup).

Phase-resolved PLIF experiments were performed to further investigate the acoustically forced behavior of the flat-flame burner, and to generate a database of the resulting PLIF images. Steady and unsteady PLIF data were collected at numerous laser excitation wavelengths and acoustic drive frequencies. Targeted species included OH, CH, CH₂O and acetone. Additionally, image chemiluminescence was also performed.

After corrections for shot-to-shot variations in the laser source, variation in spatial distribution of the laser sheet, and progressive absorption of the laser sheet by the target species, the PLIF data were used to produce cinematographic sequences of the unsteady flame. These sequences provided useful insight into the actions of the flame under acoustically forced conditions. Variations in the size and shape of the reaction zone were observed with OH, CH and CH₂O PLIF. CH₂O PLIF also allowed identification of combustion product recirculation at the edges of the flame. Furthermore, acetone PLIF provided visualization of the reactant flow and confirmation of the presence of the unsteady shear layer. Structures on the jet's outer boundary were observed to develop and convect into the reaction zone. Tracking of these structures indicated a transport time delay of 18 ms to 20 ms.

PLIF images were integrated to produce global combustion response values for OH, CH, CH₂O and the pixel-by-pixel product combination of OH and CH₂O at numerous drive frequencies. The values were then compared with the results from the global measurements of chemiluminescence using the PMT. Notable variations in magnitude and substantial variations in phase were seen across datasets. The OH-CH₂O combination proposed by Paul and Najm (1998) showed the closest agreement with the PMT measurements (aside from the spatially resolved chemiluminescence data).

In addition to the production of cinematographic sequences, the PLIF data were also used to generate plots of the spatially resolved combustion response function and the spatially resolved forced Rayleigh index. These plots were instrumental in discerning the mechanisms and interaction involved in producing the global response. Spatially resolved combustion response plots illuminated the direct modulation of the flow crossing the reaction zone and showed the elevation in response magnitude at the nozzle cavity resonant frequency. The forced Rayleigh index plots revealed the driving and damping regions and their ability to swap character. They also assisted in clarifying how the convecting shear layer structures interact with the outer edges of the flame to produce a contribution to the unsteady combustion response.

Ultimately, a detailed library of the PLIF data and the associated experimental parameters was generated to aid in future research, principally in the validation of numerical models; however, use in the advancement of theory is certainly not ruled out. The library data can be found in appendix H. Efforts were made to document the experimental equipment, its configuration, and the operational conditions and parameters as thoroughly as was practical within this thesis.

Finally, generation of simplified transfer function models for the combustion response was demonstrated as a starting point for future modeling work. Transfer functions were produced to match the bulk chemiluminescence data for the given standard reference case. Three successive functions were produced, each with more regard to the coupling mechanisms involved. It was shown that the occasional notch or null in the magnitude response (and the associated phase jump) were the product of two competing coupling mechanisms with opposite phases at their crossover point. It was also determined that the function relating the fluctuating pressure to the fluctuating chemiluminescence signal must violate linearity in some way for the given experimental data, lest the response be non-causal. Construction of a sample non-linear function block (within the complete response function) which meets the necessary requirements was demonstrated.

6.2 Future Work

The work presented leverages the acoustically forced, phased-resolved PLIF technique previously developed and refined here. It can certainly be applied to countless other burner configurations to help evaluate their dynamics under unsteady conditions. However, the burner evaluated in this work, despite its utter simplicity, remains elusive with the details of its dynamic character. Further investigation is certainly warranted. Questions that could be addressed include:

1. How does the system respond at higher drive amplitudes? - The burner was found to exhibit a linear response in amplitude for the ranges where data were collected. However, unrecorded tests at higher drive amplitudes (near the limits of the apparatus) revealed a sudden change in behavior similar to a triggering phenomenon. A limit cycle appeared to be present but with non-unity periodicity.
2. How does the system respond to bi-tonal acoustic drive? - All experiments performed in this work used a single frequency acoustic drive (i.e. monotone). Investigation in the modeling section alluded to the possible failure of superposition due to the “required” nonlinearity proposed. Future experiments employing bi-tonal or multi-tonal drive could verify or discredit this supposition.
3. What is the nature of the “anomalous” phase transitions observed in the higher flow and higher equivalence ratio experiments? - During the bulk chemiluminescence measurements, a few experiments at high flow and equivalence ratio produced unusual (and unexplainable) transitions in the phase curve. It is unclear if these were related to an issue within the experimental apparatus; however, a real, physical phenomenon could not be excluded. Is it possible that they are related to the phenomenon discussed in item 1 above? All the PMT chemiluminescence experiments performed involved gradually

stepping the acoustic drive from low frequency to high frequency. An interesting adjunct would be to reverse this sweep direction to see if any hysteresis exists.

4. How well do the modeled species concentrations match the PLIF measurements and what improvements to the model can be made? - The modeling efforts presented in chapter 5 were very simplistic and were produced only as a starting point. Improvements can definitely be made. Additionally, coupling between the final transfer function presented and a chemical kinetics package like Cantera may produce interesting results. Indeed, with proper combination, it would be possible to directly interrogate the species concentrations of interest, allowing direct comparison to the collected PLIF data. However, it is certainly arguable that a more warranted approach would be to perform a full, unsteady numerical simulation of the acoustically forced burner, including the kinetics. In either case, this is left as future work for an industrious researcher.

In addition to the work proposed above, great strides can certainly be made in the technique itself with improved equipment. Many years have passed since the first experiments in 1999 and 2000, and the initial conception, design and fabrication of the apparatus used in this work. Technology has advanced greatly since then, perhaps in ways that seemed almost impossible to the researchers involved at the time. Very high speed imaging systems (both CMOS and CCD based) have been developed. Megapixel resolutions have been achieved and continuous image collections at thousands of frames per second are possible. For short burst operation, frame rates as high as one million fps have been touted. In a similar way (although not as dramatically) high-energy, pulsed UV laser sources have also advanced. Burst-pulse Nd:YAG lasers are under development that can produce a short series of very closely spaced laser pulses suitable for collection of brief cinematographic PLIF sequences.

Instrumentation electronics and computing power have also gained phenomenal ground in recent years. The development of a custom instrument (the AFC-100) was deemed necessary at the time to achieve the data collection rates and timing performance needed (along with operation and control of many other critical functions). Now, with inexpensive and very powerful processors available (both in PCs and in stand-alone DSP boards) along with nearly plug-and-play FPGA development kits, it is undoubtedly possible to assemble an improved system from “off the shelf” components. Such a control could provide many improved features. Something as simple as high-speed data communication and storage of the collected acoustic waveforms would reduce the experimental run time substantially.

With a faster laser, imager and data collection and control system, it would be possible (if not feasible) to make a giant leap forward in the phase-resolved PLIF technique. The hope would be to also sweep the imager gating pulse while collecting PLIF data in a similar fashion to what has been described in chapter 4. Necessarily, much more data would need to be collected. The information on the imaged species fluorescence decay as a function of time after the laser pulse would allow direct inference of the collisional quenching for that species. This would remove a major (and very annoying) unknown from the technique, leading to a possible direct relation between the fluorescence signal and the absolute species concentration.

A p p e n d i x A

SPATIAL AVERAGING IN SIMPLE THERMOACOUSTIC SYSTEMS

A.1 Introduction

In investigating thermoacoustic oscillations such as those found in combustion instabilities, a frequent objective is to compute or predict the oscillatory modes of the system and their associated growth or decay rates. This seemingly innocent goal has proved to be a daunting task for generations of researchers. Fundamentally, the difficulty arises from the complexity and limited understanding of the mechanisms involved. As a result, most of these mechanisms are modeled and, as such, are approximations. In addition, attempts to validate models against experimental data have produced limited results due to the difficulty in collecting the data and the resulting uncertainties. Even so, the necessity remains and efforts are made to grapple with these problems through approximate methods, both analytical and numerical.

Culick proposed one such approximate method in 1961, based on a method of spatial averaging. The mathematical technique itself was not new, having been used in various branches of mechanics. It involves solving the unperturbed, homogeneous system, that being the classical acoustic solution to the combustor, to arrive at the normal modes for the chamber. The inhomogeneous problem is then investigated assuming that it is a small perturbation from the homogenous case. Using a modal expansion of the admitted pressure for the classical case as a Green's function, an integral equation of the difference of the two systems is formed. The integral equation simplifies since one of the terms is identically zero. Formally, the volume integral involving the boundary conditions is transformed into a surface integral using Green's theorem and an equation for the pressure field as a function of position is obtained. Next, exploiting the orthogonality of the classical modes, it is possible to solve for the coefficients of the terms in the

Green's function. Further manipulation of the result allows one to arrive at a relation for the perturbed wave number and resulting frequency. Detailed bases of this technique are covered in chapter 4 of AGARD RTO-AG-AVT-039 (Culick 2006); applications are covered in chapters 6, 7 and 9. We will proceed with two simple, yet interesting sample cases.

A.2 The Rijke Tube

The simplest device to examine with this technique is the Rijke tube. Rijke first experimented with this device in 1859, although references to similar devices date back as far as 1777 when Byron Higgins recorded his experience with a “singing flame.” In its basic form, the Rijke tube is a duct with open acoustic conditions at both ends and a planar heat source located somewhere inside. Airflow through the duct is either driven by natural convection (when the duct is erected vertically) or forced by a fan or blower. In Rijke’s original configuration, the heating grid was a section of wire gauze that was heated by a flame. Once the flame was removed, the apparatus began to oscillate acoustically (sing) with ever increasing amplitude. As heat energy was extracted from the gauze and the heat source began to cool substantially, the oscillations would subside. This simple device has fascinated researchers for 150 years and work continues even at the present time. Probably the most detailed investigation was performed on a horizontal configuration; results were published by Matveev and Culick (2003). Figure A-1 is an illustration of the Rijke tube used by Matveev while Figure A-2 shows a simplified cross-section of the device.

A.2.1 – Rijke Tube Exact Solution

Making a few ideal assumptions, including the assumption of a simple velocity coupling model for the heat transfer from the grid to the air, it is possible to directly or “exactly” solve this problem using wave matching.

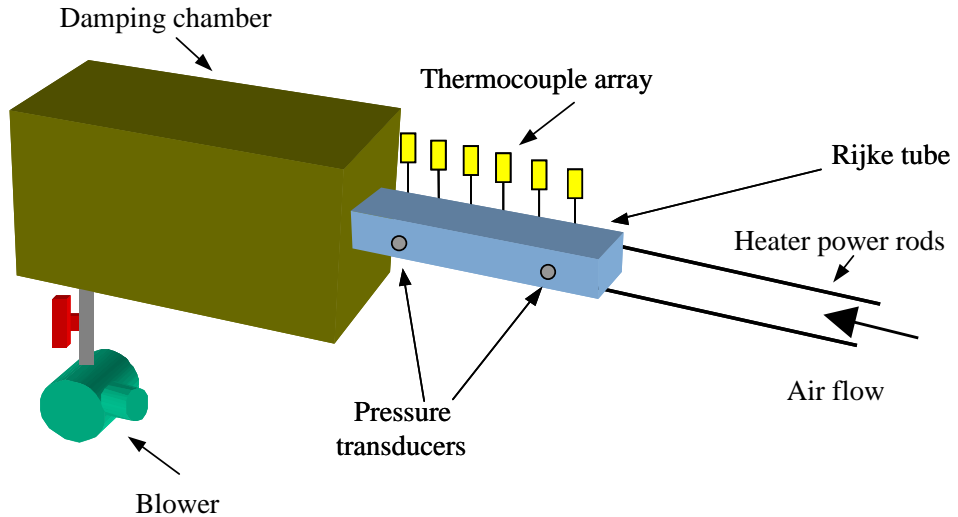


Figure A-1: Horizontal Rijke tube apparatus as used by Matveev et. al.

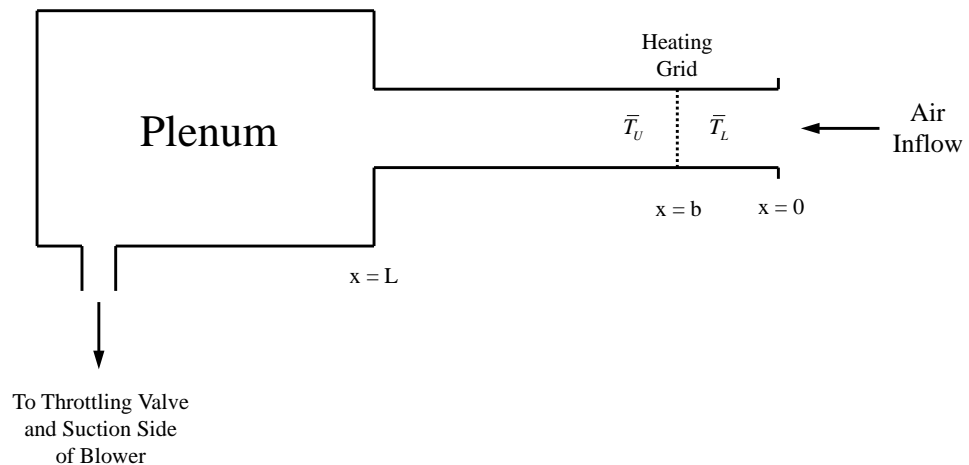


Figure A-2: Simplified cross-section of Rijke tube used by Matveev et. al.

We begin with the following idealizations:

- The only acoustic modes in the tube are longitudinal along the axis of flow.
- There are no acoustic losses at either end of the tube, nor are there losses within the tube due to viscous effects.
- The average pressure is uniform throughout the tube.
- There are no heat losses through the walls of the tube.
- The heating grid located at station $x = b$ is infinitesimally thin and the heat transfer to the air occurs in this infinitesimally thin space.
- Fluctuating quantities as well as jumps in governing parameters across the heater are small enough that classical linear acoustics apply and entropy waves are negligible.

Given these assumptions, we begin by expressing the principal variables as sums of their average and fluctuating parts: $p = \bar{p} + p'$, $\rho = \bar{\rho} + \rho'$, $u = \bar{u} + u'$, $\dot{Q} = \dot{Q}_0 + \dot{Q}'$, while the temperature and speed of sound are assumed to be constant throughout each region. The basic conservation equations along with the ideal gas equation are used to relate the average variables:

$$(A-1) \quad \bar{\rho}_U \bar{u}_U = \bar{\rho}_L \bar{u}_L,$$

$$(A-2) \quad \bar{p}_U = \bar{p}_L,$$

$$(A-3) \quad \bar{T}_U = \bar{T}_L + \frac{\dot{Q}_0}{C_p \bar{\rho}_L \bar{u}_L},$$

or

$$\bar{T}_U = \bar{T}_L \left(1 + \frac{\gamma - 1}{\gamma} \frac{\dot{Q}_0}{\bar{p} \bar{u}_L} \right)$$

and consequently:

$$(A-4) \quad \bar{\rho}_U = \bar{\rho}_L \left(1 + \frac{\gamma - 1}{\gamma} \frac{\dot{Q}_0}{\bar{p} \bar{u}_L} \right)^{-1}$$

and

$$(A-5) \quad \bar{a}_u = \bar{a}_L \left(1 + \frac{\gamma-1}{\gamma} \frac{\dot{Q}_0}{\bar{p} \bar{u}_L} \right)^{\frac{1}{2}}.$$

Here, the subscript $()_u$ corresponds to the upper part of the tube, or the part convectively downstream of the heater. The subscript $()_L$ corresponds to the lower part of the tube, or the part convectively upstream of the heater.

With the mean parameters addressed, it is possible to begin with the classical equations for linear acoustics and arrive at the equations for the jump conditions at the heater. We begin with the one-dimensional linear acoustic equations, neglecting the mean flow contributions:

$$(A-6) \quad \frac{\partial \rho'}{\partial t} + \frac{\partial}{\partial x} (\bar{\rho} u') = 0, \quad (\text{Mass})$$

$$(A-7) \quad \bar{\rho} \frac{\partial u'}{\partial t} + \frac{\partial p'}{\partial x} = 0, \quad (\text{Momentum})$$

$$(A-8) \quad \frac{\partial p'}{\partial t} + \gamma \bar{p} \frac{\partial u'}{\partial x} = (\gamma-1) \dot{Q}' \delta(x-b). \quad (\text{Energy})$$

If a differential volume is taken across the grid at location $x = b$, each of these equations can be integrated over this volume to arrive at the corresponding jump condition. Let the differential volume be of total length 2δ . Then integrating the mass equations produces

$$(A-9) \quad \int_{b-\delta}^{b+\delta} \frac{\partial \rho'}{\partial t} dx + \int_{b-\delta}^{b+\delta} \frac{\partial}{\partial x} (\bar{\rho} u') dx = 0.$$

In the limit as δ goes to zero, the first integral vanishes and the remaining integral collapses to just the jump across the heater:

$$(A-10) \quad \bar{\rho}_u u'(b_+) = \bar{\rho}_L u'(b_-).$$

In exactly the same way, the momentum equation becomes

$$(A-11) \quad \int_{b-\delta}^{b+\delta} \bar{\rho} \frac{\partial u'}{\partial t} dx + \int_{b-\delta}^{b+\delta} \frac{\partial p'}{\partial x} dx = 0.$$

The first integral can be integrated by parts. The resulting equation is

$$(A-11a) \quad \bar{\rho} u' \Big|_{b-\delta}^{b+\delta} - \int_{b-\delta}^{b+\delta} u' \frac{\partial \bar{\rho}}{\partial t} dx + \int_{b-\delta}^{b+\delta} \frac{\partial p'}{\partial x} dx = 0.$$

The first term now goes to zero by using (A-10) and the second term is zero since $\bar{\rho}$ is independent of t . The last term collapses to the condition across the jump, which is simply:

$$(A-12) \quad p'(b_+) = p'(b_-).$$

The pressure is continuous across the heater.

Similarly, the integral form of the energy equation across the grid becomes

$$(A-13) \quad \int_{b-\delta}^{b+\delta} \frac{\partial p'}{\partial t} dx + \int_{b-\delta}^{b+\delta} \gamma \bar{p} \frac{\partial u'}{\partial x} dx = \int_{b-\delta}^{b+\delta} (\gamma - 1) \dot{Q}' \delta(x - b) dx.$$

Taking the limit as δ goes to zero, the first integral vanishes and the remaining jump condition becomes

$$(A-14) \quad u'(b_+) - u'(b_-) = \frac{(\gamma - 1)}{\gamma} \frac{1}{\bar{p}} \dot{Q}'.$$

Given these preliminary results, it only remains to assume a model for \dot{Q}' , the fluctuating portion of the heat transferred from the grid to the flow. One such model was proposed by Merk (1957):

$$(A-15) \quad \frac{\dot{Q}'(t)}{\dot{Q}_0} = Tr \left(\frac{u'(b_-, t)}{u_0} \right) \quad \text{for } x = b, \text{ otherwise } = 0.$$

Here, $Tr(U)$ is a transfer function, which is in general complex valued. Its magnitude is typically between 0 and 1, and its phase delay is between 0 and 90 degrees, corresponding to a first order thermal inertia lag. For our test case, however, we will simplify this transfer function to a scalar

multiplier, κ ; consequently, there is no phase contribution. We will assume that the magnitude is $0 \leq \kappa \leq 1$. As a result, equation (A-15) becomes

$$(A-15a) \quad \frac{\dot{Q}'(x,t)}{\dot{Q}_0} = \kappa \frac{u'(b_-,t)}{\bar{u}_L} \quad \text{for } x = b, \text{ otherwise } = 0.$$

Or, it can be said that, at the heating grid,

$$(A-15b) \quad \kappa = \frac{\bar{u}_L}{u'(b_-,t)} \frac{\dot{Q}'(b,t)}{\dot{Q}_0}.$$

With this result, it is now possible to work out a solution using the wave-matching method.

We begin with the derivation of the classical 1-D wave equation for the regions up and downstream of the grid. The momentum equation (A-7) is differentiated with respect to x , while the energy equation (A-8) with no heat addition (i.e. $\dot{Q}'(t)\delta(x-b) = 0$) is differentiated with respect to time. The difference of these results is taken and the term $\frac{\partial^2 u'}{\partial x \partial t}$ is eliminated. The resulting wave equation is

$$(A-16) \quad \frac{\partial^2 p'}{\partial t^2} - \frac{\gamma \bar{p}}{\bar{\rho}} \frac{\partial^2 p'}{\partial x^2} = 0 \quad \text{or} \quad \frac{\partial^2 p'}{\partial t^2} - \bar{a}^2 \frac{\partial^2 p'}{\partial x^2} = 0,$$

where \bar{p} , $\bar{\rho}$, and \bar{a}^2 are taken constant in the regions on either side of the heater. This equation admits solutions of the form

$$(A-17) \quad p'(x,t) = e^{-i\Omega t} [P_1 \cos(kx) + P_2 \sin(kx)].$$

where Ω is the complex frequency and k is the complex wavenumber defined as

$$(A-18) \quad \Omega = \omega + i\alpha \quad \text{and} \quad k = \frac{1}{\bar{a}}(\omega + i\alpha).$$

Here, α is the growth or decay rate of the wave, with α positive indicating growth. In general, growth rates are typically small in comparison to the period of the wave. (i.e. $\alpha \ll \omega$) For the example case, only the frequency and mode shapes are of interest and α will be taken as zero.

For the Rijke tube with acoustically open ends, the pressure fluctuations must vanish at the entrance and exit:

$$(A-19) \quad p'(0, t) = 0 \quad \text{and} \quad p'(L, t) = 0.$$

This requires that the equation for the pressure fluctuations in the lower (right) section of the tube becomes

$$(A-20) \quad p'_L(x, t) = P_L e^{-i\omega t} \sin(k_L x).$$

For the upper (left) part of the tube, a coordinate substitution is made where $\xi = L - x$. Then the pressure equation for this region is

$$(A-21) \quad p'_U(x, t) = P_U e^{-i\omega t} \sin(k_U \xi).$$

The equations for the velocity fluctuations can now be determined by combining the relations for the fluctuating pressure with the momentum equation (A-7):

$$(A-22) \quad u'_L(x, t) = -iP_L \frac{1}{\bar{\rho}_L \bar{a}_L} e^{-i\omega t} \cos(k_L x),$$

$$(A-23) \quad u'_U(x, t) = iP_U \frac{1}{\bar{\rho}_U \bar{a}_U} e^{-i\omega t} \cos(k_U (L - x)).$$

Using the previously derived jump conditions (A-12) and (A-14), it is possible to eliminate P_L and

P_U . Equation (A-12) establishes the requirement for pressure continuity across the grid:

$$(A-24) \quad P_U \sin(k_U (L - b)) = P_L \sin(k_L b),$$

and equation (A-14) constrains the velocity jump across the grid:

$$(A-25) \quad P_U \frac{1}{\bar{\rho}_U \bar{a}_U} e^{-i\omega t} \cos(k_U (L - b)) + P_L \frac{1}{\bar{\rho}_L \bar{a}_L} e^{-i\omega t} \cos(k_L b) = -i \frac{(\gamma - 1)}{\gamma} \frac{1}{\bar{p}} \dot{Q}'(t).$$

The RHS of (A-25) can be expanded using the model for the heat transfer from the grid to the flow as presented in equation (A-15a) along with velocity fluctuation for the lower section of the tube

given in (A-22):
$$RHS = -P_L \frac{1}{\bar{\rho}_L \bar{a}_L} \frac{(\gamma-1)}{\gamma} \frac{\kappa}{\bar{p}} \frac{\dot{Q}_0}{\bar{u}_L} e^{-i\omega t} \cos(k_L b).$$

Equation (A-25) then becomes

$$(A-25a) \quad P_U \frac{1}{\bar{\rho}_U \bar{a}_U} \cos(k_U (L-b)) = -P_L \frac{1}{\bar{\rho}_L \bar{a}_L} \left(1 + \frac{(\gamma-1)}{\gamma} \frac{\kappa}{\bar{p}} \frac{\dot{Q}_0}{\bar{u}_L} \right) \cos(k_L b).$$

or

$$\frac{P_U}{P_L} \frac{\cos(k_U (L-b))}{\cos(k_L b)} = -\frac{\bar{\rho}_U \bar{a}_U}{\bar{\rho}_L \bar{a}_L} \left(1 + \frac{(\gamma-1)}{\gamma} \frac{\kappa}{\bar{p}} \frac{\dot{Q}_0}{\bar{u}_L} \right).$$

Substituting (A-24) into (A-25a) for P_U/P_L gives

$$(A-26) \quad \frac{\tan(k_L b)}{\tan(k_U (L-b))} = -\frac{\bar{\rho}_U \bar{a}_U}{\bar{\rho}_L \bar{a}_L} \left(1 + \frac{(\gamma-1)}{\gamma} \frac{\kappa}{\bar{p}} \frac{\dot{Q}_0}{\bar{u}_L} \right).$$

For the case where \dot{Q}_0 goes to zero (i.e. the heater is disabled), the mean density and speed of sound, as well as the wave numbers become uniform throughout the tube. The governing equation then becomes:

$$(A-27) \quad \frac{\tan(kb)}{\tan(k(L-b))} = -1 \quad \text{for} \quad \dot{Q}_0 \rightarrow 0.$$

Expanding this in terms of sines and cosines, and applying the angle difference formulas along with the Pythagorean relation leads to the simple and expected result

$$(A-28) \quad \sin(kL) = 0 \quad \text{implying} \quad k = 0, \frac{\pi}{L}, \frac{2\pi}{L}, \dots, \frac{n\pi}{L}.$$

These are just the wave numbers associated with an open-open pipe.

The solution of (A-26) in the non-trivial case (where $T_U > T_L$) can be achieved by numerical means. The equation can be simplified by the use of the mean flow relations (A-4) and (A-5):

$$(A-29) \quad \begin{aligned} \frac{\tan(k_L b)}{\tan(k_U (L-b))} &= - \left(1 + \frac{(\gamma-1)}{\gamma} \frac{1}{\bar{p}} \frac{\dot{Q}_0}{\bar{u}_L} \right)^{-\frac{1}{2}} \left(1 + \frac{(\gamma-1)}{\gamma} \frac{\kappa}{\bar{p}} \frac{\dot{Q}_0}{\bar{u}_L} \right) \\ &= - \left(\frac{\bar{T}_U}{\bar{T}_L} \right)^{-\frac{1}{2}} \left(1 + \kappa \left(\frac{\bar{T}_U}{\bar{T}_L} - 1 \right) \right). \end{aligned}$$

Here it can be seen that if there is no unsteady heat release (i.e. $\kappa \rightarrow 0$), then (A-29) becomes

$$(A-30) \quad \frac{\tan(k_L b)}{\tan(k_U (L-b))} = - \left(1 + \frac{(\gamma-1)}{\gamma} \frac{1}{\bar{p}} \frac{\dot{Q}_0}{\bar{u}_L} \right)^{-\frac{1}{2}} = - \left(\frac{\bar{T}_U}{\bar{T}_L} \right)^{-\frac{1}{2}} \quad \text{for } \kappa \rightarrow 0.$$

On the other hand, if $\kappa \rightarrow 1$, then (A-29) becomes

$$(A-31) \quad \frac{\tan(k_L b)}{\tan(k_U (L-b))} = - \left(1 + \frac{(\gamma-1)}{\gamma} \frac{1}{\bar{p}} \frac{\dot{Q}_0}{\bar{u}_L} \right)^{\frac{1}{2}} = - \left(\frac{\bar{T}_U}{\bar{T}_L} \right)^{\frac{1}{2}} \quad \text{for } \kappa \rightarrow 1.$$

By noting that the wave numbers can be written in terms of the frequency and the speed of sound,

namely $k_L = \frac{\omega}{\bar{a}_L}$ and $k_U = \frac{\omega}{\bar{a}_U}$, it is possible to rewrite the arguments of the tangent functions in

(A-29), (A-30) and (A-31) in terms of dimensionless frequency:

$$(A-29a) \quad \begin{aligned} \frac{\tan\left(\frac{\omega L}{\pi \bar{a}_L} \pi \frac{b}{L}\right)}{\tan\left(\frac{\omega L}{\pi \bar{a}_L} \left(\frac{\bar{T}_L}{\bar{T}_U}\right)^{\frac{1}{2}} \pi \left(1 - \frac{b}{L}\right)\right)} &= - \left(1 + \frac{(\gamma-1)}{\gamma} \frac{1}{\bar{p}} \frac{\dot{Q}_0}{\bar{u}_L} \right)^{-\frac{1}{2}} \left(1 + \frac{(\gamma-1)}{\gamma} \frac{\kappa}{\bar{p}} \frac{\dot{Q}_0}{\bar{u}_L} \right) \\ &= - \left(\frac{\bar{T}_U}{\bar{T}_L} \right)^{-\frac{1}{2}} \left(1 + \kappa \left(\frac{\bar{T}_U}{\bar{T}_L} - 1 \right) \right), \end{aligned}$$

$$(A-30a) \quad \frac{\tan\left(\frac{\omega L}{\pi \bar{a}_L} \pi \frac{b}{L}\right)}{\tan\left(\frac{\omega L}{\pi \bar{a}_L} \left(\frac{\bar{T}_L}{\bar{T}_U}\right)^{\frac{1}{2}} \pi \left(1 - \frac{b}{L}\right)\right)} = -\left(1 + \frac{(\gamma-1)}{\gamma} \frac{1}{\bar{p}} \frac{\dot{Q}_0}{\bar{u}_L}\right)^{-\frac{1}{2}} = -\left(\frac{\bar{T}_U}{\bar{T}_L}\right)^{-\frac{1}{2}},$$

$$(A-31a) \quad \frac{\tan\left(\frac{\omega L}{\pi \bar{a}_L} \pi \frac{b}{L}\right)}{\tan\left(\frac{\omega L}{\pi \bar{a}_L} \left(\frac{\bar{T}_L}{\bar{T}_U}\right)^{\frac{1}{2}} \pi \left(1 - \frac{b}{L}\right)\right)} = -\left(1 + \frac{(\gamma-1)}{\gamma} \frac{1}{\bar{p}} \frac{\dot{Q}_0}{\bar{u}_L}\right)^{\frac{1}{2}} = -\left(\frac{\bar{T}_U}{\bar{T}_L}\right)^{\frac{1}{2}}.$$

The curves for these relations are plotted in Figure A-3.

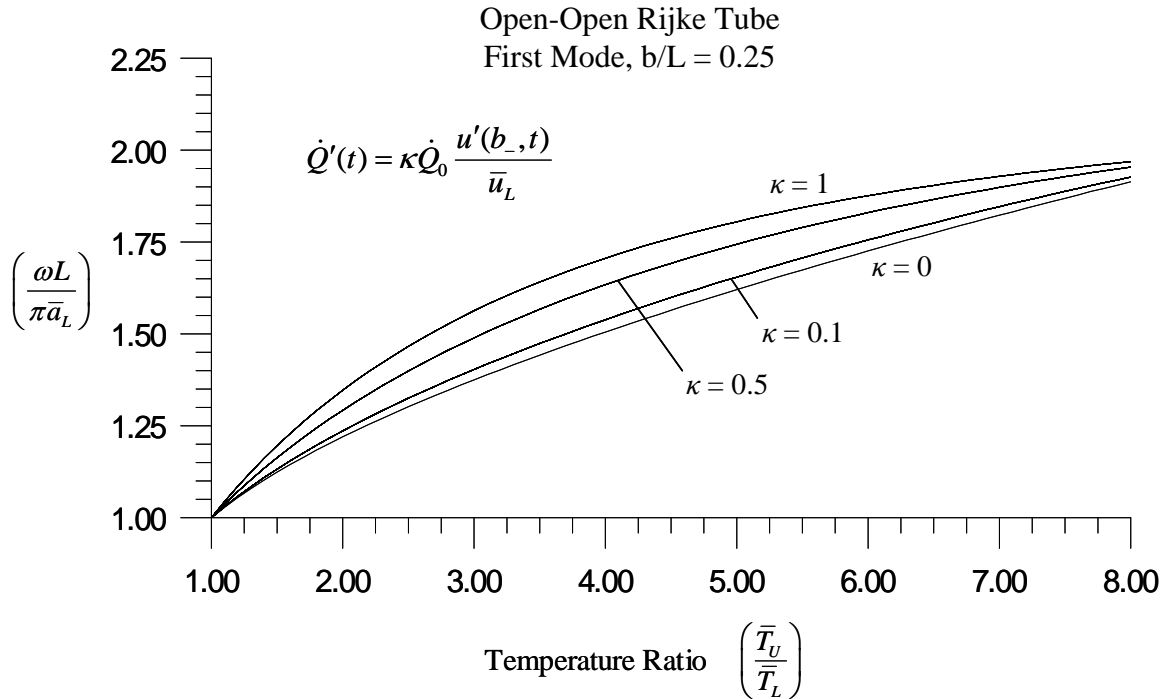


Figure A-3: Plots of the exact solution of the Rijke tube as given by equation (A-29a). The heated grid is located at a distance from the inlet that is one quarter of the total length of the tube. The parameter κ is a dimensionless coupling constant that scales the magnitude of the unsteady heat input in relation to the velocity fluctuation just upstream of the heater. The model used for $\dot{Q}'(x, t)$ is due to Merk as presented in equation (A-15a). $\kappa = 0$ corresponds to the acoustic case where only the temperature jump exists and no unsteady heat input is present.

A.2.2 – Rijke Tube Solution by Spatial Averaging

For the method of spatial averaging, we begin with the energy equation including the heat addition term on the right hand side. Following the same procedure used to arrive at the wave equation in (A-16), we find

$$(A-32) \quad \frac{\partial^2 p'}{\partial t^2} - \frac{\gamma \bar{p}}{\bar{\rho}} \frac{\partial^2 p'}{\partial x^2} = (\gamma - 1) \frac{\partial \dot{Q}'}{\partial t} \delta(x - b) + \frac{\gamma \bar{p}}{\bar{\rho}} \frac{\partial \bar{\rho}}{\partial x} \frac{\partial u'}{\partial t}.$$

Note the last term on the RHS of the equation involving the spatial derivative of the mean density.

For the case of the plane heater, it is recognized that

$$(A-33) \quad \frac{1}{\bar{\rho}} \frac{\partial \bar{\rho}}{\partial x} = \frac{\partial}{\partial x} \ln(\bar{\rho}) = [\ln(\bar{\rho}_U) - \ln(\bar{\rho}_L)] \delta(x - b) = \ln\left(\frac{\bar{\rho}_U}{\bar{\rho}_L}\right) \delta(x - b).$$

Substituting this into (A-32) gives:

$$(A-34) \quad \frac{\partial^2 p'}{\partial t^2} - \bar{a}^2 \frac{\partial^2 p'}{\partial x^2} = \left[(\gamma - 1) \frac{\partial \dot{Q}'}{\partial t} + \gamma \bar{p} \ln\left(\frac{\bar{\rho}_U}{\bar{\rho}_L}\right) \frac{\partial u'}{\partial t} \right] \delta(x - b).$$

The goal is to now solve this equation approximately by examining the perturbed solution of the classical acoustic problem. This is done by assuming that the mode shapes of the system with unsteady heat addition are close to those of the classical system and that the difference is only seen in the time dependent amplitudes. We start with the wave equation for the classical system that includes the jump in average temperature. Considering only the first mode, we have

$$(A-35) \quad \frac{\partial^2 p'_1}{\partial t^2} - \bar{a}^2 \frac{\partial^2 p'_1}{\partial x^2} = \frac{\gamma \bar{p}}{\bar{\rho}} \frac{\partial \bar{\rho}}{\partial x} \frac{\partial u'_1}{\partial t} \quad \text{with} \quad \begin{aligned} p'_1(0, t) &= 0 \\ p'_1(b_-, t) &= p'_1(b_+, t) \\ p'_1(L, t) &= 0. \end{aligned}$$

A spatially averaged, weighted difference is constructed by multiplying (A-34) by p'_1 and (A-35) by p' , and then subtracting. This difference is then integrated over the length of the tube. Formally,

this integral is over the volume of the tube, but we choose to solve in one dimension since the Rijke tube is of uniform cross-sectional area.

$$(A-36) \quad \int_0^L \left[p'_1 \frac{\partial^2 p'}{\partial t^2} - p' \frac{\partial^2 p'_1}{\partial t^2} \right] dx - \int_0^L \bar{a}^2 \left[p'_1 \frac{\partial^2 p'}{\partial x^2} - p' \frac{\partial^2 p'_1}{\partial x^2} \right] dx = \int_0^L (p'_1 h - p' h'_1) dx,$$

$$\text{where } h = \left[(\gamma - 1) \frac{\partial \dot{Q}'}{\partial t} + \gamma \bar{p} \ln \left(\frac{\bar{\rho}_U}{\bar{\rho}_L} \right) \frac{\partial u'}{\partial t} \right] \delta(x - b),$$

$$\text{and } h'_1 = \gamma \bar{p} \ln \left(\frac{\bar{\rho}_U}{\bar{\rho}_L} \right) \frac{\partial u'_1}{\partial t} \delta(x - b).$$

The second integral can be split into the regions upstream and downstream of the heater:

$$(A-37) \quad \int_0^L \left[p'_1 \frac{\partial^2 p'}{\partial t^2} - p' \frac{\partial^2 p'_1}{\partial t^2} \right] dx - \bar{a}_L^2 \int_0^b \left[p'_1 \frac{\partial^2 p'}{\partial x^2} - p' \frac{\partial^2 p'_1}{\partial x^2} \right] dx - \bar{a}_U^2 \int_b^L \left[p'_1 \frac{\partial^2 p'}{\partial x^2} - p' \frac{\partial^2 p'_1}{\partial x^2} \right] dx = \int_0^L (p'_1 h - p' h'_1) dx.$$

The second and third terms can then be integrated by parts and the boundary conditions can be applied:

(A-38a,b)

$$\begin{aligned} \bar{a}_L^2 \int_0^b \left[p'_1 \frac{\partial^2 p'}{\partial x^2} - p' \frac{\partial^2 p'_1}{\partial x^2} \right] dx &= \bar{a}_L^2 \left[p'_1 \frac{\partial p'}{\partial x} - p' \frac{\partial p'_1}{\partial x} \right]_0^b - \bar{a}_L^2 \int_0^b \left[\frac{\partial p'_1}{\partial x} \frac{\partial p'}{\partial x} - \frac{\partial p'}{\partial x} \frac{\partial p'_1}{\partial x} \right] dx, \\ \bar{a}_U^2 \int_b^L \left[p'_1 \frac{\partial^2 p'}{\partial x^2} - p' \frac{\partial^2 p'_1}{\partial x^2} \right] dx &= \bar{a}_U^2 \left[p'_1 \frac{\partial p'}{\partial x} - p' \frac{\partial p'_1}{\partial x} \right]_b^L - \bar{a}_U^2 \int_b^L \left[\frac{\partial p'_1}{\partial x} \frac{\partial p'}{\partial x} - \frac{\partial p'}{\partial x} \frac{\partial p'_1}{\partial x} \right] dx. \end{aligned}$$

So, (A-37) simply becomes

$$\begin{aligned}
 \text{(A-39)} \quad & \int_0^L \left[p'_1 \frac{\partial^2 p'}{\partial t^2} - p' \frac{\partial^2 p'_1}{\partial t^2} \right] dx - \bar{a}_L^2 \left[p'_1 \frac{\partial p'}{\partial x} - p' \frac{\partial p'_1}{\partial x} \right]_{x=b_-} + \bar{a}_U^2 \left[p'_1 \frac{\partial p'}{\partial x} - p' \frac{\partial p'_1}{\partial x} \right]_{x=b_+} \\
 & = \int_0^L (p'_1 h - p' h_1) dx .
 \end{aligned}$$

Now, from our earlier analysis, the form of the pressure in the tube for the unperturbed case is

$$\text{(A-40)} \quad p'_1(x, t) = \begin{cases} P_L e^{-i\omega t} \sin(k_{L_1} x) & 0 \leq x < b \\ P_U e^{-i\omega t} \sin(k_{U_1} (L - x)) & b < x \leq L \end{cases} .$$

However, by the matching condition at the heater:

$$\text{(A-41)} \quad P_U = P_L \frac{\sin(k_{L_1} b)}{\sin(k_{U_1} (L - b))} .$$

And, consequently, (A-40) becomes

$$\text{(A-42)} \quad p'_1(x, t) = \begin{cases} P_L e^{-i\omega t} \sin(k_{L_1} x) & 0 \leq x < b \\ P_L e^{-i\omega t} \frac{\sin(k_{L_1} b)}{\sin(k_{U_1} (L - b))} \sin(k_{U_1} (L - x)) & b < x \leq L \end{cases} .$$

Now, by inspection, one can see that

$$\text{(A-43)} \quad \frac{\partial^2 p'_1}{\partial t^2} = -\omega_1^2 p'_1 .$$

Additionally, as mentioned earlier, we assume that the spatial distribution of the pressure is similar for the perturbed and unperturbed cases, and that the primary difference is in the time dependence. Consequently, we assume a form for the first mode fluctuating pressure in the perturbed case of

$$\text{(A-44)} \quad p' = \begin{cases} \bar{p} \eta_1(t) \sin(k_{L_1} x) & 0 \leq x < b \\ \bar{p} \eta_1(t) \frac{\sin(k_{L_1} b)}{\sin(k_{U_1} (L - b))} \sin(k_{U_1} (L - x)) & b < x \leq L \end{cases} .$$

Substituting (A-42) and (A-44) into (A-39), our equation becomes

$$\begin{aligned}
& P_L \bar{p} e^{-i\omega_l t} (\ddot{\eta}_l(t) + \omega_l^2 \eta_l(t)) \left[\int_0^b \sin^2(k_{L_l} x) dx + \frac{\sin^2(k_{L_l} b)}{\sin^2(k_{U_l}(L-b))} \int_b^L \sin^2(k_{U_l}(L-x)) dx \right] \\
(\text{A-45}) \quad & = P_L e^{-i\omega_l t} \left[\int_0^b h \sin(k_{L_l} x) dx + \frac{\sin(k_{L_l} b)}{\sin(k_{U_l}(L-b))} \int_b^L h \sin(k_{U_l}(L-x)) dx \right] \\
& - \bar{p} \eta_l(t) \left[\int_0^b h_l \sin(k_{L_l} x) dx + \frac{\sin(k_{L_l} b)}{\sin(k_{U_l}(L-b))} \int_b^L h_l \sin(k_{U_l}(L-x)) dx \right].
\end{aligned}$$

Reorganizing:

$$\begin{aligned}
& \ddot{\eta}_l(t) + \omega_l^2 \eta_l(t) = \frac{1}{\bar{p} E_l} \left[\int_0^b h \sin(k_{L_l} x) dx + \frac{\sin(k_{L_l} b)}{\sin(k_{U_l}(L-b))} \int_b^L h \sin(k_{U_l}(L-x)) dx \right] \\
(\text{A-46}) \quad & - \frac{\eta_l(t)}{P_L E_l e^{-i\omega_l t}} \left[\int_0^b h_l \sin(k_{L_l} x) dx + \frac{\sin(k_{L_l} b)}{\sin(k_{U_l}(L-b))} \int_b^L h_l \sin(k_{U_l}(L-x)) dx \right],
\end{aligned}$$

$$\text{where } E_l = \int_0^b \sin^2(k_{L_l} x) dx + \frac{\sin^2(k_{L_l} b)}{\sin^2(k_{U_l}(L-b))} \int_b^L \sin^2(k_{U_l}(L-b)) dx.$$

The integrals in E_l are directly solvable:

$$\int_0^b \sin^2(k_{L_l} x) dx = \frac{b}{2} - \frac{\sin(2k_{L_l} b)}{4k_{L_l}} \quad \text{and} \quad \int_b^L \sin^2(k_{U_l}(L-x)) dx = \frac{L-b}{2} - \frac{\sin(2k_{U_l}(L-b))}{4k_{U_l}}.$$

Thus, E_l becomes

$$(\text{A-47}) \quad E_l = \left[\frac{b}{2} - \frac{\sin(2k_{L_l} b)}{4k_{L_l}} \right] + \frac{\sin^2(k_{L_l} b)}{\sin^2(k_{U_l}(L-b))} \left[\frac{L-b}{2} - \frac{\sin(2k_{U_l}(L-b))}{4k_{U_l}} \right].$$

Then, substituting for h and h_l from (A-36) produces the eyesore

(A-48)

$$\begin{aligned}
\ddot{\eta}_1(t) + \omega_1^2 \eta_1(t) = & \frac{1}{\bar{p}E_1} \left\{ \int_0^b \left[(\gamma-1) \frac{\partial \dot{Q}'}{\partial t} + \gamma \bar{p} \ln \left(\frac{\bar{\rho}_U}{\bar{\rho}_L} \right) \frac{\partial u'}{\partial t} \right] \sin(k_{L_1} x) \delta(x-b) dx \right. \\
& + \frac{\sin(k_{L_1} b)}{\sin(k_{U_1}(L-b))} \int_b^L \left[(\gamma-1) \frac{\partial \dot{Q}'}{\partial t} + \gamma \bar{p} \ln \left(\frac{\bar{\rho}_U}{\bar{\rho}_L} \right) \frac{\partial u'}{\partial t} \right] \sin(k_{U_1}(L-x)) \delta(x-b) dx \left. \right\} \\
& - \frac{\gamma \bar{p} \eta_1(t)}{P_L E_1 e^{-i\omega_1 t}} \left\{ \int_0^b \ln \left(\frac{\bar{\rho}_U}{\bar{\rho}_L} \right) \frac{\partial u_1'}{\partial t} \sin(k_{L_1} x) \delta(x-b) dx \right. \\
& \left. + \frac{\sin(k_{L_1} b)}{\sin(k_{U_1}(L-b))} \int_b^L \ln \left(\frac{\bar{\rho}_U}{\bar{\rho}_L} \right) \frac{\partial u_1'}{\partial t} \sin(k_{U_1}(L-x)) \delta(x-b) dx \right\}.
\end{aligned}$$

It is now convenient to substitute for the terms containing fluctuating quantities. As given before,

(A-15a) represents the model for the thermal coupling. Differentiating with respect to time gives

$$(A-49) \quad \frac{\partial \dot{Q}'}{\partial t} = \kappa \frac{\dot{Q}_0}{\bar{u}_L} \frac{\partial u'}{\partial t} \Big|_{x=b} \quad \text{for } x=b.$$

Additionally, to arrive at relations for the fluctuating velocities one can appeal to the acoustic energy equation. By plugging in the pressure fluctuation relations for the unperturbed case, the solutions for the classical velocity fluctuations differentiated with respect to time can be determined:

$$(A-50) \quad \frac{\partial u_1'}{\partial t} = \begin{cases} -\frac{P_L}{\gamma \bar{p}} \frac{\omega^2}{k_{L_1}} e^{-i\omega_1 t} \cos(k_{L_1} x) & 0 \leq x < b \\ \frac{P_L}{\gamma \bar{p}} \frac{\omega^2}{k_{U_1}} e^{-i\omega_1 t} \frac{\sin(k_L b)}{\sin(k_U(L-b))} \cos(k_{U_1}(L-x)) & b < x \leq L. \end{cases}$$

Similarly, the velocity fluctuations in the system of interest can be approximated by the same means. Differentiated with respect to time, these velocity fluctuations are

$$(A-51) \quad \frac{\partial u'}{\partial t} = \begin{cases} \frac{1}{\gamma k_{L_1}} \ddot{\eta}_1(t) \cos(k_{L_1} x) & 0 \leq x < b \\ -\frac{1}{\gamma k_{U_1}} \ddot{\eta}_1(t) \frac{\sin(k_L b)}{\sin(k_U (L-b))} \cos(k_{L_1} (L-x)) & b < x \leq L \end{cases}$$

Substituting these relations into (A-48) and using the ideal and thermally perfect gas relations as

well as the identity $\frac{k_{L_1}}{k_{U_1}} = \left(\frac{\bar{T}_U}{\bar{T}_L}\right)^{\frac{1}{2}}$, the result becomes

(A-52)

$$\ddot{\eta}_1(t) + \omega_1^2 \eta_1(t) = \frac{1}{E_1 k_{L_1}} \ddot{\eta}_1(t) \kappa \left(\frac{\bar{T}_U}{\bar{T}_L} - 1 \right) \cos(k_{L_1} b) \sin(k_{L_1} b) - \frac{1}{2} \frac{1}{E_1 k_{L_1}} (\ddot{\eta}_1(t) + \omega_1^2 \eta_1(t)) \ln \left(\frac{\bar{T}_U}{\bar{T}_L} \right) \left[\cos(k_{L_1} b) \sin(k_{L_1} b) - \left(\frac{\bar{T}_U}{\bar{T}_L} \right)^{\frac{1}{2}} \frac{\sin^2(k_{L_1} b)}{\tan \left(\left(\frac{\bar{T}_U}{\bar{T}_L} \right)^{-\frac{1}{2}} k_{L_1} (L-b) \right)} \right].$$

This assumed Heavyside step behavior across the heater so that derivatives of jumps with respect to x could be Lebesgue integrated as Dirac delta functions.

The above can be made more manageable by the assignment of two definitions:

(A-53)

$$\begin{aligned} \beta_1 &= \cos(k_{L_1} b) \sin(k_{L_1} b), \\ \beta_2 &= \left(\frac{\bar{T}_U}{\bar{T}_L} \right)^{\frac{1}{2}} \frac{\sin^2(k_{L_1} b)}{\tan \left(\left(\frac{\bar{T}_U}{\bar{T}_L} \right)^{-\frac{1}{2}} k_{L_1} (L-b) \right)}. \end{aligned}$$

With these, (A-52) becomes

$$(A-54) \quad \ddot{\eta}_1(t) + \omega_1^2 \eta_1(t) = \frac{\beta_1}{E_1 k_{L_1}} \kappa \left(\frac{\bar{T}_U}{\bar{T}_L} - 1 \right) \ddot{\eta}_1(t) - \frac{1}{2} \frac{(\beta_1 - \beta_2)}{E_1 k_{L_1}} \ln \left(\frac{\bar{T}_U}{\bar{T}_L} \right) (\ddot{\eta}_1(t) + \omega_1^2 \eta_1(t)).$$

Rearranging:

$$(A-54a) \quad \ddot{\eta}_1(t) + \omega_1^2 \frac{1 + \frac{1}{E_1 k_{L_1}} \frac{(\beta_1 - \beta_2)}{2} \ln\left(\frac{\bar{T}_U}{\bar{T}_L}\right)}{1 - \frac{1}{E_1 k_{L_1}} \left[\kappa \beta_1 \left(\frac{\bar{T}_U}{\bar{T}_L} - 1 \right) - \frac{(\beta_1 - \beta_2)}{2} \ln\left(\frac{\bar{T}_U}{\bar{T}_L}\right) \right]} \eta_1(t) = 0.$$

Inspecting this result, it is noticed that two of the terms involve the difference $(\beta_1 - \beta_2)$.

Looking back through the previous work, we can see that this difference directly results from the evolution of the last term on the RHS of equation (A-32), that being the one involving the spatial derivative of the average density. We reassemble the difference for closer examination:

$$(A-55) \quad (\beta_1 - \beta_2) = \cos(k_{L_1} b) \sin(k_{L_1} b) - \left(\frac{\bar{T}_U}{\bar{T}_L} \right)^{\frac{1}{2}} \frac{\sin^2(k_{L_1} b)}{\tan\left(\left(\frac{\bar{T}_U}{\bar{T}_L} \right)^{-\frac{1}{2}} k_{L_1} (L - b) \right)}.$$

This can be regrouped such that

$$(A-55a) \quad (\beta_1 - \beta_2) = \cos(k_{L_1} b) \sin(k_{L_1} b) \left(\frac{\bar{T}_U}{\bar{T}_L} \right)^{\frac{1}{2}} \left[\left(\frac{\bar{T}_U}{\bar{T}_L} \right)^{-\frac{1}{2}} - \frac{\tan(k_{L_1} b)}{\tan(k_{U_1} (L - b))} \right].$$

Examining the term in brackets on the right and comparing this with the result in equation (A-30) for the exact solution with no unsteady heat addition, it is quickly realized that (A-55a) simply reduces to

$$(A-56) \quad (\beta_1 - \beta_2) = 2 \cos(k_{L_1} b) \sin(k_{L_1} b) = 2\beta_1.$$

Consequently, the result from (A-54a) becomes

$$(A-57) \quad \ddot{\eta}_1(t) + \omega_1^2 \frac{1 + \frac{1}{E_1 k_{L_1}} \beta_1 \ln\left(\frac{\bar{T}_U}{\bar{T}_L}\right)}{1 - \frac{\beta_1}{E_1 k_{L_1}} \left[\kappa \left(\frac{\bar{T}_U}{\bar{T}_L} - 1 \right) - \ln\left(\frac{\bar{T}_U}{\bar{T}_L}\right) \right]} \eta_1(t) = 0.$$

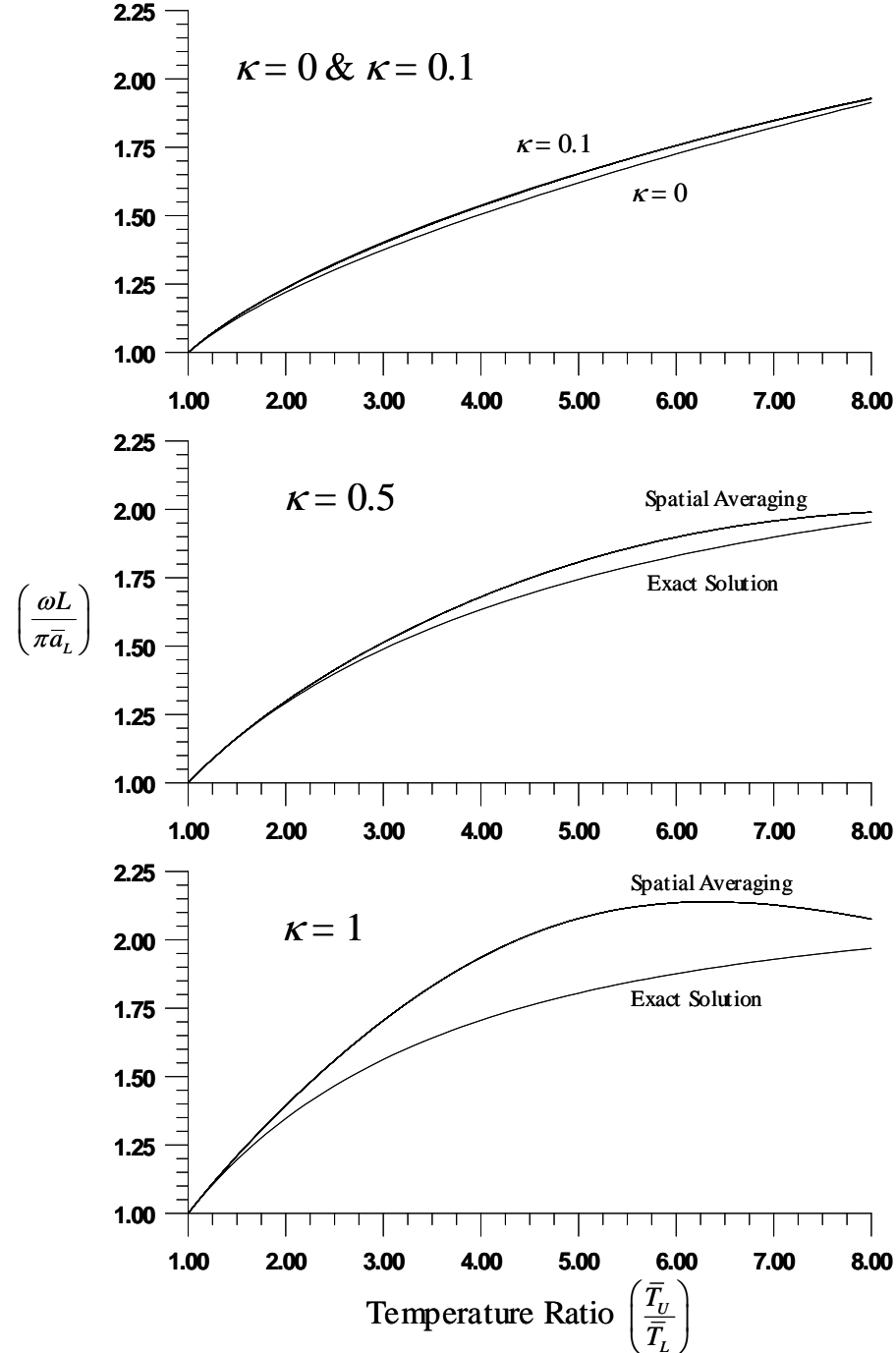


Figure A-4: Plots of the spatial averaging (equation A-54, dashed lines) and exact solutions (A-29, solid lines) of the Rijke tube. The heated grid is located at $x = 0.25 L$, where L is the total length of the tube and $x = 0$ is the inlet. The parameter κ is a dimensionless coupling constant that scales the magnitude of the unsteady heat input in relation to the velocity fluctuation just upstream of the heater. $\kappa = 0$ corresponds to the acoustic case where only the temperature jump exists and no unsteady heat input is present. As $\kappa \rightarrow 0$, the spatial averaging and exact solutions become coincident.

And by inspection, it is now possible to see that

$$(A-58) \quad \tilde{\omega}_1^2 = \frac{1 + \frac{1}{E_1 k_{L_1}} \ln \left(\frac{\bar{T}_U}{\bar{T}_L} \right)}{1 - \frac{\beta_1}{E_1 k_{L_1}} \left[\kappa \left(\frac{\bar{T}_U}{\bar{T}_L} - 1 \right) - \ln \left(\frac{\bar{T}_U}{\bar{T}_L} \right) \right]} \omega_1^2,$$

where $\tilde{\omega}_1$ is the estimated frequency of the first perturbed mode and ω_1 is the frequency of the first mode of the classical system with only the temperature jump at the heater.

Equation (A-58) can now be plotted for various values of κ on the same graph along with the results for the exact solution method. This is shown in Figure A-4. Here, the exact solution for $\kappa = 0$ defines the classical acoustic solution for the tube with a temperature jump at $b/L = 0.25$. Once the unsteady thermal coupling is introduced, (i.e. $\kappa > 0$), the exact solution lies above the acoustic solution, with first mode frequencies increasing with κ . The spatial averaging method shows good agreement for cases where the temperature jump across the heater is small. More importantly, however, it also shows good agreement for large temperature jumps when the coupling constant, κ , is small. For the case where $\kappa = 0.1$, the spatial averaging solution is nearly coincident with the exact solution.

A.3 A Closed-Open Tube

A similar system to the Rijke tube is that of a cavity with an acoustically open exit, but an acoustically closed entrance. A diagram of such a system is shown in Figure A-5. One can image a sintered plate at the entrance of the tube, forcing the acoustically closed condition at that location while allowing the mean flow to be driven through it.

Dowling (1995) proposed such a problem (containing no mean flow, however) and analyzed the case using various methods. The intent was to propose a model case that was solvable exactly with a specified heat release model and set of boundary conditions. Various approximate

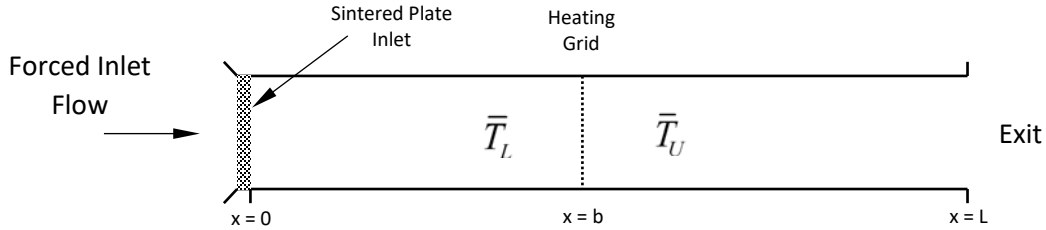


Figure A-5: Acoustically closed-open cavity with heater. Similar to the case presented by Dowling (1995).

methods were then applied and compared against the exact solution. One such approximate method tested was that of spatial averaging. Dowling called this technique the linearized Galerkin method and her results showed a large discrepancy between the exact solution and the approximate method.

Dowling chose a heat release model postulated by Bloxsidge et al. (1988). This model, shown in equation (A-59), is based on experiments with a confined premixed flame.

$$(A-59) \quad \dot{Q}'(t) = \kappa C_p (\bar{T}_U - \bar{T}_L) \bar{\rho}_L u'_L(t - \tau).$$

Here, κ represents a coupling factor while τ represents a time delay. Both these factors are functions of frequency. If a mean flow is assumed, equation (A-3) can be immediately used to make the substitution

$$(A-3a) \quad C_p (\bar{T}_U - \bar{T}_L) \bar{\rho}_L = \frac{\dot{Q}_0}{\bar{u}_L}.$$

Thus, the model in (A-59) becomes

$$(A-60) \quad \dot{Q}'(t) = \kappa \frac{\dot{Q}_0}{\bar{u}_L} u'_L(t - \tau).$$

By inspection, this is functionally equivalent to the model due to Merk presented earlier. Now, it is reasonable to assume that for a physically realizable heater that the total instantaneous heat

release must always be greater than or equal to zero. i.e. $\dot{Q}_0 + \dot{Q}'(t) \geq 0$. If this is true, then (A-60) implies

$$(A-61) \quad \bar{u}_L + \kappa u'_L(t) \geq 0.$$

Since, by definition, the mean of $u'_L(t)$ is zero, it takes on both positive and negative values. Consequently, (A-61) cannot hold true as \bar{u}_L tends to zero and the model case assuming no mean flow is physically invalid. Nonetheless, the presented case accepts a mean flow without additional troubles.

A.3.1 – Closed-Open Tube Exact Solution

The procedure to arrive at the exact solution for this problem is identical to that used for the Rijke tube presented earlier. The only difference lies in one boundary condition. The boundary conditions for the closed-open case are

$$(A-62) \quad \left. \frac{\partial p'}{\partial x} \right|_{x=0,t} = 0 \quad \text{and} \quad p'(L,t) = 0.$$

These admit solutions for the lower and upper portions of the tube in the forms

$$(A-63) \quad p'_L(x,t) = P_L e^{-i\omega t} \cos(k_L x) \quad \text{and} \quad p'_U(x,t) = P_U e^{-i\omega t} \sin(k_U(L-x)).$$

The corresponding velocity fluctuations in each region are

$$(A-64) \quad u'_L(x,t) = i P_L \frac{1}{\bar{\rho}_L \bar{a}_L} e^{-i\omega t} \sin(k_L x) \quad \text{and} \quad u'_U(x,t) = i P_U \frac{1}{\bar{\rho}_U \bar{a}_U} e^{-i\omega t} \cos(k_U(L-x)).$$

The pressure matching condition at $x = b$ requires

$$(A-65) \quad P_U \sin(k_U(L-x)) = P_L \cos(k_L b).$$

Additionally, the velocity jump condition at the grid demands

$$(A-66) \quad P_U \frac{1}{\bar{\rho}_U \bar{a}_U} e^{-i\omega t} \cos(k_U(L-b)) - P_L \frac{1}{\bar{\rho}_L \bar{a}_L} e^{-i\omega t} \sin(k_L b) = -i \frac{(\gamma-1)}{\gamma} \frac{1}{\bar{p}} \dot{Q}'.$$

As before, the selected model for the heat transfer is combined with the relation for the velocity on the lower side of the heating grid:

$$RHS = P_L \frac{1}{\bar{\rho}_L \bar{a}_L} \frac{(\gamma-1) \kappa}{\gamma} \frac{\dot{Q}_0}{\bar{p} \bar{u}_L} e^{-i\omega t} \sin(k_L b).$$

Equation (A-66) then becomes

$$(A-66a) \quad \frac{P_U}{P_L} \frac{\cos(k_U(L-b))}{\sin(k_L b)} = \frac{\bar{\rho}_U \bar{a}_U}{\bar{\rho}_L \bar{a}_L} \left[1 + \frac{(\gamma-1) \kappa}{\gamma} \frac{\dot{Q}_0}{\bar{p} \bar{u}_L} \right].$$

Substituting (A-65) into (A-66a) gives

$$(A-67) \quad \tan(k_L b) \tan(k_U(L-b)) = \frac{\bar{\rho}_L \bar{a}_L}{\bar{\rho}_U \bar{a}_U} \frac{1}{\left[1 + \frac{(\gamma-1) \kappa}{\gamma} \frac{\dot{Q}_0}{\bar{p} \bar{u}_L} \right]}.$$

Finally, making substitutions for the density and speed of sound ratios as well as using (A-3) to substitute for the term involving \dot{Q}_0 , the exact solution simply becomes

$$(A-68) \quad \tan(k_L b) \tan(k_U(L-b)) = \frac{\left(\frac{\bar{T}_U}{\bar{T}_L} \right)^{1/2}}{\left[1 + \kappa \left(\frac{\bar{T}_U}{\bar{T}_L} - 1 \right) \right]}.$$

A.3.2 – Dowling’s Solution by Modal Expansion

Dowling begins by deriving the classic wave equation with the heat addition term present on the right hand side. The derivation involves a linearization step in the thermal coupling that is justified for “linear perturbations in a region where there is no mean heat input or mean velocity” present. This rationalization based on the lack of mean heat input or velocity is unnecessary and alludes to a configuration that is simply not physical. As shown above, the addition of a mean flow does not affect the construct of the problem nor does it change the heat release model chosen by

Dowling other than to make it physically realizable. The resulting wave equation, which in 1-D is functionally equivalent to (A-32), is given as

$$(A-69) \quad \frac{1}{\bar{a}^2} \frac{\partial^2 p'}{\partial t^2} - \bar{\rho} \nabla \cdot \left(\frac{1}{\bar{\rho}} \nabla p' \right) = \frac{(\gamma-1)}{\bar{a}^2} \frac{\partial \dot{Q}'}{\partial t} \delta(x-b).$$

In proceeding, the fluctuating pressure for the perturbed system is expanded as a series:

$$(A-70) \quad p'(x, t) = \sum_{m=1}^{\infty} \eta_m(t) \psi_m(x) \quad m = 1, 2, \dots$$

Here, the basis functions, $\psi_m(x)$, are taken as the eigensolutions of the homogeneous wave equation:

$$(A-71) \quad \frac{\omega_m^2}{\bar{a}^2} \psi_m + \bar{\rho} \frac{d}{dx} \left(\frac{1}{\bar{\rho}} \frac{d\psi_m}{dx} \right) = 0, \quad \frac{d\psi_m}{dx} = 0 \quad \text{at } x = 0$$

$$\text{and} \quad \psi_m = 0 \quad \text{at } x = L.$$

Dowling goes on to state that since the temperature is uniform in the two regions ahead of and behind the heater, the wave equation simplifies to:

$$(A-72) \quad \frac{d^2 \psi_m}{dx^2} + \frac{\omega_m^2}{\bar{a}_k^2} \psi_m = 0, \quad k = 1 \text{ for } 0 \leq x < b$$

$$\text{and} \quad k = 2 \text{ for } b < x \leq L,$$

along with the associated jump conditions

$$(A-73) \quad [\psi_m]_{x=b_-}^{x=b_+} = 0 \quad \text{and} \quad \left[\frac{1}{\bar{\rho}} \frac{d\psi_m}{dx} \right]_{x=b_-}^{x=b_+} = 0.$$

The solution to this basis system is simply

$$(A-74) \quad \psi_m(x) = \begin{cases} \cos(k_{L_m} x) & 0 \leq x < b \\ \frac{\cos(k_{L_m} b)}{\sin(k_{U_m} (L-b))} \sin(k_{U_m} (L-x)) & b < x \leq L. \end{cases}$$

It is at this point that a mistake is made in the analysis. Dowling states that substituting the series expansion (A-70) into the 1-D version of the wave equation with heat addition (A-69) leads to

$$(A-75) \quad \sum_{m=1}^{\infty} (\ddot{\eta}(t) + \omega_m \eta(t)) \psi_m(x) = (\gamma - 1) \frac{\partial \dot{Q}'}{\partial t} \delta(x - b).$$

This is incorrect. Dowling assumes that the mean density is constant throughout the tube. This is true everywhere except at the heater where the average density experiences a discontinuous jump.

As such, the wave equation should appear as seen in (A-32) with the term containing $\frac{\partial \bar{\rho}}{\partial x}$ appearing explicitly on the right hand side. This is a term that Dowling neglects.

It may appear at first glance that this term is insignificant since it only has value at an infinitesimally thin location within the heater. However, in the next step of the analysis, equation (A-75) is multiplied by $\psi_n(x)$ and integrated over the length of the tube. Suddenly, the aforementioned term takes on new meaning as it appears as a delta function under integration resulting in a quantity that scales with the difference in density across the jump, a value that is not negligible. The motivation for this multiplication and integration is to exploit the orthogonality of the modes of the system. The result is:

$$(A-76) \quad \ddot{\eta}_n(t) + \omega_n \eta_n(t) = \frac{(\gamma - 1)}{E_n} \int_0^L \psi_n(x) \frac{\partial \dot{Q}'}{\partial t} \delta(x - b) dx ,$$

$$\text{where } E_n = \int_0^L \psi_n^2(x) dx .$$

After selecting the first mode for evaluation, substituting for the unsteady heat release model (with $\kappa = 1.0$) and applying the approximation that $\ddot{\eta}_1(t) \approx -\omega_1^2 \eta_1(t)$, Dowling arrives at the following result for the approximation to the first mode frequency as a function of heater position and temperature ratio:

$$(A-77) \quad \tilde{\omega}_1^2 = \omega_1^2 - \frac{\omega_1(\gamma-1)C_p(\bar{T}_U - \bar{T}_L)\sin(k_{L_1}b)\cos(k_{L_1}b)}{E_1\bar{a}_1}.$$

After linearizing using the binomial expansion the results is simplified to

$$(A-78) \quad \tilde{\omega}_1 = \omega_1 - \frac{(\gamma-1)C_p(\bar{T}_U - \bar{T}_L)\sin(k_{L_1}b)\cos(k_{L_1}b)}{2E_1\bar{a}_1}.$$

Figure A-6 shows these results plotted for the case where $b/L = 0.5$. Also plotted are the results for the exact solution where $\kappa = 1.0$ and $\kappa = 0$. Based on these results, Dowling claims that the method of spatial averaging “diverges significantly for larger temperature ratios” and that “by

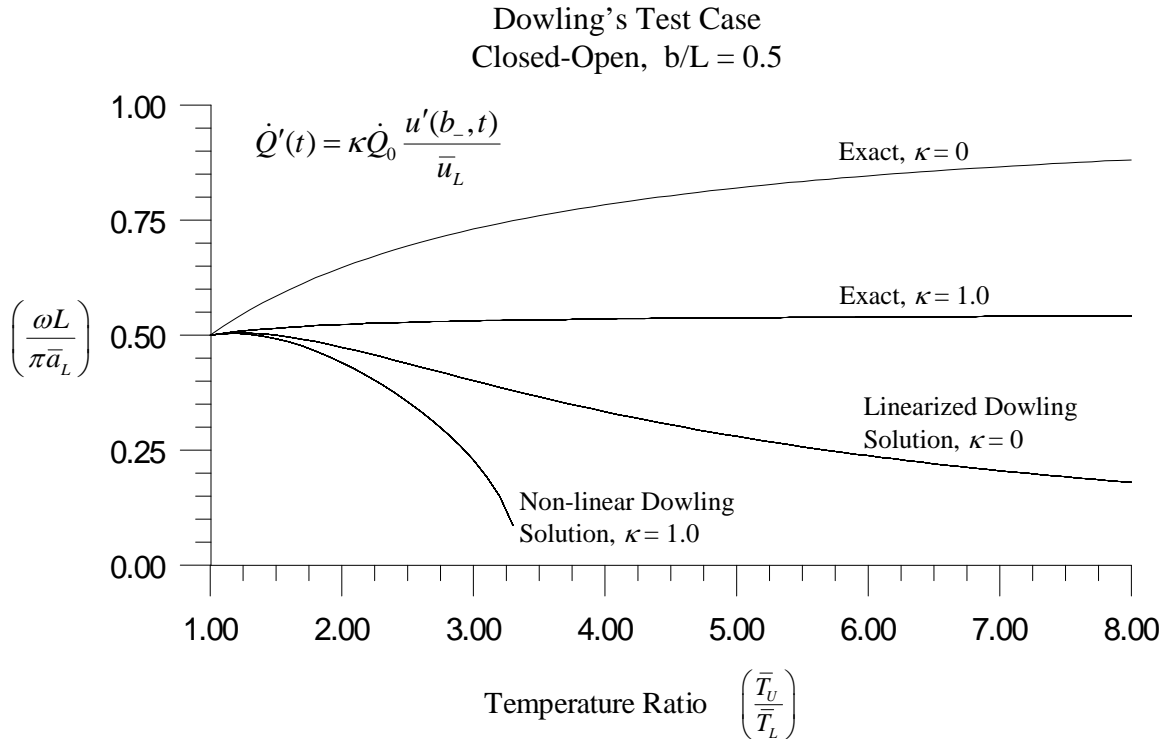


Figure A-6: Solutions by Dowling (1995) for the closed-open system. The heating grid is located at $x = 0.5 L$ where L is the total length of the tube. The parameter κ is a dimensionless coupling constant that scales the magnitude of the unsteady heat input in relation to the velocity fluctuation just upstream of the heater. $\kappa = 0$ corresponds to the acoustic case with the temperature discontinuity present but without unsteady heat input. $\kappa = 1$ corresponds to Dowling's chosen unsteady heat input model based on work by Bloxsidge et. al. (1988).

temperature ratio of six, the Galerkin method predicts a frequency which is less than half the exact value.” As will be shown in the next section, the combination of the missing average density term along with the approximation used to arrive at (A-77) results in this erroneous conclusion. On the contrary, when executed properly, the method of spatial averaging produces an approximation that is quite reasonable.

A.3.3 – Closed-Open System Spatial Averaging Solution - Corrected

The solution to the closed-open problem by spatial averaging is completely analogous to the previous solution for the classic Rijke tube given in section A.2.2. The method is identical and only the boundary condition at the entrance of the tube is different. As such, the solution presented here is highly abridged and only focuses on the differences.

The first difference appears in (A-35) which represents the wave equation for the classical system that includes the temperature jump at the heater. Here the boundary condition at the

entrance of the duct becomes $\left. \frac{\partial p'_1}{\partial x} \right|_{x=0,t} = 0$. As a consequence, the solution to the system becomes

$$(A-79) \quad p'_1(x,t) = \begin{cases} P_L e^{-i\omega t} \cos(k_{L_1} x) & 0 \leq x < b \\ P_U e^{-i\omega t} \sin(k_{U_1} (L-x)) & b < x \leq L \end{cases}$$

And the matching condition at the heater implies

$$(A-80) \quad P_U = P_L \frac{\cos(k_{L_1} b)}{\sin(k_{U_1} (L-b))}$$

Resulting in p'_1 becoming

$$(A-81) \quad p'_1(x,t) = \begin{cases} P_L e^{-i\omega t} \cos(k_{L_1} x) & 0 \leq x < b \\ P_L e^{-i\omega t} \frac{\cos(k_{L_1} b)}{\sin(k_{U_1} (L-b))} \sin(k_{U_1} (L-x)) & b < x \leq L \end{cases}$$

Following the same assumptions as given in the Rijke tube solution, p' is chosen to be

$$(A-82) \quad p' = \begin{cases} \bar{p}\eta_1(t)\cos(k_{L_1}x) & 0 \leq x < b \\ \bar{p}\eta_1(t)\frac{\cos(k_{L_1}b)}{\sin(k_{U_1}(L-b))}\sin(k_{U_1}(L-x)) & b < x \leq L \end{cases}$$

Substituting these into the equation for the spatially averaged weighted difference as derived in (A-39) produces the result

$$(A-83) \quad \begin{aligned} & P_L \bar{p} e^{-i\omega_1 t} (\ddot{\eta}_1(t) + \omega_1^2 \eta_1(t)) \left[\int_0^b \cos^2(k_{L_1}x) dx + \frac{\cos^2(k_{L_1}b)}{\sin^2(k_{U_1}(L-b))} \int_b^L \sin^2(k_{U_1}(L-x)) dx \right] \\ & = P_L e^{-i\omega_1 t} \left[\int_0^b h \cos(k_{L_1}x) dx + \frac{\cos(k_{L_1}b)}{\sin(k_{U_1}(L-b))} \int_b^L h \sin(k_{U_1}(L-x)) dx \right] \\ & \quad - \bar{p}\eta_1(t) \left[\int_0^b h_1 \cos(k_{L_1}x) dx + \frac{\cos(k_{L_1}b)}{\sin(k_{U_1}(L-b))} \int_b^L h_1 \sin(k_{U_1}(L-x)) dx \right]. \end{aligned}$$

Defining the term in brackets on the LHS as E_1 in the usual way and solving leads to:

$$(A-84) \quad E_1 = \left[\frac{b}{2} + \frac{\sin(2k_{L_1}b)}{4k_{L_1}} \right] + \frac{\cos^2(k_{L_1}b)}{\sin^2(k_{U_1}(L-b))} \left[\frac{L-b}{2} - \frac{\sin(2k_{U_1}(L-b))}{4k_{U_1}} \right].$$

Then substituting for h and h_1 in (A-83) as given in (A-36), produces the equivalent monstrosity to (A-48):

$$\begin{aligned}
\ddot{\eta}_1(t) + \omega_1^2 \eta_1(t) = & \frac{1}{\bar{p}E_1} \left\{ \int_0^b \left[(\gamma - 1) \frac{\partial \dot{Q}'}{\partial t} + \gamma \bar{p} \ln \left(\frac{\bar{\rho}_U}{\bar{\rho}_L} \right) \frac{\partial u'}{\partial t} \right] \cos(k_{L_1} x) \delta(x - b) dx \right. \\
& + \frac{\cos(k_{L_1} b)}{\sin(k_{U_1}(L - b))} \int_b^L \left[(\gamma - 1) \frac{\partial \dot{Q}'}{\partial t} + \gamma \bar{p} \ln \left(\frac{\bar{\rho}_U}{\bar{\rho}_L} \right) \frac{\partial u'}{\partial t} \right] \sin(k_{U_1}(L - x)) \delta(x - b) dx \left. \right\} \\
& - \frac{\gamma \bar{p} \eta_1(t)}{P_L E_1 e^{-i\omega_1 t}} \left\{ \int_0^b \ln \left(\frac{\bar{\rho}_U}{\bar{\rho}_L} \right) \frac{\partial u_1'}{\partial t} \cos(k_{L_1} x) \delta(x - b) dx \right. \\
& \left. + \frac{\cos(k_{L_1} b)}{\sin(k_{U_1}(L - b))} \int_b^L \ln \left(\frac{\bar{\rho}_U}{\bar{\rho}_L} \right) \frac{\partial u_1'}{\partial t} \sin(k_{U_1}(L - x)) \delta(x - b) dx \right\}.
\end{aligned} \tag{A-85}$$

At this point it is necessary to substitute for the fluctuating quantities. The model for the fluctuating heat release is as presented in (A-49); however u' and its derivative are now different. Generating these needed time derivatives using the acoustic energy equation gives

$$\frac{\partial u_1'}{\partial t} = \begin{cases} \frac{P_L}{\gamma \bar{p}} \frac{\omega^2}{k_{L_1}} e^{-i\omega_1 t} \sin(k_{L_1} x) & 0 \leq x < b \\ \frac{P_L}{\gamma \bar{p}} \frac{\omega^2}{k_{U_1}} e^{-i\omega_1 t} \frac{\cos(k_L b)}{\sin(k_U(L - b))} \cos(k_{L_1}(L - x)) & b < x \leq L \end{cases} \tag{A-86}$$

and

$$\frac{\partial u'}{\partial t} = \begin{cases} -\frac{1}{\gamma k_{L_1}} \ddot{\eta}_1(t) \sin(k_{L_1} x) & 0 \leq x < b \\ -\frac{1}{\gamma k_{U_1}} \ddot{\eta}_1(t) \frac{\cos(k_L b)}{\sin(k_U(L - b))} \cos(k_{L_1}(L - x)) & b < x \leq L. \end{cases} \tag{A-87}$$

Making the substitutions into (A-85) and wading through the algebra produces the final result

(A-88)

$$\ddot{\eta}_1(t) + \omega_1^2 \eta_1(t) = -\frac{1}{E_1 k_{L_1}} \ddot{\eta}_1(t) \kappa \left(\frac{\bar{T}_U}{\bar{T}_L} - 1 \right) \cos(k_{L_1} b) \sin(k_{L_1} b) + \frac{1}{2} \frac{1}{E_1 k_{L_1}} (\ddot{\eta}_1(t) + \omega_1^2 \eta_1(t)) \ln \left(\frac{\bar{T}_U}{\bar{T}_L} \right) \left[\cos(k_{L_1} b) \sin(k_{L_1} b) + \left(\frac{\bar{T}_U}{\bar{T}_L} \right)^{1/2} \frac{\cos^2(k_{L_1} b)}{\tan \left(\left(\frac{\bar{T}_U}{\bar{T}_L} \right)^{-1/2} k_{L_1} (L-b) \right)} \right].$$

As earlier, defining a couple of quantities allows for easier rearrangement:

(A-89)

$$\beta_1 = \cos(k_{L_1} b) \sin(k_{L_1} b),$$

$$\beta_3 = \left(\frac{\bar{T}_U}{\bar{T}_L} \right)^{1/2} \frac{\cos^2(k_{L_1} b)}{\tan \left(\left(\frac{\bar{T}_U}{\bar{T}_L} \right)^{-1/2} k_{L_1} (L-b) \right)}.$$

Then (A-88) can be written as

$$(A-90) \quad \ddot{\eta}_1(t) + \omega_1^2 \frac{1 - \frac{1}{E_1 k_{L_1}} \frac{(\beta_1 + \beta_3)}{2} \ln \left(\frac{\bar{T}_U}{\bar{T}_L} \right)}{1 + \frac{1}{E_1 k_{L_1}} \left[\kappa \beta_1 \left(\frac{\bar{T}_U}{\bar{T}_L} - 1 \right) - \frac{(\beta_1 + \beta_3)}{2} \ln \left(\frac{\bar{T}_U}{\bar{T}_L} \right) \right]} \eta_1(t) = 0.$$

This time it is noticed that two terms in the above equation involve the sum $(\beta_1 + \beta_3)$.

Similar to before, this combination is the direct result of the term in equation (A-32) involving the spatial derivative of the average density. Reassembling the difference gives

$$(A-91) \quad (\beta_1 + \beta_3) = \cos(k_{L_1} b) \sin(k_{L_1} b) + \left(\frac{\bar{T}_U}{\bar{T}_L} \right)^{1/2} \frac{\cos^2(k_{L_1} b)}{\tan \left(\left(\frac{\bar{T}_U}{\bar{T}_L} \right)^{-1/2} k_{L_1} (L-b) \right)},$$

which can then be regrouped as

$$(A-91a) \quad (\beta_1 + \beta_3) = \frac{\cos^2(k_{L_1}b)}{\tan(k_{U_1}(L-b))} \left[\tan(k_{L_1}b) \tan(k_{U_1}(L-b)) + \left(\frac{\bar{T}_U}{\bar{T}_L} \right)^{1/2} \right].$$

Comparing the portion in brackets on the right with the result in (A-68) for the case with $\kappa = 0$ (i.e. no unsteady heat input), it becomes apparent that

$$(A-92) \quad (\beta_1 + \beta_3) = 2 \cos^2(k_{L_1}b) \tan(k_{L_1}b) = 2\beta_1.$$

Consequently, (A-90) becomes

$$(A-93) \quad \ddot{\eta}_1(t) + \omega_1^2 \frac{1 - \frac{1}{E_1 k_{L_1}} \beta_1 \ln\left(\frac{\bar{T}_U}{\bar{T}_L}\right)}{1 + \frac{\beta_1}{E_1 k_{L_1}} \left[\kappa \left(\frac{\bar{T}_U}{\bar{T}_L} - 1 \right) - \ln\left(\frac{\bar{T}_U}{\bar{T}_L}\right) \right]} \eta_1(t) = 0.$$

And then, by inspection,

$$(A-94) \quad \tilde{\omega}_1^2 = \frac{1 - \frac{1}{E_1 k_{L_1}} \beta_1 \ln\left(\frac{\bar{T}_U}{\bar{T}_L}\right)}{1 + \frac{\beta_1}{E_1 k_{L_1}} \left[\kappa \left(\frac{\bar{T}_U}{\bar{T}_L} - 1 \right) - \ln\left(\frac{\bar{T}_U}{\bar{T}_L}\right) \right]} \omega_1^2.$$

Figure A-7 shows this result plotted for various values of κ ranging from 0 to 1.0 and for $b/L = 0.5$. Also plotted are the exact solutions as well as the solutions presented by Dowling. As can be seen, the new solution fares far better in approximating the exact solution versus the one

previously presented. For $\frac{\bar{T}_U}{\bar{T}_L} = 8.0$, the difference between the exact and approximate solutions

is only 18.8% for $\kappa = 1.0$, where $\frac{\dot{Q}'}{\dot{Q}_0}$ takes its maximum value according to Merk's model. This

difference drops to 15.0% for $\kappa = 0.5$. As with the Rijke tube example, this approximation improves rapidly as κ becomes small with the difference diminishing to 5.6% for $\kappa = 0.1$.

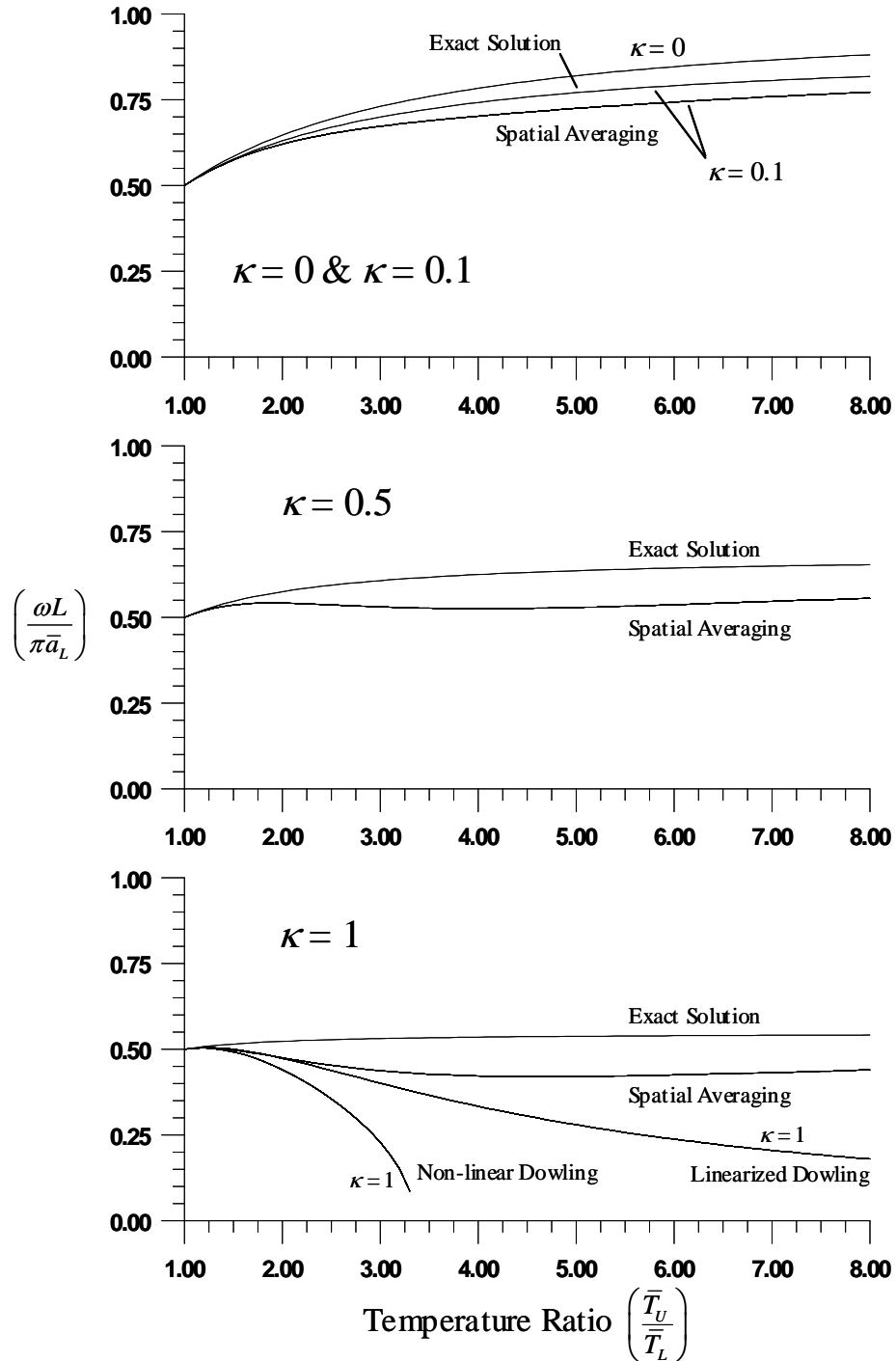


Figure A-7: Plots of the spatial averaging (equation A-94, dashed lines) and exact solutions (A-68, solid lines) of the closed-open system. The heated grid is located at $x = 0.5 L$, where L is the total length of the tube. The parameter κ is a dimensionless coupling constant that scales the magnitude of the unsteady heat input in relation to the velocity fluctuation just upstream of the heater. $\kappa = 0$ corresponds to the acoustic case where only the temperature jump exists and no unsteady heat input is present. As $\kappa \rightarrow 0$, the spatial averaging and exact solutions become coincident. Solutions by Dowling (1995) are shown for reference

A p p e n d i x B

A STAGNATION PLANE STABILIZED FLAT-FLAME BURNER

B.1 Overview

In choosing a burner to investigate, a principal goal was to select an element that produced a simple, premixed methane/air flame whose characteristics under steady operation are well understood. The device chosen was based on a stagnation stabilized, flat-flame burner used by Vagelopoulos and Egolfopoulos (1998) at USC to evaluate laminar flame speeds. This simple device employs a jet of premixed fuel and air impinging against a flat-face stagnation body. The jet is generated by an aerodynamic contraction and approaches the stagnation body normal to the surface. The flame stabilizes in the space between the nozzle and the stagnation plane at a location where the local flame speed at the centerline is equal to the axial jet velocity.

In the experiments run at USC, nozzle exit diameters of 14, 22, and 30 mm were used. Additionally, various distances between the nozzle exit plane and the stagnation plane were also tried. In most experiments, however, these distances corresponded to H/Ds of 1.0 to 1.5. For all the experiments presented herein, a nozzle with a 14 mm exit diameter was used. The stagnation plane was positioned at a distance of 21 mm from the nozzle exit plane, corresponding to an H/D of 1.5. Details of these components are presented below.

B.2 Nozzle Design

The principal goal in designing the burner nozzle was to create an aerodynamic contraction that would generate a nearly uniform velocity profile at its exit while having internal cavity dimensions such that L_c/D_c was of order one. Having a cavity with near unity aspect ratio helps idealize the Helmholtz resonance of the device. Localizing and characterizing this behavior is

important in later understanding its contribution to the measured combustion response functions of the burner.

The method outlined by Chmielewski (1974) was used in generation of the contour for the nozzle. This method specifies an average streamwise acceleration through the contraction. The chosen acceleration function is

$$(B-1) \quad f(z) = \left\{ \frac{1}{2} \left[1 - \cos 2\pi \left(\frac{z - z_i}{L} \right)^n \right] \right\}^p.$$

Here, the exponents n and p are selectable. For the experimental nozzle, $n = 4.0$, and $p = 0.8$. These were chosen to match the test cases examined by Chmielewski where separation data were available. A contraction ratio of 10 was chosen along with a nozzle L/D of 1.75. This combination results in the desired cavity L_c/D_c of roughly unity, while placing the contraction operational point just to the right of the separation curve as presented in Figure 5 of the Chmielewski paper.

Figure B-1 shows the fabrication drawing for the nozzle. It is machined from 6061-T6 aluminum round bar stock. The inside of the component was rough machined prior to CNC contour machining. The nozzle exit region was also unfinished during this operation, being left in an intermediate configuration to allow for fixturing. After completion of the contour, this end was finished to create the nozzle discharge knife-edge, as well as the register for the chamber bottom plates.

Included in the nozzle is a radial port located 6.35 mm from the bottom face. This port is 6.05 mm in diameter and allows for the placement of a 6 mm microphone cartridge element. The element used here (and elsewhere) is a Panasonic WM-60A electret type. The cartridge is bottomed in the hole and the port is back-filled with five-minute epoxy. Electrical terminations are made to a Molex KK-style, gold-plated, 2 pin connector. A 1.6 mm diameter hole between the port and the

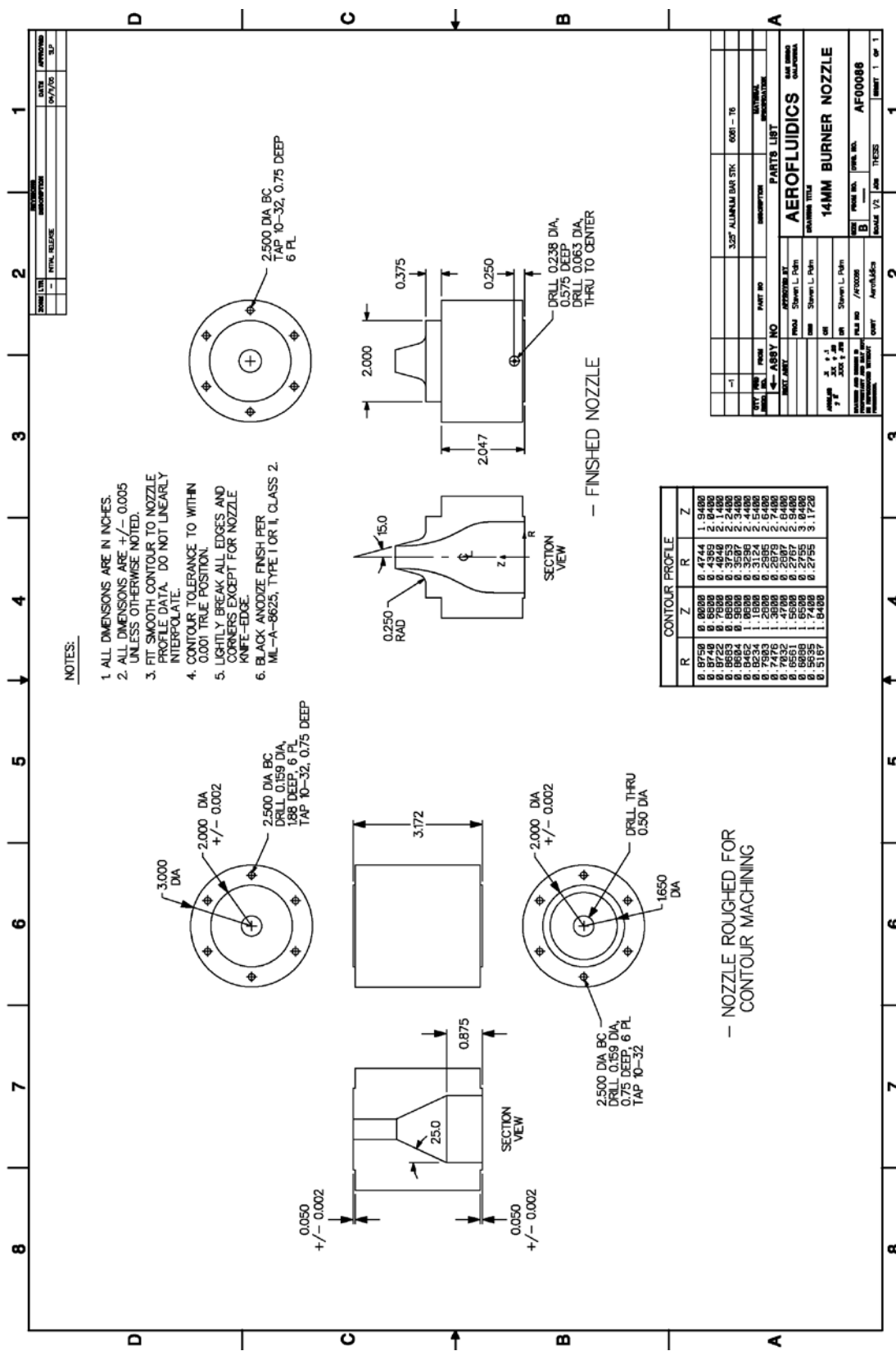


Figure B-1: Manufacturing drawing for 14 mm burner nozzle.

nozzle cavity provides the necessary acoustic coupling. This connection length is approximately 1.3 mm.

Figure B-2 shows the overall nozzle assembly. This assembly is formed from a stack of four major components. The top element in this stack is the aforementioned contraction. The next two components are spool sections used to position and seal two sintered metal discs. Finally, a base plate seals to the bottom of the assembly while providing a feed port for the fuel/air mixture. Additionally, this plate provides mounting points for the burner. Internal to the burner and on the top side of the bottom-plate is a small radial diffuser. This element is pressed into the plate and redirects the incoming flow in several radial directions, preventing it from jetting against the bottom sintered disc.

The sintered discs were custom fabricated for this burner by Capstan California of Los Angeles. Each disc is sintered bronze and is 50.8 mm in diameter and 3.1 mm thick. The average pore size is 30 um. These discs serve two purposes. First and foremost, they are used to equalize the axial velocity at all radial positions. For optimal aerodynamic performance of the contraction, the axial velocity at the inlet must be uniform and the scale of the turbulence must be much smaller than the inlet diameter. The sintered discs provide these conditions. The pressure drop across the discs encourages the flow to distribute itself evenly. The very small pore size and close spacing generate a nearly ideal porous-wall condition with turbulence scales on the order of the pore spacing (tens of microns). Two discs are used in series to produce coarse and fine corrections.

In addition to being flow conditioners, the second disc is used as a flow meter. A pressure port in the side of the middle ring is used to measure the differential pressure between the cavity below the upper disc and the outside environment. The very small pores in the sintered disc act similarly to the channels in a laminar flow element. This differential pressure is measured using a Datametrics barocel, model 572D-10T, and displayed on a Hewlett Packard model 3456A precision digital voltmeter.

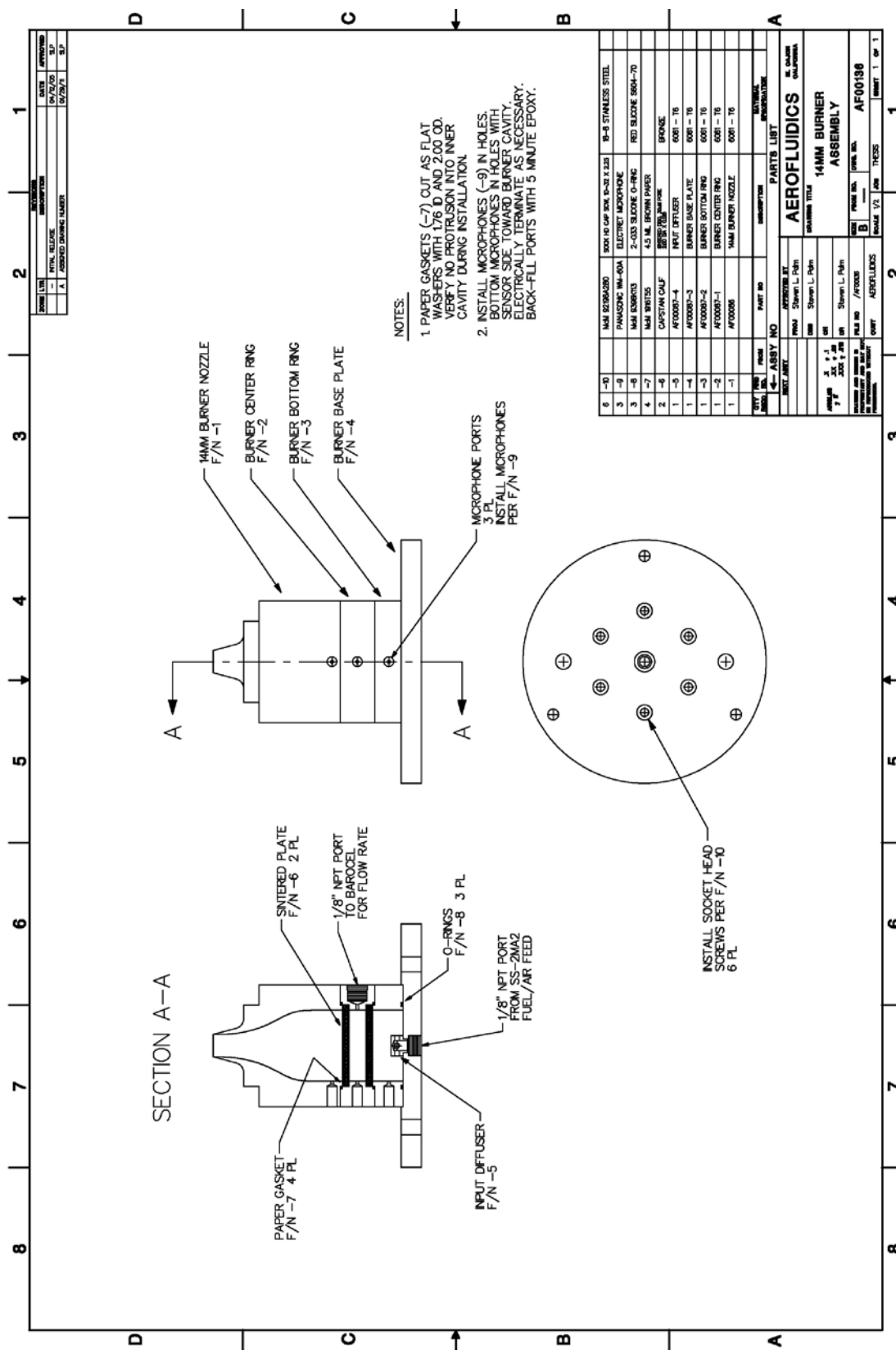


Figure B-2: Assembly of 14 mm nozzle components.

Calibration of the sintered plate flow meter was accomplished by temporarily inserting a precision rotameter and pressure gauge in line with the circuit feeding the burner. Calibration runs were made with two different rotameters. An Omega model PMR1-010181 was used to calibrate flows below 2300 standard milliliters per minute. For flow ranges above this value, an Omega model PMR1-010191 rotameter was used. All calibration runs were performed with dry air at 21.5 C and corrections were made for the back-pressure on the discharge side of the rotameters. The results were reduced and curve-fit producing a relation for actual volumetric flow of air at the discharge versus pressure transducer output signal. This relation was further modified to correct for gas composition when methane was added to the mixture. The correction compensated for both the change in average molecular weight as well as the mixture viscosity. The final result was an equation yielding the actual volumetric flow rate (and consequently mean nozzle exit velocity) given the differential pressure reading and the mixture equivalence ratio.

To verify that the contraction was producing an acceptable velocity distribution a miniature Pitot probe was constructed. The probe was fabricated from miniature stainless steel tubing with an outside diameter of 0.71 mm and a wall thickness of 0.10 mm. One end of the probe was connected to a brass support boss with a diameter of 6.3 mm which then fed a section of Tygon instrument tubing leading to a Datametrics precision barocel, model 536-15. The resulting voltage signal was displayed on an Extech CMM-15 precision multimeter. The brass support boss was fastened to a 6.3 mm diameter stainless support tube, which in turn was attached to a micrometer traverse stage. This stage provided a means for sweeping the probe across the top of the nozzle exit. The other end of the probe was bent downward at 90 degrees and slightly flattened along an axis perpendicular to the direction of motion. The residual opening was approximately 0.25 mm wide in the direction of movement. The two resulting flat sides were dressed with a jeweler's file to thin the profile even further. The completed end was then deburred and polished with crocus cloth. Figure B-3 shows a sketch of the configuration.

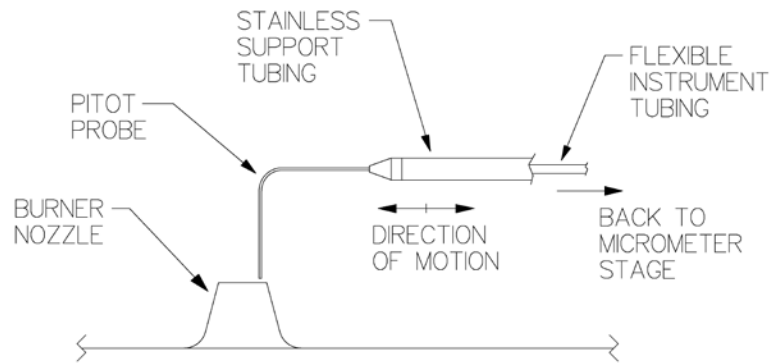


Figure B-3: Configuration of Pitot probe used to measure the jet velocity profile at the exit of the contraction.

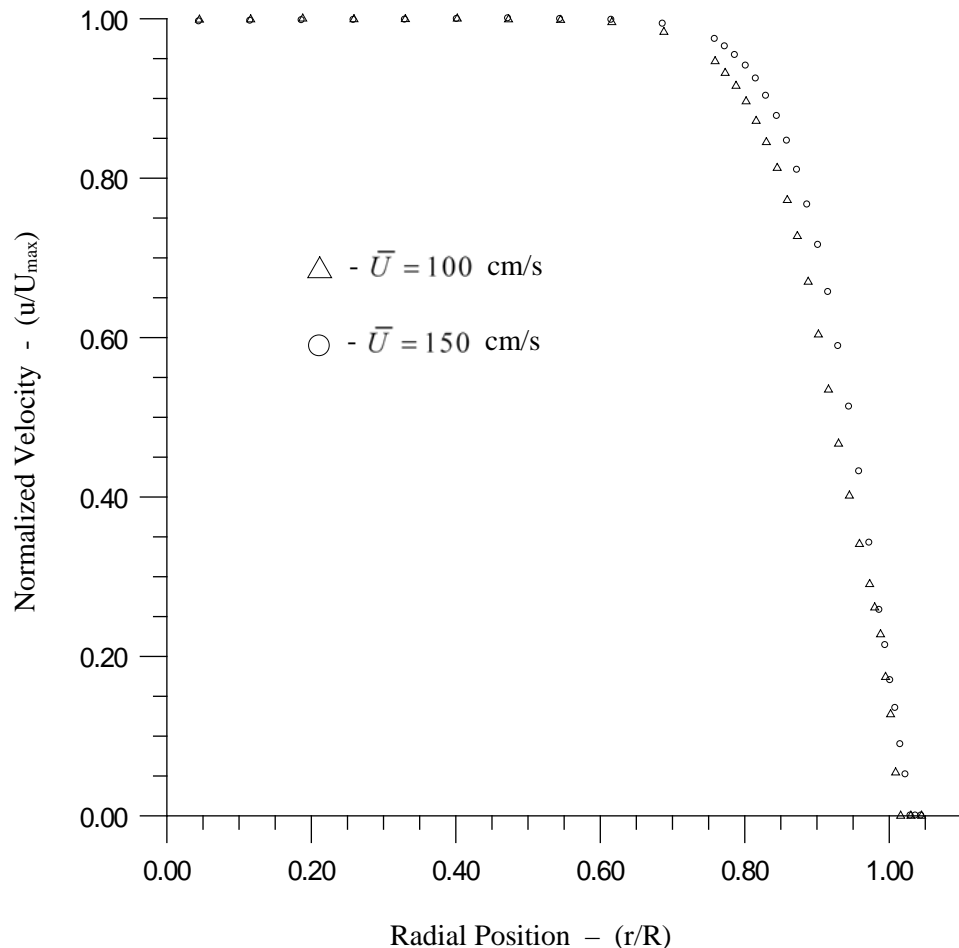


Figure B-4: Measured velocity profiles at exit of aerodynamic contraction with $D_{exit} = 14$ mm ($R = 7$ mm). Profiles shown for average exit velocities of 100 cm/s and 150 cm/s.

During velocity profile measurement, the Pitot probe was positioned vertically such that its end was in a plane approximately 1 mm above the nozzle exit plane. The probe was then swept, starting from outside to flow field, traveling inward toward the burner nozzle centerline. Several passes were made, both at mean exit velocities of 100 cm/sec and 150 cm/sec. Typical results are shown in Figure B-4.

B.3 Stagnation Body

A stagnation body was designed to create a flat face upon which the jet from the nozzle could impinge. The body was generally shaped as a cone with a sloped top and a flat bottom to act as the stagnation face. A sloped top was chosen so that during acoustic driving, it would present a more spatially distributed change in impedance. It was believed that this would reduce the likelihood of having abrupt changes in the acoustic characteristics of the chamber as a function of drive frequency.

The first stagnation body was fabricated from solid 6061-T6 aluminum bar stock. By design, it was cooled simply by radiation. It was approximately 14 cm tall and 7.6 cm at its maximum diameter near the base. The diameter of the planar section of the face (away from the edge fillet) was 5.7 cm. The body was solid throughout except for a 3.2 mm diameter port for a type K thermocouple that was buried in its center. A 3/8"-16 port was tapped in the top of the body for mounting and positioning.

Numerous experiments were run with this stagnation body; however, it was soon discovered that under certain operating conditions (at higher burner flow rates and equivalence ratios) the core temperature of the body was approaching 550 C. Radiation alone was not sufficient to cool the body effectively and a substantial amount of uncertainty existed in estimating the face temperature. Consequently, it was decided that a water-cooled stagnation body would be designed

and constructed. The goal here was to produce a device that would result in a much lower and more controlled face temperature. The resulting design is shown in Figure B-5.

The major components of the new stagnation body are machined from 304 stainless steel (AMS 5639). It is split into two parts, the top section being the body (F/N -1) and the bottom section being the face (F/N -2). A drilled manifold in the body routes cooling water down its center, creating stagnation-point flow against the backside of the face element. Here, the flow spreads out radially, past the diffuser ring (F/N -3) and up through a narrow radial slot generated by the outer edge of the diffuser ring and the inner wall of the face element. The pressure drop through this slot balances the flow to assure an even distribution at all positions at a given radius. The flow is then collected behind the diffuser ring and returned to another drilled passage to leave the body through the exit port.

Attached to the center of the inner surface of the face section is an RdF patch-style heat flux gauge. It is RdF part number 27036-1 and has a sensitivity of 0.164 $\mu\text{V}/\text{BTU}\cdot\text{ft}^2\cdot\text{hr}$. It is bonded to the surface using OmegaBond-200 thermally conductive epoxy. The thickness of the epoxy layer is very thin (< 0.03 mm) and does not contribute significantly to the resistance in the thermal circuit. The heat flux gauge employs type-T thermocouple junctions and reports both the local temperature and the heat flux per unit area. By knowing these as well as the material properties and thickness of the face component, it is possible to compute the stagnation plane surface temperature. The measured thickness of the metal between the flux gauge and the external stagnation surface at ambient conditions is 7.70 mm. In addition, the cooling water flow rate, inlet temperature and exit temperature are also measured. This allows the computation of the average total heat load into the stagnation body.

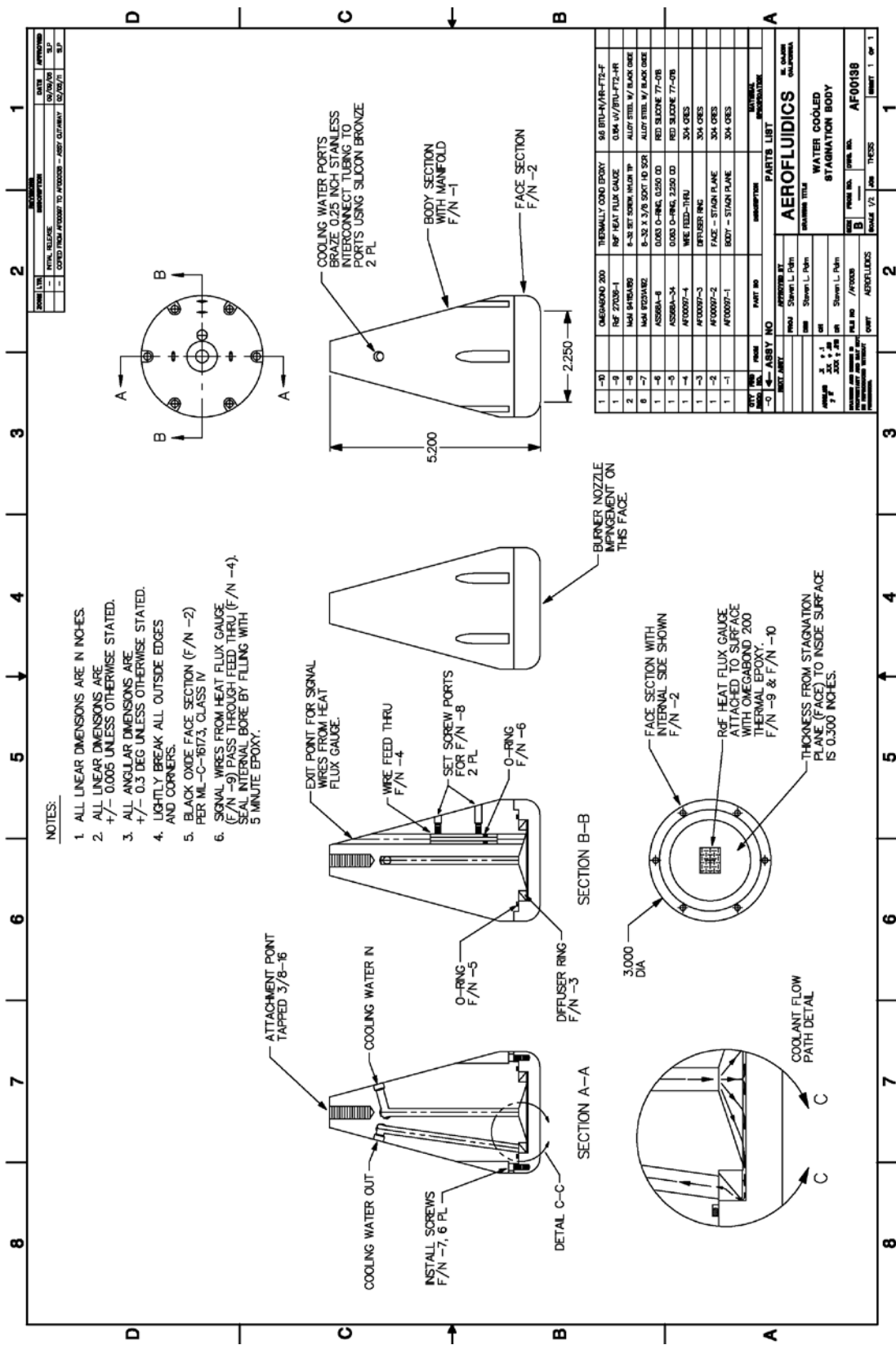


Figure B-5: Upgraded stagnation body with water cooling and fabricated from stainless steel.

B.4 Burner Assembly

The aforementioned nozzle and stagnation body, as well as numerous other support components, are combined into the complete burner assembly. Figure B-6 shows a sketch of the upper portion of this unit while Figure B-7 shows photographs of the completed system.

The stagnation body is supported above the burner nozzle by four cylindrical posts and an x-frame. A section of 3/8"-16 threaded rod allows for adjustment of the gap between the nozzle exit plane and face of the stagnation body. For all the experiments, this gap was set to 21 mm, corresponding to an H/D of 1.5. This height was set to within 0.05 mm using a specially machined gauge pin. The height was reset or verified after any changes to the burner assembly or test section. The stagnation body support structure is, in turn, fastened to an octagonal aluminum plate that forms the bottom of the test section. This plate is 12.7 mm thick and is fabricated in two pieces

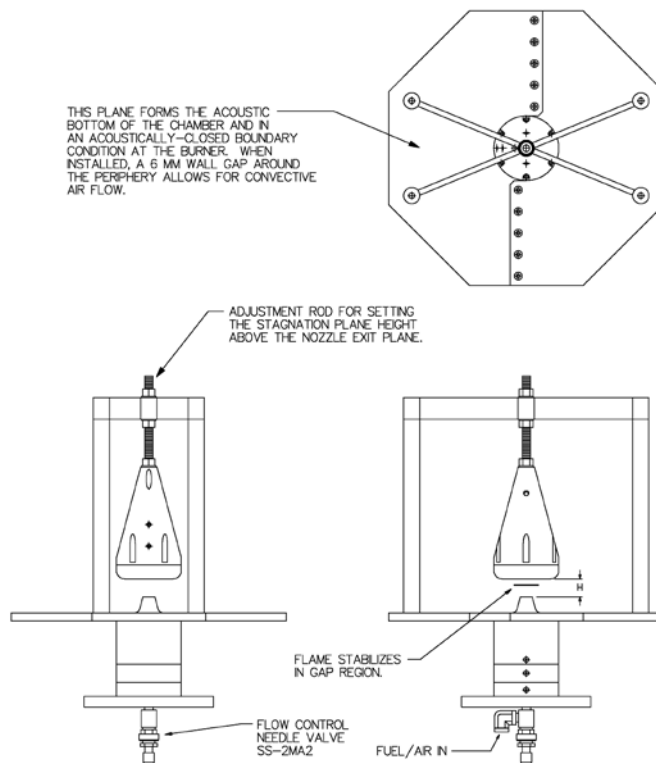


Figure B-6: Simplified burner assembly. Stagnation body height, H, is shown as 21 mm. This corresponds to an $H/D = 1.5$, which is the value used for all experiments.

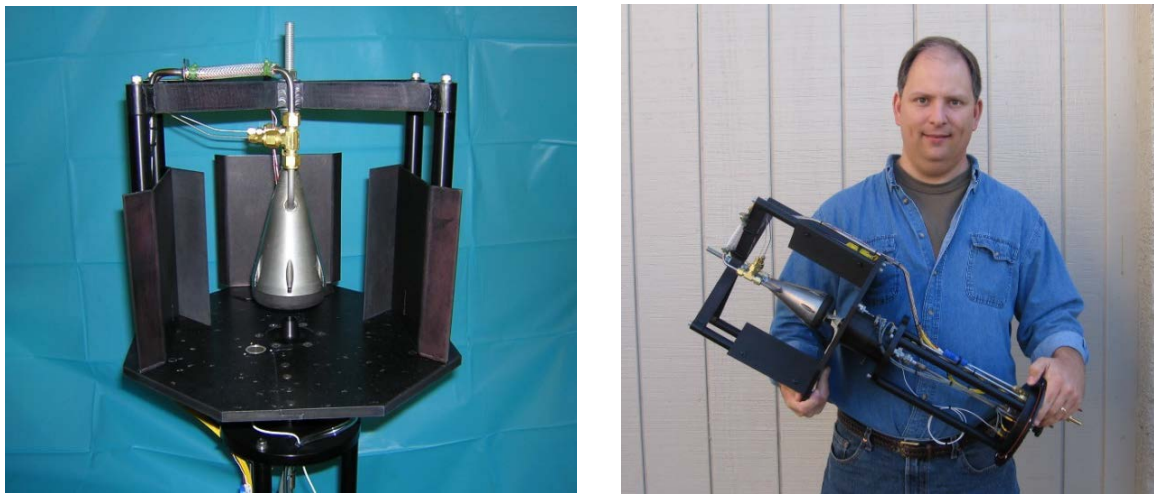


Figure B-7: Left - upper end of completed burner assembly with plumbing, electrical and optical shields in place. Right – entire burner assembly as installed in the test chamber; shown for size reference.

that bolt together using ten 8-32 flat-head screws. This split-part fabrication allows the plate to be passed through one of the test section access ports and assembled in situ. A hole in the center of the plate attaches to a register on the top of the nozzle assembly using six 10-32 flat-head screws. When installed, a wall gap is formed around the outer edge of the plate. This gap between the edge of the octagonal plate and the walls of the test section is approximately 6 mm wide and allows for ambient air to be naturally convected into the lower part of the test section.

Also attached to the test section base plate are various optical guards fabricated from aluminum or stainless steel sheet metal. The guards have ports or slits strategically located to allow the passage of the laser sheet or to provide camera optical access. However, they improve the signal-to-noise ratio in PLIF experiments dramatically by blocking scattered light that can be inadvertently received by the camera optics. All the guards are conversion coated with black anodize or black oxide.

As can be seen in Figure B-7, the cooling lines and electrical leads for the stagnation body are routed across the top of the x-brace and down the backside of one of the optical guards. They

are then passed through a slot in the edge of the base plate where they enter the cavity below the test section. Care was taken to minimize the apparent frontal area of the lines in the test section in order to minimize the resulting acoustic impedance mismatch. Ultimately, all connections to the burner assembly pass through connectors in a bulkhead disk that mounts in the bottom of the forcing chamber. This disk can be seen on the right side of the right photograph in Figure B-7.

B.5 Fuel/Air Feed System

A fuel/air feed system was needed to supply the experimental burner during operation. One of the critical design objectives was to create a feed system that would produce steady operation, both in equivalence ratio and in total burner flow rate, while also allowing for fine control of the burner flow rate. Figure B-8 shows a plumbing and instrumentation diagram of the resulting design.

In the implemented scheme, ultra-high purity (UHP) methane is fed from a high-pressure cylinder, through a pressure regulator (PR301) and into a Brooks FC8900 mechanical flow controller (FE201). This flow controller is purely a pneuma-mechanical device that attempts to hold the flow rate of methane constant for small fluctuations in downstream pressure. The target flow rate is adjustable through a knob on the side of the unit. From here the fuel gas flows through a Fathom GR112-1-A-PO thermal mass flow meter (FE202) and then into the primary mixing element (ME201).

Air for the combustible mixture is acquired from a facility air compressor. As such, this air is contaminated with moisture, oil and particulates. Before use, it is first brought through two stages of conventional filter/separators (FL101 & FL102). These remove the condensed moisture and oil droplets, as well as the bulk of the particulate matter. The air is then passed through a pressure regulator (RV101) and into a SpeedAir 5VC90 desiccant air drier (DR201). This device

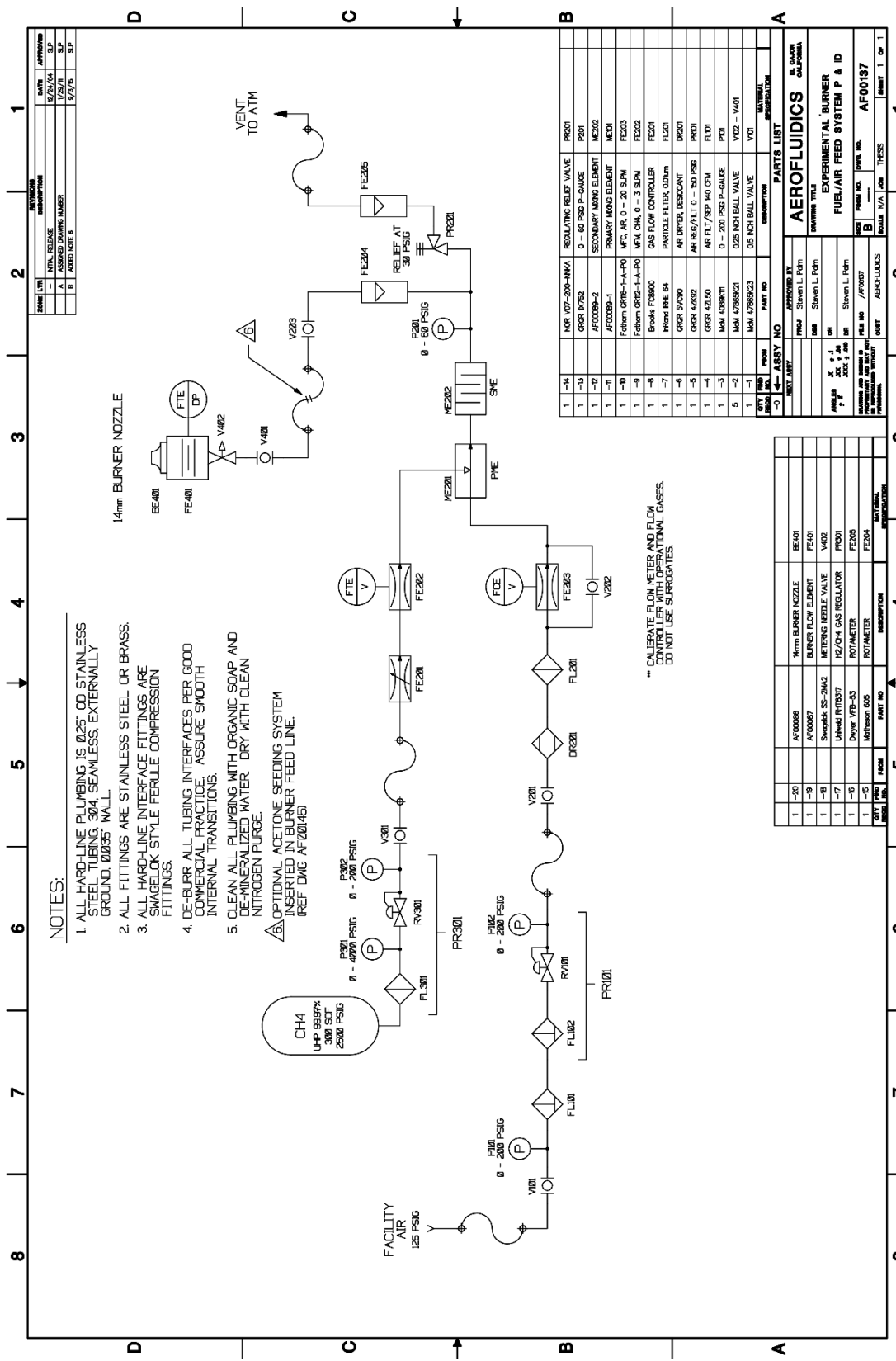


Figure B-8: Plumbing and instrumentation diagram for the experimental burner fuel/air feed system.

removes the bulk of the remaining moisture, reducing the air's dew point to less than -20 C . Finally, the air is directed through an Ingersol-Rand IRHE-84 0.01 micron polishing filter (FL201). This stage removes any remaining particulates or contamination from the silica drier that might be of concern. Remaining particles in the air stream are an order of magnitude smaller than the laser wavelengths involved in the experimental diagnostics. At this point, the air is passed through a Fathom GR116-1-A-PO thermal mass flow controller (FE203) and into the primary mixing unit (ME201).

The primary mixing element consists of an aluminum body with an internal spool. This spool contains a 3.2 mm diameter central port through which the combustion air is passed. In the side walls of this spool are two injection orifices, each 0.58 mm in diameter, through which the combustion methane is injected. The methane is injected into the freestream of air as jets in cross-flow. The typical jet Mach numbers are low ($M < 0.1$) and the jet velocities range from 12 m/s to 20 m/s. Their corresponding jet Reynolds numbers range from 1300 to 2200. The free stream air Mach number is also low ($M < 0.1$) with a velocity that is approximately 13 m/s. The corresponding Reynolds number based on the port diameter is 7000.

The fuel/air combination is then passed into the secondary premixer (ME202). This is a simple device that consists of a stack of approximately twenty machined Delrin discs pressed into a section of 12.7 mm diameter stainless steel tubing that is approximately 76 mm long. Each disc is machined as a small square-bottom cup with an off-center hole approximately 2.5 mm in diameter penetrating the bottom. The discs are pressed into the stainless tube with these penetrations alternating back and forth along a single axis. The ends of the tube are then coupled to a pair of reducer fittings to allow for interfacing to the 6.3 mm diameter tubing used throughout the system. As the gas passes through the device, it is forced to alternate directions, passing down through an orifice, turning and moving parallel to a disc bottom, and then dropping through the next hole. The

turns required to pass through the orifices in the discs, and the accompanying jets generated, result in induced secondary flows. It is these secondary flows that are exploited to enhance mixing.

After leaving the secondary mixing element, the flow is fed into a distribution manifold. The pressure is held constant in this manifold by a Norgren V07-200-NNKA adjustable, ported relief valve (PR201) that is set for 206.7 kPaG. Flow that is bypassed by this relief is routed through a rotameter (FE205) and then discharged to an atmospheric vent external to the laboratory. The rotameter in this bypass is used only as a visual indicator of flow and no quantitative data is recorded from it.

A second line from this manifold passes through a second rotameter (FE204), then through a ball valve (V203), and finally onto either the acetone seeding system, or directly to the burner assembly. Once again, the rotameter here is only used for qualitative measurement of the flow. The precision rotameters used for calibration of the sintered-plate flow meter were temporarily installed in the flexible line just ahead of ball valve V401.

With the given configuration of the feed system, it is possible to operate the thermal mass flow meters and controllers higher in their flow ranges resulting in better accuracy. The equivalence ratio of the mixture can be set and held constant with relative ease while the total flow rate to the burner is varied. Any unused fuel/air mixture is dumped overboard through the external vent. Furthermore, the flow control needle valve (V402) is always fed with a constant pressure from the feed manifold, allowing it to operate in a fixed position for a given flow rate. In practice this setup was found to work very well. Typical variations in equivalence ratio throughout a four-hour burner run were estimated to be less than $\pm 1.5\%$ while the variation in the total burner flow rate was estimated to be less than $\pm 0.05\%$.

It should be noted that the methane thermal mass flow meter (FE202) was specially calibrated at the factory for use with methane. Under normal circumstances, thermal mass flow

meters and controllers are calibrated with surrogate gases when the operational gas requires special handling. For methane flow meters, nitrogen gas is typically used as a surrogate. However, the use of surrogate calibration gases can result in significantly increased error margins. In this case, special arrangements were made with the manufacturer and UHP methane was used in its factory calibration, eliminating this concern.

Operation of the methane flow meter (FE202) and air mass flow controller (FE203) was accomplished through a custom electronics package. This system provided a simple interface allowing individual parameter control as well as specific control of the equivalence ratio through a partially closed-loop (feed-forward/feedback) control system. In equivalence-ratio-control mode, it is possible to set a desired equivalence ratio while also setting the total methane flow such that the flow elements are utilized near their maximum range. This results in maximum measurement accuracy and minimizes the error between the desired and actual equivalence ratios. In control mode, the methane flow rate is measured by FE202. Based on this signal and the desired equivalence ratio, a corresponding air flow rate is computed (feed-forward). This demand signal



Figure B-9: Left – mixing panel used to generate fuel/air mixture for experimental burner. Right – mixing system control electronics.

is then fed to the air mass flow controller (FE203), which attempts to flow the desired amount of air to the mixer (feedback). Pictures of this controller, as well as the mixing panel, are shown in Figure B-9.

B.6 Burner Operational Range and Characteristics

After completion of all the burner components and ancillary equipment, the burner assembly was installed in the test section of the experimental apparatus and detailed experiments were performed to evaluate its operational range. Fixed values of equivalence ratio were taken while the jet exit velocity was swept. Equivalence ratios ranged from 0.6 to 1.0 in steps of 0.25.

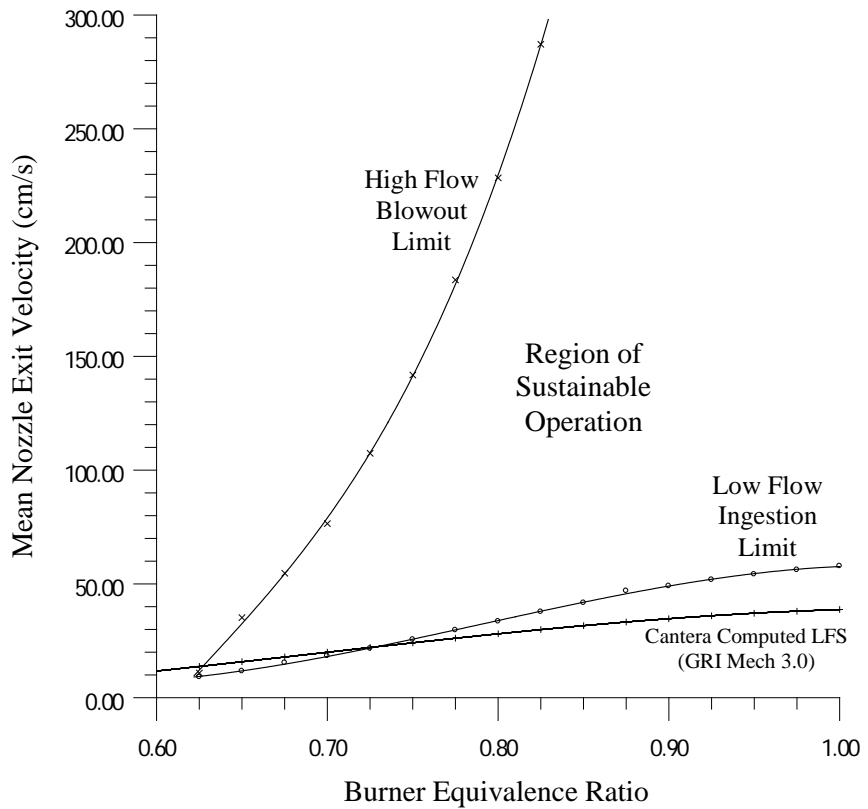


Figure B-10: Operational envelope of the stagnation plane flat-flame burner with 14 mm diameter nozzle. Fuel is methane (99.97%) and oxidizer is dry air. The mixture laminar flame speed (computed using Cantera and GRI Mech 3.0) is shown for reference.

Jet exit velocities ranged from approximately 10 cm/s to 280 cm/s. For all runs, the temperature of the fuel/air mixture as well as the ambient air was 21.5 ± 0.8 C. Figure B-10 shows a map of the experimentally determined limits.

Both high-flow and low-flow limits are shown. Above and to the left of the high-flow limit, the local strain rate is too high support combustion at the given equivalence ratio. This results in the flame spontaneously extinguishing. Below the low-flow limit, the jet exit velocity is less than the local flame speed and the flame propagates back inside the burner nozzle. The region between is labeled as the “region of sustainable operation.” This is operating space in which the burner will run indefinitely.

Within this operating region, there are three principal operating modes. These modes can be classified as Flat, Attached, and TopHat as shown in Figure B-11. At higher flow rates (following, but below the high blow-out limit) a flat flame is established. This is shown in the left side of Figure B-11. This is the condition under which all the thermoacoustic response experiments were run. At lower flow rates there is a tendency for the flame to attach itself to the lip of the nozzle and operate as a Bunsen style flame. This is shown in the middle image. Finally, under some operating conditions at low flow rate, the flame transitions to a form that looks similar to a

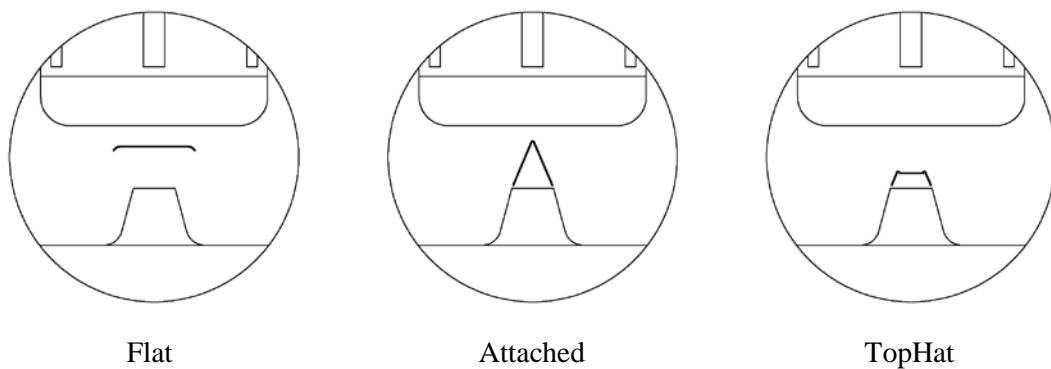


Figure B-11: The principal operating modes of the burner within the region of sustainable operation. Transitions between operating modes are typically sharp and accompanied by hysteretic behavior.

top hat. This is shown in the right side of figure B-11. It is essentially a Bunsen style flame that has a truncated and slightly inverted top.

At equivalence ratios of 0.80 or higher, the transitions between these forms are abrupt and exhibit hysteresis. Figure B-12 shows these transition boundaries on an operating regime diagram similar to that presented in Figure B-10. In the range of equivalence ratios from 0.75 to 0.80, the transitions become ambiguous or difficult to distinguish. Finally, below this range in equivalence ratios, no transitions occur at all. As the flow rate is reduced, the flat flame smoothly descends until it appears to be level with the nozzle lip.

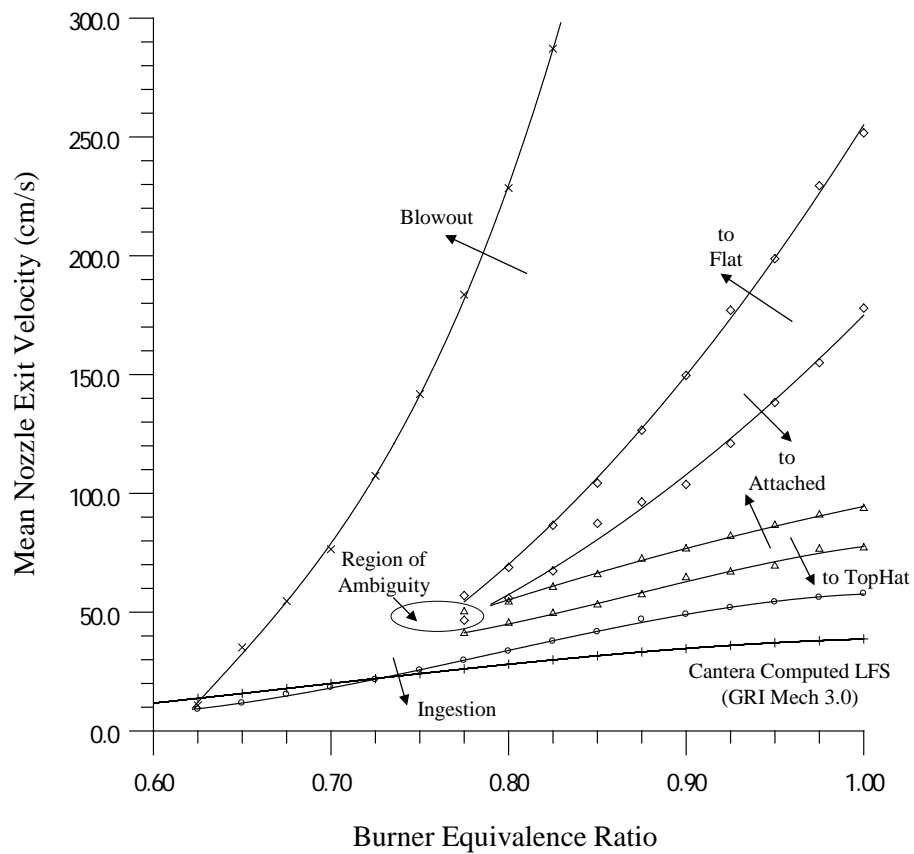


Figure B-12: Burner operational envelope shown with transition boundaries. Transitions between operating modes exhibit hysteresis. Two lines are shown for each mode (branch) pair – one for each transition direction.

A p p e n d i x C

ACETONE SEEDING SYSTEM

C.1 Overview

Early in the execution of the acoustically forced imaging experiments, it was realized that improved knowledge of the unsteady behavior of the incident reactant flow field was desirable. After initial data reduction of images from the OH PLIF experiments, it was observed that portions of the flame sheet exhibited large, unsteady motions and partial roll-up under certain ranges of drive frequencies. To better visualize how the premixed reactants flow into these regions, acetone PLIF experiments were added to the test matrix. By accurately seeding a small amount of acetone into the fuel/air mixture and inducing fluorescence of the acetone molecules through laser stimulation, it is not only possible to spatially resolve the location of the incoming combustible mixture but also deduce the scalar field to some degree. This additional concentration information provides insight into the transport of the combustibles into the reaction zone as well as to the entrainment rate of air at the jet boundary.

C.2 Seeder Design

A supplementary acetone seeding system needed to be designed and constructed, and integrated into the existing fuel/air feed system. After careful evaluation of the existing feed system (as presented in appendix B, Figure B-8) it was decided that the most desirable insertion location for the seeder would be in the flexible line connecting the fuel mixing panel to the burner assembly. This is represented by the flex-line shown between ball valves V203 and V401 in Figure B-8. The operating pressure in this section is nominally 206.7 kPaG; as such, it was necessary to engineer the seeding system to accurately and safely meter the acetone flow against this opposing pressure.

A principal requirement of the seeding system was to have it capable of precisely metering the acetone flow rate in order to achieve a constant and tightly controlled molar concentration ratio. In many experiments by others, the tracer was seeded into the fuel simply by bubbling the gas mixture through a reservoir of liquid acetone. The result is a reactant mixture that is essentially saturated with acetone vapor at the given pressure and temperature conditions. This produces a marked shift in the gas composition and its associated parameters such as average molecular weight and viscosity. Furthermore, for experiments where combustion is present (i.e. non cold-flow) the change in fuel composition and the resulting reaction kinetics can be substantial.

Acetone exhibits very strong fluorescence when excited between 225 nm and 320 nm. In practice, a very small molar fraction of acetone is needed to visualize the reactant flow through laser-induced fluorescence. It was decided that the seeding system would be designed to regulate the acetone flow rate such that mole fractions down to 0.2% were achievable across the majority of the burner operating range. During seeding, the flow of methane would be slightly reduced in order match the heating value per unit mass of the gas mixture with the unseeded reference case. Furthermore, the burner nozzle exit velocity would be held constant between the two cases. The goal of this was simply to minimize the impact of the acetone seeding on the flame behavior.

The resulting design is shown in Figure C-1. The seeding panel is attached to the side of the experiment table, in close proximity to the test section and burner. A plumbing and instrumentation diagram for the system is shown in Figure C-2.

The premixed combustible reactants are supplied to the seeder from the fuel/air feed system. The mixture enters the panel's input manifold where it is branched to ball valves V502 and V503. During normal (unseeded) operation, valve V503 is opened while valves V502 and V504 are closed. In this configuration, the fuel/air mixture bypasses the seeding system and flows directly from the input manifold to the output manifold. A pressure gauge (P501) indicates the



Figure C-1: Left – acetone seeding panel installed on the side of the experiment table. A glass Pyrex bottle serves as the acetone reservoir. The clear, braided PVC hose in the lower right brings the incoming fuel/air mixture to the panel. The black polypropylene hose in the lower left carries the seeded mixture to the burner. Right – view of the back side of the panel showing the body of the precision syringe pump.

pressure in the output manifold for reference and supply availability verification. The flow at the output manifold exits through polypropylene tubing (6.35 mm ID) and is directed to the burner assembly.

If acetone seeding is required, valve V503 is closed and valves V502 and V504 are opened. This allows the fuel/air mixture to pass through mixing element ME501 and then filter FL501 prior to proceeding to the burner. The mixing element incorporates a section of 21 gauge stainless steel hypodermic tubing which is partially embedded in a cylindrical section of wool felt. Liquid acetone is introduced into the felt medium through the hypodermic tubing at a precisely controlled rate.

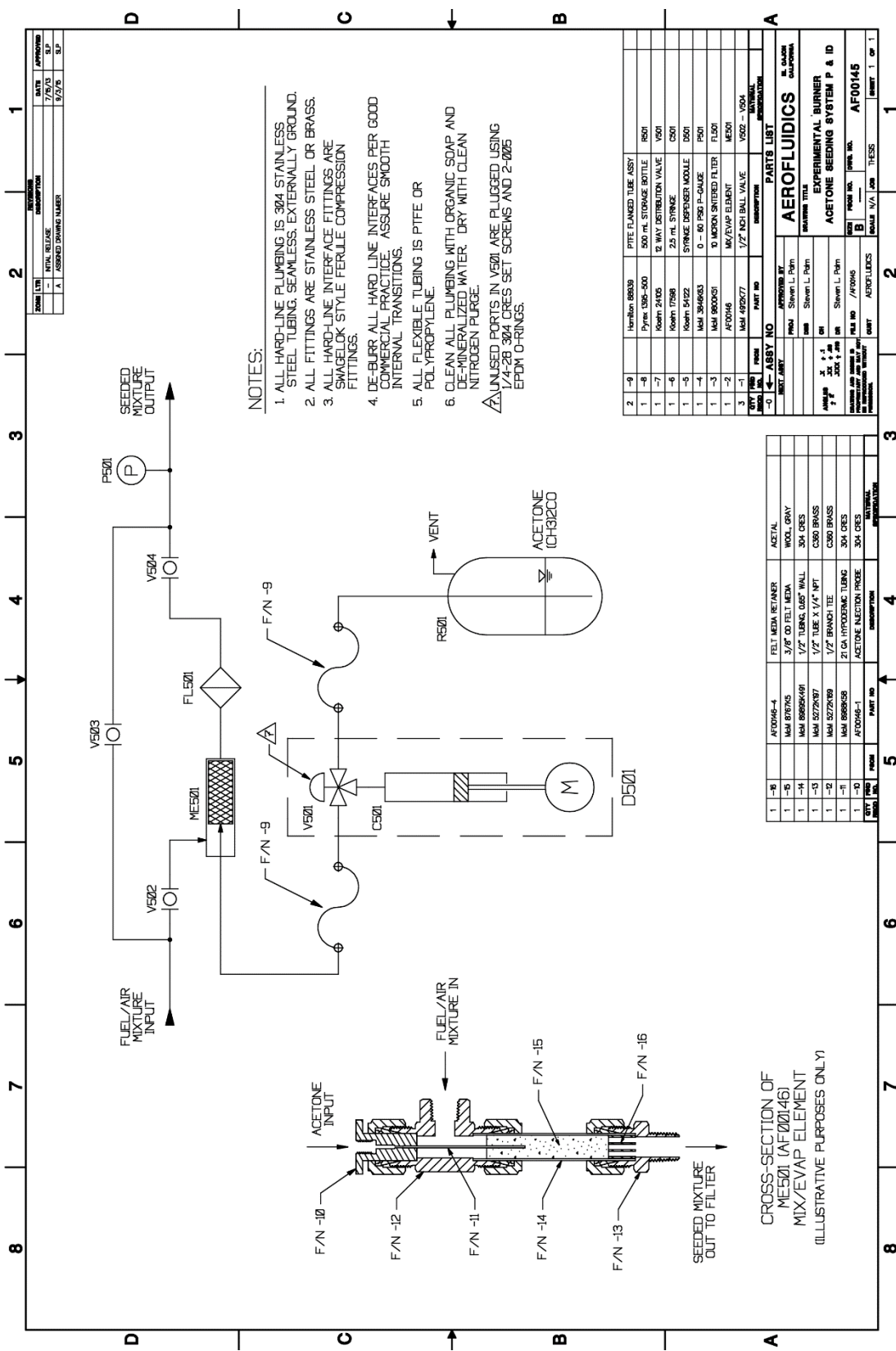


Figure C-2: Plumbing and instrumentation diagram for the acetone seeding system.

The reactant gas mixture is passed through the felt medium in order to evaporate this acetone. The wicking action within the felt distributes the acetone, and equilibrium between the supply rate and evaporation rate is quickly reached. An illustration of the mixer/evaporator can be seen on the left side of Figure C-2.

A Norgren Kloehn precision syringe dispenser module (D501 - P/N 54122) is used to control the injection of acetone into the fuel/air flow. This unit is remotely programmable and operable through an RS-232 communications port. This port is interfaced to the Master Control Computer in the experimental setup, allowing the computer to direct the acetone seeding process. A 2.5 mL syringe (C501 - Kloehn P/N 17598) and a 12 port distribution valve (V501 - Kloehn P/N 24105) are integrated with the dispenser module. It should be noted that only two of the distribution ports on V501 are used. The remainder are plugged.

C.3 Seeder Operation

During typical operation, the acetone system is bled prior to dispensing to the mixer. The control computer commands valve V501 to select the acetone reservoir. The plunger is then stroked two times from the fully dispensed position to the fully withdrawn position and then back to the fully dispensed position again. This expels any air within the syringe, valve, and plumbing to the reservoir. Following this, the plunger is fully withdrawn, filling the syringe with acetone. When seeding is to begin, valve V501 is automatically rotated to the output position and the plunger is commanded to expel acetone at a constant and precise rate. This rate is controlled by the integrated electronics within the dispenser and no attendance is required by the control computer. A transport delay is encountered for the first dispense operation after a long idle period. This is the time it takes to fill the PTFE capillary tubing between valve V501 and the mixing element. Typical delays are up to 30 seconds. Once the system is primed and dispense operations are being performed sequentially, delays become negligible.

While performing acetone PLIF experiments, control of the seeding system is orchestrated by the control software running on the master control computer (OPO.exe, version 1.25). Commands are included in the OPO scripting language that allow the user to specify the seeding rate as well as to sequence bleed, reload and dispense operations. In particular, the seeding rate is established by providing values for two system parameters; these are the reactant gas flow rate in liters per minute, and the volume fraction of acetone desired in mole percent. The required equivalence ratio decrement to match the heating value per unit mass, and the adjusted flow reading to establish a matched burner nozzle exit velocity are computed by a separate program.

During a typical experiment, the system is bled and loaded prior to data collection. Once dispensing has begun and sufficient time has passed to account for the possible transport delay, image capture commences. Once a block of data has been captured (typically 200 images along with the corresponding supplementary data), it is automatically retrieved and stored. During this retrieval and storage period, the seeding system is automatically re-bled, reloaded and restored to the dispense mode. By the time the data storage is complete, acetone seeding has been fully reestablished and the next set of images can be captured. This continues until all image captures are complete. After the final block of images have been collected, valve V501 is selected to the reservoir position and all remaining acetone in the dispenser is ejected back into the reservoir.

A p p e n d i x D

**ACOUSTIC FORCING CHAMBER
MAGNITUDE AND PHASE CALIBRATION**

D.1 Description and Necessity

By the very nature of the work at hand, knowing the magnitude and phase of the pressure fluctuations at the location of the flame is essential to nearly all the experiments performed in the acoustic forcing chamber. Having this data makes it possible to evaluate the numerous response characteristics including the local and global combustion response functions.

During experiments, two PCB 106B50 pressure transducers were used to measure the pressure in the test section. These transducers have an in-phase magnitude response of 72.5 mV/kPa from 0.5 Hz to nearly 40 kHz. One transducer was located in the wall of the test section at approximately the same elevation as the flame. The second transducer was located in the floor of the chamber, approximately 4 cm below the plane of the flame and at a radial distance of 5 cm from the centerline.

The need for calibration arises from the fact that at higher driving frequencies, the magnitude and phase of the pressure field at the flame location is not represented by the field felt at the two pressure transducers. Indeed, at frequencies above approximately 100 Hz, the chamber no longer contains a bulk mode and instead the first pressure node appears in the drive section. As the drive frequency increases, more nodes in the longitudinal direction arise. In addition, radial and tangential modes also begin to be excited.

Several problems arose from this behavior at higher frequencies. One such problem was that it was not possible to drive the chamber well at frequencies that corresponded to having a pressure node directly in line with the drive speakers. Constructing a variable length chamber was

considered; however, the complexity of doing this far outweighed the benefits and it was ultimately decided to map the frequencies at which weak drive coupling occurred and simply avoid them during the experiments.

Another problem was that the excited tangential modes were not spatially stable. Instead, these modes appeared to rotate arbitrarily leading to a relation between the pressure transducer readings and the pressure at the flame that was not one to one. Installing a set of radial baffles in the tubular section between the driver ducts and the top of the test section solved this difficulty. The baffle system is a welded assembly consisting of six equally spaced radial blades constructed from 3.2 mm thick 5052 aluminum sheet. The blade assembly is 66 cm long and 30.0 cm in diameter. This diameter is roughly 2 mm smaller than the inside diameter of the chamber tubular sections. The baffle group is rigidly supported from the top of the chamber and is spatially fixed in the region between the top of the test section and the bottom of the horizontal driver tubes.

D.2 Calibration Method

With the uniqueness issue resolved, the remaining difficulty was to arrive at the one-to-one relation (i.e. calibration) between the pressure at the transducers and at the flame location. This was accomplished by performing “cold” calibration runs using a specially designed probe microphone. A small 6 mm microphone (Panasonic WM-60AY) was mounted on the end of a 6.35 mm diameter section of stainless steel tubing. The electrical leads from the microphone were passed through the center of the tube to a BNC connector on the opposing end. The tube was inserted through a special boss in the side of the test section and positioned so the face of the microphone was at a centerline location roughly halfway between the burner nozzle and the burner stagnation plane. Photos of this probe assembly can be seen in Figure D-1.

Once installed, the signal output from the probe microphone as well as the signals from the two pressure transducers were fed to the AFC-100. The calibration routine on the central control

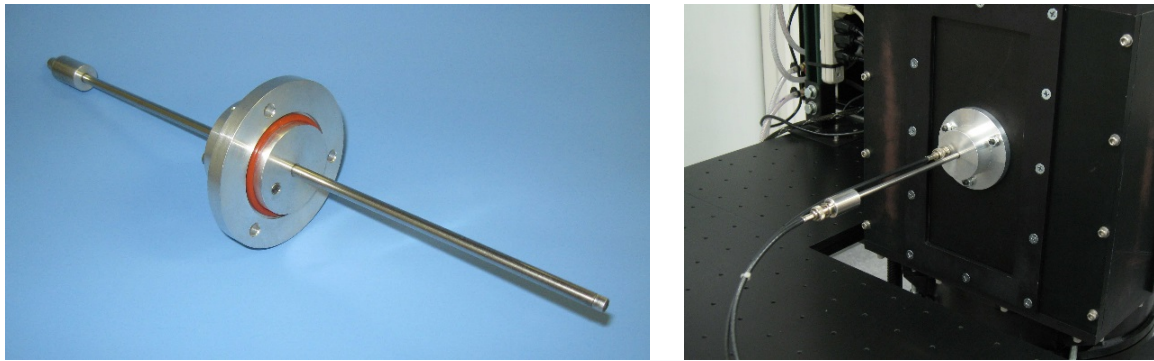


Figure D-1: Left – probe microphone assembly used for acoustic calibration of the test chamber. Right – assembly installed in the chamber test section.

and data acquisition computer (DAQ) was then started. The routine instructed the AFC-100 to sweep the acoustic drive frequency from 20 Hz to 2000 Hz in one Hertz steps. The driving amplitude was adjusted to achieve good signal-to-noise ratio while also ensuring that the microphone was in its linear response regime. The signals from the pressure transducers and microphone were then captured and fast Fourier transformed by the AFC-100, generating a magnitude multiplier and phase offset for each drive frequency. This data was relayed back to the DAQ for storage in the preliminary calibration table.

After collection, the preliminary data was post processed to tag frequencies where the chamber exhibited poor behavior. These consisted of regions where the drive coupling was weak or where there was a large disparity in signal magnitude between the probe microphone and one of the pressure transducers. Frequency ranges where the phase difference between the microphone and the transducer of interest was varying rapidly (in relation to frequency) were also tagged. This “poor behavior” flag was included in the final calibration file and was subsequently used in the experimental runs to automatically avoid these drive frequencies.

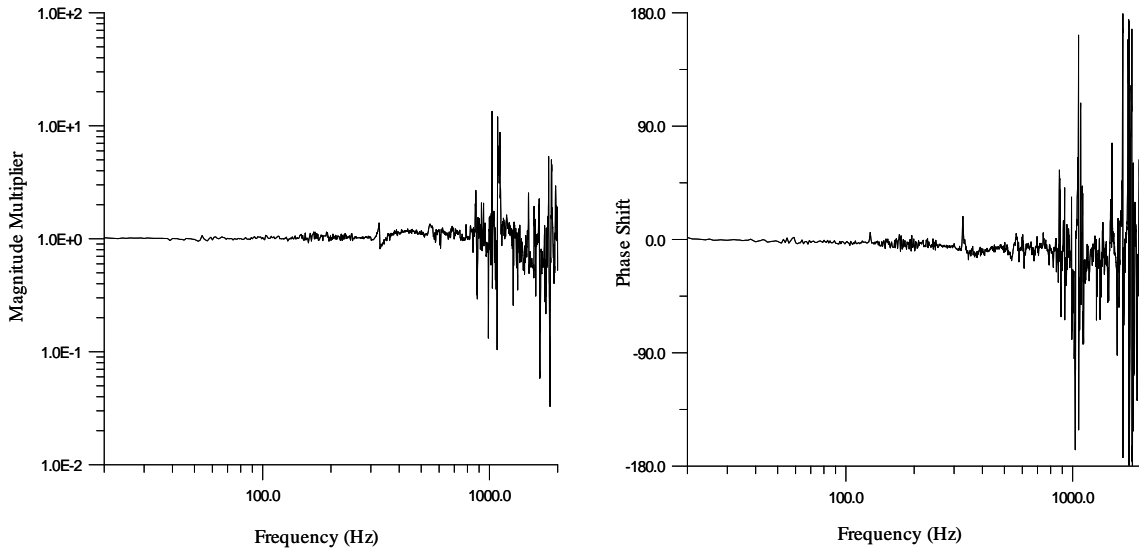


Figure D-2: Magnitude and phase calibration plots for the acoustic forcing chamber. For a signal received at the pressure transducer in the test section floor, the above corrections can be applied to determine the magnitude and phase of the pressure at the flame location. The magnitude correction is multiplicative while the phase correction is additive.

D.3 Resulting Calibration

The resulting calibration curves for the chamber are shown in Figure D-2. These curves represent the magnitude and phase differences between the unsteady pressure measured at the transducer in the test section floor, and those seen by the flame. More precisely, for a given drive frequency, the magnitude shown is the multiplier applied to the signal measured at the floor transducer to arrive at the magnitude at the flame. Similarly, the phase presented is the offset that is added to the measured pressure signal phase at the floor transducer to arrive at the phase of the pressure local to the flame.

As can be seen, the corrections are small for frequencies below 800 Hz. However, for frequencies above this the acoustic wavelength is on the same order as (or smaller than) the diameter of the chamber. At still higher frequencies, the wavelength can be on the order of the distance between the floor transducer and the flame. As a result, the corrections for some

frequencies are large, and in some cases no steady or usable correction can be found. These regions are tagged as having poor behavior and are avoided in the automated experiments.

D.4 Verification Through Simulated Response Testing

After generating the final calibration file, it was deemed necessary to do a system-wide verification to check not only the validity of the calibration but also the operation of the software, hardware and setup being used in the chemiluminescence experiments (See chapter 3). This was accomplished using a carefully controlled experiment in which the normal PMT used for chemiluminescence was replaced with the probe microphone connected to a custom, selectable filter network. Figure D-3 shows the normal experimental configuration while Figure D-4 shows the setup for verification.

The filter network was designed to provide bias current for the microphone and to generate various filtered outputs to act as surrogate combustion response transfer functions. A first order low-pass filter, a second order high-pass filter (with high Q), and a second order low-pass filter

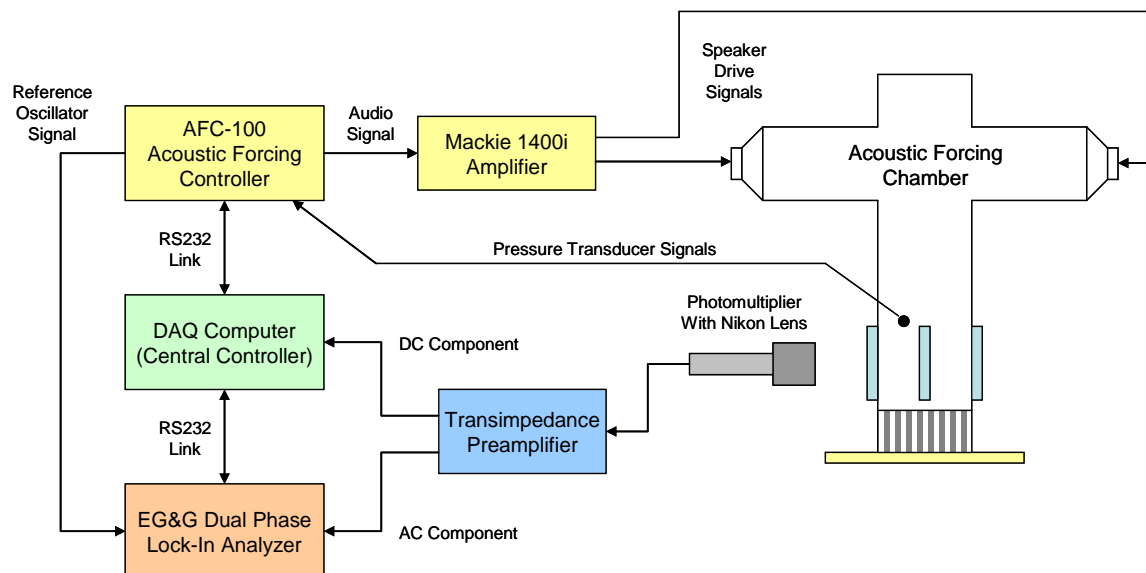


Figure D-3: Single-line schematic for experimental setup used in chemiluminescence experiments.

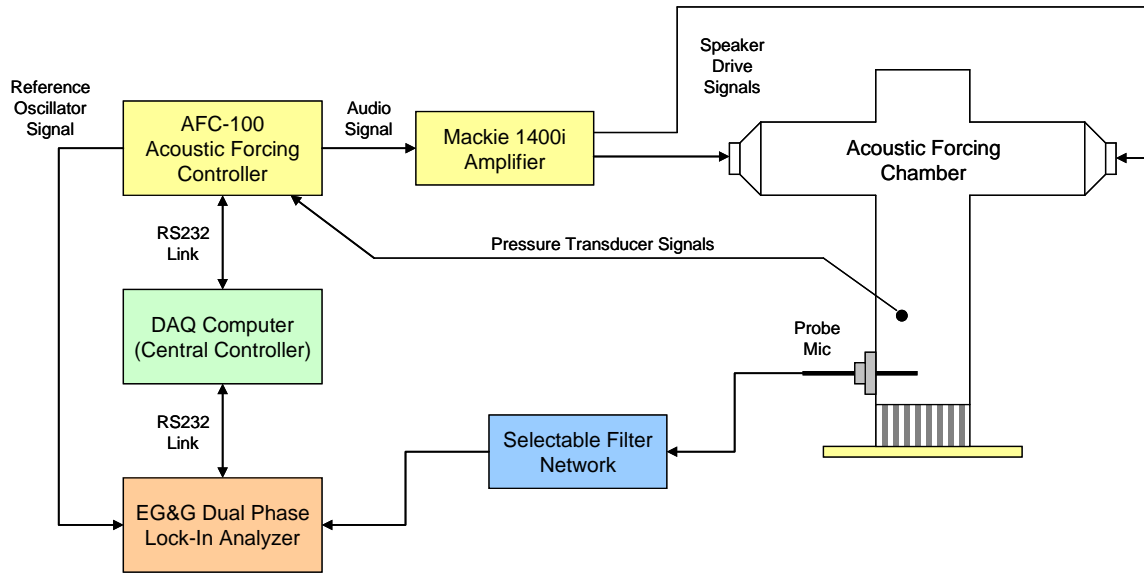


Figure D-4: Single-line schematic for acoustic calibration setup. Here, the probe microphone replaces the photomultiplier tube. A selectable filter network generates the surrogate response transfer function.

(with high Q) were all constructed. In addition, a straight-through path (i.e. unity transfer function) was also provided. Figure D-5 shows a schematic of the filter network circuit while Figure D-6 shows the computed filter transfer functions. It should be noted that the computed filter responses were based on idealized components. Nominal resistor values were assumed while capacitor values were measured with a capacitance meter. The operational amplifiers were assumed to be ideal. At the drive frequencies of interest, the ideal amplifier assumption is justified; however, each of the passive components has an associated tolerance and these must be considered when evaluating the results. All of the resistors used were 1% metal film devices. The capacitors employed were of the polyester or polystyrene dielectric type and had tolerances varying from 2% to 5%.

The verification experiments were performed in the same manner and with the same routines prepared for the PMT based chemiluminescence scans. Test runs were made with each of the three filters in line as well as with no filter (i.e. just the microphone bias circuit). Figures D-7

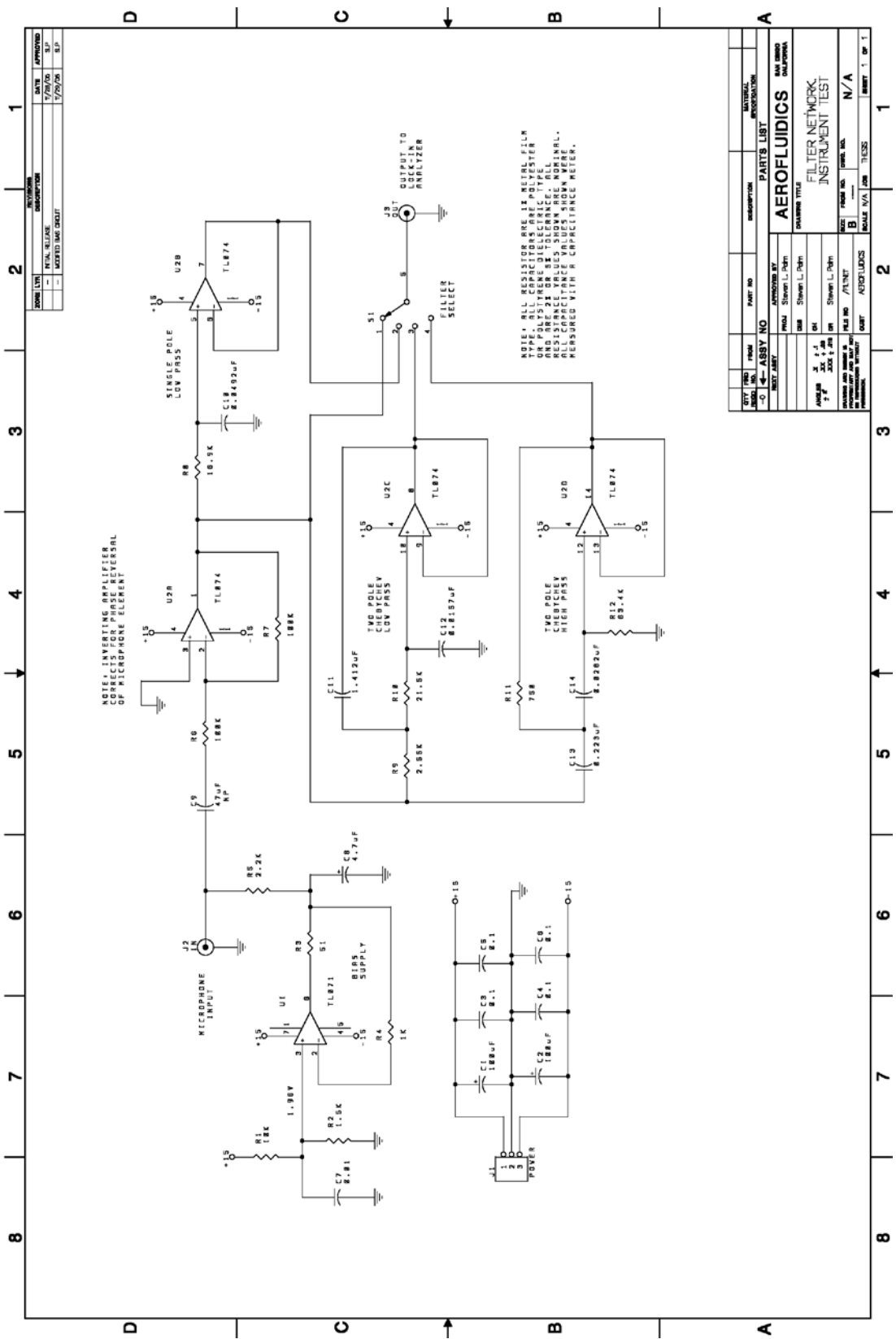


Figure D-5: Microphone filter network for verifying acoustic calibration as well as system software and hardware.

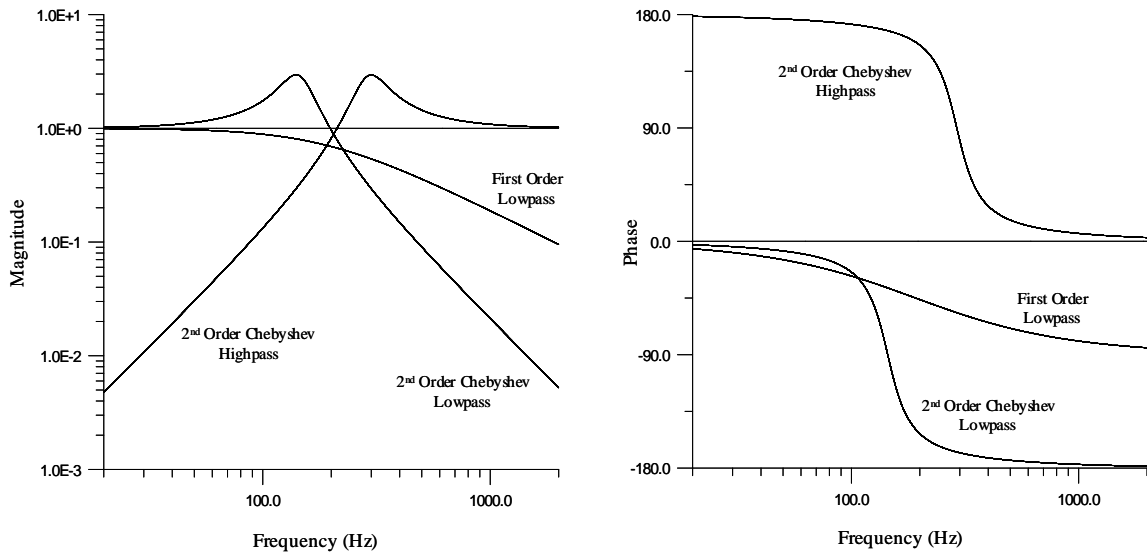


Figure D-6: Computed magnitude and phase responses of the microphone filter networks. Magnitude responses are normalized by the pass-through gain.

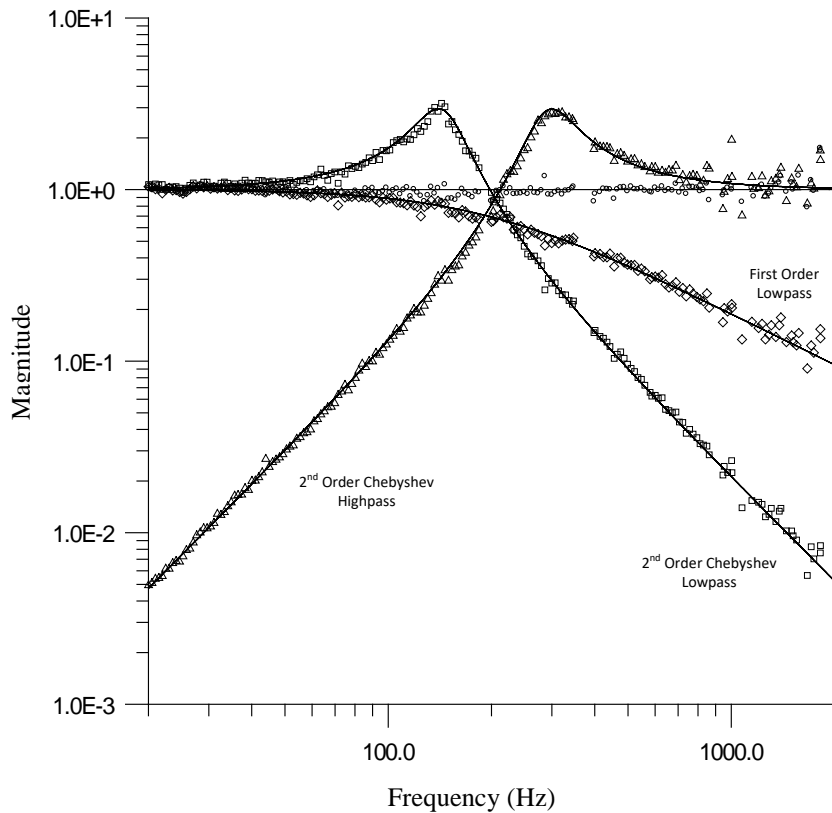


Figure D-7: Measured magnitude responses overlaid on computed transfer functions. Each symbol corresponds to a measurement data point.

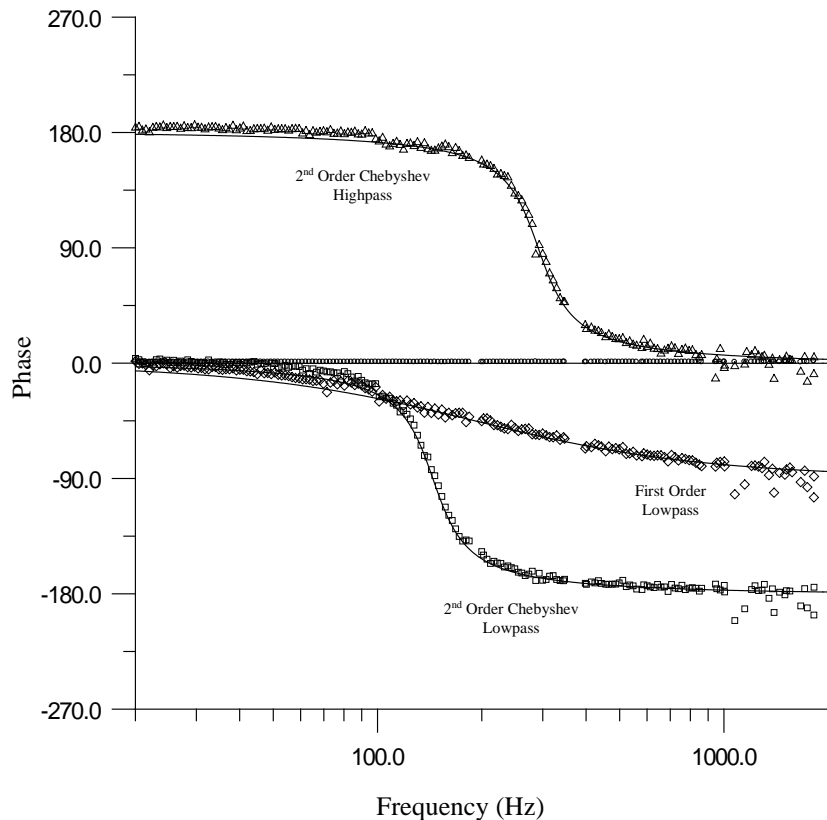


Figure D-8: Measured phase responses overlaid on computed transfer functions. Each symbol corresponds to a measurement data point.

and D-8 show the results of the tests. In these graphs, lines correspond to the computed or predicted responses based on the particular inline filter. The individual symbols correspond to data points collected by the experimental system. As can be seen, the correlation between the computed and measured results for both magnitude and phase responses in all the cases is good.

A p p e n d i x E

LASER SOURCES: DESIGN, FABRICATION AND PERFORMANCE

E.1 Introduction and Overview

One particular technique used in the presented work to measure the time-varying heat release rate of the flame under examination involves phase-resolved planar laser-induced fluorescence (PLIF). Pun, Palm and Culick introduced the basic method in 2000. Since then, the technique has been applied to several burners by various researchers including Pun et al. (2002, 2003), Ratner et al. (2002, 2003) and Kang et al. (2005). A major advantage of this technique is the ability to non-intrusively acquire not only temporally resolved, but spatially resolved data on the unsteady combustion process.

A specific goal of the work at hand was to advance this technique by producing custom equipment specifically designed to tackle previously encountered problems with the method. One such problem stemmed from the laser source. Unlike traditional laser-induced fluorescence (LIF), PLIF requires that the stimulating laser source be formed into a sheet to facilitate spatial imaging. This places a substantial demand on the laser source, itself. To achieve usable signal-to-noise ratios, pulse energies on the order of many, if not tens of millijoules, are typically required. The desire to fluoresce multiple species at wavelengths varying from 390 nm to 226 nm places further constraints on the system. As a solution, a custom laser system was designed and fabricated at the component level. A general system diagram is shown in Figure E-1.

In this system, a reengineered short-pulse Nd:YAG laser is used as the primary optical source. The laser operates at 10 Hz and produces an 8 mm diameter output beam at a wavelength

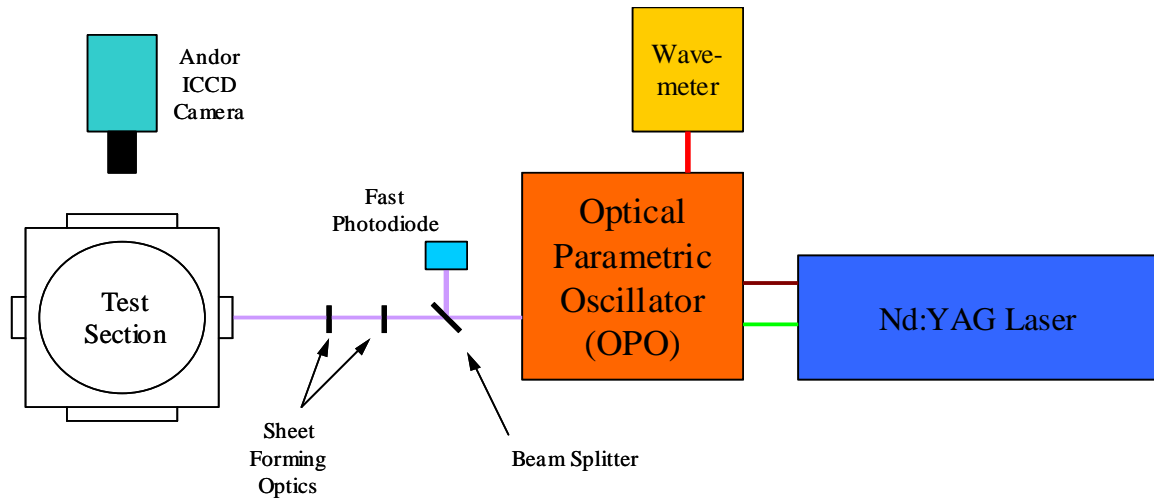


Figure E-1: The laser source general system diagram. An Nd:YAG laser (2 joule-per-pulse capable) pumps an optical parametric oscillator (OPO) to produce tunable UV emission. This output is used to fluoresce targeted chemical species in planar laser induced fluorescence (PLIF). The fluorescence signal is detected using an Andor iStar ICCD camera. A fast photodiode is used to monitor laser shot timing and shot-to-shot energy variation. A Burleigh WA-4500 wavemeter monitors the OPO cavity fundamental wavelength for OPO tuning.

of 1064 nm. The pulse duration is approximately 8-10 ns. The oscillator cavity employs an unstable resonator design, resulting in an output beam with an approximately Gaussian profile in the far field. The maximum output energy is 2 joules per pulse. This 1064 nm fundamental is then doubled to 532 nm using a KTP nonlinear optical crystal in Type II operation. The 1064 nm pump beam passed into the crystal is diagonally polarized while the 532 nm output is horizontally polarized. At large pump energies, doubling efficiency can be in excess of 50 percent resulting in outputs greater than one Joule per pulse at 532 nm. The fundamental and second harmonic beams are separated using a dichroic mirror.

Initial plans called for the design and construction of a dye laser, which in turn would pump a doubling/mixing stage employing BBO non-linear optical crystals. This scheme for generating tunable UV light is similar to that used by others engaged in combustion related PLIF, including those at Caltech. The design of the dye laser would allow it to accept to the full output energy of

the Nd:YAG laser at 532 nm. It would also be capable of accepting tripled output at 355 nm, used for pumping Exalite dyes in p-dioxane solvent. Design of the dye laser system was completed along with fabrication of all the control electronics. Manufacturing of the machined mechanical components was started and a completed pattern for the laser base plate was released to the aluminum foundry.

It was at this juncture that advice from a colleague, Sheng Wu, led to a change in strategy. Wu suggested that an Optical Parametric Oscillator (OPO) could be constructed to produce the desired UV output. He further proposed the idea of a ring cavity OPO, similar to work done by Smith et al. (2001) and Armstrong et al. (2002), and also the introduction of intra-cavity harmonic generation as seen in work by Fix et al. (1998, 2002). Wu offered to supply the nonlinear optical crystals at a substantially reduced cost if the development was undertaken.

As a result construction on the dye laser was halted and development began on the unique OPO for UV light generation. As suggested, the OPO incorporates a ring cavity with intra-cavity nonlinear optics to produce the wavelengths of interest. It is capable of producing output wavelengths for CH PLIF at 390nm, formaldehyde PLIF at 352nm (with mirror upgrades), acetone and OH PLIF at 277 nm and 283 nm, and NO PLIF at 226 nm.

The UV output is separated from the unwanted residuals using one or two Pellin-Broca prisms. Beam steering is accomplished using MgF coated, fused silica, right angle prisms. The beam is formed into a laser sheet using cylindrical optics prior to being passed into the test section. These cylindrical optics are UV-BBAR coated fused silica.

E.2 Nd:YAG Laser Design

The Nd:YAG laser was constructed by rebuilding and heavily modifying a Quantel YG-581-C system. (Photos of the laser and power supply are shown in Figure E-2.) During this

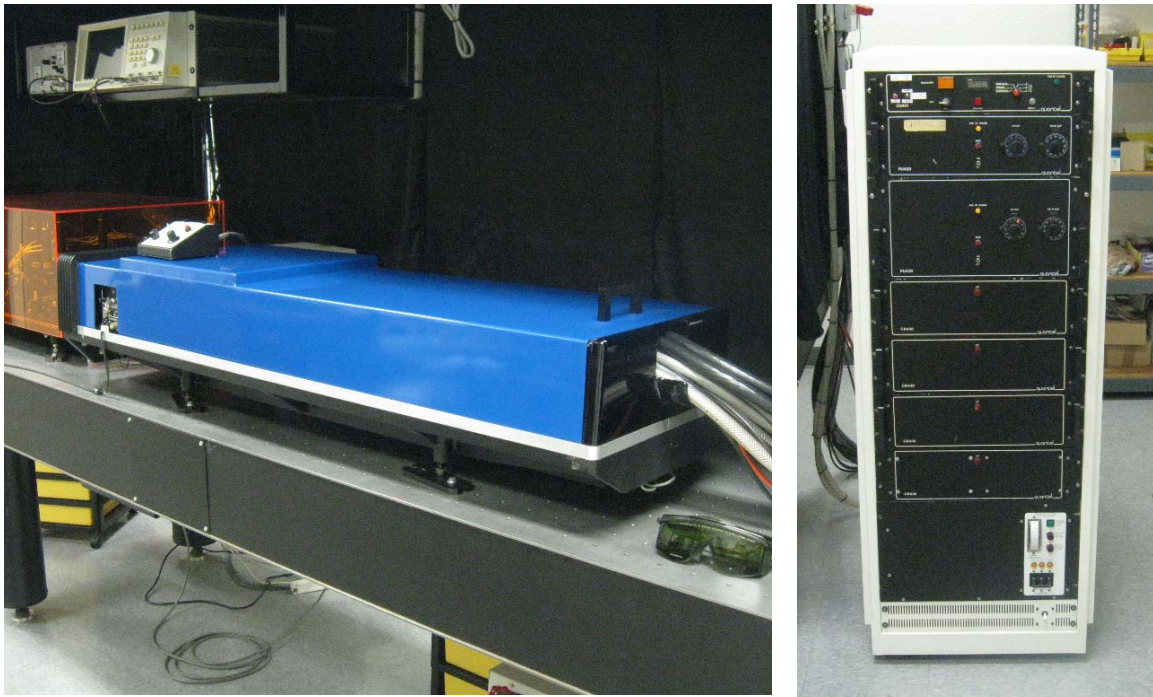


Figure E-2: Nd:YAG laser (left) and power supply (right) used as the principal light source in the phase-resolved PLIF experiments. Laser is built on the bed of a Quantel YG-581-C. Many sections were completely re-engineered to achieve usable system performance.

process, the oscillator cavity was completely redesigned. The original oscillator was of a stable resonator configuration and proved to be far too temperamental. It had poor mode selection and unacceptably bad long term stability. An unstable resonator was designed and implemented using an output coupler with a Gaussian reflectivity profile. This vastly improved the performance of the system.

Additionally, a second amplifier rod and pump chamber was installed to increase the output to 2 Joules per pulse at 1064 nm. A custom capacitor bank was fabricated to support the additional amplifier head. With the additional bank, the nominal electrical output from the power supply was increased from ~80 to ~130 Joules per pulse. A Quantel PU430 power supply was upgraded to support the increased electrical load from the two amplifiers. New control electronics were fabricated and the power input stage of the parallel resonant converter was redesigned to employ

IGBTs. All heavily loaded components were modified to be water cooled. In order to reject the additional heat from this increased output, a custom cooling group was also fabricated.

The firing control electronics were also modified. An additional trigger management circuit was added to the control unit to allow the laser to be triggered by a single rising-edge pulse. The circuit sequences the necessary signals to fire the laser and then recharge the capacitor banks for the next shot. It also incorporates a rate limiter that prevents the laser from being fired too rapidly, resulting in possible damage. Additional alarm electronics were also added to detect charging unit faults and to shut down the laser in the event of an anomaly.

A custom pendant was designed and built to allow remote operation of the laser. Additional signals were added to the pendant umbilical to enable remote adjustment of the Q-switch timing. This allows the laser output power to be varied during operation without removing the laser cover.

E.2.1 Optical Layout

Figure E-3 shows the optical layout of the Nd:YAG laser. It consists of an oscillator, two amplifier stages, and a second harmonic generator. The oscillator itself is comprised of two subsections. These are the oscillator rod and cavity mirrors, and the Q-switch. In its simplest form, the oscillator is formed by the rear cavity mirror (M101), the output coupler (M102) and a 7 mm, flashlamp pumped Nd:YAG rod (Y101). This combination, when properly aligned, forms a resonant cavity. When rod Y101 is pumped sufficiently, an energy level population inversion occurs. Unlike three level systems such as the ruby laser, Nd:YAG is a four-level lasing medium. This greatly reduces the pump requirement to achieve the inversion. Spontaneous emission from the rod seeds the cavity and quickly leads to stimulated emission and growth of the dominant modes. Some of this circulating energy in the cavity escapes through the output coupler and constitutes the oscillator output.

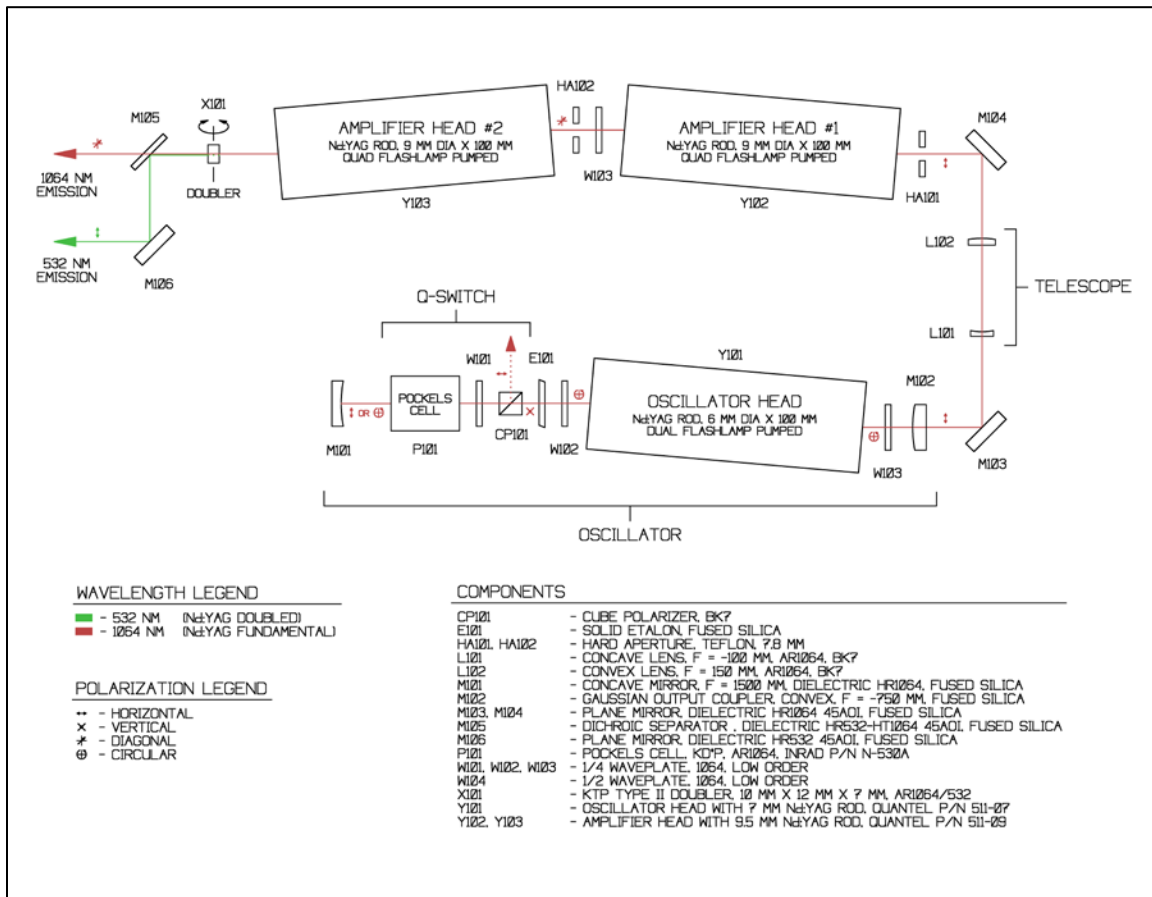


Figure E-3: Nd:YAG laser optical layout and component description.

In its original configuration, the oscillator used a stable resonator design. In this case, the output coupler had a uniform reflectivity profile across its face. In addition, the rear of the cavity included a concave lens and a mode selection aperture. The size and placement of the aperture were chosen to favor the TEM_{00} mode. Although functional, this stable resonator design was plagued with difficulties. Spatial mode stability was poor and the mirror alignment sensitivity made the long-term thermal stability of the laser unacceptably bad. In the end, the stable resonator design was abandoned.

A new, unstable resonator was designed from scratch. A computer code was written to model the resonator using matrix methods described by Magni, Silvestri, and Cybo-Ottone (1989),

as well as Gerrard and Burch (1975). Measurements of the thermal lensing of the oscillator rod were taken using a collimated diode laser. The rod was pumped under nominal flashlamp energies at 10 Hz. Simultaneously, the collimated beam was passed through the rod, and the distance from the rod face to the resulting beam waist was measured. This data was incorporated in the simulation. In addition, a Gaussian output coupler which was on hand was evaluated and found to be appropriate. It was measured to have a focal length of -750 mm and a centerline reflectivity of 14.4%. Figure E-4 shows the reflectivity profile.

Simulations for positive-branch, unstable operation were performed and the cavity length along with the ROC of the rear cavity mirror were optimized. It was found that a cavity length of 46 cm combined with a +1500 mm focal length rear mirror performed well. It should be noted that the simulations were run with the complete balance of intra-cavity components. These additional components are discussed below.

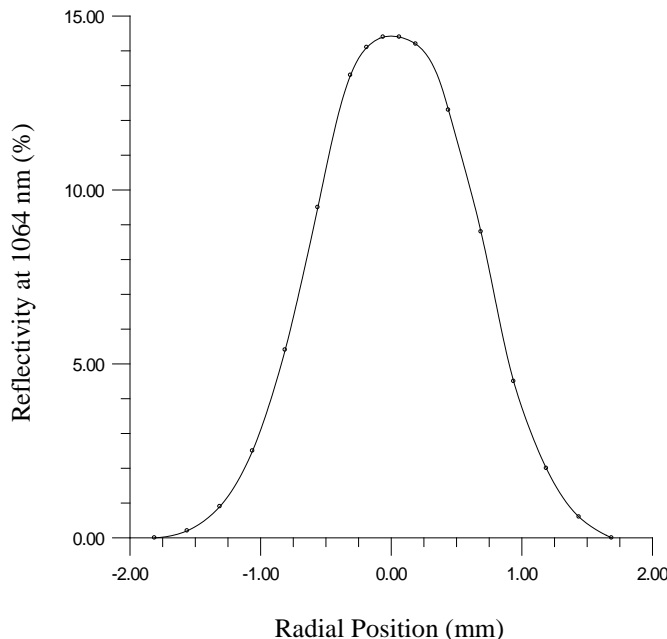


Figure E-4: Oscillator cavity output coupler reflectivity profile. Data was taken along a single diameter.

Unfortunately, with the basic oscillator described above, lasing begins at the threshold where the rod gain just exceeds the cavity losses. Since the flashlamp pumping time is significantly longer than the cavity build-up time (10^{-4} sec versus 10^{-8} sec), this results in either a series of many short, low energy pulses or one long pulse with the energy being distributed throughout. The instantaneous power, in either case, is relatively low, usually on the order of a few kilowatts.

To resolve this issue, a Q-switch is introduced. Figure E-3 shows the final configuration with the Q-switch optics included. The Q-switch is comprised of a Pockels cell (P101), a quarter-waveplate (W101) and a cube polarizer (CP101). Polarizer CP101 rejects any light in the cavity that is horizontally polarized. Vertically polarized photons are allowed to pass. Waveplate W101 performs a “quarter” rotation. Linearly polarized light passing through W101 is transformed into circularly polarized light, and vice versa. Pockels cell P101 contains a KD*P optical crystal with parallel electrodes along two opposing longitudinal sides. This crystal is passive in the absence of an electric field. However, when a potential of 3600V DC is applied across the electrodes, the crystal behaves as an additional quarter-waveplate for 1064 nm light.

Spontaneously emitted light from the YAG rod that is vertically polarized at CP101 passes through the cube polarizer, and then through W101 and P101 sequentially on its way to the rear cavity optics. W101 introduces a quarter rotation and transforms the light to circular polarization. After reflecting from M101, the light passes back through L101, P101 and W101. Once again, W101 performs another quarter rotation, causing the light to become horizontally polarized. As the light reaches the cube polarizer, CP101, it is rejected from the oscillator. This loss “spoils the Q” of the cavity, making it unable to resonate.

However, if P101 has a 3600V potential applied to it, it also acts as a quarter waveplate. In combination with W101, this forms a “half-wave” rotation per pass through the Q-switch optics. Since the Q-switch optics are traversed twice, the total polarization rotation encountered is 180 degrees. Thus, vertically polarized light departing CP101 toward M101, returns to CP101

vertically polarized and passes through it. Consequently, the cavity Q becomes very large. In practice, the oscillator cavity is “Q-switched” approximately 150 microseconds after the flashlamps have been fired. This allows the Nd:YAG rod to establish a strong population inversion prior to lasing. The result is a laser pulse from the oscillator that is approximately 8-10 ns in duration and has a peak instantaneous power of roughly 20 megawatts.

Finally, various optics are added to improve performance and to narrow the laser line width. A solid quartz etalon (E101) is installed within the cavity to reduce the number of longitudinal modes. This etalon provides photon selectivity during the onset of lasing. Photons with wavelengths that are integer divisors of the thickness of the etalon are favored. As a result, more of these photons are available in the early stages of build up to stimulate emission.

Another improvement in oscillator mode selection is achieved by installing quarter waveplates (W102 and W103) on either side of Y101. Without these waveplates, the cavity standing wave with linear polarization passes through the rod. Nodes in this wave appear at regular intervals along the longitudinal axis. These nodes are regions that quantum mechanically exhibit low photon density. This results in two undesirable effects. The first is that, for a given longitudinal mode, these regions of the rod are underutilized since little stimulated emission occurs. This phenomenon is known as spatial burning. The second effect, being a consequence of the first, is that unwanted modes that have good overlap with underutilized regions tend to be driven resulting in multimode output and broader line width.

By inserting quarter waveplates on either side of Y101, the light passing through the rod is circularly polarized. It is right-hand polarized when travelling in one direction, and left-hand polarized when returning the other direction. As result, no longitudinal nodes appear within the rod. The addition of the etalon and quarter waveplates reduces the line width of the YAG fundamental from about one wavenumber to approximately 0.2 wavenumbers.



Figure E-5: Left – redesigned Nd:YAG laser oscillator cavity. Right – oscillator output burn (near-field) taken with Kodak Linagraph paper, type 1895.

The new oscillator design proved to be a substantial improvement. Performance of the cavity was exceptional. Beam quality was found to be good and long term stability was excellent. Typical pulse energies for the oscillator cavity were found to be 140 mJ; sufficient for driving the amplifier stages. Figure E-5 shows the redesigned oscillator cavity as well as a near-field oscillator burn profile.

The oscillator output is used to feed two stages of amplification. The vertically polarized light from the cavity exits through output coupler (M102) and is turned 90 degrees by a dielectric mirror. It is then passed through a telescope where the beam is expanded from 5 mm to 8 mm. Following the telescope, the beam is again turned 90 degrees and directed down the amplifier leg. The amplifier leg consists of two 9.5 mm, flashlamp pumped Nd:YAG rods (Y102 and Y103) operated in series. The beam entering the amplification leg is first clipped to a diameter of 7.8 mm by passing through aperture HA101. It then passes through rod Y102, after which it is spatially filtered again by another 7.8 mm diameter aperture (HA102). At this location the beam is passed through a 1064 nm half waveplate that is rotated such that the light emerges diagonally polarized. Since each amplifier rod is pumped by four linear flashlamps (positioned 90 degrees apart), performing a 45 degree rotation of polarization between the two amplifiers enables the second

amplifier to partially correct for the phase-front distortion introduced by the thermal birefringence of the first amplifier. After this 45° polarization rotation, the beam passes through the final amplifier rod (Y103) and enters the second harmonic generator.

The second harmonic generator consists simply of a type II KTP doubling crystal (X101), an HR532-HT1064 dichroic separator (M105) and an HR532 dielectric mirror (M106). The 1064 nm emission from the laser enters the doubling crystal (X101) with diagonal polarization. Second order, nonlinear doubling occurs yielding 532 nm laser light that is horizontally polarized. With a properly sized doubling crystal, conversion efficiency can be in excess of 50 percent. The combined 1064 nm/532 nm is passed through a dichroic separator (M105). The separator allows the 1064 nm component to pass while the 532 nm light is reflected. The final dielectric mirror (M106) is used to return the 532 nm beam to a path that is parallel to the residual 1064 nm emission.

E.3 Optical Parametric Oscillator (OPO)

In order to perform laser-induced fluorescence on the combustion species of interest, it was necessary to create a tunable UV laser light source. Conventionally, researchers have used a combination of YAG or Excimer pumped dye lasers along with UV doubling and mixing systems. However, in recent years, great strides have been made in the production of high quality, nonlinear optical crystals, and as a result interest has grown in the use of all solid state optical parametric oscillators (OPO) and optical parametric amplifiers (OPA).

E.3.1 OPO Theory

The optical parametric effect is possible due to nonlinear susceptibilities found in many transparent, inorganic crystals. These nonlinearities have been used for many years to perform optical frequency multiplication and heterodyning (mixing) of laser beams. It is a special case of the second order heterodyning behavior that gives rise to basic optical parametric oscillation.

Given incident light on a nonlinear optical crystal, the material polarization vector $\underline{\mathbf{P}}(t)$ describes the dipole moment per unit volume that is induced into the crystal by the electric fields of the applied waves. In terms of the order of the interactions, this can be written as

$$(E-1) \quad \underline{\mathbf{P}}(t) = \underline{\mathbf{P}}^{(0)}(t) + \underline{\mathbf{P}}^{(1)}(t) + \underline{\mathbf{P}}^{(2)}(t) + \dots,$$

where superscripts indicate the order of interaction. The zeroth order term corresponds to a static polarization found in some crystals. The first order term is just the typical linear interaction. Using notation from Butcher and Cotter (1990), this can be written as

$$(E-2) \quad \underline{\mathbf{P}}^{(1)}(t) = \epsilon_0 \int_{-\infty}^{+\infty} \underline{\underline{\chi}}^{(1)}(\omega) \cdot \underline{\mathbf{E}}(\omega) e^{-i\omega t} d\omega.$$

Here, $\underline{\underline{\chi}}^{(1)}(\omega)$ is a second order tensor called the linear susceptibility. $\underline{\mathbf{E}}(\omega)$ is the applied electric field in the frequency domain and ϵ_0 ($\approx 8.85 \times 10^{-12}$ F-m $^{-1}$) is the permittivity of free space. The second order polarization vector provides the behavior of interest, and can be written as

$$(E-3) \quad \underline{\mathbf{P}}^{(2)}(t) = \epsilon_0 \int_{-\infty}^{+\infty} \int_{-\infty}^{+\infty} \underline{\underline{\chi}}^{(2)}(\omega_1, \omega_2) : \underline{\mathbf{E}}(\omega_1) \underline{\mathbf{E}}(\omega_2) e^{-i(\omega_1 + \omega_2)t} d\omega_2 d\omega_1.$$

In this case, $\underline{\underline{\chi}}^{(2)}(\omega)$ is the quadratic susceptibility, which is a tensor of order three.

In order to continue in the present illustration, the following simplifications and assumptions are made in order to reduce equation (E-3):

- i. All the beams lie along a single, principal axis.
- ii. There are two incoming wavelengths of interest and they are both monochromatic and coherent.
- iii. The susceptibility tensor is taken to be frequency independent.

The first assumption eliminates much of the vector notation, which is not essential to understanding the basics of the phenomenon. The second condition introduces Dirac delta

functions in the electric field, $\underline{E}(\omega)$. This in turn reduces the convolution presented in (E-3) to simple multiplications. The final simplification of having a frequency independent susceptibility tensor serves to reduce algebra bookkeeping and, once again, does not interfere with understanding the basic physics. One can imagine an ideal material in which the molecular dipoles respond infinitely fast to the applied electric field, and without loss.

Given the above simplifications, the material polarization (in one dimension) can be written

$$(E-4) \quad P(t) = \epsilon_0 \left(\chi^{(0)} + \chi^{(1)} E(t) + \chi^{(2)} E^2(t) + \dots \right).$$

Furthermore, the two monochromatic input signals can be represented by

$$(E-5) \quad E(t) = E_1 e^{-i\omega_1 t} + E_1^* e^{+i\omega_1 t} + E_2 e^{-i\omega_2 t} + E_2^* e^{+i\omega_2 t}.$$

Here, E_n^* is the complex conjugate of E_n . Combining (E-4) and (E-5), and discarding the uninteresting parts containing the static and linear susceptibilities gives

$$(E-6) \quad \begin{aligned} P^{(2)}(t) = \epsilon_0 \chi^{(2)} & \left[2 \left(E_1 E_1^* + E_2 E_2^* \right) + \left(E_1^2 e^{-i2\omega_1 t} + E_1^{*2} e^{i2\omega_1 t} \right) + \left(E_2^2 e^{-i2\omega_2 t} + E_2^{*2} e^{i2\omega_2 t} \right) \right. \\ & \left. + 2 \left(E_1 E_2 e^{-i(\omega_1+\omega_2)t} + E_1^* E_2^* e^{i(\omega_1+\omega_2)t} \right) + 2 \left(E_1 E_2^* e^{-i(\omega_1-\omega_2)t} + E_1^* E_2 e^{i(\omega_1-\omega_2)t} \right) \right]. \end{aligned}$$

The first term on the right hand side is an induced time-invariant electric field in the crystal that is commonly referred to as optical rectification. The remaining terms are all the second order harmonics that are possible. Terms two and three correspond to homodyne mixing where one of the input frequencies is doubled. The last two terms correspond to heterodyne mixing where the sum or difference of the two input signals is produced.

It should be noted that although all these terms are present in the polarization equation, not all harmonics are produced simultaneously. Indeed, under most conditions, no harmonic output is produced. Along with the restrictions produced by equation (E-6), as well as energy conservation, there is also the constraint of phase matching. In the case of heterodyning, phase matching is achieved by exploiting the variation in the crystal's index of refraction as a function of optical

wavelength, as well as the birefringence of the nonlinear crystal used. When properly tuned, the phased array of dipoles in the crystal, which are driven in the nonlinear regime by a combination of the input beams, will be in phase with the desired output. This tuning is accomplished by either varying the crystal temperature or physically rotating the crystal in relation to the optical axis. In the constructed OPO, all crystals are tuned by rotation.

During frequency conversion, energy conservation is maintained on a photon-by-photon basis. For example, in frequency doubling, two photons at ω_1 vanish and a single photon at $\omega_2 = 2\omega_1$ appears simultaneously. In positive heterodyning, two incoming photons with different frequencies, ω_1 and ω_2 , vanish and a third photon at $\omega_3 = \omega_1 + \omega_2$ appears. This can be seen in the energy diagrams shown in Figure E-6.

The question arises if it is possible to convert a single photon into two lower energy photons through this process. Fortunately, the answer is “yes.” This is shown as the third case in Figure E-6 and corresponds to the frequency difference terms present in equation (E-6). This “negative heterodyning” still requires two input signals, ω_1 and ω_2 in order to produce the difference output

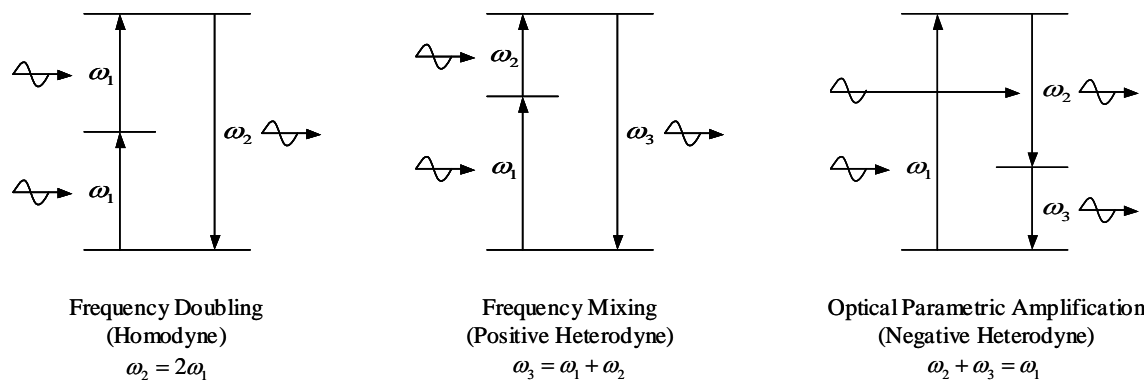


Figure E-6: Energy level diagrams for three different cases of frequency conversion in nonlinear optical crystals.

ω_3 . However, due to energy conservation, photons at both ω_2 and ω_3 are produced as photons at ω_1 disappear. The result is that the signal at ω_2 is amplified much the same way traditional laser amplification occurs through stimulated emission. This effect is called Optical Parametric Amplification (OPA).

With this method of amplification it is now possible to construct an oscillator by surrounding the crystal with a cavity that has high-Q at frequency ω_2 but is transparent (or has significant loss) at frequencies ω_1 and ω_3 . Energy is coupled into the cavity by a pump beam at frequency ω_1 . The cavity resonance at frequency ω_2 allows the intra-cavity crystal to produce its own stimulus for the OPA effect. As a result, cavity circulating energy builds rapidly at ω_2 . This circulating energy is typically called the “signal.” The remaining pump energy and the output produced at ω_3 are allowed to escape the cavity. The unused output beam at ω_3 is typically dubbed the “idler.” This formation of an optical parametric amplifier within a resonant cavity is called an optical parametric oscillator (OPO).

E.3.2 OPO Design

A unique OPO was designed and built to fulfill the need for a tunable UV light source. Pictures of the completed device are presented in Figure E-7 while a schematic of the optical layout is shown in Figure E-8.

E.3.2.1 Oscillator Cavity (Circulator)

The core of the UV source is the ring cavity oscillator. A layout drawing and corresponding photo are shown in Figure E-9. The fundamental design of the ring cavity is based on work by Smith and Bowers (2001), as well as Armstrong and Smith (2002). The cavity is designed to be

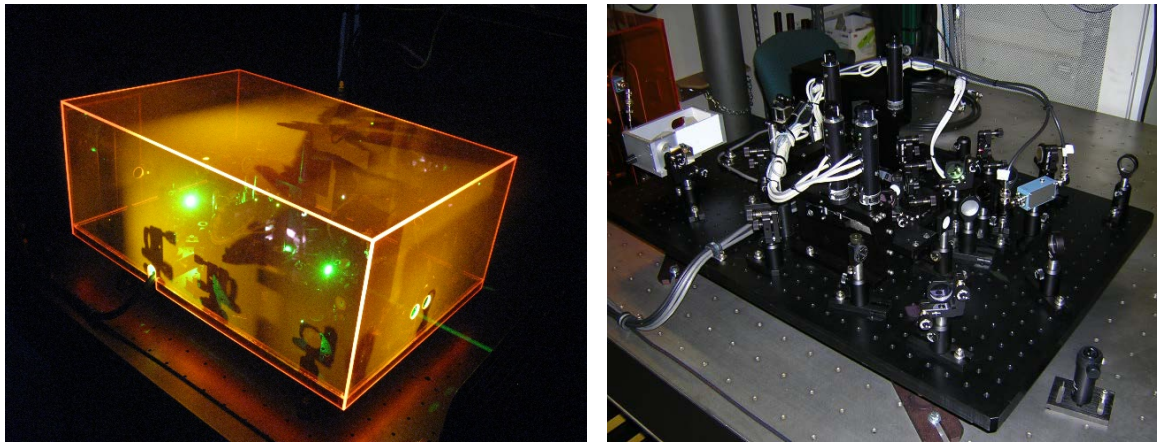


Figure E-7: Completed optical parametric oscillator (OPO). Left - in operation with cover in place. Right - cover removed, revealing optics, actuators, and ancillary components.

pumped with 532 nm, horizontally polarized laser light and is engineered to oscillate with fundamental wavelengths from 720 nm to 795 nm. It is bounded by four custom-engineered dielectric mirrors, M201 through M204. The performance specifications for these mirrors are listed in Table E-1. The mirrors are arranged in a planar-rectangular configuration. Within the cavity, the basic oscillator components are the OPO crystal (X201), a fused silica corrector (C201), a dove prism (P201), and a half waveplate (W201). The OPO crystal used is a 17 mm long KTP (potassium titanyl phosphate) element with an 8 mm x 9 mm cross section. The crystal is cut for Type II phase matching in the XZ plane with $\theta = 56.0^\circ$ and $\varphi = 0.0^\circ$. The total round-trip cavity length is ~ 260 mm. With a beam diameter of 6 mm and a signal wavelength of 780 nm, the resulting cavity Fresnel number is $N_F = d^2/\lambda L \simeq 180$.

The pump beam enters through M201, passes through X201, then C201, and then exits through M202, as shown. A signal and idler beam are developed from the crystal due to the optical parametric effect. The resulting long-wave idler is unused and leaves the cavity through M202. It passes through M210 and is absorbed by beam-stop S201. However, the short-wave signal beam

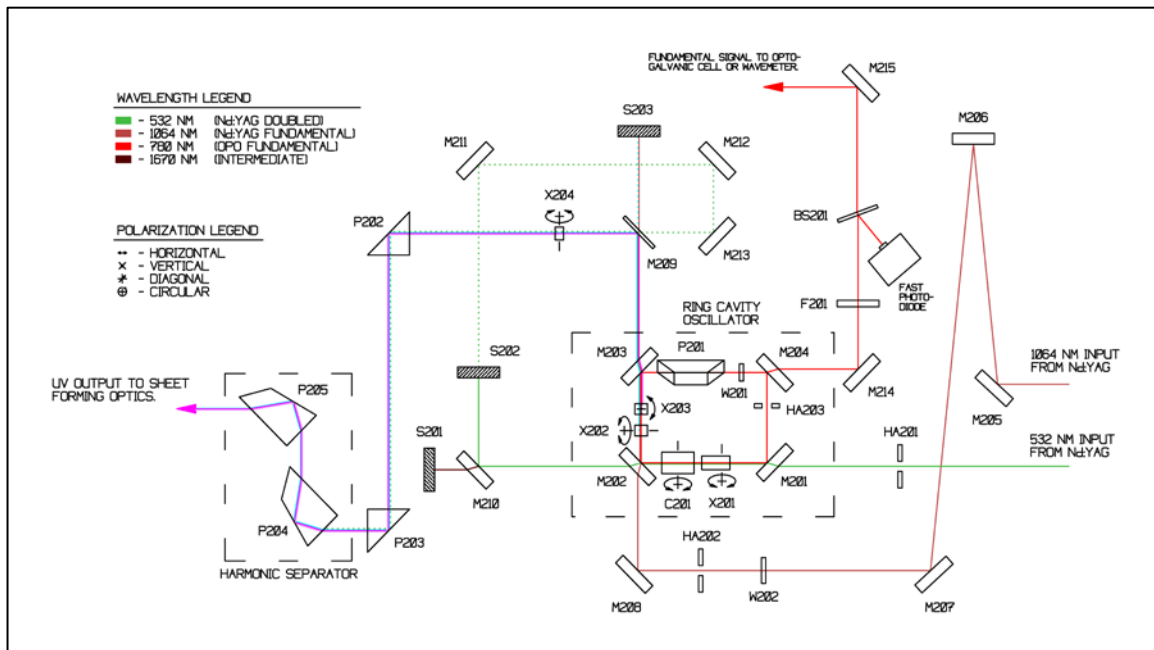


Figure E-8: General layout of optical parametric oscillator. Some optics are repositioned or removed for specific wavelength configurations.

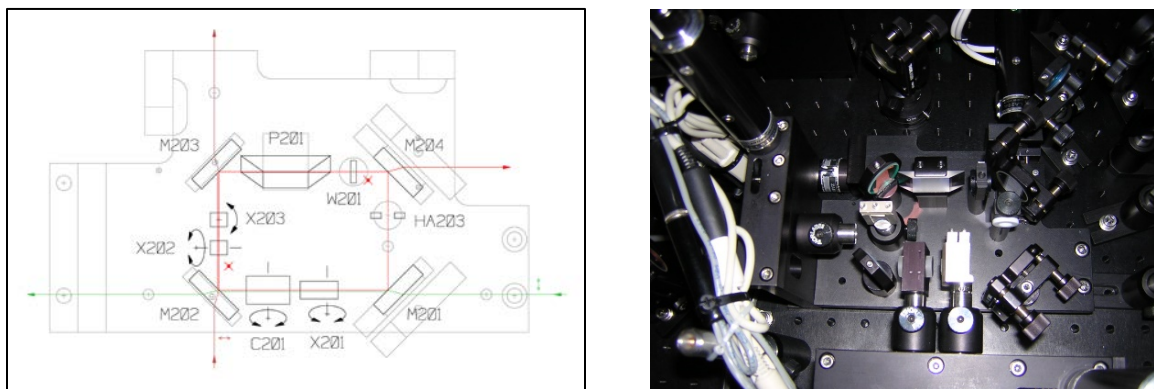


Figure E-9: OPO ring cavity oscillator fabricated on a custom sub-plate. Left – sketch showing components and beam paths. Right – photo of actual oscillator hardware.

Mirror	Transmission Bands	Reflective Bands	AOI and Pol	Substrate	Dielectric
M201 thru M203	280-320/380-400/532/1064 nm	720-795 nm	45p	Fused Silica	High Energy
M204		720-795/532 nm	45p	Fused Silica	Standard
M209	532/1064 nm	270-290/380-400 nm	45p	Fused Silica	High Energy

Table E-1: Specifications for the four OPO cavity mirrors as well as the output separator M209.

circulates in the cavity, but only in the forward direction. This wave is a mode of the cavity, but it lacks a reverse traveling component. This prevents the development of a standing wave and consequently there is no spatial burning within the oscillator crystal. This narrows the cavity line width and also improves conversion efficiency.

Tuning of the cavity is accomplished by rotating crystal X101 about a horizontal axis that is perpendicular to the beam direction. Rotation is performed by a precision linear actuator (Zaber model T-LA28 with ball end) extending against a sine bar. This rotation scheme is used for all crystals in the system as well as the fused silica corrector. The single step size of the actuator is 0.1 um. With a sine bar fulcrum distance of 76.2 mm, this equates to an angular step size of approximately 1.6 μ rad. The result is a tuning resolution of roughly 0.0005 nm per step at the fundamental. This is substantially smaller than the line width of the OPO fundamental, which was determined to be about 0.09 nm or 1.5 wavenumbers using a Burleigh WA-4500 pulsed laser wavemeter.

Rotation of X201 results in a beam offset that misaligns the cavity. In order to correct this, C201 is rotated to generate a displacement in the opposite direction. In addition, fine adjustment of alignment in the horizontal plane is accomplished by a translation stage under M204. The stage is oriented so that M204 moves in a direction perpendicular to the approaching beam. The stage is moved with the same model actuator used in the rotation stages.

As demonstrated in simulations by Smith and Bowers (2001), beam spread in the plane of rotation of X201 tends to be narrow due to the limited acceptance angle of the KTP crystal. However, in the direction perpendicular to this (along the axis of rotation), spatial gain narrowing and back-conversion lead to a wide beam spread. The solution is to introduce P201. This dove prism is inserted along its axis in the beam path between mirrors M203 and M204. It is rotated 45 degrees about its longitudinal axis as can be seen in Figure E-9. This results in the cavity beam experiencing an inversion and physical rotation of 90 degrees on every pass through the prism. In a four-mirror cavity, this results in the beam alternating between two states, interchanging the horizontal and vertical axis on each pass. The ultimate result is a great improvement in the quality of the signal beam. The signal fluence in the far-field shows a divergence that is small and roughly uniform in all directions.

It was initially believed that the physical rotation produced by the dove prism would also rotate the beam polarization. As such, a half waveplate (W201) was inserted just downstream of the prism in order to rotate the polarization of the cavity beam from horizontal back to vertical. During cavity alignment, W201 was simply rotated until peak circulating energy at the fundamental wavelength was detected. Then W201 was locked in place with a setscrew. However, it was later discovered through work by Moreno et al. that the polarization of the light passing through the dove prism rotates only slightly and becomes mildly elliptic. Consequently, the correction induced by W201 is very small. Indeed, replacing W201 with a quarter waveplate may result in improved cavity performance since this could be used to correct for the rotating portion of the electric field, which appears to be the dominant part of the distortion. Nevertheless, this custom waveplate has not been procured and tried.

Qualitative monitoring of the cavity pulse length and circulating energy is accomplished through observation of the light leaked through M204. This weak signal is redirected by a silvered mirror (M214) and passed through an RG-665 Schott glass filter (F201). This filter allows the OPO

fundamental (> 700 nm) to pass while blocking any residuals from the 532 nm pump or from harmonic generation. The remaining signal is then divided by a 30/70 beam splitter (BS201), directing 30% to a fast photodiode and the balance to either an optogalvanic cell or a Burleigh pulsed laser wavemeter for wavelength determination.

The fast photodiode used is a Thor Labs model FDS010. This photodiode is biased with 12 volts through a current limiting, R-C noise filter. The output is fed to a Hewlett Packard 54100D digitizing oscilloscope where it is displayed along with the Nd:YAG laser Q-switch signal which is used as a trigger reference. The photodiode signal provides qualitative information about the circulating energy within the ring cavity, and is principally used during cavity alignment. Fine adjustments can be made to M201 and M204 while observing the oscilloscope in order to maximize the area under the displayed curve, resulting in peak circulating energy.

E.3.2.2 Generation of 350-390 nm Output

Generation of 390 nm light for CH PLIF or 352 nm light for CH₂O PLIF is accomplished by doubling the oscillator fundamental. Doubling is achieved by introducing an intra-cavity BBO crystal. A schematic of the scheme can be seen in Figure E-10. It should be noted that the presently installed cavity mirrors do not support operation down to 704 nm. Consequently, CH₂O PLIF at 352 nm is not currently possible. However, this can be easily rectified with the procurement of a set of upgraded dielectric mirrors. This improvement has been reserved for future work.

The doubling crystal is installed in the X203 position and is rotated about a vertical axis. The oscillator fundamental enters the crystal vertically polarized. When properly tuned, type I doubling occurs and the resulting second harmonic exits the crystal with horizontal polarization. Cavity mirror M203 allows this harmonic to pass while reflecting the cavity fundamental. The output is turned by M209 and directed into a Pellin-Broca harmonic separator by a pair of right

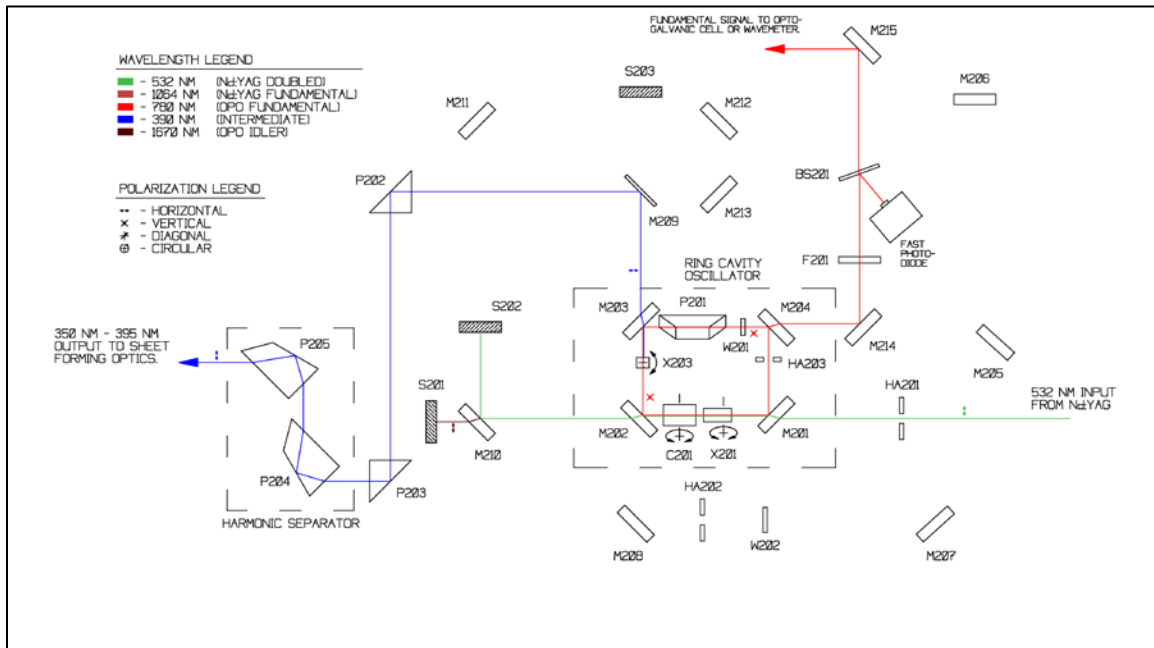


Figure E-10: Optical parametric oscillator configuration for generating 390 nm UV light for CH PLIF or 352 nm UV light for formaldehyde PLIF.

angle prisms. The harmonic separator removes any unwanted residuals and the clean UV beam exits the assembly and proceeds to the sheet forming optics.

Figure E-11 shows the performance of the OPO in this configuration while producing output at 390 nm. Energy measurements were taken at the exit of the YAG laser for the 532 nm pump beam and just after the harmonic separator for the 390 nm output. Conversion efficiency is defined as the ratio of the 390 nm output energy to the 532 nm pump energy. As can be seen, a peak conversion efficiency of approximately 3.5% was obtained, with an output energy of 16.9 mJ per pulse. Higher output energies were obtained beyond this peak efficiency point; however, substantially increased 532 nm pump energies resulted in damage to the anti-reflective coating on the OPO crystal (X201) and pitting of the crystal surface. Consequently, pump energies in future experiments were limited to 600 mJ.

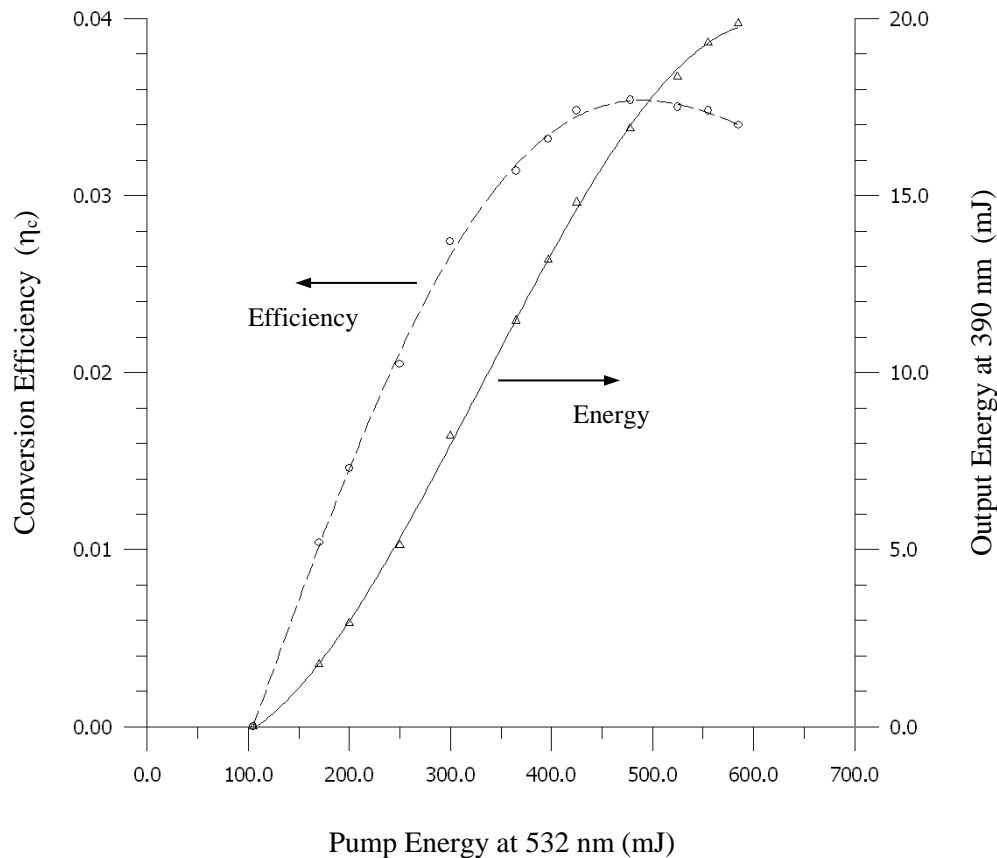


Figure E-11: Optical parametric oscillator performance generating 390 nm output. Energies listed are per pulse. YAG laser firing rate is 10 Hz. Peak conversion efficiency is 3.5% with a 390 nm output of 16.9 mJ. With a pump energy of 585 mJ, the output energy rises to 19.9 mJ.

Unfortunately, it was not possible to determine the line width of the 390 nm emission using the Burleigh wavemeter as was previously done with the OPO fundamental. With the given internal configuration, the wavemeter was not capable of measuring wavelengths shorter than 400 nm. Nonetheless, it is known that for doubling or mixing of narrow linewidth beams of Gaussian distribution, the output linewidth is approximately the square root of the sum of the input linewidths. For wider input linewidths, the resulting output is constrained by the acceptance bandwidth of the NLO crystal. Given this, the estimated linewidth of the 390 nm output is between 1.5 cm^{-1} and 2.0 cm^{-1} .

E.3.2.3 Generation of 283 nm (and 277 nm) Output

Generation of UV light at 283 nm and 277 nm for OH and acetone PLIF is accomplished by two stages of intra-cavity mixing. In this approach, residual 1064 nm IR from the YAG laser is delayed and then mixed with the OPO cavity fundamental. The resulting product is then mixed again with the cavity fundamental to produce the desired output. A schematic of this configuration is shown in Figure E-12.

As before, the OPO ring cavity is pumped with the doubled Nd:YAG output at 532 nm to produce the circulating cavity fundamental. The residual 1064 nm from the pump laser is delayed in order to synchronize it with this fundamental, which requires time to build. A delay line implemented with dielectric mirrors M205 through M208 fulfills this requirement and directs the beam down the mixing leg of the cavity. Half waveplate W202 rotates the 1064 nm polarization from diagonal to horizontal to prepare it for mixing.

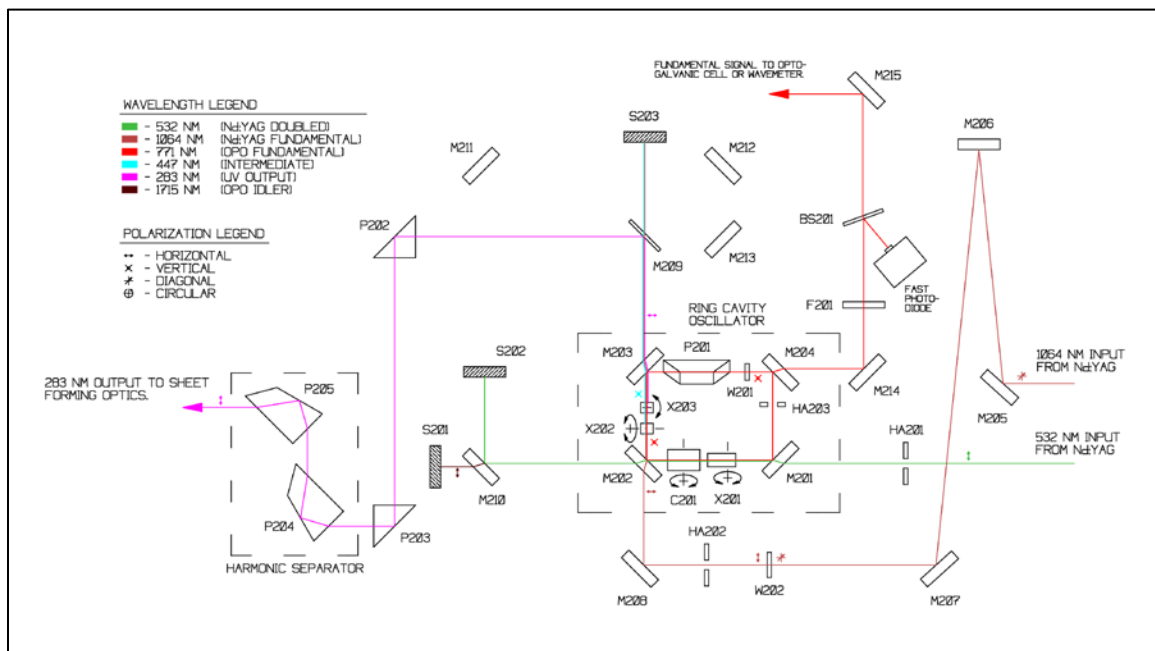


Figure E-12: Optical parametric oscillator configuration for generating 283 nm UV light for OH PLIF.

BBO mixing crystals are installed in positions X202 and X203. The crystal in the X202 position is cut for type II mixing and is rotated about a horizontal axis while the crystal in the X203 position is cut for type I mixing and is rotated about a vertical axis. When the angle of X202 is adjusted properly, the horizontally polarized 1064 nm mixes with the vertically polarized 771 nm cavity fundamental to produce a 447 nm vertically polarized output. The beam then passes through X203 where it is mixed again (assuming proper tuning) with the 771 nm fundamental. The result is a horizontally polarized output at 283 nm. The 1064 nm IR, 447 nm intermediate and the 283 nm UV all exit the cavity through M203. After M203, the desired output is reflected off M209 and

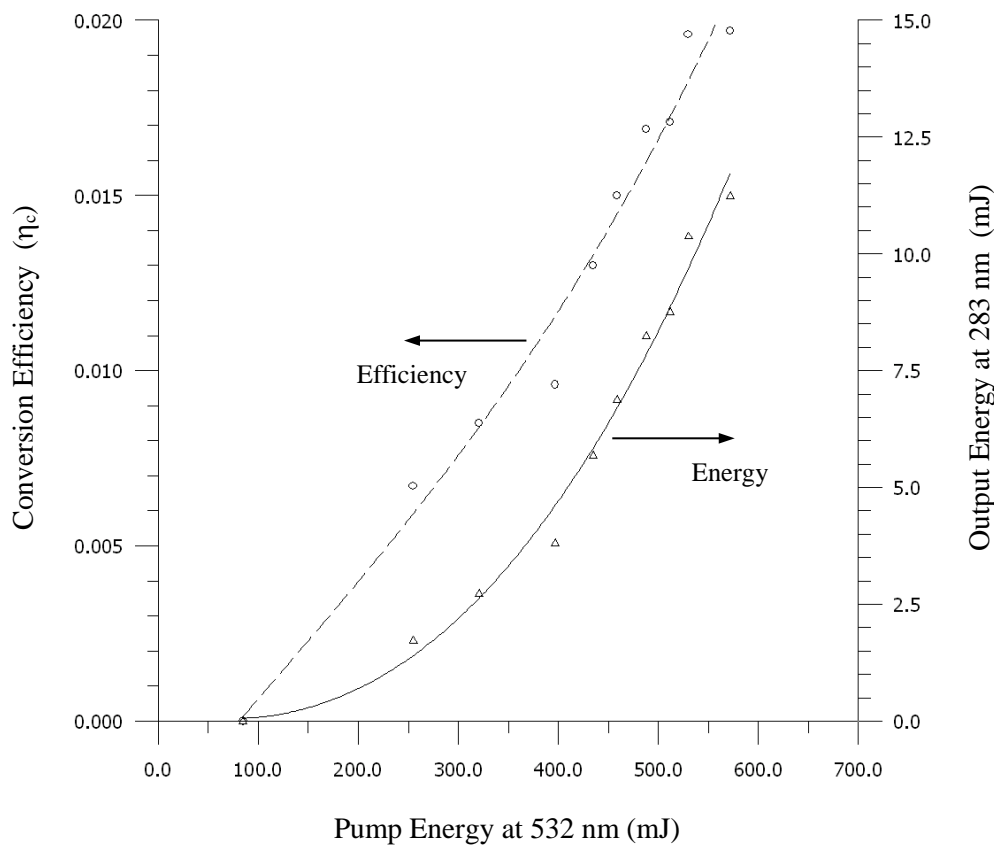


Figure E-13: Optical parametric oscillator performance generating 283 nm output. Energies listed are per pulse. YAG laser firing rate is 10 Hz. The peak conversion efficiency seen in this experiment was approximately 2.0% with a pump energy of 572 mJ and an output energy of 11.2 mJ. Both conversion efficiency and output energy were still rising with increasing pump energy.

directed to the Pellin-Broca harmonic separator. After traversing the harmonic separator, the clean 283 nm UV beam exits the OPO assembly. The remaining 1064 nm and 447 nm light exiting the oscillator passes through M209 and is captured in a beam stop (S203).

Figure E-13 shows the performance of the OPO in this configuration. The conversion efficiency is seen to be continually climbing with pump energies at this level. At a pump energy of 572 mJ, the conversion efficiency is seen to be 2.0% with an output energy of 11.2 mJ per pulse. Maximum observed output energies exceeded 12 mJ per pulse; again, this was limited by the damage threshold of the OPO crystal. Similar to the 390 nm output, the 283 nm line width was estimated to be approximately 1.5 cm^{-1} to 2.0 cm^{-1} .

E.3.2.4 Generation of 226 nm Output

In order to generate 226 nm UV for NO PLIF, the cavity is operated in the same configuration as for 390 nm production. The cavity output at 393 nm is externally mixed with the residual 532 nm pump beam to produce 226 nm light. A schematic of this configuration is shown in Figure E-14.

In this configuration, beam stop S202 is removed and a BBO crystal for type I mixing is installed in the X204 location. This crystal is tuned by rotating it around a horizontal axis that is normal to the beam path. The residual energy from the horizontally polarized 532 nm pump beam is looped around the back side of the cavity by mirrors M210 through M213 and then passed through M209 and finally X204. At the same time, the horizontally polarized 393 nm from the cavity output reflects off M209 and is also directed through X204. The path formed by mirrors M210 through M213 results in a delay that synchronizes the 532 nm pump with the 393 nm cavity emission. With proper adjustment, mixing occurs in X204 and a vertically polarized, 226 nm output is generated. This output along with residuals is steered by two right angle prisms to a single Pellin-Broca prism

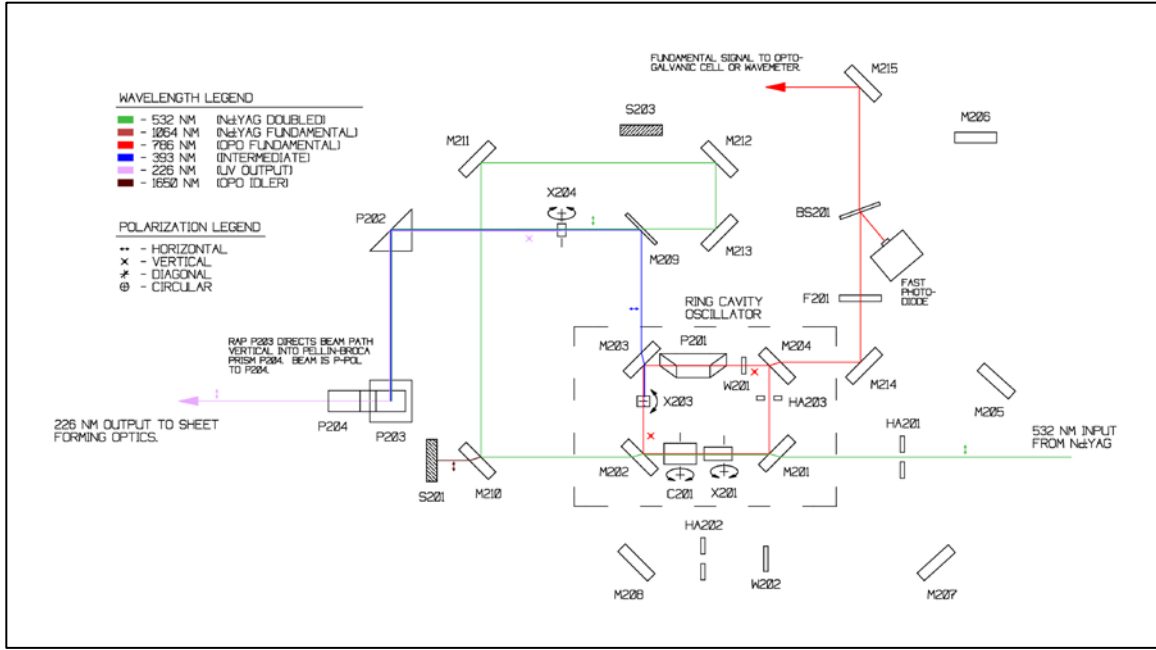


Figure E-14: Optical parametric oscillator configuration for generating 226 nm UV light for OH PLIF.

for separation. Unlike the previous cases, the desired output here is vertically polarized and requires that the Pellin-Broca prism be rotated about a horizontal axis in order to match the Brewster angle. Right-angle prism P203 turns the beam vertically where it enters the Pellin-Broca (P204) from below. The output from P204 is horizontal in direction. After separation, the unwanted residuals are stopped and the 226 nm UV beam exits the OPO assembly.

No measurements of conversion efficiency or line width were made at 226 nm. Due to the poor efficiency of mixing at short wavelengths (i.e. at 393 nm and 532 nm) the output energy was very low, reaching a maximum of only 1.62 mJ per pulse with a 532 nm pump energy of 577 mJ. In addition, the crystal mixing acceptance angle at these wavelengths is less than 0.5 mrad, which makes tuning to maximize the output energy arduous at best. Ultimately, no PLIF experiments were performed at 226 nm in the presented work. It may be possible to improve system

performance at 226 nm to support running unsteady, phase resolved PLIF experiments using NO fluorescence. This is left for future work.

E.3.3 OPO Control Software

Wavelength selection and harmonic generation optimization is achieved in the optical parametric oscillator by controlling the six Zaber T-LA28 actuators that rotate crystals X201 through X204, as well as fused silica corrector C201, and also translate mirror M204. For proper operation, the movements of the actuators must be very precisely orchestrated. Some of the crystals have acceptance angle requirements that are so restrictive that actuators must track trajectories to within a couple microns. As a consequence, simple operation of the OPO through manual adjustment was not possible.

To solve this dilemma, custom control software was written to operate the OPO. This software communicates with the actuators through an RS-232 interface using a proprietary Zaber control protocol. By design, the actuators can be connected in a daisy chain configuration allowing the use of a single computer serial port to control all devices. The software, written in C, is compiled using Borland Turbo C 3.0 and currently consists of over 3800 lines of code. The binary executable runs under DOS or the DOSBox emulator (v0.74), originally written by Peter Veenstra. Figure E-15 shows a screenshot of the interface.

The interface allows actuators to be positioned or jogged individually or together as a synchronous group. Individual movements allow fine adjustments of doubling or mixing crystals while group movements allow tracking as the OPO is tuned or scanned to different wavelengths. Calibration functions enable the operator to log optimized positions to a pair of lookup tables. One table contains the optimal relations between the position of the OPO crystal (X201) and the other actuators in the system. The second table relates the position of X201 to the fundamental wavelength of the cavity. Once these tables have been populated, a position or scan command can

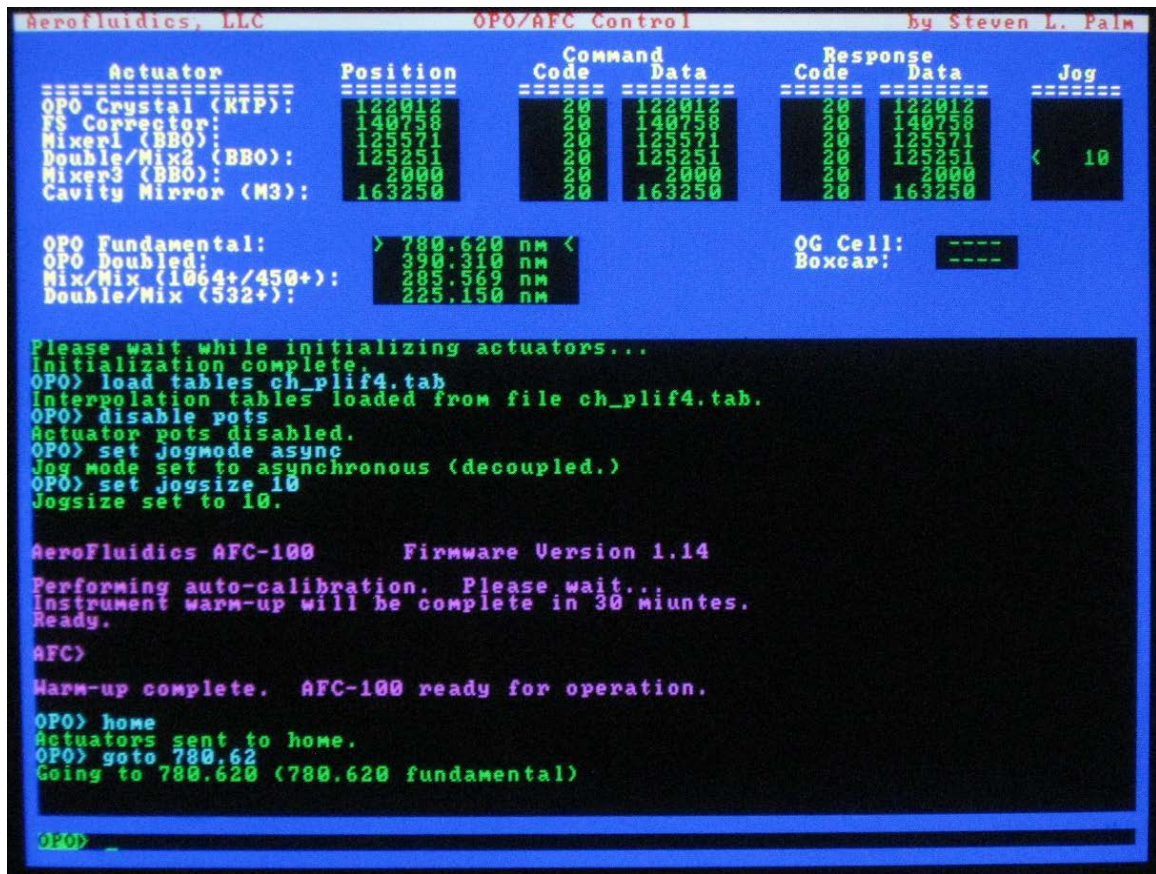


Figure E-15: Screenshot of the OPO control and interface software. The code is written in C and compiled under Borland Turbo C 3.0 for DOS.

be issued and the software will move the actuators to their necessary locations or along a trajectory based on interpolated data from the tables.

The software also incorporates minimal spectroscopic functions. Two analog inputs accept external sensor signals, one from an optogalvanic cell and another from an optional Stanford Research boxcar integrator. Spectroscopic scans can be performed semi-automatically in order to calibrate the OPO wavelength using the OG cell. Wavelength calibration is discussed in section E.3.4.

Aside from operating the optical parametric oscillator, the software package also provides the user and data storage interface for the AFC-100 acoustic forcing controller. Communications

with the AFC-100 traverse a second RS-232 serial port and incorporate a custom, hybrid ASCII/Binary protocol. This interface is discussed in more detail in appendix F.

In addition, the control software also provides the control interface for the acetone seeding system. Functional details of the seeding system can be found in appendix C. The command structure and syntax can be found in appendix F.

Finally, the code also provides the interface and automated control of the Princeton Applied Research 5206 dual phase lock-in analyzer used in the acoustically driven chemiluminescence experiments. Further details of the interface are discussed in chapter 3 and appendix D.

E.3.4 OPO Wavelength Calibration

In order to tune the optical parametric oscillator to the precise wavelengths required while performing species-specific laser-induced fluorescence, the system requires precision calibration against a standard. This was originally accomplished by the use of an optogalvanic cell that received the 70 percent balance of the OPO cavity fundamental monitor beam (as was mentioned in section E.3.2.1). This detection system is constructed around a hollow cathode lamp (Photron model P826) with a neon gas fill; the OPO fundamental beam is directed at the ionized gas in the tube's cathode well.

A high voltage, current regulating power supply drives the hollow cathode lamp. After striking, the average current across the lamp is held constant at 12 mA using closed-loop control. The control monitors the voltage across a current sensing resistor which is in line with the lamp. The time constant of the control is long compared to any optogalvanic effect stimulated by the laser, and a filter capacitor upstream of the lamp holds the lamp voltage roughly constant during such a transient. During a laser shot, incident photons stimulate electron mobility in the ionized gas within the lamp. This mobility sharply increases when the wavelength of the photons corresponds to natural electrical transitions of the ionized gas. This change in mobility manifests

as an abrupt change in the lamp current during a laser shot. In turn, the current pulse becomes a voltage pulse superimposed on the steady voltage drop seen across the sensing resistor. This pulse is amplified and integrated using a custom boxcar integrator. The signal is recorded as the OPO wavelength is slowly scanned. A resulting spectrum is generated that can be compared with the fill gas standard electrical transitions in order to calibrate the OPO tuning.

As previously mentioned, the P826 HC lamp uses neon as the fill gas. Neon has a number of electrical transitions in the wavelength range of interest (between 720 nm and 800 nm). Table E-2 shows a list of the transitions from 760 nm to 800 nm, which were the lines used to initially calibrate the OPO in the presented work. A sample optogalvanic spectrum taken during a calibration is shown in Figure E-16. It is immediately noticed that the peaks in the spectra are quite broad. This was puzzling at first. However, it was finally surmised that although the OPO principal bandwidth was relatively narrow, the output exhibits very broad, low amplitude wings. It is believed that the very low fluences required by the OG cell in combination with the OPO's broadly distributed spectral components result in the poorly resolved spectra.

Spectrum	Wavelength Air (nm)	Relative Intensity	Configuration
Ne I	772.462	60	$2s2.2p5.(2P^<1/2>).3p - 2s2.2p5.(2P^<3/2>).5s$
Ne I	783.303	56	$2s2.2p5.(2P^<3/2>).3p - 2s2.2p5.(2P^<1/2>).3d$
Ne I	783.905	230	$2s2.2p5.(2P^<3/2>).3p - 2s2.2p5.(2P^<1/2>).3d$
Ne I	783.999	7	$2s2.2p5.(2P^<3/2>).3p - 2s2.2p5.(2P^<1/2>).3d$
Ne I	792.711	300	$2s2.2p5.(2P^<3/2>).3p - 2s2.2p5.(2P^<1/2>).3d$
Ne I	793.700	1300	$2s2.2p5.(2P^<3/2>).3p - 2s2.2p5.(2P^<1/2>).3d$
Ne I	794.318	7900	$2s2.2p5.(2P^<3/2>).3p - 2s2.2p5.(2P^<1/2>).3d$
Ne I	794.414	200	$2s2.2p5.(2P^<3/2>).3p - 2s2.2p5.(2P^<1/2>).3d$

Table E-2: List of observable neon I electrical transitions used in wavelength calibration of the OPO. These transitions were correlated with measured spectra taken with an optogalvanic cell.

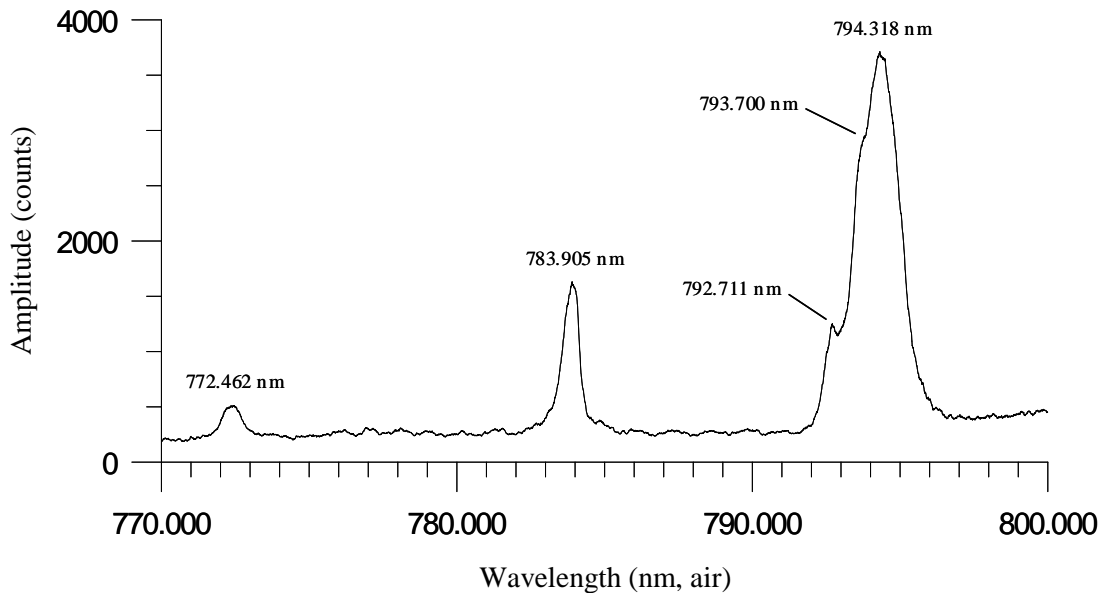


Figure E-16: Typical neon optogalvanic spectrum recorded during OPO calibration scan. The measured peaks are correlated against known neon electrical transitions in order to relate the X201 actuator position to cavity fundamental wavelength.

Nonetheless, given the spectra, a semi-automated reduction program processes the spectrum and attempts to identify the peaks. In some cases human intervention is required. Nonetheless, once the peaks are identified, a calibration file is generated for the OPO control software. This allows the user to perform single point tuning or scan operations within the OPO control software by directly entering the wavelengths of interest.

Fortunately, before serious data collection began, a Burleigh WA-4500 pulsed laser wavemeter was obtained. This unit uses interferometry signals from a pair of etalons (one coarse, one fine) to compute the input beam wavelength on a shot-by-shot basis. The device automatically calibrates itself against a single-mode, stabilized helium-neon laser once per minute. The measured laser wavelength and line width appear on screen within the control software window in real time. The acquisition of this device eliminated the need for the optogalvanic calibration scans. The wavemeter was used to measure the OPO fundamental wavelength continuously while tuning the laser and performing the experiments. This proved to be a substantial (if not invaluable) improvement to the experimental setup.

A p p e n d i x F

CUSTOM INSTRUMENTATION: THE AFC-100

F.1 Motivation and Overview

In the late 1990s, a method of measuring the unsteady combustion response of a flame or burner using phase-resolved planar laser induced fluorescence (PLIF) was developed by Pun, Palm and Culick (2000). During these early experiments, many issues arose (some technical, some logistical) which limited the amount, quality and range of the data collected.

The most fundamental shortcoming of the experimental setup was the lack of automation. The original configuration required two individuals to run the experiment, and demanded operator intervention every two minutes. The total continuous runtime to collect data for one operating condition (one burner operational point, and one drive frequency and amplitude) was roughly three and a half to four hours. The intervention required by the operators involved transitioning from sitting to standing, leaning over equipment as well as squatting to make adjustments, and then sitting again. As one can imagine, performing these actions thirty times an hour for hours on end became nothing short of torturous.

Another problem with the original setup was the way in which the acoustic drive signal was measured and recorded along with the laser shot timing signal. The measured acoustic pressure signal along with the laser Q-switch trigger were collected using a DAS-20 data acquisition card. Data was recorded continuously during each two-minute period in which PLIF images were being collected. The data was then post-processed to filter the pressure signal and determine the phase relation between the fundamental drive mode and the laser shot. The shortcoming of this method is that the data was collected continuously over the two-minute period and that the sampling rate

needed to be fast enough to provide the required phase resolution between the laser trigger and the acoustic signal. The result was spectacularly large data files that consumed a great deal of disk space but contained very little real information. In addition, the size of these files grew linearly with the acoustic forcing frequency, making data collection at drive frequencies above 100 Hertz impractical (at the time).

Finally, with the original experimental configuration it was not possible to actively control the laser timing in order to target a specific pressure phase angle for acquiring PLIF images. Instead, drive frequencies were selected that allowed the 10 Hz laser to naturally precess in its phase relation to the pressure signal. The collected data was then post-processed and sorted into N equally spaced phase bins for averaging, where the number of bins was typically 12, but sometimes as high as 24. Even so, with 24 bins, it was possible to have images with phase differences as great as 15 degrees being averaged together. The ultimate consequence was spread in the data and a resulting uncertainty that was undesirable.

At the inception of the new experimental apparatus it was decided to resolve these issues along with others by designing and constructing a custom instrument. Not only would this instrument incorporate hardware and features to address the issues mentioned above, but it would also handle functions previously performed by small, separate circuits. One of these circuits controlled the acoustic drive frequency and amplitude. It incorporated a PID closed-loop controller to hold the amplitude of the acoustic standing wave in the chamber at a constant level. Another circuit was responsible for processing the signal from a pyroelectric energy detector or a photodiode to measure and record the UV laser energy on a shot-per-shot basis. This data was used later in the post-processing step to apply corrections to the PLIF images based on the incident UV laser energy.



Figure F-1: First version of AFC-100 acoustic forcing controller. (Right) – assembled enclosure with front panel showing. (Left) – cover removed revealing the main circuit board.

F.2 Base Instrument – Acoustic Forcing Controller

In order to keep the task from being overwhelming, it was decided to build the instrument in stages. The first stage incorporated the foundational components, which included the enclosure, power supply, front panel interface, and microprocessor controller. It also included the input channel conditioning and amplification as well as the closed-loop acoustic forcing controller. The completed package was dubbed the AFC-100. Figure F-1 shows pictures of this early version.

In the early stages of the instrument development, attempts were made to minimize the cost of construction by designing around all through-hole components. This would allow the board assembly to be performed in house with a conventional soldering station versus requiring operations by an outside vendor to IR solder surface mount components. This goal was achievable in the first stage as can be seen in the left photograph above. Unfortunately, later stages required components that could not be obtained in any footprint other than surface mount. This resulted in additional capital expenditures later in the instrument development to pay for custom tooling and outside services.

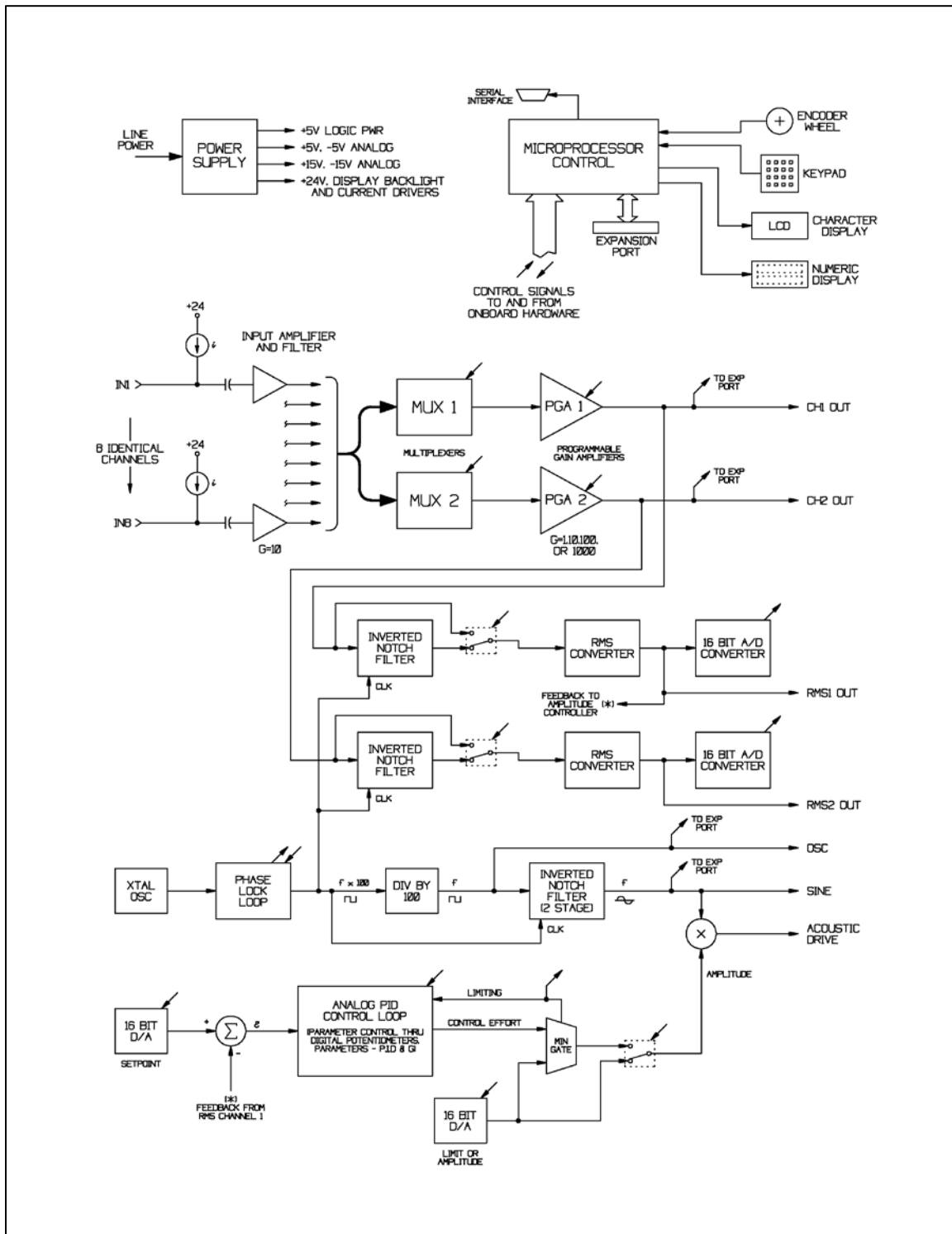


Figure F-2: Block diagram of the base system of the AFC-100 acoustic forcing controller.

Figure F-2 shows a block diagram of the base instrument. The unit is constructed from seven fundamental sections. These are:

- i) The Microprocessor Based System Controller
- ii) The Input Signal Conditioning Stage
- iii) The Signal Selector and Amplification Stage
- iv) The Measurement Stage
- v) The Oscillator Section
- vi) The Amplitude Control Section
- vii) The Power Supply

The basic function of these sections is discussed below.

F.2.1 – Digital Controller

At the heart of the AFC-100 is a system controller based on a Zilog Z180 microprocessor. The Z180 is assembled on a small circuit board with a Flash ROM, static RAM, real time clock IC, bus interface connector, and assorted interconnect logic. This “core module” is then plugged into a connector on the base system, allowing it to interface with the rest of the logic in the AFC-100.

The main board incorporates a pair of Xilinx XC95108 complex programmable logic devices (CPLDs) to implement special logic functions and to interface to the balance of components on the main board. Design and implementation of the CPLD logic was accomplished using the Xilinx Foundation development suite. Programming was performed *in situ* through the JTAG programming interface on each device.

Also included on the mainboard are logic and connectors for interfacing the controller to a rotary hand-wheel encoder, a 4x4 keypad, a 4x20 LCD alphanumeric display and a separate, larger LED numeric display. These components form the man-machine interface for the AFC-100. The keypad contains digits 0 through 9, a decimal point, [Enter], [Escape], [Delete], [Up-Arrow], and

[Down-Arrow]. These allow the operator to scroll through on-screen menus, select functions and enter specific parameters. The encoder wheel also aids in menu navigation while additionally allowing operating parameters to be changed smoothly (i.e. semi-continuously).

F.2.2 - Input Signal Conditioning

The signal input stage of the instrument contains eight identical channels, labeled IN1 through IN8. Each channel contains an integral current source to supply power for a piezoelectric pressure transducer or for connection to an electret microphone. The first two channels are configured for pressure transducers and are accessible through BNC connectors on the front face of the instrument. The remaining six channels are setup for attaching condenser-type elements and have interface connectors on the rear panel.

Each channel also incorporates a non-polar blocking capacitor and bleed resistor that forms a high-pass network. These networks block the supply bias while allowing the signals of interest to pass to the input amplifiers. The corner frequency is less than 0.02 Hertz resulting in virtually no phase shift at the lowest frequency of interest, which is 20 Hertz. Non-inverting gain stages constructed around TL034A operational amplifiers accompany each input channel, providing times-ten amplification prior to proceeding.

F.2.3 – Signal Selection and Amplification

The eight inputs are then fed, in parallel, to two MAX4708 eight-to-one-line multiplexers for signal selection. The outputs of these two selectors form the starting points of the two internal signal channels. Each output is directed next to a PGA202 programmable gain instrument amplifier. Gain steps for these devices are x1, x10, x100, and x1000. The resulting total gain range of the input signal conditioning, selection and amplification sections is 10^1 through 10^5 in decade steps. These two conditioned channels are routed to different sections of the instrument as well as

to two BNC connectors on the front face. The connectors are labeled CH1 and CH2. The total gain error for either channel is less than 0.15% for frequencies up to 5 kHz. The total phase error at 5 kHz is less than 0.3 degrees. The full power bandwidth of each channel is greater than 400 kHz for gains up to 1000 and greater than 100 kHz for a gain setting of 10000.

F.2.4 – Measurement Stage

One terminus for the conditioned signals is the measurement section. Here the RMS amplitude of each signal is measured using an Analog Devices AD637 precision RMS to DC converter. The time constant of the each converter is configured to be approximately 250ms. This results in a maximum measurement error of 0.2% at the lowest frequency of interest, which is 20 Hz. The DC output of each block is directed to a MAX195 16-bit A/D converter for measurement and display by the controller. The RMS analog signals are also buffered and fed to BNC connectors on the instrument front panel.

Input filtering for the stage is also provided using an LMF100 switched-capacitor filter IC. The device incorporates two independent filter blocks per integrated circuit. One block is used for each channel. Each block is configured as a second-order inverted notch filter (bandpass) with a Q of approximately 20. This produces an attenuation of 30 dB for the nearest harmonic of the signal of interest. The filters are driven with a clock signal derived from the onboard oscillator. This allows the notch to track the acoustic drive frequency. Analog switches are used to independently route the incoming signals either through the filter networks, or around them. Consequently, the resulting measurements made by the RMS converters are either of the broadband amplitude or of the amplitude of the fundamental mode.

F.2.5 – Oscillator Section

An onboard phase-lock-loop (PLL) stabilized oscillator is used as the principal timing reference for the instrument. It is responsible for producing the acoustic drive signal as well as the clock signals for the switched-capacitor filters. The PLL uses a 1.0 MHz crystal oscillator as a master reference.

The acoustic drive frequency is generated by running the phase-locked oscillator near its maximum operating limit, at a frequency that is 2×10^N times the desired signal (where N is a non-negative integer). The oscillator is divided by two with a flip-flop to insure symmetry, and then divided by decades to reach the desired output frequency. This maximizes the resolution of the oscillator and also generates the necessary x100 clock required by the filter blocks. The total tuning range spans from 20 Hz to 5 kHz. From 20.00 Hz to 49.99 Hz, the frequency is adjustable in steps of 0.01 Hz. From 50.0 Hz to 499.9 Hz, the minimum step size is 0.1 Hz. For frequencies of 500 Hz and above, adjustment can only be made in single Hertz steps.

Passing the oscillator square wave through a two-stage inverted notch filter generates the sine wave for the acoustic output. Each stage is configured similarly to those used in the channel filters. The resulting attenuation at the nearest harmonic of the fundamental is 60 dB, or one thousand times. As a result, it is essentially only the Fourier component of the fundamental that is retained, producing the sine wave. The two switched-capacitor filter blocks are clocked 180 degrees out of phase to reduce switching noise.

F.2.6 – Amplitude Control Section

In order to control the amplitude of the acoustic forcing in the test section, the sine wave is combined with a DC control-effort signal in an AD534 precision analog multiplier. The result is that the sine wave is simply scaled in amplitude by the control effort. The signal is then directed

to a BNC connector on the rear of the instrument, which is ultimately connected to a power amplifier feeding the acoustic drivers.

Under conditions of closed-loop control, an analog PID controller generates the control-effort signal. The set-point signal is produced through a MAX541 16-bit D/A converter. The difference between this signal and the measured CH1 RMS signal produces the error signal at the input to the controller. The controller is implemented with four gain parameters labeled P, I, D and G. Here P, I, and D are the traditional gains for the proportional, integral and derivative terms. The G parameter is a loop gain that scales all parameters. In the circuit, the gains are implemented through a Dallas Semiconductor DS1844 digital potentiometer IC. The IC contains four individual potentiometers, each constructed as a 64-step ladder. In the control system, the potentiometers are used in a voltage divider configuration, allowing the gains to span from zero to maximum.

The control system also implements a limiter to prevent the control effort from swinging to an excessive value in the event of controller instability. The limiting value is generated through another MAX541 D/A converter and is directed in parallel with the control signal through a min-gate circuit. Alternatively, the operator is allowed to directly set the acoustic output amplitude through this same channel. This is accomplished through analog switches that direct the D/A signal directly to the analog multiplier.

F.2.7 – Power Supply

An onboard power supply generates the necessary voltages for the entire system. To ensure very low noise, all the voltage rails are produced through linear regulation. Three separate transformers produce the input AC voltages to the board. Each transformer covers a different voltage range, allowing the linear regulators to operate with lower overhead, thus producing less heat. The inputs from the transformers are rectified and then passed through PI-network filters to minimize line-side ripple to the regulators.

The regulated DC voltages that are generated are +5 VDC for logic power, ± 5 VDC for low-voltage analog systems, ± 15 VDC for high-voltage analog sections, and +24 VDC for current drivers and the alphanumeric display backlight. The +5 volt rail for the analog and digital sections are derived from the same source; however, region isolation is maintained and noise coupling from the digital to analog components is mitigated through the use of inductive elements.

F.3 AFC-100-EX1 – Phase Targeter Expansion

After the base system was constructed, programmed, debugged and calibrated, work began on the expansion board to perform phase targeting and pressure signal data collection. In designing the expansion, it quickly became clear that it would not be possible to maintain the strategy of using only through-hole components. Board space was at a premium and some components, such as the high-speed, high-accuracy analog-to-digital converters were simply not available in any package other than surface mount. As a result, the board design was hybridized, containing both surface mount and through-hole components. Given the space constraints, SMT components were distributed on both sides of the board.

Figure F-3 shows a picture of the phase targeter board while Figure F-4 presents a block diagram of the board level architecture. The vast majority of custom logic functions are implemented in a Xilinx XC95216 SMT CPLD shown at the right hand side of the diagram. A functional block diagram of the CPLD implemented logic is shown in Figure F-5. The primary functions of the expansion can be divided into four sections:

- i) The Pressure Signal Conditioning and Conversion Block
- ii) The Data Collection Timing and Storage Subsystem
- iii) The Laser and Camera Timing Control Block
- iv) Laser Energy and Timing Measurement Block

Discussions of each of these blocks are given in the following sections.

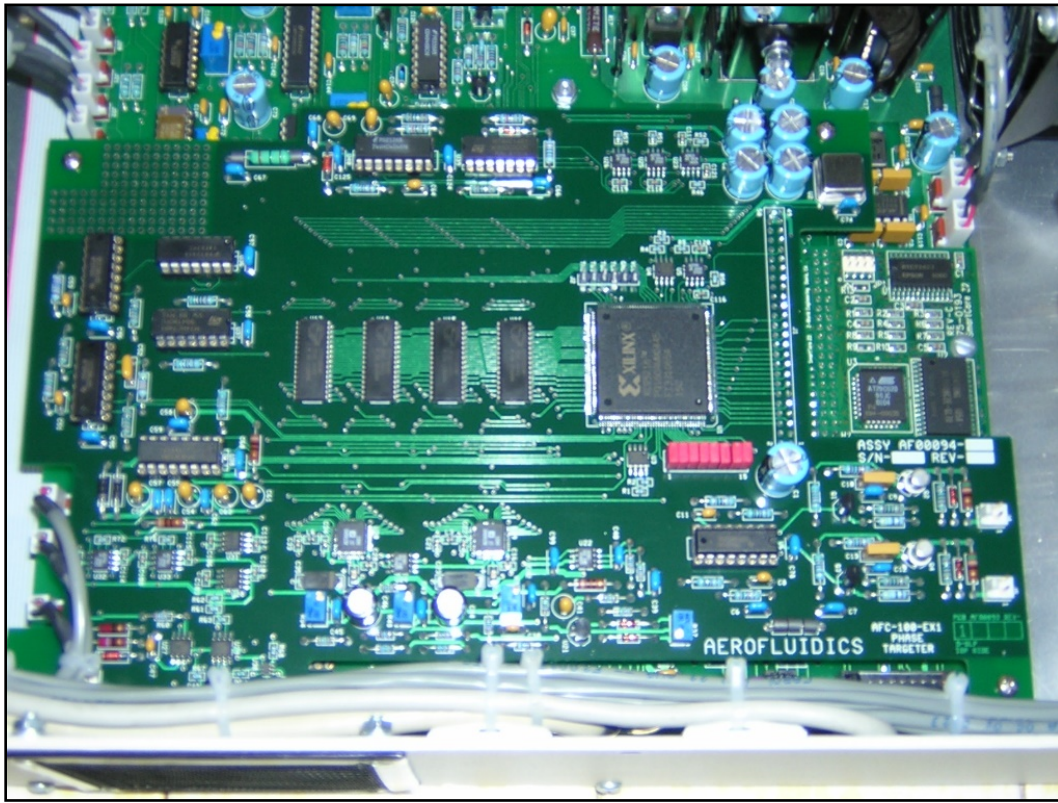


Figure F-3: EX1 phase targeter expansion board as it was being installed in the AFC-100 instrument. The large, square integrated circuit is the Xilinx CPLD. To the left are the four 128K x 8 static RAMs for storage of the acoustic waveforms.

F.3.1 – Pressure Signal Conditioning and Conversion

The amplified (but unfiltered) pressure signals collected on the base system are routed to the expansion board where they are scaled properly for measurement by high speed, high precision analog-to-digital converters. The devices used are a pair of Analog Devices AD7484 14 bit, parallel output, SAR converters. These devices incorporate integral track-and-hold amplifiers to stabilize the signal at the start of conversion. Conversions are performed using a proprietary pipelined successive approximation algorithm resulting in a one-sample latency. Corrections for this offset are made elsewhere in the circuit and are discussed later. Converter throughputs are as high as three million samples per second.

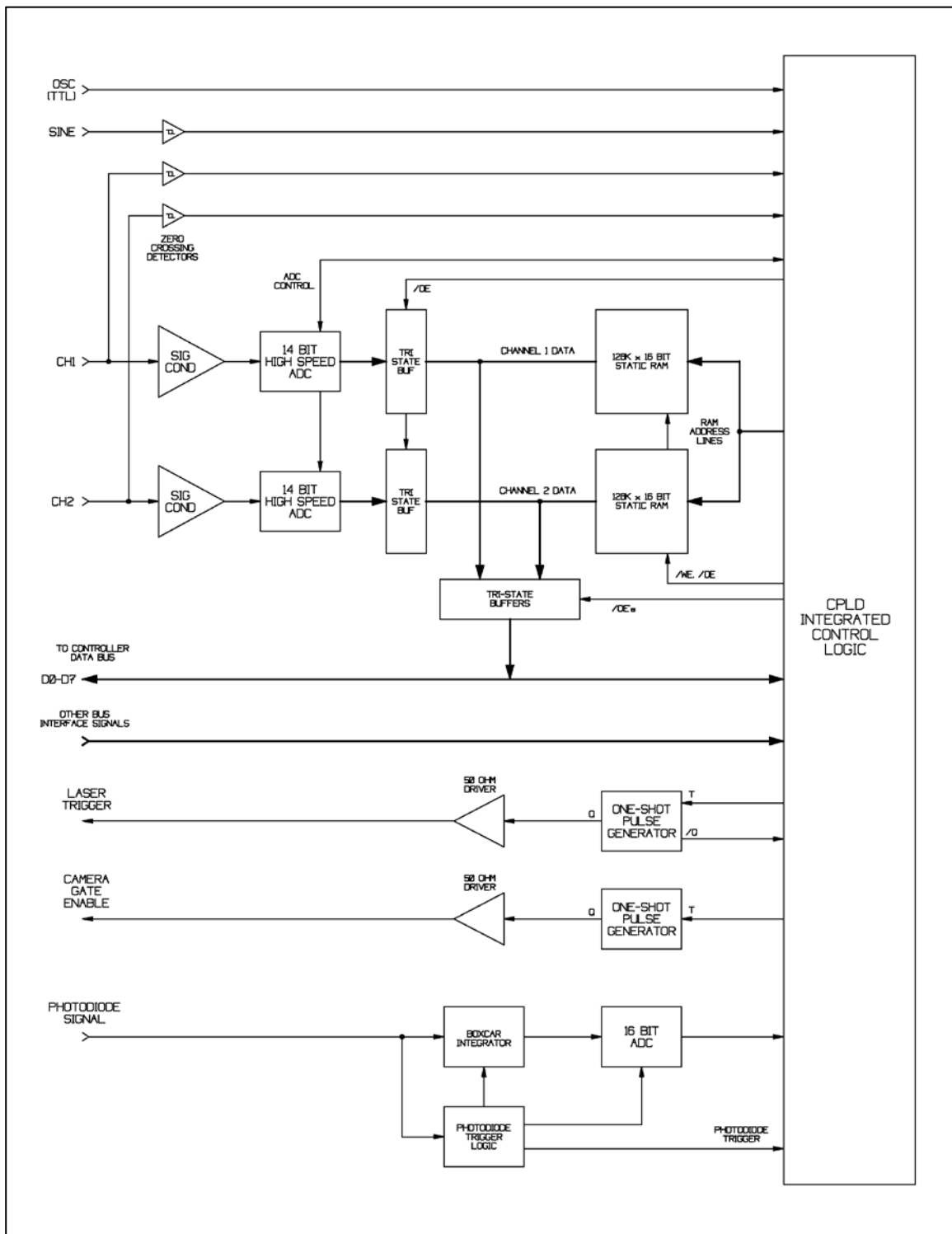


Figure F-4: Block diagram of the board level structure of the AFC-100-EX1 phase targeter expansion.

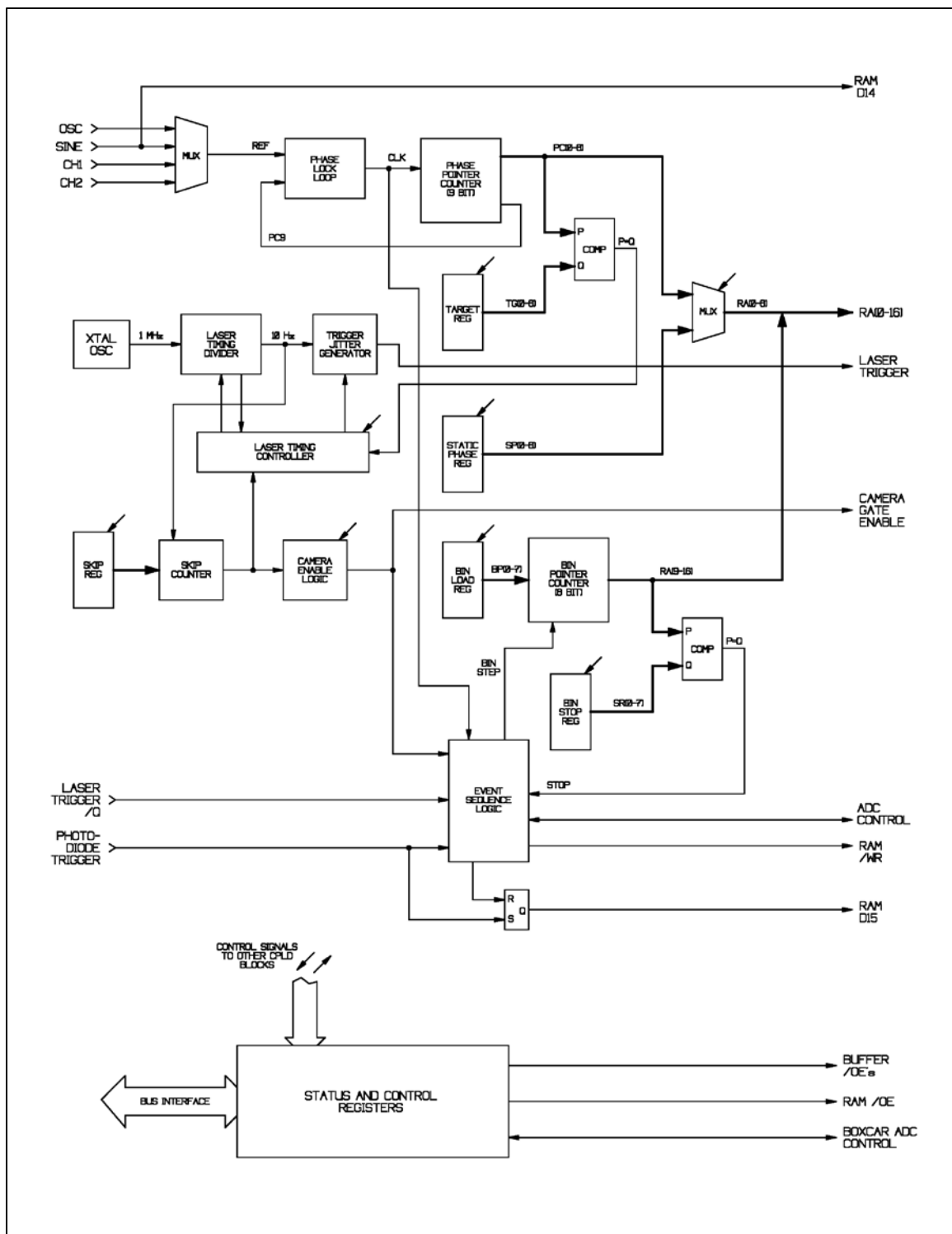


Figure F-5: Block diagram of the logic implemented in the phase targeter CPLD.

Great care was taken in the circuit layout around the analog to digital converters. A four-layer circuit board was used with solid signal-power and signal-ground planes incorporated in the middle layers around the signal conditioning and converter sections. Rigorous power filtering and bypassing techniques were employed (as per the Analog Devices design guidelines) to maximize the signal-to-noise-and-distortion ratio (SINAD). It is estimated that at the sampling frequencies of interest, the converter system SINAD is approximately 78 dB, compared with the theoretical limit of an ideal 14 bit converter which is 86 dB.

F.3.2 – Data Collection Timing and Storage

Data collection and storage from the two analog channels constitutes a primary function of the phase targeter expansion board. As mentioned earlier, a principal goal of the system is to collect the data needed in order to evaluate the combustion response to the applied acoustic field, while simultaneously eliminating the volumes of useless interim data that were collected in previous experiments. To accomplish this, only data in the time period around the laser shot is stored.

In practice, a phase-locked sample-rate clock is synthesized at a frequency that is 512 times that of the acoustic drive mode. During an imaging laser shot, 512 samples from each converter are stored in memory. Since 512 is a 2^N number (i.e. $2^9 = 512$) and since the drive frequency and all of its harmonics are periodic on this window, a fast Fourier transform (FFT) can be performed directly without the inaccuracies introduced by padding data or applying windowing functions. The details of this implementation are given below.

The collected data is stored in on-board static RAM that is organized into two banks, one for each channel. Each bank is 128 Kbytes by 16 bits in size. The lower 14 bits store the output of the associated analog-to-digital converter while the upper two bits contain information related to the drive phase and laser shot timing. Each bank, in turn, is divided into 256 bins, each containing 512 sample words. Communication with the memory is controlled by two sets of tri-

state buffers. One set directs the data from the ADCs to the memory while the other set allows the RAM to communicate directly with the system data bus. This interface can be seen in Figure F-4.

To generate the aforementioned divisions, the RAM address lines are split into two groups. The lower nine address lines are driven by either a nine-bit phase counter or from a nine-bit phase pointing register. A two-to-one multiplexer controls the selection between these two. The upper eight address lines are driven from a bin pointing register/counter. Together, these span the full 17 bit address space. This architecture can be seen in Figure F-5. Prior to data collection, the bin counter is loaded with the value of the first bin in the sequence. Next, a stop register is loaded with the bin value at which data collection should be terminated. During the collection process, the bin counter advances upward in single increment steps, starting from the loaded value and terminating at the stop value.

Also while in collection mode, a voltage controlled oscillator (VCO) drives the phase counter. The most significant bit of the counter is phase locked with the input reference signal from the acoustic drive system. The output from the phase comparator is filtered and fed to the input of the VCO. The result is that the VCO drives the counter at a frequency that is 512 times the acoustic forcing frequency, and phase feedback locks the counter in such a way that the initial count at zero corresponds with the rising edge of the reference signal.

Data collection is initiated by first setting the “ready” bit followed by the “collect” bit, both in the control register. Slightly more than one acoustic drive cycle must pass between the setting of the “ready” bit prior to setting the “collect” bit. This assures that the circular buffer of the first bin has been populated. Once recording begins, signal data from the ADCs is stored in RAM within the current bin as the phase pointer continuously counts in a circular manner. This amounts to a circular buffer for each channel. When a laser shot is detected by the photodiode, the corresponding trigger sets the MSB of each data channel for the associated data words. This marks the location in the acoustic cycle where the laser shot occurred and where the PLIF image was taken. Once

these words are written to memory, the bin pointer is automatically incremented to the next bin. If the value in the bin pointer prior to incrementing is equal to the value in the stop register, then the auto-increment logic also clears the “collect” bit, stopping data collection.

F.3.3 – Laser and Camera Timing Control

Generation of laser and camera timing signals is accomplished through clock division and delay gates implemented in the EX1 CPLD. This logic can be seen in the block diagram presented in Figure F-5. Here, a 1 MHz crystal oscillator is passed through a clock divider in order to produce the master timing reference. The fundamental output of this divider is a 10 Hz clock that is fed to both the laser trigger control logic as well as the camera timing control logic.

The laser trigger logic incorporates a timing control block and a jitter generator. It offers two modes of operation. The first is free-running mode. In this state, the jitter generator is disabled and the 10 Hz clock from the timing reference is fed directly to the laser trigger output. This fires the laser at 10 Hz, but asynchronously to the acoustic drive signal.

The second mode is for targeting operation. During targeting, the laser timing is jittered in order to have the laser shot correspond with a specific phase angle of the acoustic drive. However, when operating in this mode, the average pulse rate of the laser is still regulated by the 10 Hz reference. Consequently, the average thermal load on the laser components (principally the Nd:YAG rods) is held constant keeping the oscillator cavity in tune and output beam quality optimized.

Targeting is achieved by use of a “target” register that holds the value of the phase angle of interest. This register value is compared with the output of the phase-lock-loop driven phase pointer. When the 10 Hz master timing reference indicates that a laser pulse is required, the timing control logic checks to see if the camera gate will be enabled on this shot. If not, the jitter generator is bypassed and the pulse is fed directly to the laser trigger output. However, if the camera gate is

enabled and an image will be collected on this pulse, the “operate” latch is set in the jitter generator. The jitter generator then monitors the output of the phase target comparator. When a match is indicated, a pulse is sent to the laser trigger output and the “operate” latch is cleared.

Control of the “camera gate enable” signal is accomplished through the same “ready” and “collect” bits mentioned in section F.3.2. In addition the “skip” register controls how often data and images are collected. More specifically, the value in the “skip” register indicates how many laser shots will be skipped between camera images. If the register value is zero, an image is taken during every laser shot. Additionally, it is this same signal that also inhibits or enables the advancement of the bin pointer for acoustic data collection. This results in the camera images and acoustic data sets being synchronized.

The inclusion of the “skip” register in the phase targeter was necessary due to the limited frame rate of the ICCD camera. At full resolution, the camera requires 270 ms to collect a frame. As a consequence, if full images are being acquired, data can only be collected on every third laser shot. In practice, only sub-images are collected from the ICCD. In this case, the ICCD controller has the option to discard the unneeded data, reducing the collection time to less than 200 ms. Under these conditions, data can be recorded every other shot.

It should be noted that the “camera gate enable” signal does not directly trigger the ICCD camera. Instead this signal is fed to an external gate control box where it toggles a flip-flop that allows a single gate trigger pulse to pass. It is actually the YAG laser Q-switch signal that acts as the trigger. Passing through this gate controller box when enabled, it initiates gating of the camera intensifier. The camera’s own internal timing generator controls the width of the gate pulse.

F.3.4 – Laser Energy and Timing Measurement

Shot-by-shot energy measurements are collected by the instrument using a high speed photodiode. A small portion of the UV beam headed toward the test section is sampled by a fused

silica window which is rotated close to the Brewster angle. The weak reflection from the window is directed through a ground quartz diffuser and into the photodiode.

A high speed comparator is used to measure the timing of the laser emission from the photodiode signal. As mentioned earlier, this bit is stored in the MSB of both channels of the storage RAM during data collection, providing shot timing information in relation to the measured acoustic signal. A shift register in the sequence logic is used to correct the shot locator bit for the one-cycle latency in the high-speed ADCs. In this way the shot indicator is synchronized with the acoustic data.

The comparator output is also used to trigger a very high speed boxcar integrator circuit which is integral to the EX1. This circuit collects the signal from the photodiode, integrates it over the pulse duration, and then passes it onto a MAX195 16 bit analog-to-digital converter. The data is then converted to a real energy value using a calibration parameter and then made available for viewing on the front panel. In addition, pulse energies measured during data collection are also stored along with their respective acoustic data sets.

F.3.5 – Data Retrieval and Storage

Once a data collection sequence is complete, the interface buffers connected to the storage RAM are transitioned to allow interface to the Z180 controller. The data is combined with other pertinent information (such as the laser shot energy, the acoustic forcing frequency and amplitude, and a host of other controller setup parameters), arranged into packets, and then transmitted to the central control PC through an RS-232 serial connection. Data is transmitted at 19.2 kbaud using a custom, lossless communications protocol that employs CRC and re-transmission on error. Packets can be transmitted in either ASCII or binary formats; however, binary communication is nearly always used as it provides the best transfer rate. The AFC-100 data packets and the corresponding images are collected from the ICCD and recombined during post-processing.

F.4 AFC-100-EX2 – Input Filter Expansion

After using the instrument for a period of time an operational difficulty was uncovered. Under certain experimental conditions, it was found that the RMS measurements of signal amplitude were sometimes incorrect. Not only did this provide erroneous data, but it also caused anomalous behavior in the automatic gain control system and wandering in the closed-loop control of the acoustic amplitude. Examination of the captured acoustic waveforms revealed that the amplified input signals were clipping against the supply voltage rails. This was due to a drift in the DC component of the signals just ahead of the programmable gain amplifiers.

Each signal channel of the AFC-100 incorporates a high-pass filter to block the DC bias generated by the input current sources, as well as any offset present in the first stage amplifiers. The corner frequency of these filters is approximately 0.02 Hz. Since the filters are simple RC types, it was necessary to have a very low corner frequency to avoid corrupting the signal phase at the lowest frequency of interest, which is 20 Hz. Placing the corner frequency at 0.02 Hz provided three decades of separation.

Unfortunately, the investigation into the measurement errors revealed that signals between 0.2 and 1.0 Hz were present at the input. These long-period signals passed through the input filter and were superimposed on the acoustic waveform. It was determined that these fluctuations were due to thermally driven convection currents in the test chamber and were only present at higher firing rates of the experimental burner. In order to solve the problem and eliminate the signal clipping it was necessary to construct an input filter expansion board; this was the EX2.

A picture of the EX2 expansion is shown in Figure F-6 while a block diagram of its basic architecture is presented in Figure F-7. The expansion was designed to interface with the system expansion bus while also intercepting the input signals at the programmable gain amplifiers. To accomplish this, the EX1 phase targeter board was raised and the oddly-shaped EX2 filter board

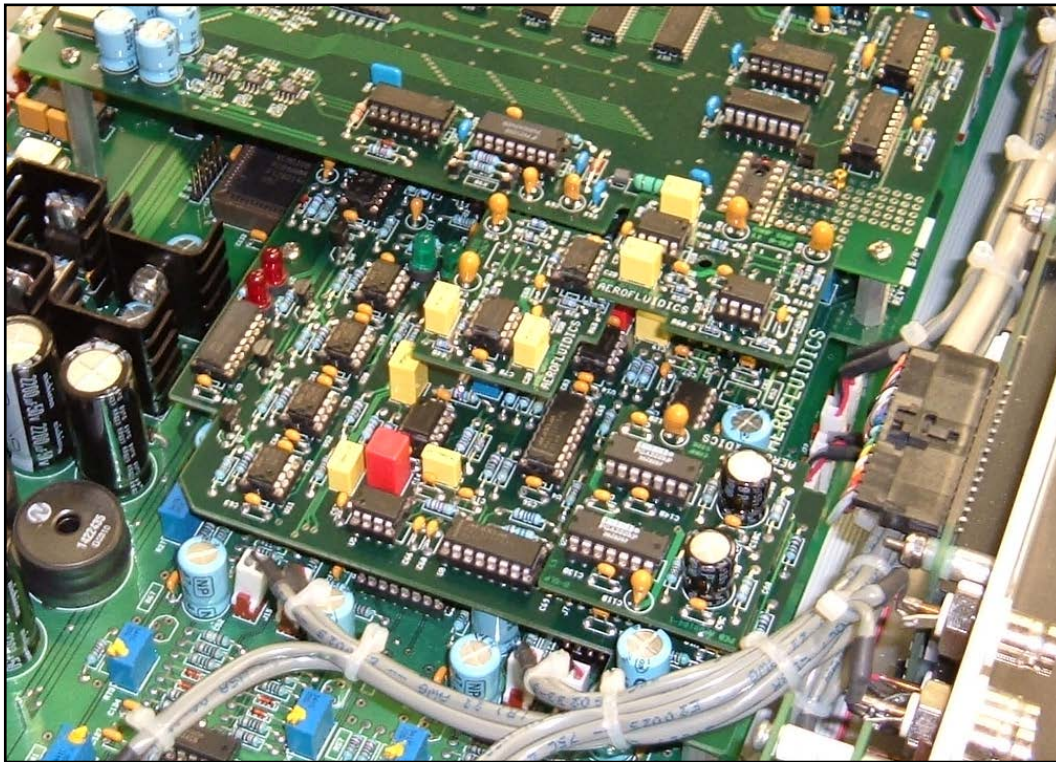


Figure F-6: EX2 input filter board as installed in the AFC-100 instrument. The unit is partially sandwiched between the mainboard and the EX-1 phase targeter expansion. A couple of mistakes in the initial layout resulted in the addition of three small daughter boards to institute corrections.

was slipped between it and the main board. The PGA202 amplifiers on the main board were removed and replaced with IC mezzanine connectors that communicated the signals up to the expansion. The programmable gain amplifiers were reinstalled in sockets on the EX2.

The expansion incorporates three filters per channel. Two of these are traditional, linear, analog filters – one high-pass and one low-pass. The third filter is a non-linear, heuristic network dubbed the “bump” filter. All the filters are in the signal path ahead of the instrument amplifier. Each filter is independently selectable to be included or excluded from the path. In addition, a set of comparators monitors the output of each instrument amplifier to look for signal clipping or saturation. Finally, RMS to DC converters coupled to 16 bit ADCs also monitor the amplifier

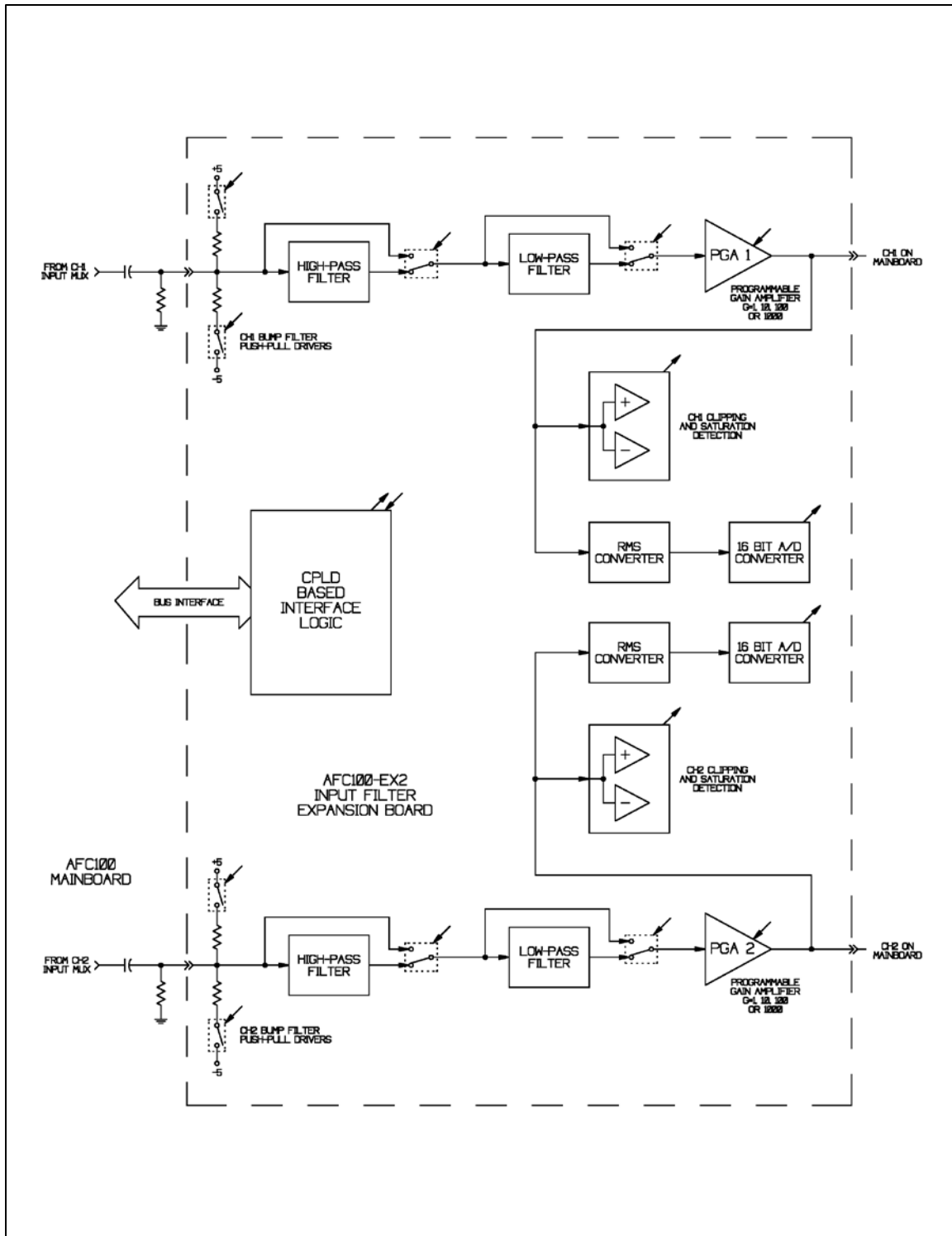


Figure F-7: Block diagram of the EX2 input filter expansion board. Components outside of the dashed line are on the AFC-100 mainboard. The mainboard RC high-pass filters are shown to clarify the interface to the “bump” filters.

outputs. These are identical in configuration to the ones present on the AFC-100 mainboard; however, the units on the EX2 monitor the amplifier outputs directly versus being downstream of the notch filters. These, along with the clipping monitors, provide much better information to the automatic gain control (AGC) system.

F.4.1 – High-Pass Filter Network

The input high-pass filter network constitutes the most critical component in the EX2 expansion. It was necessary to design a high-pass filter that would preserve phase down to a frequency of 20 Hz while still having a very steep roll-off below 3.0 Hz. Accomplishing this with an analog filter proved to be challenging. The goal was to reach an attenuation level of roughly 40 dB at 1 Hz. Figure F-8 shows a best effort Chebyshev filter with 0.1 dB maximum pass-band ripple.

This second order filter meets the requirements for attenuation. At 20 Hertz, the gain is 0.992 while at 1.0 Hertz the gain is 0.007. However, the phase error at 20 Hertz is almost 49 degrees and at 100 Hertz is still greater than 8 degrees. This was clearly unacceptable.

After some investigation it was decided to implement the filter in two stages. The first stage would be the high-pass block that generated the attenuation at low frequencies. The second block would be the phase correction stage that would be used to neutralize the phase error generated by the first stage. It was initially believed that the second stage could be generated using a traditional all-pass filter, producing the phase correction with unity gain throughout. However, it was quickly realized that a causal, all-pass filter can only produce an increasing phase lag with increasing frequency. This was the opposite of what was required. What was truly needed was the phase response of a pair of left-half plane zeros with the resulting gain change being mitigated. In reality, the system gain between 1.0 Hz and 20 Hz was not critical as long as it was not too large

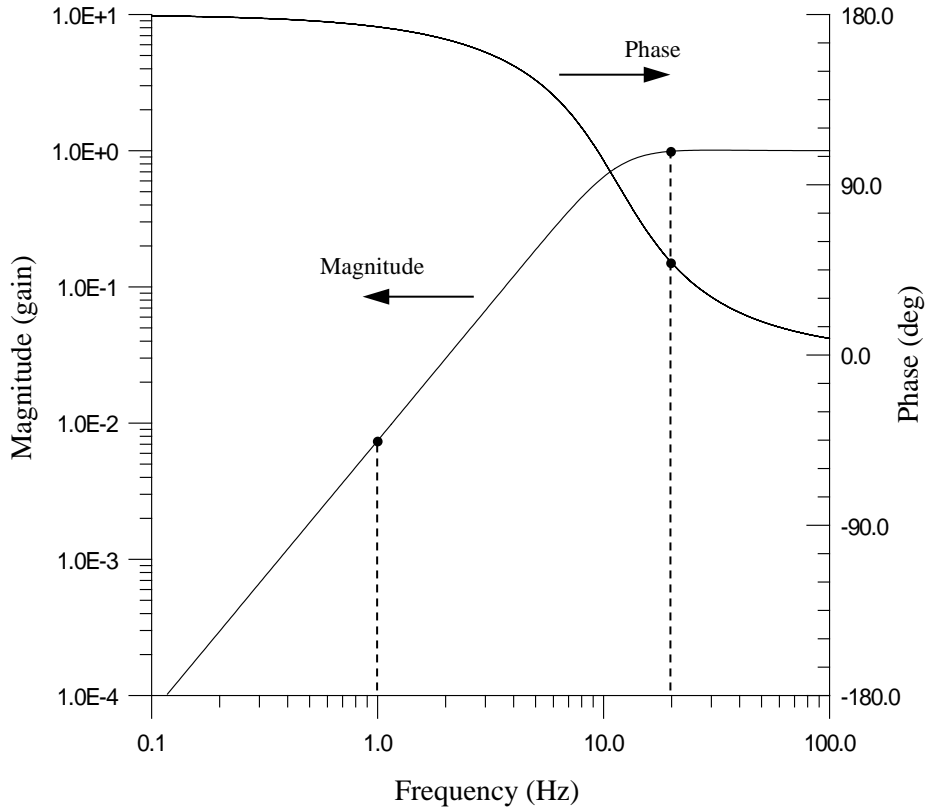


Figure F-8: Best effort 2nd order Chebyshev filter. This filter meets the amplitude attenuation requirements but is highly phase distorting at frequencies less than 100 Hz.

and the gains beyond this range met the requirements stated above. Consequently, it was possible to introduce a pole pair at a frequency slightly lower than that of the LHP zeros in order to return the slope of the gain curve to zero. In this way, a sacrificial but still acceptable change was made to the interim gain in order to achieve the required phase correction. Through an iterative design process, the filter transfer functions were chosen to be:

$$(F-1) \quad G_1(s) = \frac{s^4}{[s^2 + (45.26)s + (1114.8)][s^2 + (5.753)s + (342.47)]},$$

$$(F-2) \quad G_2(s) = K \frac{s^2 + (86.90)s + (5864.4)}{s^2 + (51.00)s + (1954.8)} \quad K \approx 3.0,$$

$$(F-3) \quad G_3(s) = G_1(s)G_2(s).$$

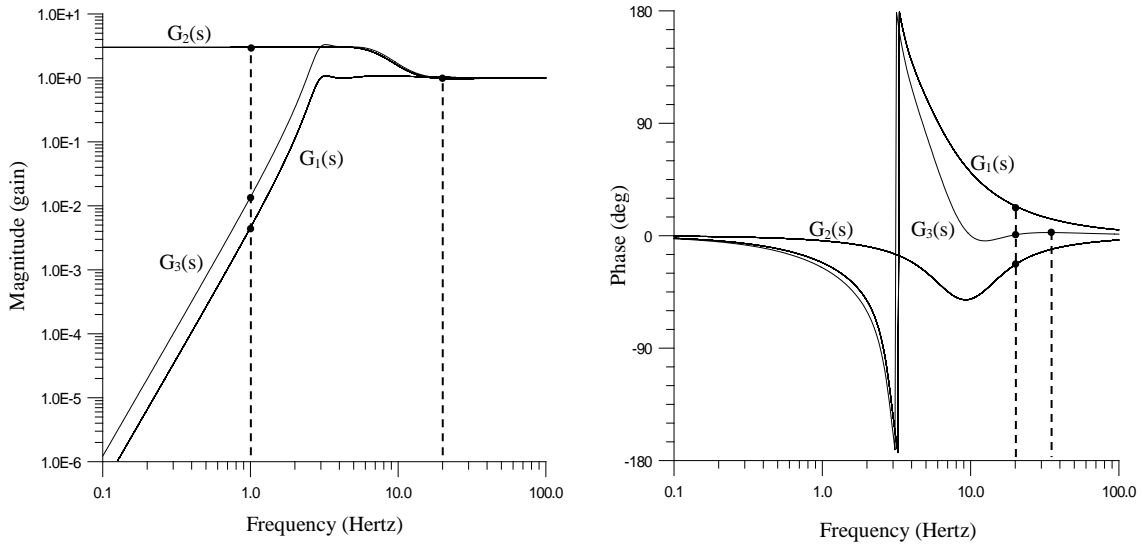


Figure F-9: Magnitude and phase responses of the two filter blocks, $G_1(s)$ and $G_2(s)$, as well as the response of their product, $G_3(s)$. The maximum errors above 20 Hertz for $G_3(s)$ are about 1.3% for magnitude (at 28 Hertz) and 2.5 degrees for phase (at 33 Hertz).

Here, $G_1(s)$ is the transfer function for a fourth order Chebeshev high-pass filter with the corner frequency located at approximately 3 Hertz. This filter was implemented in two operational amplifiers stages using the Sallen-Key topology. The second transfer function, $G_2(s)$, provides the necessary phase correction using a closely-spaced pair of complex poles and complex zeros. The pole-pair corner frequency is located at 7.0 Hertz, while the zero-pair corner frequency is at 12.2 Hertz. The Q for each pair is 0.87. The transfer function is generated using a Tow-Thomas biquad topology. Figure F-9 shows the response of each filter section along with the combined response. Gain constant K is calibrated to produce unity gain from $G_2(s)$ at high frequency.

The resulting filter has an attenuation of 37.2 dB at 1.0 Hertz and maximum 1.3% (0.11 dB) error in the pass-band, occurring at 28 Hertz. The maximum phase error in the pass-band is 2.5 degrees, occurring at 33 Hertz.

F.4.2 – Low-Pass Filter Network

A low-pass filter network was incorporated into the expansion to provide an option for attenuation of high frequency noise. Although no high frequency noise troubles had been previously encountered, including the additional filters in the EX2 was simple and deemed proactive.

The filter (one per channel) is simply a second order Chebyshev filter with a corner frequency of 50 kHz and a maximum ripple of 1 dB. Figure F-10 presents a Bode plot of the resulting response. The attenuation at 500 kHz is 39 dB. The maximum amplitude variation below

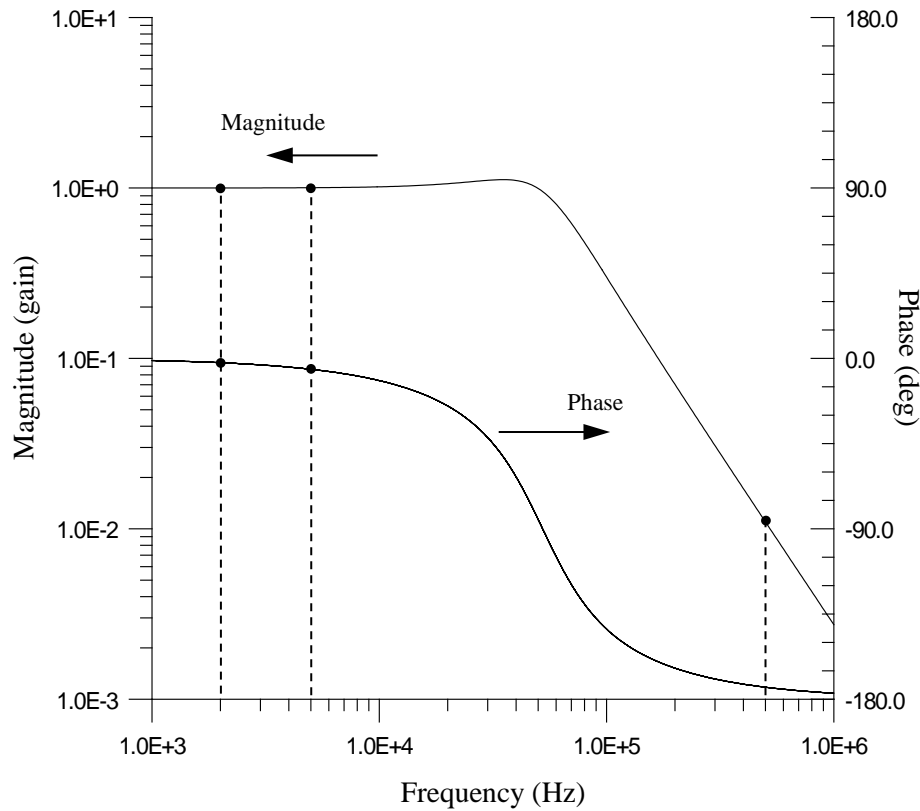


Figure F-10: Magnitude and phase of the high-pass filter block. Attenuation at 500 kHz is 39 dB. The maximum amplitude error below 2 kHz is 0.006 dB. The phase error at 2 kHz is 2.3 degrees.

5 kHz is less than 0.04 dB and below 2 kHz is less than 0.006 dB. However, the phase error at 5 kHz is nearly 6 degrees and at 2 kHz is 2.3 degrees.

Although included in the EX2 and fully tested and calibrated, the low pass filter was ultimately never required. High frequency signal noise never became an issue and the filter was never enabled in any of the formal experiments that were performed.

F.4.3 – Bump Filter

An ad-hoc, heuristic filter, dubbed the “bump filter,” was also added to each input channel. This filter is simply a device that migrates charge to or from the blocking capacitors that are present at the output of the mainboard multiplexers. This arrangement can be seen in Figure F-7. A set of comparators at the output of each programmable gain amplifier monitors the output for signal clipping or saturation. If clipping is detected, high-speed analog switches at the EX2 input section are pulsed appropriately to move charge to or from the blocking capacitor. This is done in the proper direction to quickly move the signal toward centerline.

This filter actually works surprisingly well and is useful under conditions where strong convective cells are present in the acoustic forcing chamber. The upsets generated when the filter is active are very short in duration and rarely appear in the windows of collected data. When they do appear, they are easily detectable allowing the exclusion of that particular record.

F.5 AFC-100 Commands and Functions

After the initial development of the AFC-100, a base firmware was written for the device. All the code was written in the C programming language and compiled to Z180 machine code. The firmware not only supports operation from the front panel interface, but also through a command-line interface (CLI) over an RS-232 port. This interface allows the central control computer

(running the OPO software) to communicate directly with the AFC-100. Packaged routines as well as scripts can be run on the control computer fully automating the operation of the AFC-100.

As hardware additions were incorporated into the AFC-100, the firmware was correspondingly expanded. Data transfer support was added to enable retrieval of captured waveforms and headers from the EX-1. These transfers occur over the same RS-232 port used for the CLI and use a custom protocol that supports error detection and retransmit requests. Data is transferred at 19.2 kilobaud.

Additionally, features were added to the firmware over time as experience was gained in its operation and use in the experimental setup. The last update to the code occurred in August of 2008, producing version 1.14. The C source for this current version constitutes over 6200 lines of code. A synopsis of the supported CLI commands is listed below in Table F-1.

Base Command	Command Syntax	Command Function
ABORT	"abort"	Aborts the current capture that is in progress.
BODE	"bode [start frequency] [stop frequency] [number of steps] [LOG LIN] [MAGONLY MAGPHASE]"	Runs a frequency scan for generating a Bode response plot. Automatically turns on AGC. Plot can be just magnitude or can be magnitude and phase. Including the phase information makes the scan much slower.
CALIBRATE	"calibrate energy [measured energy]"	Calibration of the shot energy monitor. The 'measured energy' should be in mJ and should be measured at the entry into the acoustic forcing chamber. This will be compared with what the controller sees at the photodiode. The photodiode signal is boxcar integrated and smoothed through an IIR filter to correct for the energy meter's thermopile thermal time-constant. The ratio of the two measurements is used to generate a calibration multiplier which is used internally.
	"calibrate phase [CH1 CH2]"	Calibrate phase targeter phase offset. This will automatically generate a phase offset value for the offset register that neutralizes the phase shift between the sync reference and the input signal of interest. The channel option picks the signal of interest. All other phase targeter and acoustic drive parameters must be set prior to this calibration. The laser must be running and acoustic forcing must be underway during the calibration.
CAPTURE	"capture"	Initiates a capture sequence. Data will be captured in bins starting at bin_ptr and stopping at stop_ptr, inclusive. Data will be collected on every Nth laser shot, where N is equal to (skip_val + 1).
CEILING_N	"ceiling_[1 2] [ON OFF]"	Enables or disables automatic gain ceiling. When the automatic gain ceiling is on for a given channel, the function prevents erroneous signal measurements in the RMS converters and phase targeter by preventing signal clipping.
DUMP	"dump [start] [stop] [CH1 CH2 BOTH] [ASCII BINARY]"	<p>The dump command is used to transfer data from the AFC100 to the host computer through the serial port. It can be used in one of three ways. The first is the full definition method:</p> <p>start -> Number of first bin to transfer</p> <p>stop -> Number of last bin to transfer</p> <p>CH1 -> Transfer only data from channel 1</p> <p>CH2 -> Transfer only data from channel 2</p> <p>BOTH -> Transfer data from both channels</p> <p>ASCII -> Transfer data in ASCII format</p> <p>BINARY -> Transfer data in binary format</p>
	"dump [start] [stop]"	This defaults to transferring both channels in binary format.
	"dump"	This will transfer the collected data from the last capture. If Dump-Mode is not set to Manual, then it will use the parameters specified for the current auto-dump. However, if Manual is selected, it will transfer both channels in binary format.
FOCUS	"focus [ON OFF null]"	Enables, disables or displays current status of focus mode. In focus mode, the ICCD free-runs and is not synchronized with a capture event. This is used during setup to focus the lens on the ICCD.
HELP	"help [topic]"	Displays the help menu. Providing a topic produces more detail.
IMPORT	"import [address]"	Imports data from a specific I/O address. Used for system debugging purposes, only.

Table F-1: AFC-100 command-line-interface (CLI) command set.

Base Command	Command Syntax	Command Function
INFO	"info [bin number] [CH1 CH2]"	Provides all information available of a specific data bin.
LASER	"laser [ON OFF]"	Used to start and stop the Nd:YAG laser.
LIFT	"lift [ceiling_1 ceiling_2]"	Used to lift the gain ceiling on a given channel.
OUTPORT	"outport [address] [data]"	Writes data to a specific I/O address. Used for system debugging purposes, only.
QUICKPROBE	"quickprobe [CH1 CH2 BOTH] <force>"	Performs a quick analysis on one or both signal channels. For the given channel, it returns the signal magnitude and phase. The magnitude is presented in RMS volts. The phase is presented as +/- 180 degrees from the rising edge of the sync reference. Positive phase is defined as lagging. The 'force' argument is optional. This forces the probe to run even if the PLL is unlocked.
REPORT	"report ceiling"	Returns the current gain ceiling status.
	"report ch1"	Returns the current RMS value on channel 1.
	"report ch2"	Returns the current RMS value on channel 2.
	"report pid_status"	Returns the current status of the PID loop controlling the acoustic forcing amplitude. Possible return values are: OFF, LIMITING, RAMPING and ON_TARGET.
SET	"set defaults"	Sets all variables to the boot-up defaults.
	"set input_1 [1..8]"	Sets channel 1 to a desired input.
	"set input_2 [1..8]"	Sets channel 2 to a desired input.
	"set gainmode_1 [AUTOMATIC MANUAL]"	Selects gain control for channel 1.
	"set gainmode_2 [AUTOMATIC MANUAL]"	Selects gain control for channel 2.
	"set gain_1 [10 100 1000 10000]"	Sets the manual gain for channel 1.
	"set gain_2 [10 100 1000 10000]"	Sets the manual gain for channel 2.
	"set hpf_1 [IN OUT]"	Enables or disables the input high pass filter on channel 1. This filter has a corner frequency of 3.5 Hz, roll-off of 80dB/dec and is phase preserving above 20 Hz.
	"set hpf_2 [IN OUT]"	Enables or disables the input high pass filter on channel 2. This filter has a corner frequency of 3.5 Hz, roll-off of 80dB/dec and is phase preserving above 20 Hz.
	"set lpf_1 [IN OUT]"	Enables or disables the input low pass filter on channel 1.
	"set lpf_2 [IN OUT]"	Enables or disables the input low pass filter on channel 2.
	"set bump_1 [ON OFF]"	Enables or disables bump filtering on channel 1.
	"set bump_2 [ON OFF]"	Enables or disables bump filtering on channel 2.
	"set filter_1 [BROADBAND NOTCH]"	Sets the input filter configuration to the channel 1 final RMS converter.
	"set filter_2 [BROADBAND NOTCH]"	Sets the input filter configuration to the channel 2 final RMS converter.
	"set frequency [20.0..5000.0]"	Sets the drive oscillator frequency.
	"set control [PID DIRECT]"	Sets the control type for acoustic forcing.
	"set amplitude [0.0..1.0]"	Sets the RMS voltage of the acoustic drive output when in the direct control mode.

Table F-1 (Cont.): AFC-100 command-line-interface (CLI) command set.

Base Command	Command Syntax	Command Function
SET (cont.)	"set limit [0.0..1.0]"	Sets the upper limit on the RMS voltage of the acoustic drive output when in the PID control mode.
	"set setpoint [1.0e-8..2.0e-1]"	Sets the desired RMS voltage setpoint for the feedback input when in PID control mode.
	"set loop_gain [0..63]"	Sets the PID loop gain.
	"set p_gain [0..63]"	Sets the PID proportional gain.
	"set i_gain [0..63]"	Sets the PID integral gain.
	"set d_gain [0..63]"	Sets the PID derivative gain.
	"set target_mode [TARGET FREERUN]"	Sets the phase targeter operating mode. Target = Capture at specific phase. Freerun = 10 Hz capture.
	"set bin_ptr [0..255]"	Sets the phase targeter bin pointer register. This is the starting point for capture operations.
	"set stop_ptr [0..255]"	Sets the phase targeter stop pointer register. This points to the last bin to be filled during a capture.
	"set skip_val [0..255]"	Sets the phase targeter skip value register. This value is the number of laser shots to skip between image (and data) collections.
	"set target [0.0..359.9]"	Sets the phase angle target for data collections. This angle is in degrees from the rising-edge-zero-crossing of the sync reference signal. Increasing phase is lagging.
	"set precession [-359.9..359.9]"	Sets the target precession rate during data capture. This is the number of degrees the target will precess after each shot. Setting this value to 0.0 disables precession.
	"set offset [0.0..359.9]"	Sets the offset angle to be applied to the target phase. The angle is in degrees and is internally subtracted from the target phase. Ideally, one would set this value so as to neutralize the phase difference between the received signal and the sync reference signal.
	"set sync_source [CH1 CH2 SINE OSC]"	Sets the source for the phase targeter sync signal. Sine is the signal used to derive the acoustic drive output signal while OSC is the internal TTL clock.
SHUTDOWN	"shutdown"	Used to park the AFC-100 in safe mode before powering down.
	"spectra [bin number] [CH1 CH2]"	Generates spectral data from a particular bin and channel for a quick review of acoustic forcing harmonic distortion.

Table F-1 (Cont.): AFC-100 command-line-interface (CLI) command set.

Appendix G

LIBRARY OF BULK CHEMILUMINESCENCE DATA

G.1 Overview

This appendix contains data from all chemiluminescence experiments relevant to the test conditions covered in this thesis. The data has been post processed and presented as plots of the combustion response function. Details of the burner and fuel system designs can be found in appendix B, while details of the acoustic forcing and response measurement schemes can be found in chapter 2 and appendix D. With the exception of the equivalence ratio and nozzle exit velocity ratio, all other controllable parameters were held constant. The relevant constant parameters are given in Table G-1 below. Experimental data is presented on the following pages.

Parameter:	Value:
Burner Nozzle Exit Diameter (D)	14.0 mm
Burner Nozzle to Bluff Body Distance (H)	21.0 mm
Resulting H/D	1.50
Fuel Gas	UHP Methane
Oxidizer	Dry Air
Ambient Temperature	20.5 to 22.8 C
Ambient Pressure	754.9 to 765.8 mm-Hg
Acoustic Drive Amplitude at Flame	6.90 Pa (RMS) 110.8 dB (SPL)

Table G-1: Parameters held constant during bulk chemiluminescence experiments.

G.2 Presented Data

As defined in chapter 3, equation (3-1), the combustion response function is given as

$$(G-1) \quad H(s) = \frac{\bar{p}}{p'(s)} \frac{q'(s)}{\bar{q}}; \quad s = i\omega,$$

where \bar{p} and \bar{q} are the average values of the local pressure and the flame heat release, respectively.

Furthermore, $p'(s)$ and $q'(s)$ are the fluctuating portions of these same quantities, which are presented here as complex valued functions.

As was also stated in chapter 3, the argument is made that the chemiluminescence intensity (CH^* and CO_2^*) measured by an optically filtered PMT can be related to the flame heat release by

$$(G-2) \quad \frac{q'(s)}{\bar{q}} \simeq \frac{I'(s)}{\bar{I}(s)}.$$

Because of quenching, absorption and other effects it has been shown that, in general, $q(s) \neq \alpha I(s)$, $\alpha = \text{const}$; however, it is conjectured that for moderate heat release rates (on average) and where fluctuations are small, $|q'(s)| \ll \bar{q}(s)$, then equation (G-2) holds approximately. The resulting relation used for the combustion response function is then

$$(G-3) \quad H(s) = \frac{\bar{p}}{p'(s)} \frac{I'(s)}{\bar{I}(s)}; \quad s = i\omega.$$

It is this function that is plotted in the following graphs. Separate plots of magnitude and phase are given for each operating condition.

Attention should be paid to the phase information presented. The phase is presented on a continuous axis versus one that wraps every 360 degrees. This is to allow better visibility of the phase lagging behavior of the response function. The inability to acoustically couple energy into the test chamber at low frequencies sets the limit on the lowest drive frequency at 20 Hz. This leads to possible ambiguity about the “unwrapped” phase value measured at 20 Hz. This is resolved

by a computer code that projects the phase trajectory back to zero frequency. It is known that for real-world systems that the phase must approach a multiple of 90° at the frequency origin. This fact is exploited by the code in finding a best-fit trajectory for the phase. Once this is done, the resulting phase-branch for the phase data at 20 Hz is computed and the corresponding offset is added to the data. It is this corrected phase that is presented in the following graphs.

Table G-2 provides a list of all the burner operating conditions that were investigated along with the datasets corresponding to each of those conditions. Additionally, the figure number for the combustion response magnitude and phase plots are also given for each operating condition.

Equivalence Ratio (ϕ)	Velocity Ratio (V_R)	Jet Velocity (cm/s)	Volumetric Flow Rate (l/min)	Mass Flow Rate (g/min)	Datasets	Figure
0.675	2.00	29.43	2.719	3.160	35	G-1
0.700	2.00	36.17	3.341	3.879	36	G-2
0.700	2.50	45.21	4.176	4.849	37	G-3
0.725	2.00	43.56	4.023	4.667	38	G-4
0.725	2.50	54.45	5.029	5.833	39	G-5
0.725	3.00	65.33	6.035	7.000	40	G-6
0.750	2.00	51.41	4.749	5.503	41	G-7
0.750	2.50	64.27	5.936	6.878	42	G-8
0.750	3.00	77.12	7.123	8.254	43	G-9
0.750	3.50	89.97	8.310	9.630	44	G-10
0.750	4.00	102.8	9.497	11.01	45	G-11
0.775	2.50	74.44	6.876	7.959	46	G-12
0.775	3.00	89.33	8.251	9.551	47	G-13
0.775	3.50	104.2	9.626	11.14	48, 49, 50, 51	G-14
0.775	4.00	119.1	11.00	12.73	53	G-15
0.775	4.50	134.0	12.38	14.33	54	G-16
0.800	3.00	101.7	9.392	10.86	55	G-17
0.800	3.50	118.6	10.96	12.67	56, 101	G-18
0.800	4.00	135.6	12.52	14.48	57, 102	G-19
0.800	4.50	152.5	14.09	16.29	58, 103	G-20
0.800	5.00	169.5	15.65	18.10	59, 104	G-21
0.825	3.00	113.9	10.52	12.16	60, 105	G-22
0.825	3.50	132.9	12.28	14.18	61, 106	G-23
0.825	4.00	151.9	14.03	16.21	62, 107	G-24
0.825	4.50	170.9	15.78	18.23	63, 108	G-25
0.825	5.00	189.9	17.54	20.26	64, 109	G-26
0.825	5.50	208.9	19.29	22.29	65, 110	G-27
0.825	6.00	227.9	21.04	24.31	66	G-28
0.850	3.50	146.7	13.55	15.64	67	G-29
0.850	4.00	167.7	15.49	17.87	68	G-30
0.850	4.50	188.6	17.42	20.11	69	G-31

Table G-2: Index of burner operating conditions and corresponding figures with bulk response function plots.

Equivalence Ratio (ϕ)	Velocity Ratio (V_R)	Jet Velocity (cm/s)	Volumetric Flow Rate (l/min)	Mass Flow Rate (g/min)	Datasets	Figure
0.850	5.00	209.6	19.36	22.34	70	G-32
0.850	5.50	230.6	21.29	24.57	71	G-33
0.850	6.00	251.5	23.23	26.81	72	G-34
0.850	6.50	272.5	25.17	29.04	73, 111	G-35
0.875	3.50	159.7	14.75	17.01	74	G-36
0.875	4.00	182.5	16.86	19.44	75	G-37
0.875	4.50	205.4	18.97	21.87	76	G-38
0.875	5.00	228.2	21.08	24.30	77	G-39
0.875	5.50	251.0	23.18	26.73	78	G-40
0.875	6.00	273.8	25.29	29.16	79, 112	G-41
0.875	6.50	296.6	27.40	31.59	80, 113	G-42
0.875	7.00	319.5	29.51	34.02	81, 114	G-43
0.900	4.00	196.1	18.12	20.86	82	G-44
0.900	4.50	220.7	20.38	23.47	83	G-45
0.900	5.00	245.2	22.65	26.08	84	G-46
0.900	5.50	269.7	24.91	28.69	85, 115	G-47
0.900	6.00	294.2	27.17	31.30	86, 116	G-48
0.900	6.50	318.7	29.44	33.91	87, 117	G-49
0.925	4.00	208.1	19.22	22.11	88	G-50
0.925	4.50	234.1	21.62	24.88	89	G-51
0.925	5.00	260.1	24.03	27.64	90, 118	G-52
0.925	5.50	286.1	26.43	30.41	91, 119	G-53
0.925	6.00	312.2	28.83	33.17	92, 120	G-54
0.950	4.50	245.3	22.66	26.04	93, 121	G-55
0.950	5.00	272.6	25.17	28.94	94, 122	G-56
0.950	5.50	299.8	27.69	31.83	95, 123	G-57
0.975	4.50	253.8	23.44	26.92	96, 124	G-58
0.975	5.00	282.0	26.05	29.91	97, 125	G-59
0.975	5.50	310.2	28.65	32.90	98, 126	G-60
1.000	5.00	288.1	26.61	30.52	99, 127	G-61
1.000	5.50	316.9	29.27	33.57	100, 128	G-62

Table G-2 (cont.): Index of burner operating conditions and corresponding figures with bulk response function plots.

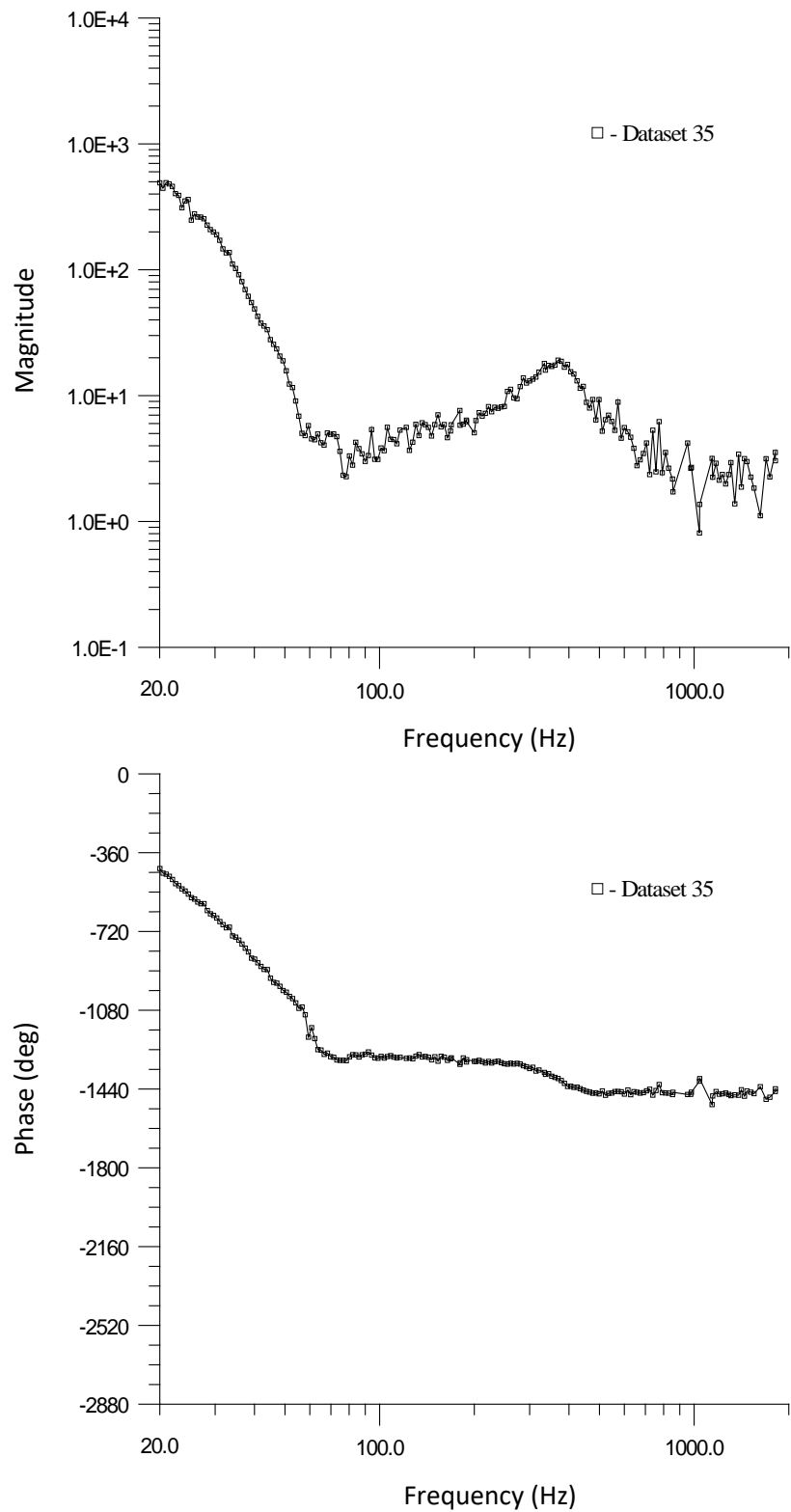


Figure G-1: Measured combustion response function for $\varphi = 0.675$ and $V_R = 2.0$.

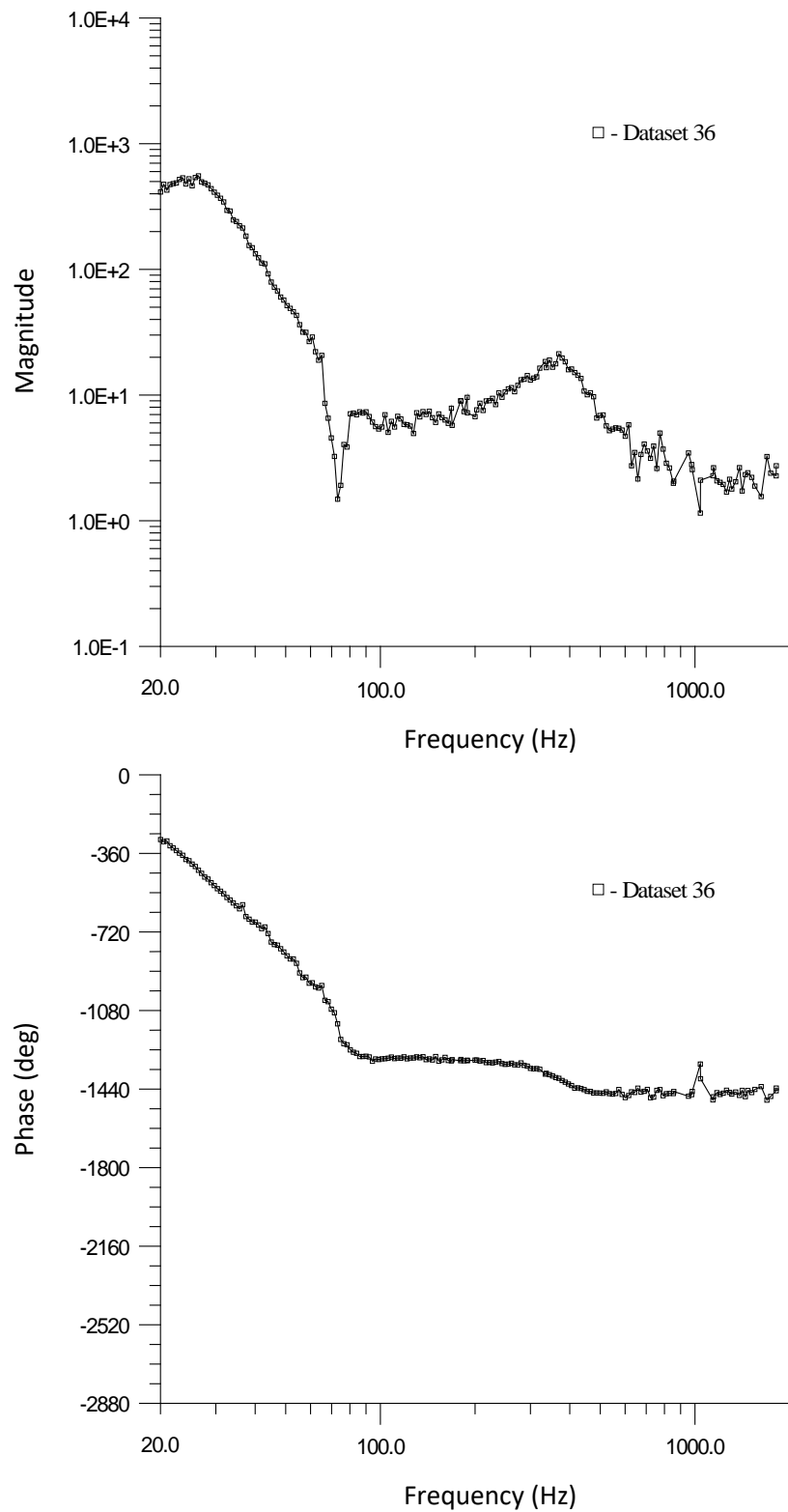


Figure G-2: Measured combustion response function for $\varphi = 0.700$ and $V_R = 2.0$.

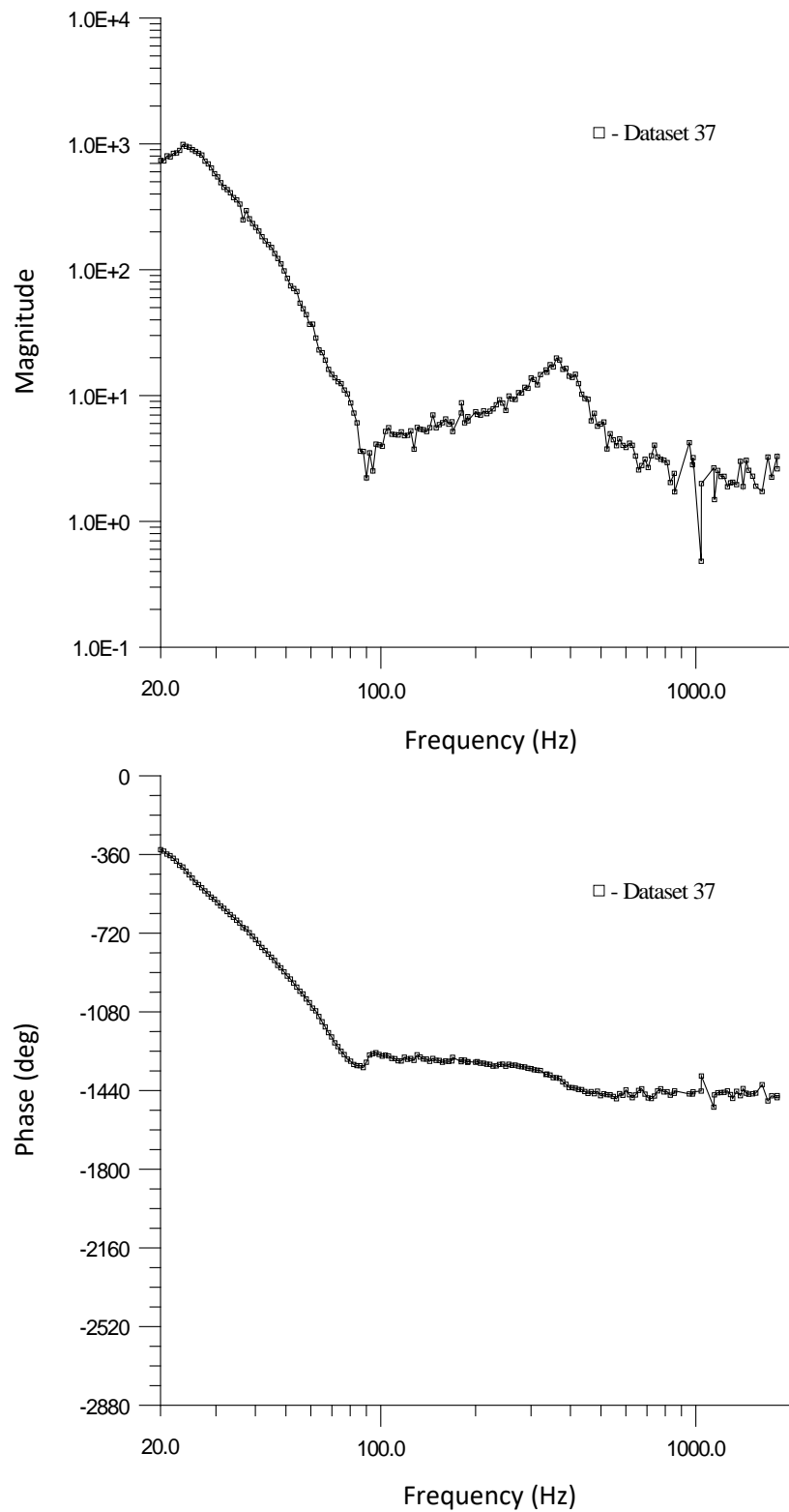


Figure G-3: Measured combustion response function for $\varphi = 0.700$ and $V_R = 2.5$.

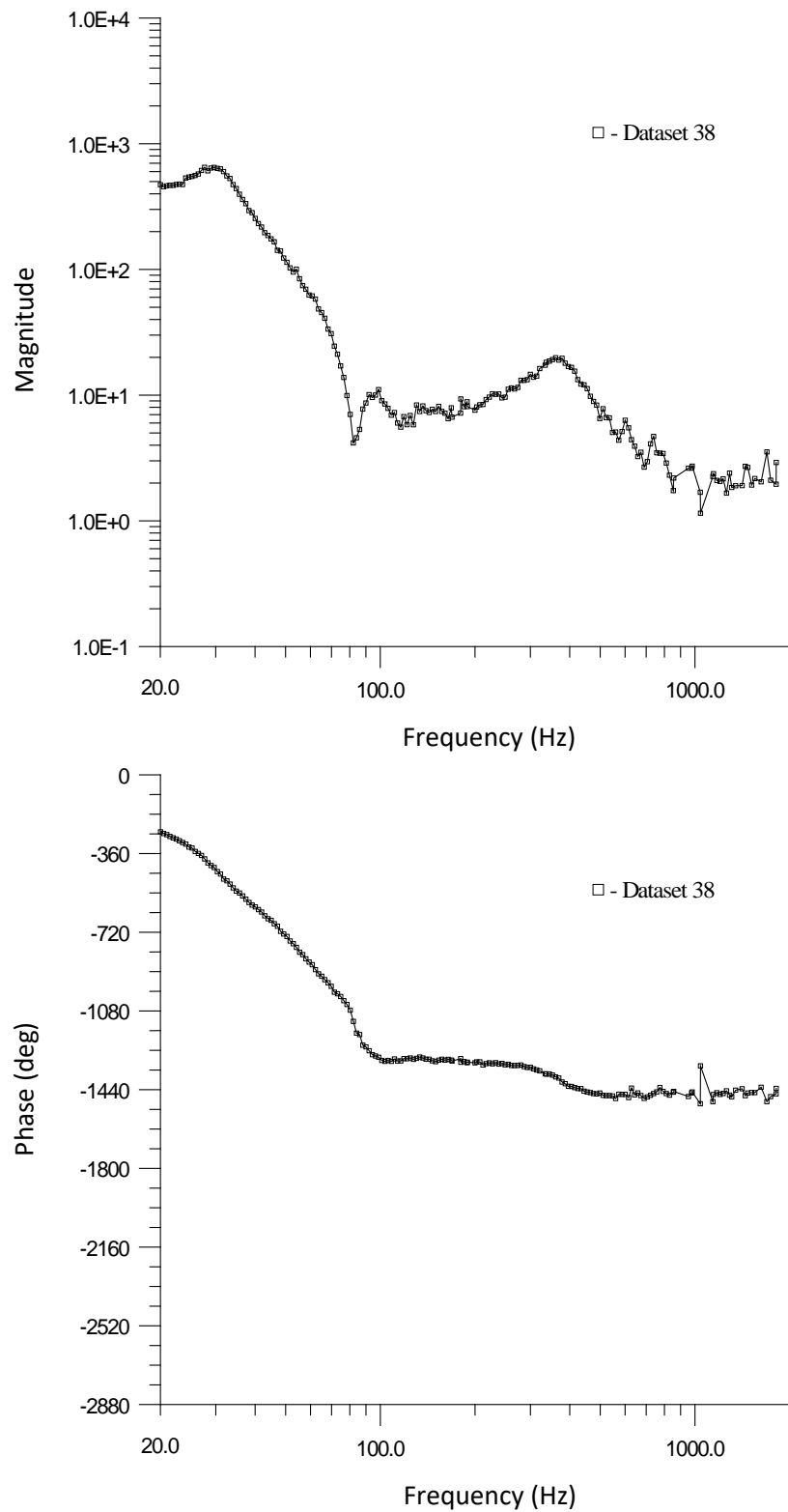


Figure G-4: Measured combustion response function for $\varphi = 0.725$ and $V_R = 2.0$.

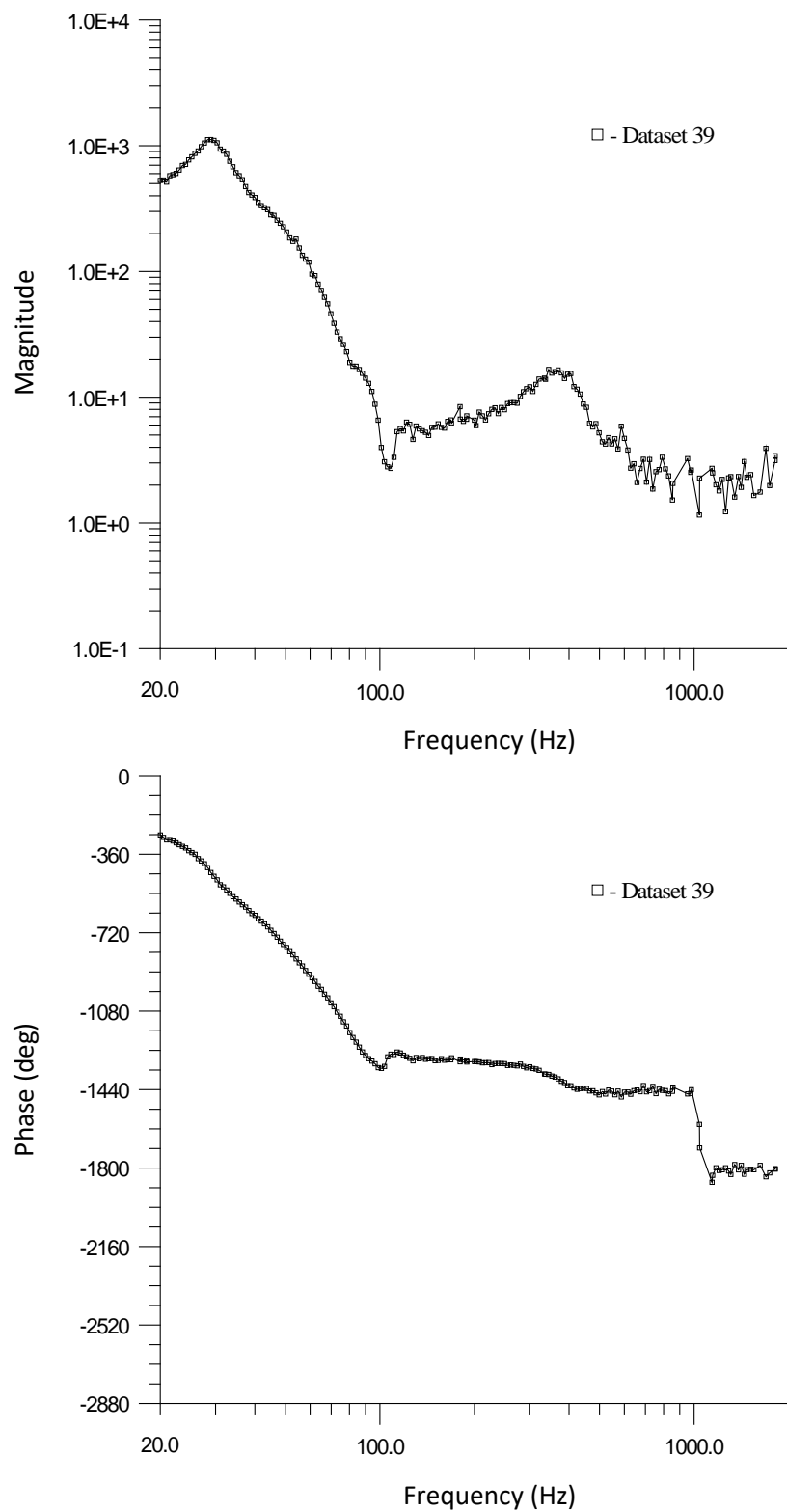


Figure G-5: Measured combustion response function for $\varphi = 0.725$ and $V_R = 2.5$.

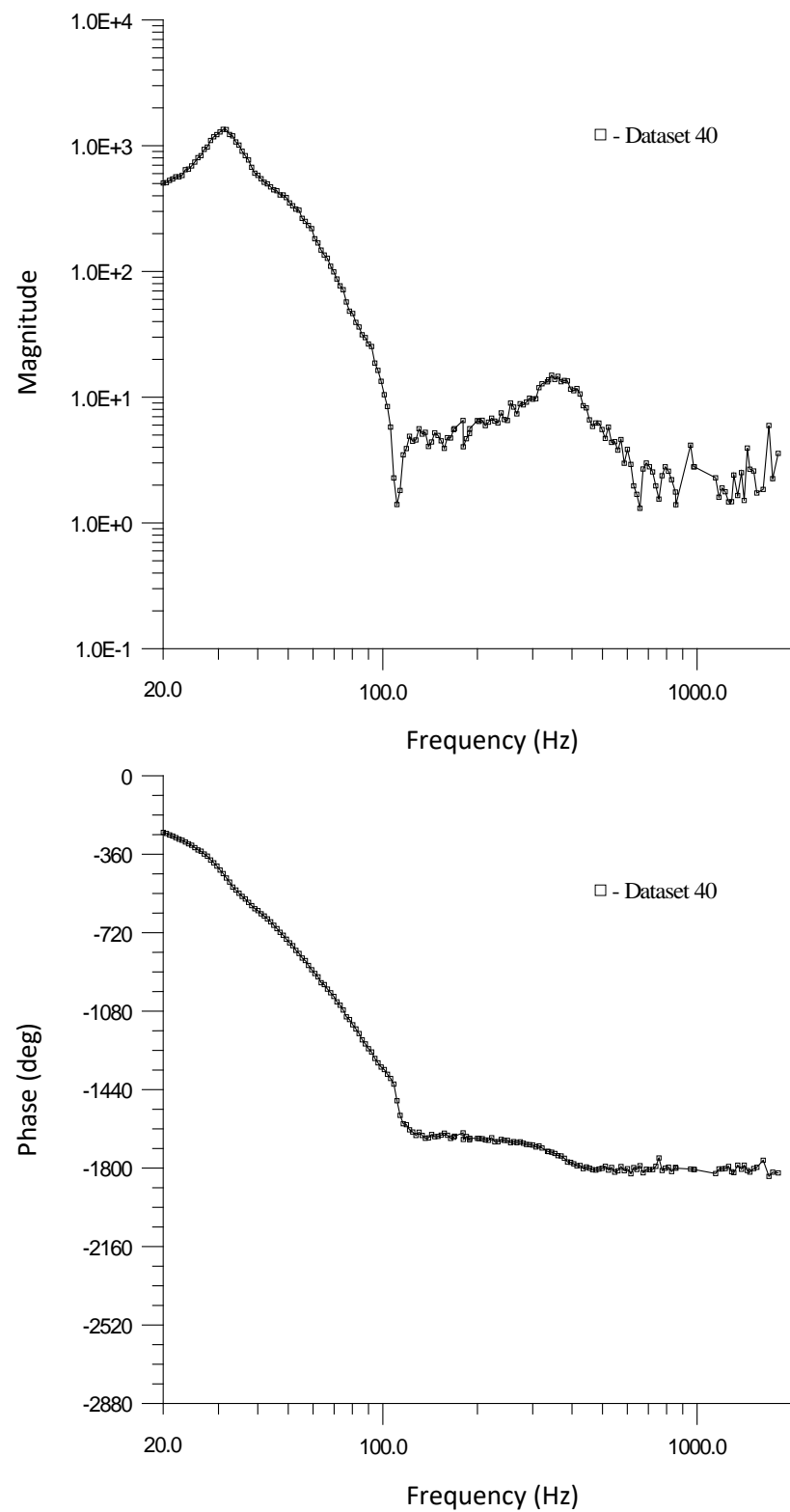


Figure G-6: Measured combustion response function for $\varphi = 0.725$ and $V_R = 3.0$.

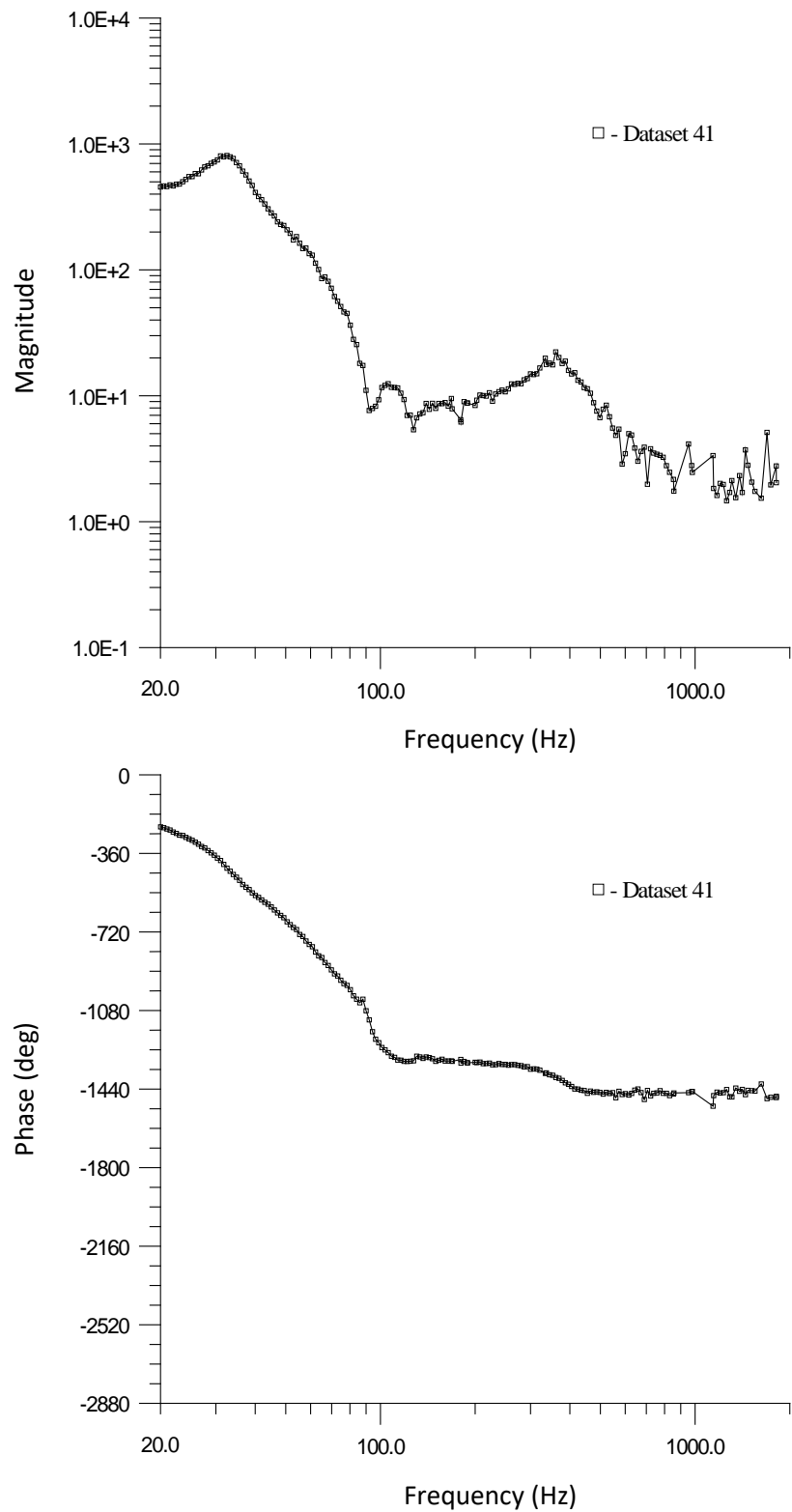


Figure G-7: Measured combustion response function for $\varphi = 0.750$ and $V_R = 2.0$.

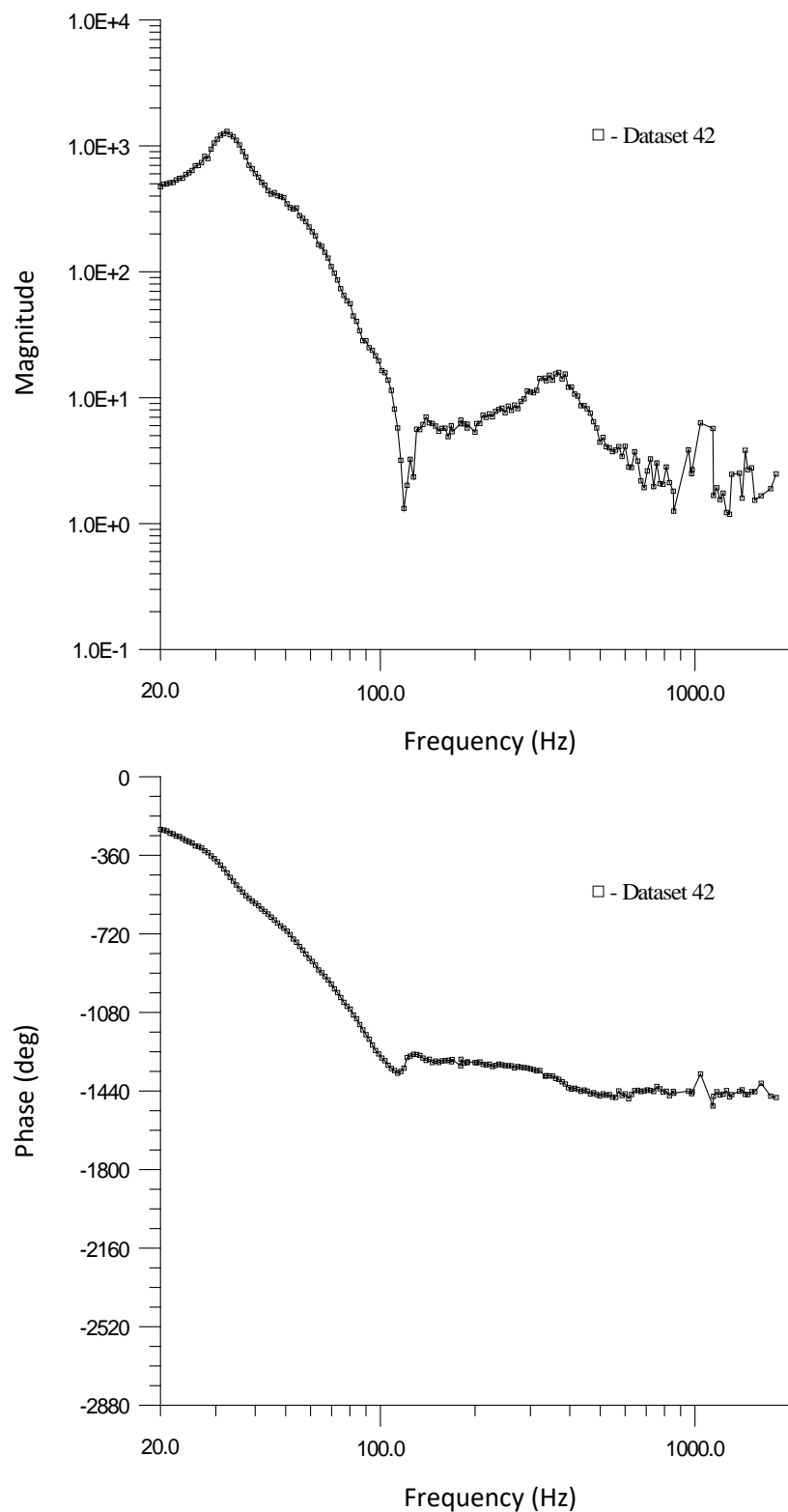


Figure G-8: Measured combustion response function for $\varphi = 0.750$ and $V_R = 2.5$.

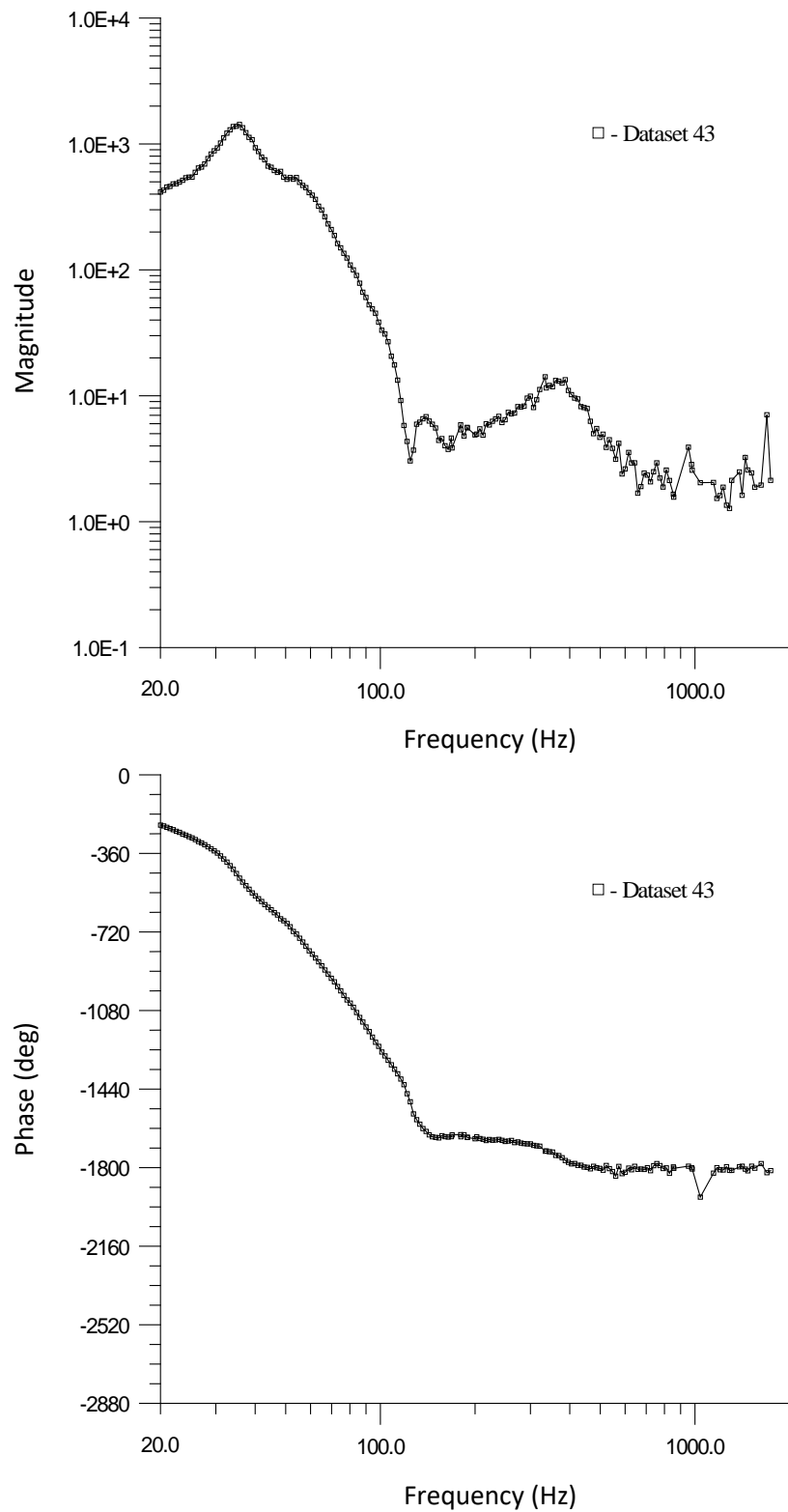


Figure G-9: Measured combustion response function for $\varphi = 0.750$ and $V_R = 3.0$.

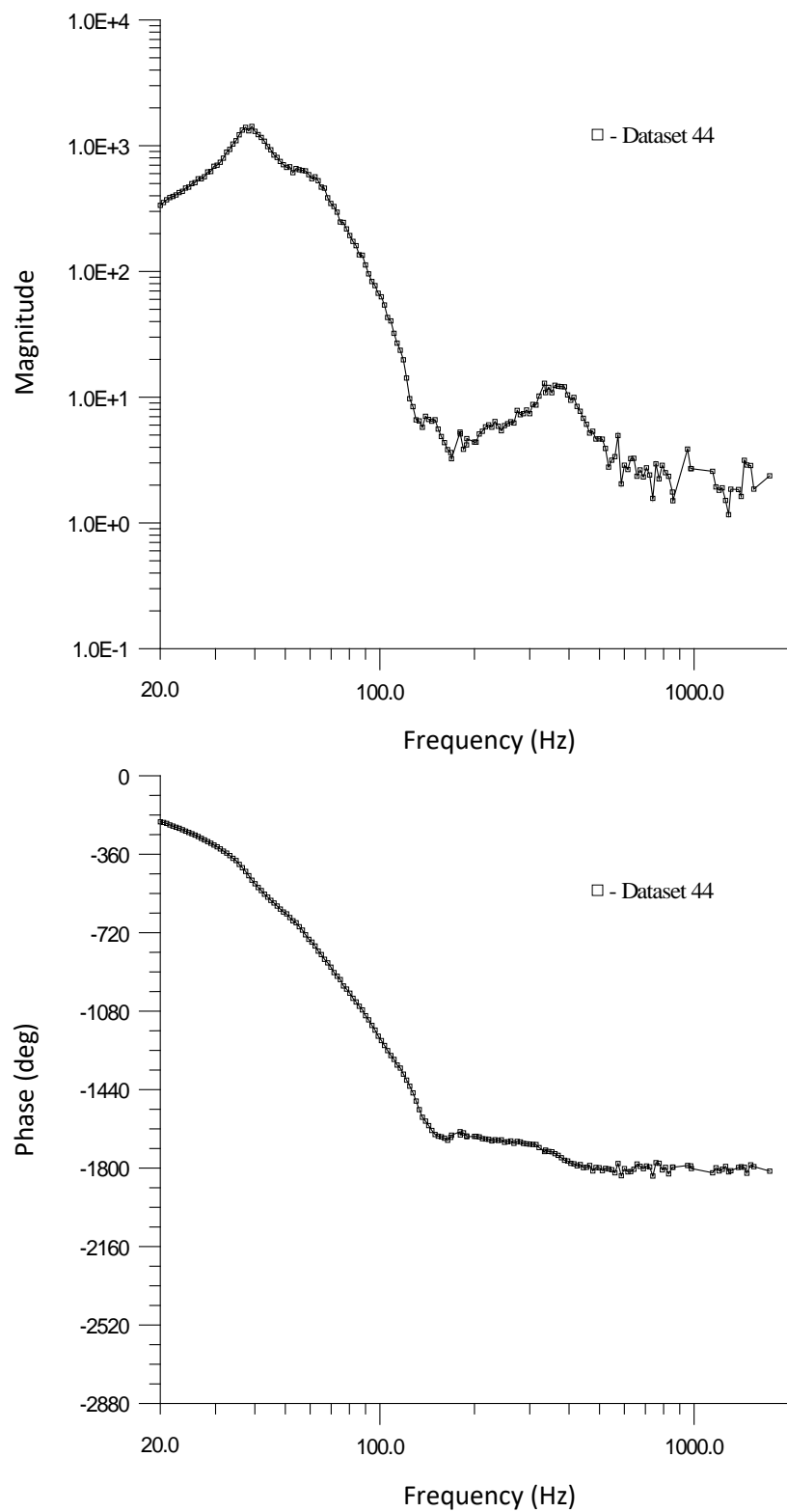


Figure G-10: Measured combustion response function for $\varphi = 0.750$ and $V_R = 3.5$.

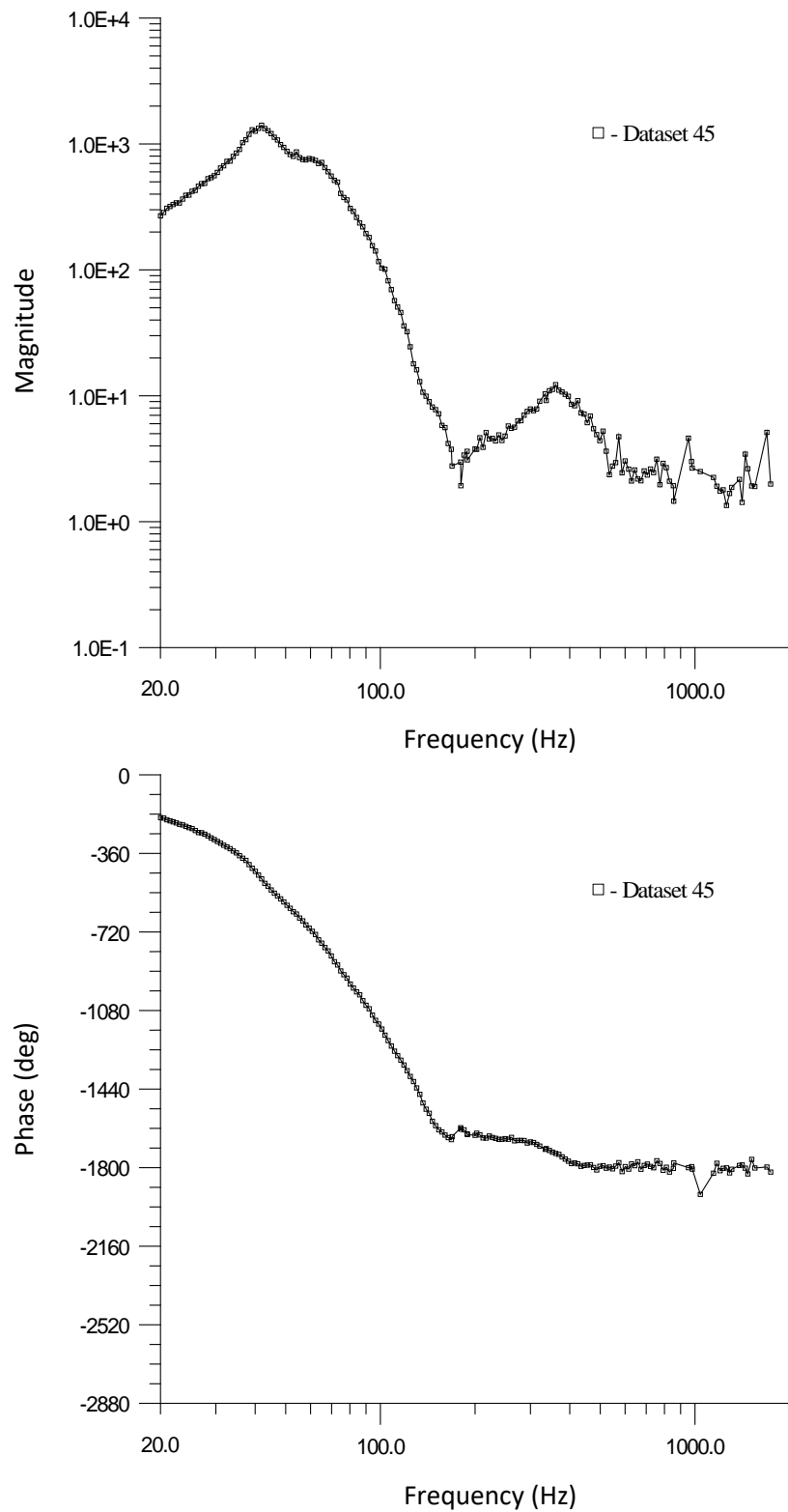


Figure G-11: Measured combustion response function for $\varphi = 0.750$ and $V_R = 4.0$.

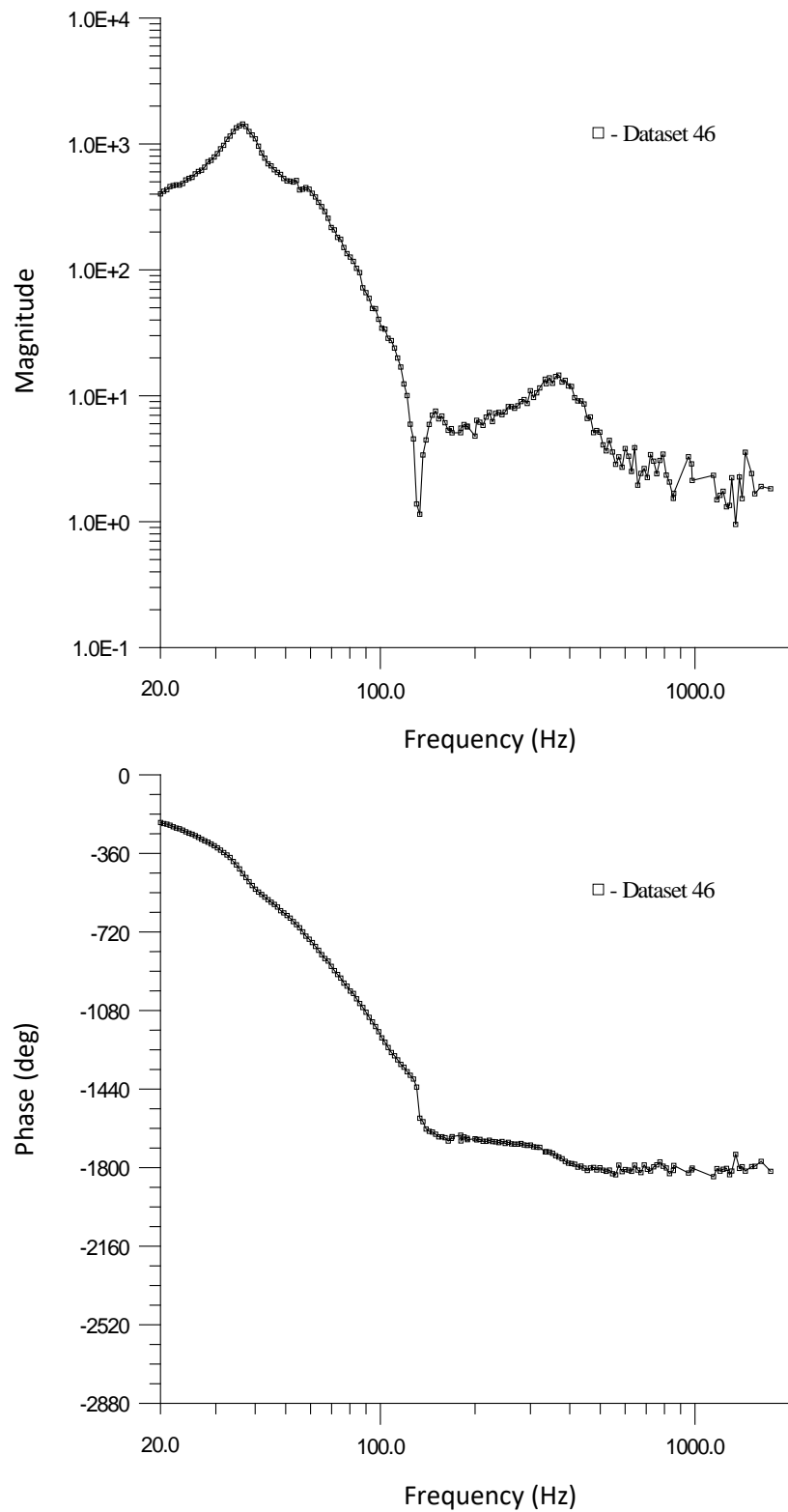


Figure G-12: Measured combustion response function for $\varphi = 0.775$ and $V_R = 2.5$.

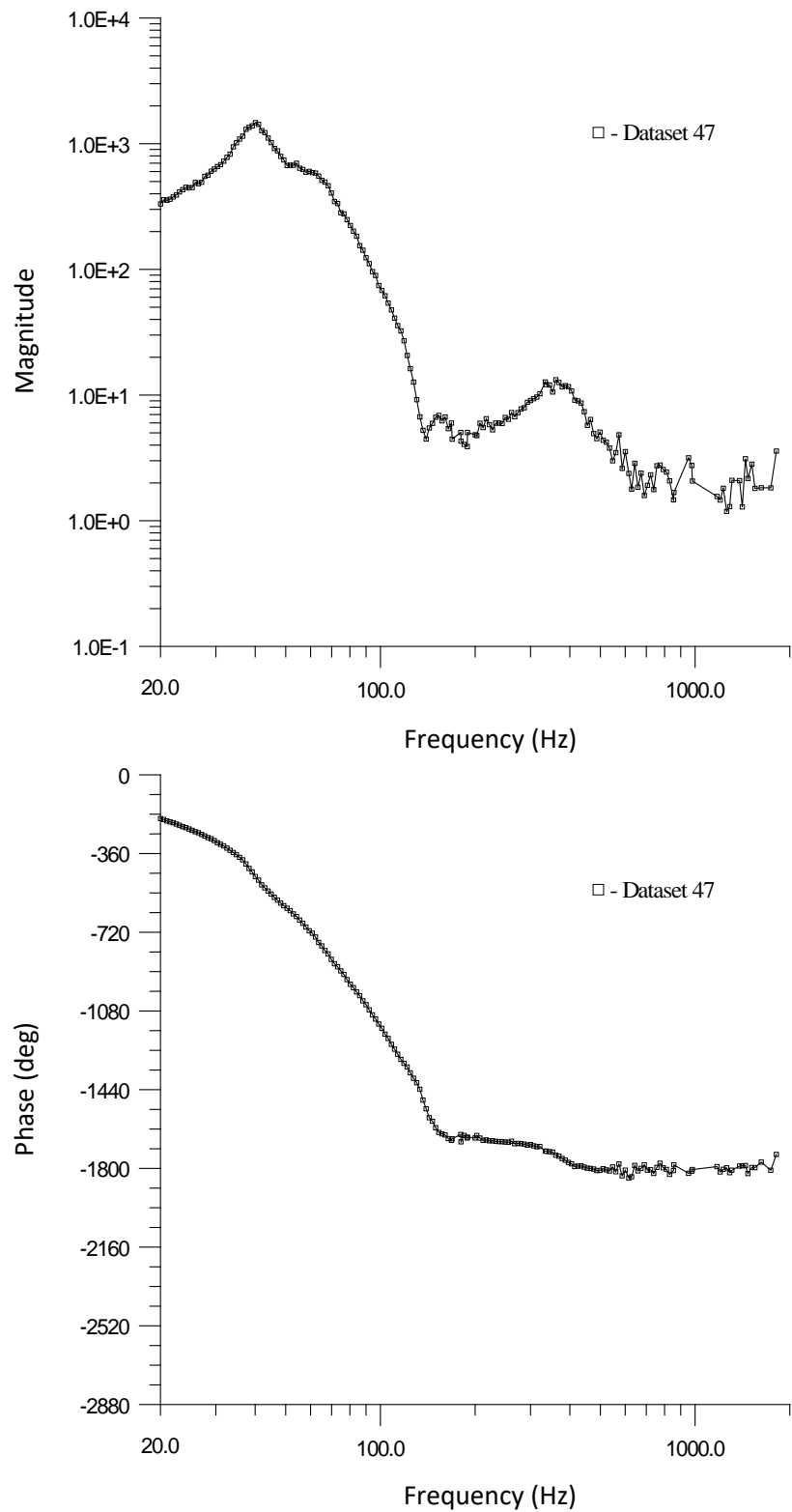


Figure G-13: Measured combustion response function for $\varphi = 0.775$ and $V_R = 3.0$.

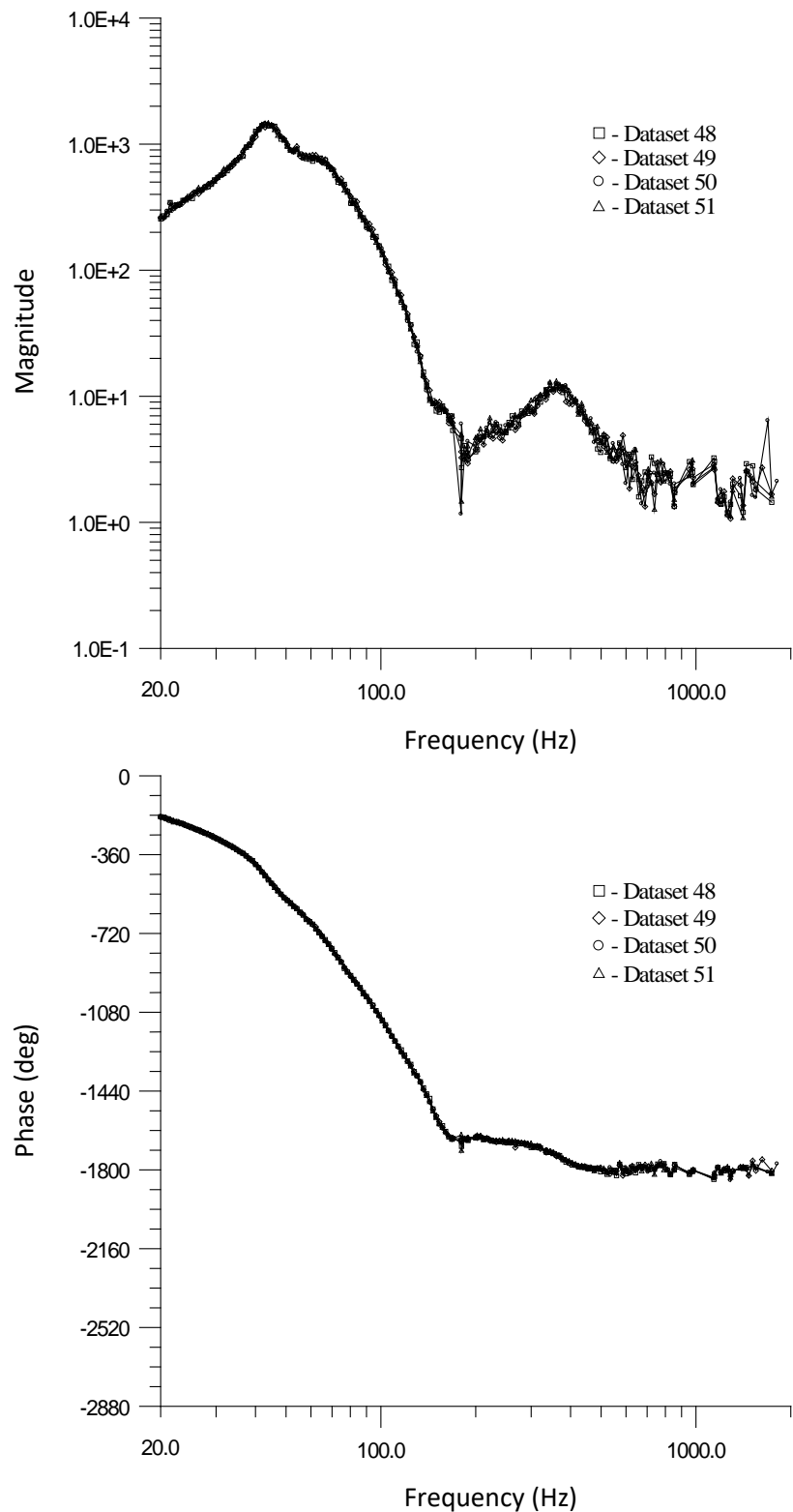


Figure G-14: Measured combustion response function for $\varphi = 0.775$ and $V_R = 3.5$.

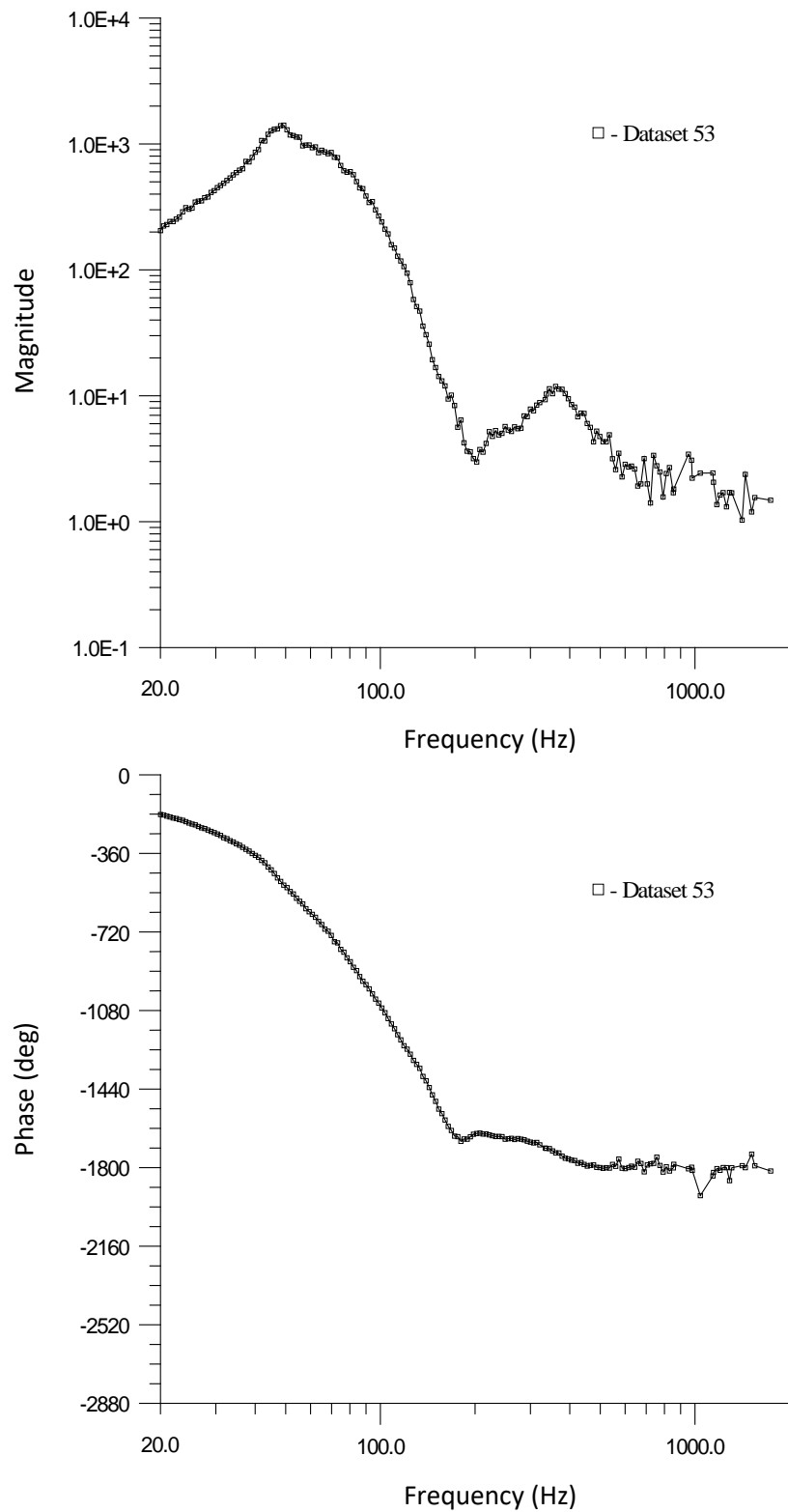


Figure G-15: Measured combustion response function for $\varphi = 0.775$ and $V_R = 4.0$.

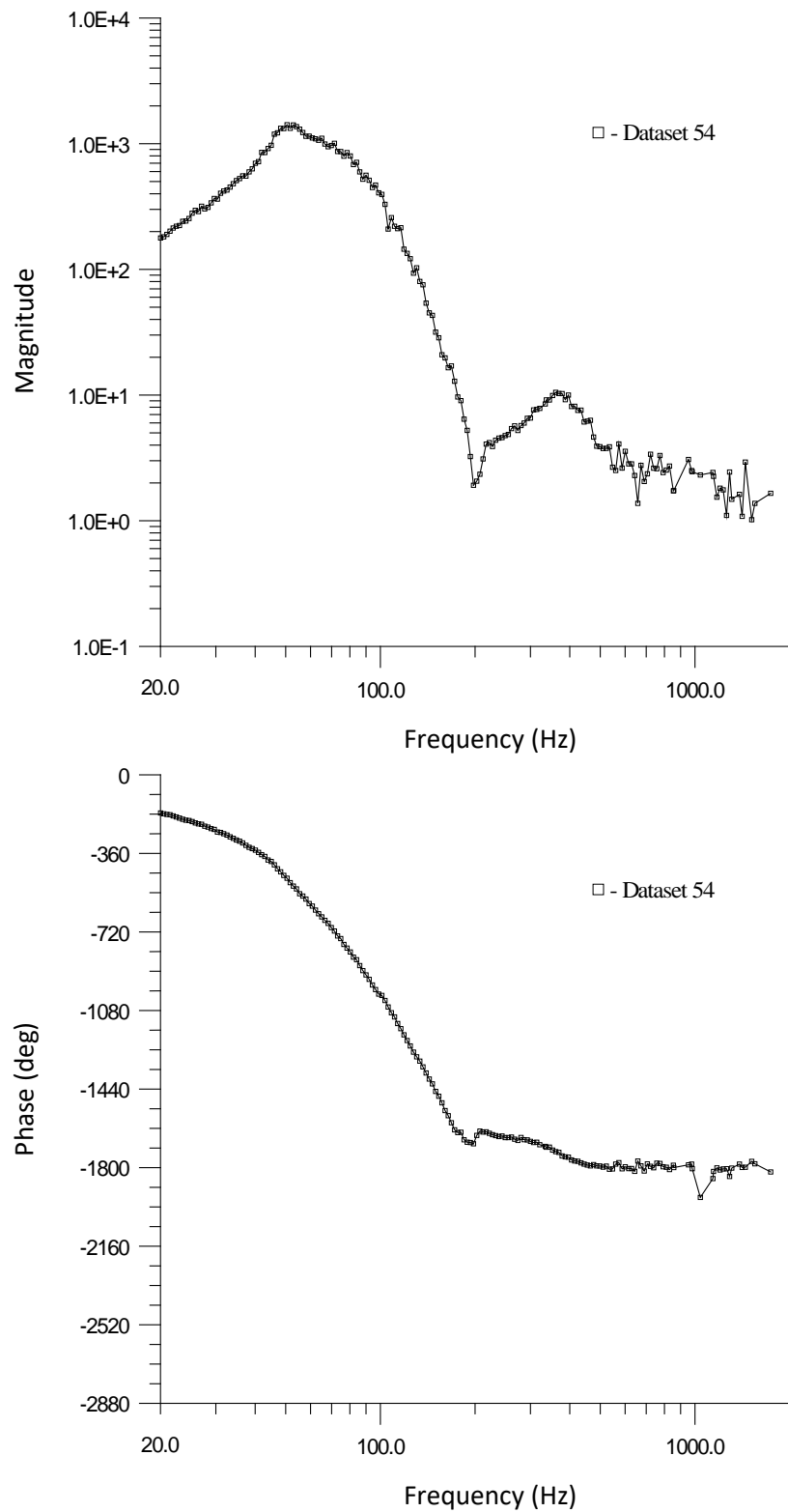


Figure G-16: Measured combustion response function for $\varphi = 0.775$ and $V_R = 4.5$.

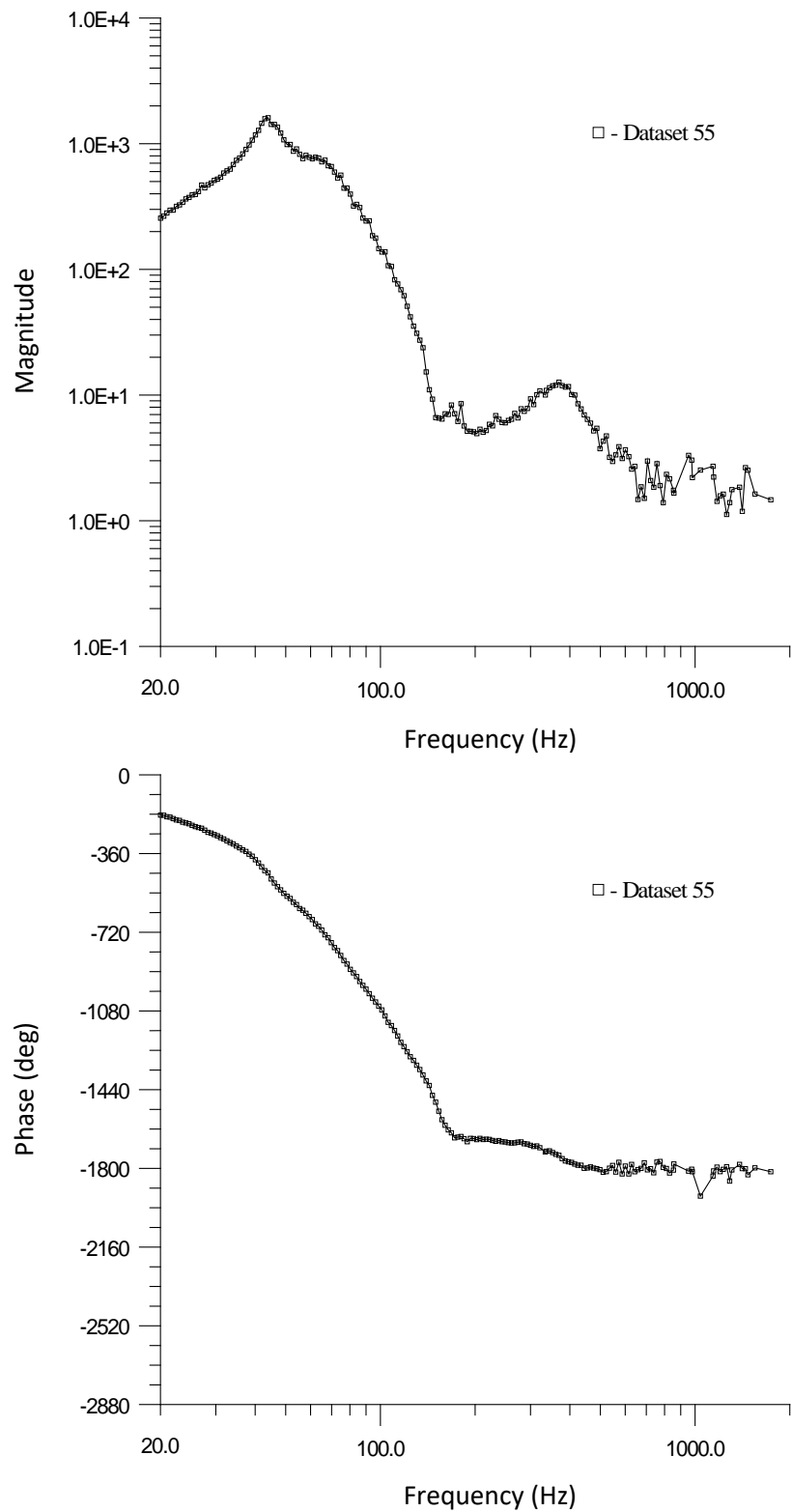


Figure G-17: Measured combustion response function for $\varphi = 0.800$ and $V_R = 3.0$.

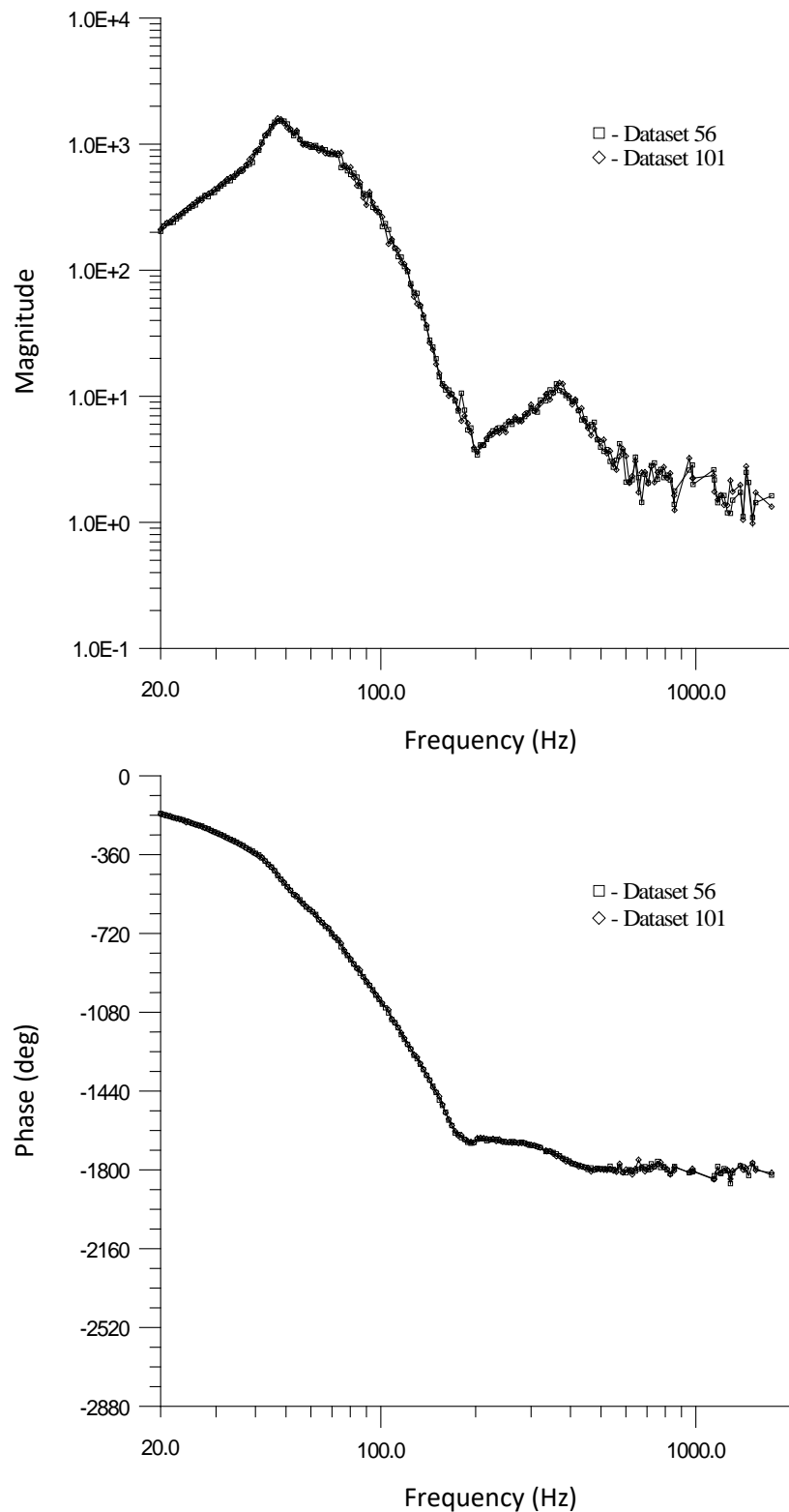


Figure G-18: Measured combustion response function for $\varphi = 0.800$ and $V_R = 3.5$.

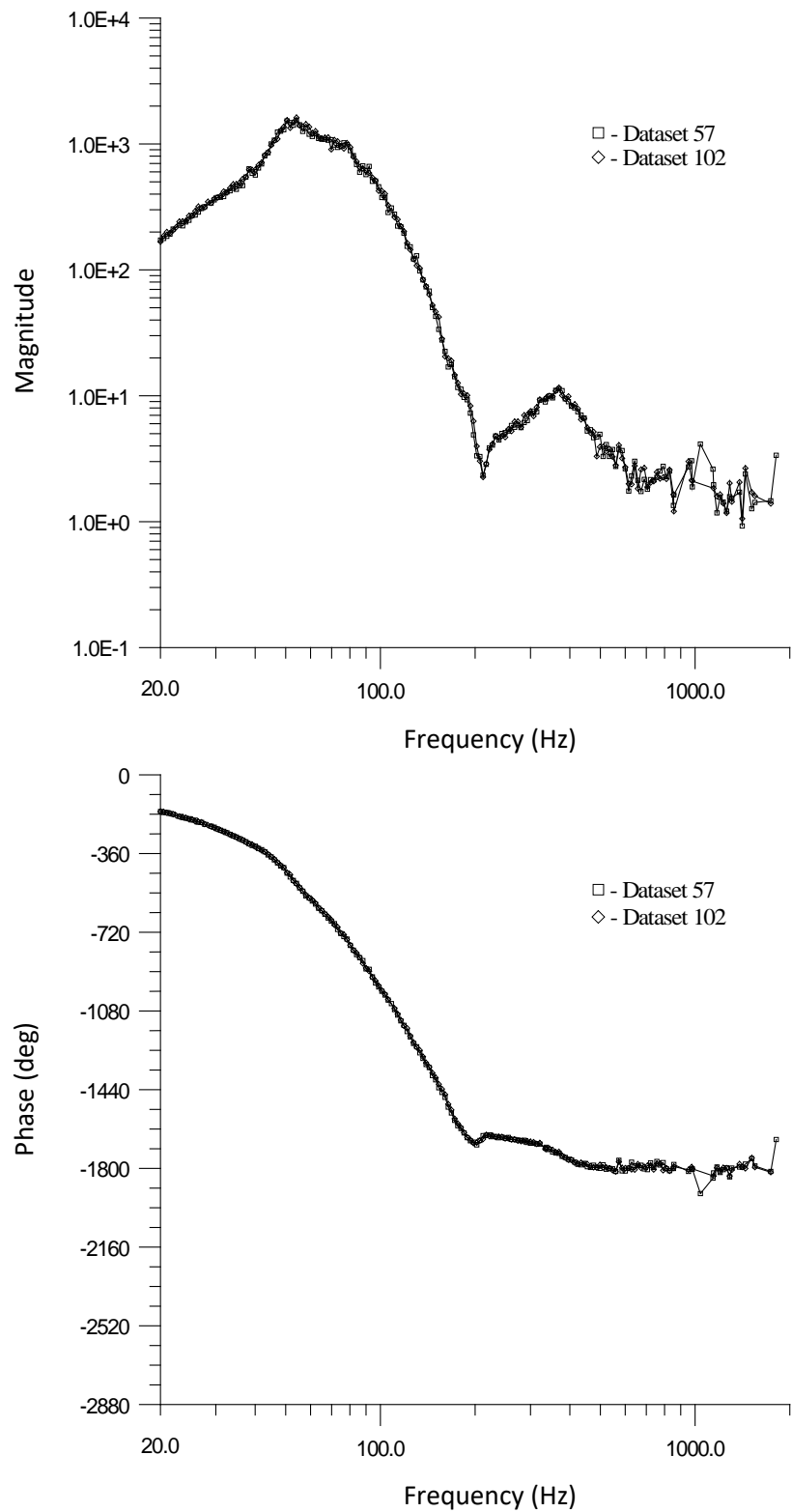


Figure G-19: Measured combustion response function for $\varphi = 0.800$ and $V_R = 4.0$.

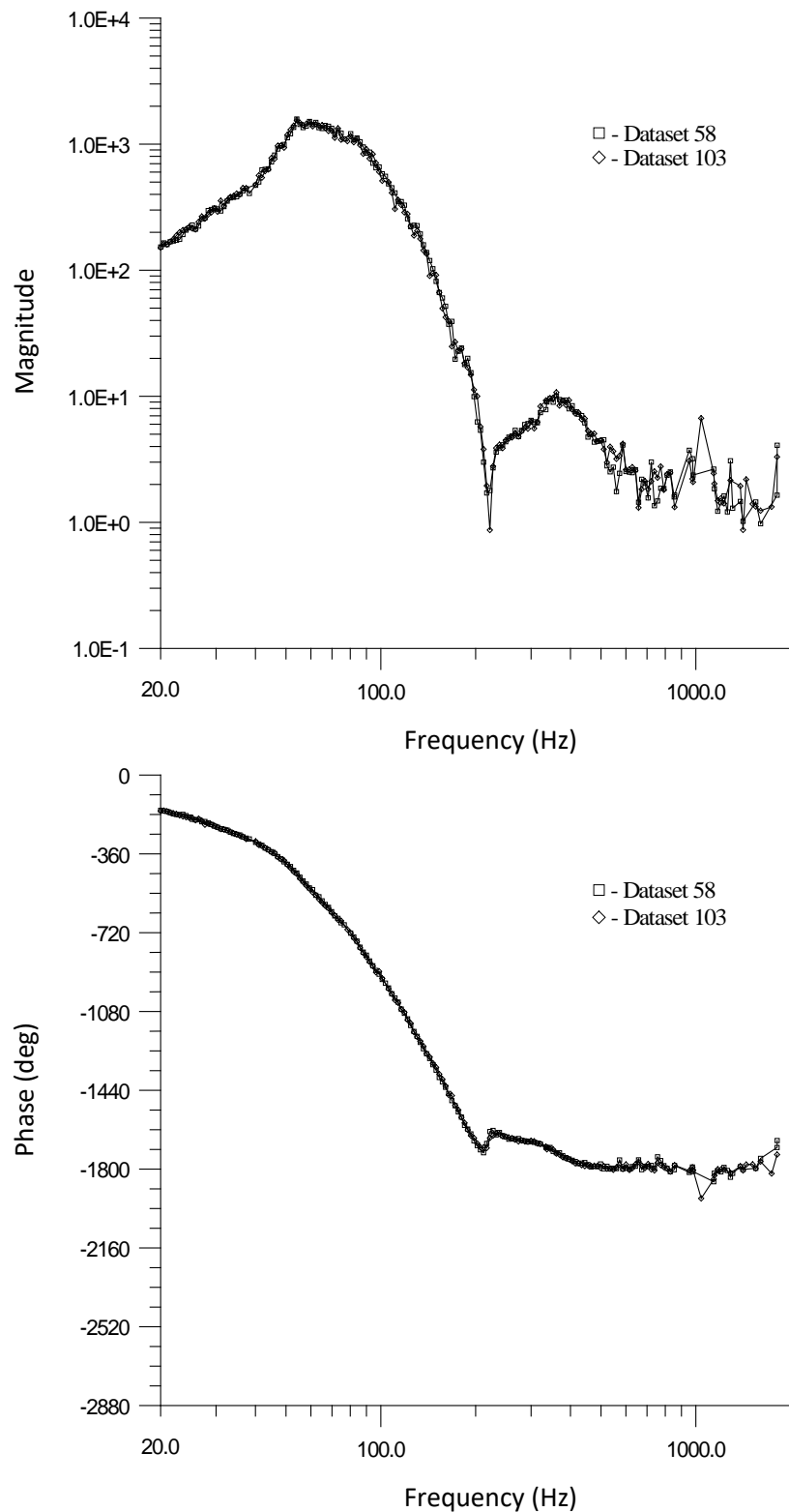


Figure G-20: Measured combustion response function for $\varphi = 0.800$ and $V_R = 4.5$.

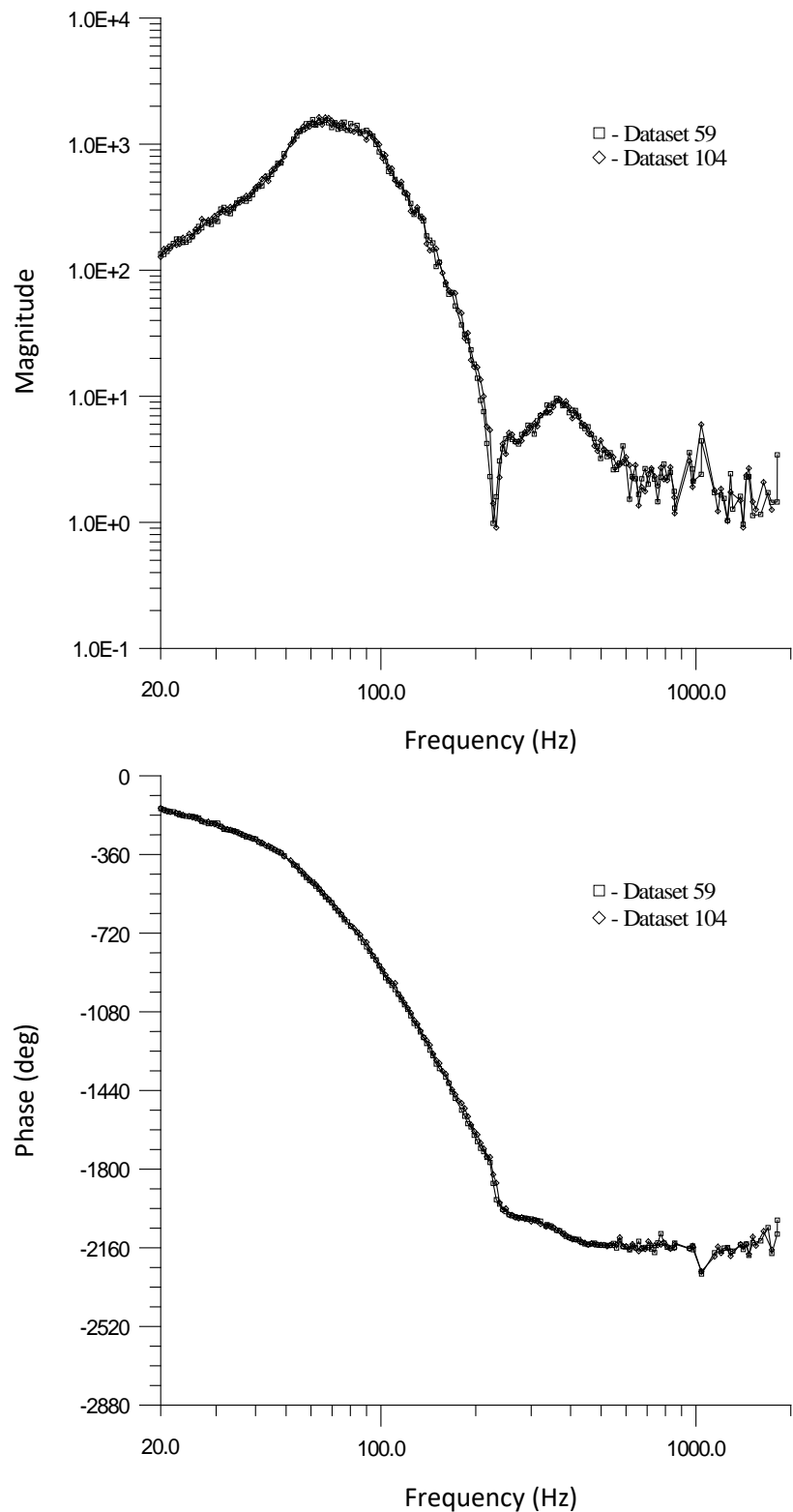


Figure G-21: Measured combustion response function for $\varphi = 0.800$ and $V_R = 5.0$.

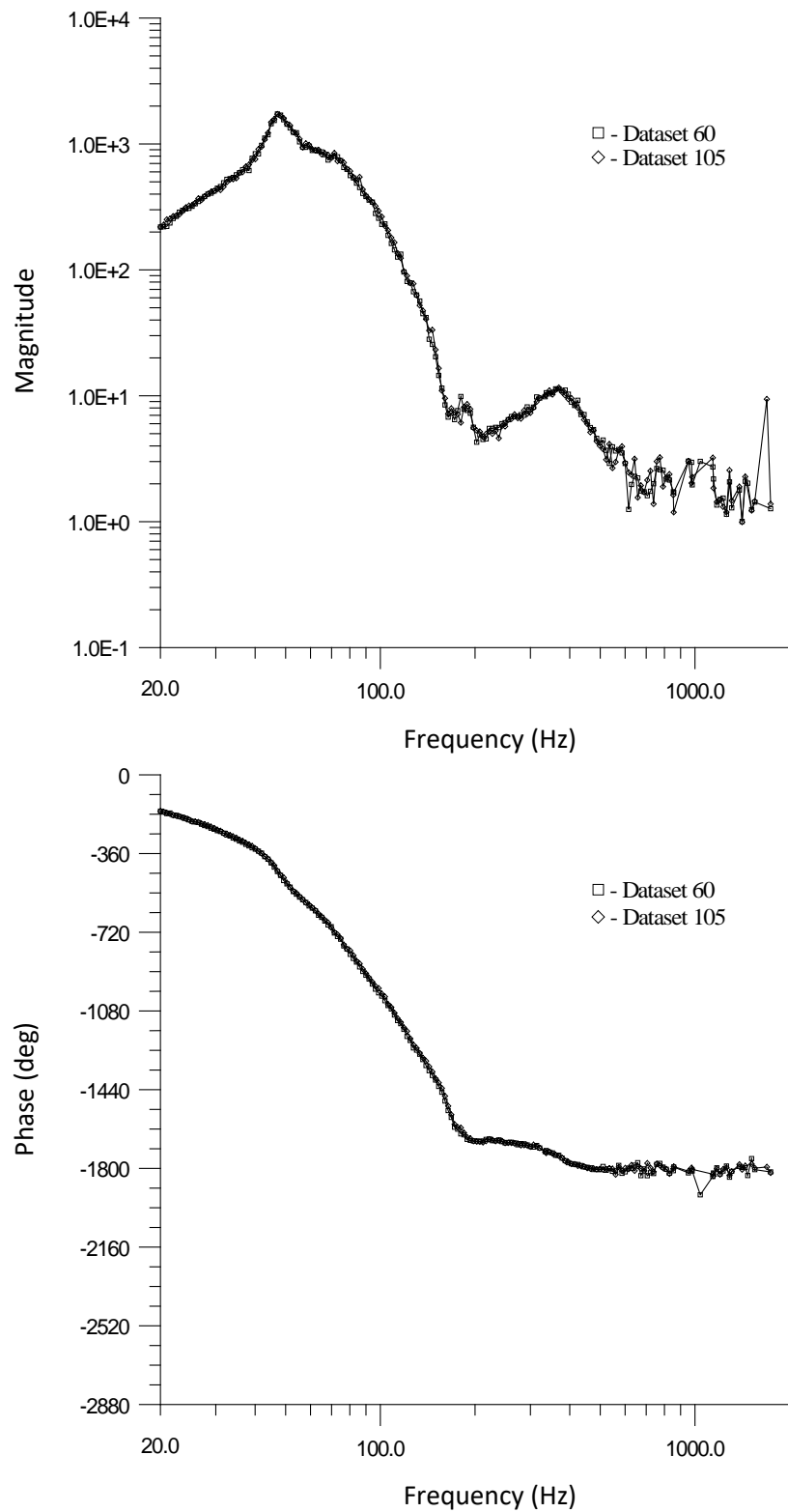


Figure G-22: Measured combustion response function for $\varphi = 0.825$ and $V_R = 3.0$.

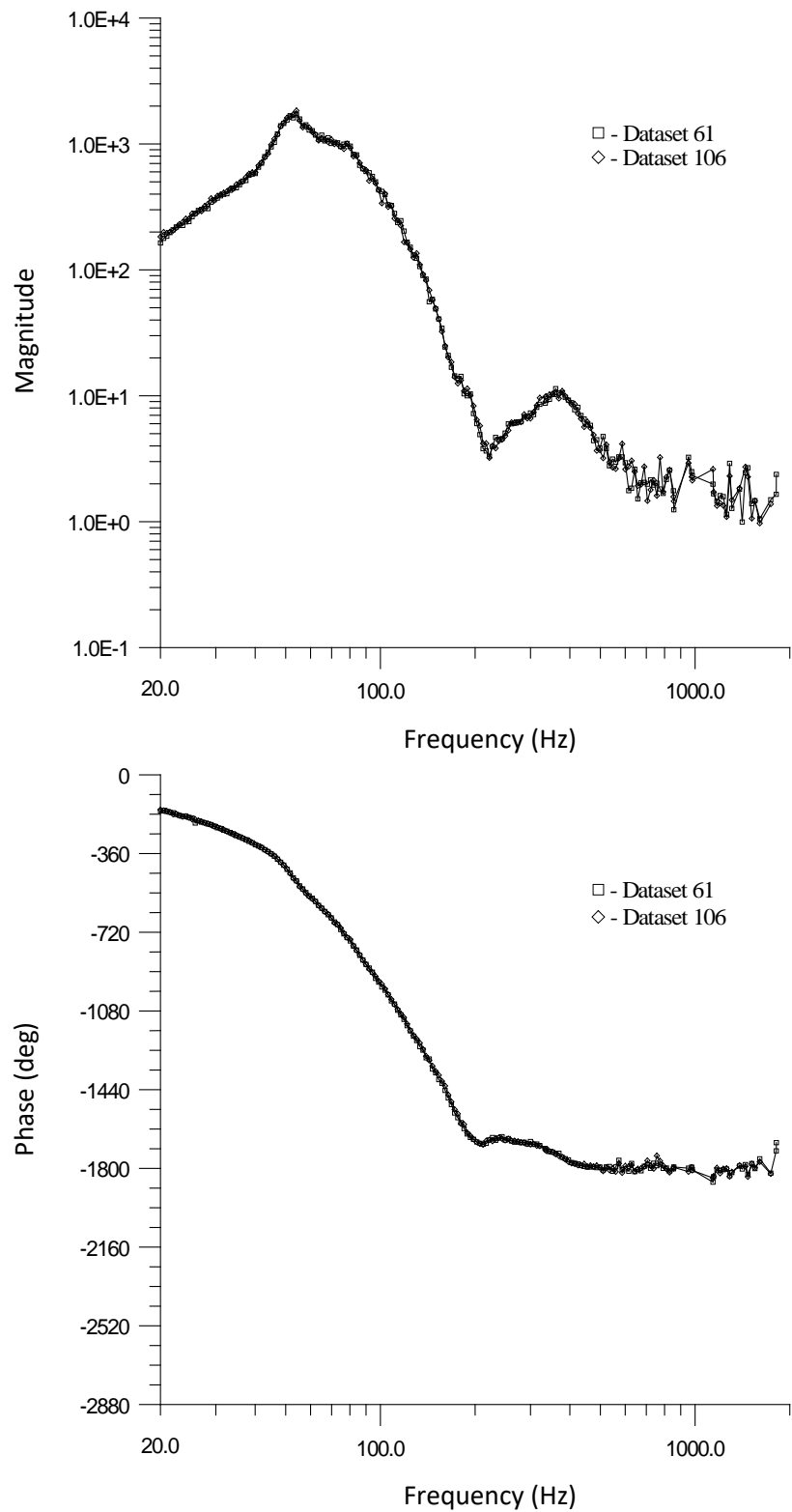


Figure G-23: Measured combustion response function for $\varphi = 0.825$ and $V_R = 3.5$.

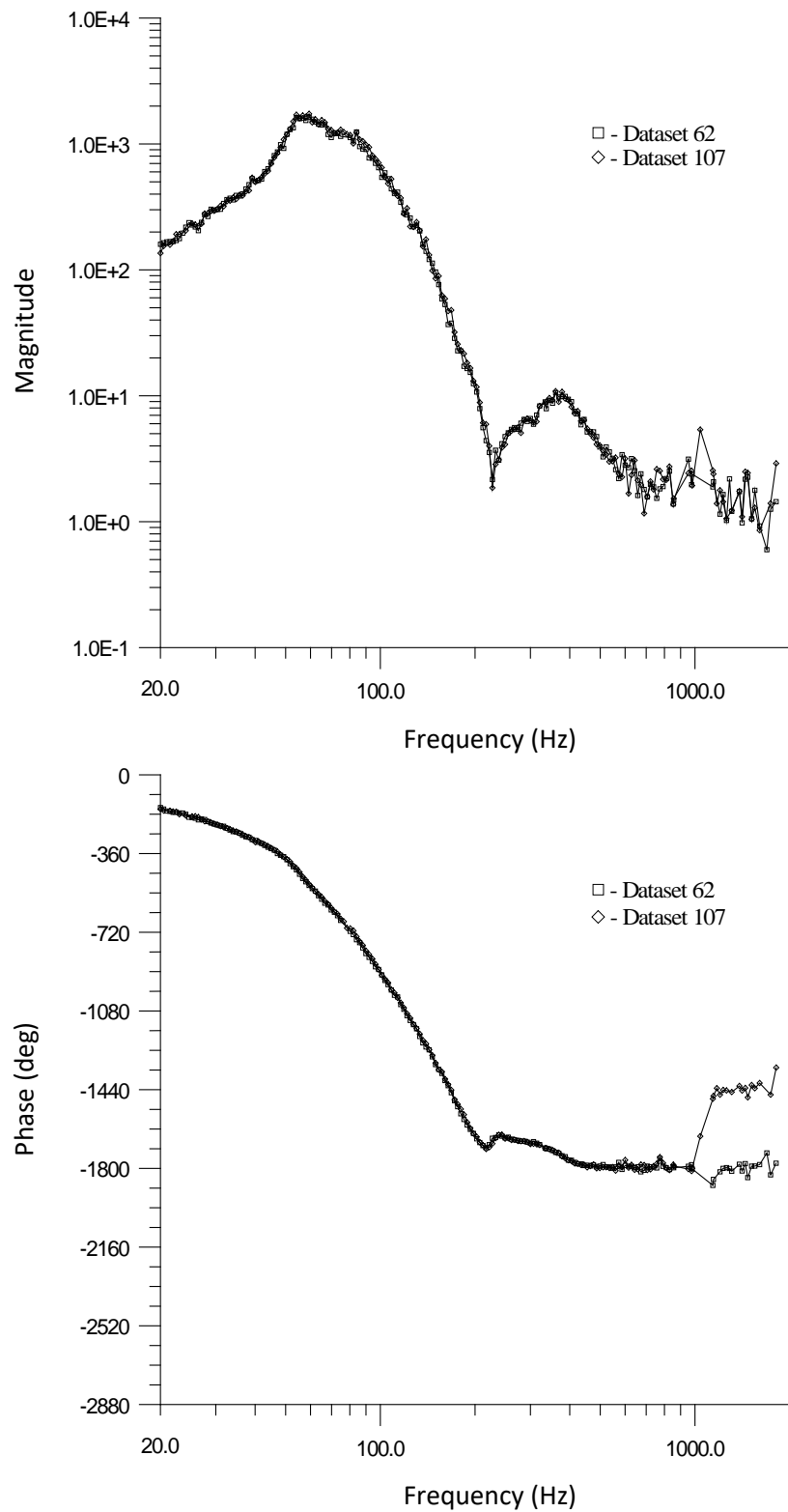


Figure G-24: Measured combustion response function for $\varphi = 0.825$ and $V_R = 4.0$.

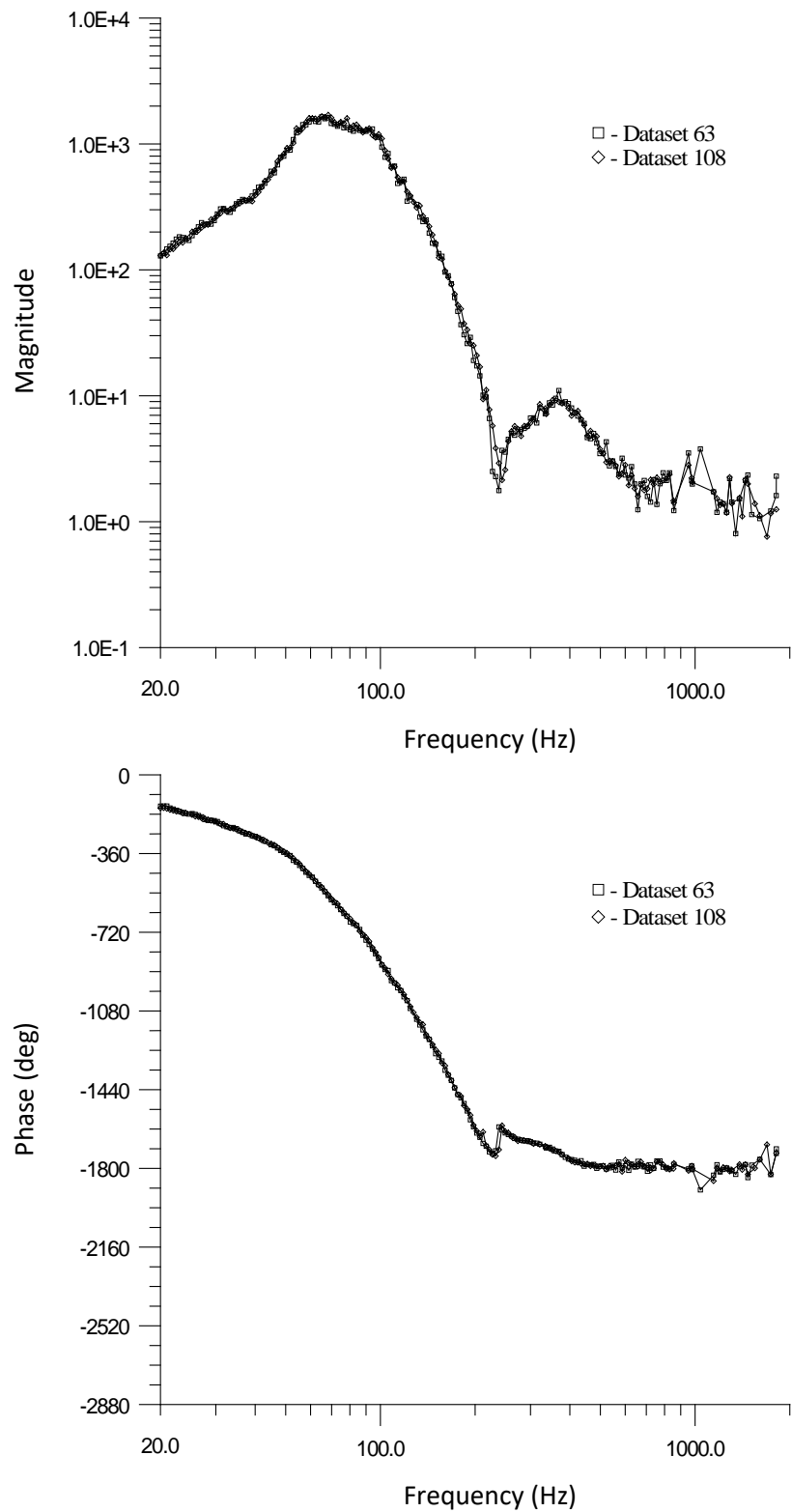


Figure G-25: Measured combustion response function for $\varphi = 0.825$ and $V_R = 4.5$.

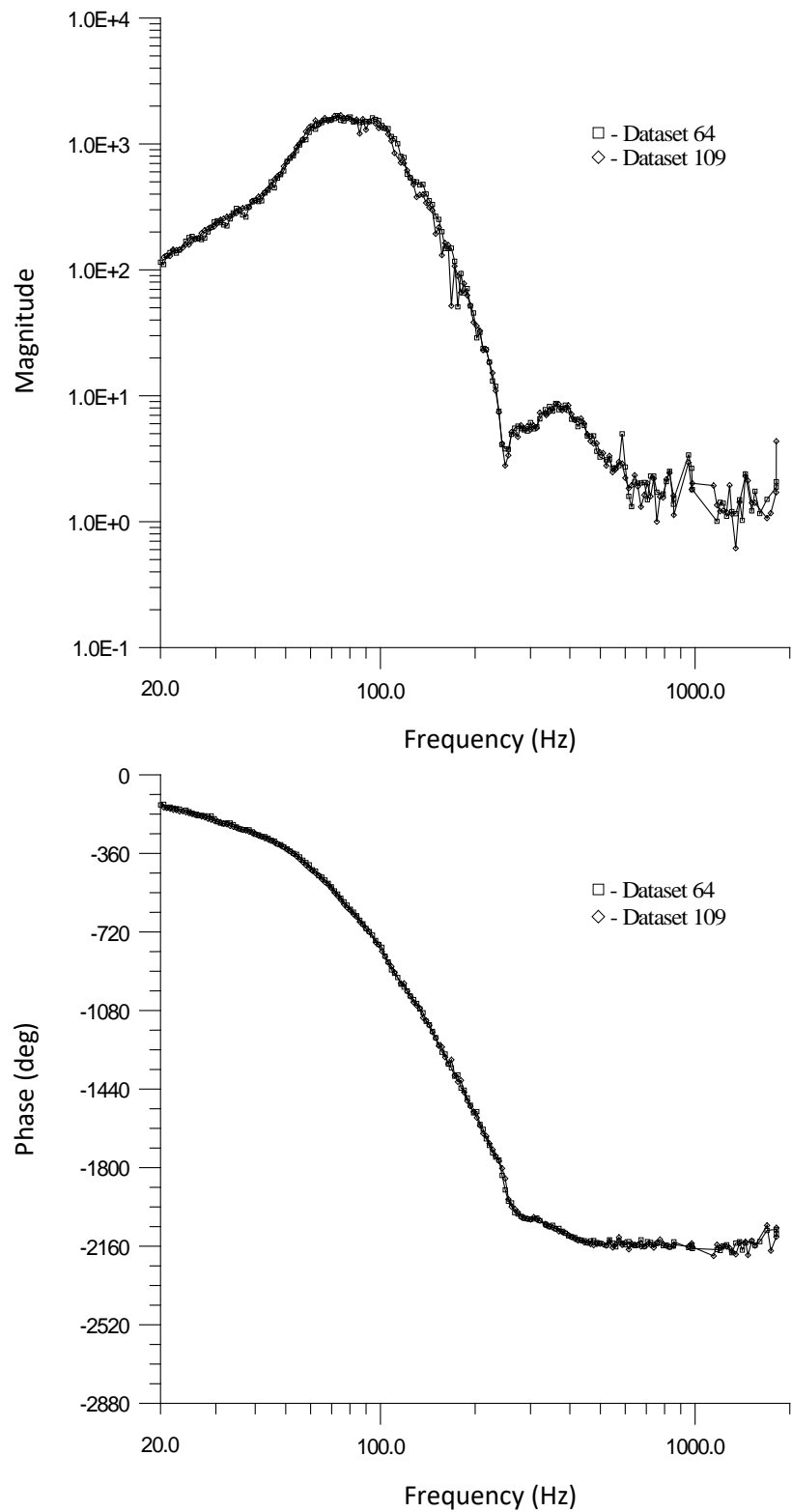


Figure G-26: Measured combustion response function for $\varphi = 0.825$ and $V_R = 5.0$.

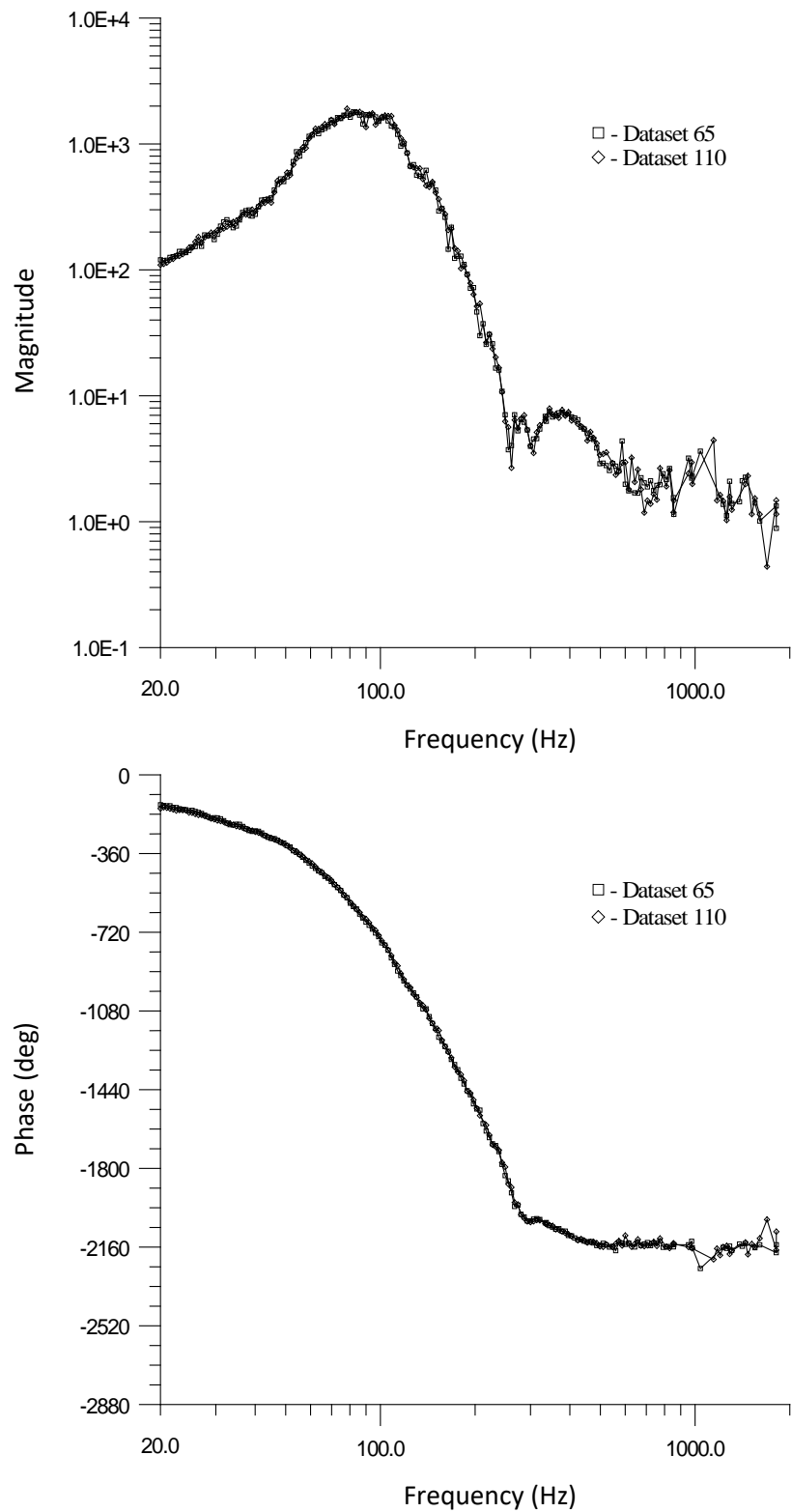


Figure G-27: Measured combustion response function for $\varphi = 0.825$ and $V_R = 5.5$.

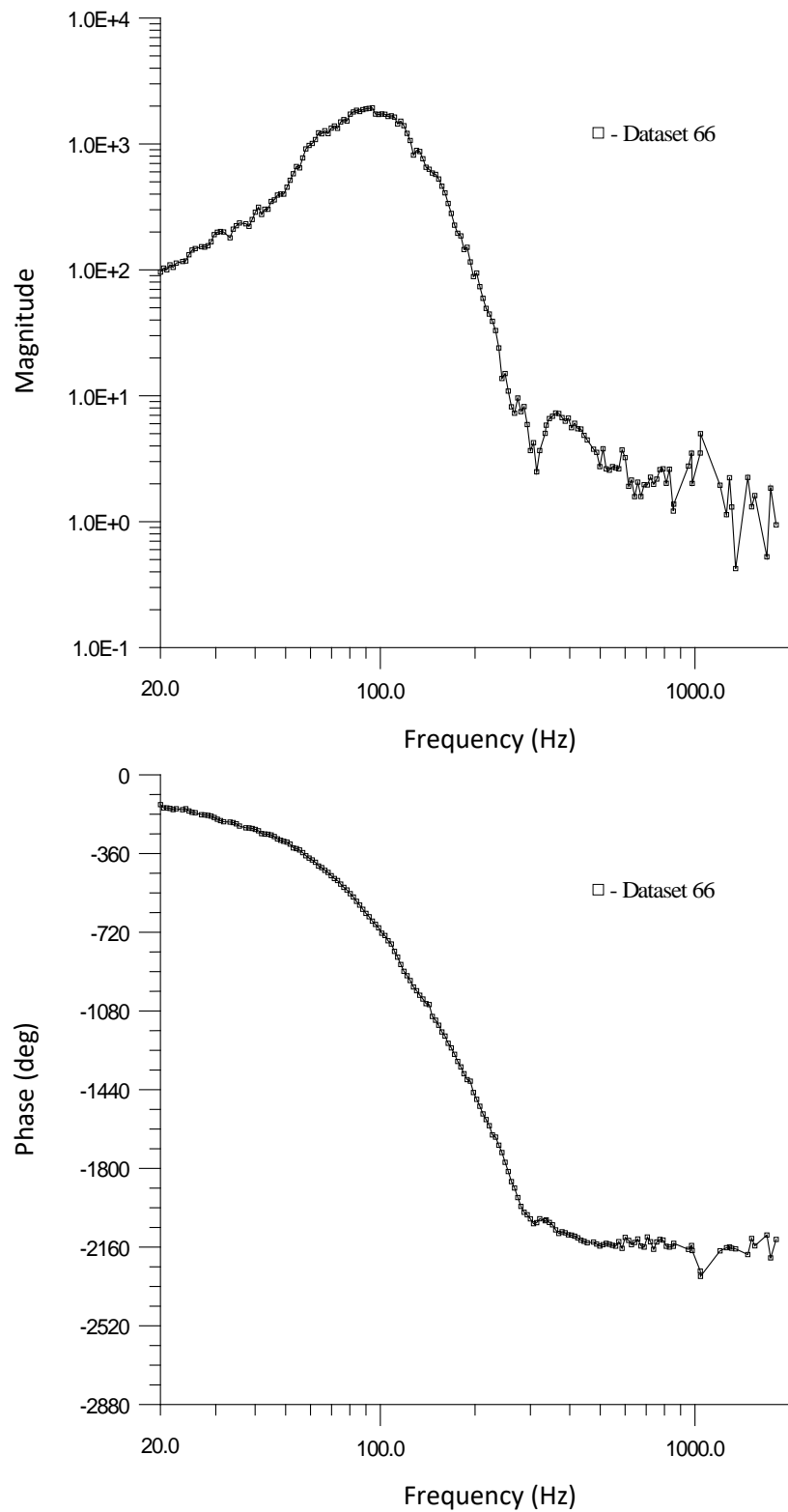


Figure G-28: Measured combustion response function for $\varphi = 0.825$ and $V_R = 6.0$.

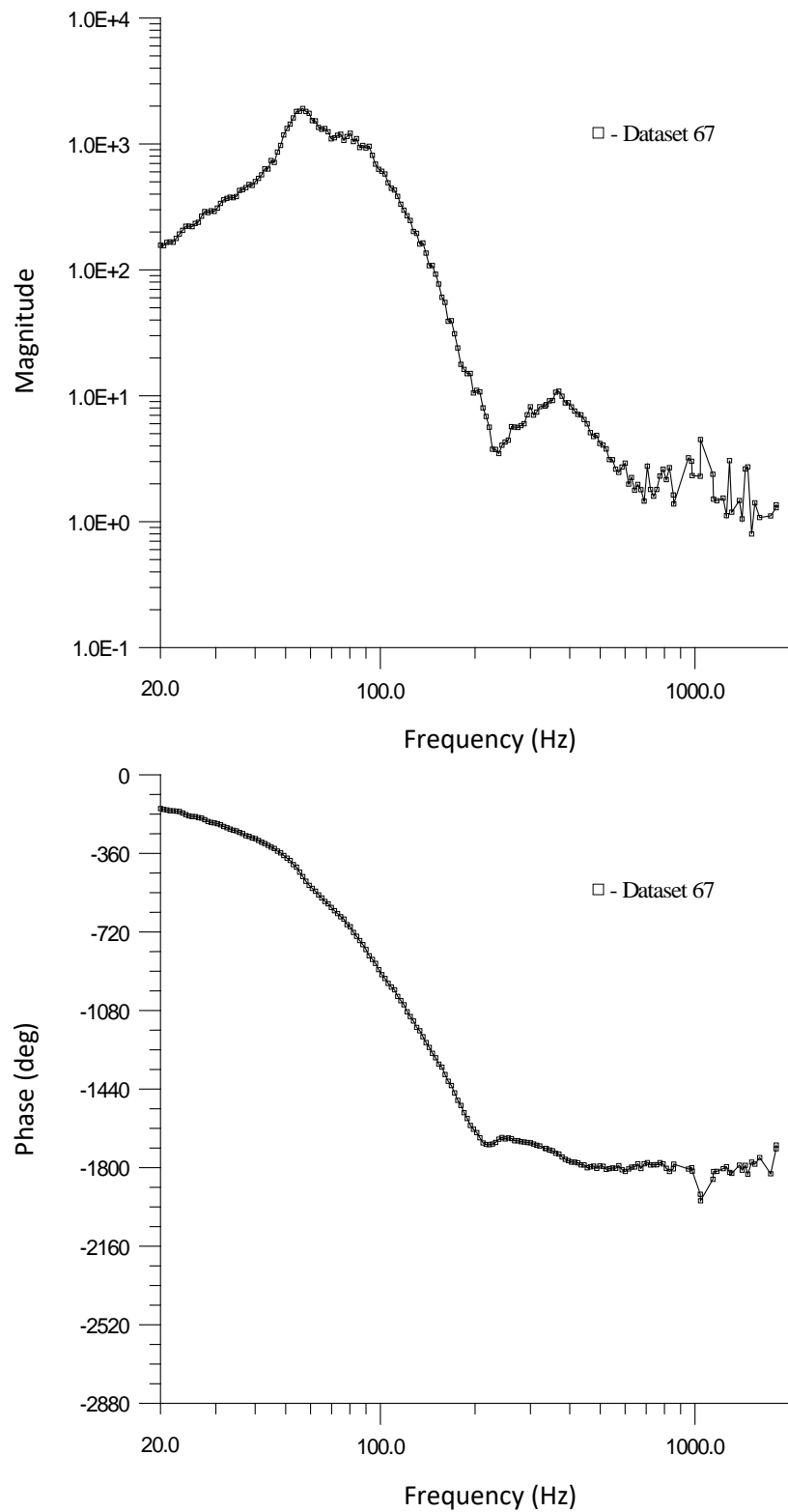


Figure G-29: Measured combustion response function for $\varphi = 0.850$ and $V_R = 3.5$.

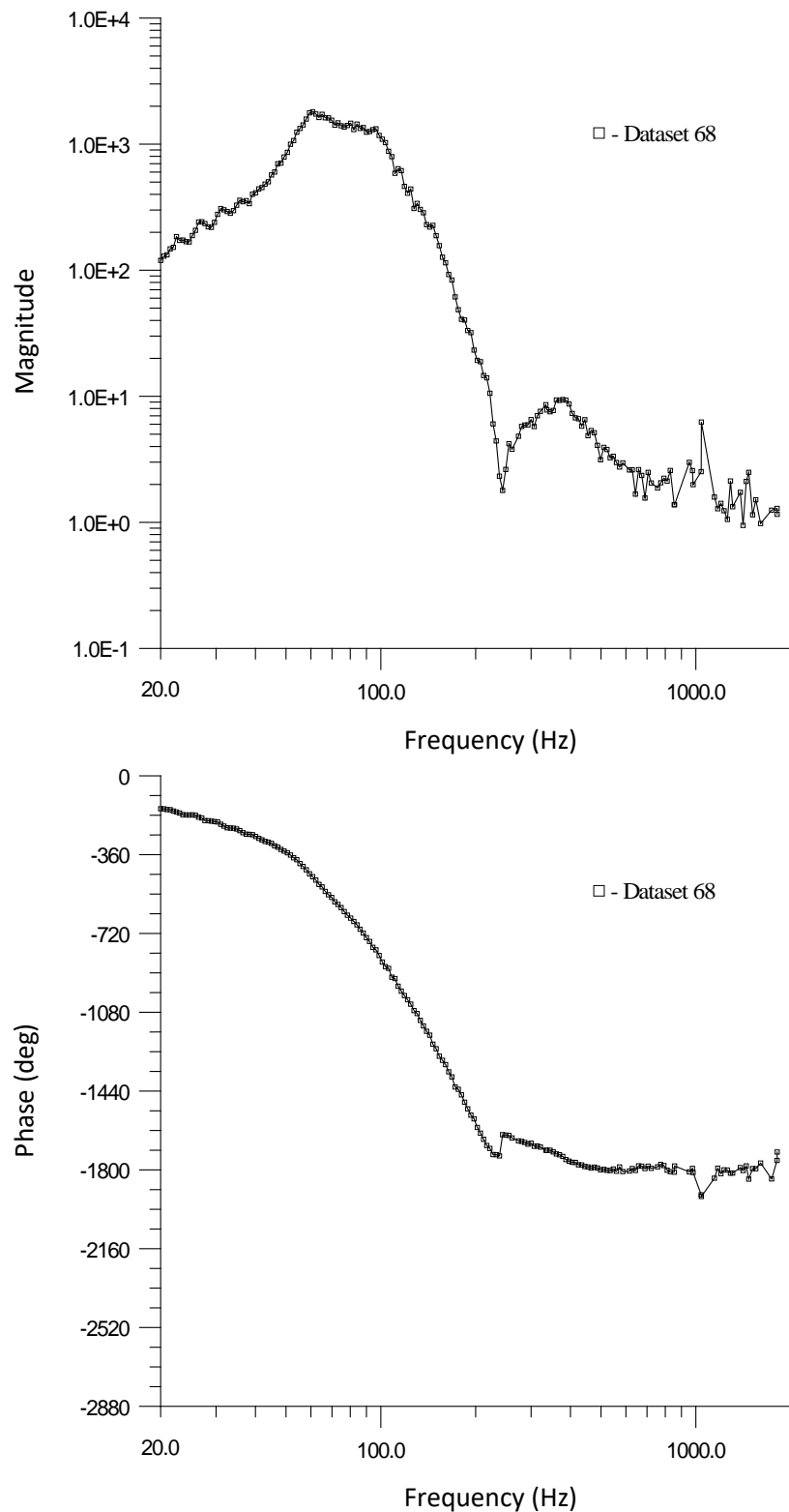


Figure G-30: Measured combustion response function for $\varphi = 0.850$ and $V_R = 4.0$.

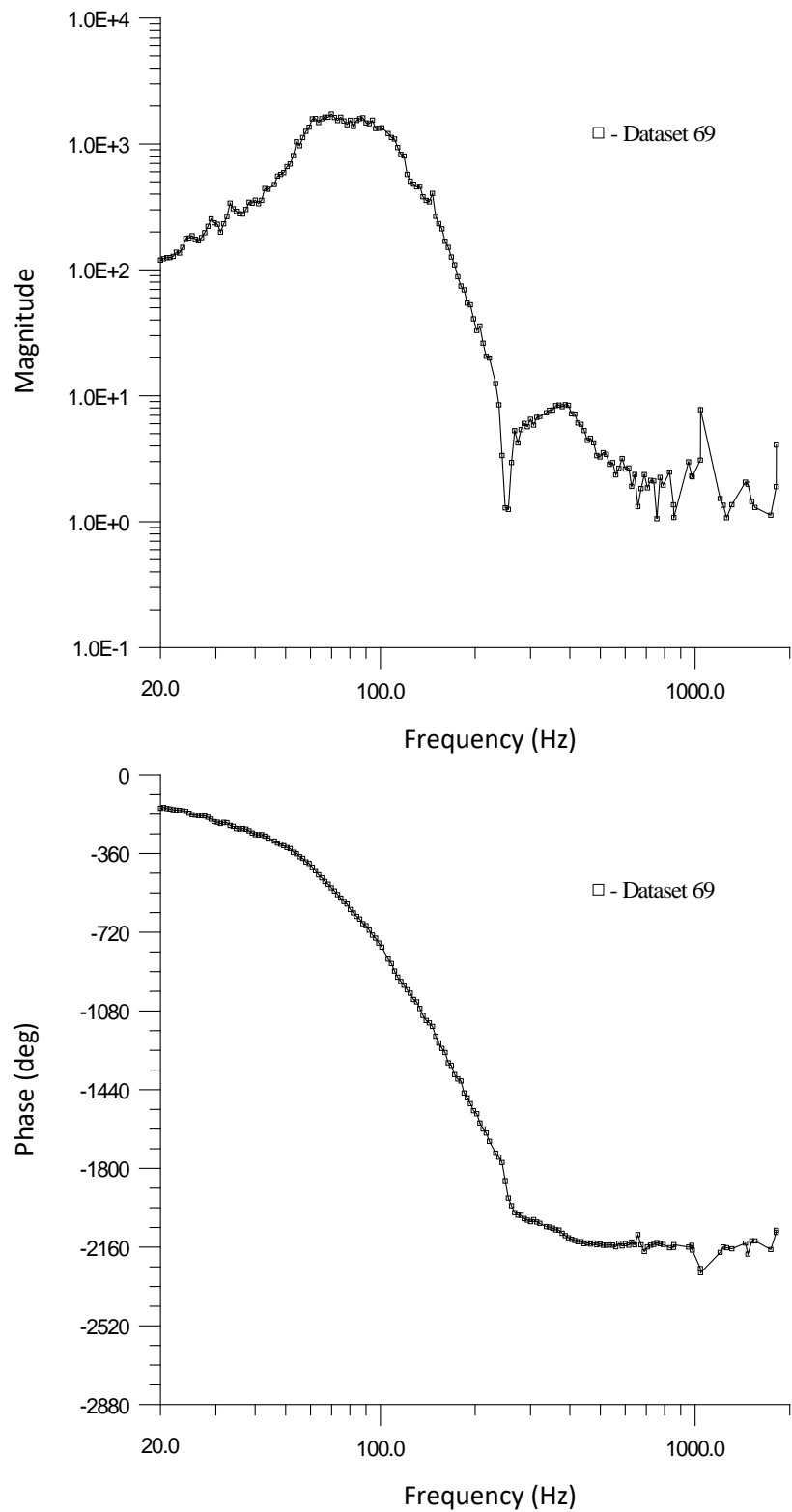


Figure G-31: Measured combustion response function for $\varphi = 0.850$ and $V_R = 4.5$.

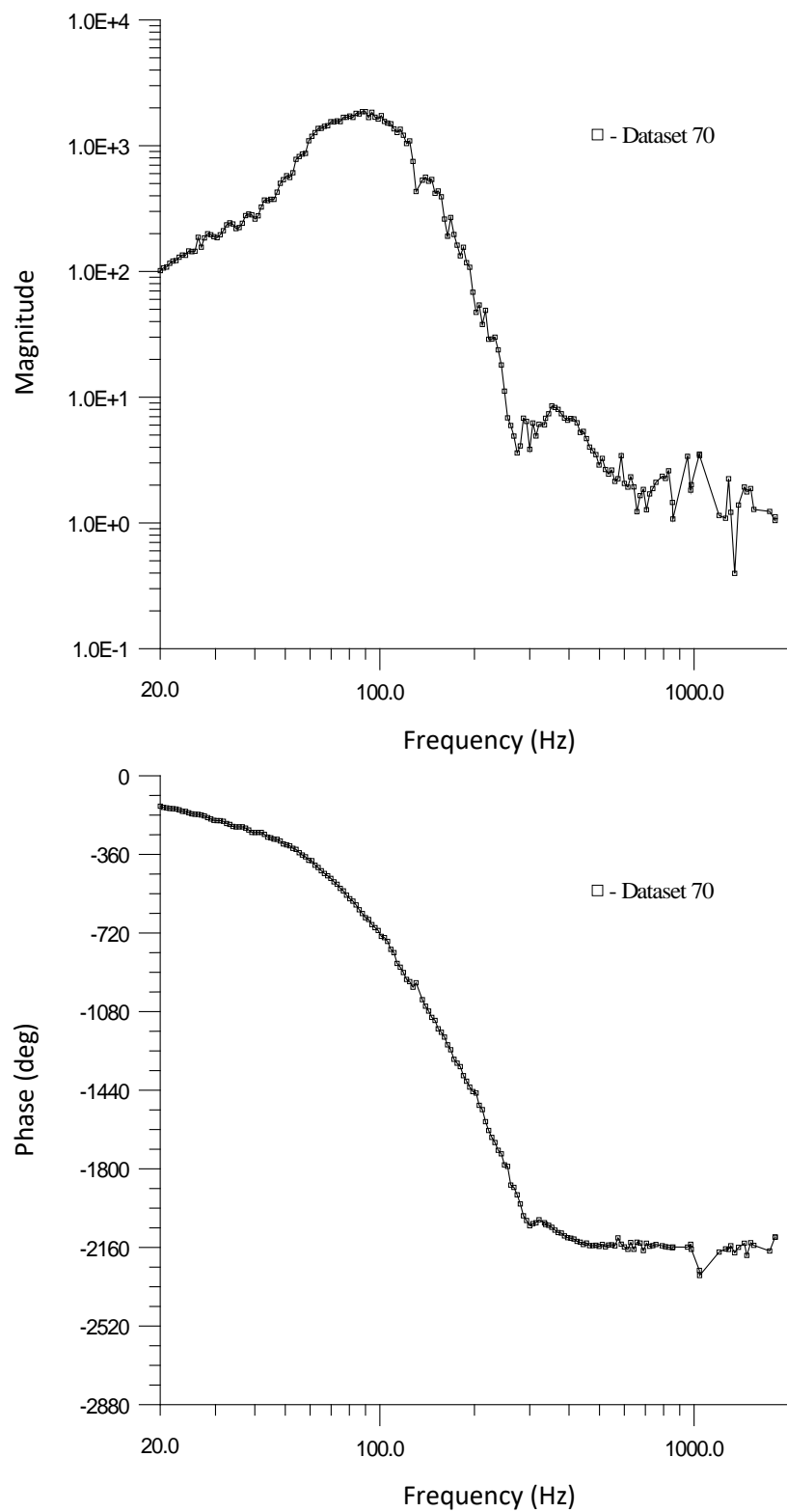


Figure G-32: Measured combustion response function for $\varphi = 0.850$ and $V_R = 5.0$.

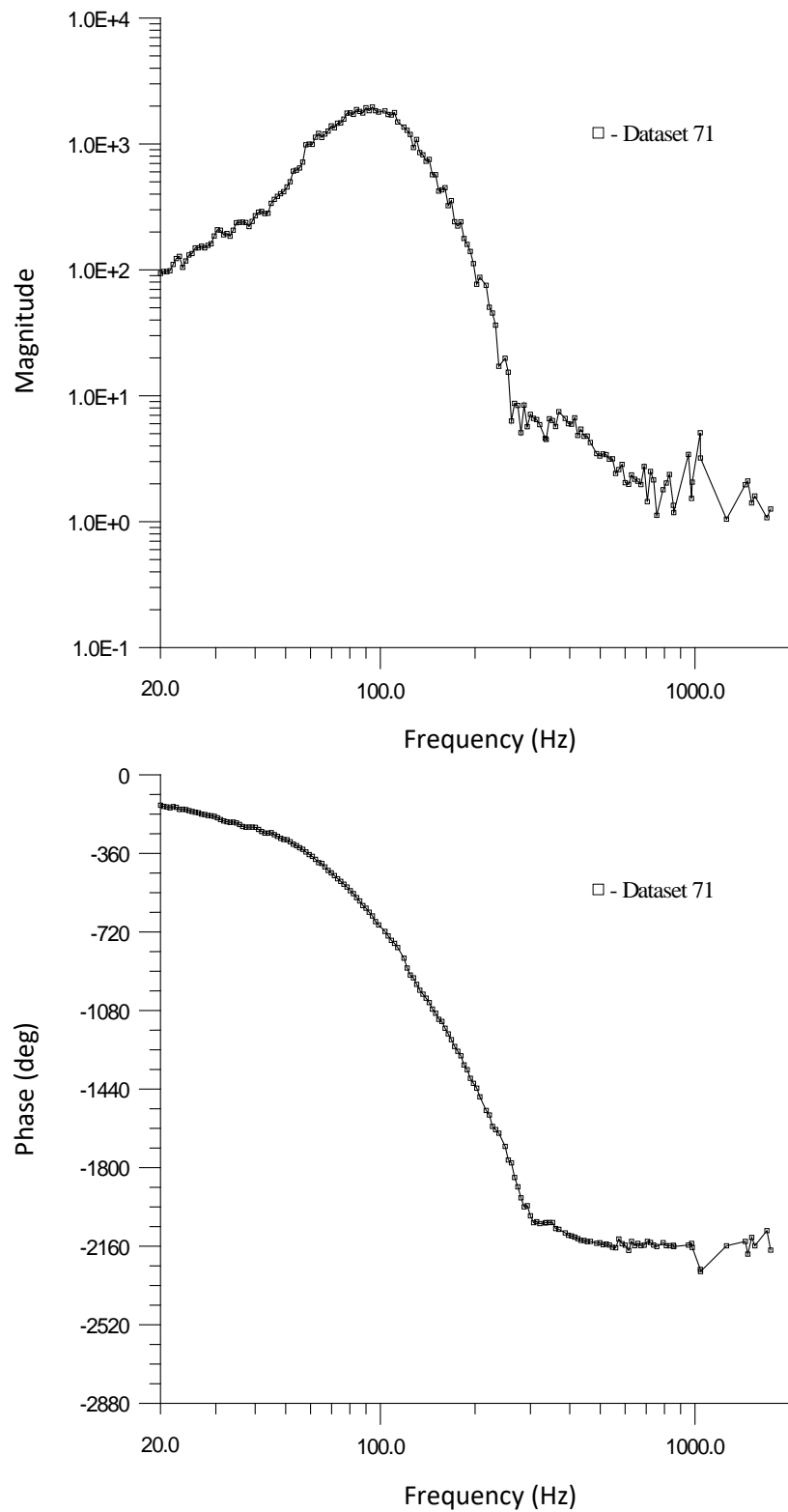


Figure G-33: Measured combustion response function for $\varphi = 0.850$ and $V_R = 5.5$.

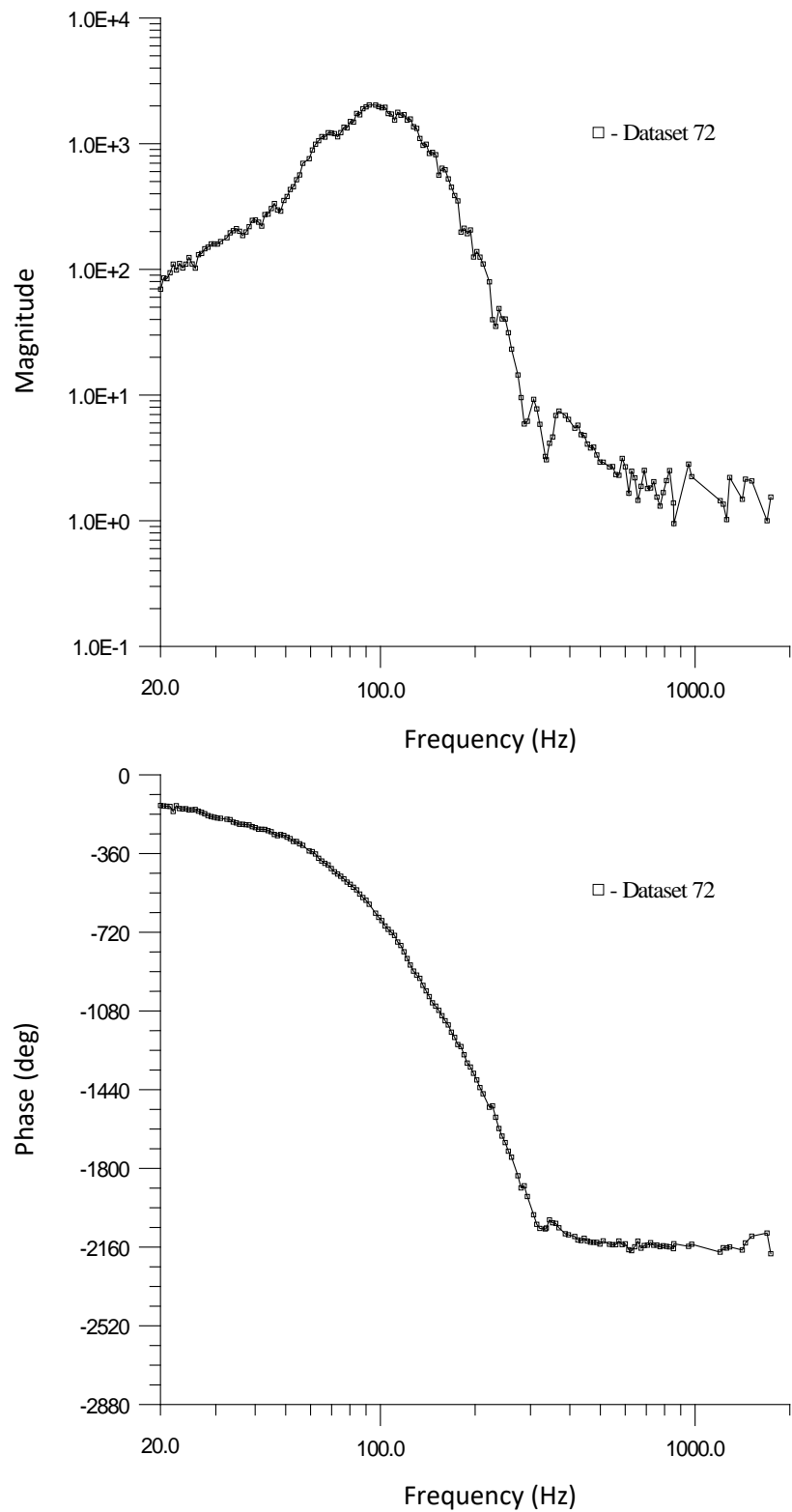


Figure G-34: Measured combustion response function for $\varphi = 0.850$ and $V_R = 6.0$.

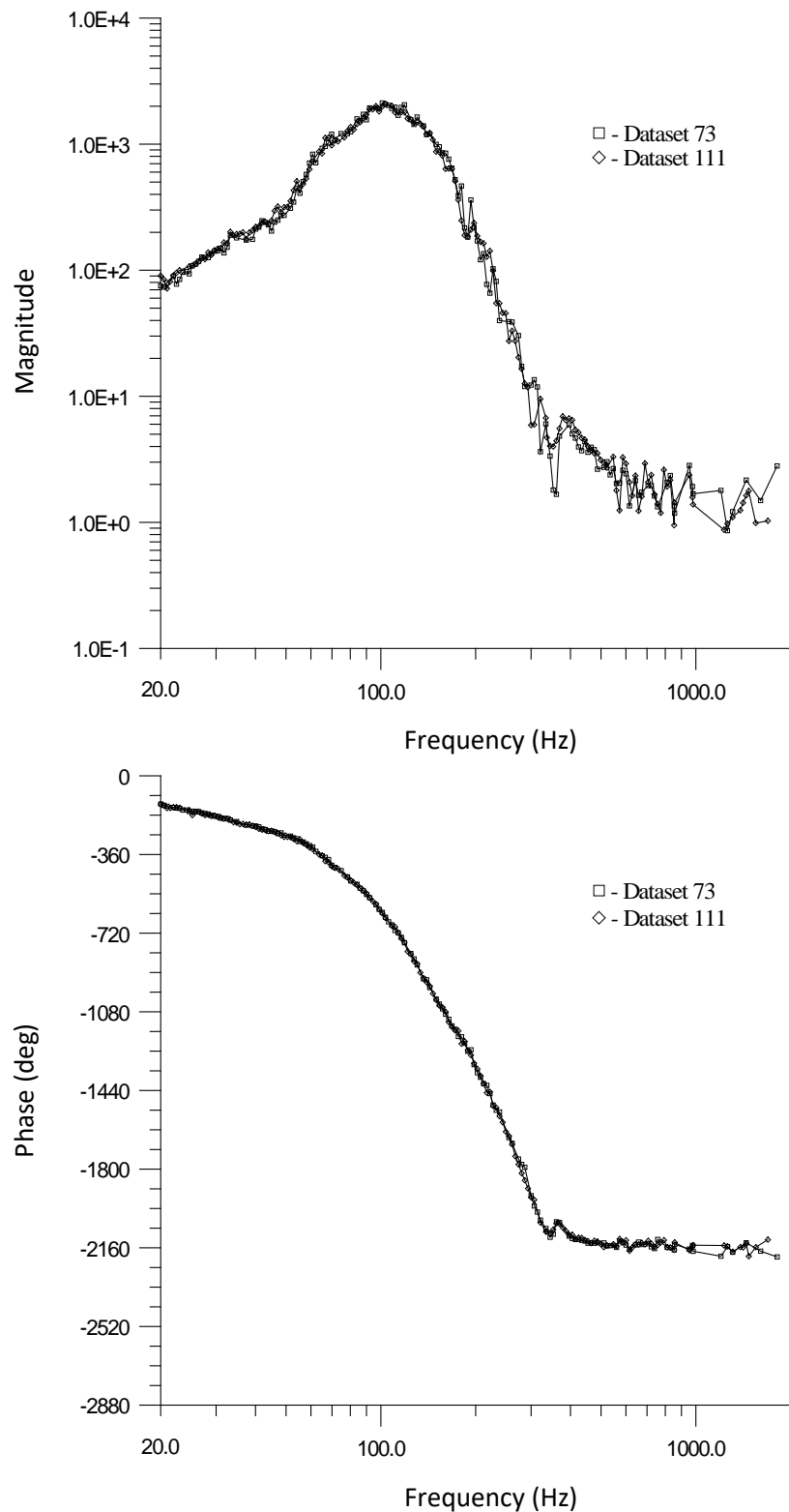


Figure G-35: Measured combustion response function for $\varphi = 0.850$ and $V_R = 6.5$.

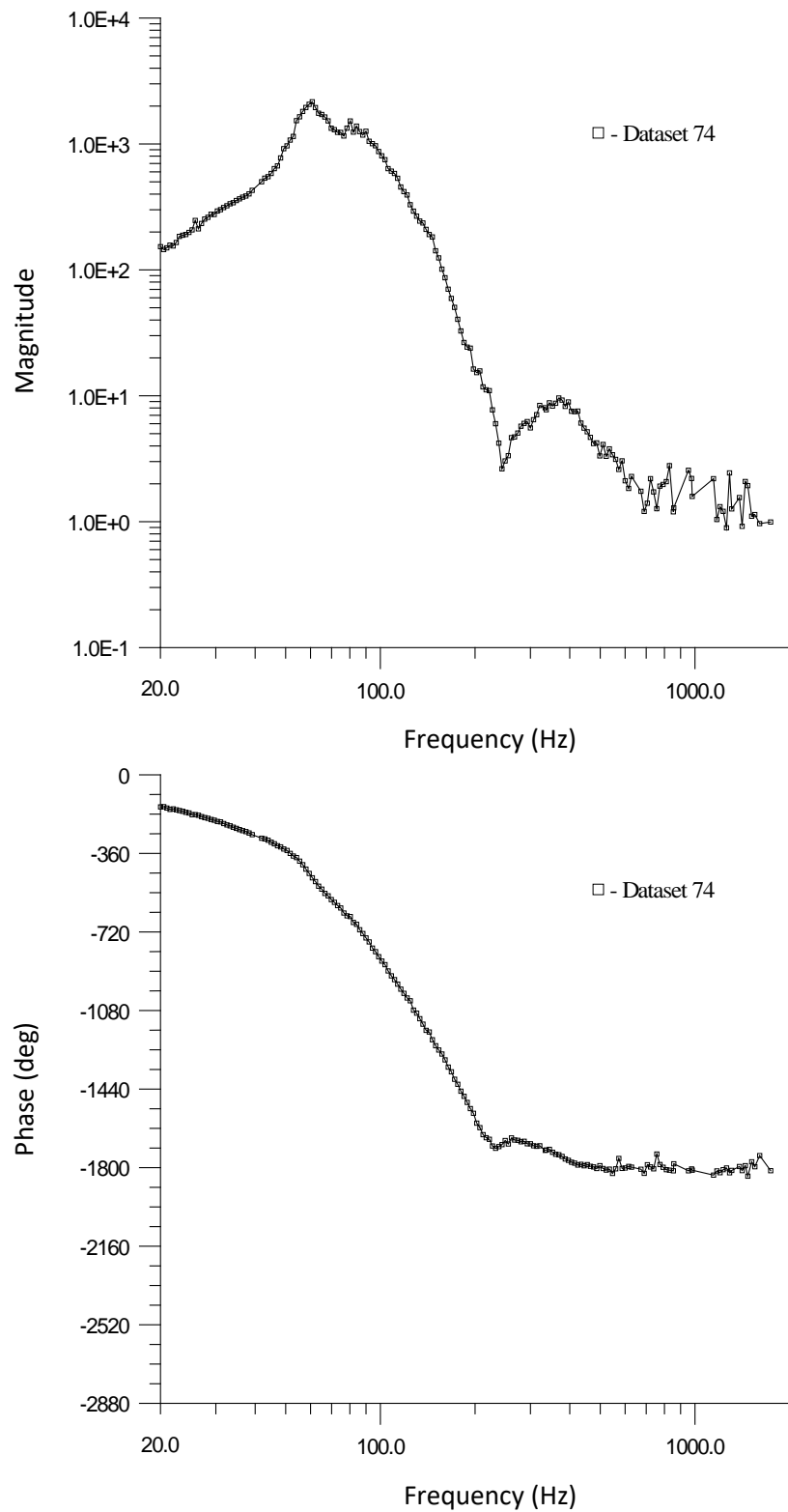


Figure G-36: Measured combustion response function for $\varphi = 0.875$ and $V_R = 3.5$.

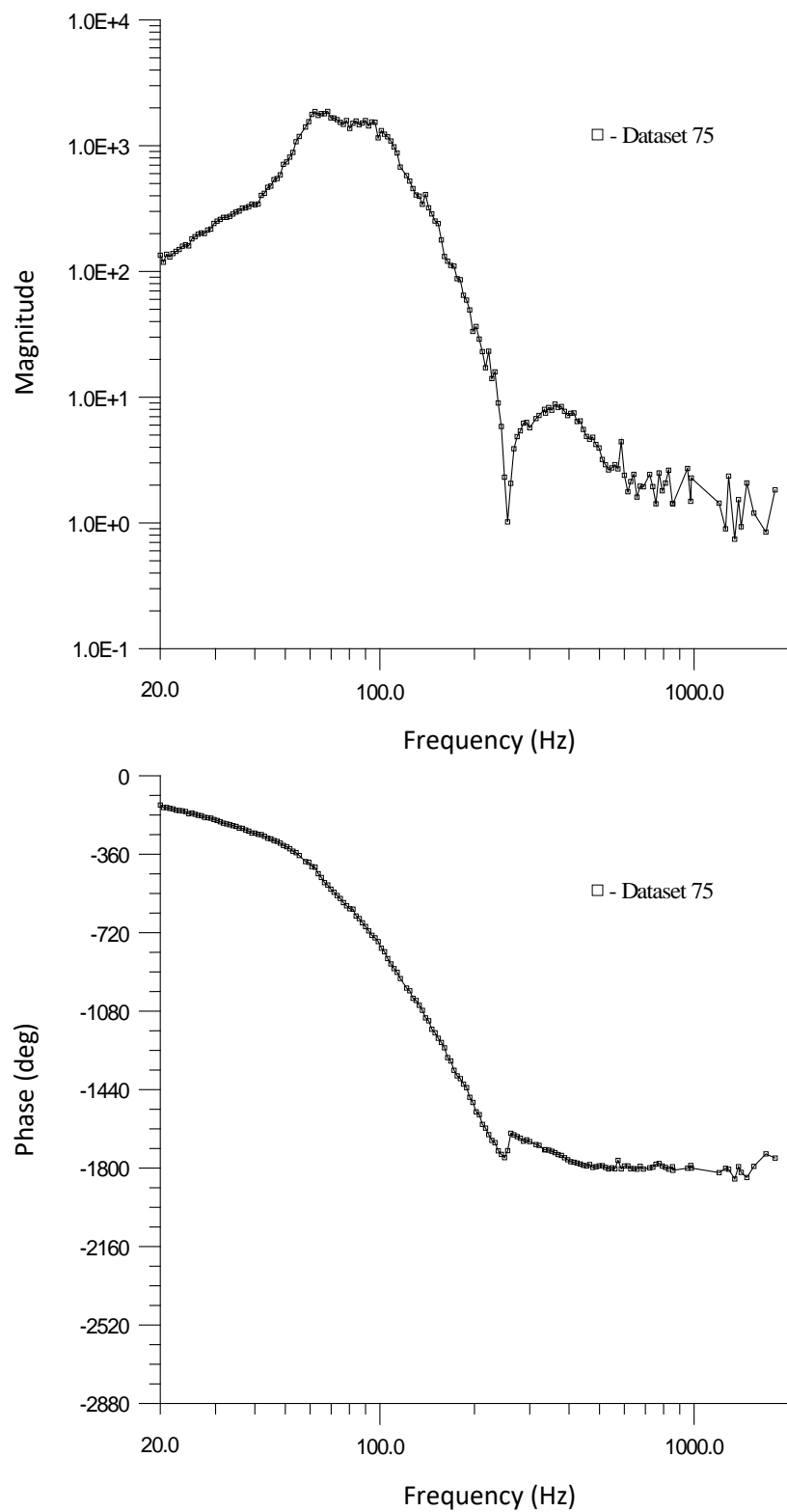


Figure G-37: Measured combustion response function for $\varphi = 0.875$ and $V_R = 4.0$.

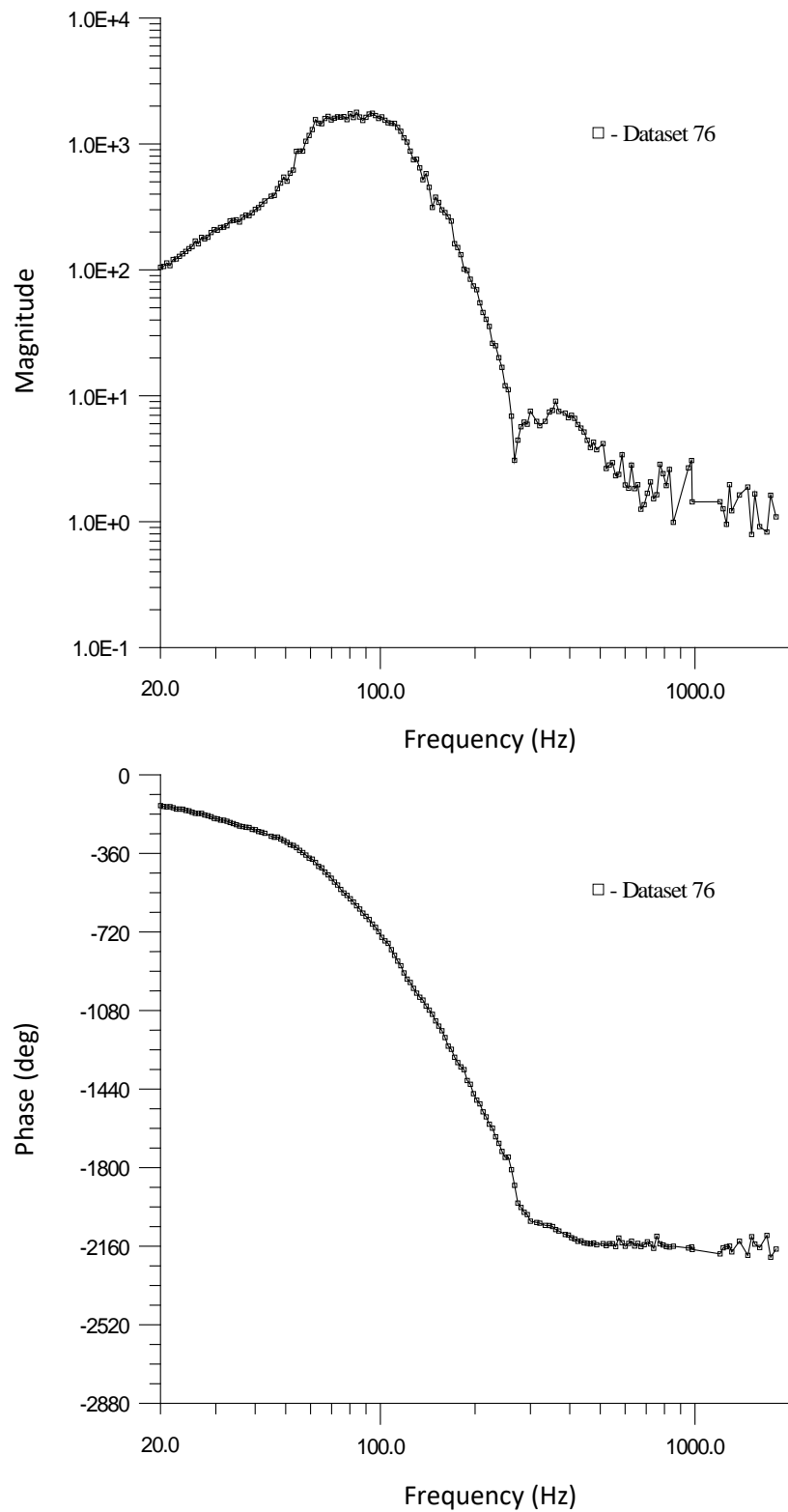


Figure G-38: Measured combustion response function for $\varphi = 0.875$ and $V_R = 4.5$.

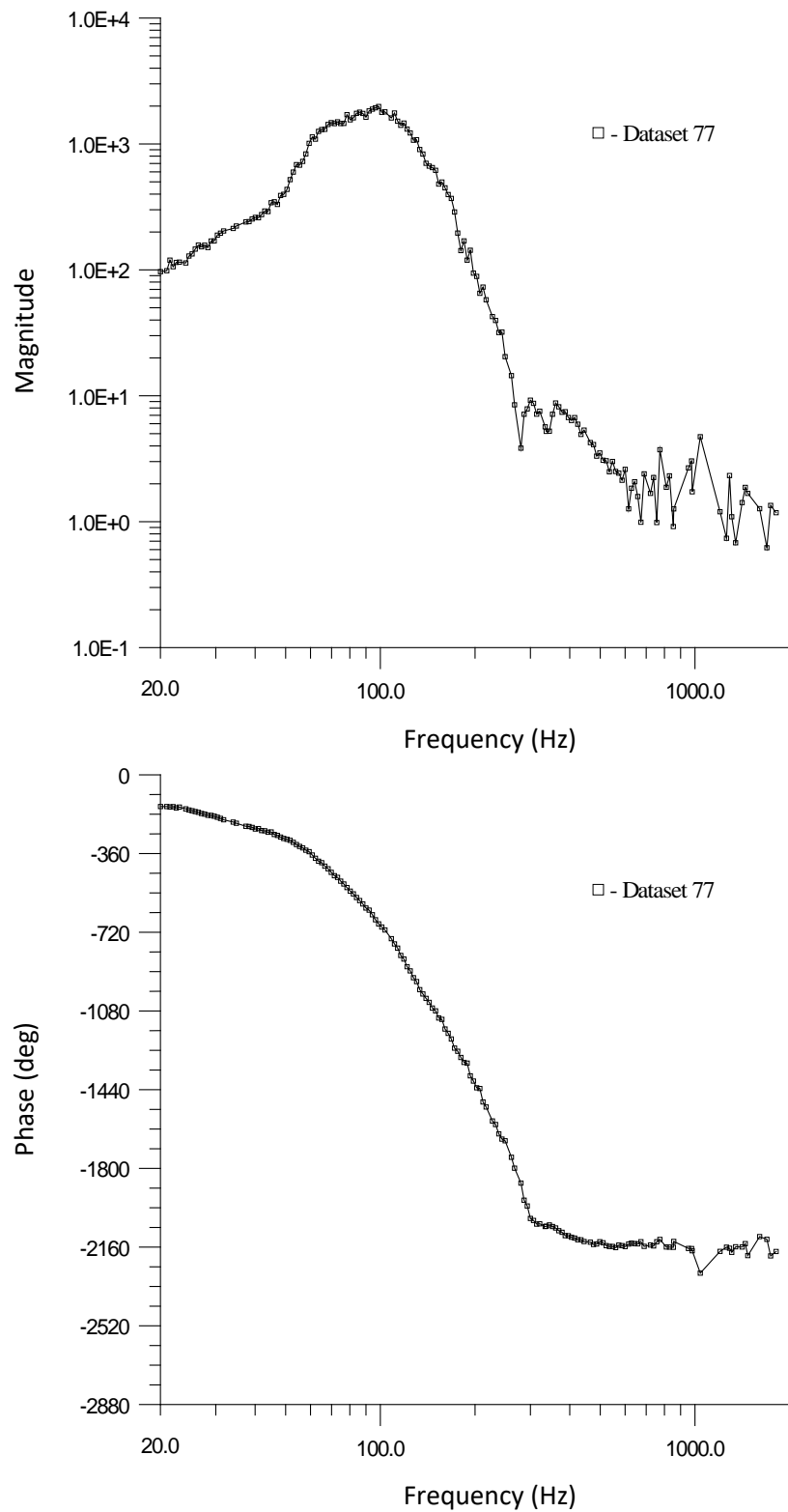


Figure G-39: Measured combustion response function for $\varphi = 0.875$ and $V_R = 5.0$.

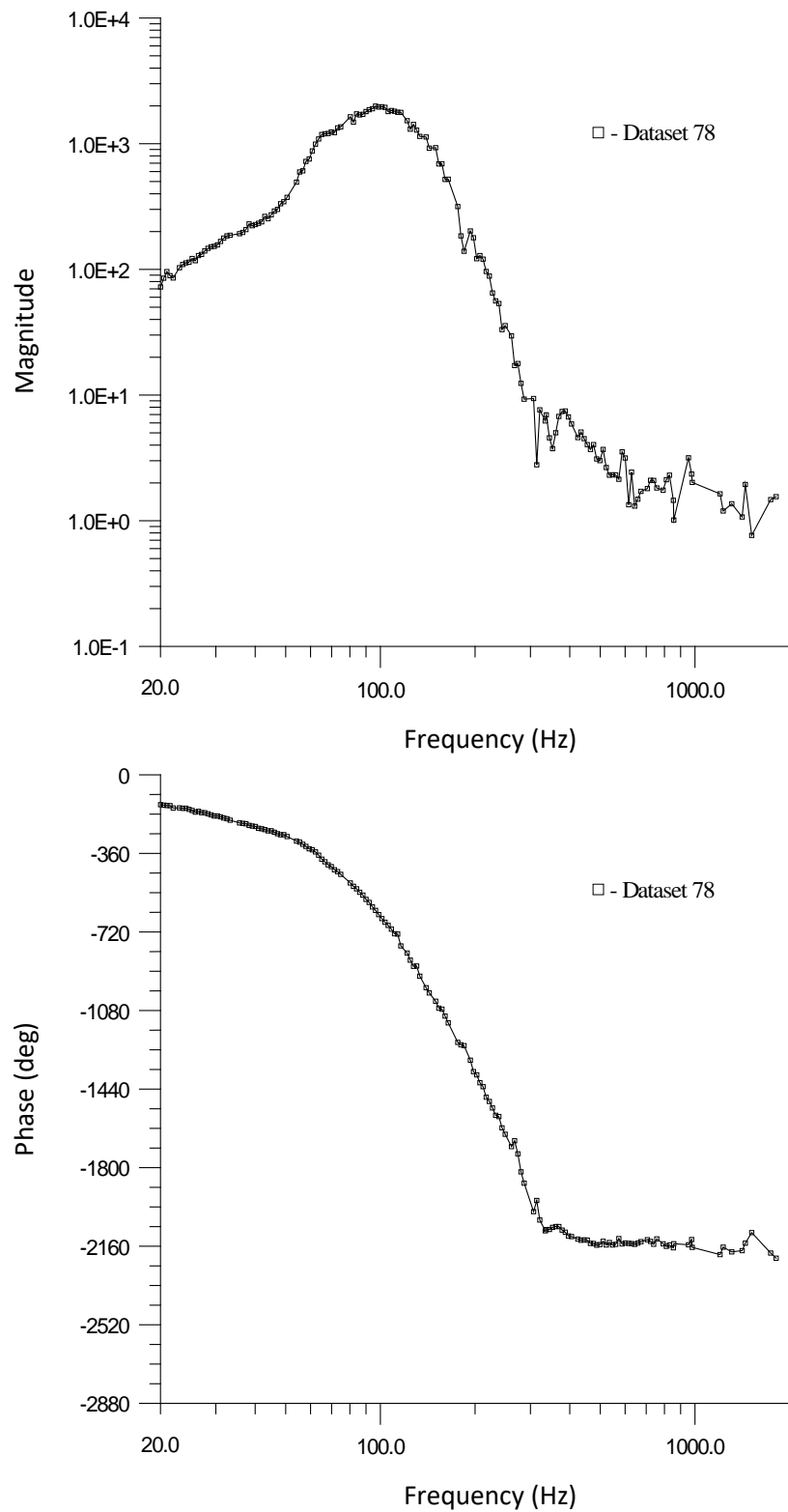


Figure G-40: Measured combustion response function for $\varphi = 0.875$ and $V_R = 5.5$.

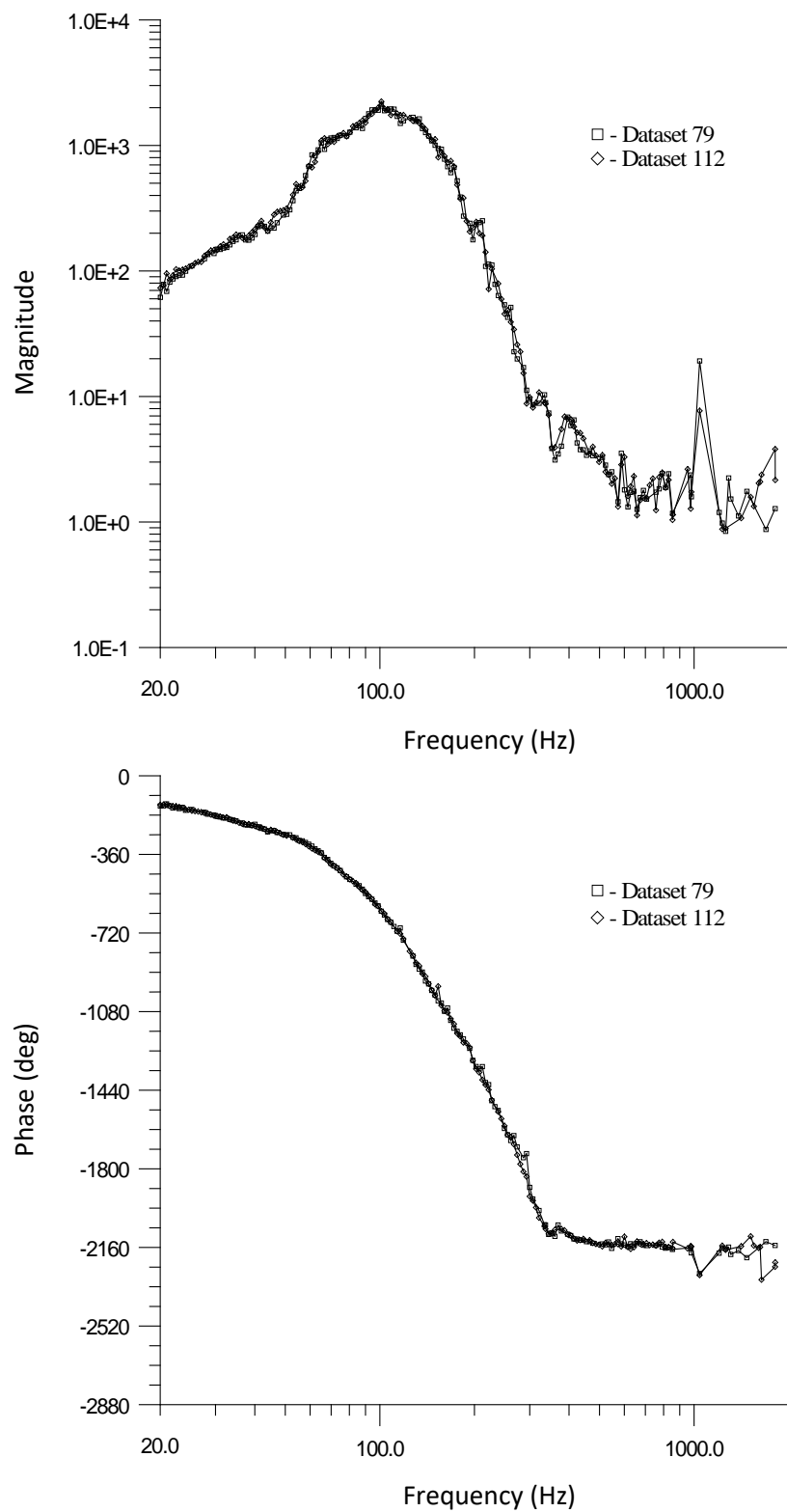


Figure G-41: Measured combustion response function for $\varphi = 0.875$ and $V_R = 6.0$.

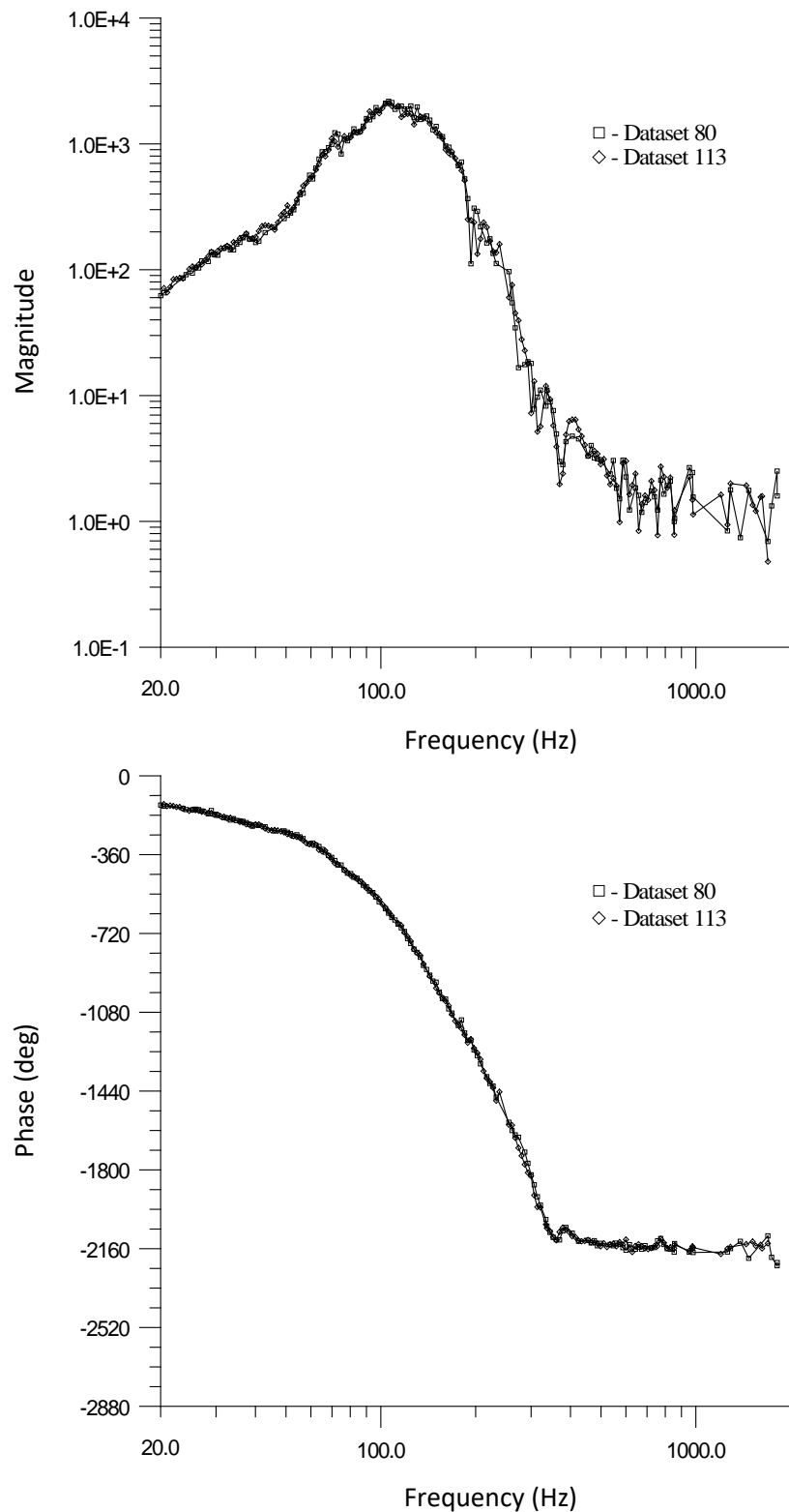


Figure G-42: Measured combustion response function for $\varphi = 0.875$ and $V_R = 6.5$.

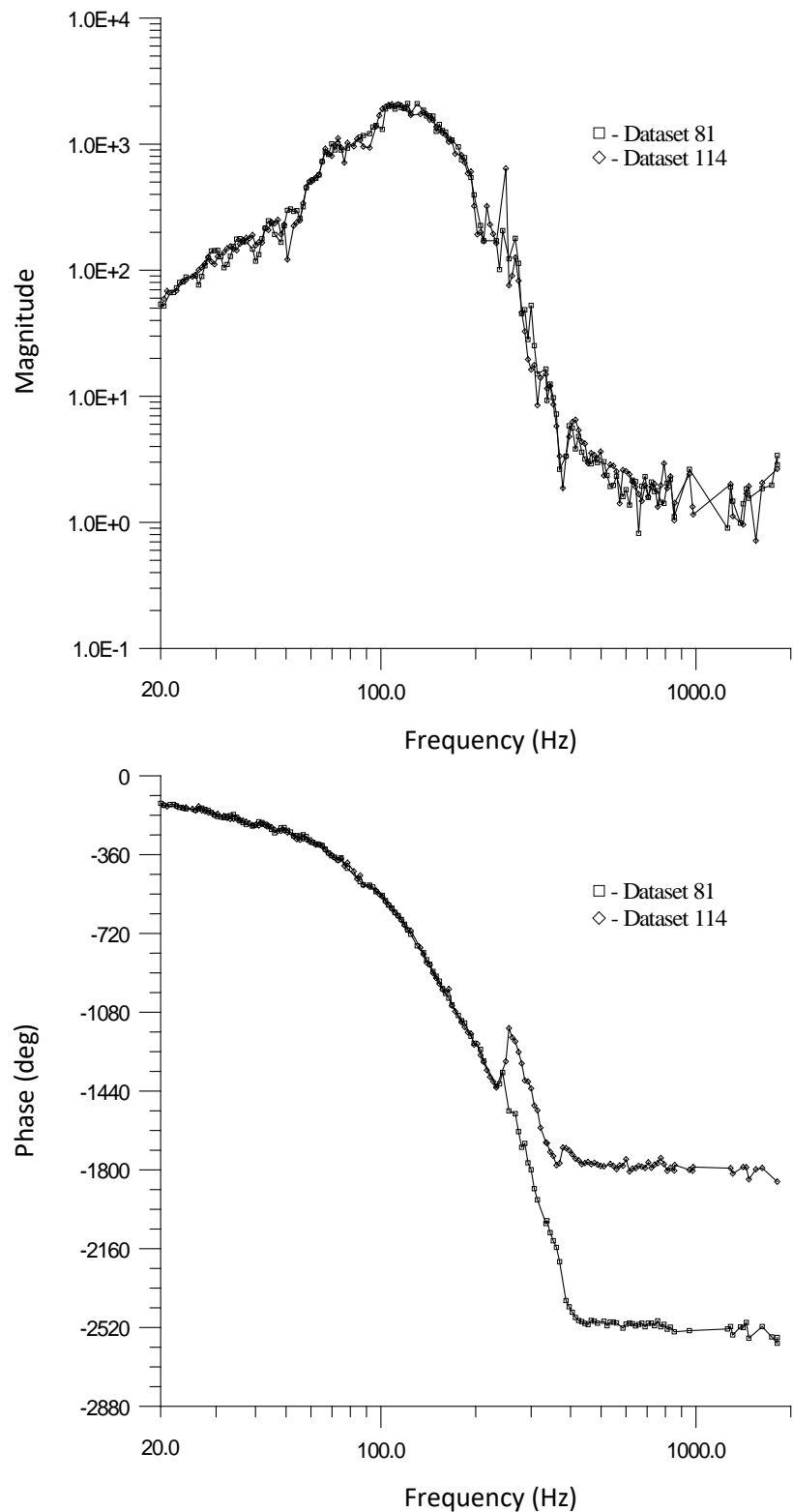


Figure G-43: Measured combustion response function for $\varphi = 0.875$ and $V_R = 7.0$.

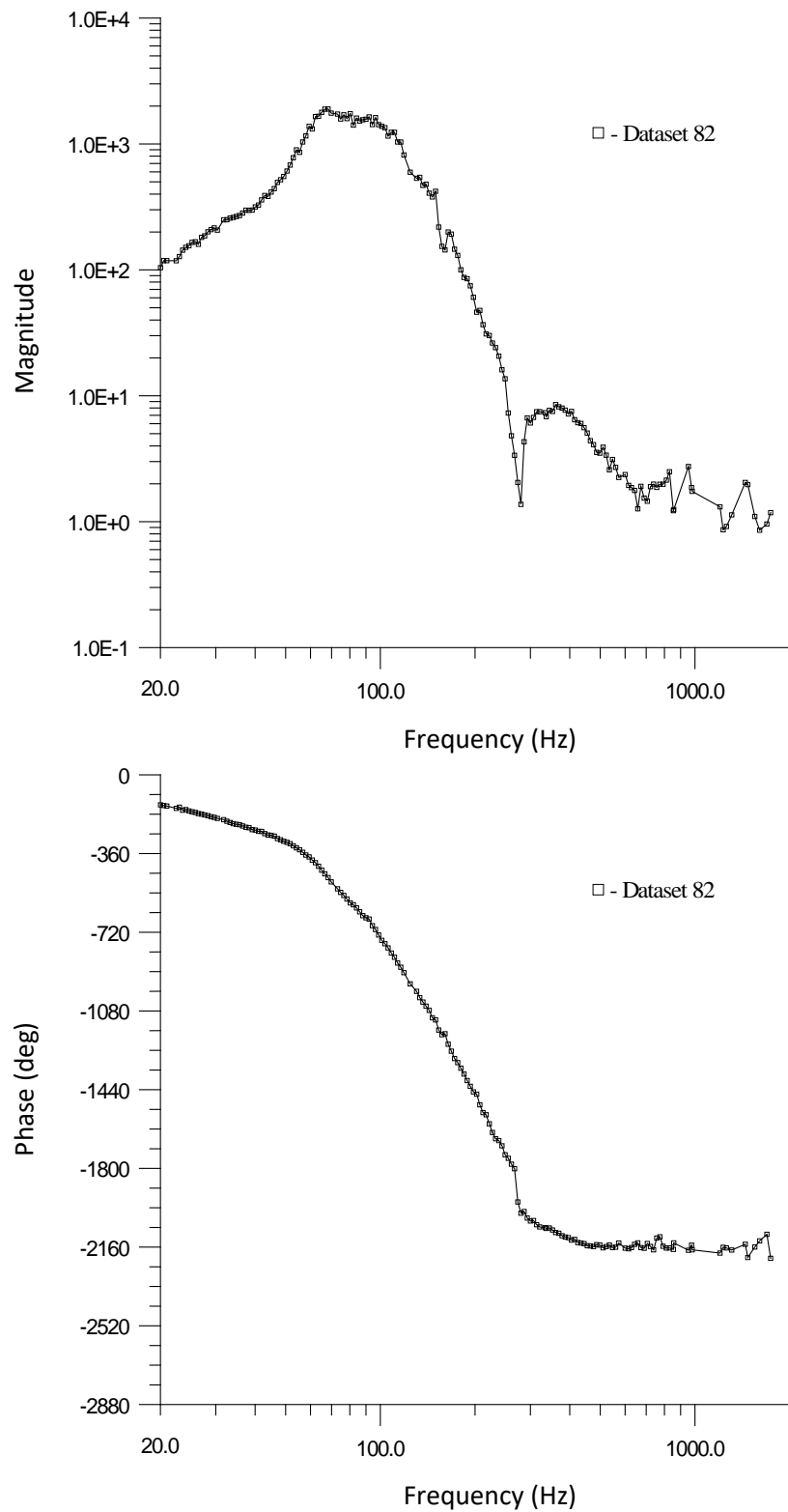


Figure G-44: Measured combustion response function for $\varphi = 0.900$ and $V_R = 4.0$.

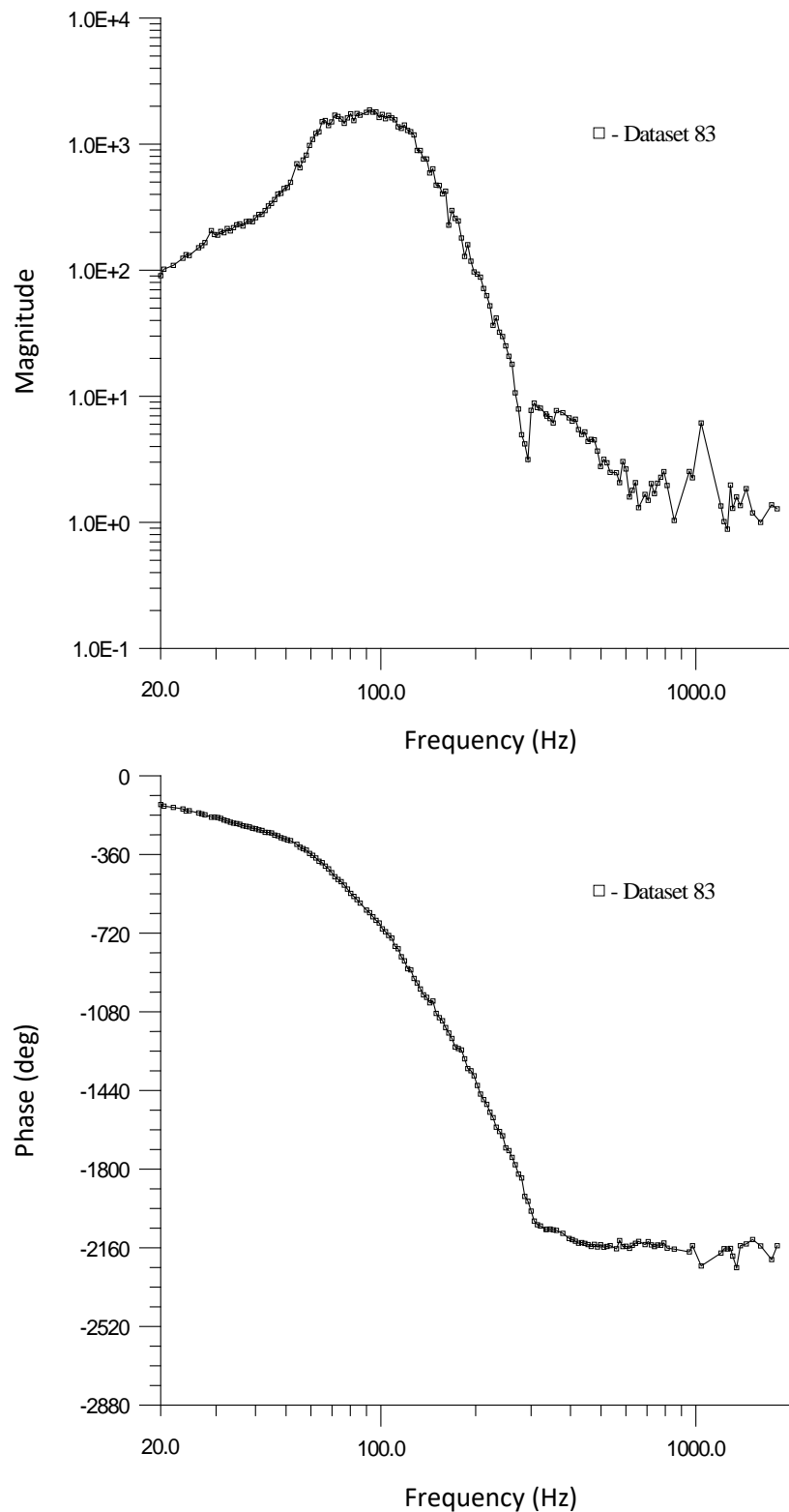


Figure G-45: Measured combustion response function for $\varphi = 0.900$ and $V_R = 4.5$.

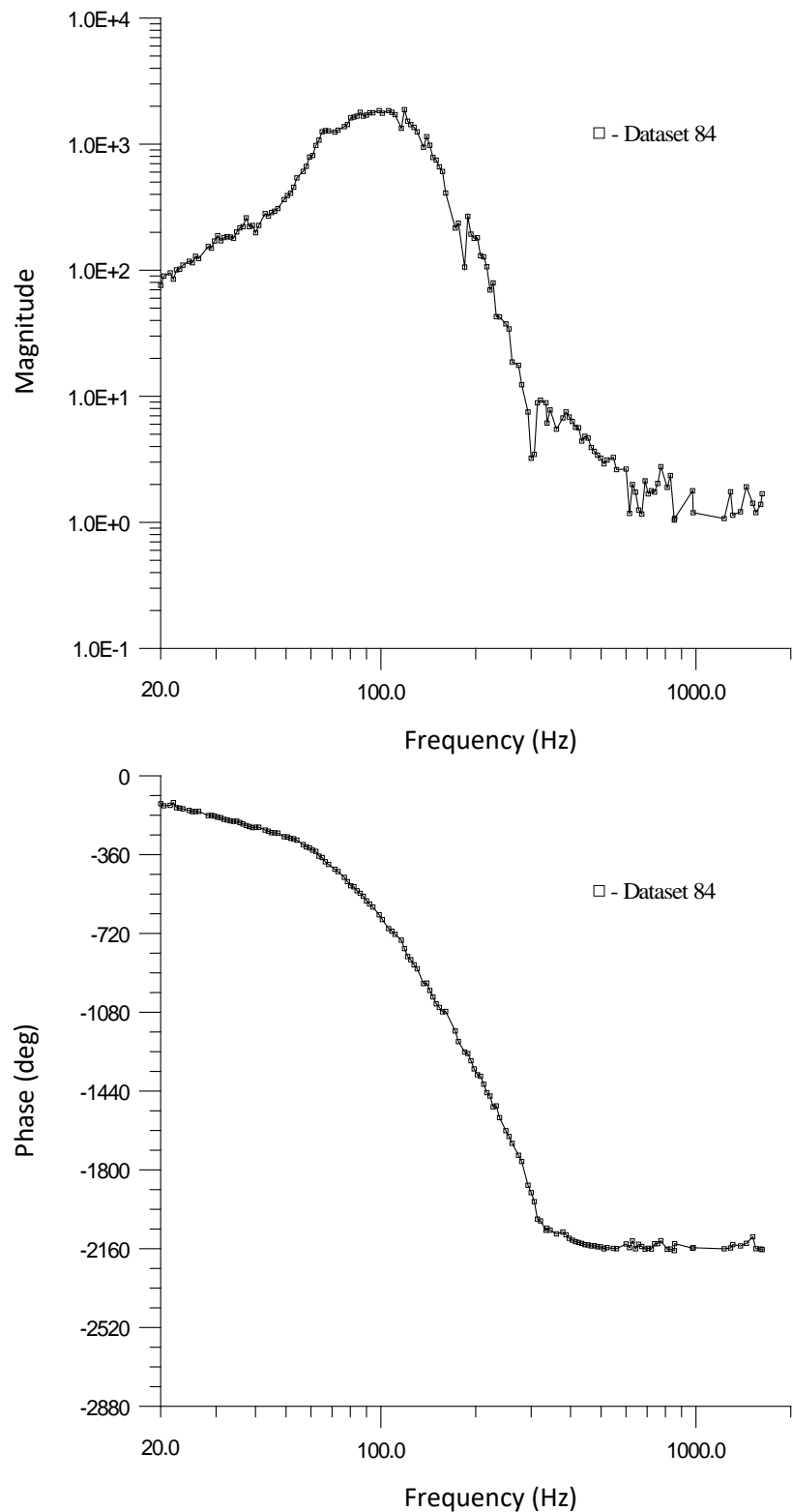


Figure G-46: Measured combustion response function for $\varphi = 0.900$ and $V_R = 5.0$.

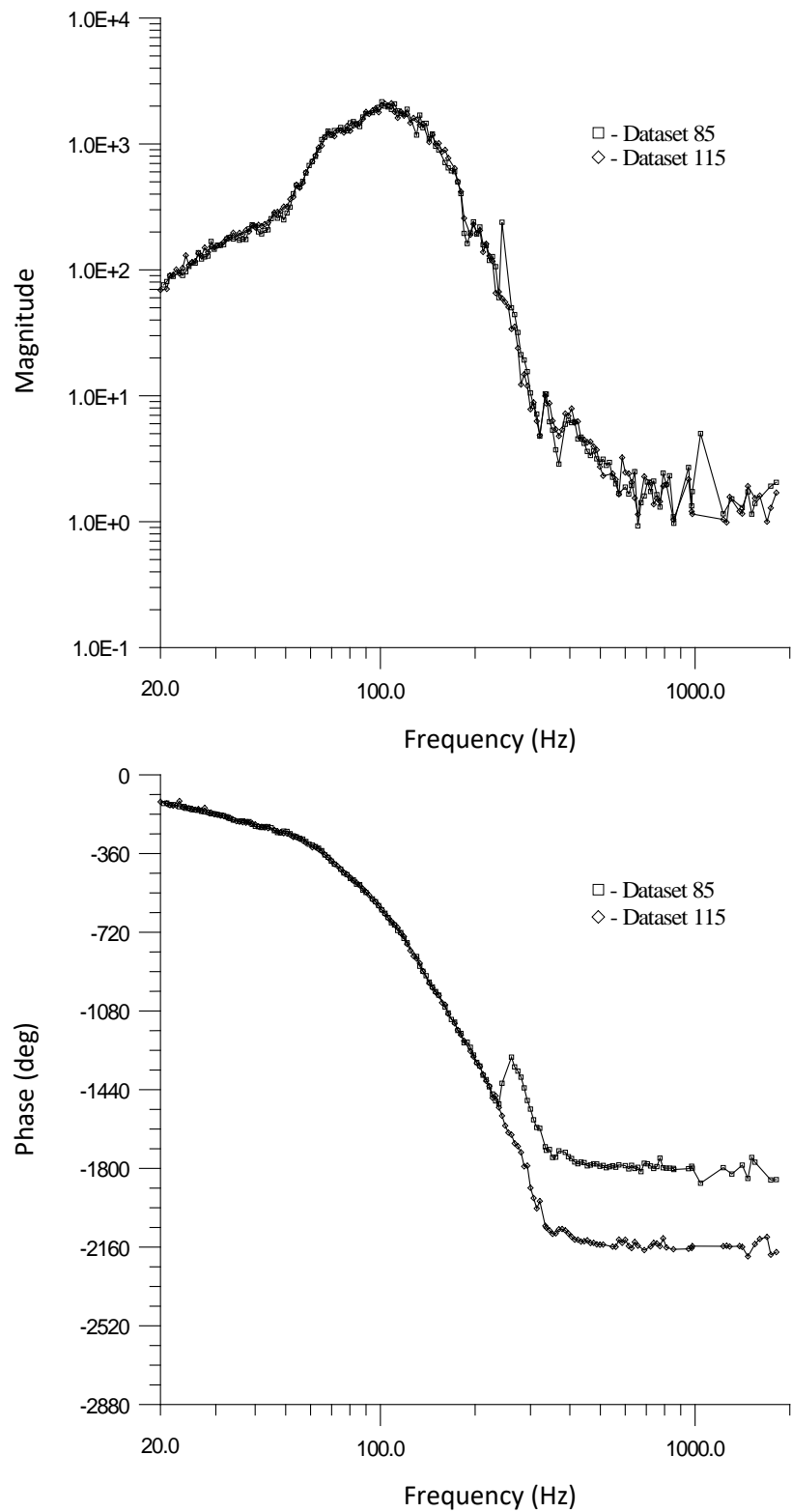


Figure G-47: Measured combustion response function for $\varphi = 0.900$ and $V_R = 5.5$.

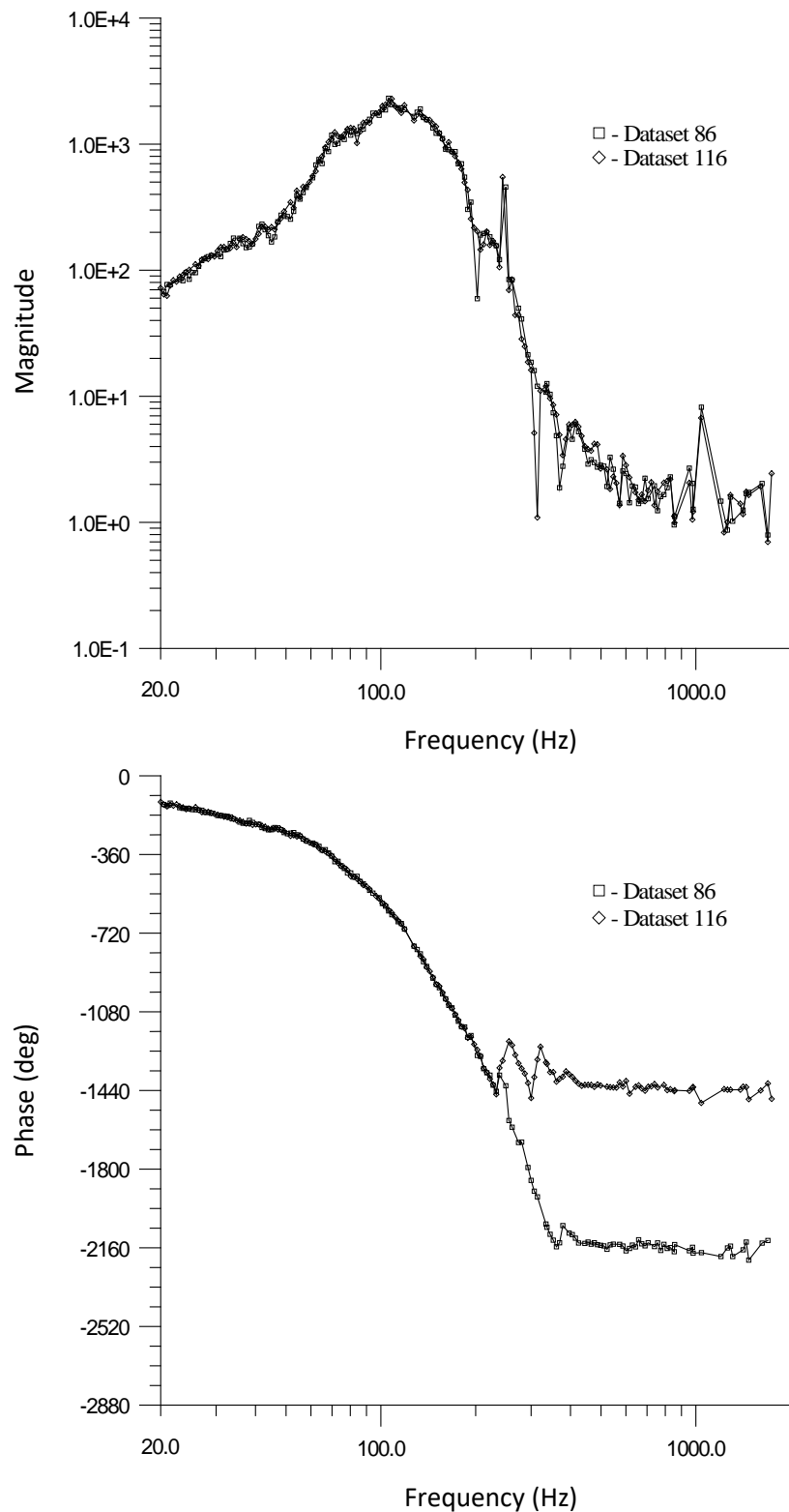


Figure G-48: Measured combustion response function for $\varphi = 0.900$ and $V_R = 6.0$.

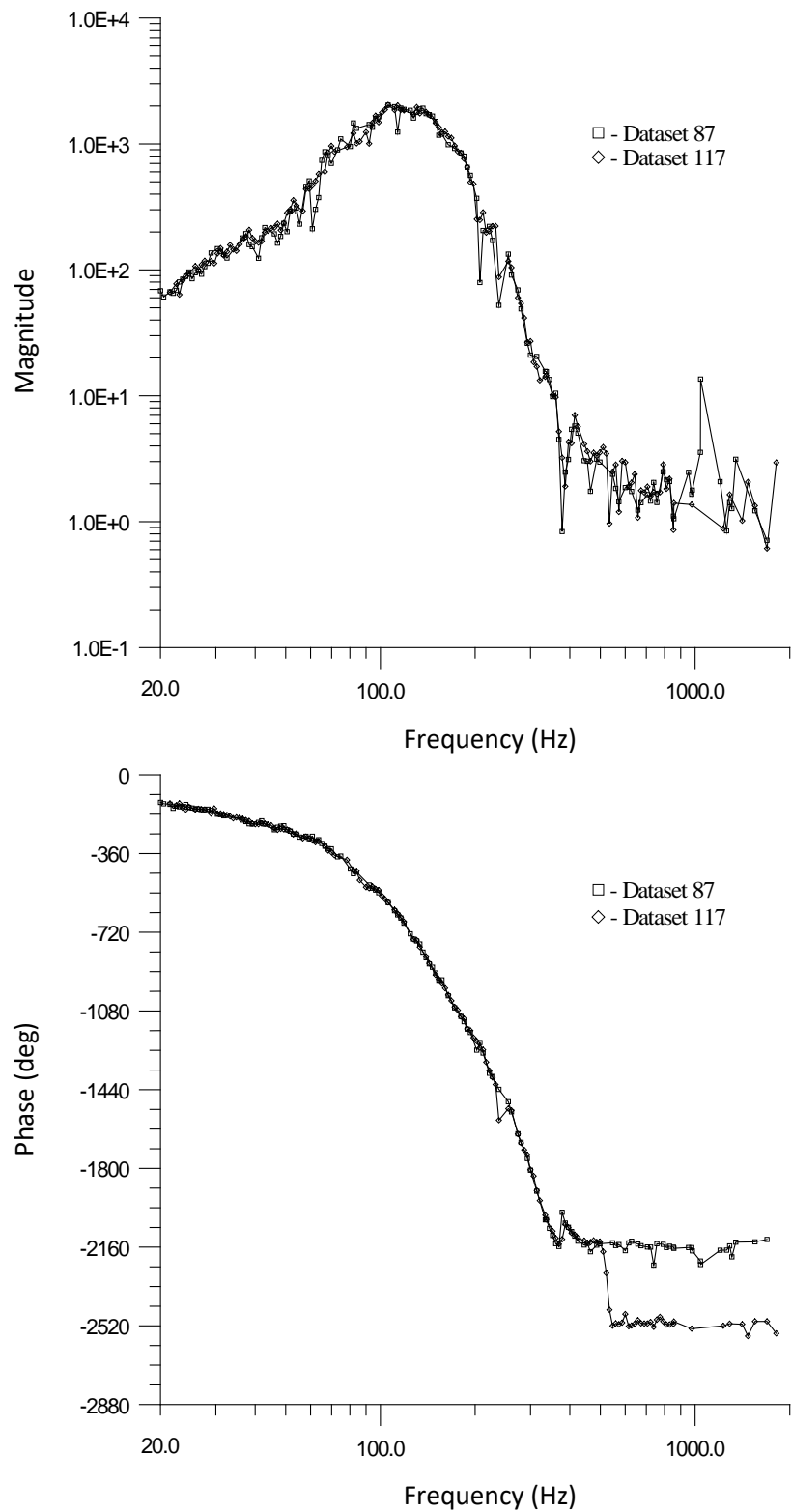


Figure G-49: Measured combustion response function for $\varphi = 0.900$ and $V_R = 6.5$.

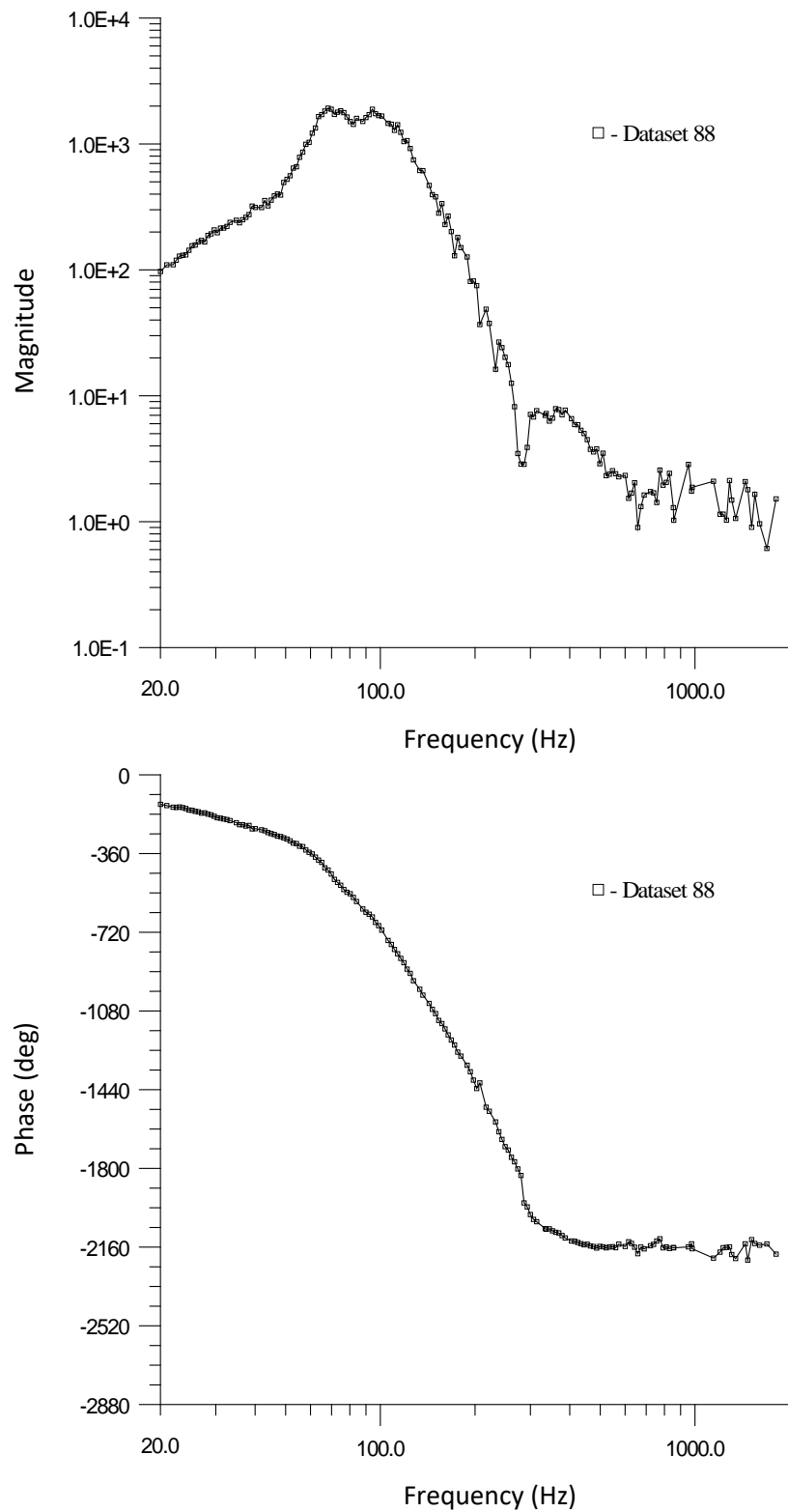


Figure G-50: Measured combustion response function for $\varphi = 0.925$ and $V_R = 4.0$.

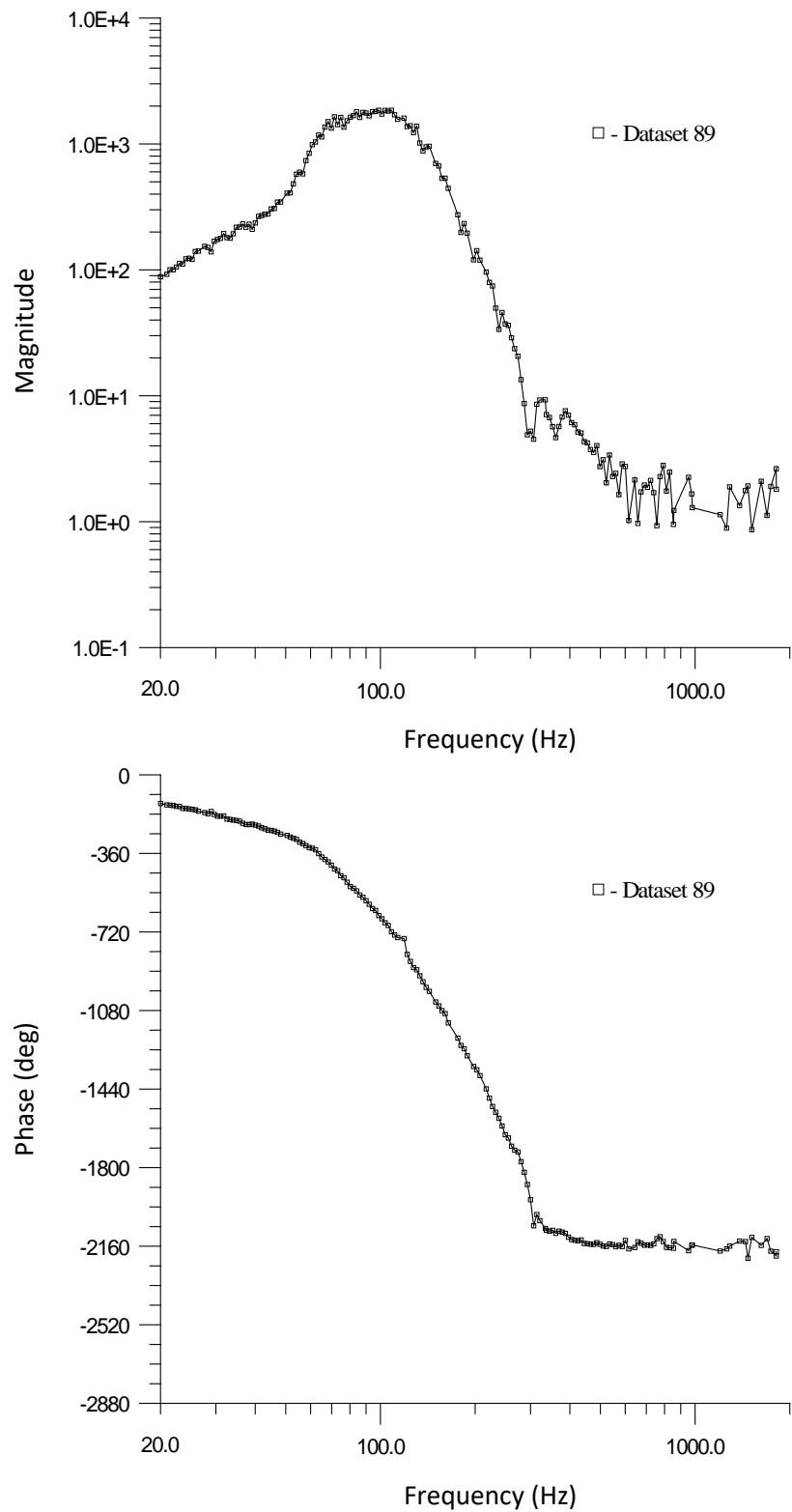


Figure G-51: Measured combustion response function for $\varphi = 0.925$ and $V_R = 4.5$.

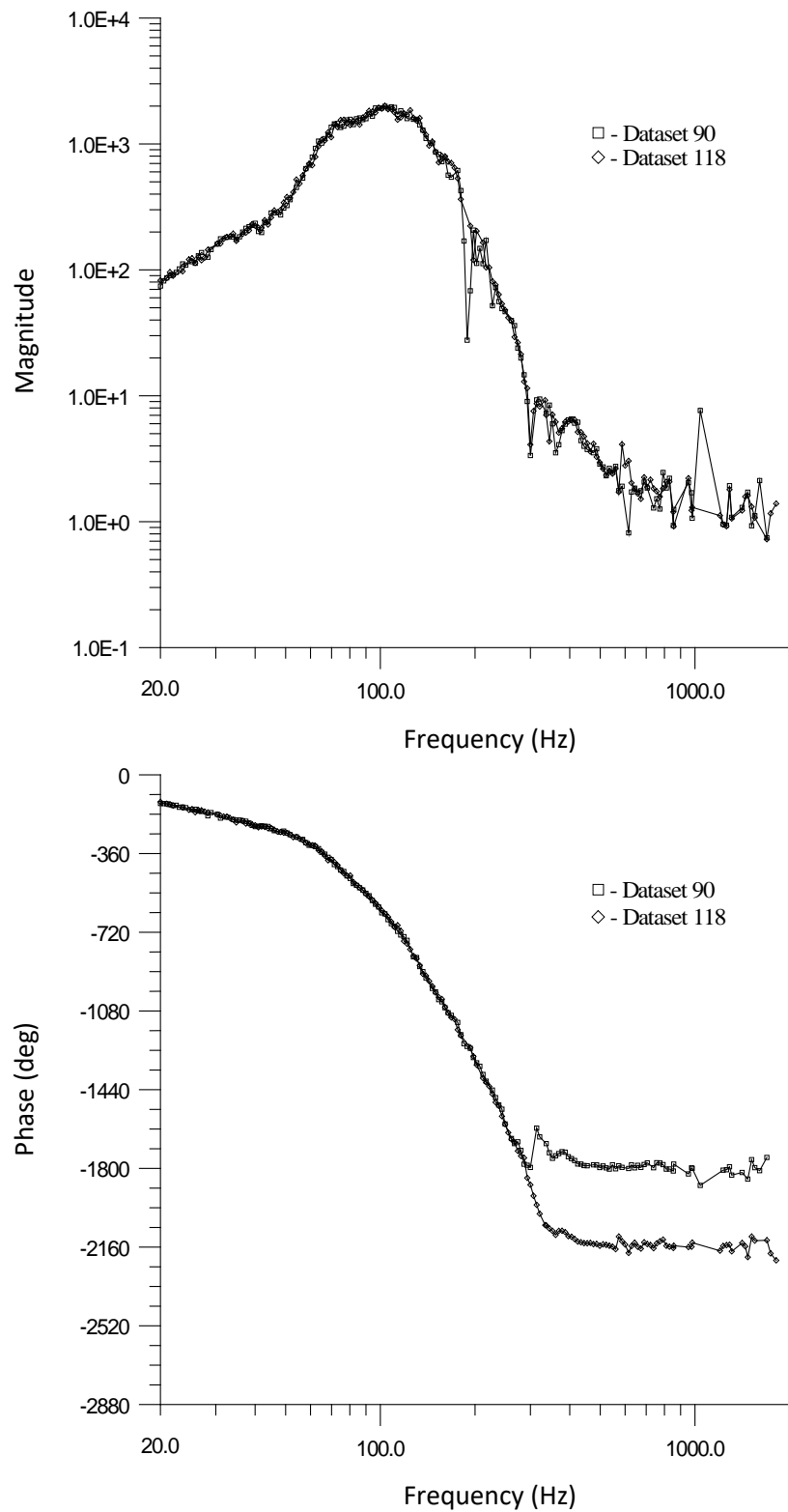


Figure G-52: Measured combustion response function for $\varphi = 0.925$ and $V_R = 5.0$.

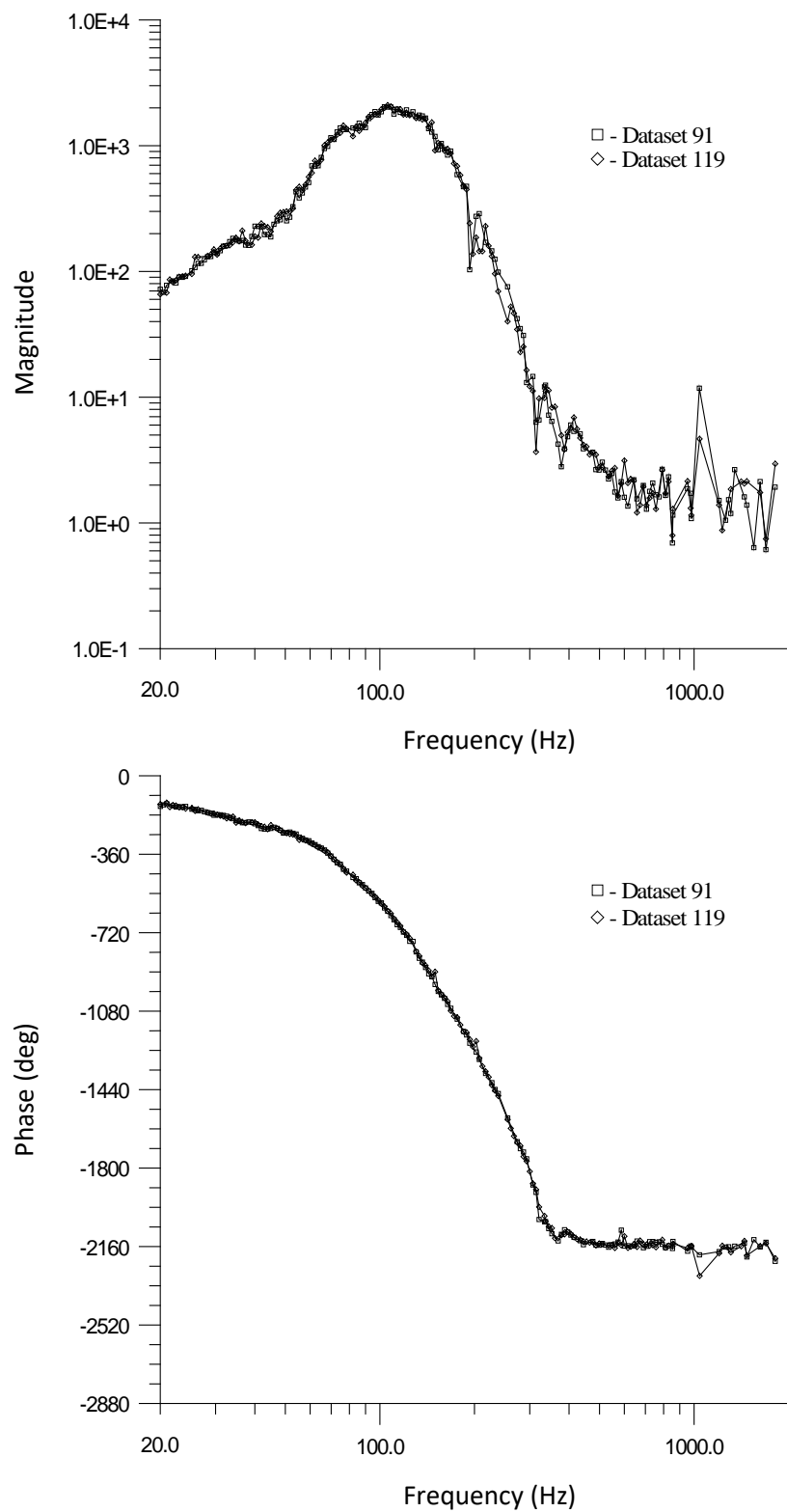


Figure G-53: Measured combustion response function for $\varphi = 0.925$ and $V_R = 5.5$.

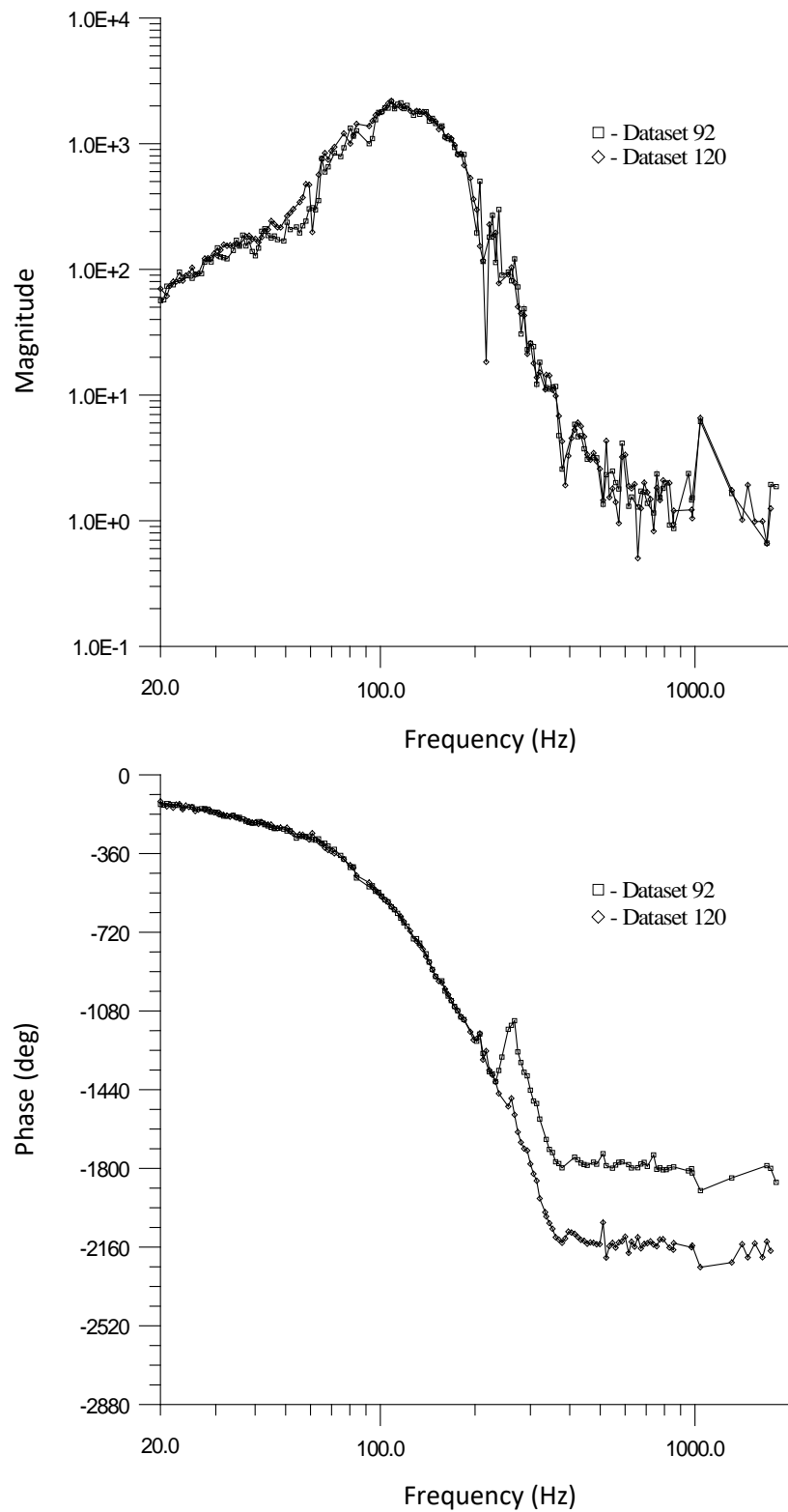


Figure G-54: Measured combustion response function for $\varphi = 0.925$ and $V_R = 6.0$.

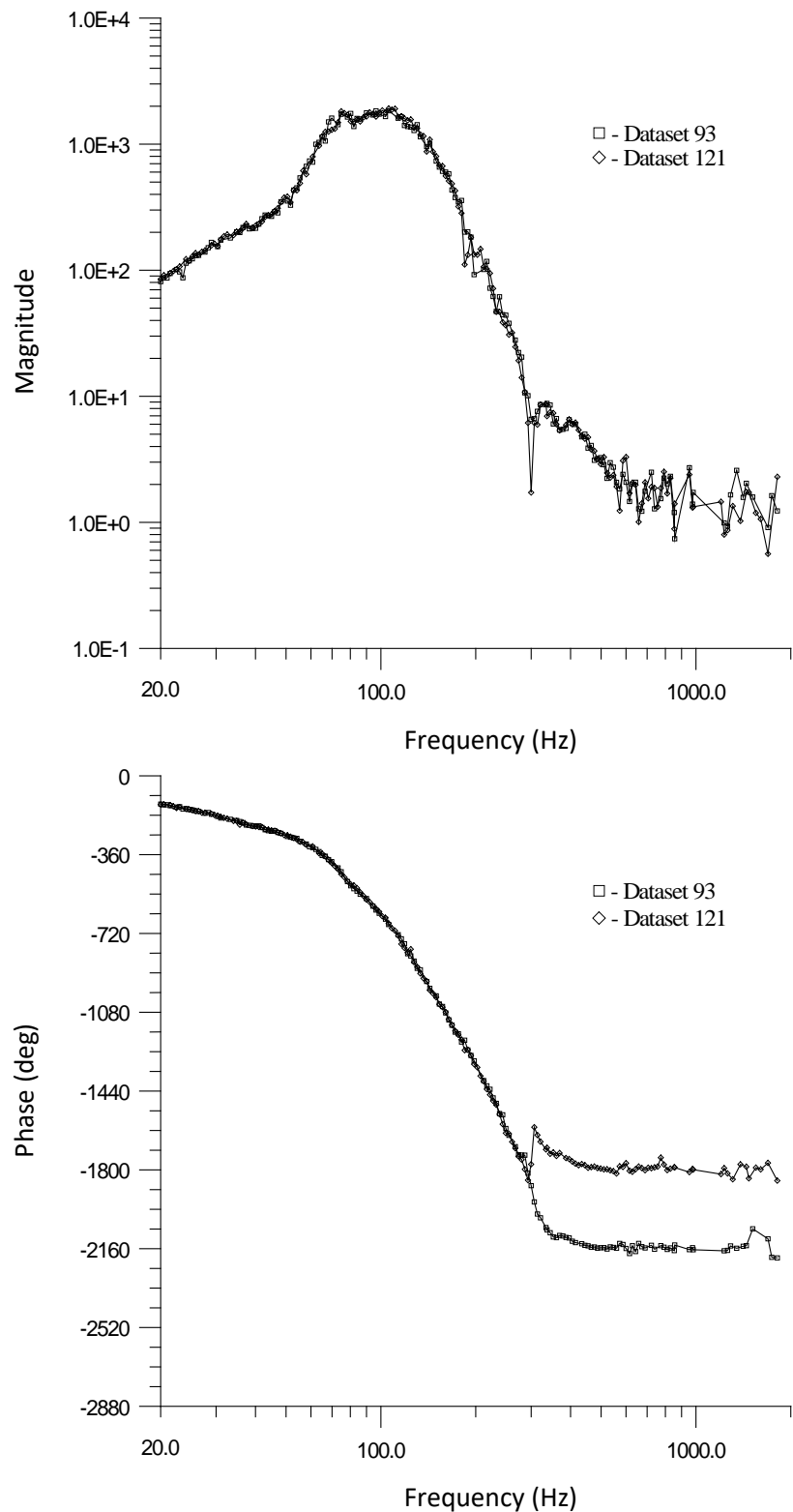


Figure G-55: Measured combustion response function for $\varphi = 0.950$ and $V_R = 4.5$.

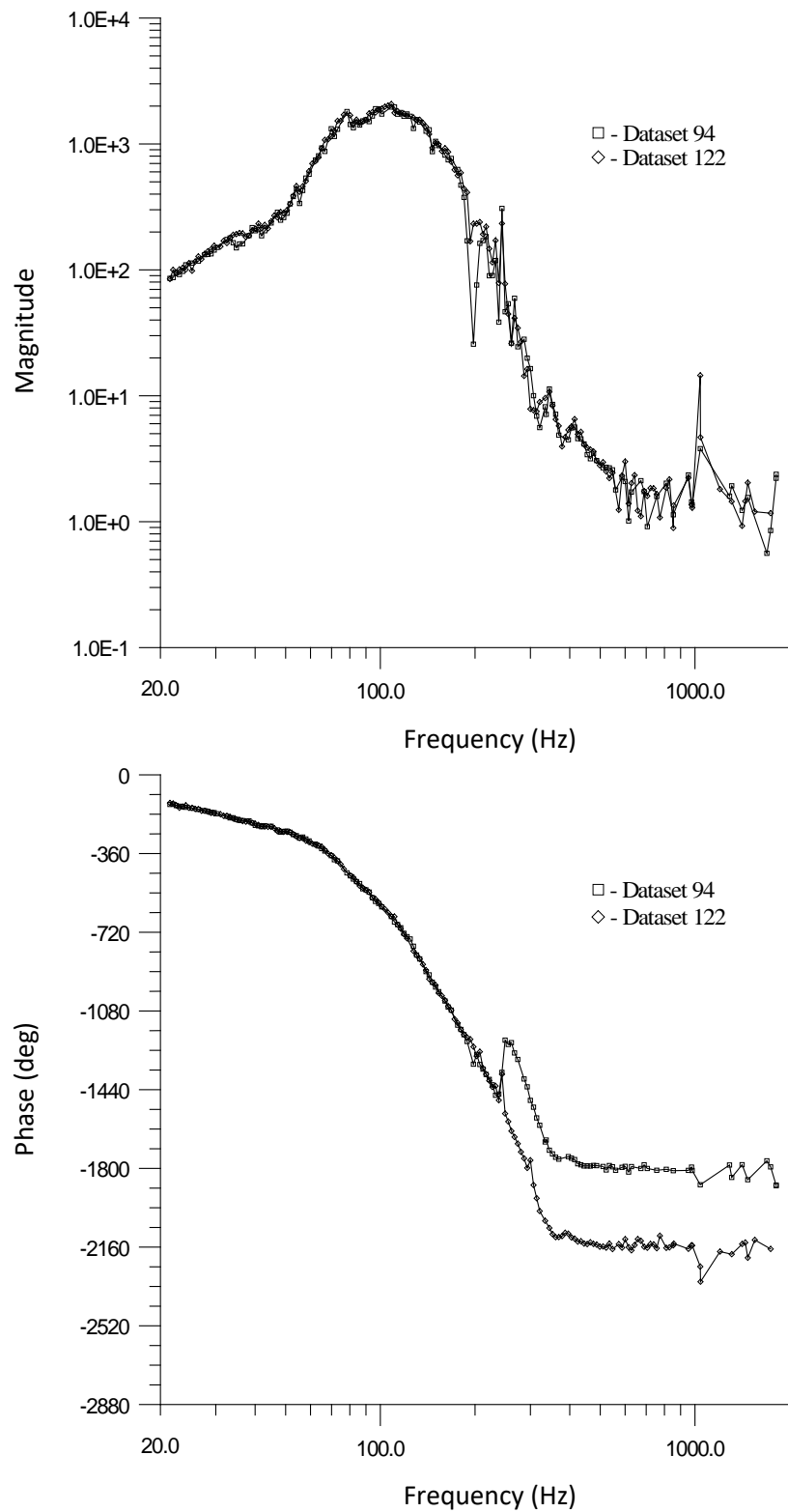


Figure G-56: Measured combustion response function for $\varphi = 0.950$ and $V_R = 5.0$.

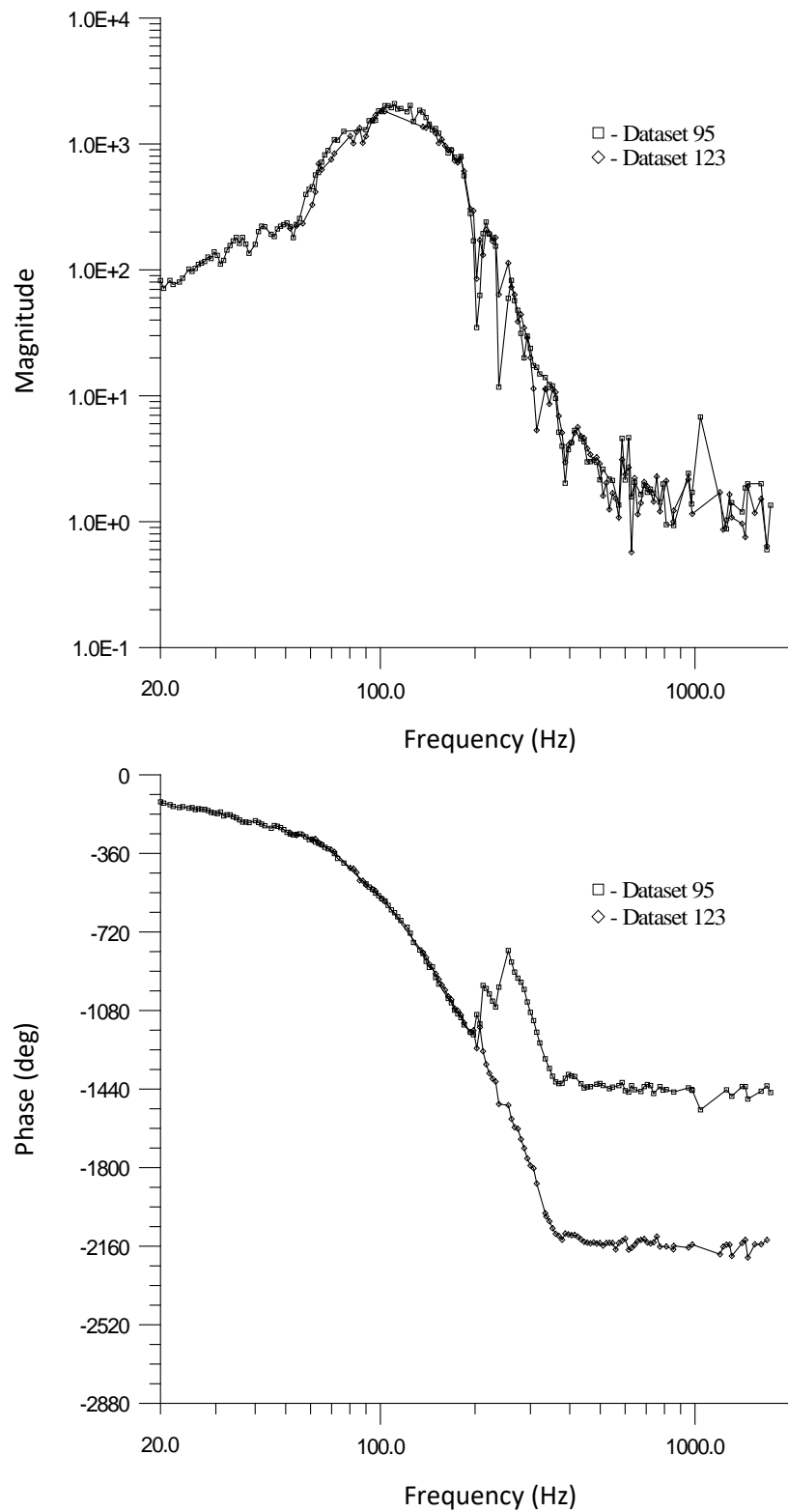


Figure G-57: Measured combustion response function for $\varphi = 0.950$ and $V_R = 5.5$.

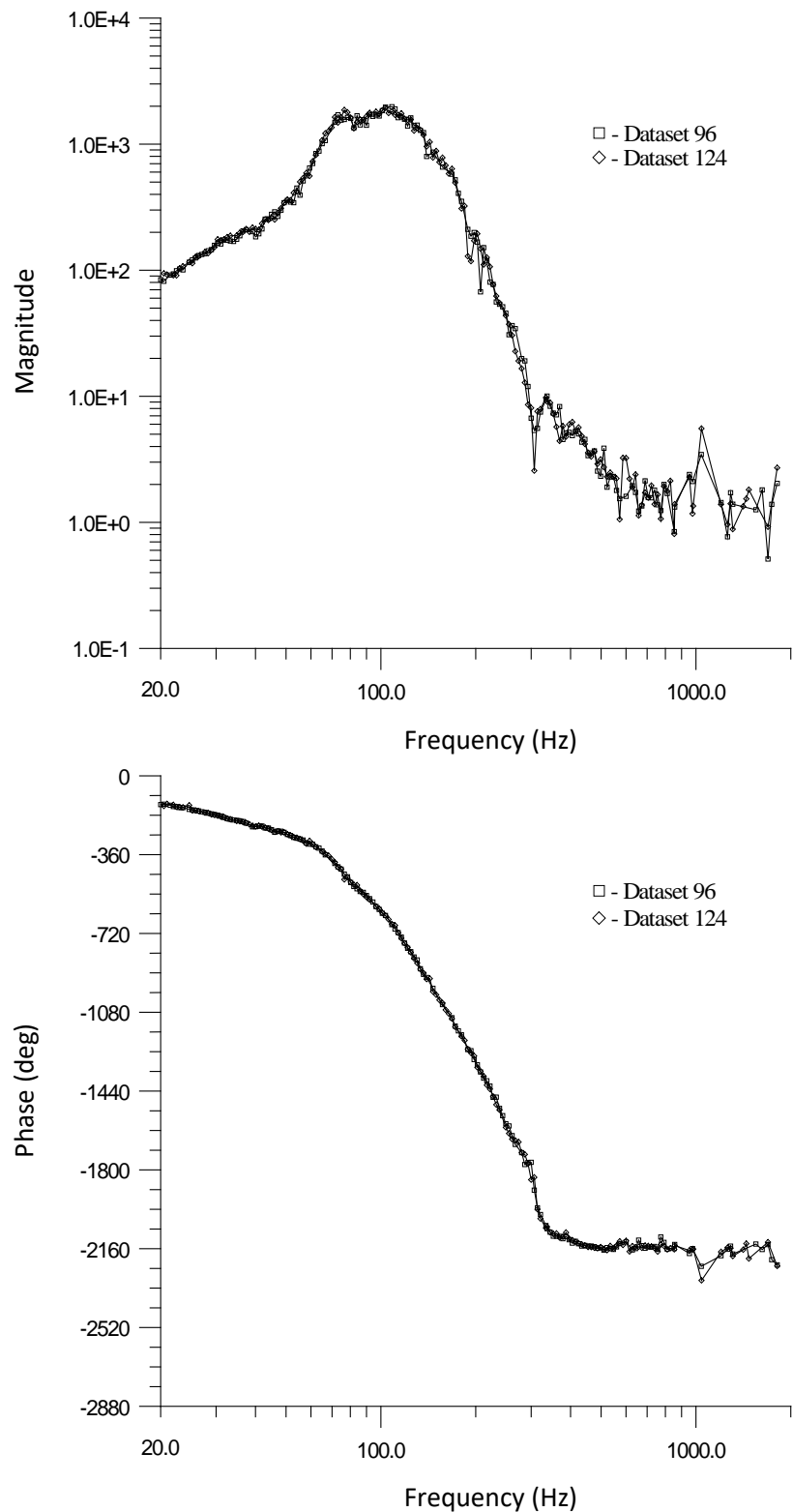


Figure G-58: Measured combustion response function for $\varphi = 0.975$ and $V_R = 4.5$.

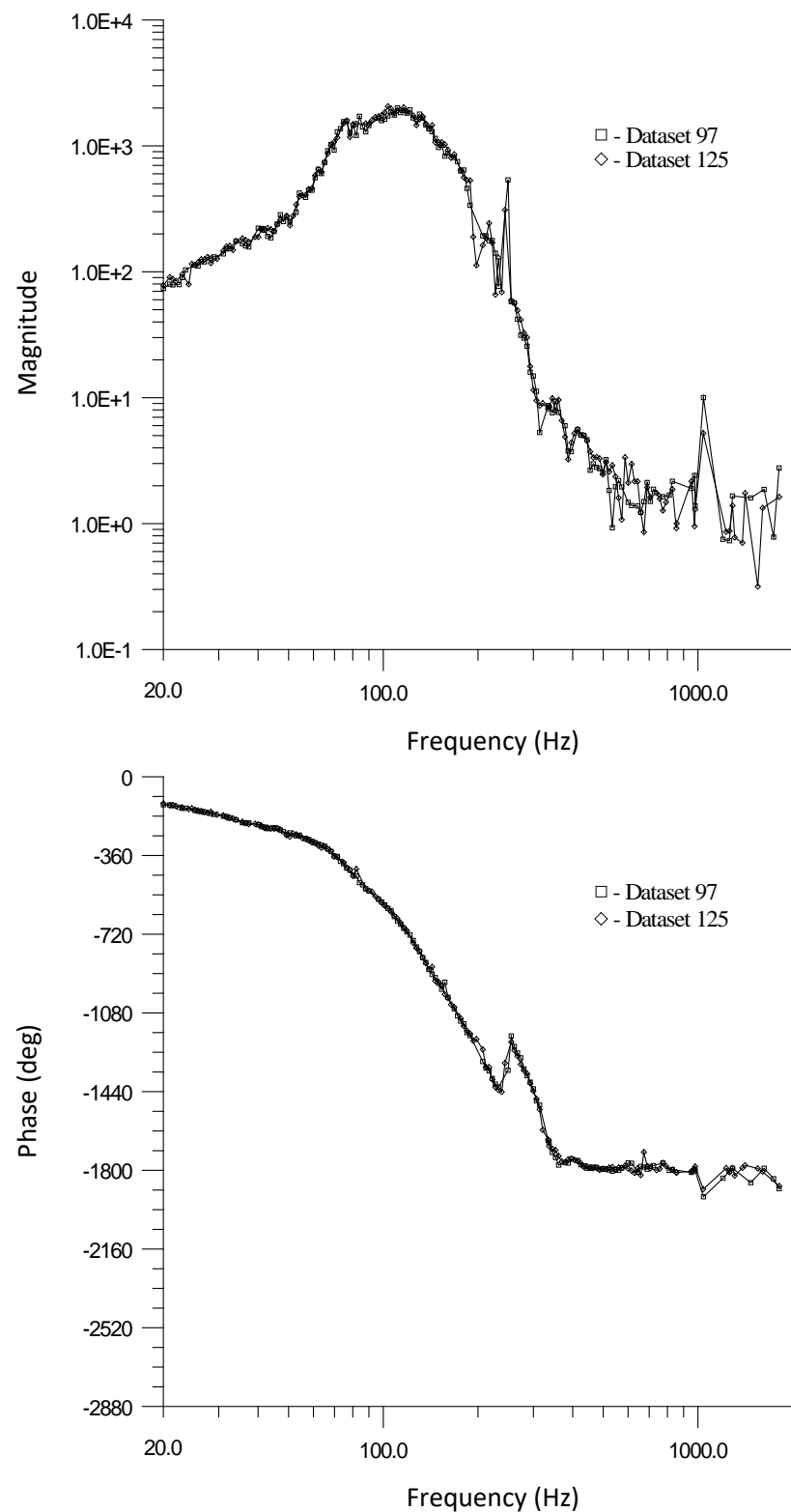


Figure G-59: Measured combustion response function for $\varphi = 0.975$ and $V_R = 5.0$.

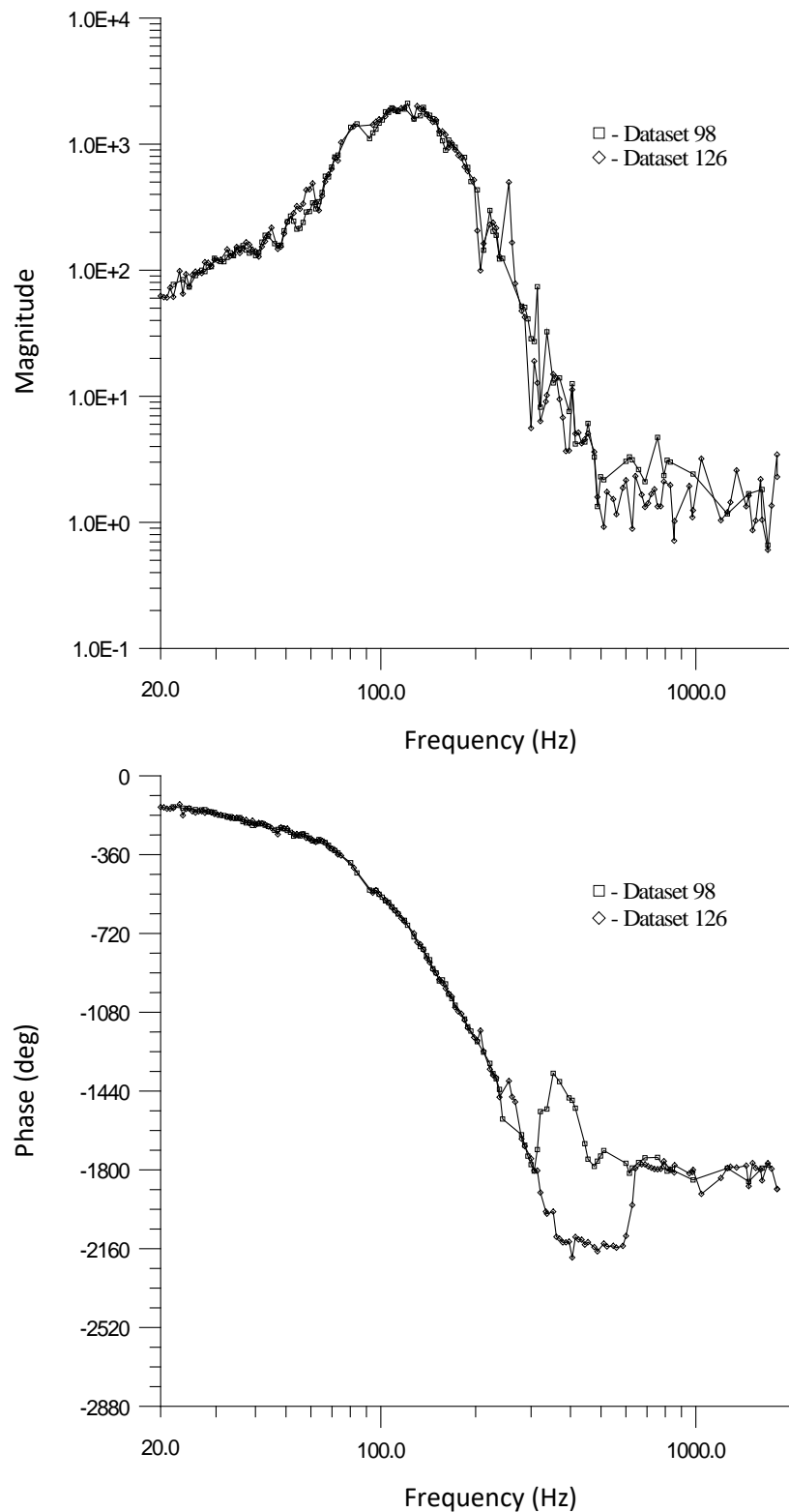


Figure G-60: Measured combustion response function for $\varphi = 0.975$ and $V_R = 5.5$.

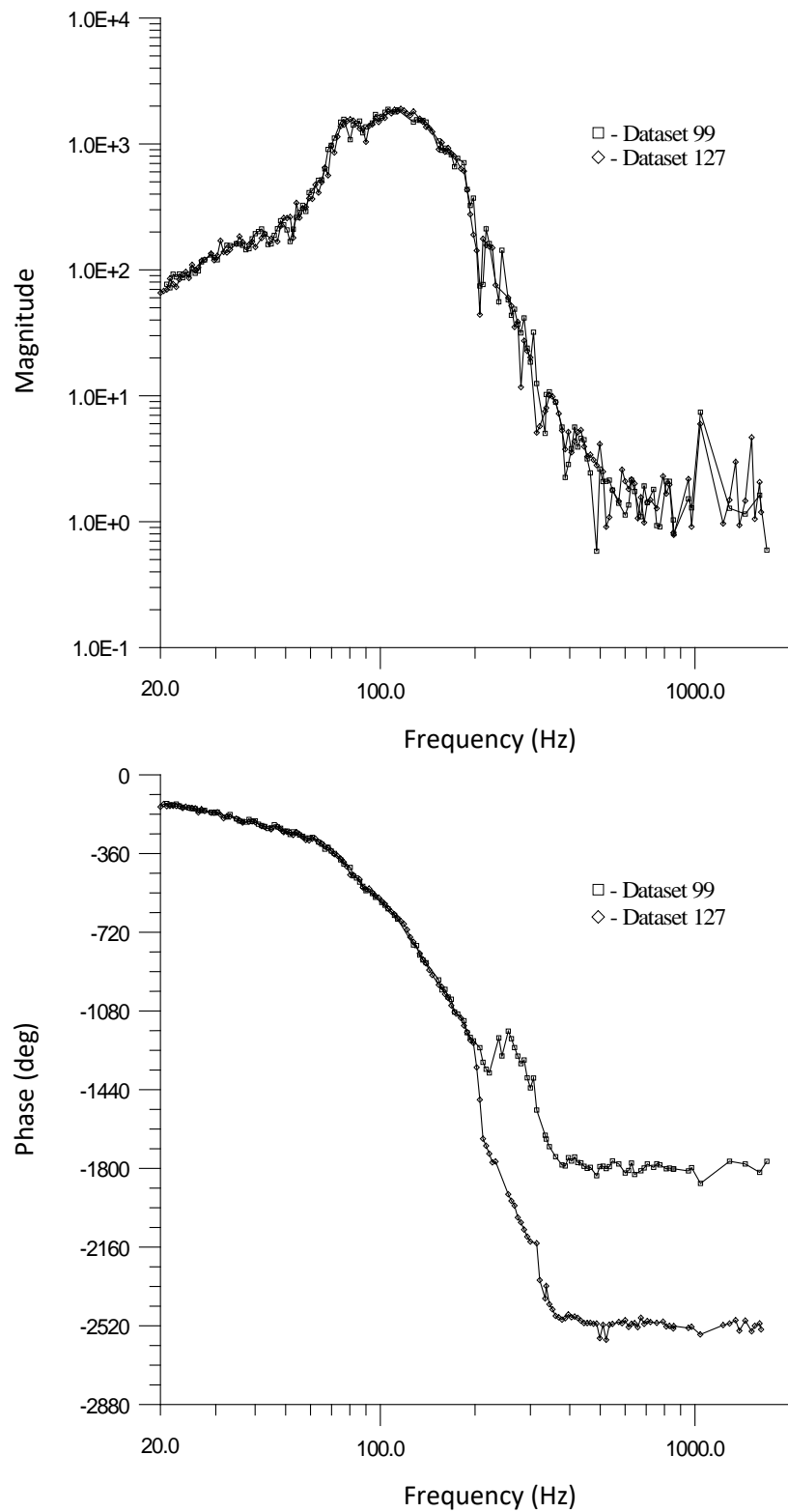


Figure G-61: Measured combustion response function for $\varphi = 1.000$ and $V_R = 5.0$.

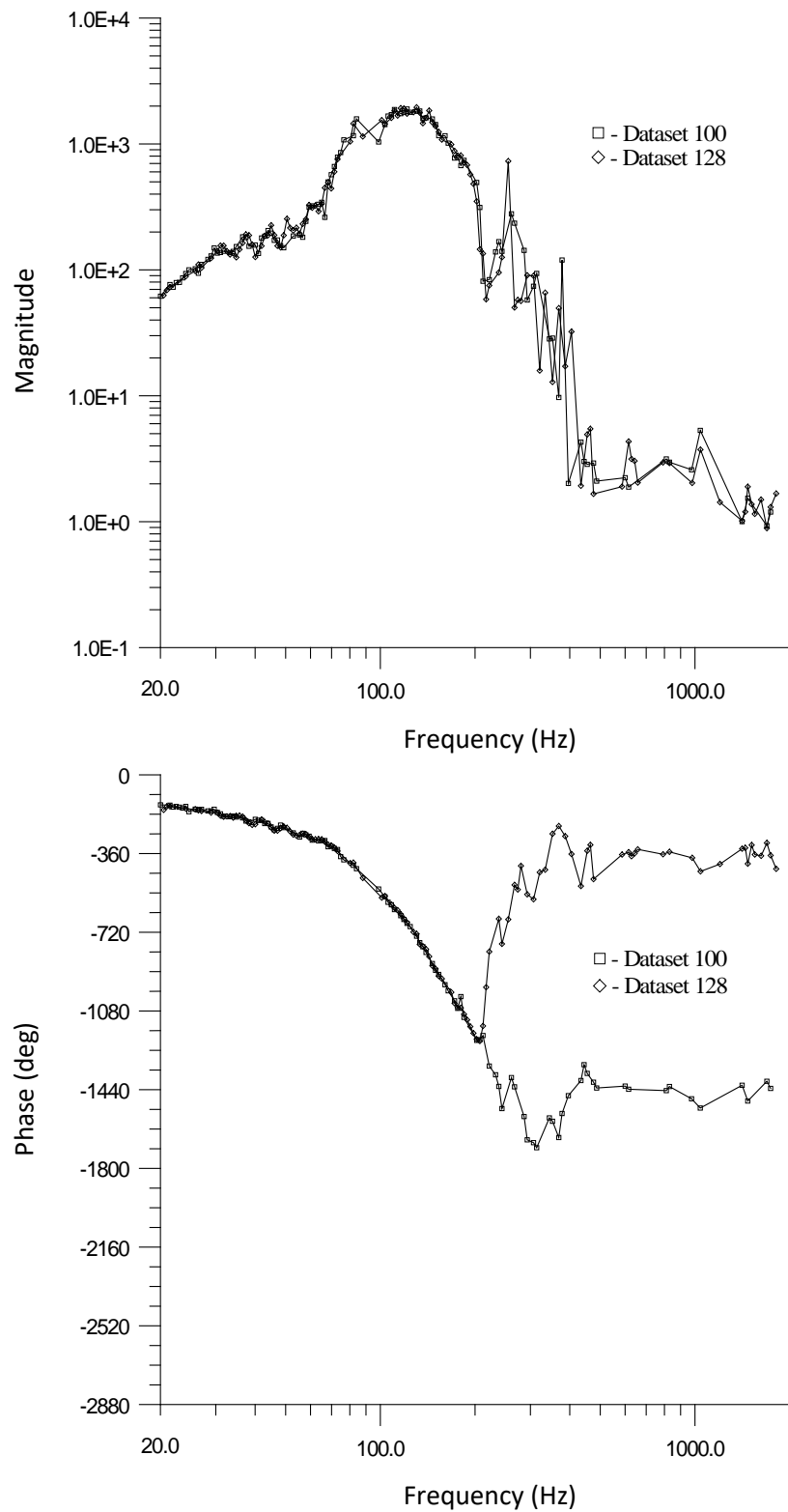


Figure G-62: Measured combustion response function for $\varphi = 1.000$ and $V_R = 5.5$.

A p p e n d i x H

LIBRARY OF SPATIALLY RESOLVED EXPERIMENTAL DATA

H.1 Overview

This appendix contains data from all PLIF and image chemiluminescence experiments relevant to the results presented in chapter 4. The data has been processed using the methods discussed in the various sections of the aforementioned chapter. Details of the burner and fuel system designs can be found in appendix B, while details of the acoustic forcing and response measurement schemes can be found in chapter 2 and appendix D. For the presented experimental data, the burner and acoustic drive parameters that were held constant are shown in Table H-1 below.

Parameter:	Value:
Burner Nozzle Exit Diameter (D)	14.0 mm
Burner Nozzle to Bluff Body Distance (H)	21.0 mm
Resulting H/D	1.50
Fuel Gas	UHP Methane
Oxidizer	Dry Air
Equivalence Ratio (ϕ)	0.85
Nozzle Exit Velocity	167.7 cm/s
Nozzle Velocity Ratio	4.0
Ambient Temperature	20.2 to 22.6 C
Ambient Pressure	755.4 to 763.5 mm-Hg
Acoustic Drive Amplitude at Flame	13.79 Pa (RMS) 116.8 dB (SPL)

Table H-1: Parameters held constant during PLIF and image chemiluminescence experiments.

H.2 Presented Data

As was stated above, the data presented in this appendix has been reduced using the methods presented in chapter 4. A brief summary of the pertinent relations is provided below. Let it be understood that barred quantities are the temporal average of the given variable while primed quantities are the fluctuating portion of that variable centered on the average. As an example, the time dependent intensity can be written as

$$I(t) = \bar{I} + I'(t).$$

In the following sections, numerous waveforms plots are presented depicting the periodic variation of the pressure (p') and the fluorescence/luminescence intensity (I'). The fluctuating intensity used in these plots is a global value, integrated over the imaged space and exploiting the axisymmetric nature of the flame. The global fluctuating intensity is computed by

$$(H-1) \quad I'(s) = 2\pi \sum_{k=1}^{Z_{size}} \sum_{j=1}^{R_{size}} I'_{pix}(s, j, k) r_j \Delta r \Delta z.$$

As was done in chapters 3 and 4, the assumption is made that the measured intensity signals (whether from CH^* and CO_2^* chemiluminescence, or from PLIF of a particular species) can be related to heat release such that

$$(H-2) \quad \frac{q'(s)}{\bar{q}} \simeq \frac{I'(s)}{\bar{I}(s)}.$$

As was shown in chapter 4, relation (H-2) allows the global combustion response function to be written in terms of values within the collected images:

$$(H-3) \quad H(s) = \frac{\bar{p}}{p'(s)} \frac{2\pi}{\bar{I}(s)} \sum_{k=1}^{Z_{size}} \sum_{j=1}^{R_{size}} I'_{pix}(s, j, k) r_j \Delta r \Delta z,$$

Where:

$$(H-4) \quad \bar{I}(s) = 2\pi \sum_{k=1}^{Z_{size}} \sum_{j=1}^{R_{size}} \bar{I}_{pix}(s, j, k) r_j \Delta r \Delta z$$

and the indices (j, k) reference the pertinent pixel in the image being reduced. From here the global forced Rayleigh index is simply

$$(H-5) \quad R_f = |H(s)| \cos(\angle H(s)) = \operatorname{Re}(H(s)).$$

It is equations (H-3) through (H-5) that are used to compute the global combustion responses and global forced Rayleigh indices presented in the following sections of this appendix.

For the spatially resolved functions, the relations used are those developed in chapter 4 and presented as equations (4-21) and (4-25). They are repeated here for convenience. The spatially resolved combustion response function is given by

$$(H-6) \quad \begin{aligned} H_{pix}(s, j, k) &= \frac{\bar{p}}{p'(s)} \frac{1}{\bar{I}_p(s)} I'_{pix}(s, j, k) \Delta r \Delta z, \\ \bar{I}_p(s) &= \sum_{k=1}^{Z_{size}} \sum_{j=1}^{R_{size}} \bar{I}_{pix}(s, j, k) \Delta r \Delta z. \end{aligned}$$

From these, the spatially resolved forced Rayleigh index is given by

$$(H-7) \quad R_f = |H(s, j, k)| \cos(\angle H(s, j, k)) = \operatorname{Re}(H(s, j, k)).$$

Table H-2 is a local index to all the remaining figures in this appendix. It provides brief descriptions as well as some ancillary information and, of course, the corresponding figure number. Table H-3 is similar, but is a local index to the data tables in the appendix.

Many of the waveform plots that are presented exhibit an upset in the p' waveform between 315° and 345° . It was determined that this is an artifact of digital switching noise internal to the AFC100 instrument. It inadvertently developed after the installation of the EX-2 filter expansion and was not discovered until most of the experimental data had been collected. The noise is coupled into the transducer signal amplification stage and is not physical or present in the actual acoustic waveform. The upset is narrow (typically one sample) and contributes negligibly to the low frequency components of the FFT. Consequently, it has virtually no effect of the experimental results.

Upon inspection, one may notice that most of the phase-resolved PLIF image plots for the higher drive frequency test cases are missing from the included library. This is a purposeful omission. For drive frequencies of 220 Hz and higher the flame motions and fluctuations in intensity are quite small - small enough that they become difficult (if not impossible) to discern within the printed images. As such, it was decided that including these images in the library provided no additional benefit. Instead, it is much more informative to examine the plots of the spatially resolved combustion response function and the spatially resolved forced Rayleigh index in these high frequency cases. The lone exception to this is the acetone PLIF images. These images allow visualization of the premixed reactant stream leaving the nozzle and approaching the reaction zone. In this case, interesting features can be resolved at drive frequencies all the way up to 375 Hz.

Table	Description	Imaging Method	Page
H-1	Parameters held constant during experiments	N/A	385
H-2	Local index of Figures in this appendix	N/A	389,390
H-3	Local index of Tables in this appendix	N/A	390-392
H-4	Values of the global (bulk) combustion response function	All	393
H-5	Values of the global (bulk) Forced Rayleigh index (R _f)	All	393
H-6	Global (bulk) harmonic content of the 55 Hz OH PLIF case	OH PLIF	395
H-7	Global (bulk) harmonic content of the 75 Hz OH PLIF case	OH PLIF	396
H-8	Global (bulk) harmonic content of the 100 Hz OH PLIF case	OH PLIF	397
H-9	Global (bulk) harmonic content of the 150 Hz OH PLIF case	OH PLIF	398
H-10	Global (bulk) harmonic content of the 220 Hz OH PLIF case	OH PLIF	399
H-11	Global (bulk) harmonic content of the 265 Hz OH PLIF case	OH PLIF	400
H-12	Global (bulk) harmonic content of the 375 Hz OH PLIF case	OH PLIF	401
H-13	Global (bulk) harmonic content of the 55 Hz CH PLIF case	CH PLIF	415
H-14	Global (bulk) harmonic content of the 75 Hz CH PLIF case	CH PLIF	416
H-15	Global (bulk) harmonic content of the 100 Hz CH PLIF case	CH PLIF	417
H-16	Global (bulk) harmonic content of the 150 Hz CH PLIF case	CH PLIF	418
H-17	Global (bulk) harmonic content of the 220 Hz CH PLIF case	CH PLIF	419
H-18	Global (bulk) harmonic content of the 240 Hz CH PLIF case	CH PLIF	420
H-19	Global (bulk) harmonic content of the 243 Hz CH PLIF case	CH PLIF	421
H-20	Global (bulk) harmonic content of the 265 Hz CH PLIF case	CH PLIF	422
H-21	Global (bulk) harmonic content of the 375 Hz CH PLIF case	CH PLIF	423
H-22	Global (bulk) harmonic content of the 55 Hz CH ₂ O PLIF case	CH ₂ O PLIF	436
H-23	Global (bulk) harmonic content of the 75 Hz CH ₂ O PLIF case	CH ₂ O PLIF	437
H-24	Global (bulk) harmonic content of the 100 Hz CH ₂ O PLIF case	CH ₂ O PLIF	438
H-25	Global (bulk) harmonic content of the 150 Hz CH ₂ O PLIF case	CH ₂ O PLIF	439
H-26	Global (bulk) harmonic content of the 220 Hz CH ₂ O PLIF case	CH ₂ O PLIF	440
H-27	Global (bulk) harmonic content of the 240 Hz CH ₂ O PLIF case	CH ₂ O PLIF	441
H-28	Global (bulk) harmonic content of the 243 Hz CH ₂ O PLIF case	CH ₂ O PLIF	442
H-29	Global (bulk) harmonic content of the 265 Hz CH ₂ O PLIF case	CH ₂ O PLIF	443
H-30	Global (bulk) harmonic content of the 375 Hz CH ₂ O PLIF case	CH ₂ O PLIF	444
H-31	Global (bulk) harmonic content of the combined 55 Hz OH-CH ₂ O PLIF case	OH-CH ₂ O PLIF	458
H-32	Global (bulk) harmonic content of the combined 75 Hz OH-CH ₂ O PLIF case	OH-CH ₂ O PLIF	459
H-33	Global (bulk) harmonic content of the combined 100 Hz OH-CH ₂ O PLIF case	OH-CH ₂ O PLIF	460
H-34	Global (bulk) harmonic content of the combined 150 Hz OH-CH ₂ O PLIF case	OH-CH ₂ O PLIF	461
H-35	Global (bulk) harmonic content of the combined 220 Hz OH-CH ₂ O PLIF case	OH-CH ₂ O PLIF	462
H-36	Global (bulk) harmonic content of the combined 265 Hz OH-CH ₂ O PLIF case	OH-CH ₂ O PLIF	463
H-37	Global (bulk) harmonic content of the combined 375 Hz OH-CH ₂ O PLIF case	OH-CH ₂ O PLIF	464

Table H-2: Index of tables appearing in appendix H. The column indicating “Imaging Method” describes the relevant imaging technique used (if any).

Table	Description	Imaging Method	Page
H-38	Global (bulk) harmonic content of the 55 Hz image chemiluminescence case	Chemiluminescence	477
H-39	Global (bulk) harmonic content of the 75 Hz image chemiluminescence case	Chemiluminescence	478
H-40	Global (bulk) harmonic content of the 100 Hz image chemiluminescence case	Chemiluminescence	479
H-41	Global (bulk) harmonic content of the 150 Hz image chemiluminescence case	Chemiluminescence	480
H-42	Global (bulk) harmonic content of the 220 Hz image chemiluminescence case	Chemiluminescence	481
H-43	Global (bulk) harmonic content of the 265 Hz image chemiluminescence case	Chemiluminescence	482
H-44	Global (bulk) harmonic content of the 375 Hz image chemiluminescence case	Chemiluminescence	483

Table H-2 (cont.): Index of tables appearing in appendix H. The column indicating “Imaging Method” describes the relevant imaging technique used (if any).

Figure	Description	Imaging Method	Page
H-1	OH PLIF image of experimental flame under steady conditions	OH PLIF	394
H-2	Waveforms generated from p' and I' data for 55 Hz OH PLIF case	OH PLIF	395
H-3	Waveforms generated from p' and I' data for 75 Hz OH PLIF case	OH PLIF	396
H-4	Waveforms generated from p' and I' data for 100 Hz OH PLIF case	OH PLIF	397
H-5	Waveforms generated from p' and I' data for 150 Hz OH PLIF case	OH PLIF	398
H-6	Waveforms generated from p' and I' data for 220 Hz OH PLIF case	OH PLIF	399
H-7	Waveforms generated from p' and I' data for 265 Hz OH PLIF case	OH PLIF	400
H-8	Waveforms generated from p' and I' data for 375 Hz OH PLIF case	OH PLIF	401
H-9	Phase-resolved OH PLIF images for the 55 Hz acoustic drive case	OH PLIF	402,403
H-10	Phase-resolved OH PLIF images for the 75 Hz acoustic drive case	OH PLIF	404,405
H-11	Phase-resolved OH PLIF images for the 100 Hz acoustic drive case	OH PLIF	406,407
H-12	Phase-resolved OH PLIF images for the 150 Hz acoustic drive case	OH PLIF	408,409
H-13	Spatially resolved combustion response function images generated from OH PLIF data	OH PLIF	410,411
H-14	Spatially resolved forced Rayleigh index images produced from the OH PLIF data	OH PLIF	412
H-15	CH PLIF image of experimental flame under steady conditions	CH PLIF	413
H-16	Waveforms generated from p' and I' data for 55 Hz CH PLIF case	CH PLIF	414
H-17	Waveforms generated from p' and I' data for 75 Hz CH PLIF case	CH PLIF	415
H-18	Waveforms generated from p' and I' data for 100 Hz CH PLIF case	CH PLIF	416
H-19	Waveforms generated from p' and I' data for 150 Hz CH PLIF case	CH PLIF	417
H-20	Waveforms generated from p' and I' data for 220 Hz CH PLIF case	CH PLIF	418

Table H-3: Index of figures appearing in appendix H. The column indicating “Imaging Methods” describes the relevant imaging technique used (if any).

Figure	Description	Imaging Method	Page
H-21	Waveforms generated from p' and I' data for 240 Hz CH PLIF case	CH PLIF	419
H-22	Waveforms generated from p' and I' data for 243 Hz CH PLIF case	CH PLIF	420
H-23	Waveforms generated from p' and I' data for 265 Hz CH PLIF case	CH PLIF	421
H-24	Waveforms generated from p' and I' data for 375 Hz CH PLIF case	CH PLIF	422
H-25	Phase-resolved CH PLIF images for the 55 Hz acoustic drive case	CH PLIF	423,424
H-26	Phase-resolved CH PLIF images for the 75 Hz acoustic drive case	CH PLIF	425,426
H-27	Phase-resolved CH PLIF images for the 100 Hz acoustic drive case	CH PLIF	427,428
H-28	Phase-resolved CH PLIF images for the 150 Hz acoustic drive case	CH PLIF	429,430
H-29	Spatially resolved combustion response function images generated from CH PLIF data	CH PLIF	431-433
H-30	Spatially resolved forced Rayleigh index images produced from the CH PLIF data	CH PLIF	433-434
H-31	CH ₂ O PLIF image of experimental flame under steady conditions	CH ₂ O PLIF	435
H-32	Waveforms generated from p' and I' data for 55 Hz CH ₂ O PLIF case	CH ₂ O PLIF	436
H-33	Waveforms generated from p' and I' data for 75 Hz CH ₂ O PLIF case	CH ₂ O PLIF	437
H-34	Waveforms generated from p' and I' data for 100 Hz CH ₂ O PLIF case	CH ₂ O PLIF	438
H-35	Waveforms generated from p' and I' data for 150 Hz CH ₂ O PLIF case	CH ₂ O PLIF	439
H-36	Waveforms generated from p' and I' data for 220 Hz CH ₂ O PLIF case	CH ₂ O PLIF	440
H-37	Waveforms generated from p' and I' data for 240 Hz CH ₂ O PLIF case	CH ₂ O PLIF	441
H-38	Waveforms generated from p' and I' data for 243 Hz CH ₂ O PLIF case	CH ₂ O PLIF	442
H-39	Waveforms generated from p' and I' data for 265 Hz CH ₂ O PLIF case	CH ₂ O PLIF	443
H-40	Waveforms generated from p' and I' data for 375 Hz CH ₂ O PLIF case	CH ₂ O PLIF	444
H-41	Phase-resolved CH ₂ O PLIF images for the 55 Hz acoustic drive case	CH ₂ O PLIF	445,446
H-42	Phase-resolved CH ₂ O PLIF images for the 75 Hz acoustic drive case	CH ₂ O PLIF	447,448
H-43	Phase-resolved CH ₂ O PLIF images for the 100 Hz acoustic drive case	CH ₂ O PLIF	449,450
H-44	Phase-resolved CH ₂ O PLIF images for the 150 Hz acoustic drive case	CH ₂ O PLIF	451,452
H-45	Spatially resolved combustion response function images generated from CH ₂ O PLIF data	CH ₂ O PLIF	453-455
H-46	Spatially resolved forced Rayleigh index images produced from the CH ₂ O PLIF data	CH ₂ O PLIF	455,456
H-47	Combined PLIF image (OH & CH ₂ O) of experimental flame under steady conditions	OH-CH ₂ O PLIF	457
H-48	Waveforms generated from I' data for 55 Hz OH-CH ₂ O PLIF combination	OH-CH ₂ O PLIF	458
H-49	Waveforms generated from I' data for 75 Hz OH-CH ₂ O PLIF combination	OH-CH ₂ O PLIF	459
H-50	Waveforms generated from I' data for 100 Hz OH-CH ₂ O PLIF combination	OH-CH ₂ O PLIF	460
H-51	Waveforms generated from I' data for 150 Hz OH-CH ₂ O PLIF combination	OH-CH ₂ O PLIF	461
H-52	Waveforms generated from I' data for 220 Hz OH-CH ₂ O PLIF combination	OH-CH ₂ O PLIF	462
H-53	Waveforms generated from I' data for 265 Hz OH-CH ₂ O PLIF combination	OH-CH ₂ O PLIF	463
H-54	Waveforms generated from I' data for 375 Hz OH-CH ₂ O PLIF combination	OH-CH ₂ O PLIF	464

Table H-3 (cont.): Index of figures appearing in appendix H. The column indicating “Imaging Methods” describes the relevant imaging technique used (if any).

Figure	Description	Imaging Method	Page
H-55	Phase-resolved OH-CH ₂ O PLIF images for the 55 Hz acoustic drive case	OH-CH ₂ O PLIF	465,466
H-56	Phase-resolved OH-CH ₂ O PLIF images for the 75 Hz acoustic drive case	OH-CH ₂ O PLIF	467,468
H-57	Phase-resolved OH-CH ₂ O PLIF images for the 100 Hz acoustic drive case	OH-CH ₂ O PLIF	469,470
H-58	Phase-resolved OH-CH ₂ O PLIF images for the 150 Hz acoustic drive case	OH-CH ₂ O PLIF	471,472
H-59	Spatially resolved combustion response function images generated from OH-CH ₂ O PLIF data	OH-CH ₂ O PLIF	473,474
H-60	Spatially resolved forced Rayleigh index images produced from the OH-CH ₂ O PLIF data	OH-CH ₂ O PLIF	475
H-61	Chemiluminescence image of experimental flame under steady conditions	Chemiluminescence	476
H-62	Waveforms generated from p' and I' data for 55 Hz chemiluminescence case	Chemiluminescence	477
H-63	Waveforms generated from p' and I' data for 75 Hz chemiluminescence case	Chemiluminescence	478
H-64	Waveforms generated from p' and I' data for 100 Hz chemiluminescence case	Chemiluminescence	479
H-65	Waveforms generated from p' and I' data for 150 Hz chemiluminescence case	Chemiluminescence	480
H-66	Waveforms generated from p' and I' data for 220 Hz chemiluminescence case	Chemiluminescence	481
H-67	Waveforms generated from p' and I' data for 265 Hz chemiluminescence case	Chemiluminescence	482
H-68	Waveforms generated from p' and I' data for 375 Hz chemiluminescence case	Chemiluminescence	483
H-69	Phase-resolved chemiluminescence images for the 55 Hz acoustic drive case	Chemiluminescence	484,485
H-70	Phase-resolved chemiluminescence images for the 75 Hz acoustic drive case	Chemiluminescence	486,487
H-71	Phase-resolved chemiluminescence images for the 100 Hz acoustic drive case	Chemiluminescence	488,489
H-72	Phase-resolved chemiluminescence images for the 150 Hz acoustic drive case	Chemiluminescence	490,491
H-73	Spatially resolved combustion response function images generated from chemiluminescence data	Chemiluminescence	492,493
H-74	Spatially resolved forced Rayleigh index images produced from the chemiluminescence data	Chemiluminescence	494
H-75	Acetone PLIF image of the burner reactant flow under steady conditions	Acetone PLIF	495
H-76	Phase-resolved acetone PLIF images for the 55 Hz acoustic drive case	Acetone PLIF	496,497
H-77	Phase-resolved acetone PLIF images for the 75 Hz acoustic drive case	Acetone PLIF	498,499
H-78	Phase-resolved acetone PLIF images for the 100 Hz acoustic drive case	Acetone PLIF	500,501
H-79	Phase-resolved acetone PLIF images for the 150 Hz acoustic drive case	Acetone PLIF	502,503
H-80	Phase-resolved acetone PLIF images for the 220 Hz acoustic drive case	Acetone PLIF	504,505
H-81	Phase-resolved acetone PLIF images for the 265 Hz acoustic drive case	Acetone PLIF	506,507
H-82	Phase-resolved acetone PLIF images for the 375 Hz acoustic drive case	Acetone PLIF	508,509

Table H-3 (cont.): Index of figures appearing in appendix H. The column indicating “Imaging Methods” describes the relevant imaging technique used (if any).

Drive Freq (Hz)	Planar Laser Induced Fluorescence (PLIF)								Chemiluminescence			
	OH PLIF		CH PLIF		CH ₂ O PLIF		OH-CH ₂ O PLIF		Image		Bulk (PMT)	
	Mag	Phase	Mag	Phase	Mag	Phase	Mag	Phase	Mag	Phase	Mag	Phase
55	1048	81.6	1575	-1.7	170	-41.9	1306	16.4	1053	21.7	1308	35.5
75	880	-58.2	1393	-150.0	125	131.6	1142	-125.3	1181	-131.9	1397	-116.3
100	376	170.7	1908	64.9	183	62.1	626	99.2	768	80.1	1130	116.7
150	57.1	-154.7	282	101.9	20.7	-51.6	65.9	152.6	134	119.9	186	168.5
220	25.4	-22.7	13.9	-12.4	6.72	1.5	44.5	-7.9	7.72	-150.3	11.9	-102.9
240	~	~	36.4	157.7	27.6	-49.8	~	~	~	~	2.12	-99.8
243	~	~	41.7	-131.7	50.9	9.8	~	~	~	~	1.83	-152.0
265	46.4	-136.6	57.4	-179.5	22.7	-28.0	76.7	-156.5	8.18	-133.5	4.13	-141.4
375	24.4	-147.1	88.7	123.8	57.0	75.8	66.8	-125.6	3.78	-76.1	9.37	-63.9

Table H-4: Global (bulk) combustion response function values ($|H(s)|$ and $\angle H(s)$) versus drive frequency and heat-release evaluation methods. Negative phase values imply I' is leading p' . For the PLIF measurements, equation (H-3) is used (incorporating the r dependence) in order to integrate the full volume of the flame. The image chemiluminescence results, on the other hand, do not incorporate this r correction since the technique is, by its nature, quasi depth integrating.

Drive Freq (Hz)	Planar Laser Induced Fluorescence (PLIF)				Chemiluminescence	
	OH	CH	CH ₂ O	OH-CH ₂ O	Image	Bulk (PMT)
55	154	1575	127	1254	979	1096
75	464	-1207	-83.3	-660	-788	-650
100	-371	810	85.9	-100	132	-501
150	-51.6	-58.0	12.8	-58.5	-66.6	-183.3
220	23.4	13.6	6.72	44.0	-6.70	-2.82
240	~	-33.7	17.8	~	~	0.02
243	~	-27.8	50.2	~	~	-1.45
265	-33.7	-57.4	20.0	-70.3	-5.63	-3.17
375	-20.5	-49.3	14.0	-38.9	0.91	4.12

Table H-5: Global (bulk) forced Rayleigh index (R_f) versus drive frequency and heat-release evaluation methods. Results are computed using values from Table H-4 and equation (H-5).

H.2.1 OH PLIF Experimental Data

The following 19 pages present the relevant collected OH PLIF data. Images were collected using an Andor iStar ICCD camera coupled to a 94 mm, f/4.1, EADS-Sodern UV lens. Optical pumping of the OH radicals of interest was performed at $\lambda_{\text{air}} = 282.93$ nm. Image data was collected and processed using the techniques described in chapter 4. For OH data, all three image correction methods were employed:

- i) Correction for the shot-to-shot variation in OPO output intensity.
- ii) Correction for the spatial variation in laser sheet intensity in the vertical direction.
- iii) Correction for the (spatially variable) attenuation of the laser sheet as it passes through the OH field.

Further information regarding the processing of this data can be found in the beginning of this appendix as well as in chapter 4.

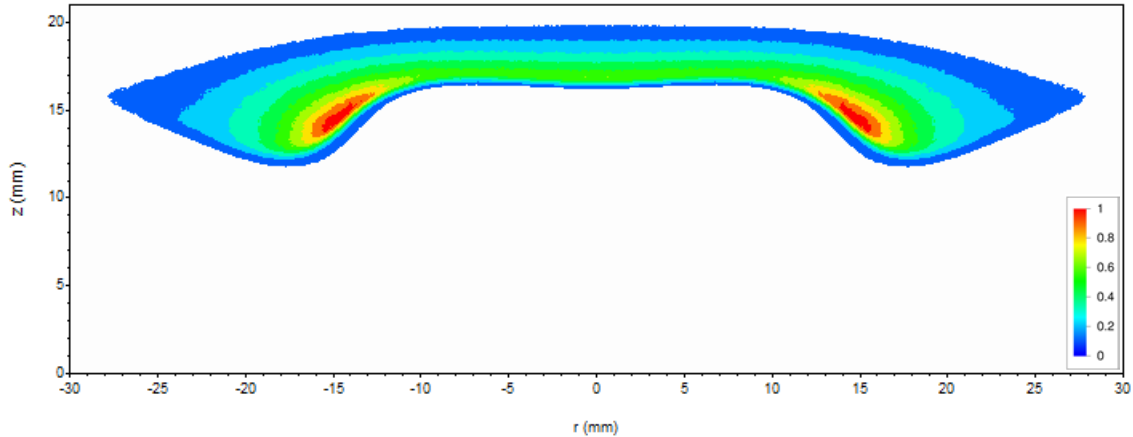


Figure H-1: OH PLIF image of flame under steady conditions (no acoustic forcing). Collected data appears on the left, and is mirrored across the centerline for a visual representation of entire flame. Burner centerline is at $r = 0$. Position $z = 0$ corresponds to the nozzle exit plane.

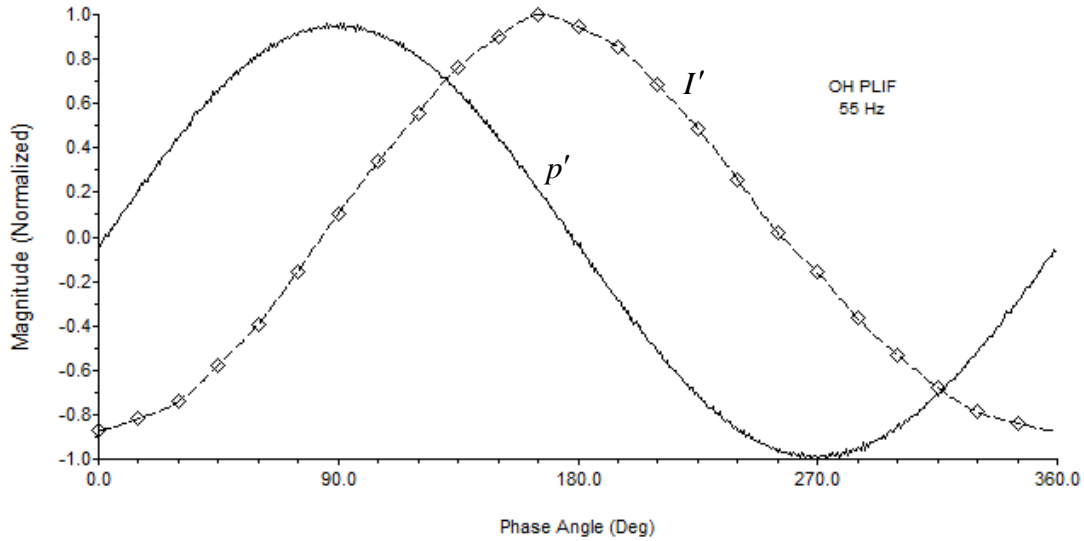


Figure H-2: Resulting waveforms from the 55 Hz OH PLIF experiment (Experiment 652). The solid curve shows the measured acoustic waveform with the rising-edge zero crossing marking the zero-degree point. Diamonds represent total (fully integrated) intensity data points computed from the phase bins. The dashed curve is a periodic cubic spline fit to this data. Signals are normalized by their peak values.

Mode	Pressure (p')		Intensity (I')	
	Mag	Phase	Mag	Phase
1	1.0000	0.0	1.0000	81.6
2	0.0107	87.6	0.0715	-137.2
3	0.0037	107.2	0.0150	85.8
4	0.0017	69.8	0.0061	-112.4
5	0.0007	164.7	0.0054	-34.2
6	0.0004	168.6	0.0058	147.1
7	0.0003	-151.6	0.0010	25.7
8	0.0004	-110.2	0.0022	-96.1
9	0.0003	-30.1	0.0013	-52.3
10	0.0003	1.4	0.0072	94.2
11	0.0003	5.7	0.0032	-15.7

Table H-6: Harmonic content of the measured acoustic and intensity fields for the 55 Hz PLIF case. The measured intensity is total (fully integrated). Magnitudes are normalized by the first mode values. All phases are in reference to the phase of the first acoustic mode. Sign convention is such that negative phases are leading while positive phases are lagging.

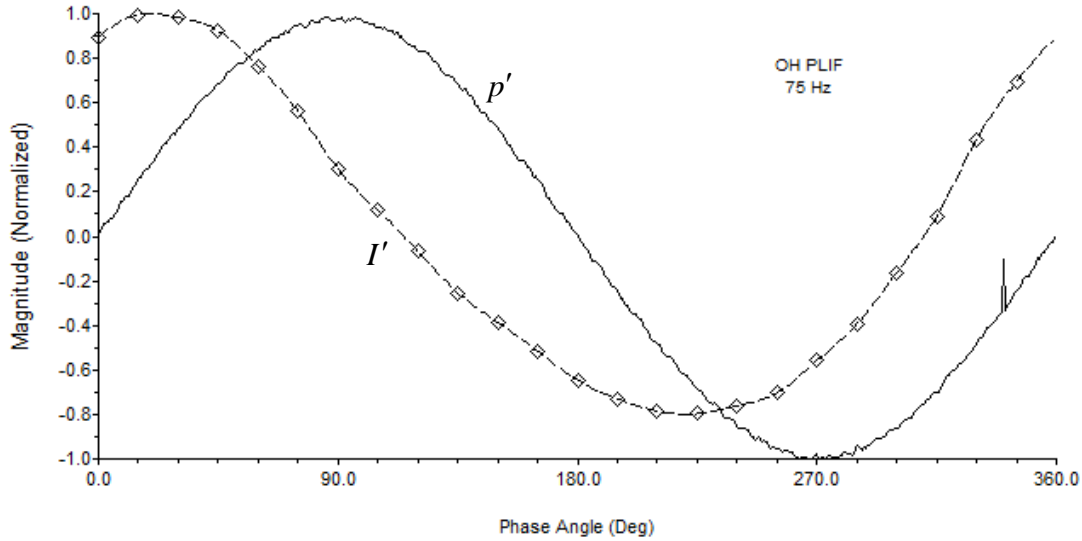


Figure H-3: Resulting waveforms from the 75 Hz OH PLIF experiment (Experiment 651). The solid curve shows the measured acoustic waveform with the rising-edge zero crossing marking the zero-degree point. Diamonds represent total (fully integrated) intensity data points computed from the phase bins. The dashed curve is a periodic cubic spline fit to this data. Signals are normalized by their peak values.

Mode	Pressure (p')		Intensity (I')	
	Mag	Phase	Mag	Phase
1	1.0000	0.0	1.0000	-58.2
2	0.0059	-74.1	0.1571	-63.6
3	0.0088	-155.9	0.0243	-49.5
4	0.0017	146.4	0.0114	-166.1
5	0.0005	154.6	0.0089	-153.9
6	0.0012	177.6	0.0067	-154.6
7	0.0010	140.1	0.0048	18.9
8	0.0001	147.5	0.0063	67.1
9	0.0009	71.8	0.0026	-102.1
10	0.0004	15.6	0.0055	5.2
11	0.0005	1.3	0.0053	-3.2

Table H-7: Harmonic content of the measured acoustic and intensity fields for the 75 Hz PLIF case. The measured intensity is total (fully integrated). Magnitudes are normalized by the first mode values. All phases are in reference to the phase of the first acoustic mode. Sign convention is such that negative phases are leading while positive phases are lagging.

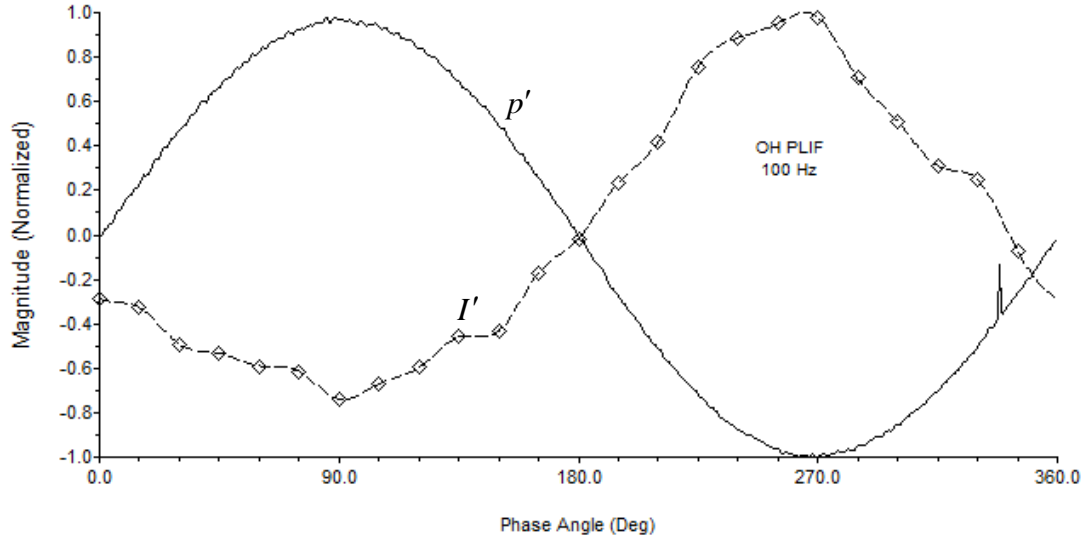


Figure H-4: Resulting waveforms from the 100 Hz OH PLIF experiment (Experiment 653). The solid curve shows the measured acoustic waveform with the rising-edge zero crossing marking the zero-degree point. Diamonds represent total (fully integrated) intensity data points computed from the phase bins. The dashed curve is a periodic cubic spline fit to this data. Signals are normalized by their peak values.

Mode	Pressure (p')		Intensity (I')	
	Mag	Phase	Mag	Phase
1	1.0000	0.0	1.0000	170.7
2	0.0125	-166.2	0.1852	53.4
3	0.0025	31.4	0.0425	-44.9
4	0.0020	-147.1	0.0405	165.6
5	0.0005	90.7	0.0317	139.3
6	0.0017	167.7	0.0114	43.3
7	0.0016	129.1	0.0475	44.3
8	0.0012	131.8	0.0104	-10.0
9	0.0015	71.8	0.0076	68.7
10	0.0007	19.7	0.0198	44.2
11	0.0018	81.0	0.0245	-36.3

Table H-8: Harmonic content of the measured acoustic and intensity fields for the 100 Hz PLIF case. The measured intensity is total (fully integrated). Magnitudes are normalized by the first mode values. All phases are in reference to the phase of the first acoustic mode. Sign convention is such that negative phases are leading while positive phases are lagging.

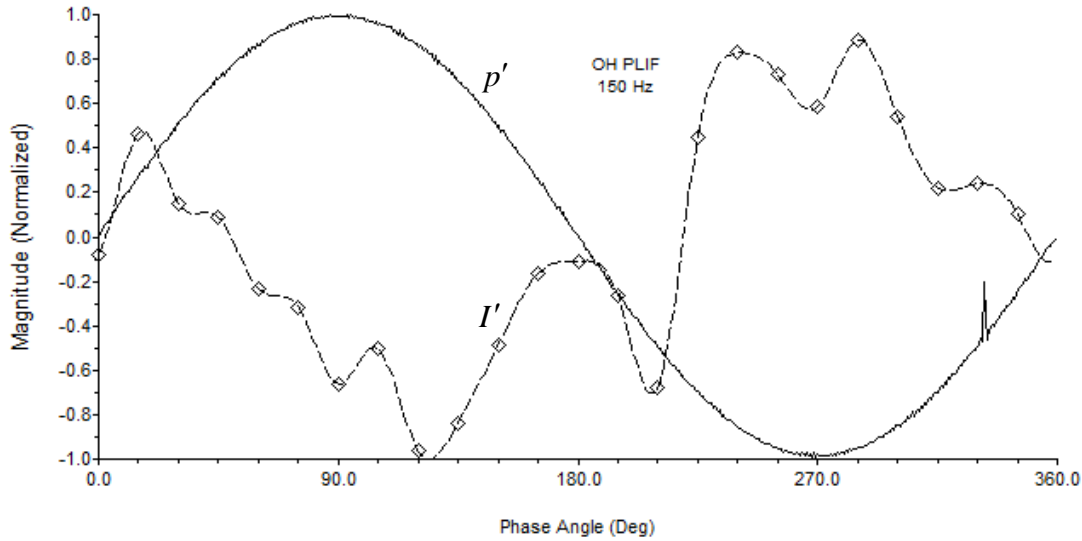


Figure H-5: Resulting waveforms from the 150 Hz OH PLIF experiment (Experiment 654). The solid curve shows the measured acoustic waveform with the rising-edge zero crossing marking the zero-degree point. Diamonds represent total (fully integrated) intensity data points computed from the phase bins. The dashed curve is a periodic cubic spline fit to this data. Signals are normalized by their peak values.

Mode	Pressure (p')		Intensity (I')	
	Mag	Phase	Mag	Phase
1	1.0000	0.0	1.0000	-154.7
2	0.0011	-59.0	0.3068	30.6
3	0.0011	-46.2	0.3299	10.5
4	0.0011	126.8	0.1475	-147.8
5	0.0013	128.4	0.2829	28.6
6	0.0011	96.0	0.1601	-135.6
7	0.0016	72.3	0.1591	99.8
8	0.0015	43.0	0.1796	21.4
9	0.0013	30.0	0.0579	127.4
10	0.0013	2.0	0.0704	1.9
11	0.0013	-31.1	0.0167	-16.6

Table H-9: Harmonic content of the measured acoustic and intensity fields for the 150 Hz PLIF case. The measured intensity is total (fully integrated). Magnitudes are normalized by the first mode values. All phases are in reference to the phase of the first acoustic mode. Sign convention is such that negative phases are leading while positive phases are lagging.

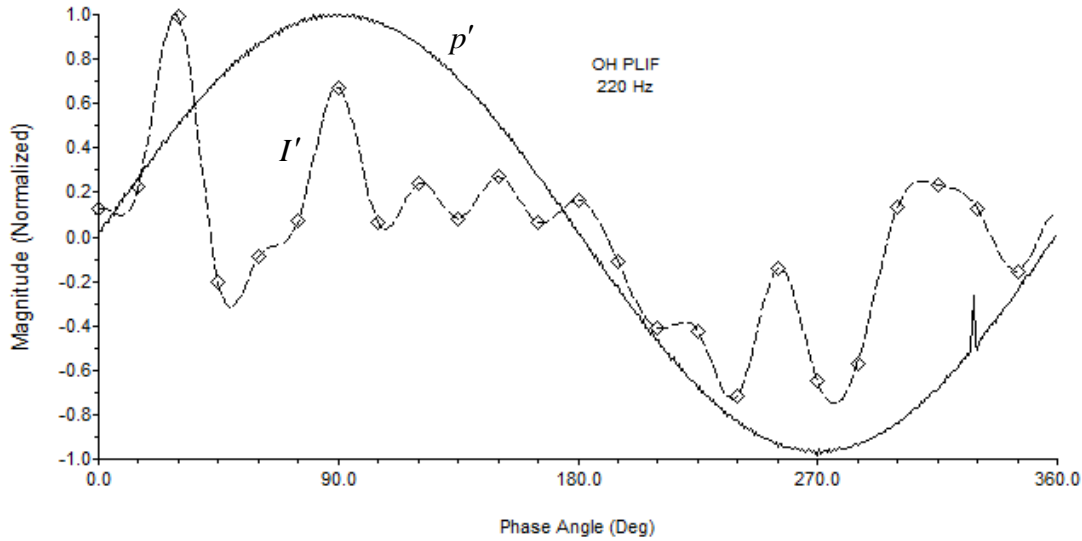


Figure H-6: Resulting waveforms from the 220 Hz OH PLIF experiment (Experiment 655). The solid curve shows the measured acoustic waveform with the rising-edge zero crossing marking the zero-degree point. Diamonds represent total (fully integrated) intensity data points computed from the phase bins. The dashed curve is a periodic cubic spline fit to this data. Signals are normalized by their peak values.

Mode	Pressure (p')		Intensity (I')	
	Mag	Phase	Mag	Phase
1	1.0000	0.0	1.0000	-22.7
2	0.0016	-92.3	0.5192	-135.0
3	0.0008	141.7	0.1109	83.1
4	0.0007	151.1	0.2414	-4.9
5	0.0006	142.4	0.6464	34.8
6	0.0007	77.7	0.4752	35.9
7	0.0005	49.1	0.1886	162.1
8	0.0007	16.1	0.3176	-179.7
9	0.0008	-27.6	0.1683	119.7
10	0.0008	-60.6	0.0981	-62.4
11	0.0008	-84.3	0.3222	-148.7

Table H-10: Harmonic content of the measured acoustic and intensity fields for the 220 Hz PLIF case. The measured intensity is total (fully integrated). Magnitudes are normalized by the first mode values. All phases are in reference to the phase of the first acoustic mode. Sign convention is such that negative phases are leading while positive phases are lagging.

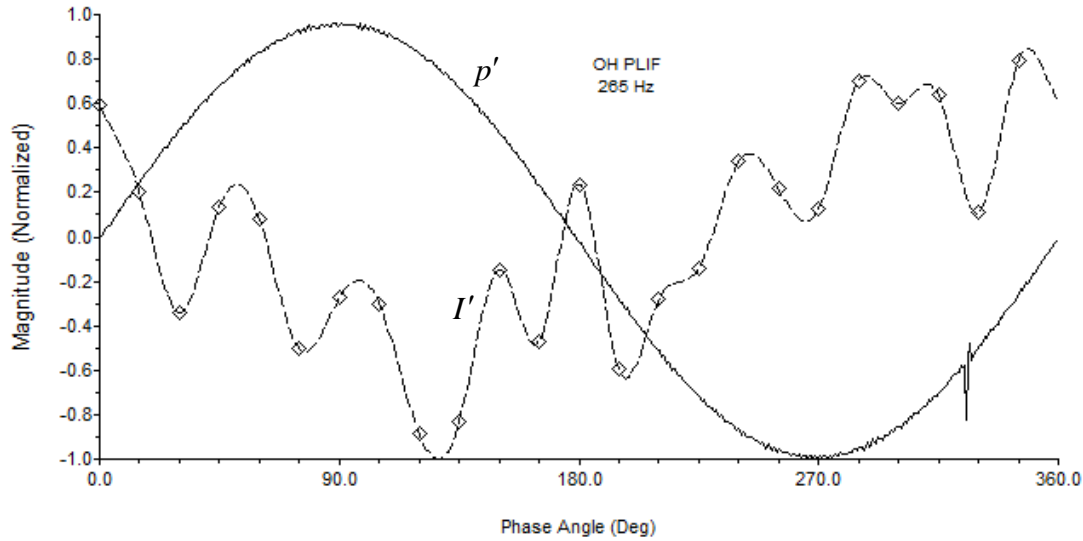


Figure H-7: Resulting waveforms from the 265 Hz OH PLIF experiment (Experiment 657). The solid curve shows the measured acoustic waveform with the rising-edge zero crossing marking the zero-degree point. Diamonds represent total (fully integrated) intensity data points computed from the phase bins. The dashed curve is a periodic cubic spline fit to this data. Signals are normalized by their peak values.

Mode	Pressure (p')		Intensity (I')	
	Mag	Phase	Mag	Phase
1	1.0000	0.0	1.0000	-136.6
2	0.0022	-150.5	0.0907	-134.0
3	0.0042	-4.6	0.1326	81.3
4	0.0008	-50.0	0.2524	-134.3
5	0.0009	-90.0	0.1491	-22.2
6	0.0008	-127.3	0.3646	-131.8
7	0.0010	-143.2	0.2395	-129.0
8	0.0008	155.6	0.1890	-33.6
9	0.0011	159.9	0.1214	92.7
10	0.0006	87.0	0.1176	-129.6
11	0.0010	80.0	0.2245	104.4

Table H-11: Harmonic content of the measured acoustic and intensity fields for the 265 Hz PLIF case. The measured intensity is total (fully integrated). Magnitudes are normalized by the first mode values. All phases are in reference to the phase of the first acoustic mode. Sign convention is such that negative phases are leading while positive phases are lagging.

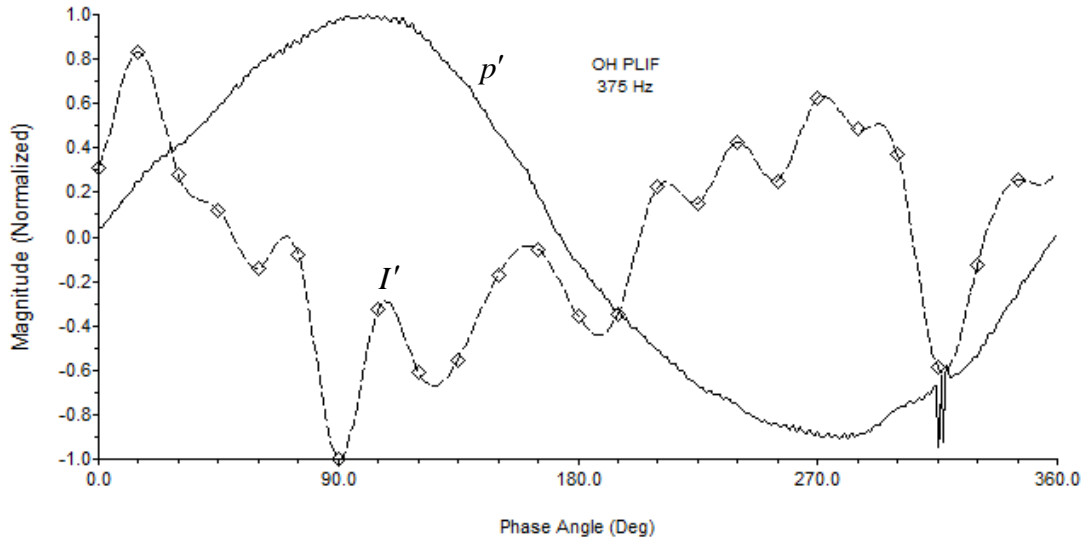


Figure H-8: Resulting waveforms from the 375 Hz OH PLIF experiment (Experiment 656). The solid curve shows the measured acoustic waveform with the rising-edge zero crossing marking the zero-degree point. Diamonds represent total (fully integrated) intensity data points computed from the phase bins. The dashed curve is a periodic cubic spline fit to this data. Signals are normalized by their peak values.

Mode	Pressure (p')		Intensity (I')	
	Mag	Phase	Mag	Phase
1	1.0000	0.0	1.0000	-147.1
2	0.0576	117.4	0.6155	-15.0
3	0.0577	-78.8	0.7051	-18.4
4	0.0102	-19.2	0.2089	-59.7
5	0.0137	-68.3	0.3690	-81.1
6	0.0082	-84.9	0.2426	-171.1
7	0.0084	-82.9	0.1762	7.7
8	0.0075	107.2	0.3937	90.0
9	0.0037	106.2	0.1059	111.9
10	0.0091	68.9	0.0733	-14.0
11	0.0013	-37.0	0.3066	15.1

Table H-12: Harmonic content of the measured acoustic and intensity fields for the 375 Hz PLIF case. The measured intensity is total (fully integrated). Magnitudes are normalized by the first mode values. All phases are in reference to the phase of the first acoustic mode. Sign convention is such that negative phases are leading while positive phases are lagging.

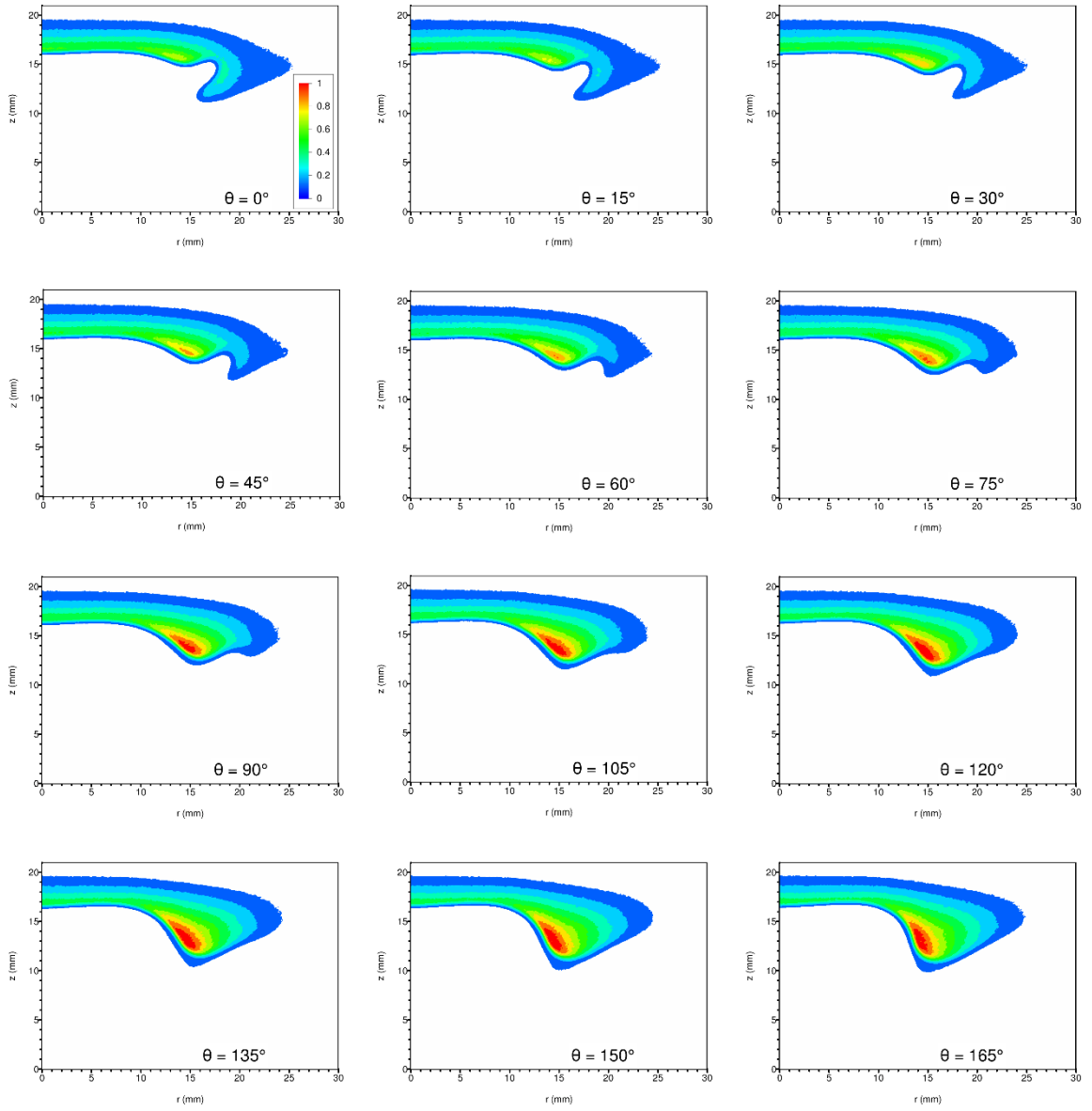


Figure H-9: Phase-resolved OH PLIF images for acoustic forcing at 55 Hz. The horizontal axis is the radius (mm) from the centerline of the burner. The vertical axis is the distance (mm) above the nozzle exit plane. (The stagnation plane is located at $z = 21\text{mm}$.) Phase angle $\theta = 0^\circ$ corresponds to the rising-edge zero crossing of the local unsteady pressure. Data from experiment 652. A total of 24 images on 15° spacing are shown. (See next page.) The magnitude scale is normalized by the peak value over all 24 images.

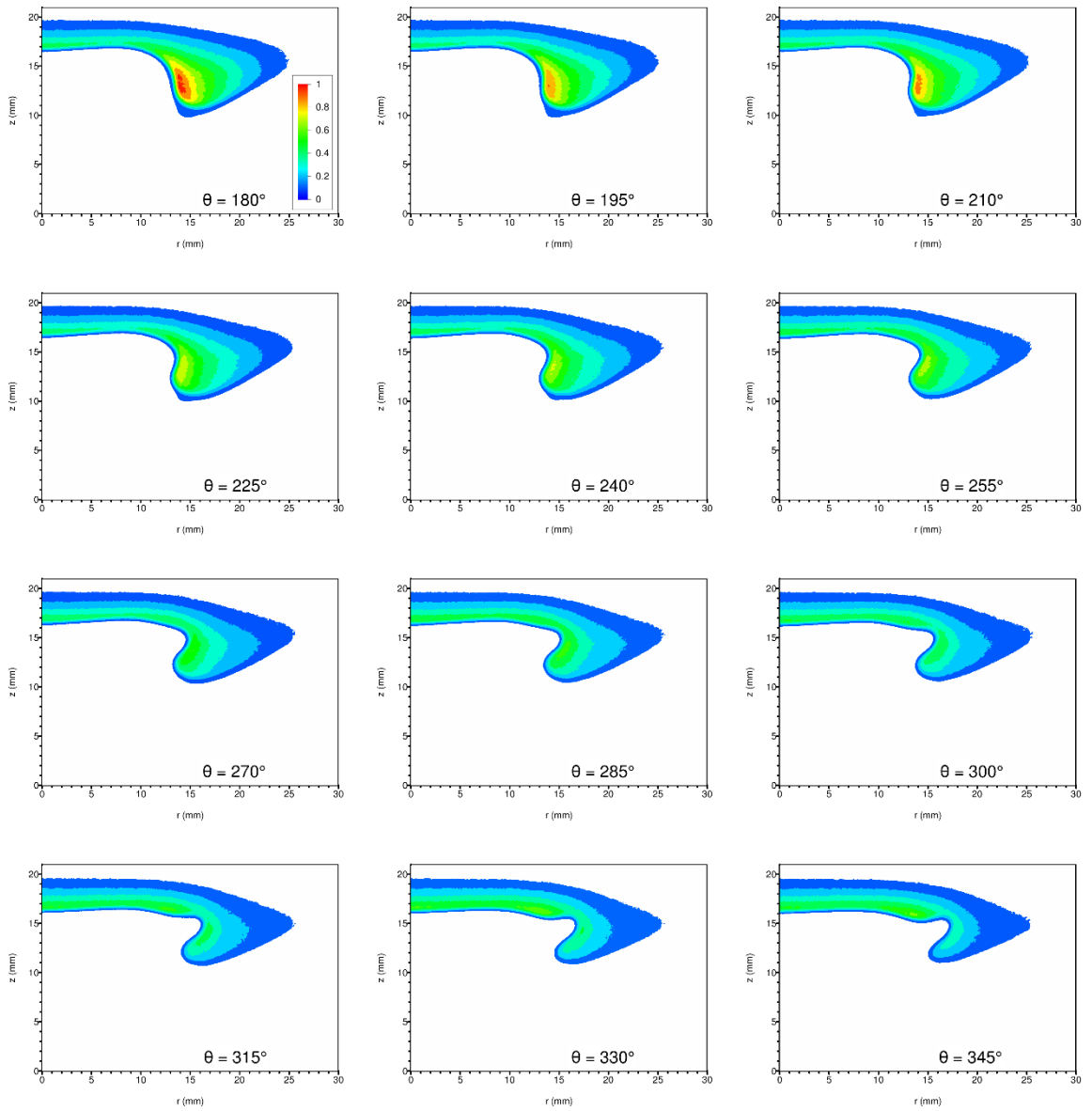


Figure H-9 (cont.): Phase-resolved OH PLIF images for acoustic forcing at 55 Hz. The horizontal axis is the radius (mm) from the centerline of the burner. The vertical axis is the distance (mm) above the nozzle exit plane. (The stagnation plane is located at $z = 21$ mm.) Phase angle $\theta = 0^\circ$ corresponds to the rising-edge zero crossing of the local unsteady pressure. Data from experiment 652. A total of 24 images on 15° spacing are shown. (See previous page.) The magnitude scale is normalized by the peak value over all 24 images.

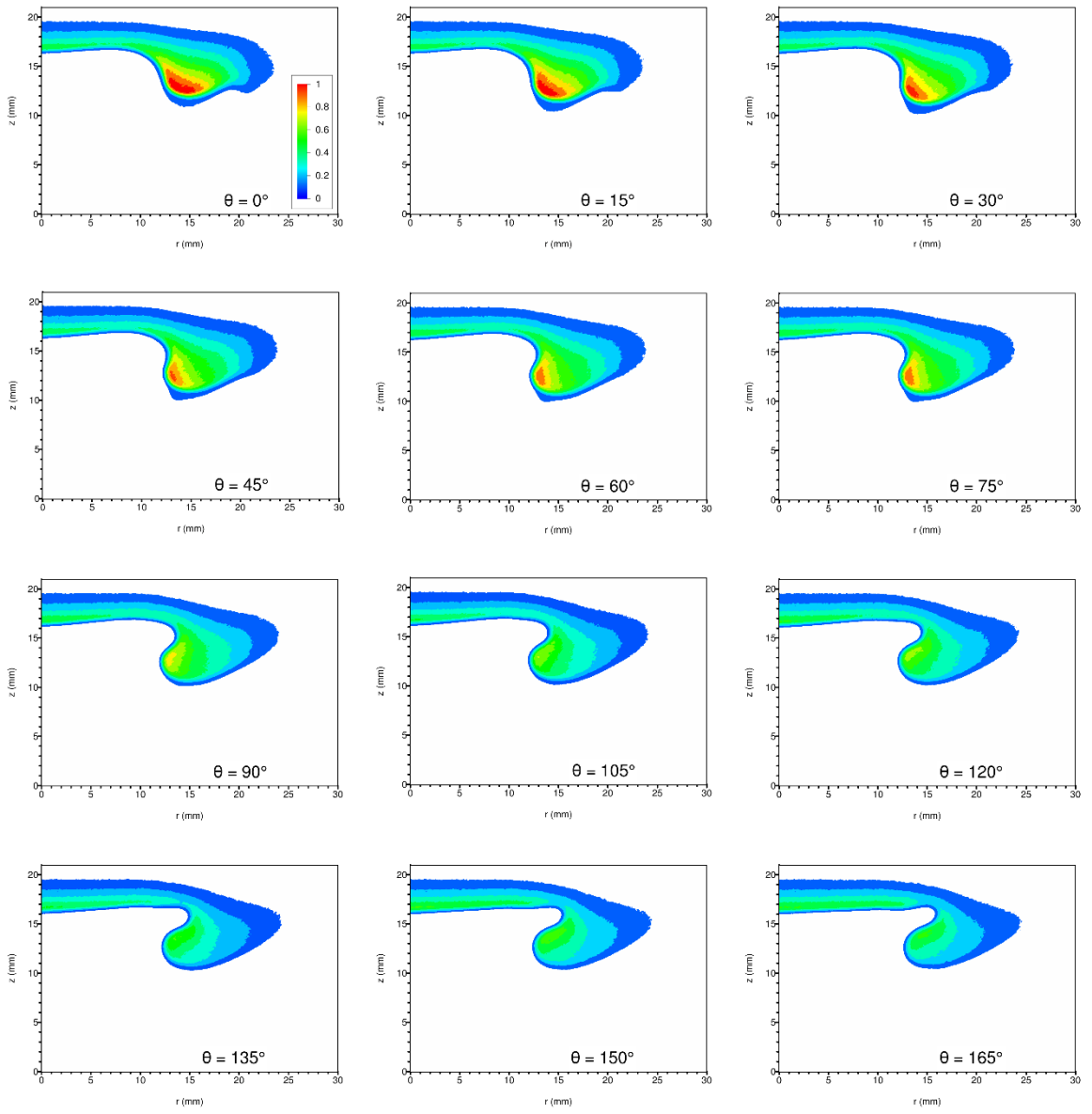


Figure H-10: Phase-resolved OH PLIF images for acoustic forcing at 75 Hz. The horizontal axis is the radius (mm) from the centerline of the burner. The vertical axis is the distance (mm) above the nozzle exit plane. (The stagnation plane is located at $z = 21\text{mm}$.) Phase angle $\theta = 0^\circ$ corresponds to the rising-edge zero crossing of the local unsteady pressure. Data from experiment 651. A total of 24 images on 15° spacing are shown. (See next page.) The magnitude scale is normalized by the peak value over all 24 images.

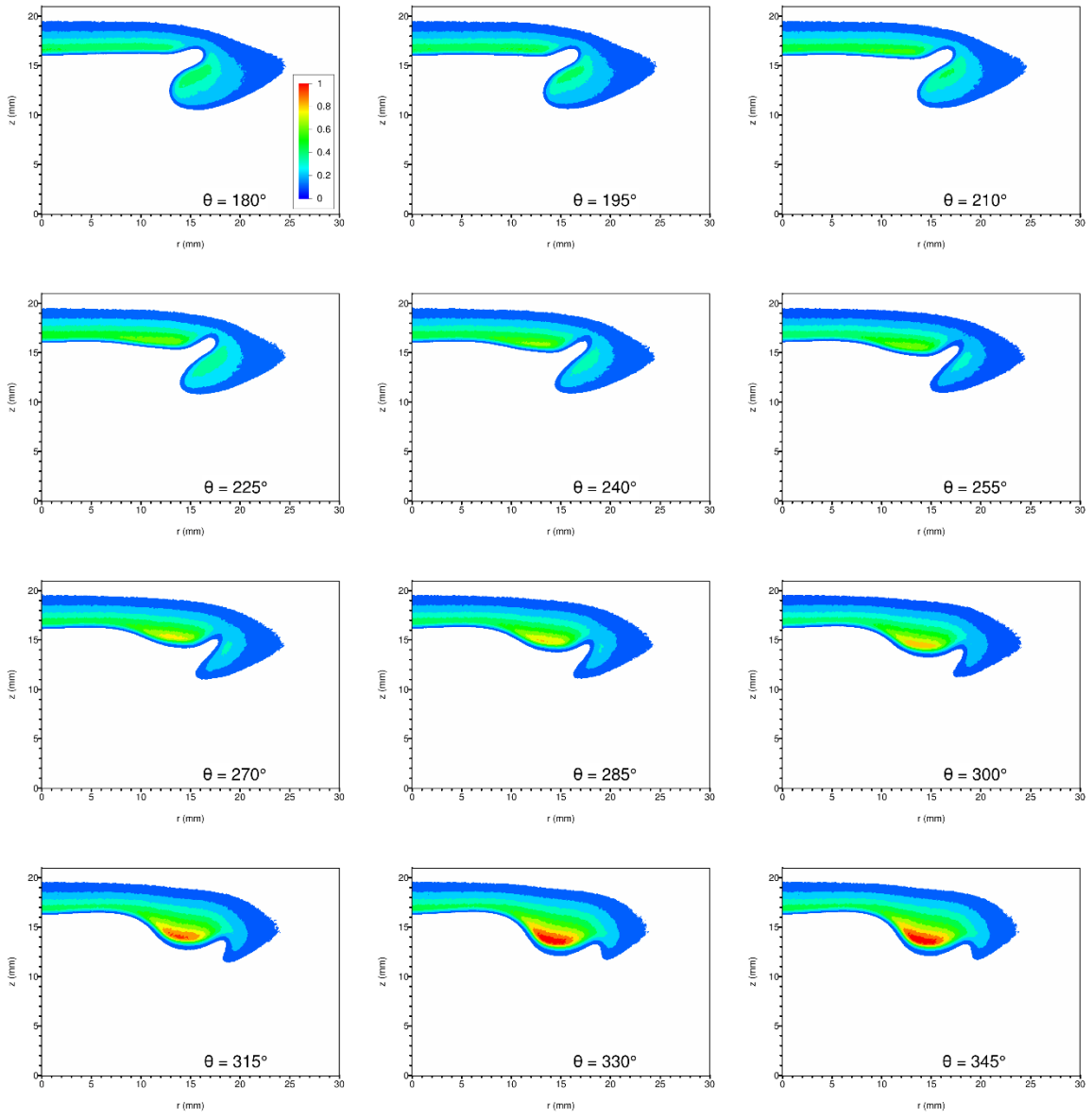


Figure H-10 (cont.): Phase-resolved OH PLIF images for acoustic forcing at 75 Hz. The horizontal axis is the radius (mm) from the centerline of the burner. The vertical axis is the distance (mm) above the nozzle exit plane. (The stagnation plane is located at $z = 21\text{mm}$.) Phase angle $\theta = 0^\circ$ corresponds to the rising-edge zero crossing of the local unsteady pressure. Data from experiment 651. A total of 24 images on 15° spacing are shown. (See previous page.) The magnitude scale is normalized by the peak value over all 24 images.

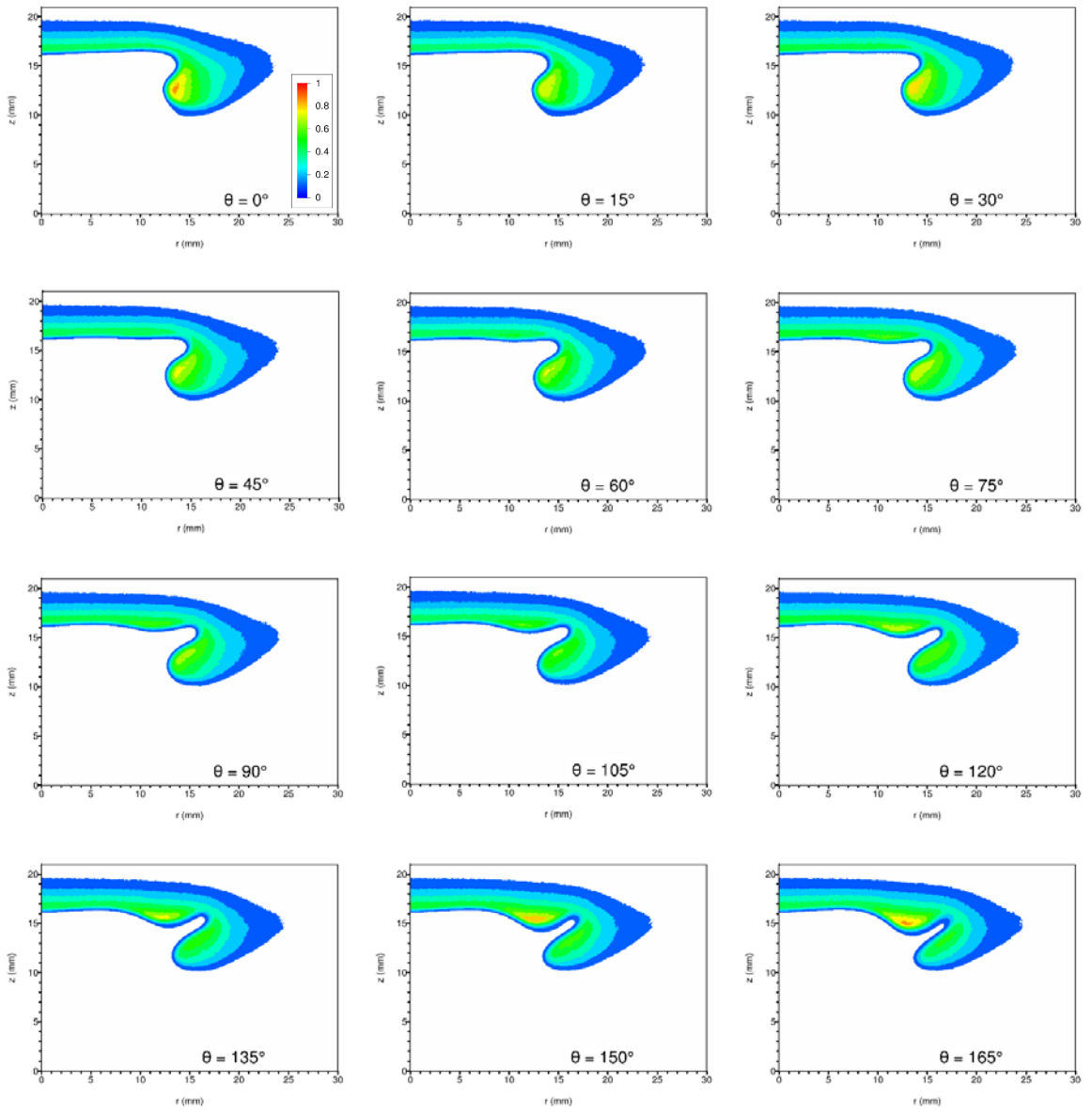


Figure H-11: Phase-resolved OH PLIF images for acoustic forcing at 100 Hz. The horizontal axis is the radius (mm) from the centerline of the burner. The vertical axis is the distance (mm) above the nozzle exit plane. (The stagnation plane is located at $z = 21$ mm.) Phase angle $\theta = 0^\circ$ corresponds to the rising-edge zero crossing of the local unsteady pressure. Data from experiment 653. A total of 24 images on 15° spacing are shown. (See next page.) The magnitude scale is normalized by the peak value over all 24 images.

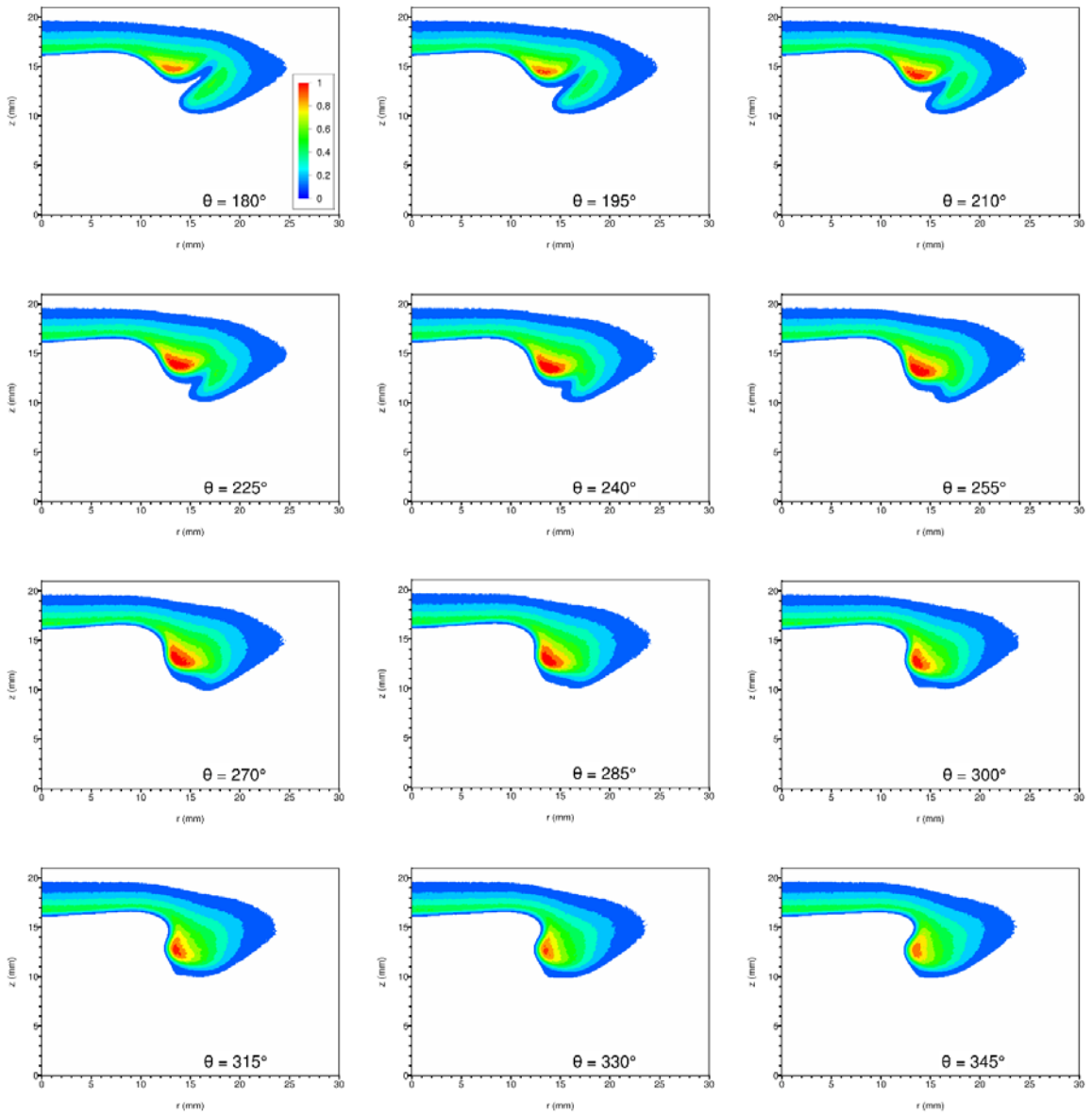


Figure H-11 (cont.): Phase-resolved OH PLIF images for acoustic forcing at 100 Hz. The horizontal axis is the radius (mm) from the centerline of the burner. The vertical axis is the distance (mm) above the nozzle exit plane. (The stagnation plane is located at $z = 21$ mm.) Phase angle $\theta = 0^\circ$ corresponds to the rising-edge zero crossing of the local unsteady pressure. Data from experiment 653. A total of 24 images on 15° spacing are shown. (See previous page.) The magnitude scale is normalized by the peak value over all 24 images.

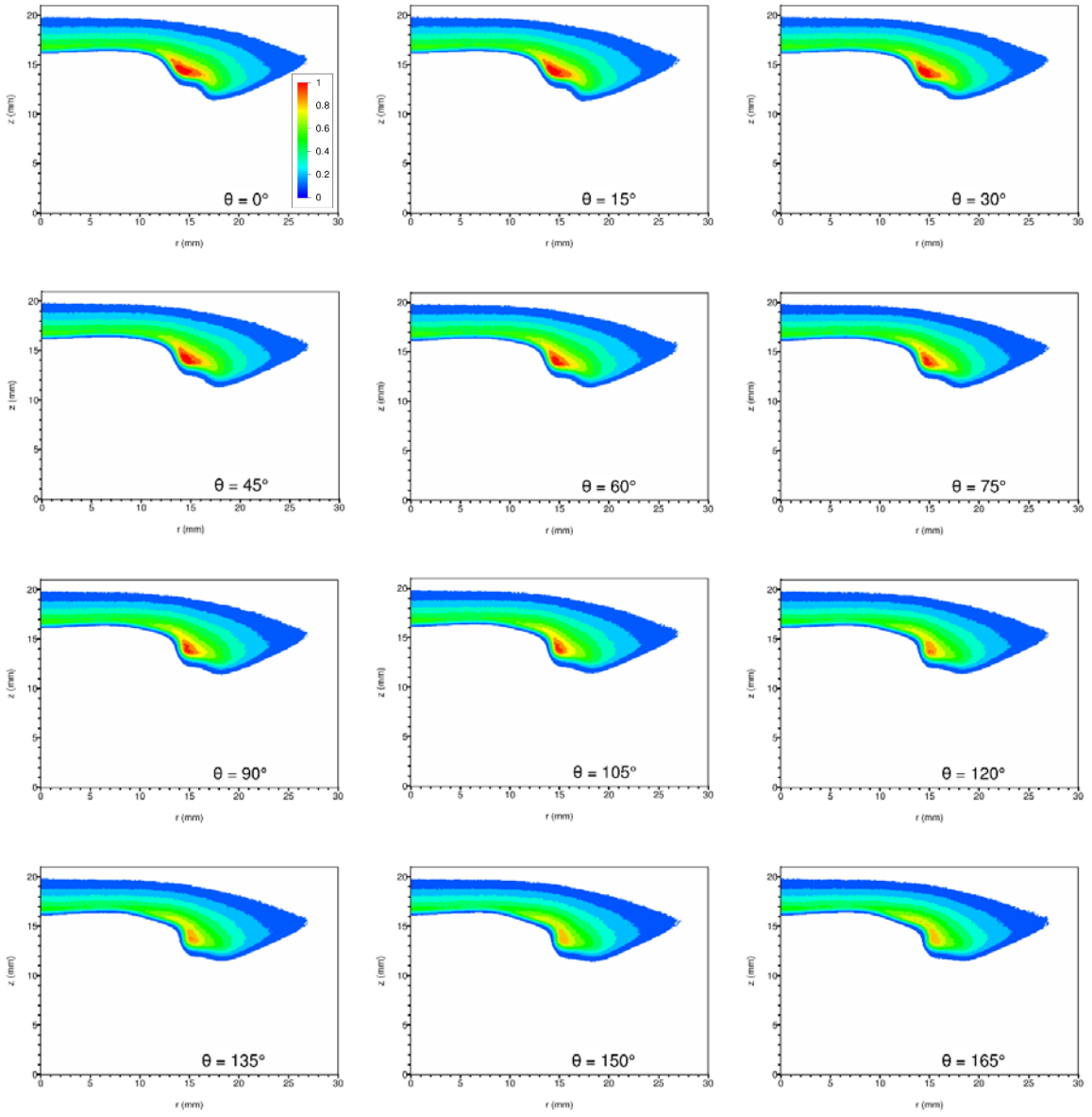


Figure H-12: Phase-resolved OH PLIF images for acoustic forcing at 150 Hz. The horizontal axis is the radius (mm) from the centerline of the burner. The vertical axis is the distance (mm) above the nozzle exit plane. (The stagnation plane is located at $z = 21\text{mm}$.) Phase angle $\theta = 0^\circ$ corresponds to the rising-edge zero crossing of the local unsteady pressure. Data from experiment 654. A total of 24 images on 15° spacing are shown. (See next page.) The magnitude scale is normalized by the peak value over all 24 images.

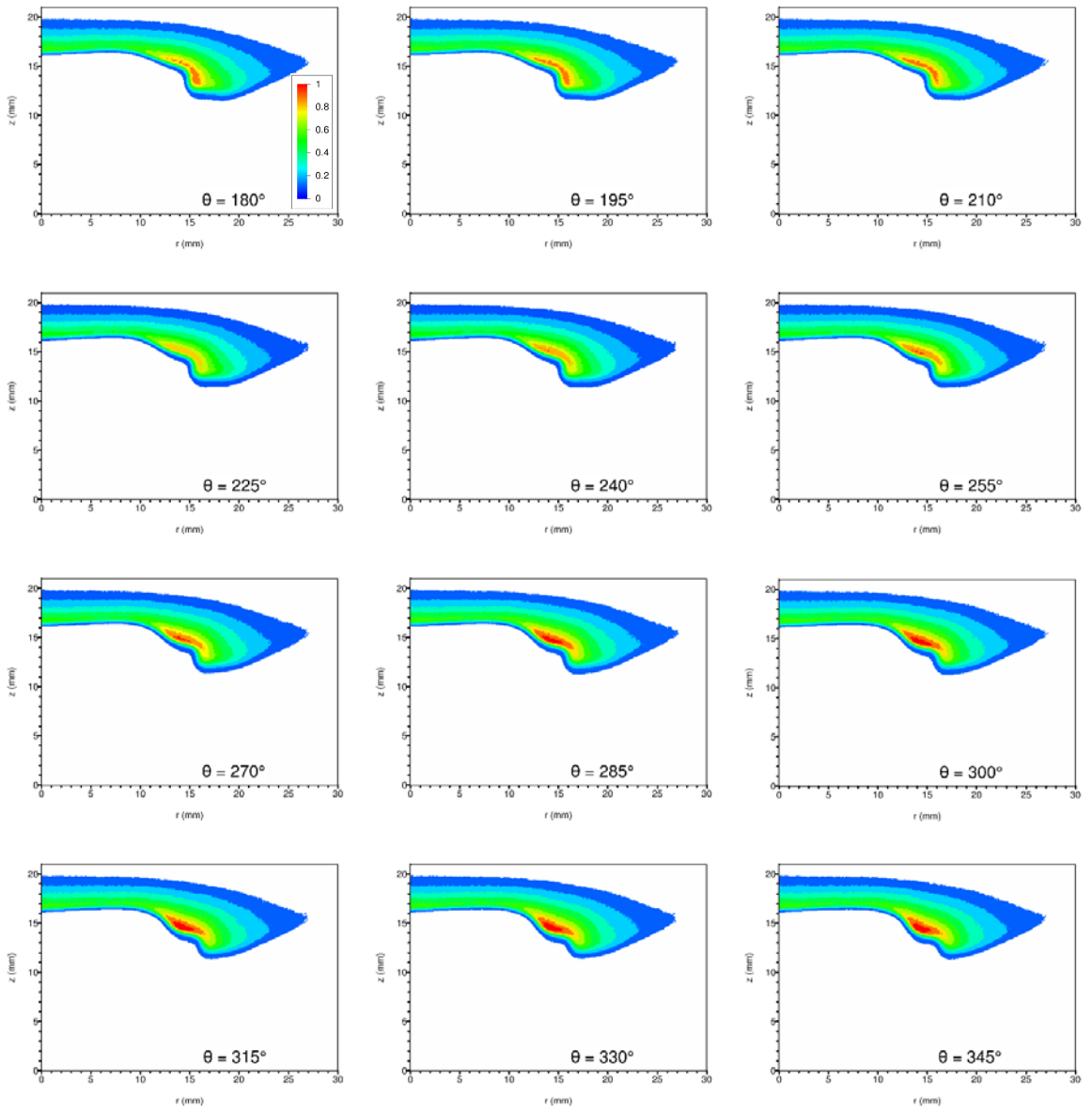


Figure H-12 (cont.): Phase-resolved OH PLIF images for acoustic forcing at 150 Hz. The horizontal axis is the radius (mm) from the centerline of the burner. The vertical axis is the distance (mm) above the nozzle exit plane. (The stagnation plane is located at $z = 21$ mm.) Phase angle $\theta = 0^\circ$ corresponds to the rising-edge zero crossing of the local unsteady pressure. Data from experiment 654. A total of 24 images on 15° spacing are shown. (See previous page.) The magnitude scale is normalized by the peak value over all 24 images.

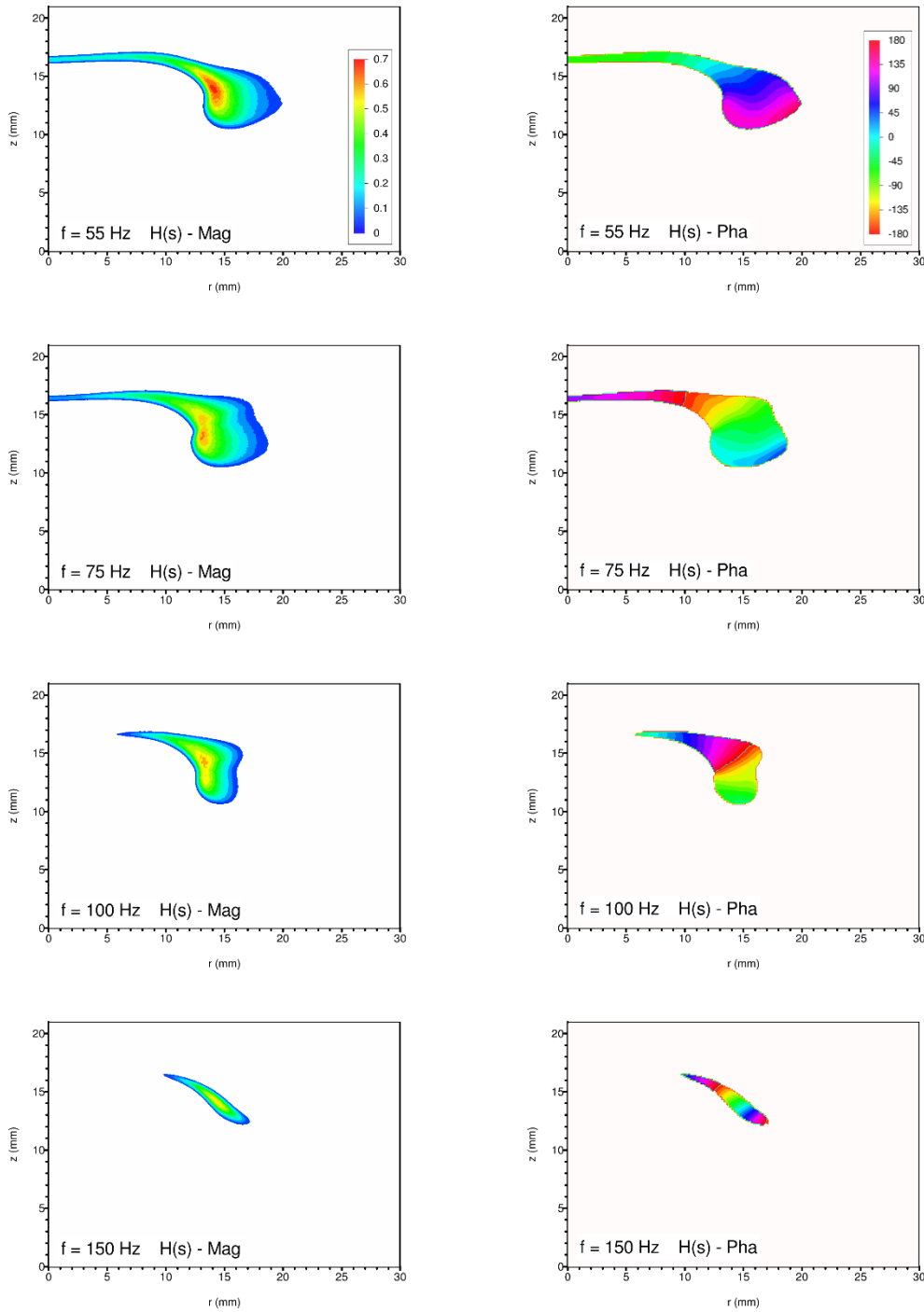


Figure H-13: Spatially resolved combustion response function produced from OH PLIF data. Magnitude plots appear in the left column while phase plots are shown on the right. Note that positive phase values correspond to I' lagging P' . The coordinate system origin is along the burner centerline at the nozzle exit plane. Data for the seven base drive frequencies are shown. (See next page.)

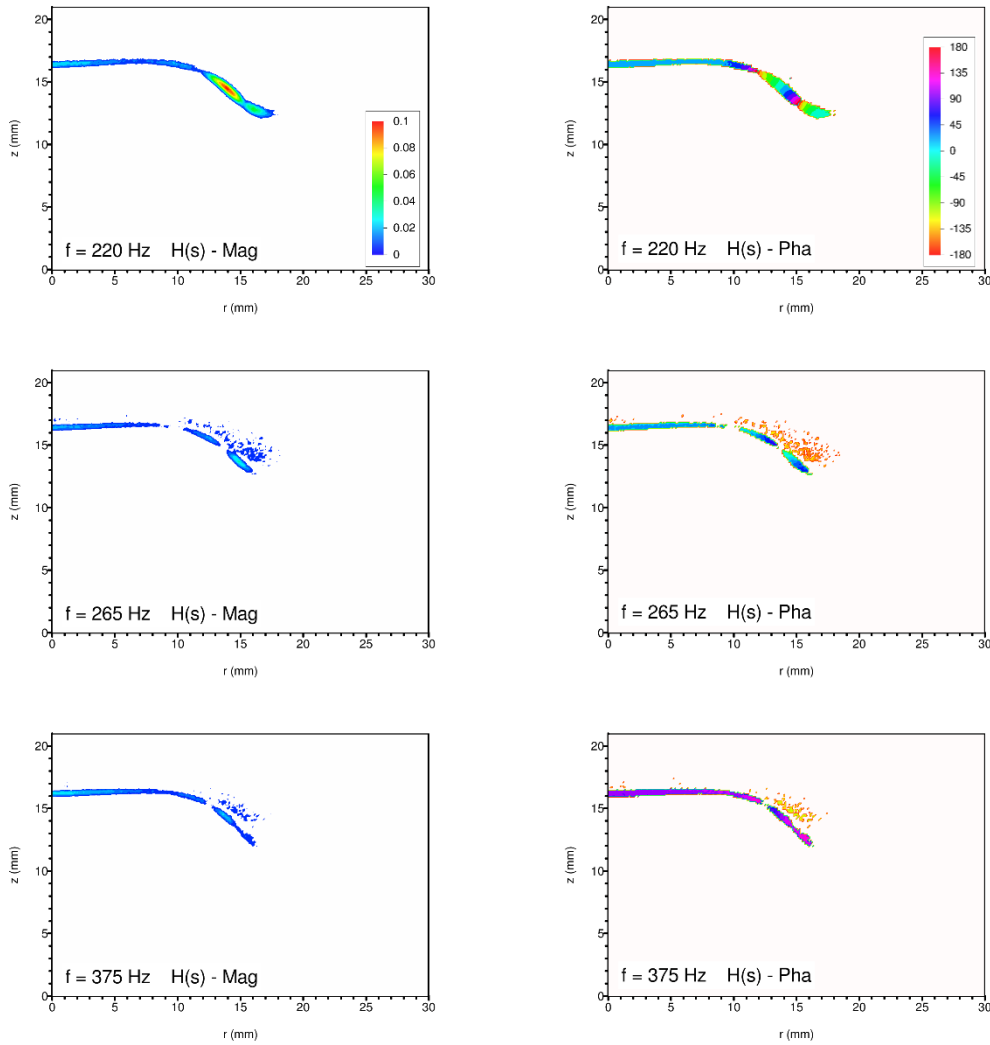


Figure H-13 (cont.): Spatially resolved combustion response function produced from OH PLIF data. Magnitude plots appear in the left column while phase plots are shown on the right. Data for the seven base drive frequencies are shown. (See previous page.) Note the change in magnitude scale versus the plots for 150 Hz and lower frequency.

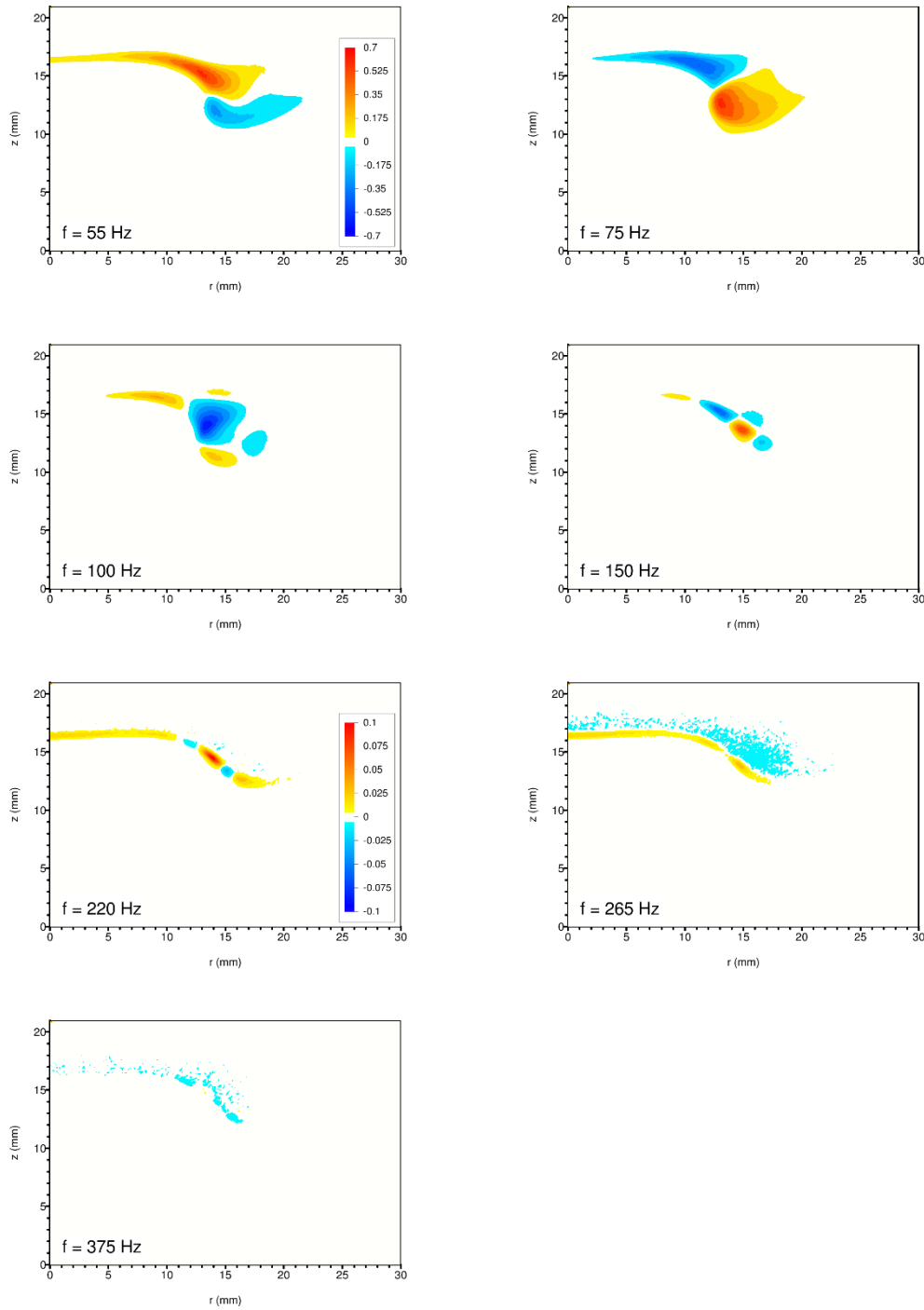


Figure H-14: Spatially resolved forced Rayleigh index produced from OH PLIF data. Data for the seven base drive frequencies are shown. Plots for the four lower frequencies use the top magnitude legend. Plots for the three higher frequencies use the bottom magnitude legend.

H.2.2 CH PLIF Experimental Data

The following 23 pages present the relevant collected CH PLIF data. Images were collected using an Andor iStar ICCD camera coupled to a 50 mm, f/1.2, Nikon macro lens. Optical pumping of the CH radicals of interest was performed at $\lambda_{\text{air}} = 390.23$ nm. Image data was collected and processed using the techniques described in chapter 4. For CH data, only two of the three image correction methods were employed:

- i) Correction for the shot-to-shot variation in OPO output intensity.
- ii) Correction for the spatial variation in laser sheet intensity in the vertical direction.

Correction for laser sheet absorption was not necessary since the fraction of absorbed energy from the sheet was very (essentially unmeasurably) small.

Further information regarding the processing of this data can be found in the beginning of this appendix as well as in chapter 4.

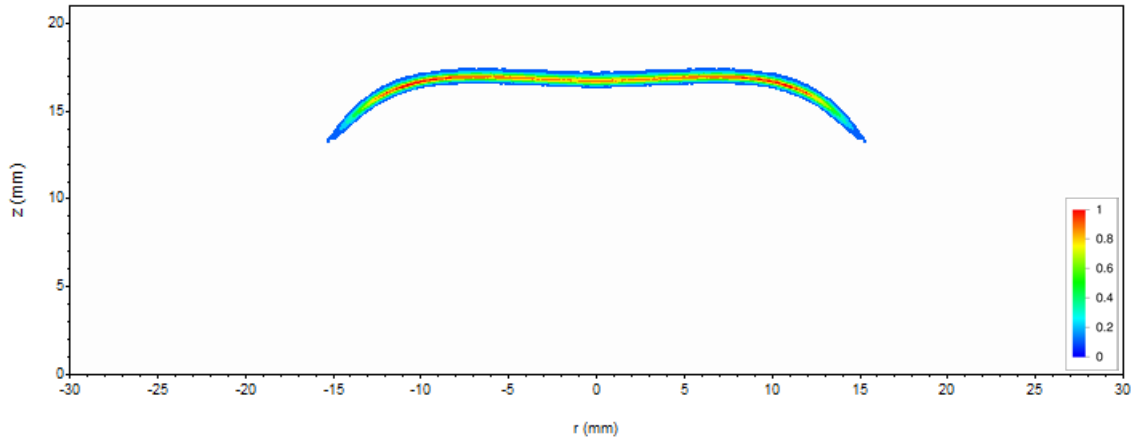


Figure H-15: CH PLIF image of flame under steady conditions (no acoustic forcing). Collected data appears on the left, and is mirrored across the centerline for a visual representation of entire flame. Burner centerline is at $r = 0$. Position $z = 0$ corresponds to the nozzle exit plane.

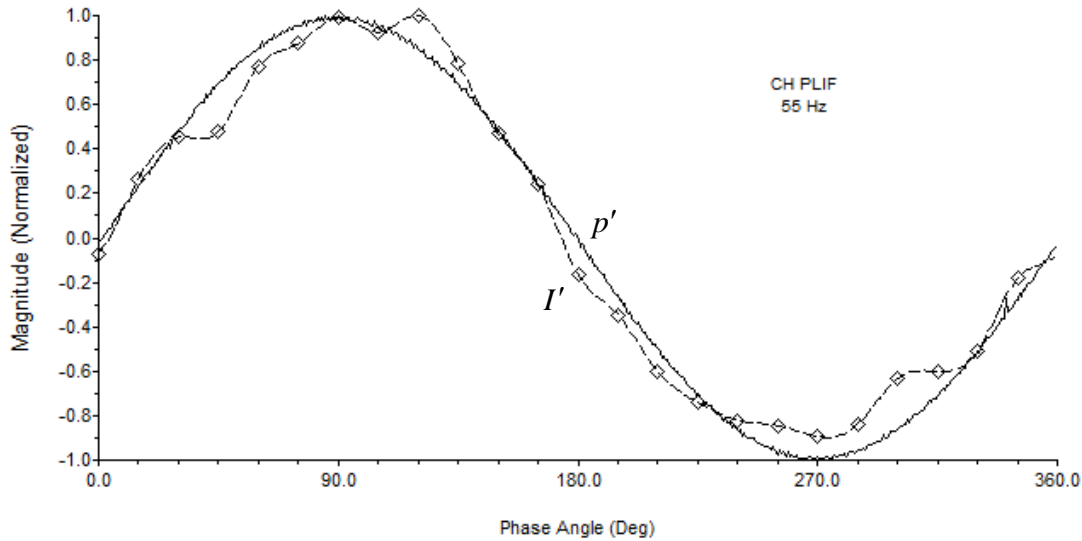


Figure H-16: Resulting waveforms from the 55 Hz CH PLIF experiment (Experiment 696). The solid curve shows the measured acoustic waveform with the rising-edge zero crossing marking the zero-degree point. Diamonds represent total (fully integrated) intensity data points computed from the phase bins. The dashed curve is a periodic cubic spline fit to this data. Signals are normalized by their peak values.

Mode	Pressure (p')		Intensity (I')	
	Mag	Phase	Mag	Phase
1	1.0000	0.0	1.0000	-0.9
2	0.0086	89.4	0.1090	144.6
3	0.0036	110.1	0.0439	-58.7
4	0.0012	91.0	0.0191	19.7
5	0.0011	-174.3	0.0191	-37.4
6	0.0009	-169.5	0.0274	-35.0
7	0.0004	-178.1	0.0108	113.6
8	0.0002	-121.2	0.0393	136.7
9	0.0002	22.9	0.0124	105.7
10	0.0005	39.2	0.0332	101.2
11	0.0006	58.8	0.0138	-158.7

Table H-13: Harmonic content of the measured acoustic and intensity fields for the 55 Hz CH PLIF case. The measured intensity is total (fully integrated). Magnitudes are normalized by the first mode values. All phases are in reference to the phase of the first acoustic mode. Sign convention is such that negative phases are leading while positive phases are lagging.

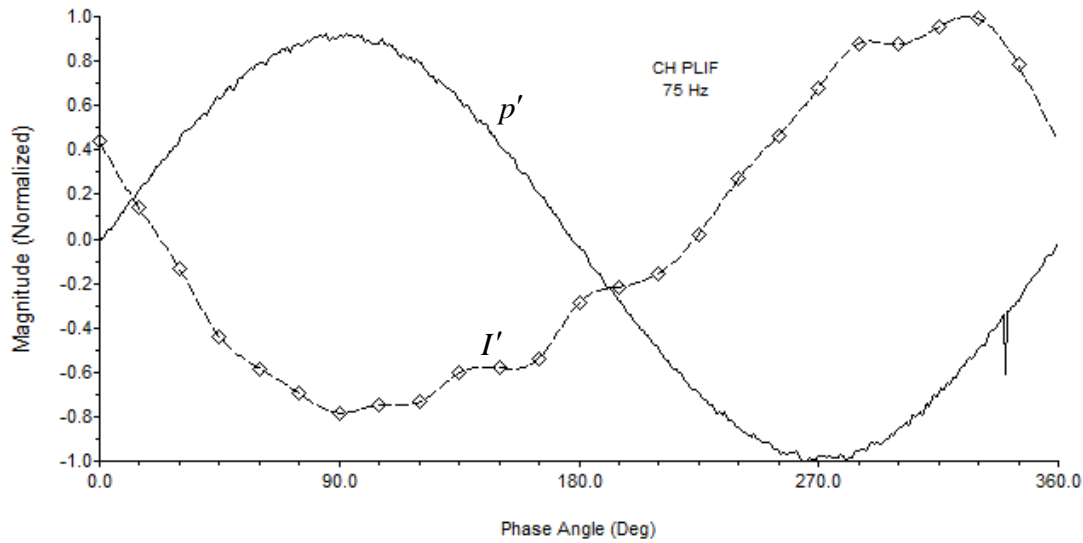


Figure H-17: Resulting waveforms from the 75 Hz CH PLIF experiment (Experiment 704). The solid curve shows the measured acoustic waveform with the rising-edge zero crossing marking the zero-degree point. Diamonds represent total (fully integrated) intensity data points computed from the phase bins. The dashed curve is a periodic cubic spline fit to this data. Signals are normalized by their peak values.

Mode	Pressure (p')		Intensity (I')	
	Mag	Phase	Mag	Phase
1	1.0000	0.0	1.0000	-150.2
2	0.0052	-44.9	0.2188	-163.3
3	0.0061	-138.7	0.0229	-166.2
4	0.0008	59.6	0.0249	-135.8
5	0.0021	25.3	0.0372	153.5
6	0.0013	-16.8	0.0090	26.1
7	0.0022	-55.5	0.0377	108.2
8	0.0014	-29.9	0.0228	7.7
9	0.0017	-80.5	0.0103	115.9
10	0.0012	-123.8	0.0161	-123.2
11	0.0014	-131.1	0.0019	91.8

Table H-14: Harmonic content of the measured acoustic and intensity fields for the 75 Hz CH PLIF case. The measured intensity is total (fully integrated). Magnitudes are normalized by the first mode values. All phases are in reference to the phase of the first acoustic mode. Sign convention is such that negative phases are leading while positive phases are lagging.

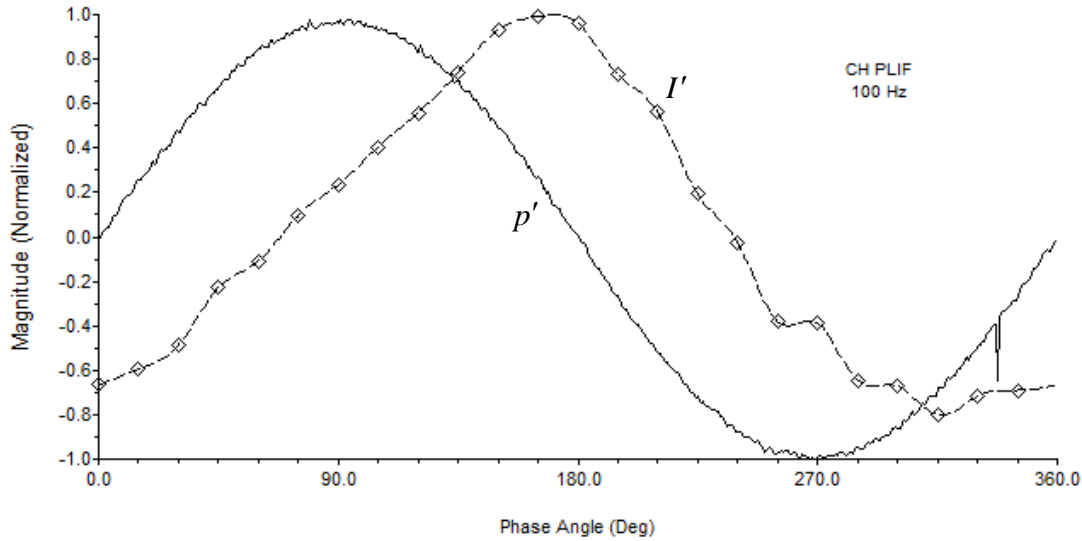


Figure H-18: Resulting waveforms from the 100 Hz CH PLIF experiment (Experiment 705). The solid curve shows the measured acoustic waveform with the rising-edge zero crossing marking the zero-degree point. Diamonds represent total (fully integrated) intensity data points computed from the phase bins. The dashed curve is a periodic cubic spline fit to this data. Signals are normalized by their peak values.

Mode	Pressure (p')		Intensity (I')	
	Mag	Phase	Mag	Phase
1	1.0000	0.0	1.0000	64.7
2	0.0103	-166.2	0.1565	-98.2
3	0.0051	10.5	0.0647	95.5
4	0.0014	-118.5	0.0274	-139.0
5	0.0020	-22.2	0.0162	-138.1
6	0.0018	-84.2	0.0243	159.8
7	0.0024	-36.1	0.0014	10.1
8	0.0020	-71.9	0.0063	-92.6
9	0.0017	-170.0	0.0022	-116.7
10	0.0008	-134.0	0.0106	62.4
11	0.0015	167.4	0.0311	21.7

Table H-15: Harmonic content of the measured acoustic and intensity fields for the 100 Hz CH PLIF case. The measured intensity is total (fully integrated). Magnitudes are normalized by the first mode values. All phases are in reference to the phase of the first acoustic mode. Sign convention is such that negative phases are leading while positive phases are lagging.

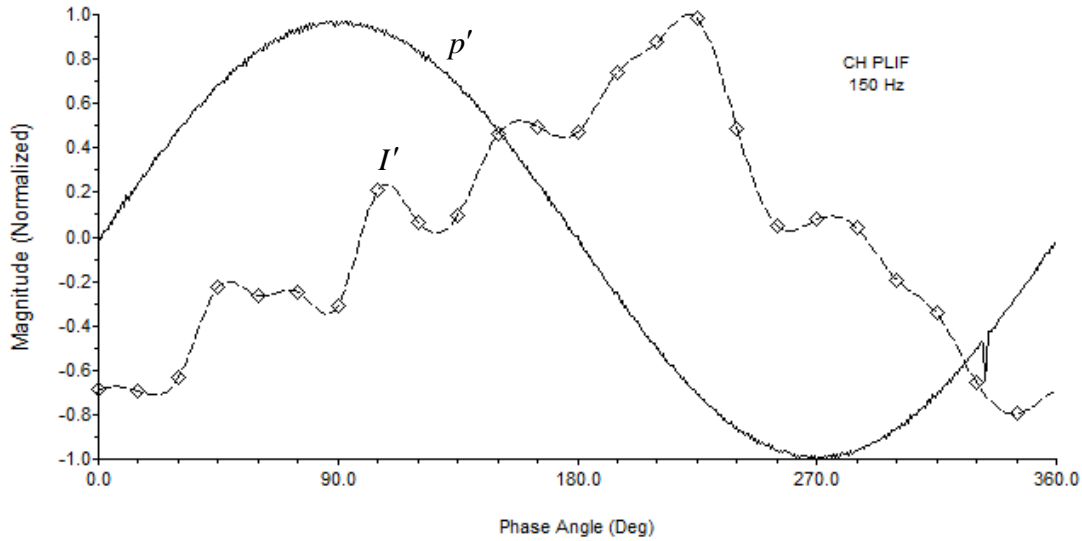


Figure H-19: Resulting waveforms from the 150 Hz CH PLIF experiment (Experiment 698). The solid curve shows the measured acoustic waveform with the rising-edge zero crossing marking the zero-degree point. Diamonds represent total (fully integrated) intensity data points computed from the phase bins. The dashed curve is a periodic cubic spline fit to this data. Signals are normalized by their peak values.

Mode	Pressure (p')		Intensity (I')	
	Mag	Phase	Mag	Phase
1	1.0000	0.0	1.0000	102.3
2	0.0013	3.1	0.2056	9.7
3	0.0029	3.2	0.0998	134.1
4	0.0016	10.0	0.1697	56.1
5	0.0010	-19.3	0.0805	-70.3
6	0.0011	-46.1	0.1358	-176.9
7	0.0006	-89.7	0.0967	-48.3
8	0.0010	-119.9	0.0720	-8.0
9	0.0009	-164.1	0.0672	-152.4
10	0.0008	163.6	0.0365	-41.9
11	0.0010	145.6	0.0247	3.2

Table H-16: Harmonic content of the measured acoustic and intensity fields for the 150 Hz CH PLIF case. The measured intensity is total (fully integrated). Magnitudes are normalized by the first mode values. All phases are in reference to the phase of the first acoustic mode. Sign convention is such that negative phases are leading while positive phases are lagging.

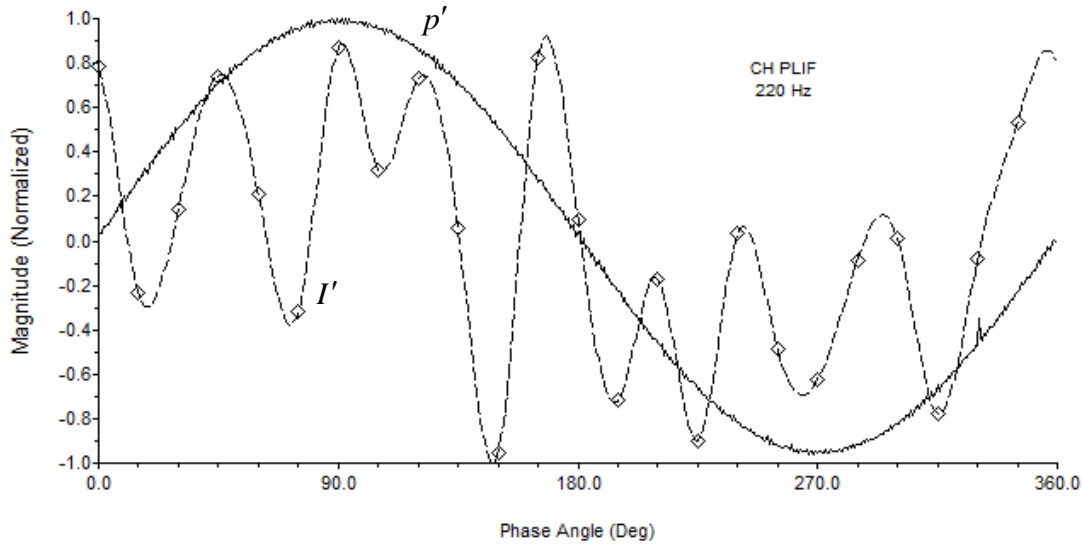


Figure H-20: Resulting waveforms from the 220 Hz CH PLIF experiment (Experiment 700). The solid curve shows the measured acoustic waveform with the rising-edge zero crossing marking the zero-degree point. Diamonds represent total (fully integrated) intensity data points computed from the phase bins. The dashed curve is a periodic cubic spline fit to this data. Signals are normalized by their peak values.

Mode	Pressure (p')		Intensity (I')	
	Mag	Phase	Mag	Phase
1	1.0000	0.0	1.0000	-25.4
2	0.0025	-98.4	0.1604	-145.8
3	0.0003	8.7	0.1971	-99.6
4	0.0006	140.0	0.3939	-84.3
5	0.0006	129.2	0.2822	107.0
6	0.0004	114.2	0.9383	-145.5
7	0.0007	84.9	0.2520	-173.5
8	0.0006	38.7	0.4549	-170.9
9	0.0006	1.6	0.7433	-20.8
10	0.0004	-13.1	0.3127	141.5
11	0.0004	-32.2	0.1194	-56.2

Table H-17: Harmonic content of the measured acoustic and intensity fields for the 220 Hz CH PLIF case. The measured intensity is total (fully integrated). Magnitudes are normalized by the first mode values. All phases are in reference to the phase of the first acoustic mode. Sign convention is such that negative phases are leading while positive phases are lagging.

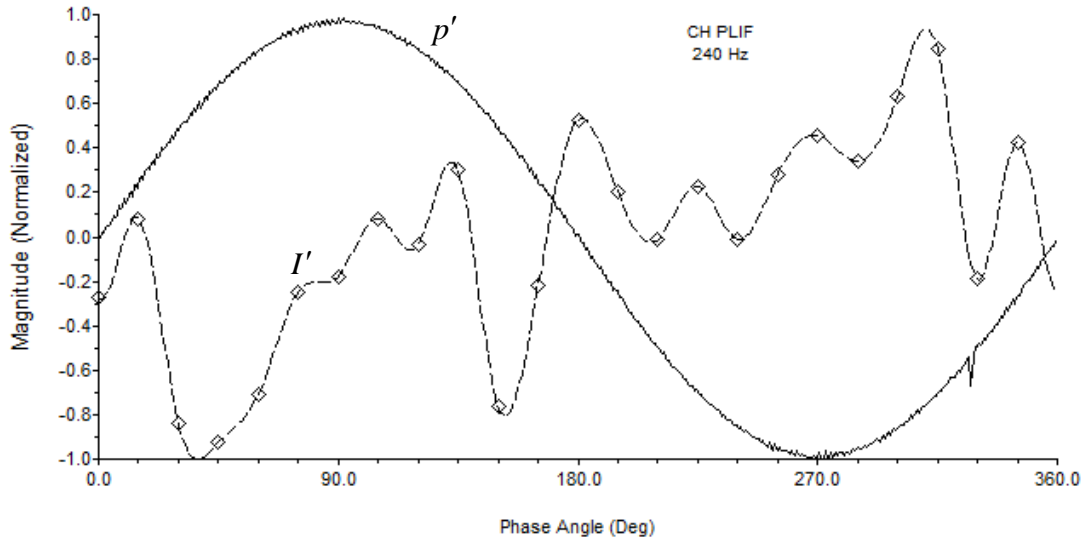


Figure H-21: Resulting waveforms from the 240 Hz CH PLIF experiment (Experiment 706). The solid curve shows the measured acoustic waveform with the rising-edge zero crossing marking the zero-degree point. Diamonds represent total (fully integrated) intensity data points computed from the phase bins. The dashed curve is a periodic cubic spline fit to this data. Signals are normalized by their peak values.

Mode	Pressure (p')		Intensity (I')	
	Mag	Phase	Mag	Phase
1	1.0000	0.0	1.0000	167.7
2	0.0017	-115.9	0.6625	164.7
3	0.0027	-8.3	0.4103	-173.4
4	0.0008	-71.5	0.4657	-42.9
5	0.0010	37.9	0.0624	68.1
6	0.0008	-100.1	0.4634	-47.3
7	0.0005	160.8	0.1985	64.9
8	0.0003	-93.6	0.3307	-119.0
9	0.0006	150.1	0.3319	103.4
10	0.0005	153.6	0.2135	136.3
11	0.0004	91.5	0.1508	70.9

Table H-18: Harmonic content of the measured acoustic and intensity fields for the 240 Hz CH PLIF case. The measured intensity is total (fully integrated). Magnitudes are normalized by the first mode values. All phases are in reference to the phase of the first acoustic mode. Sign convention is such that negative phases are leading while positive phases are lagging.

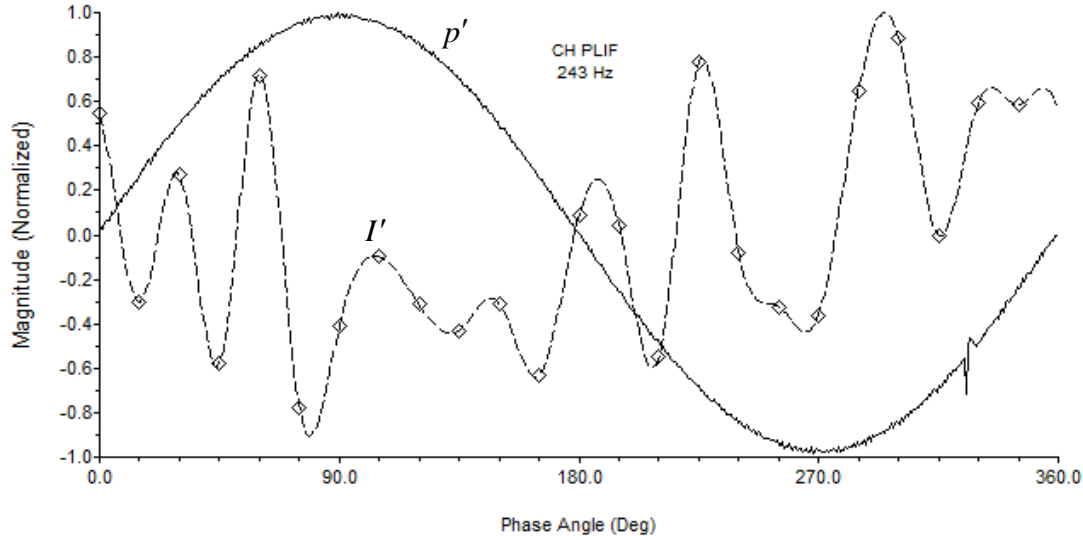


Figure H-22: Resulting waveforms from the 243 Hz CH PLIF experiment (Experiment 707). The solid curve shows the measured acoustic waveform with the rising-edge zero crossing marking the zero-degree point. Diamonds represent total (fully integrated) intensity data points computed from the phase bins. The dashed curve is a periodic cubic spline fit to this data. Signals are normalized by their peak values.

Mode	Pressure (p')		Intensity (I')	
	Mag	Phase	Mag	Phase
1	1.0000	0.0	1.0000	-135.6
2	0.0015	-109.6	0.2742	-125.9
3	0.0036	-65.5	0.3539	163.2
4	0.0007	-120.5	0.2544	53.2
5	0.0006	-12.7	0.2541	-104.8
6	0.0006	-119.4	0.7768	-133.6
7	0.0004	104.2	0.3040	124.6
8	0.0005	163.6	0.3831	17.0
9	0.0003	125.4	0.5721	119.7
10	0.0004	28.6	0.1039	-77.9
11	0.0004	86.6	0.5121	-131.5

Table H-19: Harmonic content of the measured acoustic and intensity fields for the 243 Hz CH PLIF case. The measured intensity is total (fully integrated). Magnitudes are normalized by the first mode values. All phases are in reference to the phase of the first acoustic mode. Sign convention is such that negative phases are leading while positive phases are lagging.

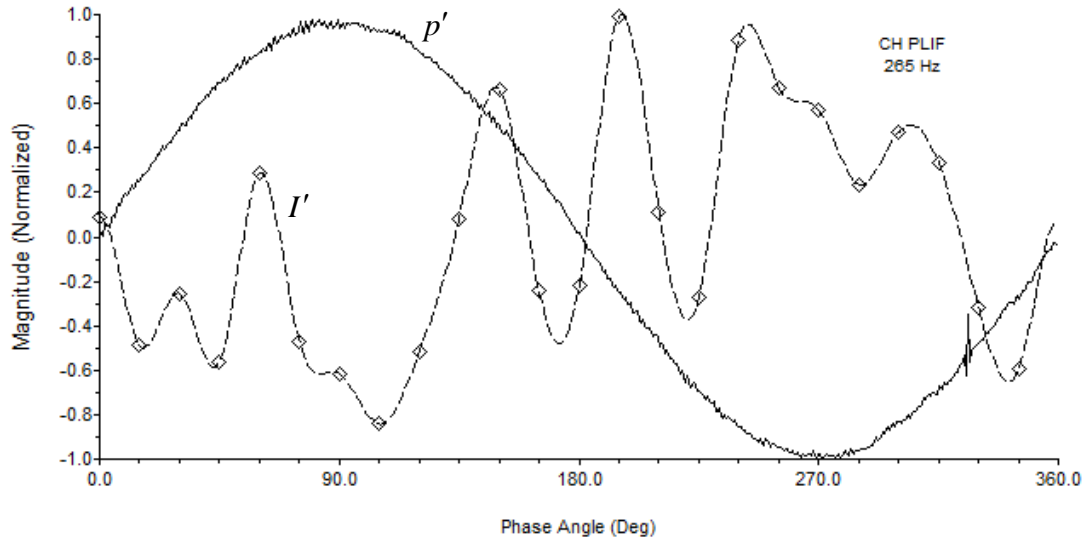


Figure H-23: Resulting waveforms from the 265 Hz CH PLIF experiment (Experiment 701). The solid curve shows the measured acoustic waveform with the rising-edge zero crossing marking the zero-degree point. Diamonds represent total (fully integrated) intensity data points computed from the phase bins. The dashed curve is a periodic cubic spline fit to this data. Signals are normalized by their peak values.

Mode	Pressure (p')		Intensity (I')	
	Mag	Phase	Mag	Phase
1	1.0000	0.0	1.0000	154.0
2	0.0105	-100.2	0.1184	47.4
3	0.0039	91.2	0.4503	30.7
4	0.0020	48.9	0.2280	142.0
5	0.0037	33.7	0.2455	-123.8
6	0.0015	24.0	0.6118	-13.7
7	0.0048	-42.0	0.4814	-129.2
8	0.0019	134.0	0.3530	24.6
9	0.0021	-27.9	0.2819	-141.0
10	0.0043	-8.6	0.1403	143.4
11	0.0046	12.6	0.1472	-116.3

Table H-20: Harmonic content of the measured acoustic and intensity fields for the 265 Hz CH PLIF case. The measured intensity is total (fully integrated). Magnitudes are normalized by the first mode values. All phases are in reference to the phase of the first acoustic mode. Sign convention is such that negative phases are leading while positive phases are lagging.

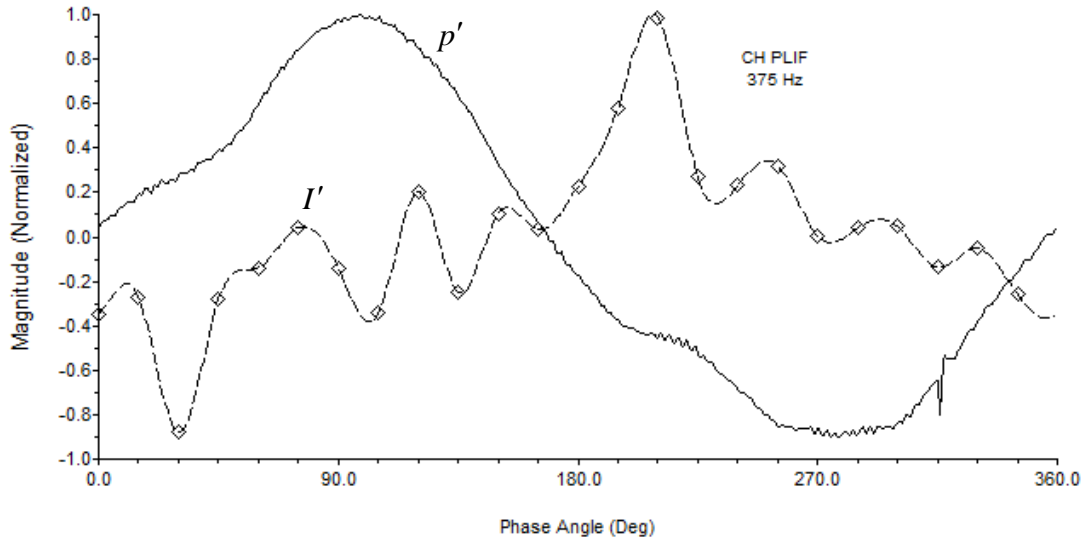


Figure H-24: Resulting waveforms from the 375 Hz CH PLIF experiment (Experiment 702). The solid curve shows the measured acoustic waveform with the rising-edge zero crossing marking the zero-degree point. Diamonds represent total (fully integrated) intensity data points computed from the phase bins. The dashed curve is a periodic cubic spline fit to this data. Signals are normalized by their peak values.

Mode	Pressure (p')		Intensity (I')	
	Mag	Phase	Mag	Phase
1	1.0000	0.0	1.0000	121.6
2	0.0747	123.7	0.1902	3.2
3	0.1465	-122.8	0.4409	162.7
4	0.0164	-99.1	0.0164	29.9
5	0.0226	-58.5	0.3143	-135.6
6	0.0094	123.6	0.1795	-13.3
7	0.0207	55.0	0.2040	-54.5
8	0.0041	-76.6	0.2057	107.3
9	0.0012	100.2	0.2418	-23.9
10	0.0063	-106.7	0.1788	5.4
11	0.0019	-47.9	0.1686	93.4

Table H-21: Harmonic content of the measured acoustic and intensity fields for the 375 Hz CH PLIF case. The measured intensity is total (fully integrated). Magnitudes are normalized by the first mode values. All phases are in reference to the phase of the first acoustic mode. Sign convention is such that negative phases are leading while positive phases are lagging.

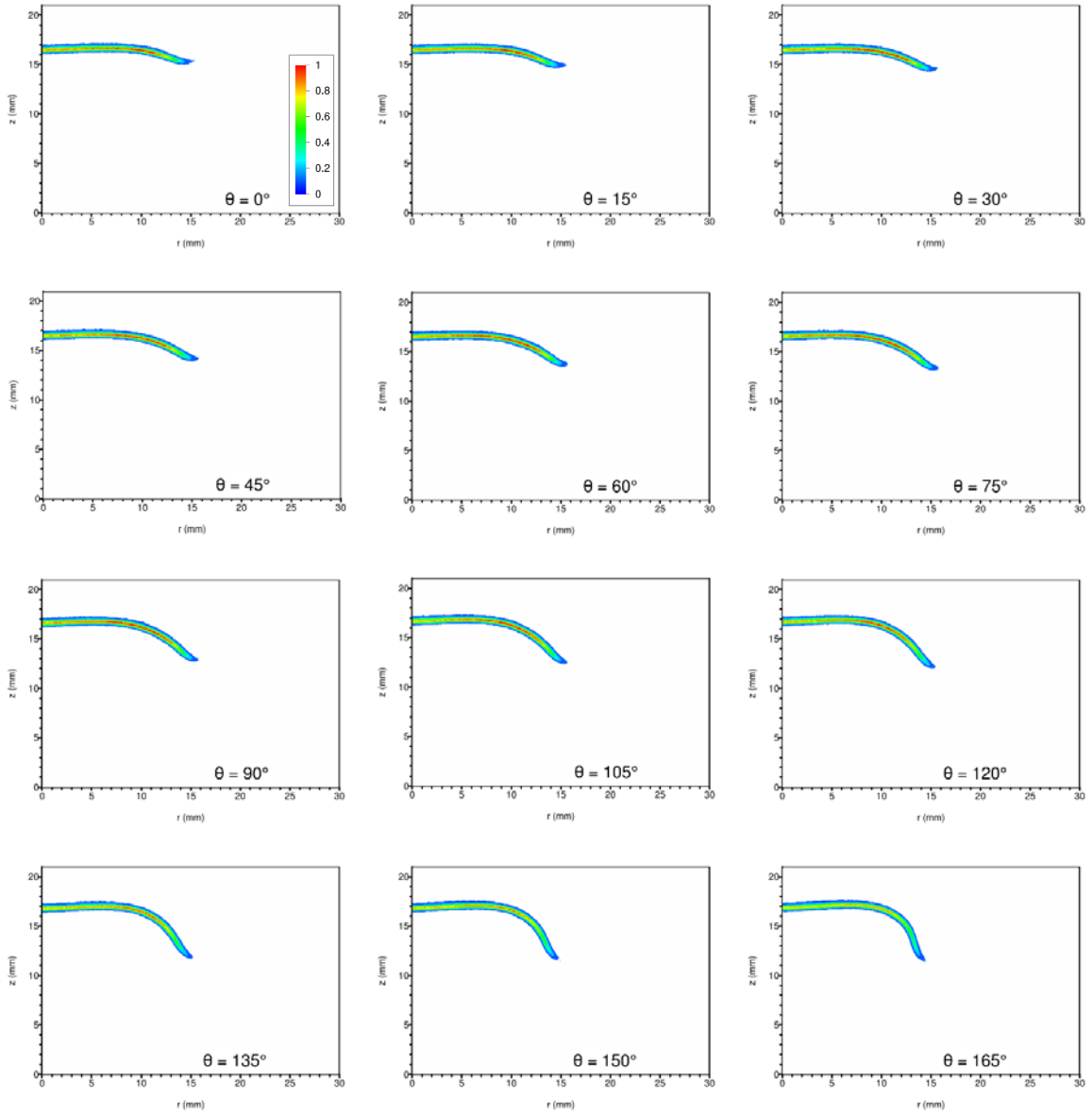


Figure H-25: Phase-resolved CH PLIF images for acoustic forcing at 55 Hz. The horizontal axis is the radius (mm) from the centerline of the burner. The vertical axis is the distance (mm) above the nozzle exit plane. (The stagnation plane is located at $z = 21\text{mm}$.) Phase angle $\theta = 0^\circ$ corresponds to the rising-edge zero crossing of the local unsteady pressure. Data from experiment 696. A total of 24 images on 15° spacing are shown. (See next page.) The magnitude scale is normalized by the peak value over all 24 images.

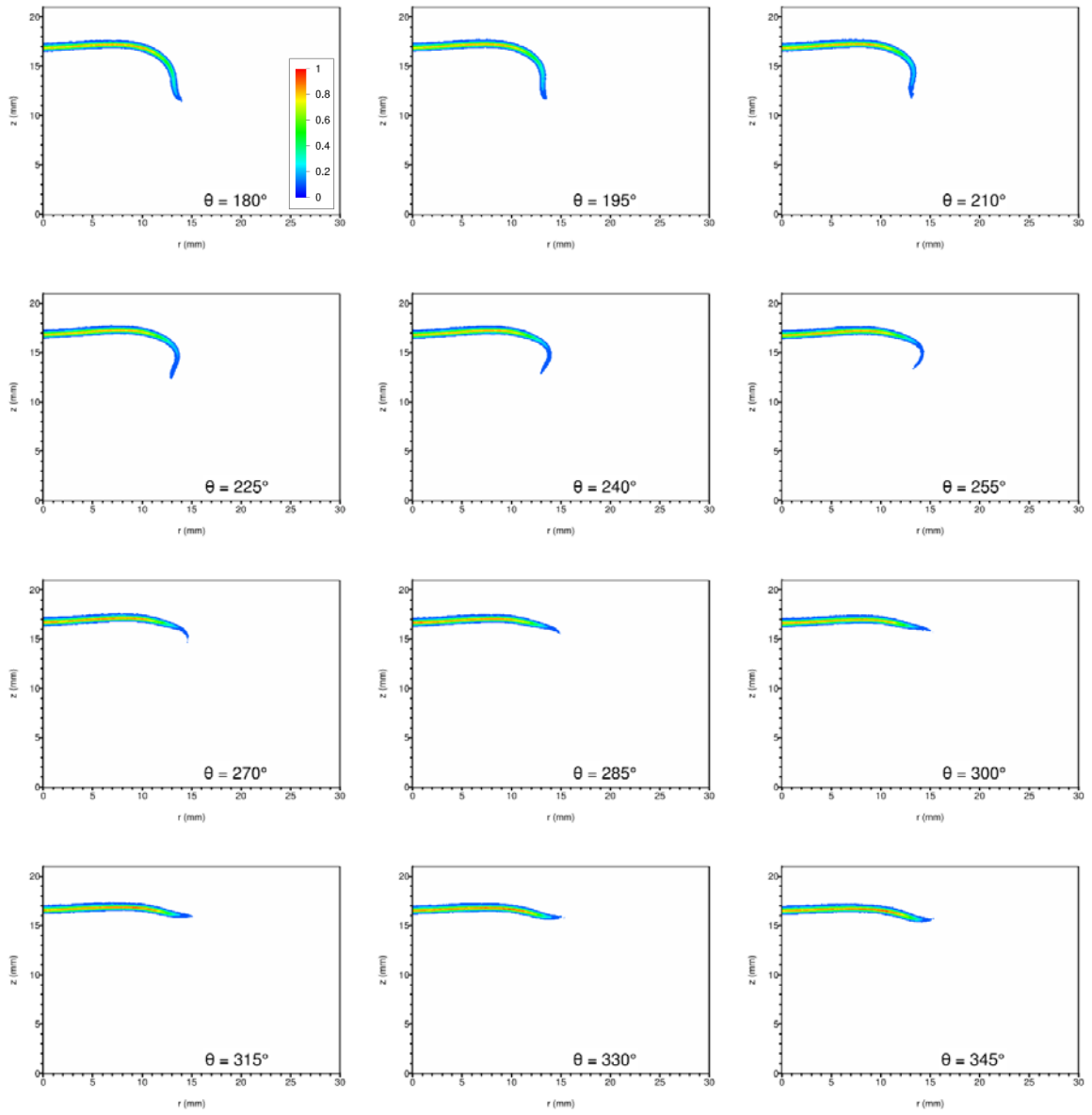


Figure H-25 (cont.): Phase-resolved CH PLIF images for acoustic forcing at 55 Hz. The horizontal axis is the radius (mm) from the centerline of the burner. The vertical axis is the distance (mm) above the nozzle exit plane. (The stagnation plane is located at $z = 21\text{mm}$.) Phase angle $\theta = 0^\circ$ corresponds to the rising-edge zero crossing of the local unsteady pressure. Data from experiment 696. A total of 24 images on 15° spacing are shown. (See previous page.) The magnitude scale is normalized by the peak value over all 24 images.

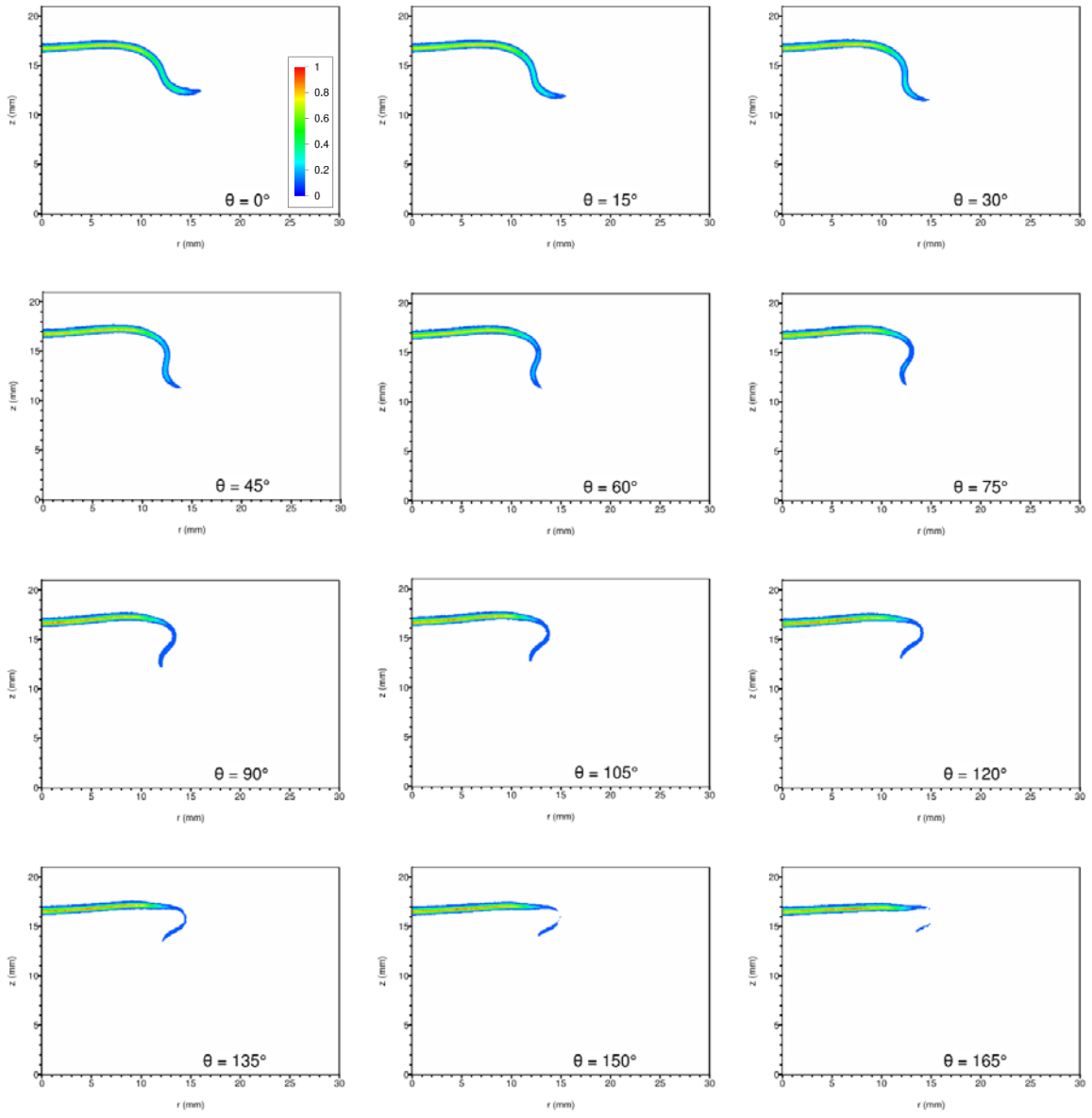


Figure H-26: Phase-resolved CH PLIF images for acoustic forcing at 75 Hz. The horizontal axis is the radius (mm) from the centerline of the burner. The vertical axis is the distance (mm) above the nozzle exit plane. (The stagnation plane is located at $z = 21\text{mm}$.) Phase angle $\theta = 0^\circ$ corresponds to the rising-edge zero crossing of the local unsteady pressure. Data from experiment 704. A total of 24 images on 15° spacing are shown. (See next page.) The magnitude scale is normalized by the peak value over all 24 images.

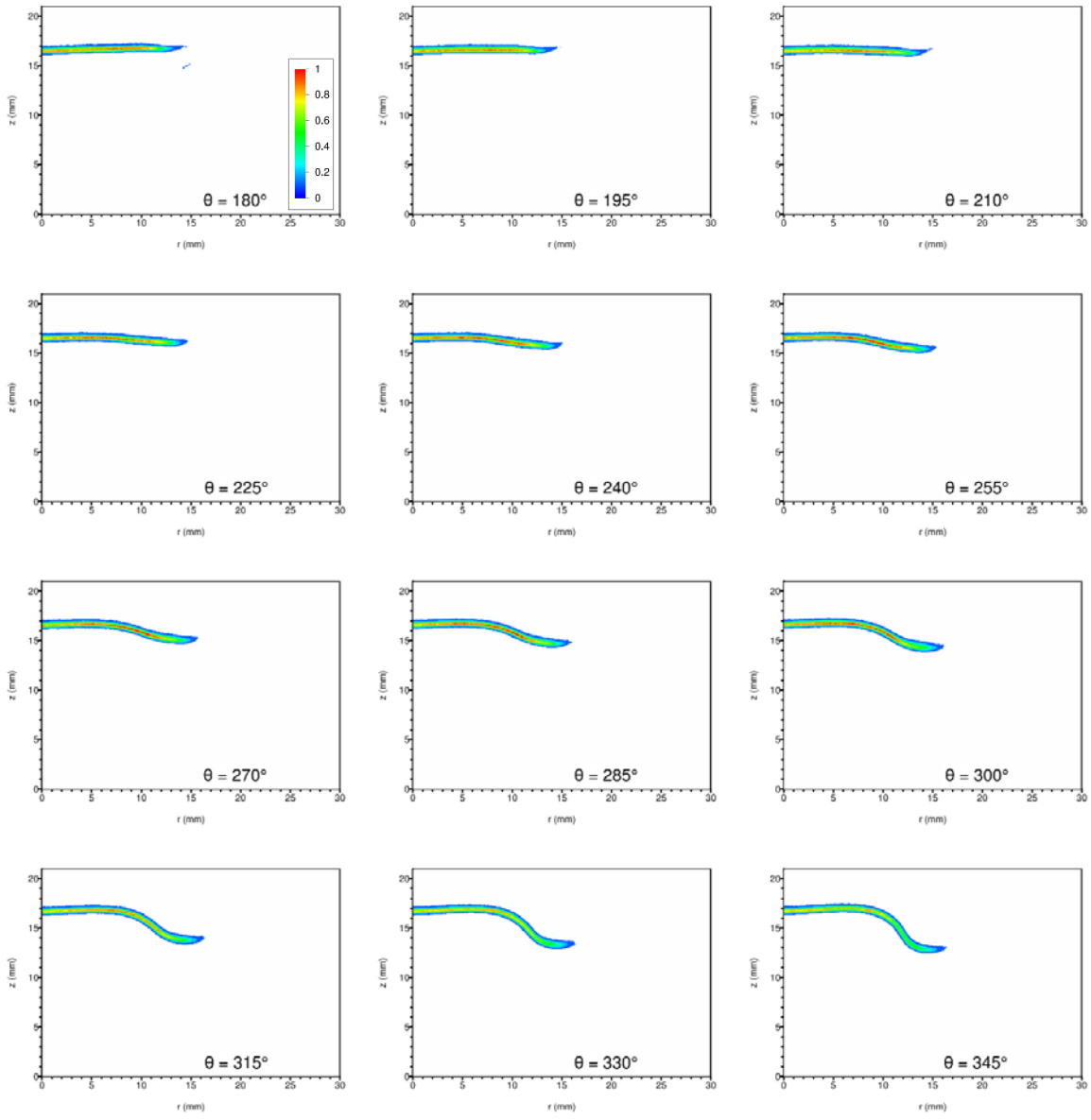


Figure H-26 (cont.): Phase-resolved CH PLIF images for acoustic forcing at 75 Hz. The horizontal axis is the radius (mm) from the centerline of the burner. The vertical axis is the distance (mm) above the nozzle exit plane. (The stagnation plane is located at $z = 21\text{mm}$.) Phase angle $\theta = 0^\circ$ corresponds to the rising-edge zero crossing of the local unsteady pressure. Data from experiment 704. A total of 24 images on 15° spacing are shown. (See previous page.) The magnitude scale is normalized by the peak value over all 24 images.

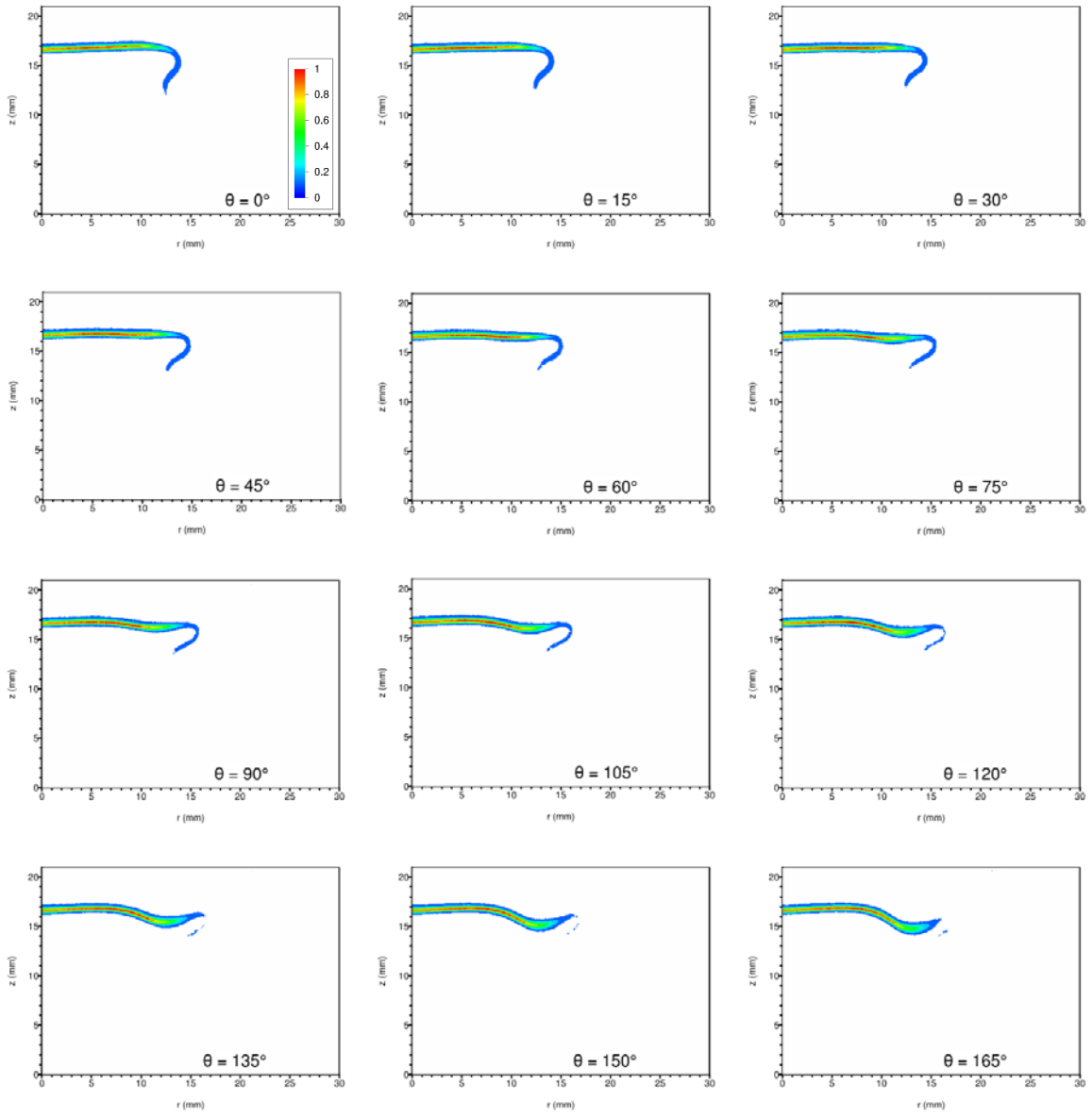


Figure H-27: Phase-resolved CH PLIF images for acoustic forcing at 100 Hz. The horizontal axis is the radius (mm) from the centerline of the burner. The vertical axis is the distance (mm) above the nozzle exit plane. (The stagnation plane is located at $z = 21\text{mm}$.) Phase angle $\theta = 0^\circ$ corresponds to the rising-edge zero crossing of the local unsteady pressure. Data from experiment 705. A total of 24 images on 15° spacing are shown. (See next page.) The magnitude scale is normalized by the peak value over all 24 images.

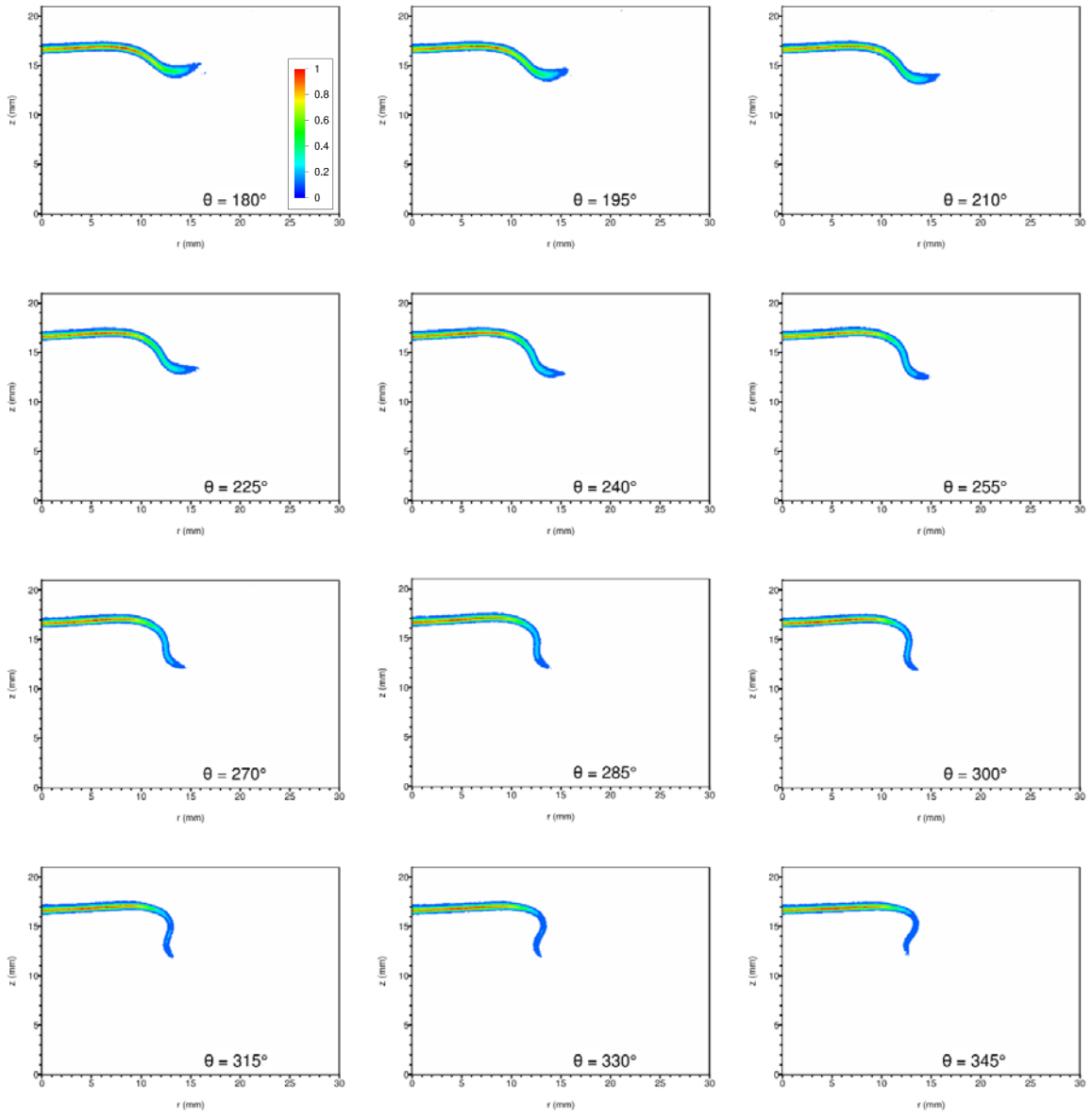


Figure H-27 (cont.): Phase-resolved CH PLIF images for acoustic forcing at 100 Hz. The horizontal axis is the radius (mm) from the centerline of the burner. The vertical axis is the distance (mm) above the nozzle exit plane. (The stagnation plane is located at $z = 21\text{mm}$.) Phase angle $\theta = 0^\circ$ corresponds to the rising-edge zero crossing of the local unsteady pressure. Data from experiment 705. A total of 24 images on 15° spacing are shown. (See previous page.) The magnitude scale is normalized by the peak value over all 24 images.

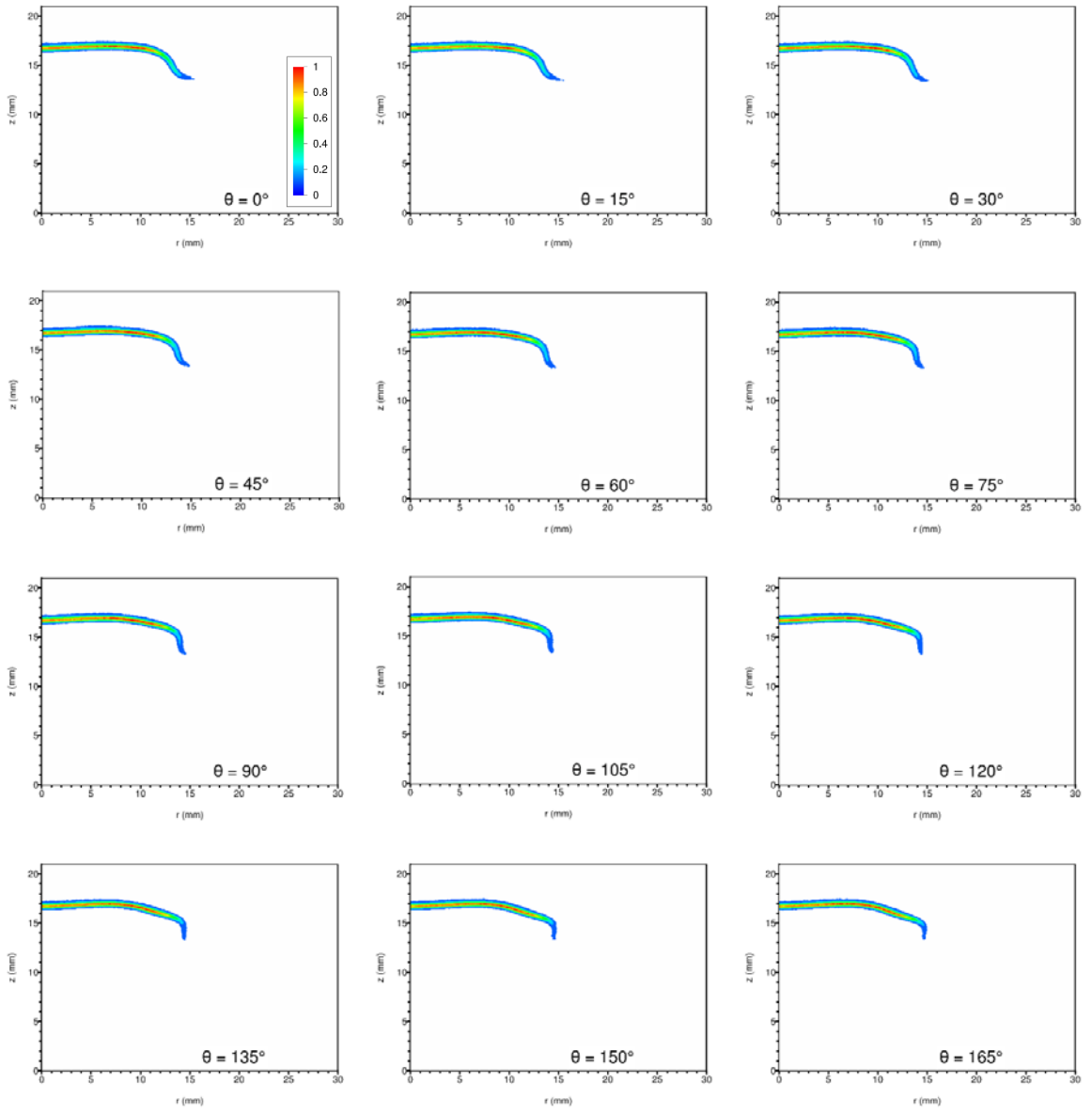


Figure H-28: Phase-resolved CH PLIF images for acoustic forcing at 150 Hz. The horizontal axis is the radius (mm) from the centerline of the burner. The vertical axis is the distance (mm) above the nozzle exit plane. (The stagnation plane is located at $z = 21\text{mm}$.) Phase angle $\theta = 0^\circ$ corresponds to the rising-edge zero crossing of the local unsteady pressure. Data from experiment 698. A total of 24 images on 15° spacing are shown. (See next page.) The magnitude scale is normalized by the peak value over all 24 images.

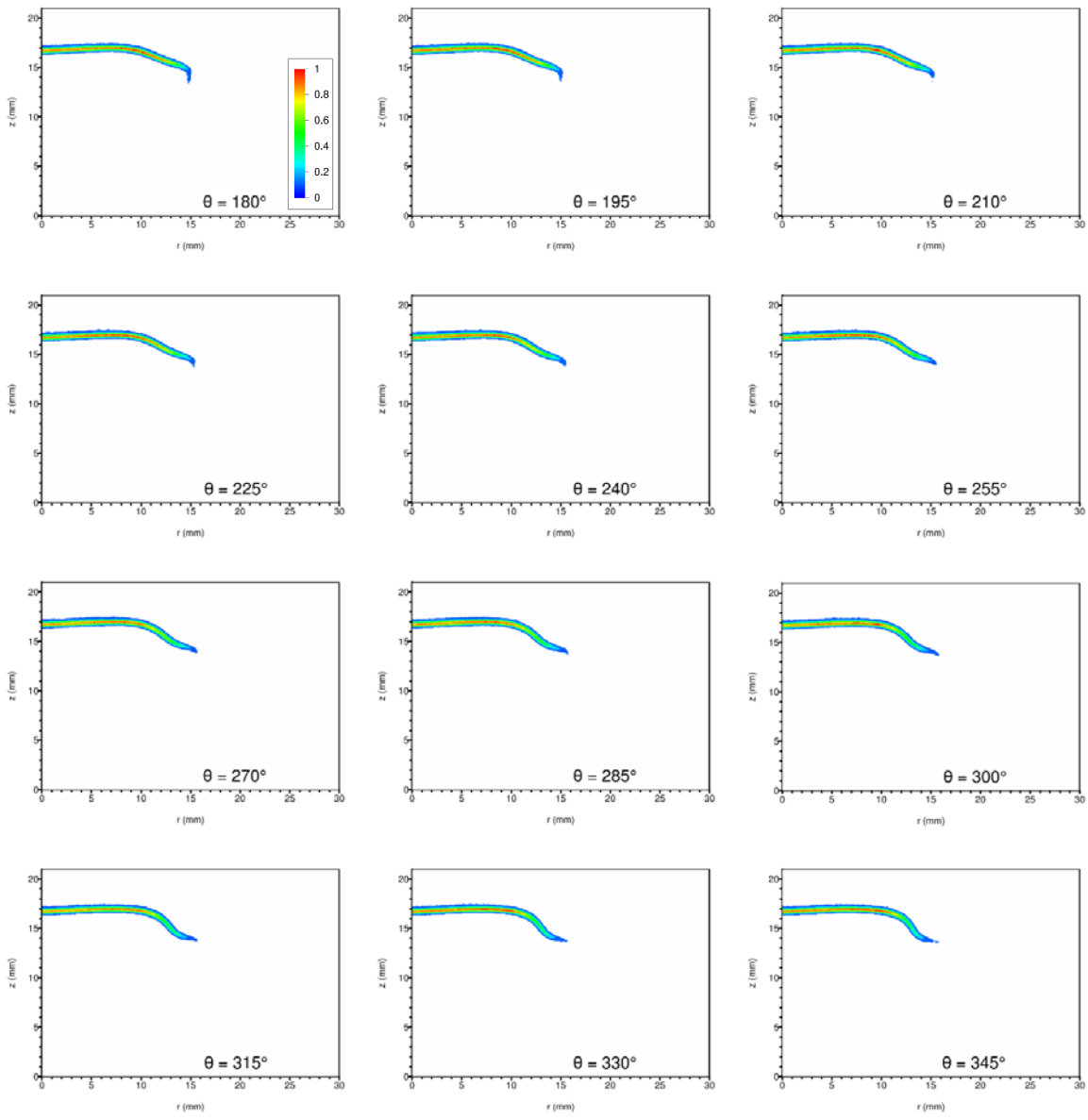


Figure H-28 (cont.): Phase-resolved CH PLIF images for acoustic forcing at 150 Hz. The horizontal axis is the radius (mm) from the centerline of the burner. The vertical axis is the distance (mm) above the nozzle exit plane. (The stagnation plane is located at $z = 21\text{mm}$.) Phase angle $\theta = 0^\circ$ corresponds to the rising-edge zero crossing of the local unsteady pressure. Data from experiment 698. A total of 24 images on 15° spacing are shown. (See previous page.) The magnitude scale is normalized by the peak value over all 24 images.

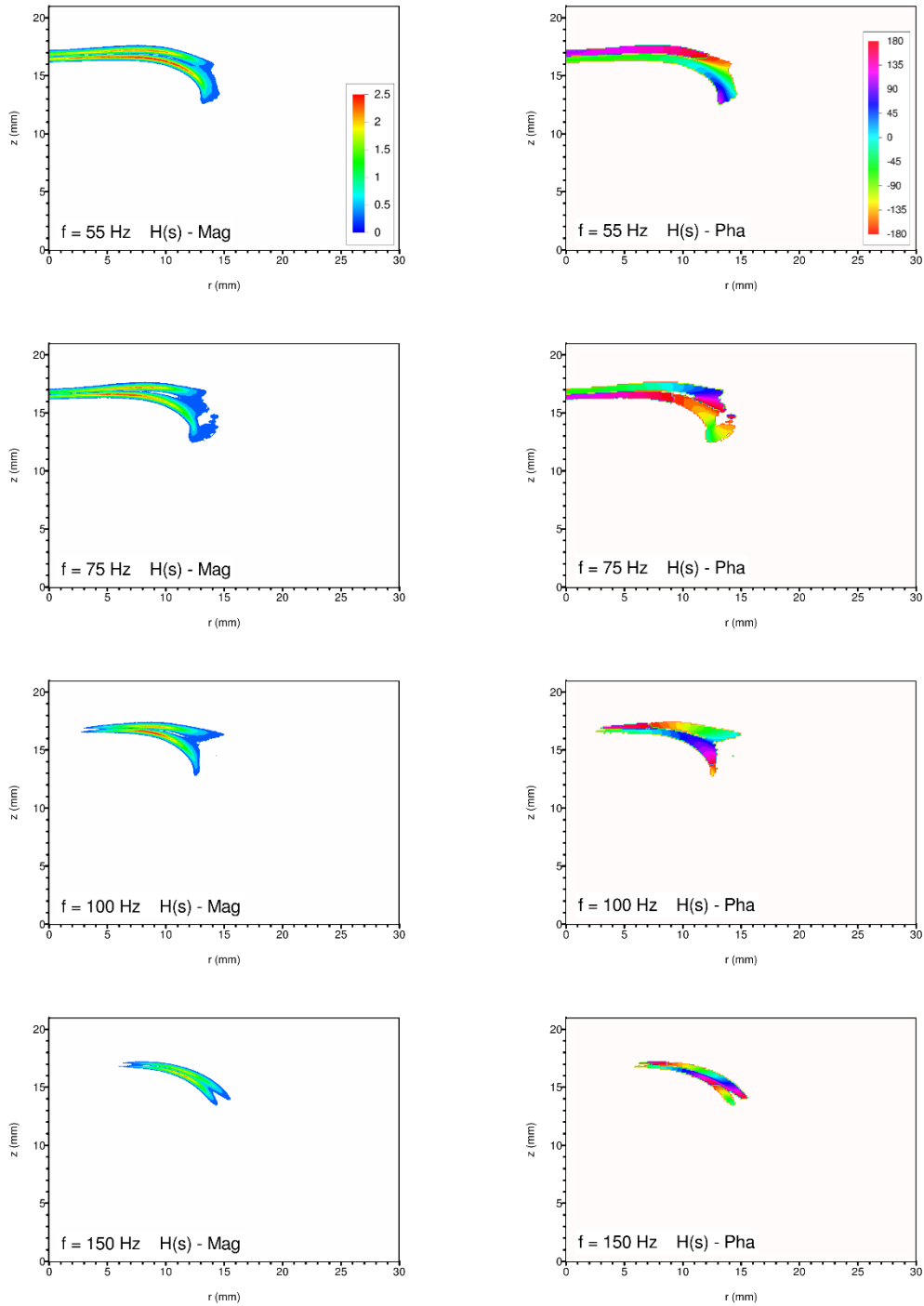


Figure H-29: Spatially resolved combustion response function produced from CH PLIF data. Magnitude plots appear in the left column while phase plots are shown on the right. Note that positive phase values correspond to I' lagging P' . The coordinate system origin is along the burner centerline at the nozzle exit plane. Data for all nine drive frequencies are shown. (See next two pages.)

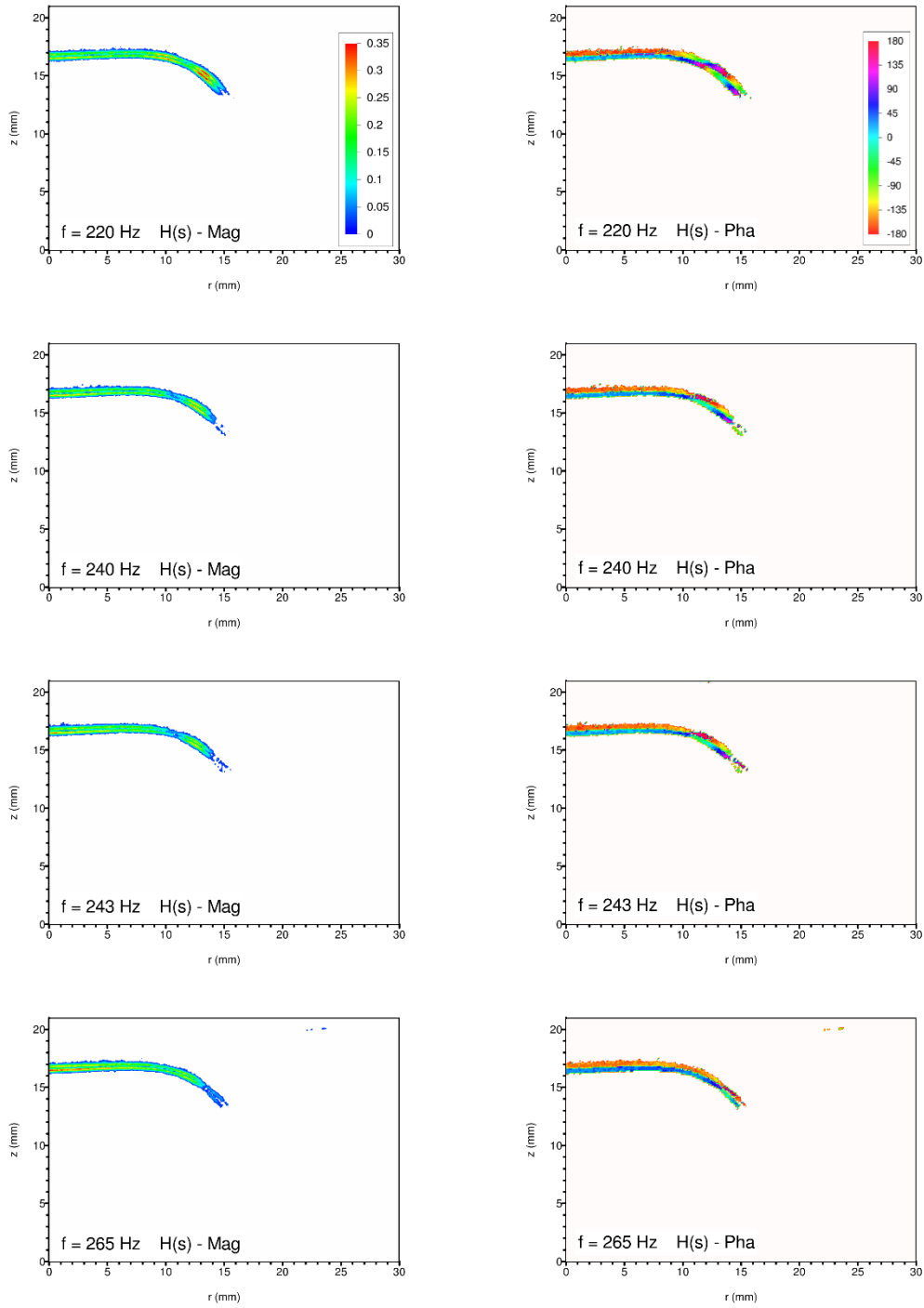


Figure H-29 (cont): Spatially resolved combustion response function produced from CH PLIF data. Magnitude plots appear in the left column while phase plots are shown on the right. Data for all nine drive frequencies are shown. (See previous and next page.) Note the change in magnitude scale versus the plots for 150 Hz and lower frequency.

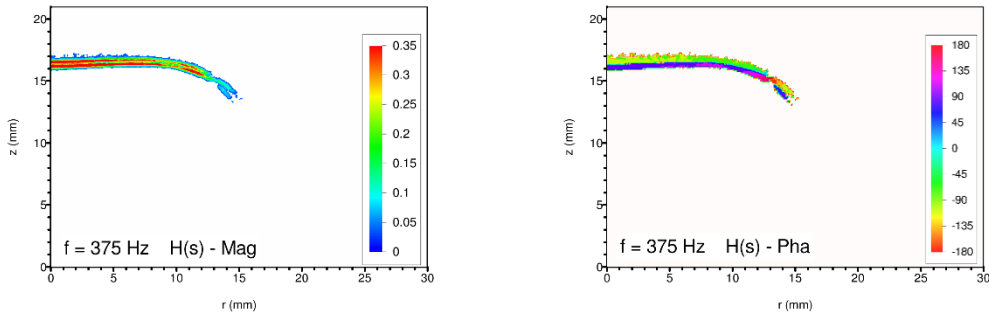


Figure H-29 (cont.): Spatially resolved combustion response function produced from CH PLIF data. Magnitude plots appear in the left column while phase plots are shown on the right. Data for all nine drive frequencies are shown. (See previous two pages.) Note the change in magnitude scale versus the plots for 150 Hz and lower frequency.

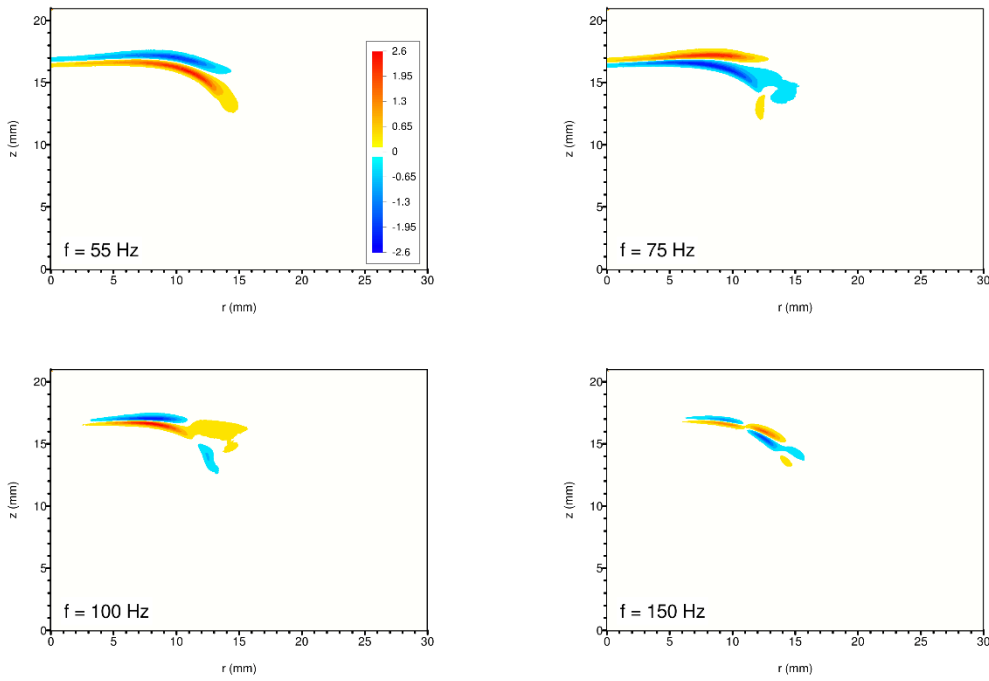


Figure H-30: Spatially resolved forced Rayleigh index produced from CH PLIF data. Data for all nine drive frequencies are shown. (See next page.) Note the difference between the magnitude legends for the lower four drive frequencies and the upper five drive frequencies.

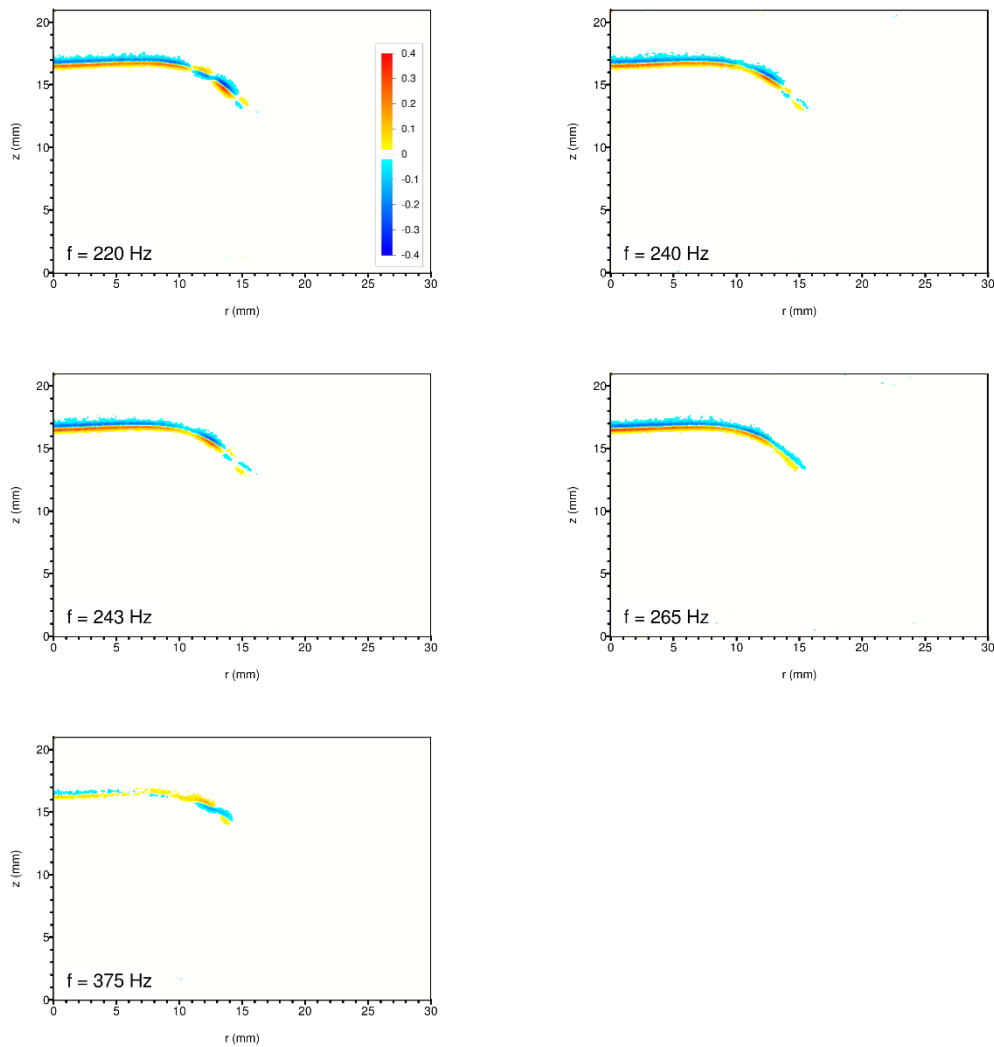


Figure H-30 (cont.): Spatially resolved forced Rayleigh index produced from CH PLIF data. Data for all nine drive frequencies are shown. (See previous page.) Note the difference between the magnitude legends for the lower four drive frequencies and the upper five drive frequencies.

H.2.3 CH₂O PLIF Experimental Data

The following 23 pages present the relevant collected CH₂O PLIF data. Images were collected using an Andor iStar ICCD camera coupled to a 50 mm, f/1.2, Nikon macro lens. Optical pumping of the CH₂O radicals of interest was performed at the Nd:YAG laser's third harmonic ($\lambda_{\text{air}} \approx 354.71 \text{ nm}$). Image data was collected and processed using the techniques described in chapter 4. For CH₂O data, only two of the three image correction methods were employed:

- i) Correction for the shot-to-shot variation in OPO output intensity.
- ii) Correction for the spatial variation in laser sheet intensity in the vertical direction.

Correction for laser sheet absorption was not necessary.

Further information regarding the processing of this data can be found in the beginning of this appendix as well as in chapter 4.

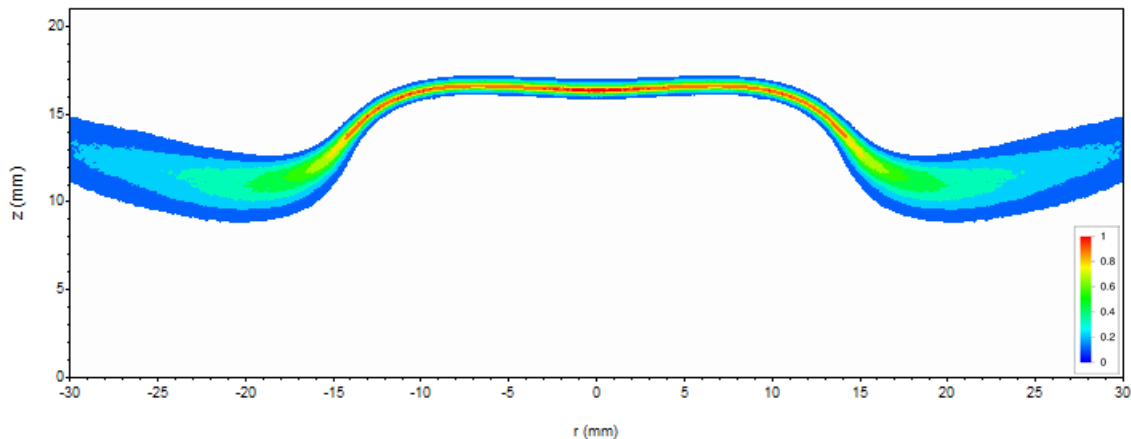


Figure H-31: CH₂O PLIF image of flame under steady conditions (no acoustic forcing). Collected data appears on the left, and is mirrored across the centerline for a visual representation of entire flame. Burner centerline is at $r = 0$. Position $z = 0$ corresponds to the nozzle exit plane.

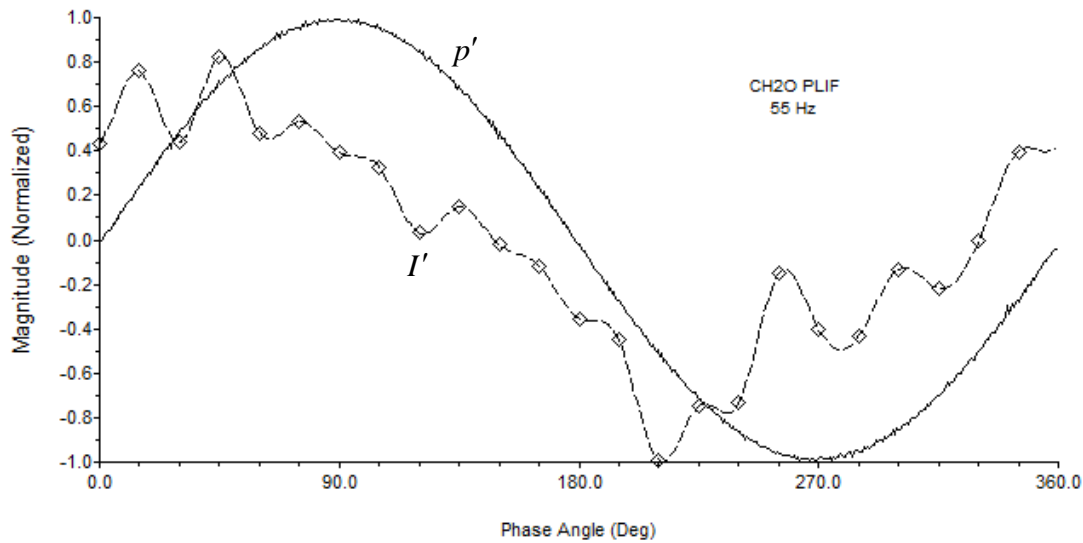


Figure H-32: Resulting waveforms from the 55 Hz CH₂O PLIF experiment (Experiment 709). The solid curve shows the measured acoustic waveform with the rising-edge zero crossing marking the zero-degree point. Diamonds represent total (fully integrated) intensity data points computed from the phase bins. The dashed curve is a periodic cubic spline fit to this data. Signals are normalized by their peak values.

Mode	Pressure (p')		Intensity (I')	
	Mag	Phase	Mag	Phase
1	1.0000	0.0	1.0000	-41.9
2	0.0104	88.7	0.0398	-126.6
3	0.0036	103.9	0.1945	-6.2
4	0.0015	82.6	0.1587	-127.2
5	0.0009	175.3	0.0557	92.6
6	0.0008	172.5	0.0631	-40.5
7	0.0004	-166.5	0.1064	-139.1
8	0.0001	-154.8	0.0167	-123.3
9	0.0001	-92.0	0.0832	72.4
10	0.0002	8.7	0.1073	17.3
11	0.0004	31.5	0.0224	-14.2

Table H-22: Harmonic content of the measured acoustic and intensity fields for the 55 Hz CH₂O PLIF case. The measured intensity is total (fully integrated). Magnitudes are normalized by the first mode values. All phases are in reference to the phase of the first acoustic mode. Sign convention is such that negative phases are leading while positive phases are lagging.

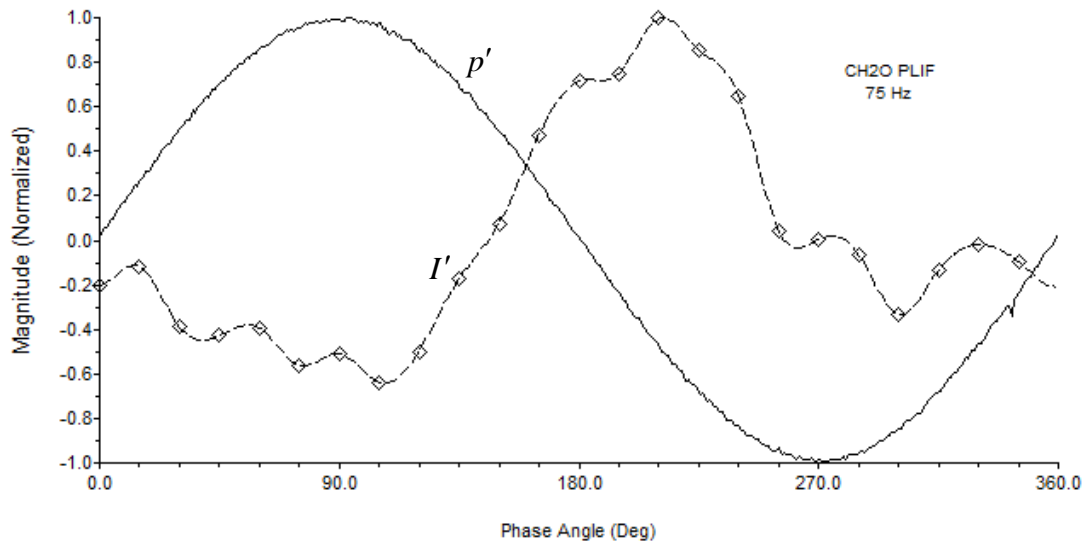


Figure H-33: Resulting waveforms from the 75 Hz CH₂O PLIF experiment (Experiment 708). The solid curve shows the measured acoustic waveform with the rising-edge zero crossing marking the zero-degree point. Diamonds represent total (fully integrated) intensity data points computed from the phase bins. The dashed curve is a periodic cubic spline fit to this data. Signals are normalized by their peak values.

Mode	Pressure (p')		Intensity (I')	
	Mag	Phase	Mag	Phase
1	1.0000	0.0	1.0000	131.6
2	0.0055	-77.4	0.6517	-56.4
3	0.0089	-160.2	0.1668	171.6
4	0.0011	110.7	0.0722	146.7
5	0.0011	88.9	0.0698	-60.6
6	0.0013	-82.8	0.0558	142.6
7	0.0006	-29.2	0.1059	50.5
8	0.0010	-34.3	0.0788	-19.4
9	0.0007	-130.9	0.0634	-8.6
10	0.0015	-51.0	0.0649	147.4
11	0.0013	-93.1	0.0362	81.9

Table H-23: Harmonic content of the measured acoustic and intensity fields for the 75 Hz CH₂O PLIF case. The measured intensity is total (fully integrated). Magnitudes are normalized by the first mode values. All phases are in reference to the phase of the first acoustic mode. Sign convention is such that negative phases are leading while positive phases are lagging.

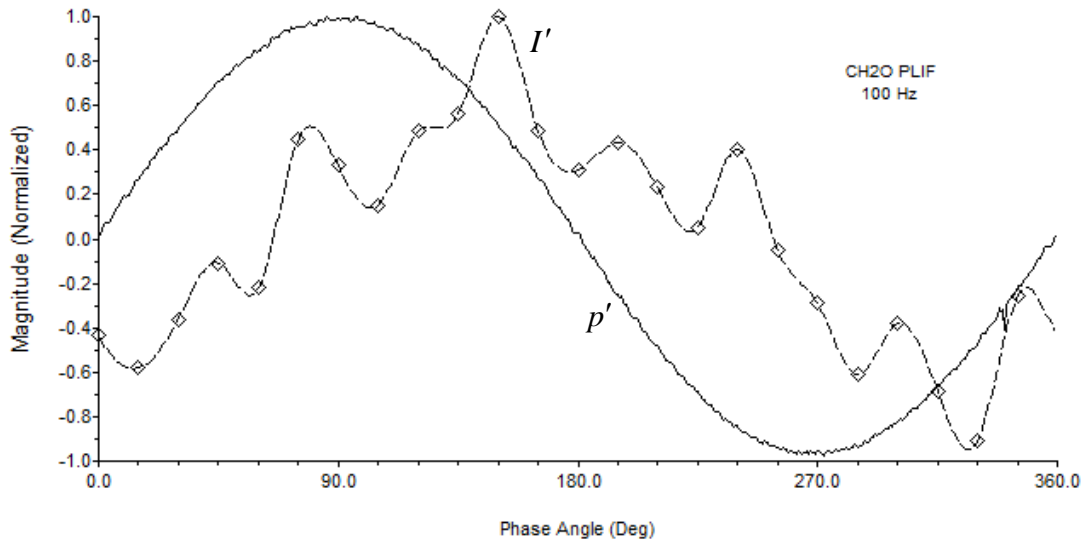


Figure H-34: Resulting waveforms from the 100 Hz CH₂O PLIF experiment (Experiment 711). The solid curve shows the measured acoustic waveform with the rising-edge zero crossing marking the zero-degree point. Diamonds represent total (fully integrated) intensity data points computed from the phase bins. The dashed curve is a periodic cubic spline fit to this data. Signals are normalized by their peak values.

Mode	Pressure (p')		Intensity (I')	
	Mag	Phase	Mag	Phase
1	1.0000	0.0	1.0000	62.1
2	0.0117	-166.5	0.0372	48.6
3	0.0031	15.3	0.1076	-60.8
4	0.0011	-84.4	0.1828	179.2
5	0.0010	-16.8	0.1401	-68.4
6	0.0005	153.9	0.0596	-20.8
7	0.0007	-31.8	0.2409	-167.2
8	0.0017	-119.9	0.1161	153.7
9	0.0006	122.5	0.1555	-141.2
10	0.0004	-169.3	0.0669	46.5
11	0.0003	-90.5	0.0895	64.5

Table H-24: Harmonic content of the measured acoustic and intensity fields for the 100 Hz CH₂O PLIF case. The measured intensity is total (fully integrated). Magnitudes are normalized by the first mode values. All phases are in reference to the phase of the first acoustic mode. Sign convention is such that negative phases are leading while positive phases are lagging.

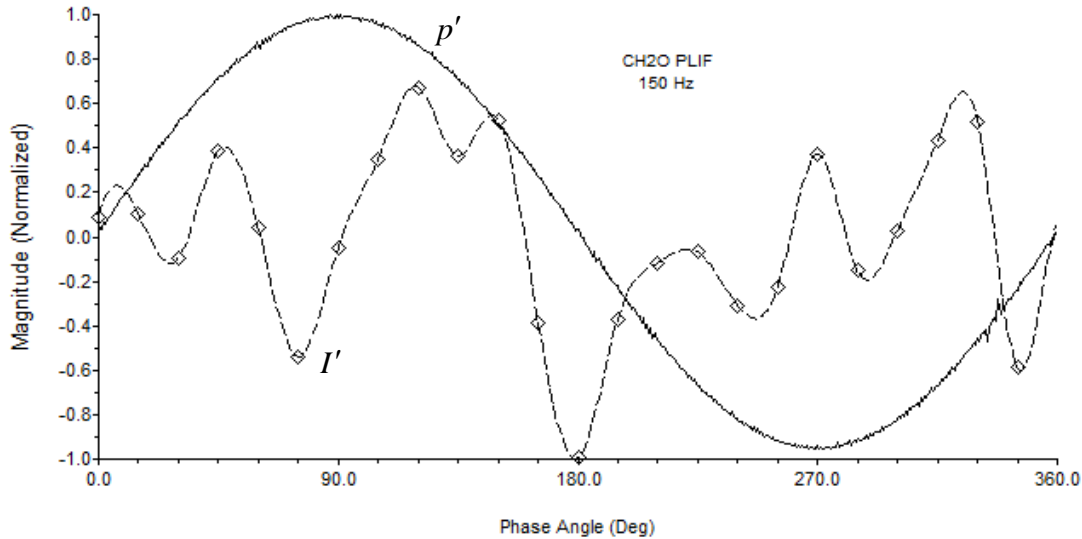


Figure H-35: Resulting waveforms from the 150 Hz CH₂O PLIF experiment (Experiment 712). The solid curve shows the measured acoustic waveform with the rising-edge zero crossing marking the zero-degree point. Diamonds represent total (fully integrated) intensity data points computed from the phase bins. The dashed curve is a periodic cubic spline fit to this data. Signals are normalized by their peak values.

Mode	Pressure (p')		Intensity (I')	
	Mag	Phase	Mag	Phase
1	1.0000	0.0	1.0000	-51.6
2	0.0010	-40.3	1.7232	147.6
3	0.0021	-16.8	1.1859	-59.1
4	0.0004	9.7	1.9710	69.6
5	0.0001	31.6	0.4814	168.8
6	0.0003	28.9	0.9301	82.1
7	0.0004	89.3	1.4644	-50.0
8	0.0003	62.0	1.0028	-25.3
9	0.0002	91.2	0.5007	-80.2
10	0.0001	131.0	0.6276	18.6
11	0.0004	57.0	0.2082	-71.6

Table H-25: Harmonic content of the measured acoustic and intensity fields for the 150 Hz CH₂O PLIF case. The measured intensity is total (fully integrated). Magnitudes are normalized by the first mode values. All phases are in reference to the phase of the first acoustic mode. Sign convention is such that negative phases are leading while positive phases are lagging.

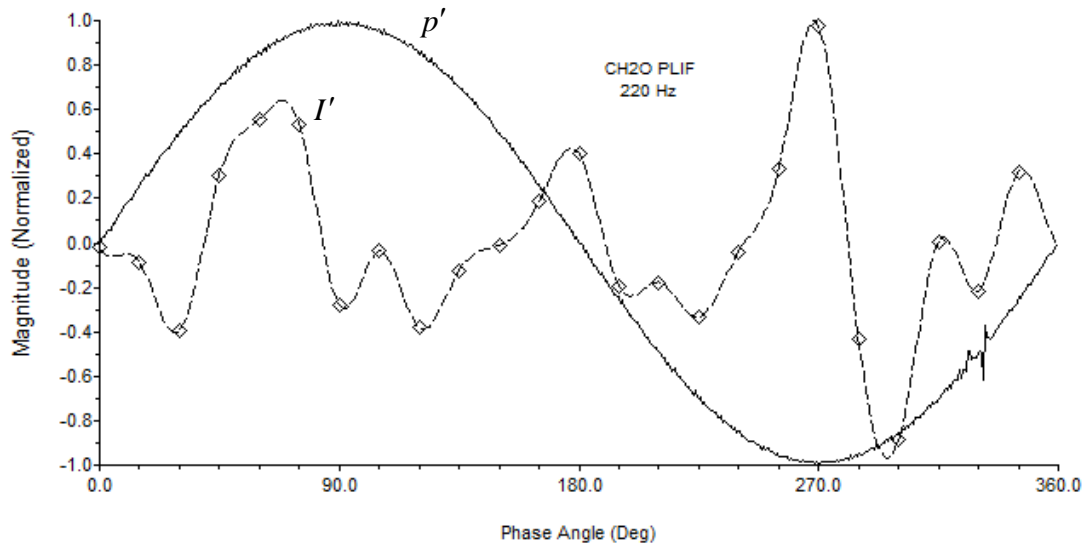


Figure H-36: Resulting waveforms from the 220 Hz CH₂O PLIF experiment (Experiment 713). The solid curve shows the measured acoustic waveform with the rising-edge zero crossing marking the zero-degree point. Diamonds represent total (fully integrated) intensity data points computed from the phase bins. The dashed curve is a periodic cubic spline fit to this data. Signals are normalized by their peak values.

Mode	Pressure (p')		Intensity (I')	
	Mag	Phase	Mag	Phase
1	1.0000	0.0	1.0000	1.5
2	0.0014	-103.9	2.7523	16.9
3	0.0006	-1.8	2.2680	32.6
4	0.0006	109.4	7.1079	-147.8
5	0.0004	87.2	4.1575	164.4
6	0.0003	48.5	0.8643	30.5
7	0.0003	62.5	3.3177	-18.4
8	0.0004	0.4	2.1327	-89.4
9	0.0002	-52.9	1.9436	168.1
10	0.0004	-127.3	1.1632	167.5
11	0.0003	-143.9	2.0598	49.9

Table H-26: Harmonic content of the measured acoustic and intensity fields for the 220 Hz CH₂O PLIF case. The measured intensity is total (fully integrated). Magnitudes are normalized by the first mode values. All phases are in reference to the phase of the first acoustic mode. Sign convention is such that negative phases are leading while positive phases are lagging.

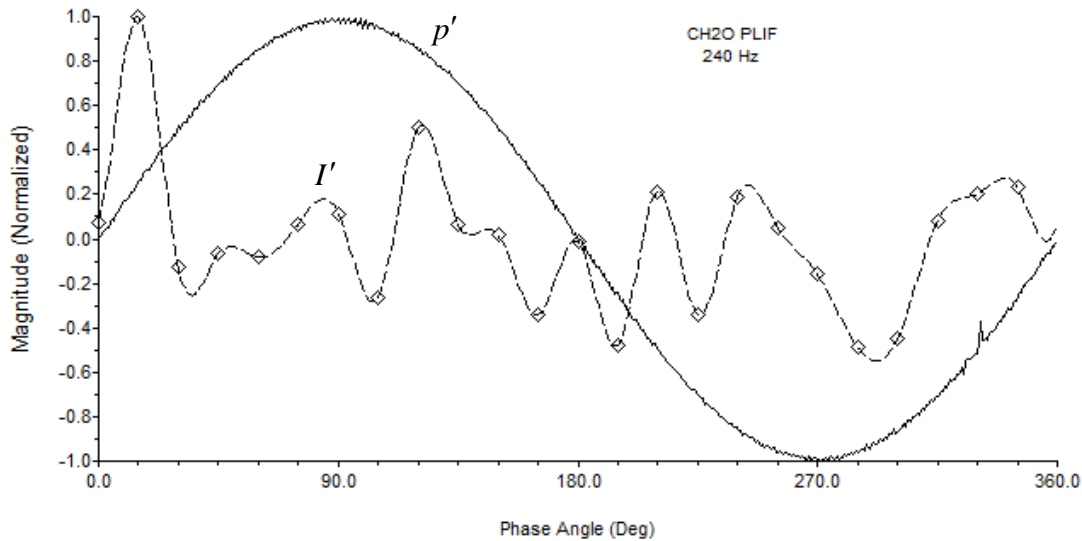


Figure H-37: Resulting waveforms from the 240 Hz CH₂O PLIF experiment (Experiment 716). The solid curve shows the measured acoustic waveform with the rising-edge zero crossing marking the zero-degree point. Diamonds represent total (fully integrated) intensity data points computed from the phase bins. The dashed curve is a periodic cubic spline fit to this data. Signals are normalized by their peak values.

Mode	Pressure (p')		Intensity (I')	
	Mag	Phase	Mag	Phase
1	1.0000	0.0	1.0000	-49.8
2	0.0020	-135.4	0.5663	-83.6
3	0.0025	-1.9	1.4048	-93.1
4	0.0011	174.3	0.1952	170.3
5	0.0007	12.7	0.1640	56.1
6	0.0003	84.8	1.0563	1.3
7	0.0008	86.4	0.7125	21.0
8	0.0006	25.6	0.1809	95.9
9	0.0004	25.8	0.6623	3.1
10	0.0009	-21.1	0.3130	70.2
11	0.0006	-68.1	0.9447	88.9

Table H-27: Harmonic content of the measured acoustic and intensity fields for the 240 Hz CH₂O PLIF case. The measured intensity is total (fully integrated). Magnitudes are normalized by the first mode values. All phases are in reference to the phase of the first acoustic mode. Sign convention is such that negative phases are leading while positive phases are lagging.

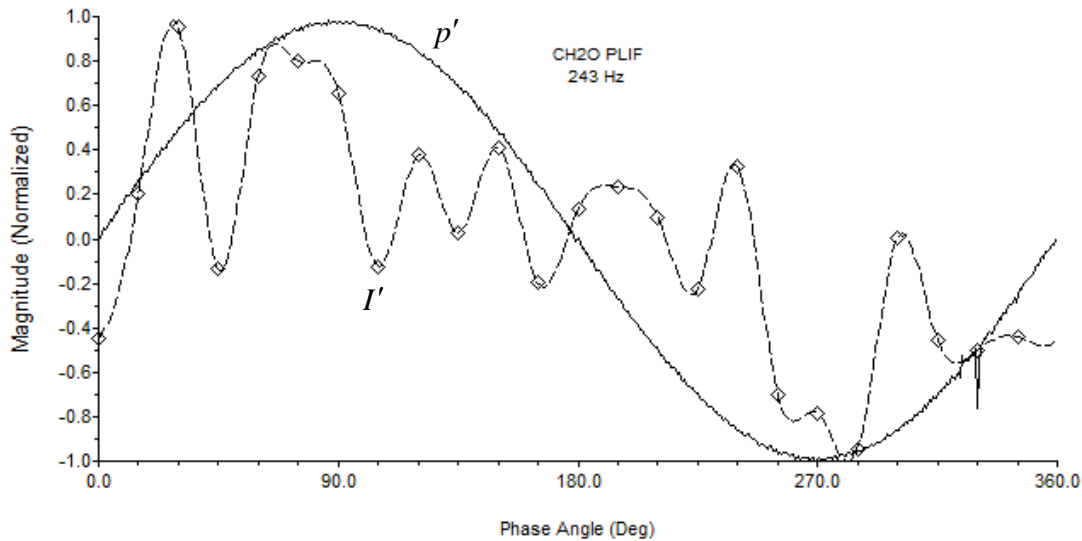


Figure H-38: Resulting waveforms from the 243 Hz CH₂O PLIF experiment (Experiment 717). The solid curve shows the measured acoustic waveform with the rising-edge zero crossing marking the zero-degree point. Diamonds represent total (fully integrated) intensity data points computed from the phase bins. The dashed curve is a periodic cubic spline fit to this data. Signals are normalized by their peak values.

Mode	Pressure (p')		Intensity (I')	
	Mag	Phase	Mag	Phase
1	1.0000	0.0	1.0000	9.8
2	0.0022	-61.6	0.4800	-4.9
3	0.0039	-49.6	0.2179	127.1
4	0.0012	-48.7	0.2550	77.4
5	0.0028	-62.1	0.3573	-9.4
6	0.0016	-99.2	0.3749	-7.3
7	0.0010	-111.9	0.3122	132.1
8	0.0015	-140.6	0.3084	104.8
9	0.0014	174.7	0.2174	171.4
10	0.0014	176.4	0.1572	109.9
11	0.0015	122.5	0.0440	141.2

Table H-28: Harmonic content of the measured acoustic and intensity fields for the 243 Hz CH₂O PLIF case. The measured intensity is total (fully integrated). Magnitudes are normalized by the first mode values. All phases are in reference to the phase of the first acoustic mode. Sign convention is such that negative phases are leading while positive phases are lagging.

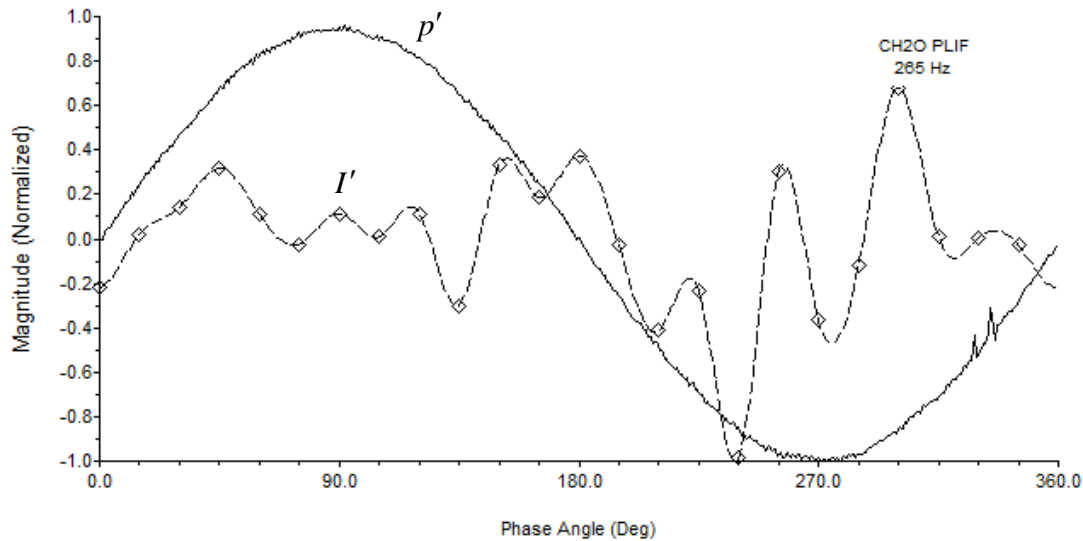


Figure H-39: Resulting waveforms from the 265 Hz CH₂O PLIF experiment (Experiment 714). The solid curve shows the measured acoustic waveform with the rising-edge zero crossing marking the zero-degree point. Diamonds represent total (fully integrated) intensity data points computed from the phase bins. The dashed curve is a periodic cubic spline fit to this data. Signals are normalized by their peak values.

Mode	Pressure (p')		Intensity (I')	
	Mag	Phase	Mag	Phase
1	1.0000	0.0	1.0000	-28.0
2	0.0088	-63.5	0.9601	-162.6
3	0.0039	101.4	1.7279	71.4
4	0.0005	158.2	0.3177	-32.8
5	0.0021	-3.2	0.7106	65.0
6	0.0013	-104.6	0.1823	-120.5
7	0.0041	-3.0	0.7214	-110.7
8	0.0004	-169.0	0.8463	161.8
9	0.0018	36.9	0.9954	87.0
10	0.0045	44.9	1.2057	-11.2
11	0.0013	5.6	0.5347	-175.6

Table H-29: Harmonic content of the measured acoustic and intensity fields for the 265 Hz CH₂O PLIF case. The measured intensity is total (fully integrated). Magnitudes are normalized by the first mode values. All phases are in reference to the phase of the first acoustic mode. Sign convention is such that negative phases are leading while positive phases are lagging.

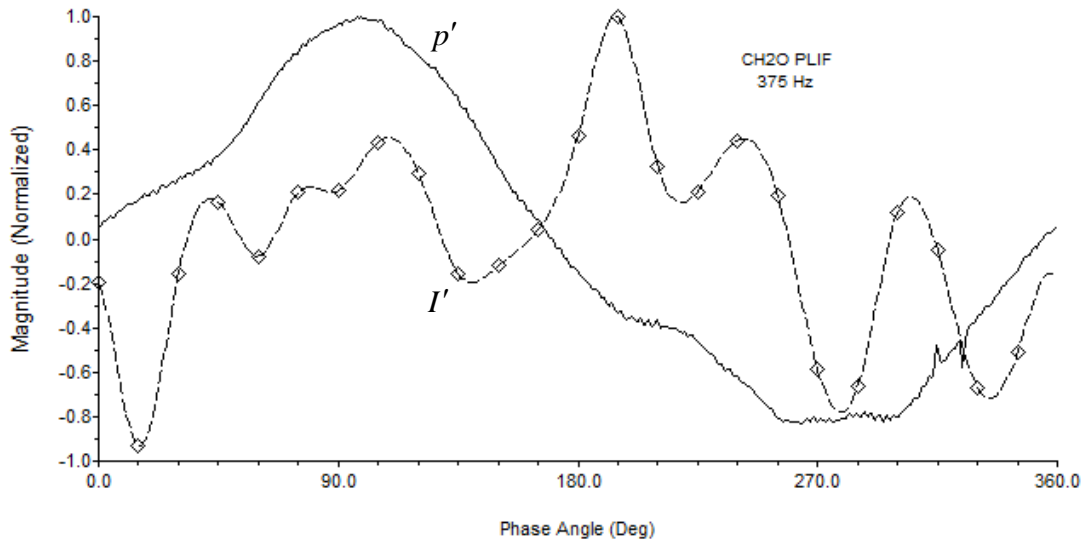


Figure H-40: Resulting waveforms from the 375 Hz CH₂O PLIF experiment (Experiment 715). The solid curve shows the measured acoustic waveform with the rising-edge zero crossing marking the zero-degree point. Diamonds represent total (fully integrated) intensity data points computed from the phase bins. The dashed curve is a periodic cubic spline fit to this data. Signals are normalized by their peak values.

Mode	Pressure (p')		Intensity (I')	
	Mag	Phase	Mag	Phase
1	1.0000	0.0	1.0000	75.8
2	0.0813	117.3	0.4351	16.2
3	0.1481	-128.0	0.5958	159.5
4	0.0181	-85.5	0.1957	30.7
5	0.0283	-66.3	0.3964	84.0
6	0.0088	143.5	0.4478	-74.1
7	0.0196	51.8	0.5441	-141.8
8	0.0069	-57.6	0.1926	-173.5
9	0.0027	-147.1	0.2912	-136.5
10	0.0132	-151.8	0.0986	-48.9
11	0.0012	109.2	0.1028	-84.4

Table H-30: Harmonic content of the measured acoustic and intensity fields for the 375 Hz CH₂O PLIF case. The measured intensity is total (fully integrated). Magnitudes are normalized by the first mode values. All phases are in reference to the phase of the first acoustic mode. Sign convention is such that negative phases are leading while positive phases are lagging.

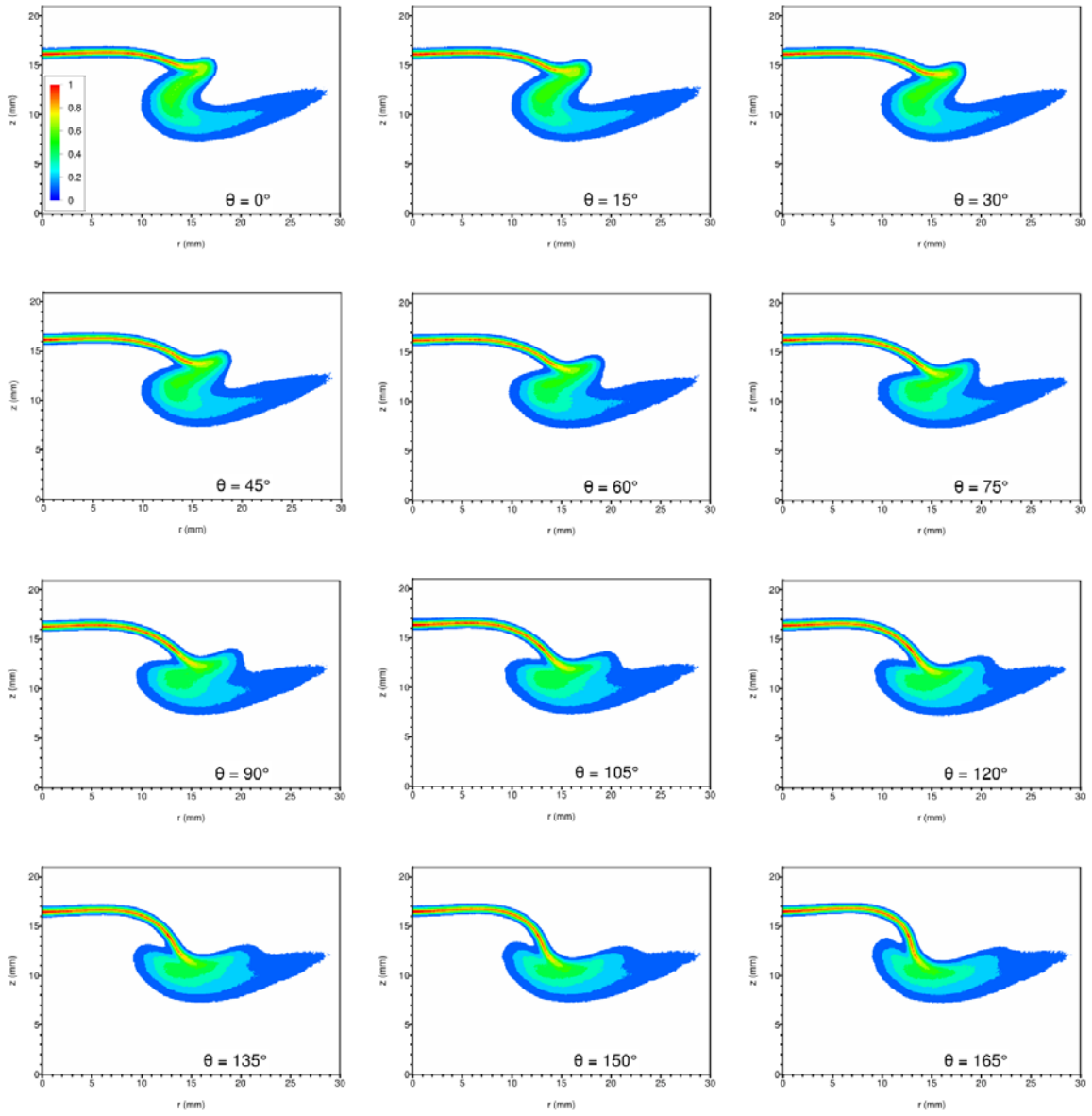


Figure H-41: Phase-resolved CH_2O PLIF images for acoustic forcing at 55 Hz. The horizontal axis is the radius (mm) from the centerline of the burner. The vertical axis is the distance (mm) above the nozzle exit plane. (The stagnation plane is located at $z = 21\text{mm}$.) Phase angle $\theta = 0^\circ$ corresponds to the rising-edge zero crossing of the local unsteady pressure. Data from experiment 709. A total of 24 images on 15° spacing are shown. (See next page.) The magnitude scale is normalized by the peak value over all 24 images.

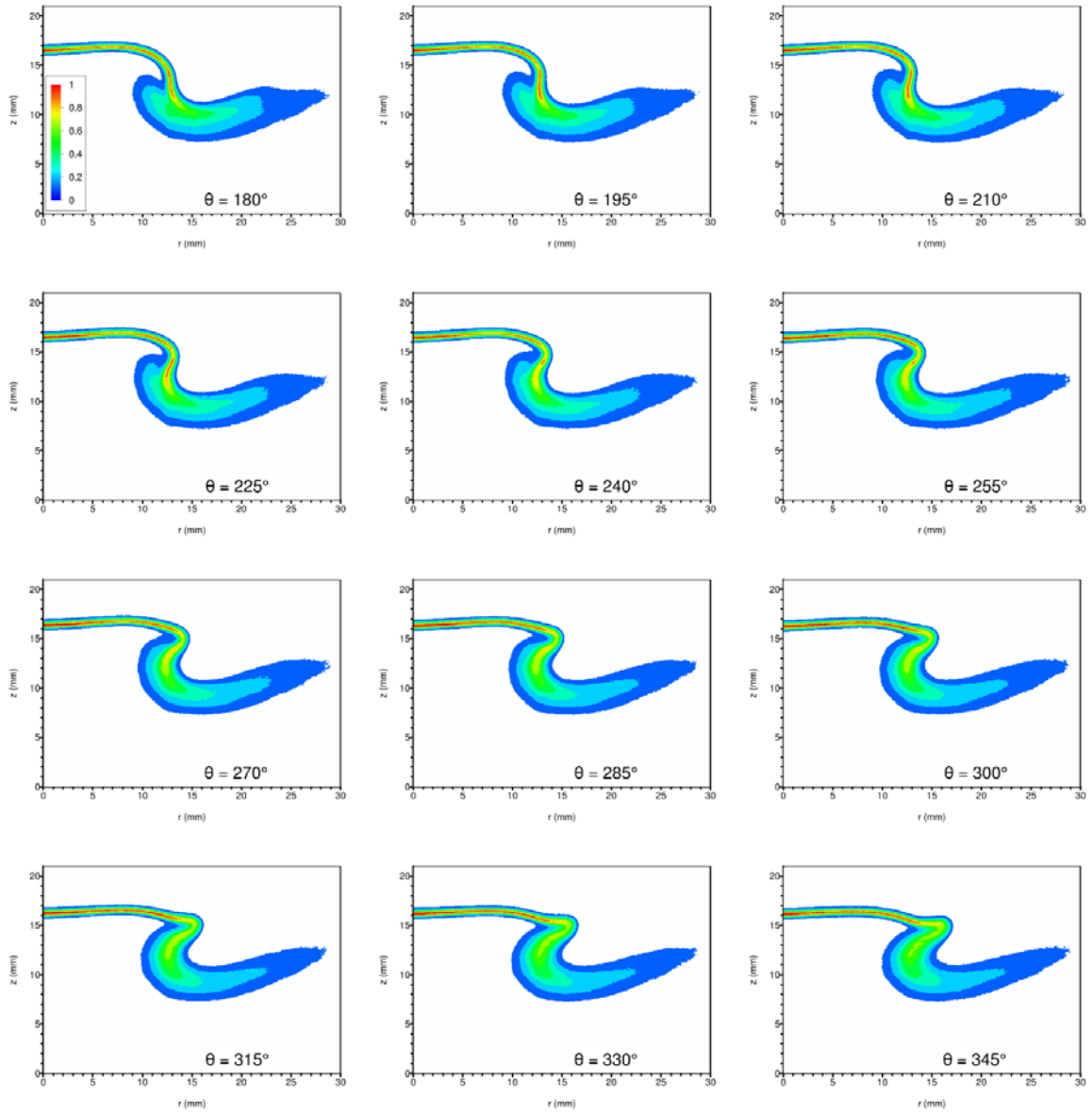


Figure H-41 (cont.): Phase-resolved CH_2O PLIF images for acoustic forcing at 55 Hz. The horizontal axis is the radius (mm) from the centerline of the burner. The vertical axis is the distance (mm) above the nozzle exit plane. (The stagnation plane is located at $z = 21\text{ mm}$.) Phase angle $\theta = 0^\circ$ corresponds to the rising-edge zero crossing of the local unsteady pressure. Data from experiment 709. A total of 24 images on 15° spacing are shown. (See previous page.) The magnitude scale is normalized by the peak value over all 24 images.

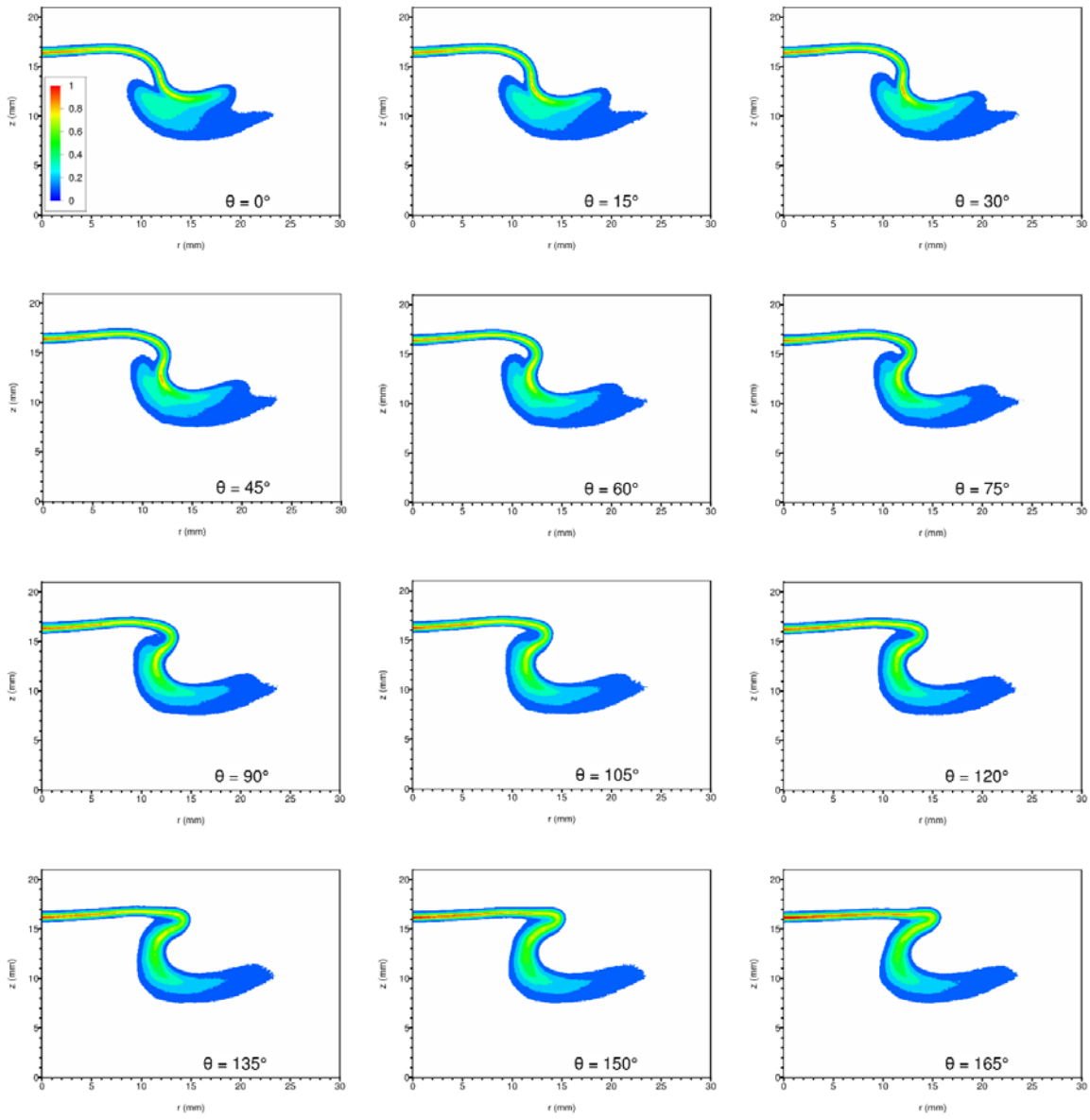


Figure H-42: Phase-resolved CH_2O PLIF images for acoustic forcing at 75 Hz. The horizontal axis is the radius (mm) from the centerline of the burner. The vertical axis is the distance (mm) above the nozzle exit plane. (The stagnation plane is located at $z = 21\text{mm}$.) Phase angle $\theta = 0^\circ$ corresponds to the rising-edge zero crossing of the local unsteady pressure. Data from experiment 708. A total of 24 images on 15° spacing are shown. (See next page.) The magnitude scale is normalized by the peak value over all 24 images.

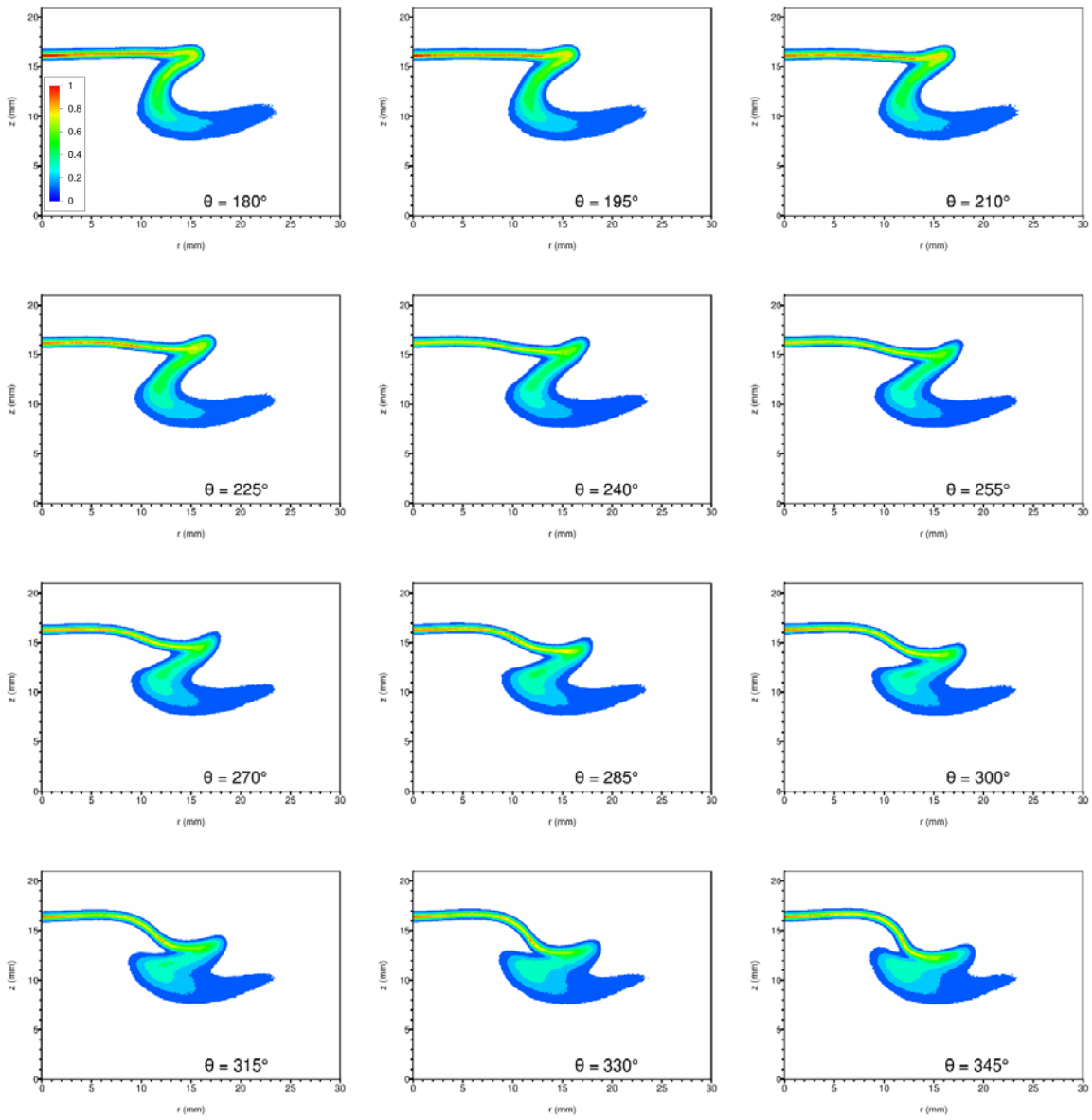


Figure H-42 (cont.): Phase-resolved CH_2O PLIF images for acoustic forcing at 75 Hz. The horizontal axis is the radius (mm) from the centerline of the burner. The vertical axis is the distance (mm) above the nozzle exit plane. (The stagnation plane is located at $z = 21\text{mm}$.) Phase angle $\theta = 0^\circ$ corresponds to the rising-edge zero crossing of the local unsteady pressure. Data from experiment 708. A total of 24 images on 15° spacing are shown. (See previous page.) The magnitude scale is normalized by the peak value over all 24 images.

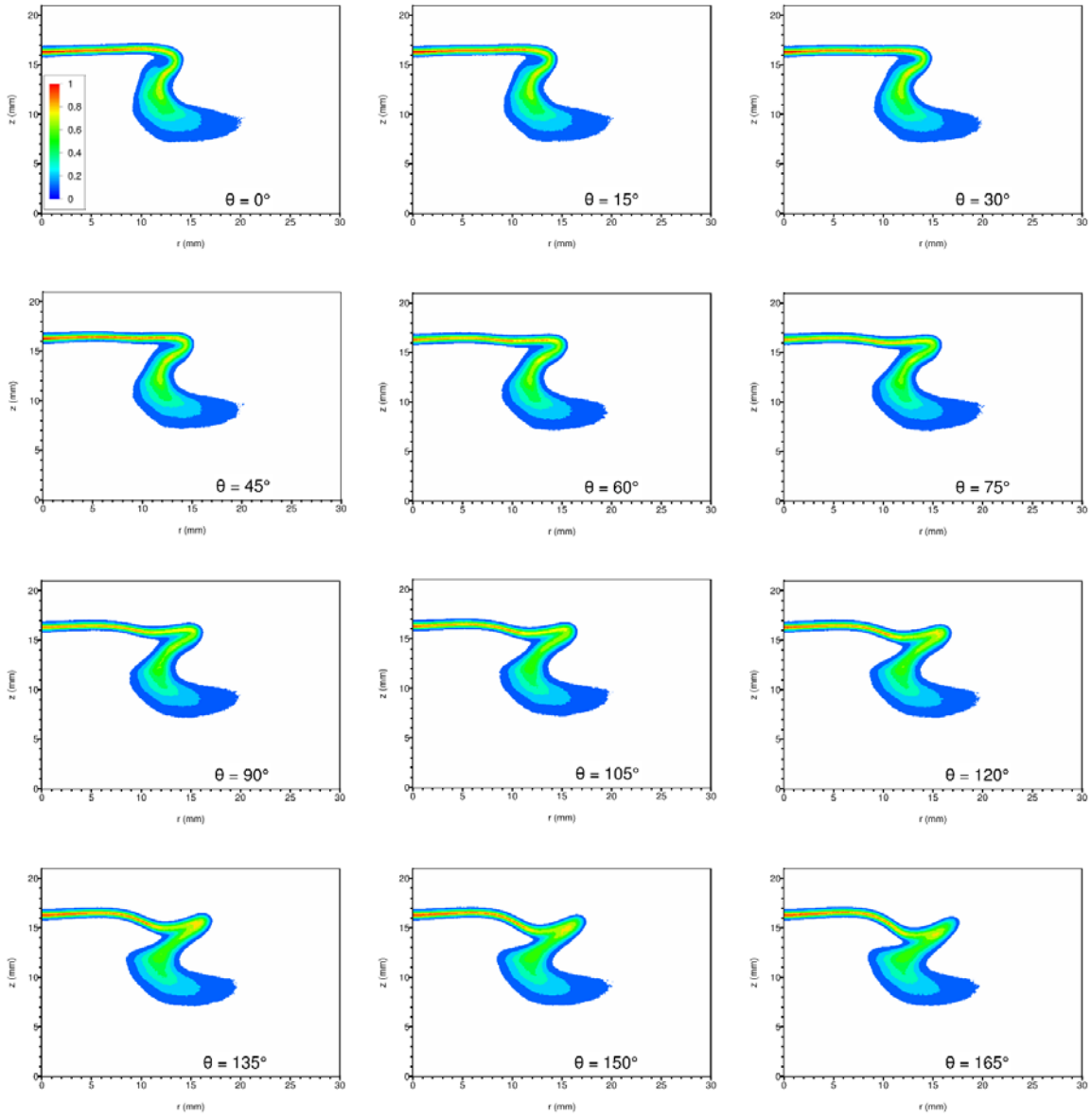


Figure H-43: Phase-resolved CH_2O PLIF images for acoustic forcing at 100 Hz. The horizontal axis is the radius (mm) from the centerline of the burner. The vertical axis is the distance (mm) above the nozzle exit plane. (The stagnation plane is located at $z = 21\text{mm}$.) Phase angle $\theta = 0^\circ$ corresponds to the rising-edge zero crossing of the local unsteady pressure. Data from experiment 711. A total of 24 images on 15° spacing are shown. (See next page.) The magnitude scale is normalized by the peak value over all 24 images.

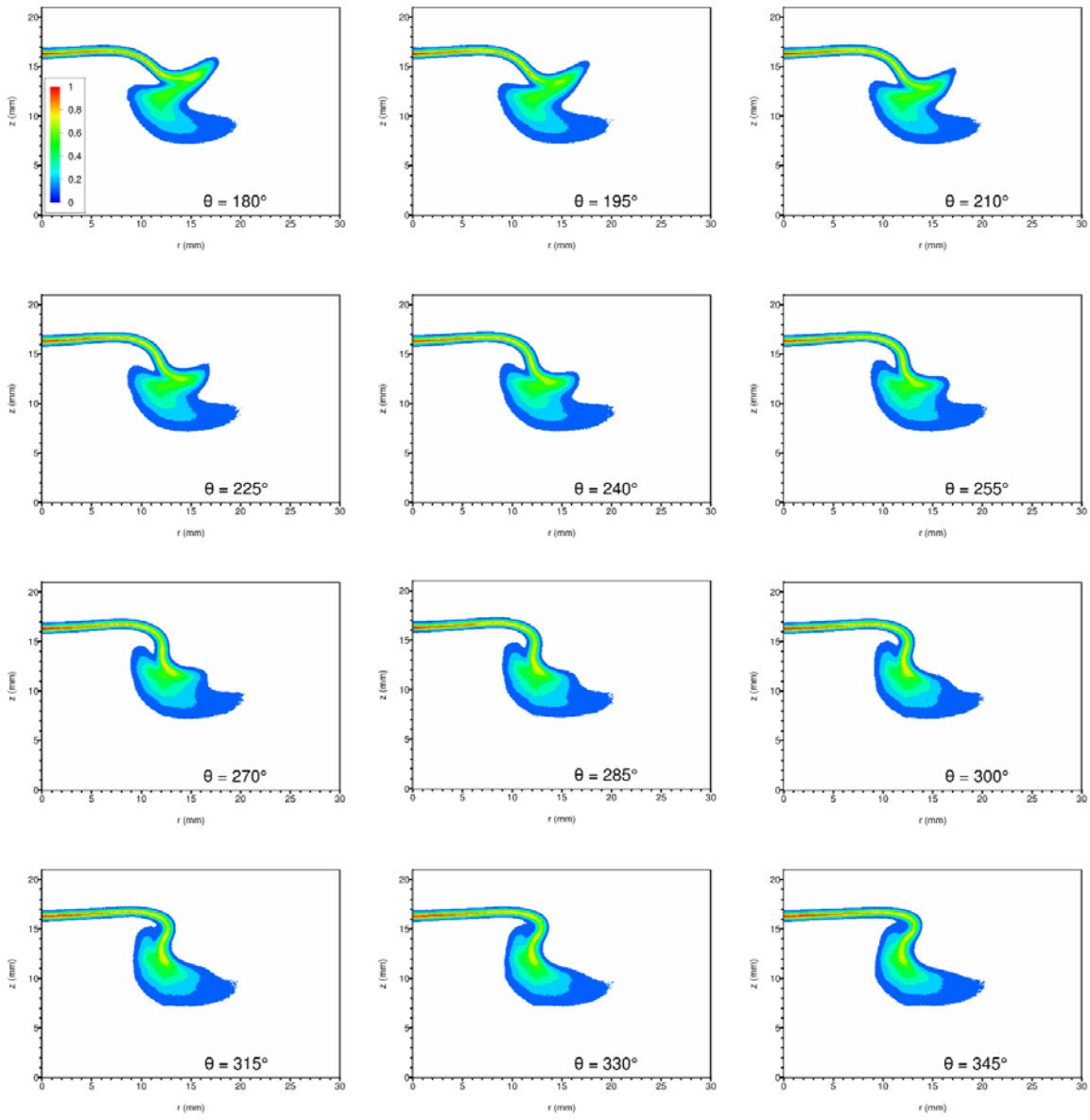


Figure H-43 (cont.): Phase-resolved CH_2O PLIF images for acoustic forcing at 100 Hz. The horizontal axis is the radius (mm) from the centerline of the burner. The vertical axis is the distance (mm) above the nozzle exit plane. (The stagnation plane is located at $z = 21\text{mm}$.) Phase angle $\theta = 0^\circ$ corresponds to the rising-edge zero crossing of the local unsteady pressure. Data from experiment 711. A total of 24 images on 15° spacing are shown. (See previous page.) The magnitude scale is normalized by the peak value over all 24 images.

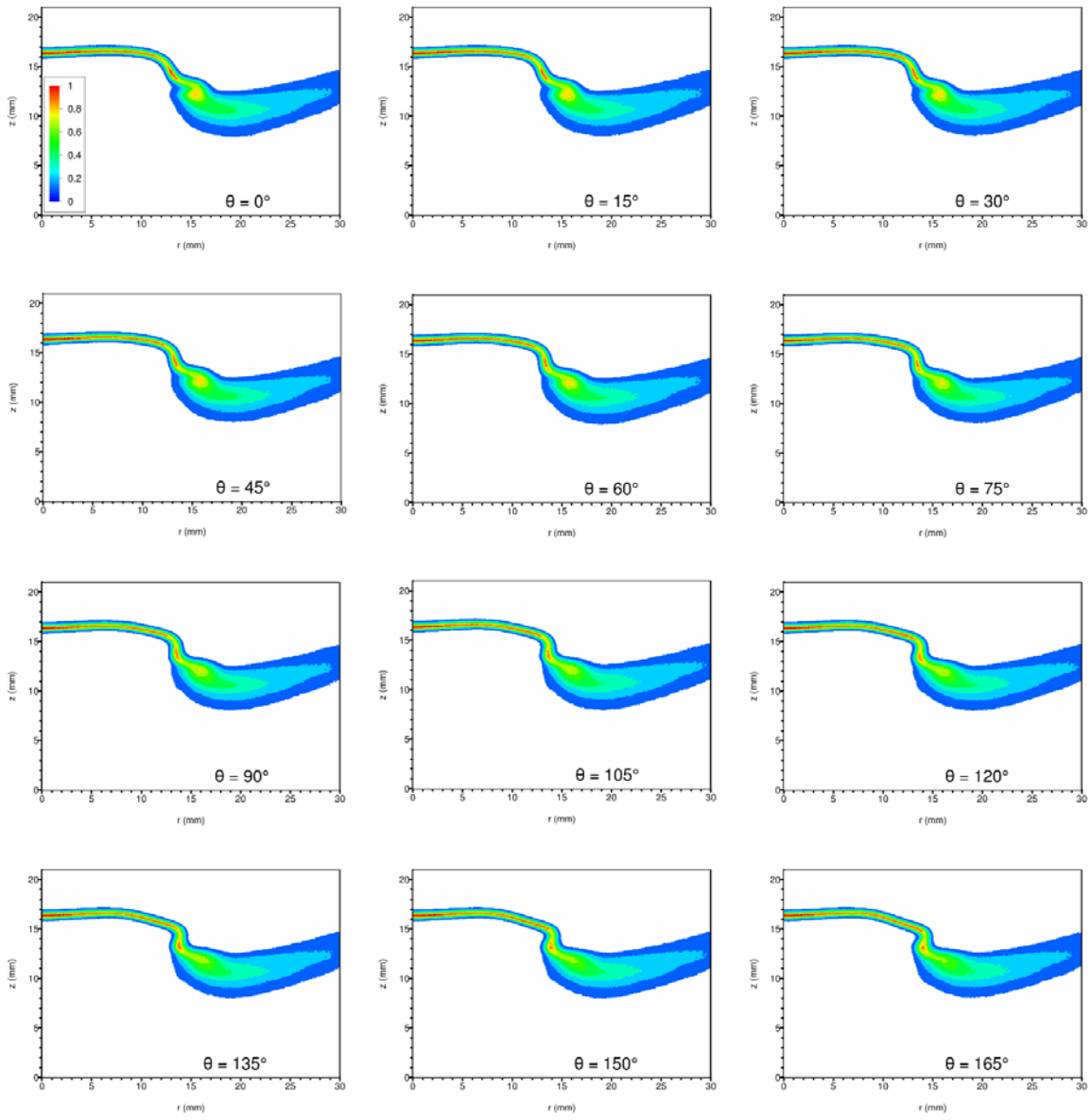


Figure H-44: Phase-resolved CH_2O PLIF images for acoustic forcing at 150 Hz. The horizontal axis is the radius (mm) from the centerline of the burner. The vertical axis is the distance (mm) above the nozzle exit plane. (The stagnation plane is located at $z = 21\text{mm}$.) Phase angle $\theta = 0^\circ$ corresponds to the rising-edge zero crossing of the local unsteady pressure. Data from experiment 712. A total of 24 images on 15° spacing are shown. (See next page.) The magnitude scale is normalized by the peak value over all 24 images.

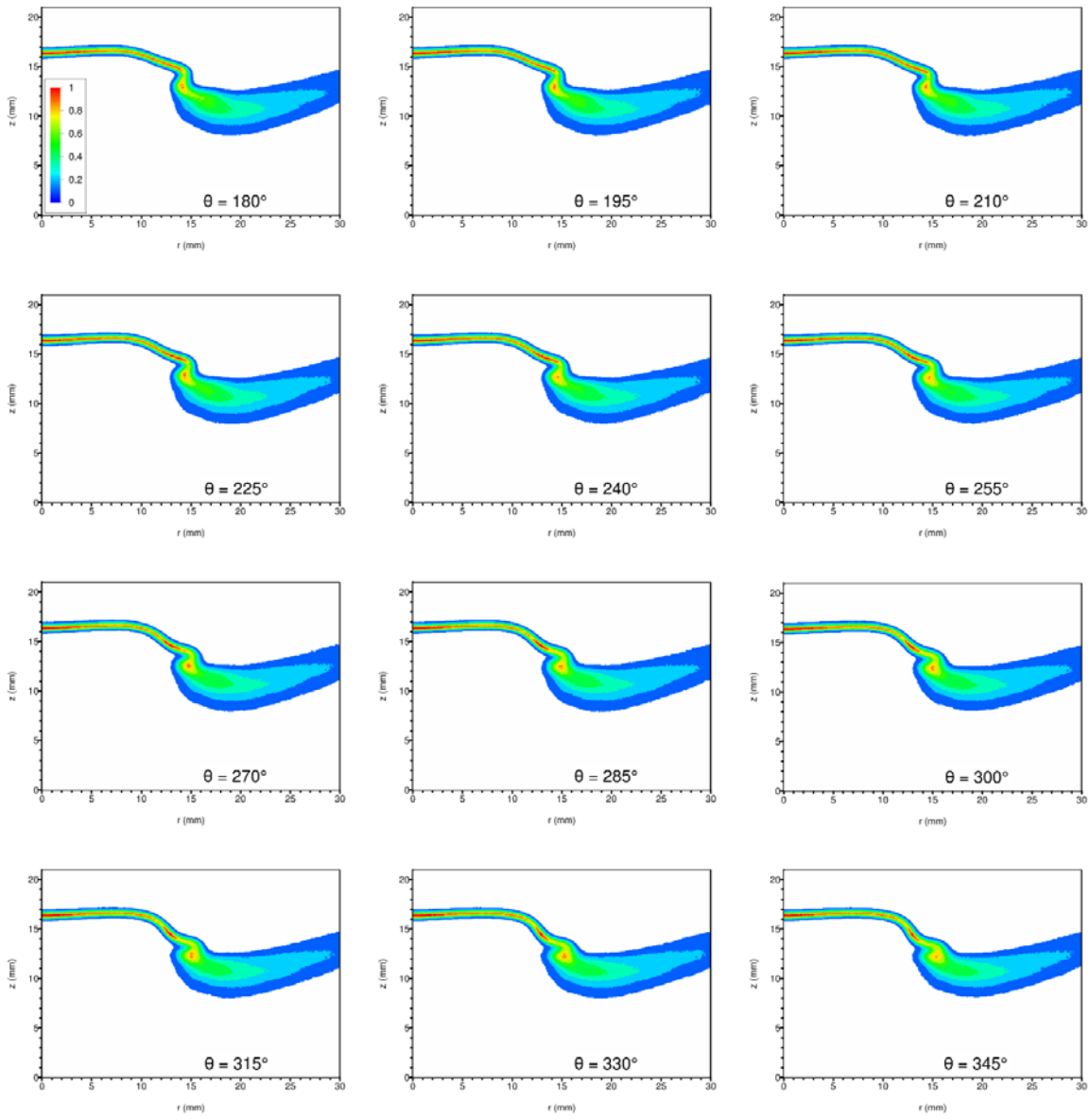


Figure H-44 (cont.): Phase-resolved CH_2O PLIF images for acoustic forcing at 150 Hz. The horizontal axis is the radius (mm) from the centerline of the burner. The vertical axis is the distance (mm) above the nozzle exit plane. (The stagnation plane is located at $z = 21\text{mm}$.) Phase angle $\theta = 0^\circ$ corresponds to the rising-edge zero crossing of the local unsteady pressure. Data from experiment 712. A total of 24 images on 15° spacing are shown. (See previous page.) The magnitude scale is normalized by the peak value over all 24 images.

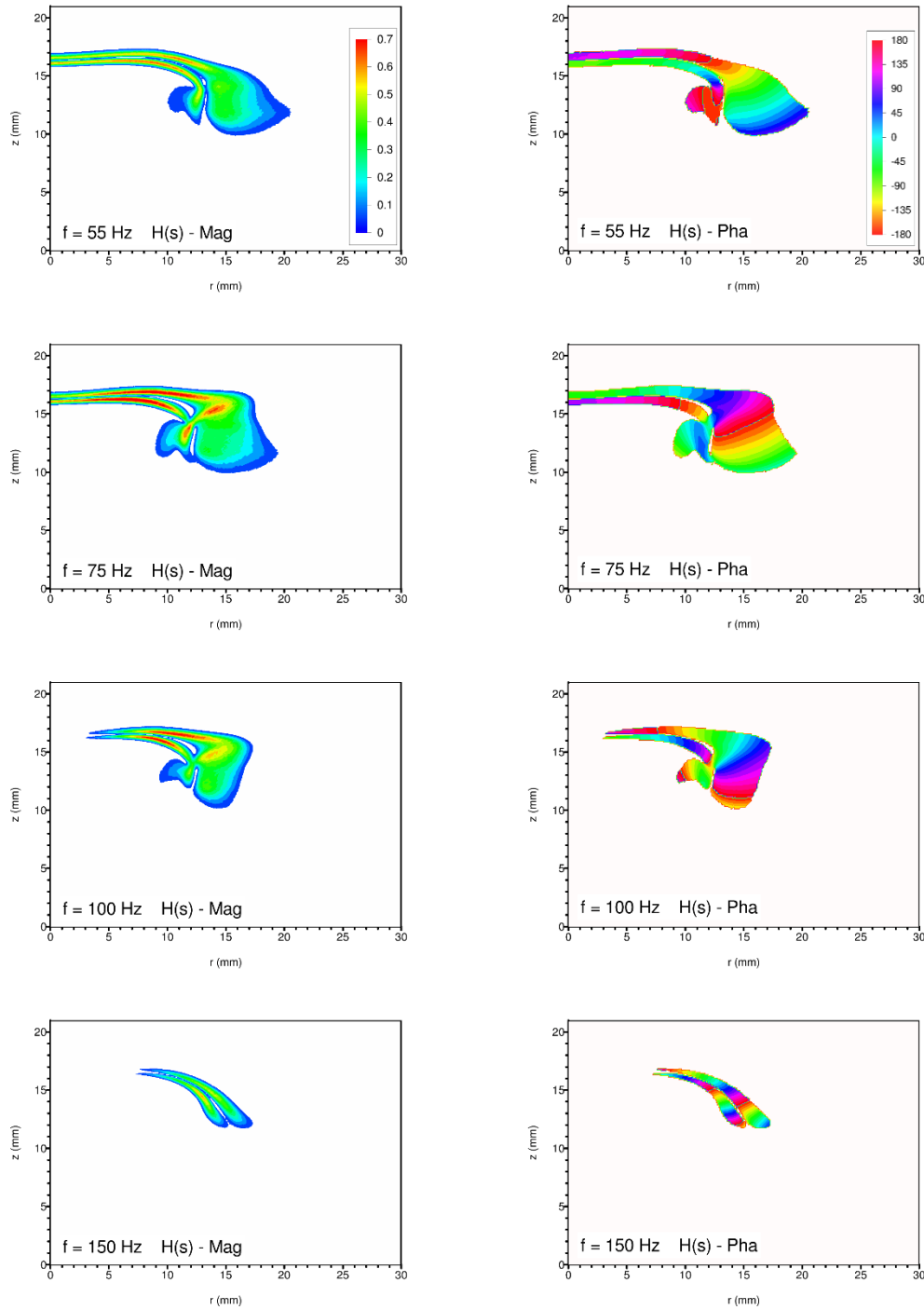


Figure H-45: Spatially resolved combustion response function produced from CH_2O PLIF data. Magnitude plots appear in the left column while phase plots are shown on the right. Note that positive phase values correspond to I' lagging P' . The coordinate system origin is along the burner centerline at the nozzle exit plane. Data for all nine drive frequencies are shown. (See next two pages.)

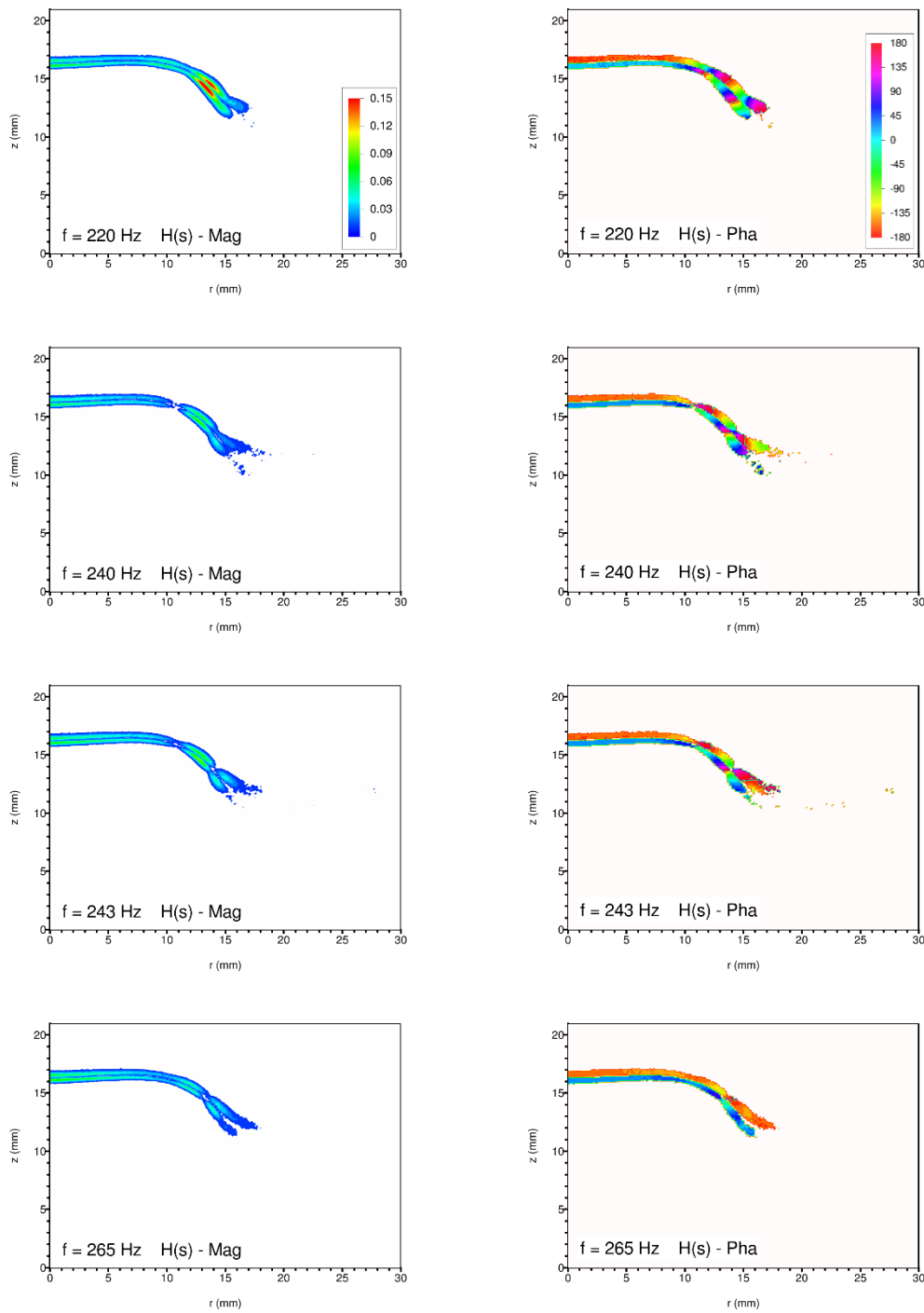


Figure H-45 (cont): Spatially resolved combustion response function produced from CH_2O PLIF data. Magnitude plots appear in the left column while phase plots are shown on the right. Data for all nine drive frequencies are shown. (See previous and next page.) Note the change in magnitude scale versus the plots for 150 Hz and lower frequency.

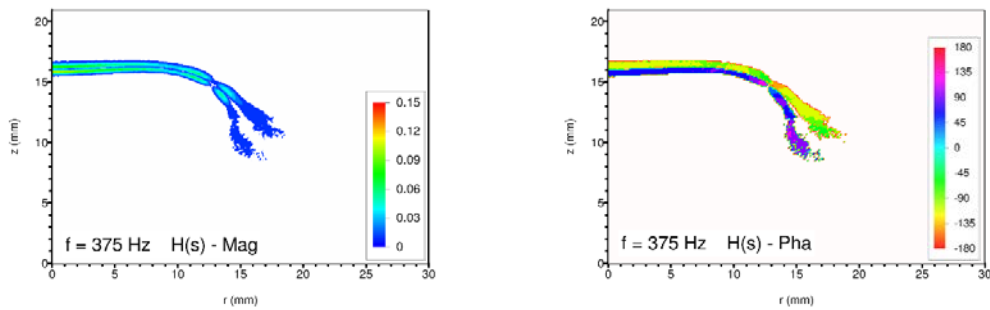


Figure H-45 (cont.): Spatially resolved combustion response function produced from CH_2O PLIF data. Magnitude plots appear in the left column while phase plots are shown on the right. Data for all nine drive frequencies are shown. (See previous two pages.) Note the change in magnitude scale versus the plots for 150 Hz and lower frequency.

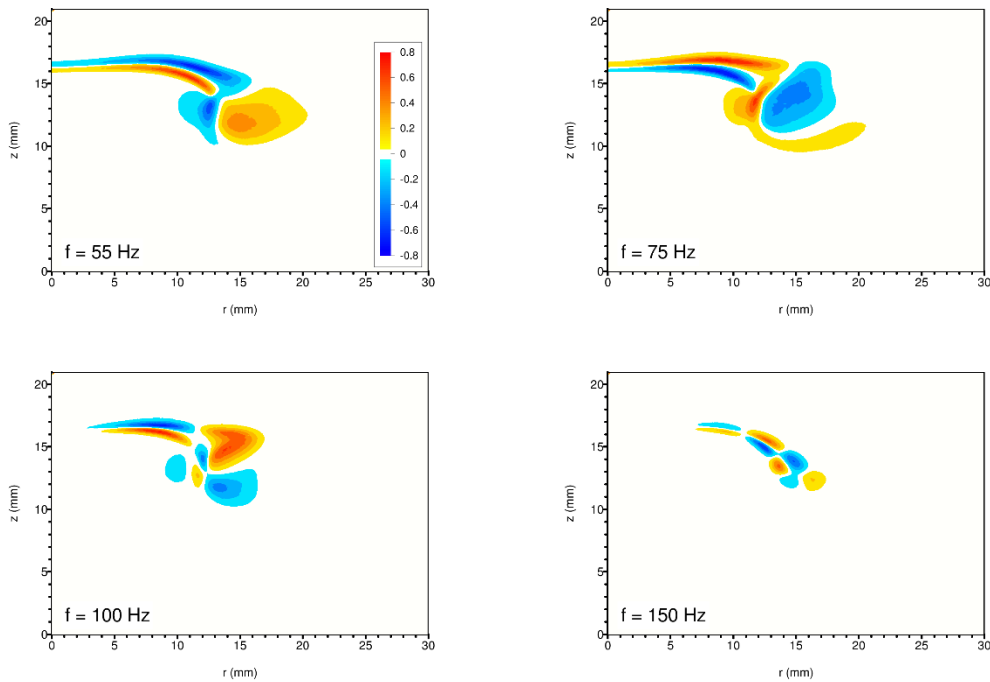


Figure H-46: Spatially resolved forced Rayleigh index produced from CH_2O PLIF data. Data for all nine drive frequencies are shown. (See next page.) Note the difference between the magnitude legends for the lower four drive frequencies and the upper five drive frequencies.

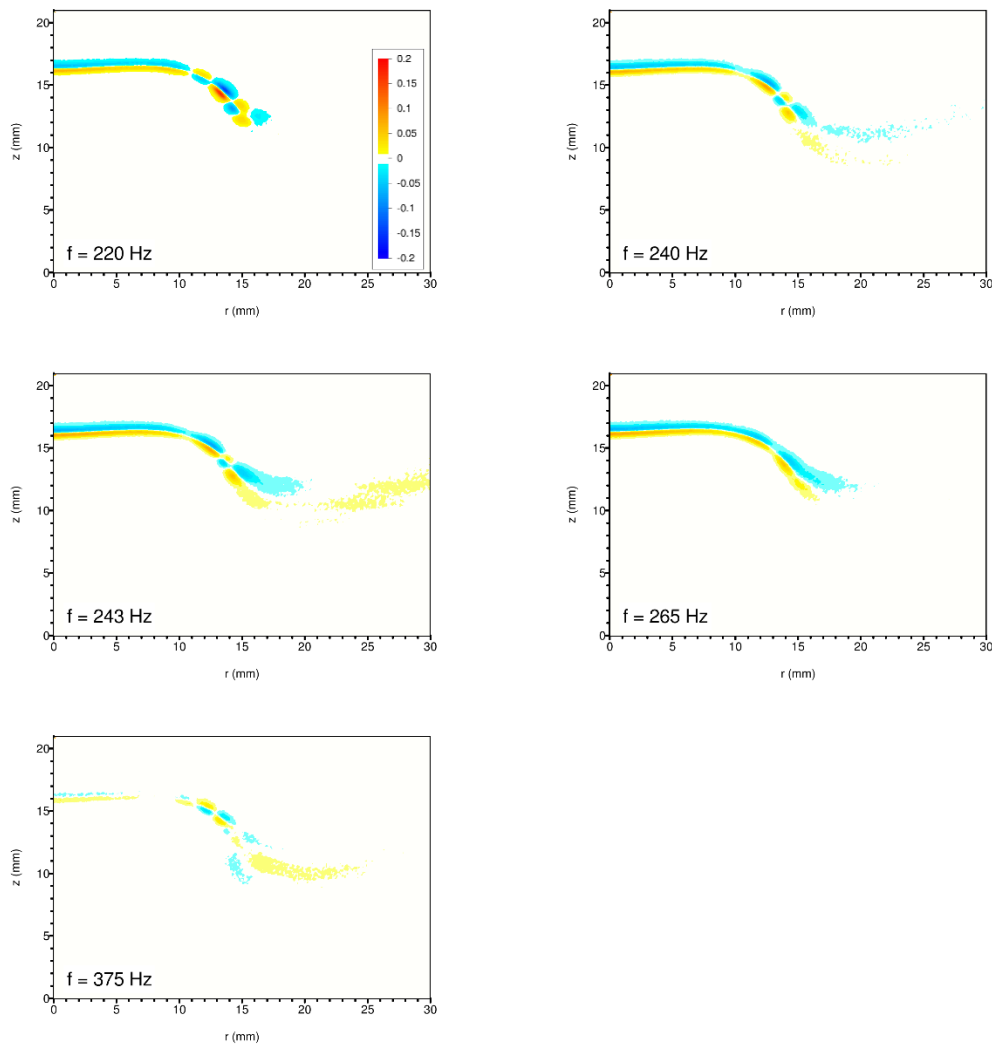


Figure H-46 (cont.): Spatially resolved forced Rayleigh index produced from CH_2O PLIF data. Data for all nine drive frequencies are shown. (See previous page.) Note the difference between the magnitude legends for the lower four drive frequencies and the upper five drive frequencies.

H.2.4 Combined OH-CH₂O PLIF Data

The following 19 pages present the combined OH-CH₂O PLIF data. This was done following the procedure outlined by Paul and Najm (1998). The claim is that the resulting images provide an improved estimate of the spatially distributed varying heat release. Images were generated by taking the pixel-by-pixel product of the paired OH and CH₂O images.

Acoustic data is not presented in the following waveform plots and spectral data tables. This is due to the combinatorial nature of the data being used. In the waveform plots, a representative sine wave is shown for the acoustic reference.

Further information regarding the processing of this data can be found in the beginning of this appendix as well as in chapter 4.

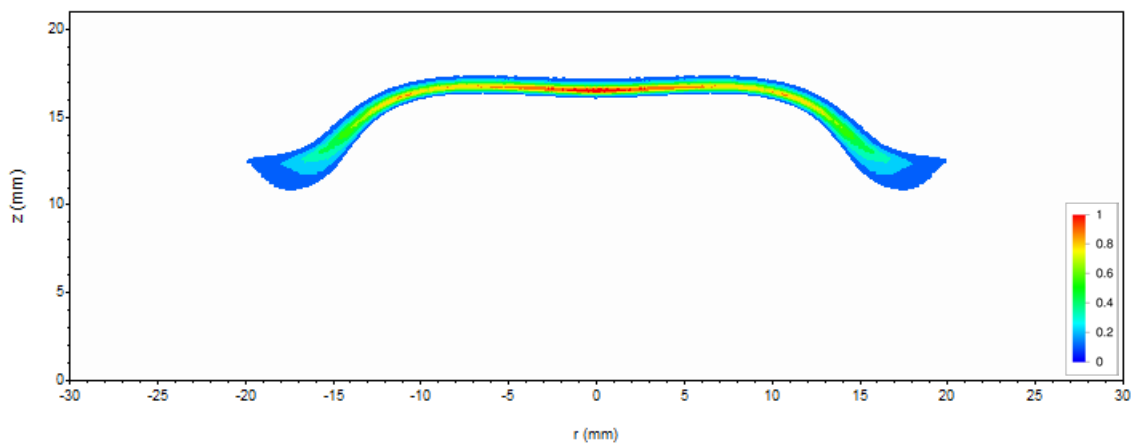


Figure H-47: Combined OH-CH₂O PLIF image of flame under steady conditions (no acoustic forcing). Collected data appears on the left, and is mirrored across the centerline for a visual representation of entire flame. Burner centerline is at $r = 0$. Position $z = 0$ corresponds to the nozzle exit plane.

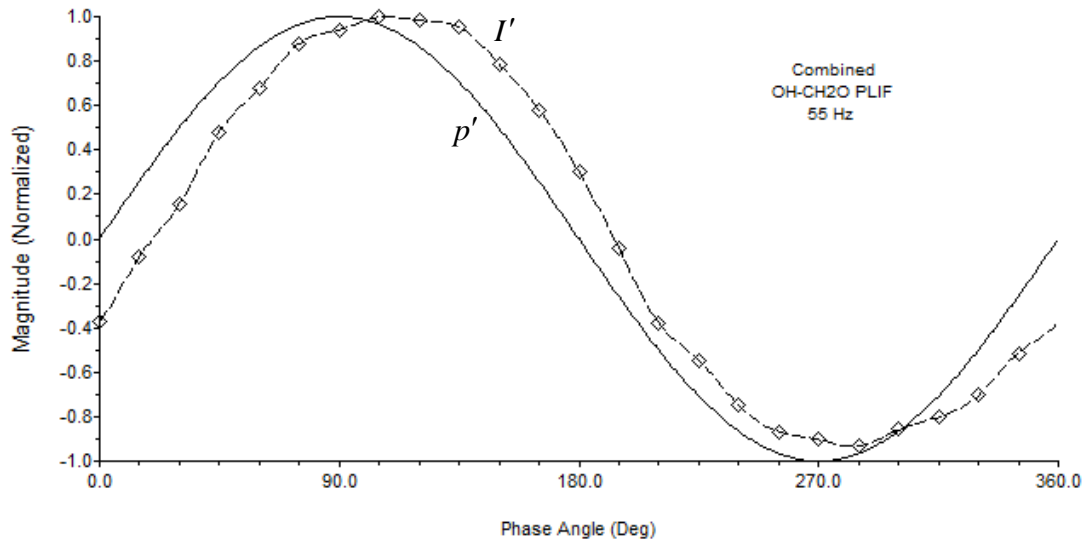


Figure H-48: Resulting waveforms from the 55 Hz OH-CH₂O PLIF combination. The solid curve shows an idealized acoustic waveform (for reference) with the rising-edge zero crossing marking the zero-degree point. Diamonds represent total (fully integrated) intensity data points computed from the phase bins. The dashed curve is a periodic cubic spline fit to this data. Signals are normalized by their peak values.

Mode	Pressure (p')		Intensity (I')	
	Mag	Phase	Mag	Phase
1	1.0000	0.0	1.0000	16.4
2			0.0694	157.9
3			0.0431	55.2
4			0.0183	163.9
5			0.0028	22.5
6			0.0073	-111.2
7			0.0079	103.7
8			0.0068	-104.8
9			0.0090	122.9
10			0.0087	39.4
11			0.0063	28.8

Table H-31: Harmonic content of the measured intensity field for the 55 Hz OH-CH₂O PLIF combination case. The measured intensity is total (fully integrated). The intensity magnitude is normalized by the first mode value. All phases are in reference to the phase of the fundamental acoustic mode. Sign convention is such that negative phases are leading while positive phases are lagging.

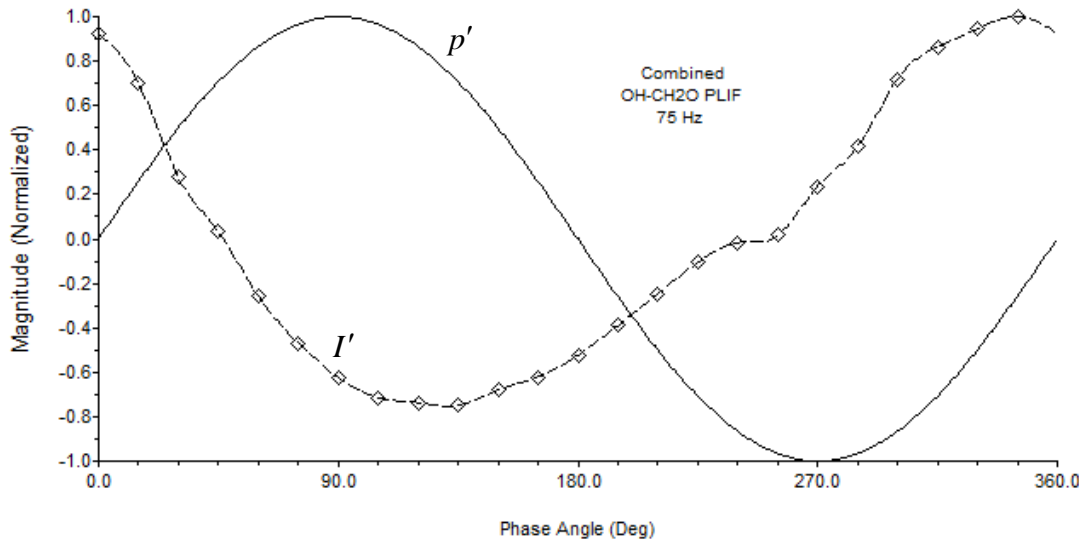


Figure H-49: Resulting waveforms from the 75 Hz OH-CH₂O PLIF combination. The solid curve shows an idealized acoustic waveform (for reference) with the rising-edge zero crossing marking the zero-degree point. Diamonds represent total (fully integrated) intensity data points computed from the phase bins. The dashed curve is a periodic cubic spline fit to this data. Signals are normalized by their peak values.

Mode	Pressure (p')		Intensity (I')	
	Mag	Phase	Mag	Phase
1	1.0000	0.0	1.0000	-125.3
2			0.2512	-107.2
3			0.0705	-138.8
4			0.0119	35.7
5			0.0331	-58.3
6			0.0203	-98.0
7			0.0119	-61.2
8			0.0094	-54.7
9			0.0036	-174.1
10			0.0168	54.2
11			0.0119	36.8

Table H-32: Harmonic content of the measured intensity field for the 75 Hz OH-CH₂O PLIF combination case. The measured intensity is total (fully integrated). The intensity magnitude is normalized by the first mode value. All phases are in reference to the phase of the fundamental acoustic mode. Sign convention is such that negative phases are leading while positive phases are lagging.

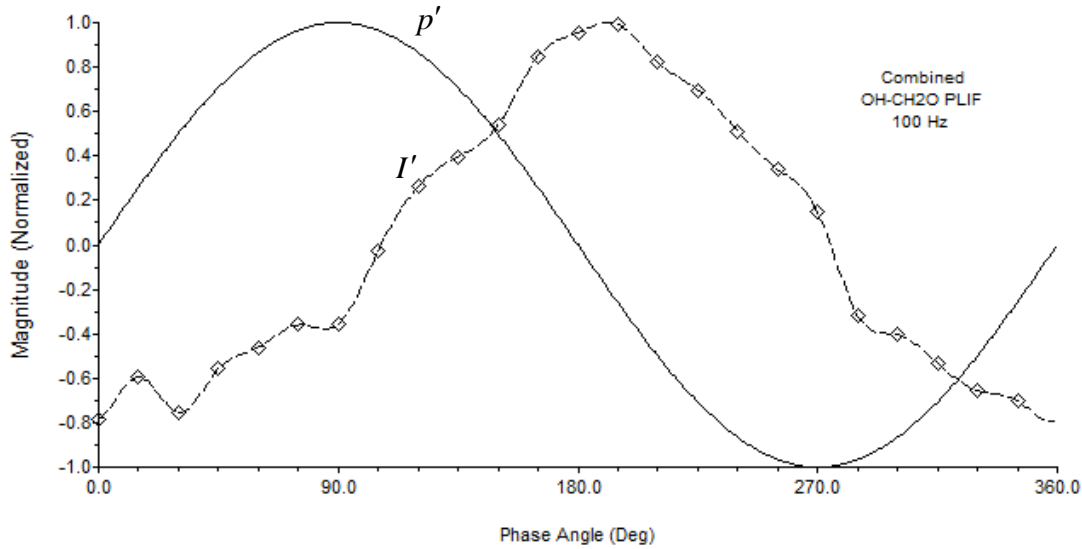


Figure H-50: Resulting waveforms from the 100 Hz OH-CH₂O PLIF combination. The solid curve shows an idealized acoustic waveform (for reference) with the rising-edge zero crossing marking the zero-degree point. Diamonds represent total (fully integrated) intensity data points computed from the phase bins. The dashed curve is a periodic cubic spline fit to this data. Signals are normalized by their peak values.

Mode	Pressure (p')		Intensity (I')	
	Mag	Phase	Mag	Phase
1	1.0000	0.0	1.0000	99.2
2			0.1491	-53.2
3			0.0176	25.7
4			0.0138	-120.8
5			0.0515	131.5
6			0.0447	-48.0
7			0.0508	-6.2
8			0.0072	131.9
9			0.0143	125.3
10			0.0355	59.0
11			0.0230	21.9

Table H-33: Harmonic content of the measured intensity field for the 100 Hz OH-CH₂O PLIF combination case. The measured intensity is total (fully integrated). The intensity magnitude is normalized by the first mode value. All phases are in reference to the phase of the fundamental acoustic mode. Sign convention is such that negative phases are leading while positive phases are lagging.

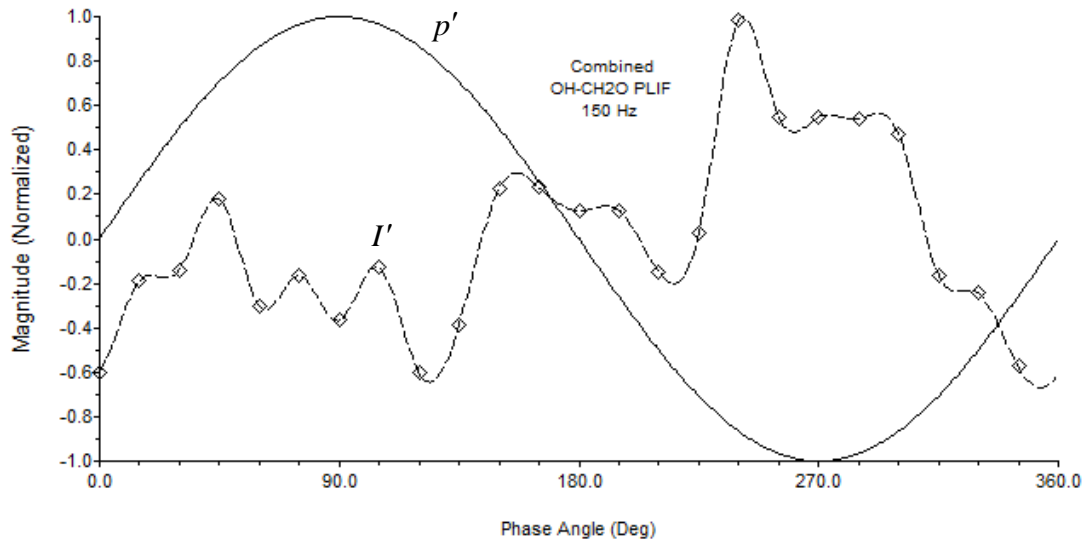


Figure H-51: Resulting waveforms from the 150 Hz OH-CH₂O PLIF combination. The solid curve shows an idealized acoustic waveform (for reference) with the rising-edge zero crossing marking the zero-degree point. Diamonds represent total (fully integrated) intensity data points computed from the phase bins. The dashed curve is a periodic cubic spline fit to this data. Signals are normalized by their peak values.

Mode	Pressure (p')		Intensity (I')	
	Mag	Phase	Mag	Phase
1	1.0000	0.0	1.0000	152.6
2			0.5615	57.5
3			0.6841	30.1
4			0.1513	-170.2
5			0.4099	33.9
6			0.1185	-158.8
7			0.2613	-171.9
8			0.3207	38.6
9			0.1023	-104.2
10			0.0724	6.1
11			0.2188	15.6

Table H-34: Harmonic content of the measured intensity field for the 150 Hz OH-CH₂O PLIF combination case. The measured intensity is total (fully integrated). The intensity magnitude is normalized by the first mode value. All phases are in reference to the phase of the fundamental acoustic mode. Sign convention is such that negative phases are leading while positive phases are lagging.

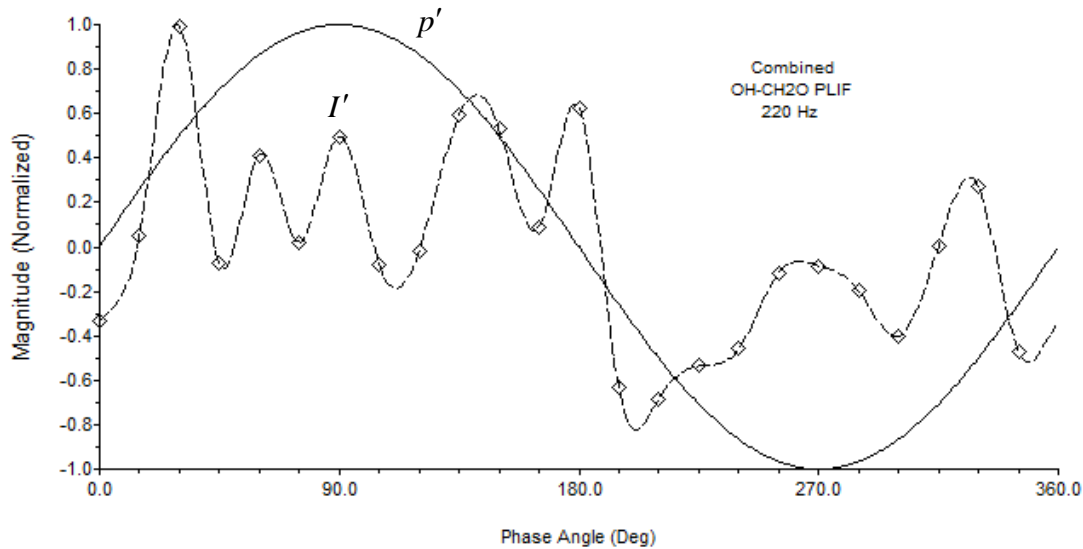


Figure H-52: Resulting waveforms from the 220 Hz OH-CH₂O PLIF combination. The solid curve shows an idealized acoustic waveform (for reference) with the rising-edge zero crossing marking the zero-degree point. Diamonds represent total (fully integrated) intensity data points computed from the phase bins. The dashed curve is a periodic cubic spline fit to this data. Signals are normalized by their peak values.

Mode	Pressure (p')		Intensity (I')	
	Mag	Phase	Mag	Phase
1	1.0000	0.0	1.0000	-7.9
2			0.3321	-173.5
3			0.7722	24.8
4			0.2782	165.8
5			0.5120	61.2
6			0.5109	55.2
7			0.5076	88.3
8			0.2605	-68.1
9			0.3550	87.0
10			0.3185	-133.6
11			0.2302	-160.2

Table H-35: Harmonic content of the measured intensity field for the 220 Hz OH-CH₂O PLIF combination case. The measured intensity is total (fully integrated). The intensity magnitude is normalized by the first mode value. All phases are in reference to the phase of the fundamental acoustic mode. Sign convention is such that negative phases are leading while positive phases are lagging.

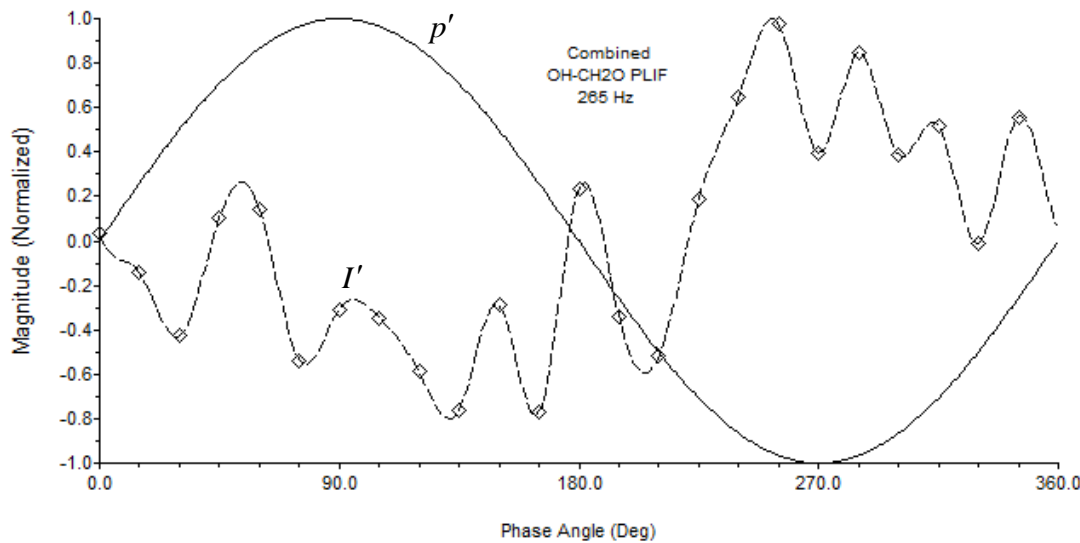


Figure H-53: Resulting waveforms from the 265 Hz OH-CH₂O PLIF combination. The solid curve shows an idealized acoustic waveform (for reference) with the rising-edge zero crossing marking the zero-degree point. Diamonds represent total (fully integrated) intensity data points computed from the phase bins. The dashed curve is a periodic cubic spline fit to this data. Signals are normalized by their peak values.

Mode	Pressure (p')		Intensity (I')	
	Mag	Phase	Mag	Phase
1	1.0000	0.0	1.0000	-156.5
2			0.3474	72.7
3			0.1065	17.3
4			0.2730	-154.6
5			0.1679	108.3
6			0.3339	-113.2
7			0.2087	-159.9
8			0.1995	-26.2
9			0.1619	108.1
10			0.0816	-83.6
11			0.2592	133.7

Table H-36: Harmonic content of the measured intensity field for the 265 Hz OH-CH₂O PLIF combination case. The measured intensity is total (fully integrated). The intensity magnitude is normalized by the first mode value. All phases are in reference to the phase of the fundamental acoustic mode. Sign convention is such that negative phases are leading while positive phases are lagging.

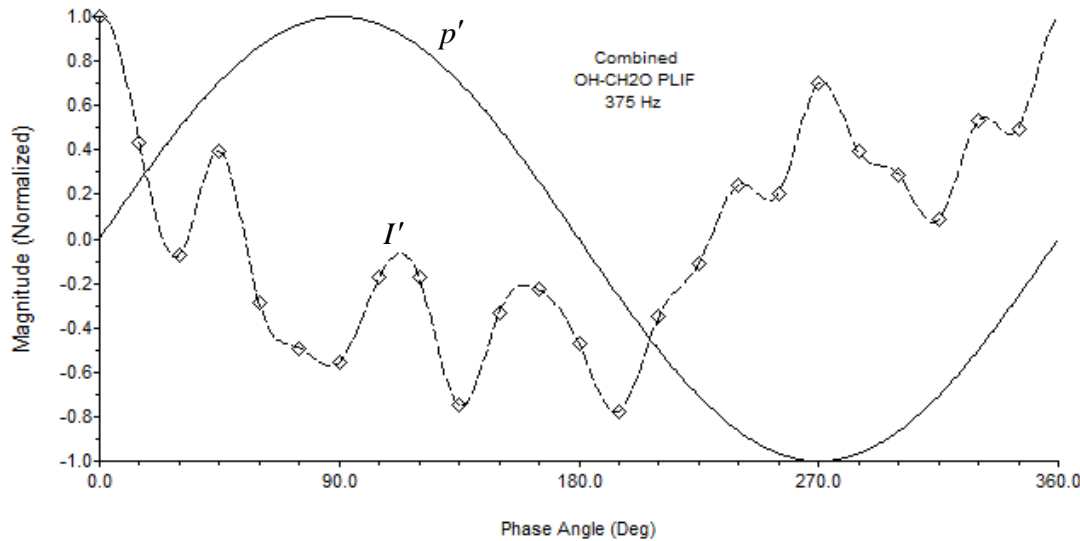


Figure H-54: Resulting waveforms from the 375 Hz OH-CH₂O PLIF combination. The solid curve shows an idealized acoustic waveform (for reference) with the rising-edge zero crossing marking the zero-degree point. Diamonds represent total (fully integrated) intensity data points computed from the phase bins. The dashed curve is a periodic cubic spline fit to this data. Signals are normalized by their peak values.

Mode	Pressure (p')		Intensity (I')	
	Mag	Phase	Mag	Phase
1	1.0000	0.0	1.0000	-125.6
2			0.0574	-141.5
3			0.4119	-50.9
4			0.1814	-114.7
5			0.0522	157.2
6			0.3332	-161.9
7			0.2209	-43.9
8			0.0786	-54.8
9			0.1477	-71.7
10			0.1332	-12.5
11			0.1164	18.4

Table H-37: Harmonic content of the measured intensity field for the 375 Hz OH-CH₂O PLIF combination case. The measured intensity is total (fully integrated). The intensity magnitude is normalized by the first mode value. All phases are in reference to the phase of the fundamental acoustic mode. Sign convention is such that negative phases are leading while positive phases are lagging.

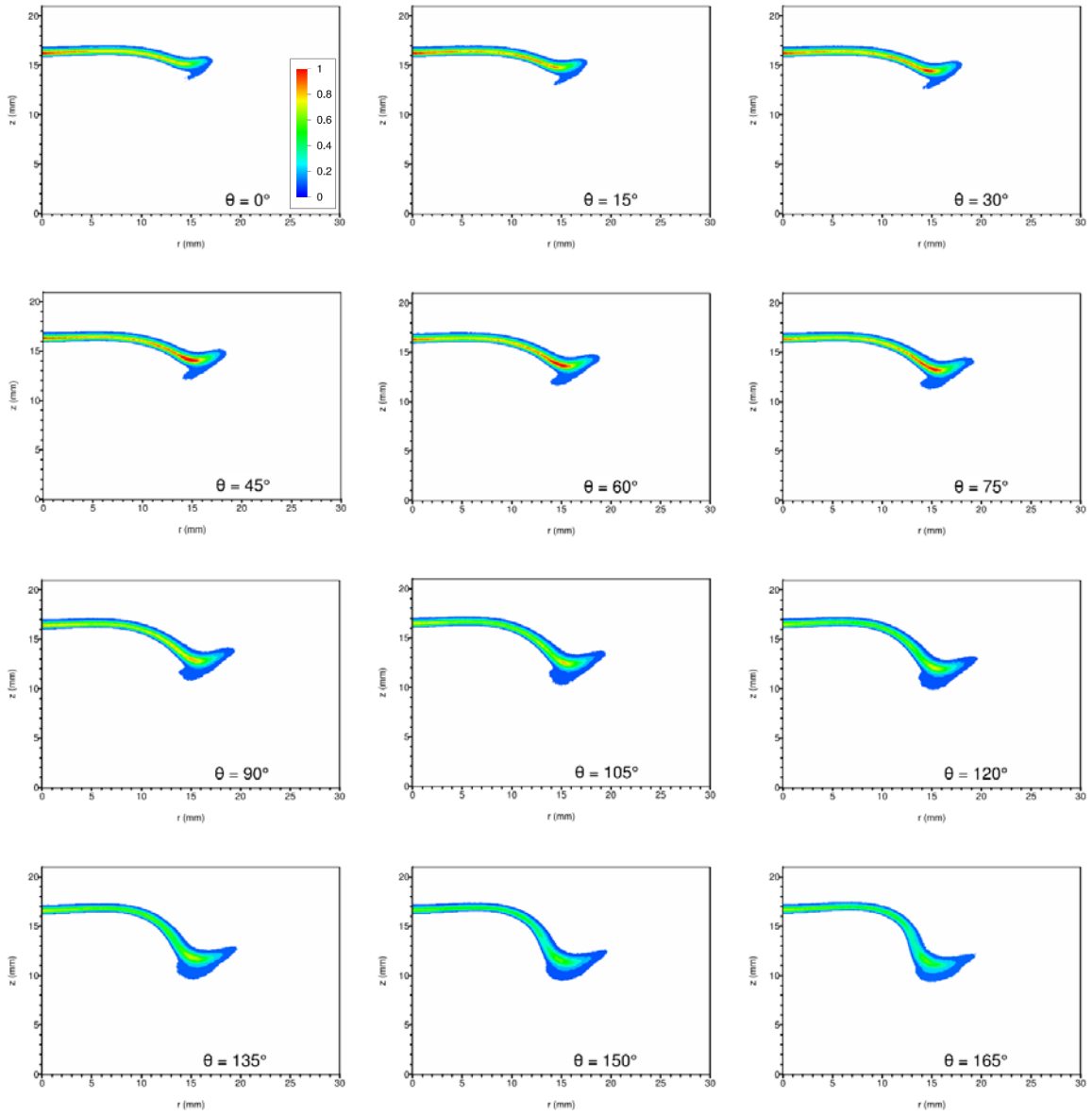


Figure H-55: Phase-resolved OH-CH₂O PLIF combination images for acoustic forcing at 55 Hz. The horizontal axis is the radius (mm) from the centerline of the burner. The vertical axis is the distance (mm) above the nozzle exit plane. (The stagnation plane is located at $z = 21\text{mm}$.) Phase angle $\theta = 0^\circ$ corresponds to the rising-edge zero crossing of the local unsteady pressure. A total of 24 images on 15° spacing are shown. (See next page.) The magnitude scale is normalized by the peak value over all 24 images.

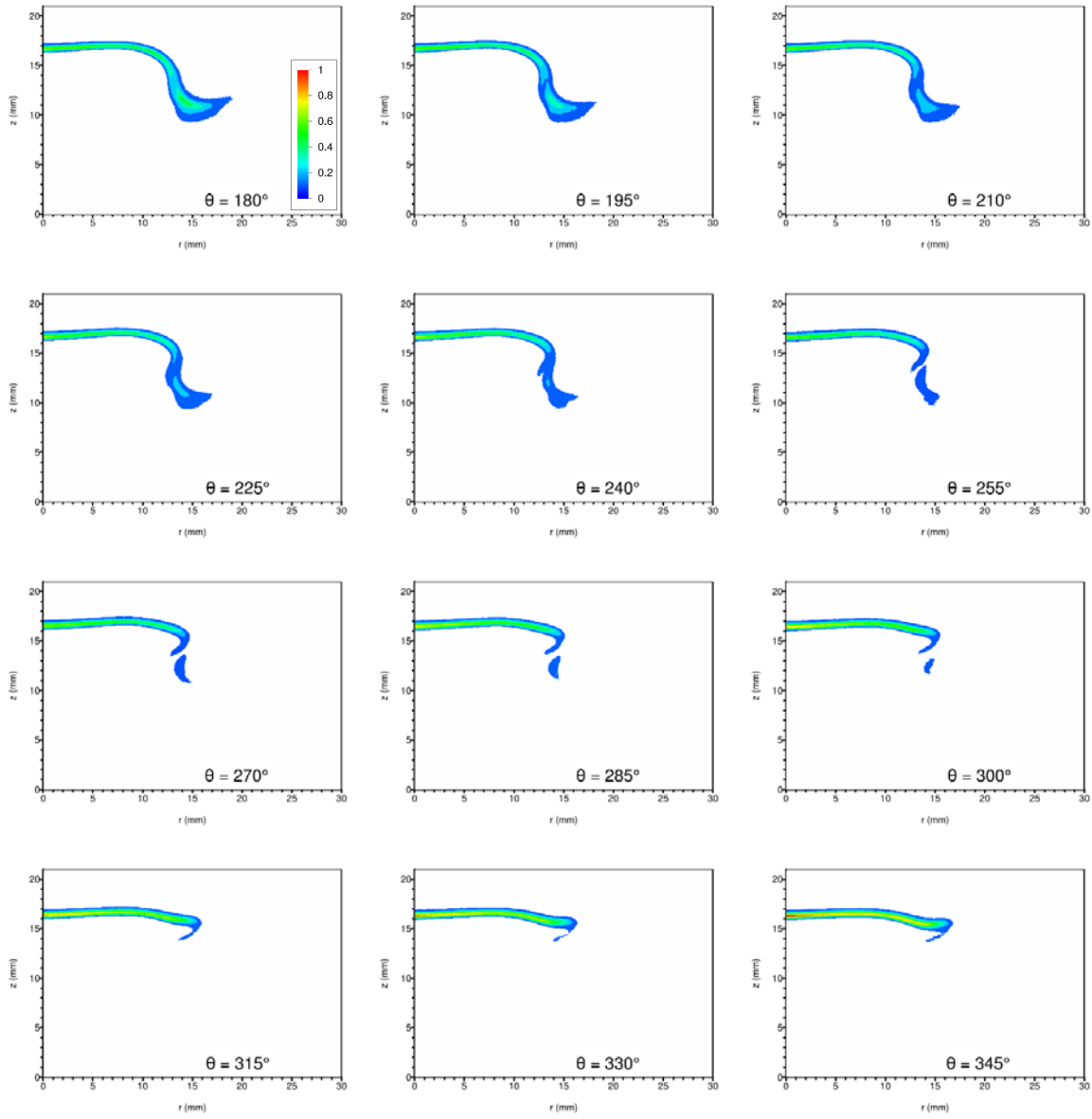


Figure H-55 (cont.): Phase-resolved OH-CH₂O PLIF combination images for acoustic forcing at 55 Hz. The horizontal axis is the radius (mm) from the centerline of the burner. The vertical axis is the distance (mm) above the nozzle exit plane. (The stagnation plane is located at $z = 21\text{mm}$.) Phase angle $\theta = 0^\circ$ corresponds to the rising-edge zero crossing of the local unsteady pressure. A total of 24 images on 15° spacing are shown. (See previous page.) The magnitude scale is normalized by the peak value over all 24 images.

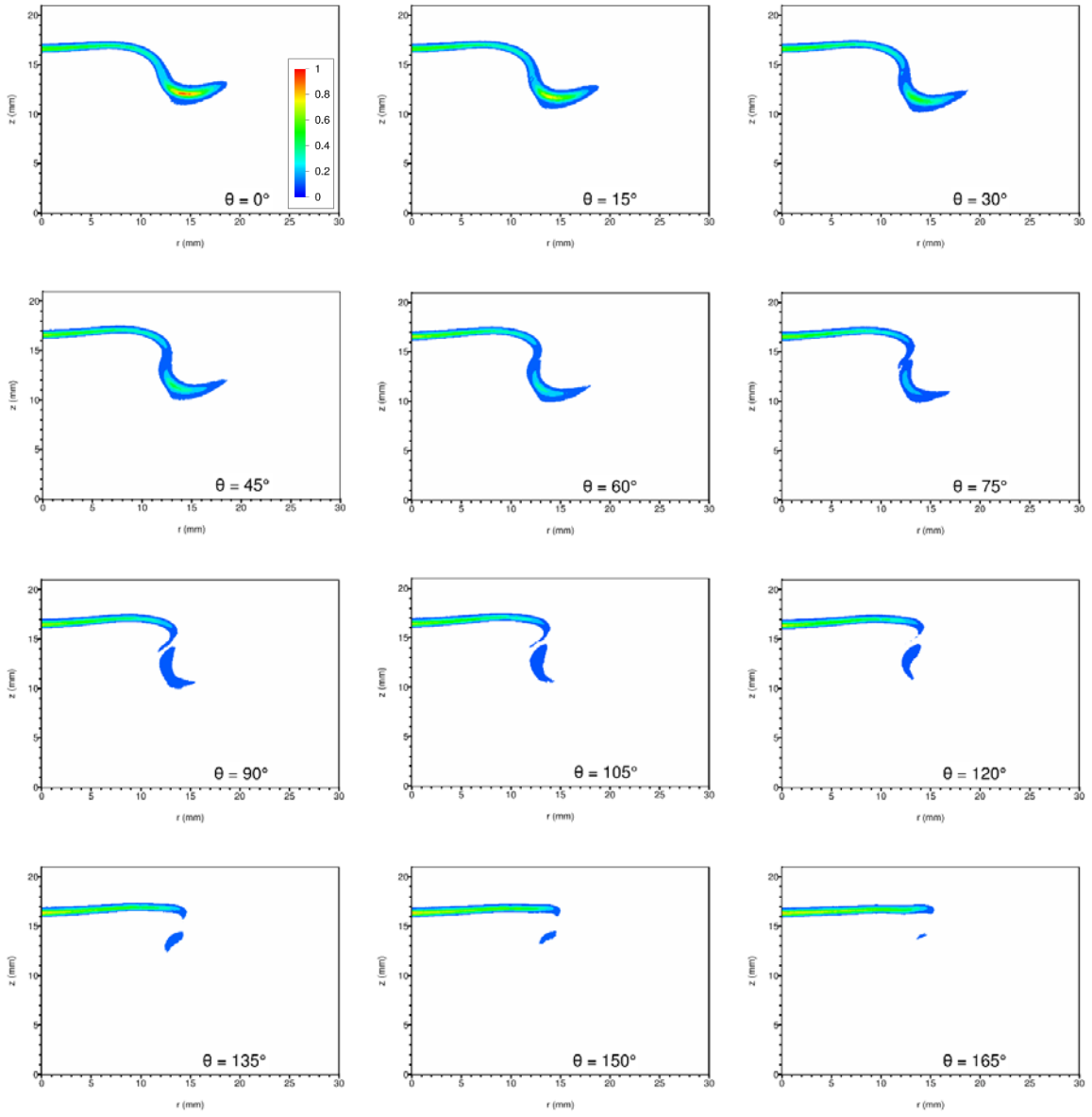


Figure H-56: Phase-resolved OH-CH₂O PLIF combination images for acoustic forcing at 75 Hz. The horizontal axis is the radius (mm) from the centerline of the burner. The vertical axis is the distance (mm) above the nozzle exit plane. (The stagnation plane is located at $z = 21\text{mm}$.) Phase angle $\theta = 0^\circ$ corresponds to the rising-edge zero crossing of the local unsteady pressure. A total of 24 images on 15° spacing are shown. (See next page.) The magnitude scale is normalized by the peak value over all 24 images.

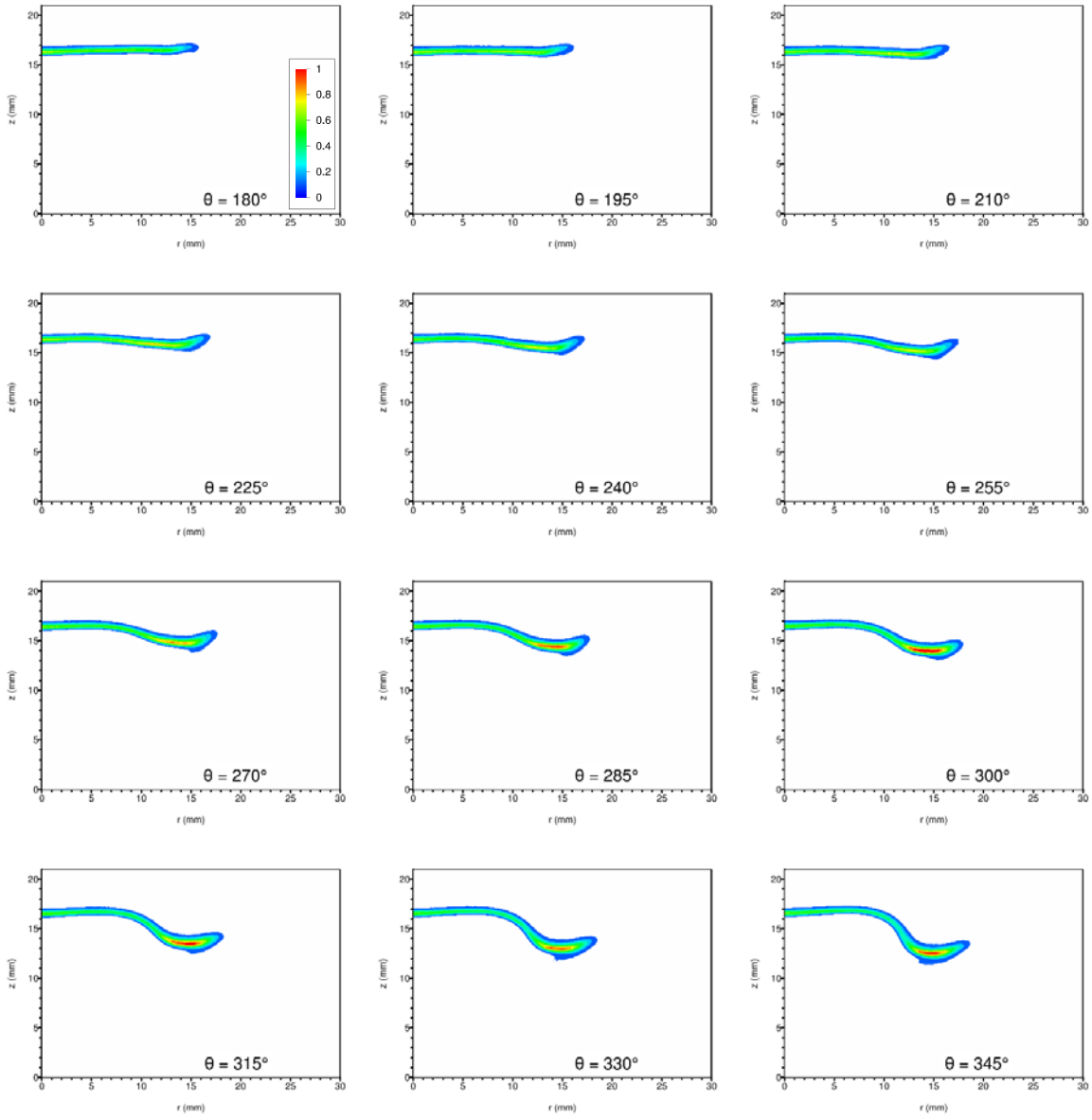


Figure H-56 (cont.): Phase-resolved OH-CH₂O PLIF combination images for acoustic forcing at 75 Hz. The horizontal axis is the radius (mm) from the centerline of the burner. The vertical axis is the distance (mm) above the nozzle exit plane. (The stagnation plane is located at $z = 21\text{mm}$.) Phase angle $\theta = 0^\circ$ corresponds to the rising-edge zero crossing of the local unsteady pressure. A total of 24 images on 15° spacing are shown. (See previous page.) The magnitude scale is normalized by the peak value over all 24 images.

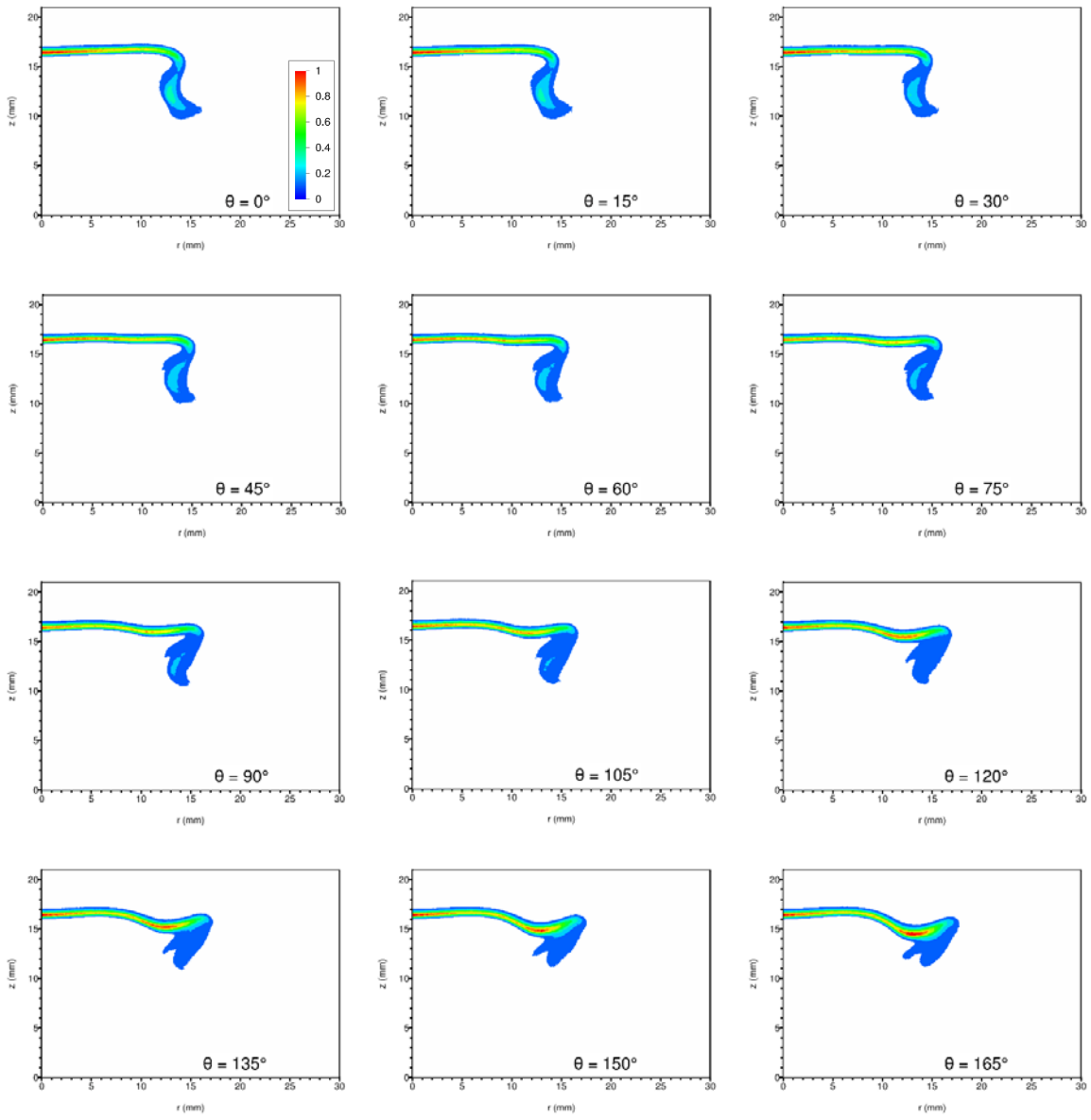


Figure H-57: Phase-resolved OH-CH₂O PLIF combination images for acoustic forcing at 100 Hz. The horizontal axis is the radius (mm) from the centerline of the burner. The vertical axis is the distance (mm) above the nozzle exit plane. (The stagnation plane is located at $z = 21$ mm.) Phase angle $\theta = 0^\circ$ corresponds to the rising-edge zero crossing of the local unsteady pressure. A total of 24 images on 15° spacing are shown. (See next page.) The magnitude scale is normalized by the peak value over all 24 images.

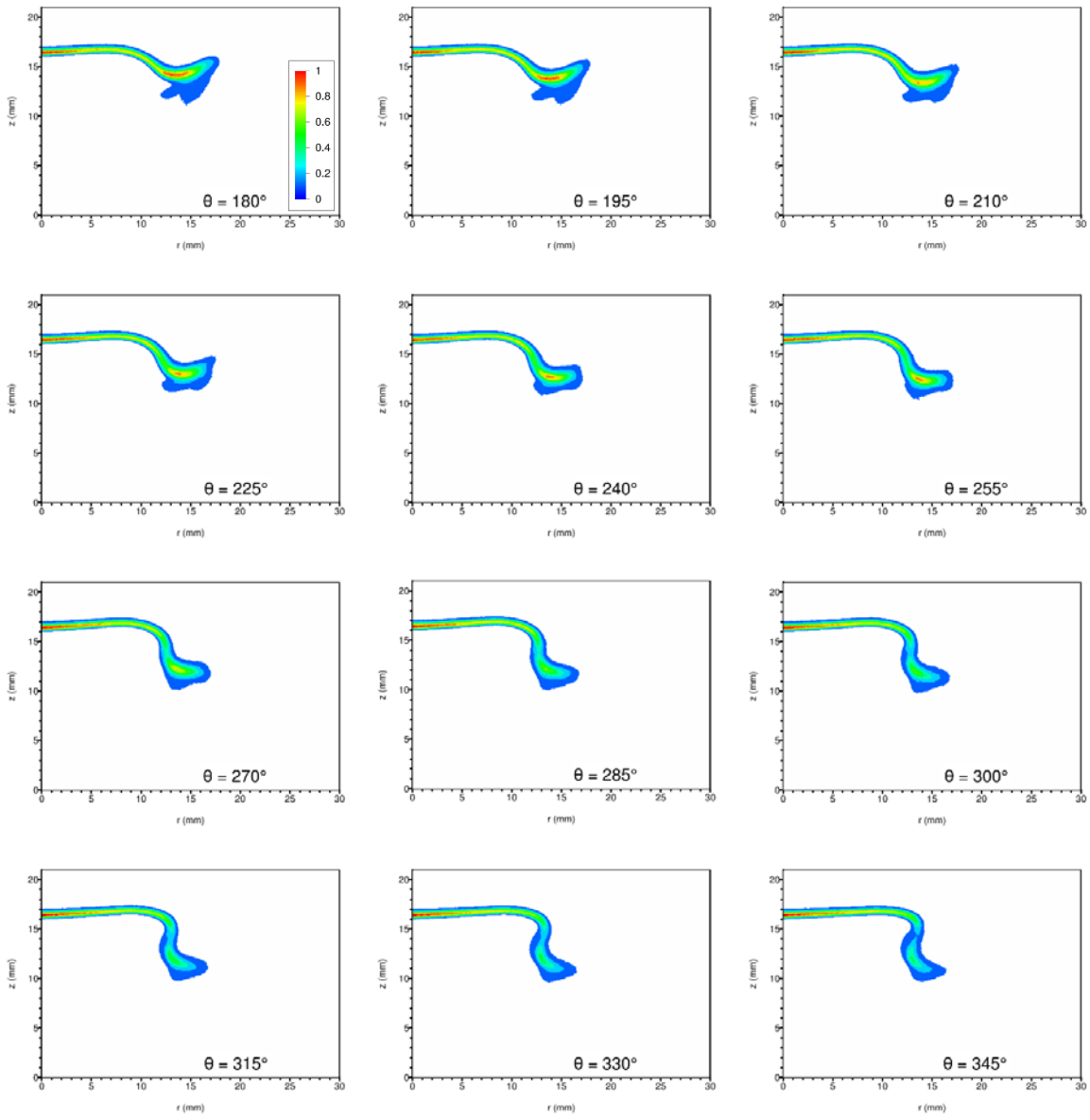


Figure H-57 (cont.): Phase-resolved OH-CH₂O PLIF combination images for acoustic forcing at 100 Hz. The horizontal axis is the radius (mm) from the centerline of the burner. The vertical axis is the distance (mm) above the nozzle exit plane. (The stagnation plane is located at *z* = 21mm.) Phase angle $\theta = 0^\circ$ corresponds to the rising-edge zero crossing of the local unsteady pressure. A total of 24 images on 15° spacing are shown. (See previous page.) The magnitude scale is normalized by the peak value over all 24 images.

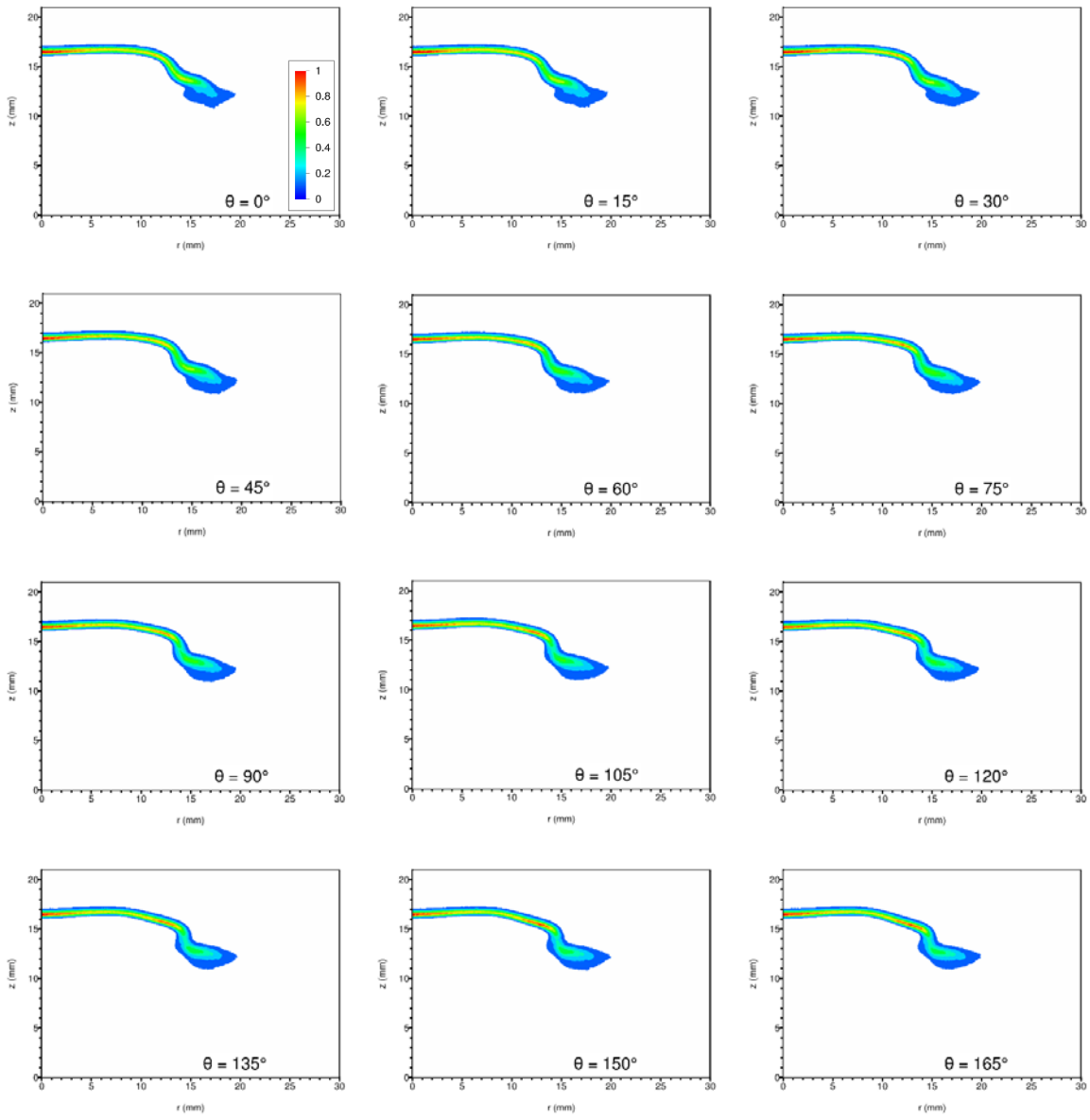


Figure H-58: Phase-resolved OH-CH₂O PLIF combination images for acoustic forcing at 150 Hz. The horizontal axis is the radius (mm) from the centerline of the burner. The vertical axis is the distance (mm) above the nozzle exit plane. (The stagnation plane is located at $z = 21\text{mm}$.) Phase angle $\theta = 0^\circ$ corresponds to the rising-edge zero crossing of the local unsteady pressure. A total of 24 images on 15° spacing are shown. (See next page.) The magnitude scale is normalized by the peak value over all 24 images.

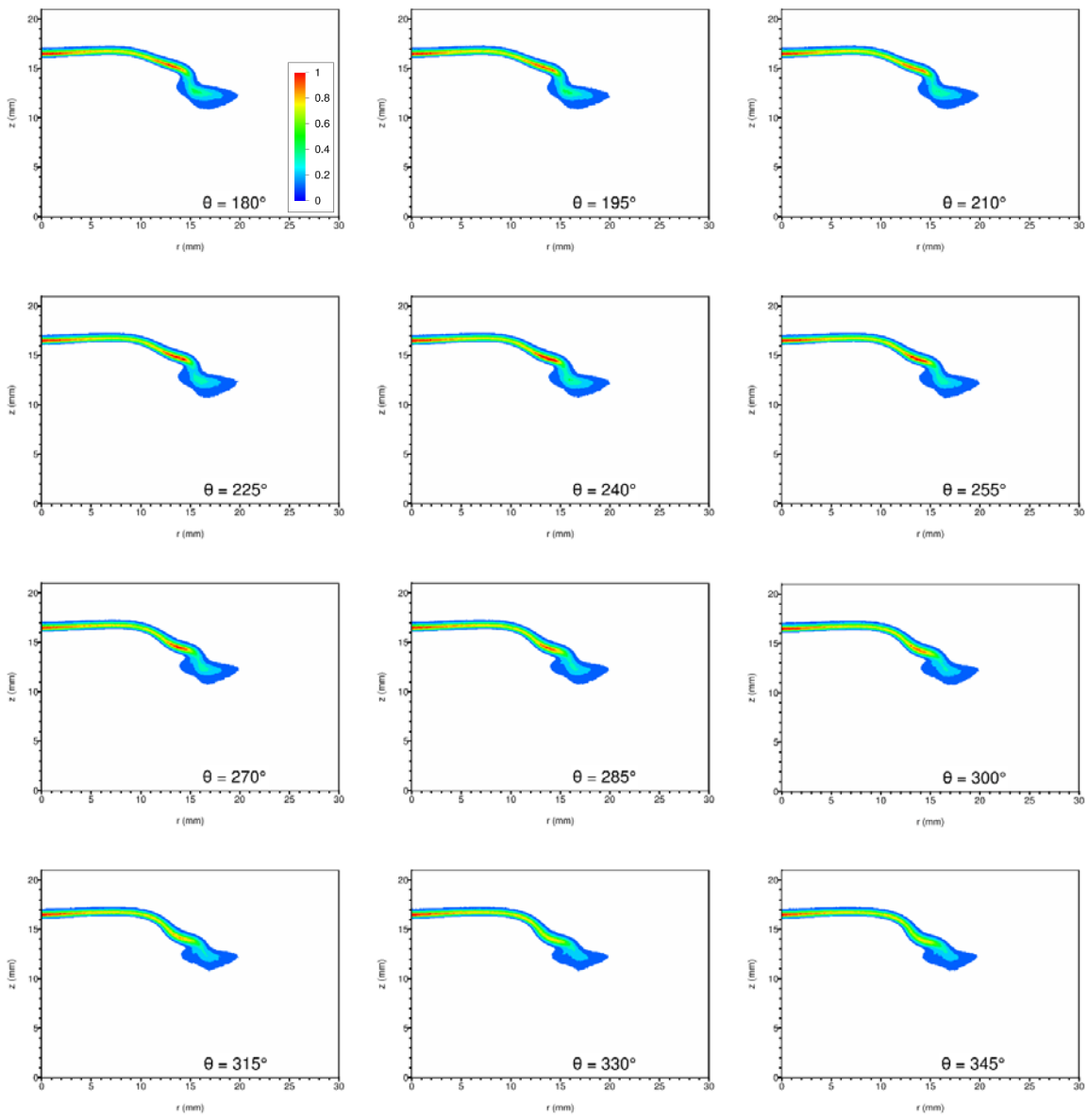


Figure H-58 (cont.): Phase-resolved OH-CH₂O PLIF combination images for acoustic forcing at 150 Hz. The horizontal axis is the radius (mm) from the centerline of the burner. The vertical axis is the distance (mm) above the nozzle exit plane. (The stagnation plane is located at $z = 21\text{mm}$.) Phase angle $\theta = 0^\circ$ corresponds to the rising-edge zero crossing of the local unsteady pressure. A total of 24 images on 15° spacing are shown. (See previous page.) The magnitude scale is normalized by the peak value over all 24 images.

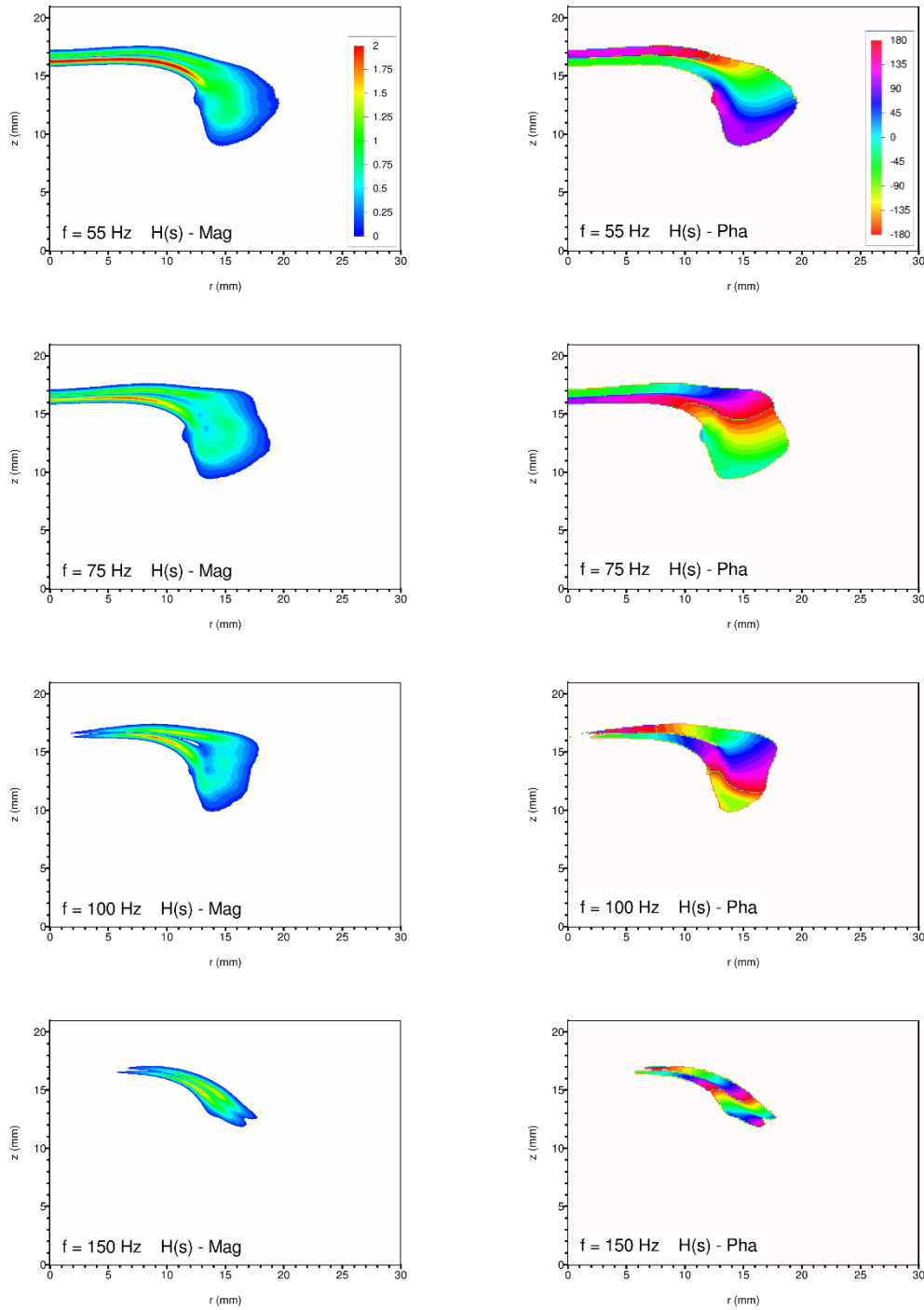


Figure H-59: Spatially resolved combustion response function produced from OH-CH₂O PLIF combination data. Magnitude plots appear in the left column while phase plots are shown on the right. Note that positive phase values correspond to I' lagging P'. The coordinate system origin is along the burner centerline at the nozzle exit plane. Data for the seven base drive frequencies are shown. (See next page.)

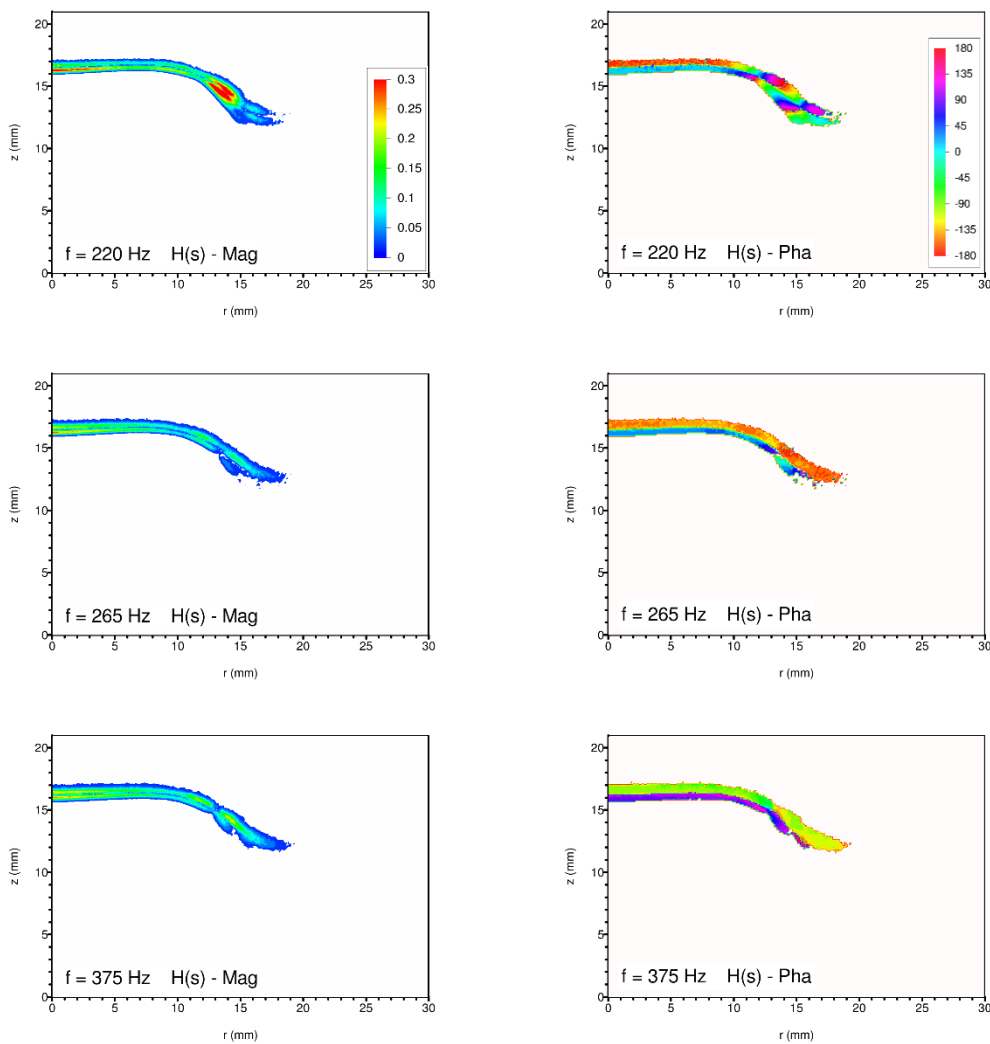


Figure H-59 (cont): Spatially resolved combustion response function produced from OH-CH₂O PLIF combination data. Magnitude plots appear in the left column while phase plots are shown on the right. Data for the seven base drive frequencies are shown. (See previous page.) Note the change in magnitude scale versus the plots for 150 Hz and lower frequencies.

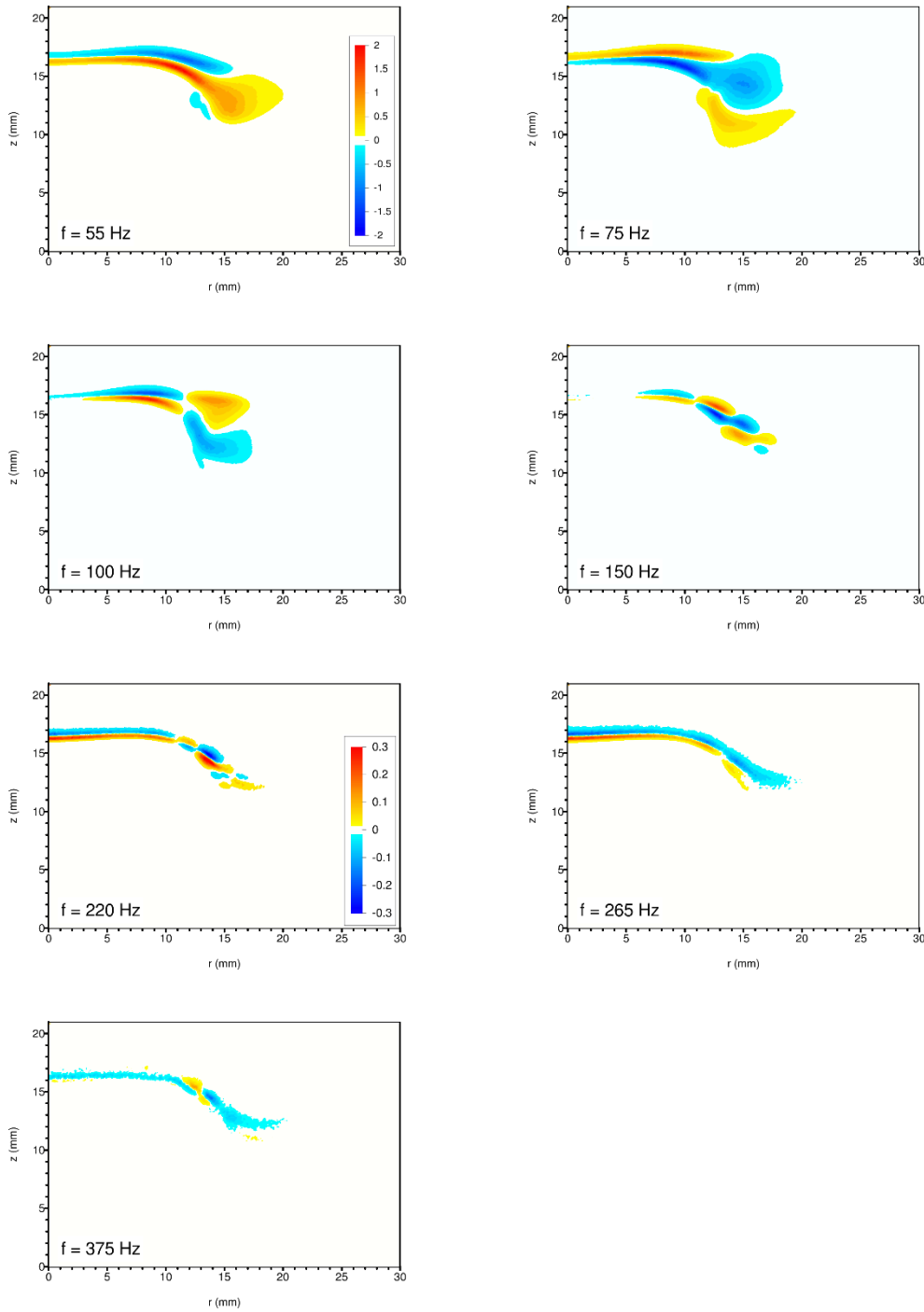


Figure H-60: Spatially resolved forced Rayleigh index produced from OH-CH₂O PLIF combination. Data for the seven base drive frequencies are shown. Plots for the four lower frequencies use the top magnitude legend. Plots for the three higher frequencies use the bottom magnitude legend.

H.2.5 Chemiluminescence Experimental Data

The following 19 pages present the relevant collected, spatially resolved chemiluminescence data. Images were collected using an Andor iStar ICCD camera coupled to a 50 mm, f/1.2, Nikon macro lens. A Semrock FF01-447/60-25 optical band-pass filter was installed to block all but the CH^* and CO_2^* chemiluminescence emission. The f-stop aperture on the lens was opened to its maximum position of f/1.2 in order to collect as much light as possible. The ICCD intensifier gate width was set to 10 μs achieve reasonable signal levels.

Further information regarding the processing of this data can be found in the beginning of this appendix as well as in chapter 4.

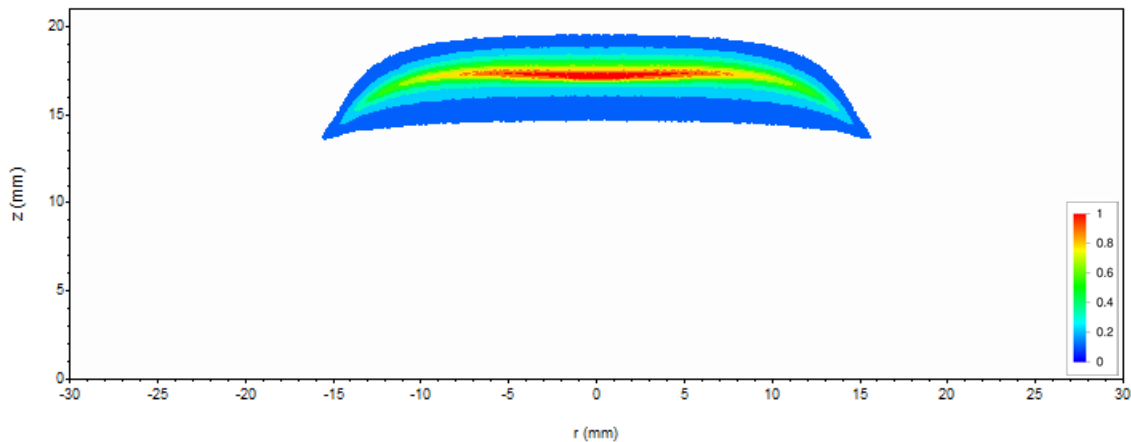


Figure H-61: Chemiluminescence image of flame under steady conditions (no acoustic forcing). Collected data appears on the left, and is mirrored across the centerline for a visual representation of entire flame. Burner centerline is at $r = 0$. Position $z = 0$ corresponds to the nozzle exit plane.

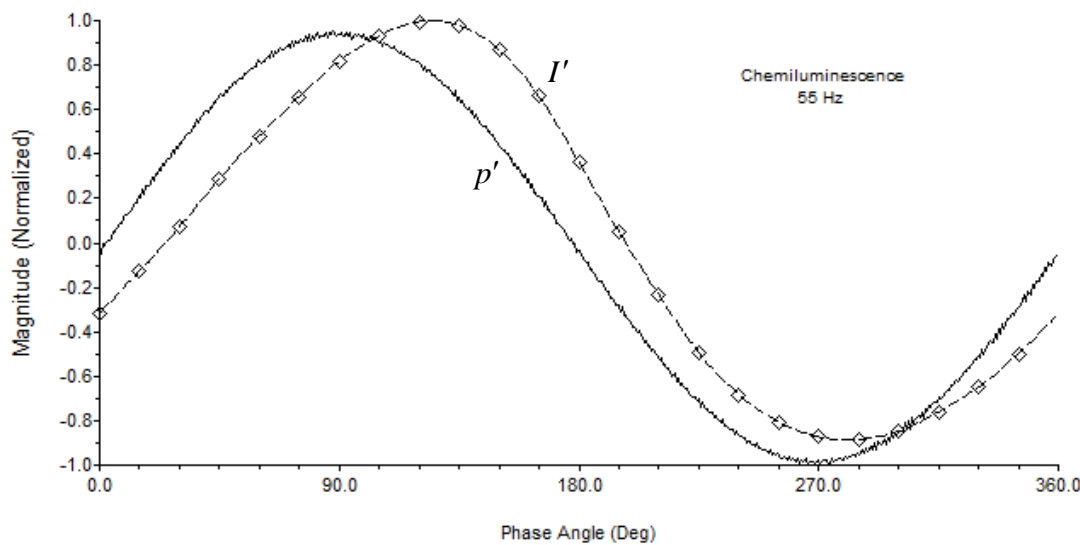


Figure H-62: Resulting waveforms from the 55 Hz chemiluminescence experiment (Experiment 668). The solid curve shows the measured acoustic waveform with the rising-edge zero crossing marking the zero-degree point. Diamonds represent total (fully integrated) intensity data points computed from the phase bins. The dashed curve is a periodic cubic spline fit to this data. Signals are normalized by their peak values.

Mode	Pressure (p')		Intensity (I')	
	Mag	Phase	Mag	Phase
1	1.0000	0.0	1.0000	21.7
2	0.0103	99.9	0.1168	-165.9
3	0.0038	110.5	0.0255	5.7
4	0.0016	71.9	0.0060	154.2
5	0.0006	-173.1	0.0022	-59.8
6	0.0006	-162.4	0.0010	129.2
7	0.0003	-120.4	0.0035	-65.2
8	0.0002	-104.0	0.0011	-127.8
9	0.0002	-62.3	0.0025	-36.9
10	0.0003	-0.4	0.0003	156.1
11	0.0003	21.3	0.0008	107.1

Table H-38: Harmonic content of the measured acoustic and intensity fields for the 55 Hz chemiluminescence case. The measured intensity is total (fully integrated). Magnitudes are normalized by the first mode values. All phases are in reference to the phase of the first acoustic mode. Sign convention is such that negative phases are leading while positive phases are lagging.

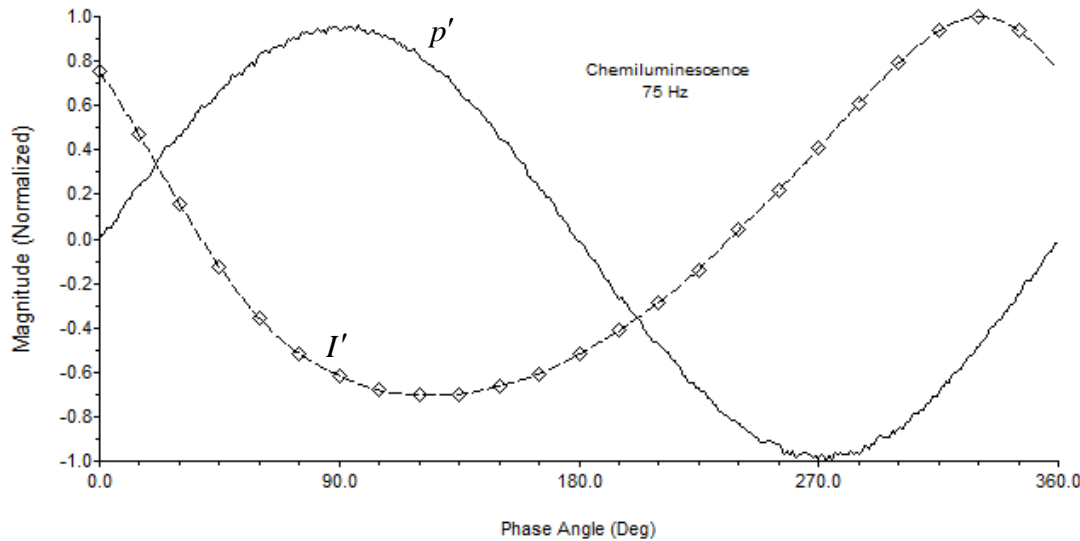


Figure H-63: Resulting waveforms from the 75 Hz chemiluminescence experiment (Experiment 667). The solid curve shows the measured acoustic waveform with the rising-edge zero crossing marking the zero-degree point. Diamonds represent total (fully integrated) intensity data points computed from the phase bins. The dashed curve is a periodic cubic spline fit to this data. Signals are normalized by their peak values.

Mode	Pressure (p')		Intensity (I')	
	Mag	Phase	Mag	Phase
1	1.0000	0.0	1.0000	-131.9
2	0.0050	-65.2	0.2039	-138.8
3	0.0078	-137.1	0.0511	-138.2
4	0.0018	104.9	0.0113	-145.5
5	0.0009	85.5	0.0020	156.2
6	0.0008	93.9	0.0003	166.8
7	0.0012	5.6	0.0018	169.1
8	0.0004	104.5	0.0008	-4.6
9	0.0010	63.9	0.0020	-74.5
10	0.0008	-87.8	0.0003	-60.2
11	0.0006	160.3	0.0006	113.6

Table H-39: Harmonic content of the measured acoustic and intensity fields for the 75 Hz chemiluminescence case. The measured intensity is total (fully integrated). Magnitudes are normalized by the first mode values. All phases are in reference to the phase of the first acoustic mode. Sign convention is such that negative phases are leading while positive phases are lagging.

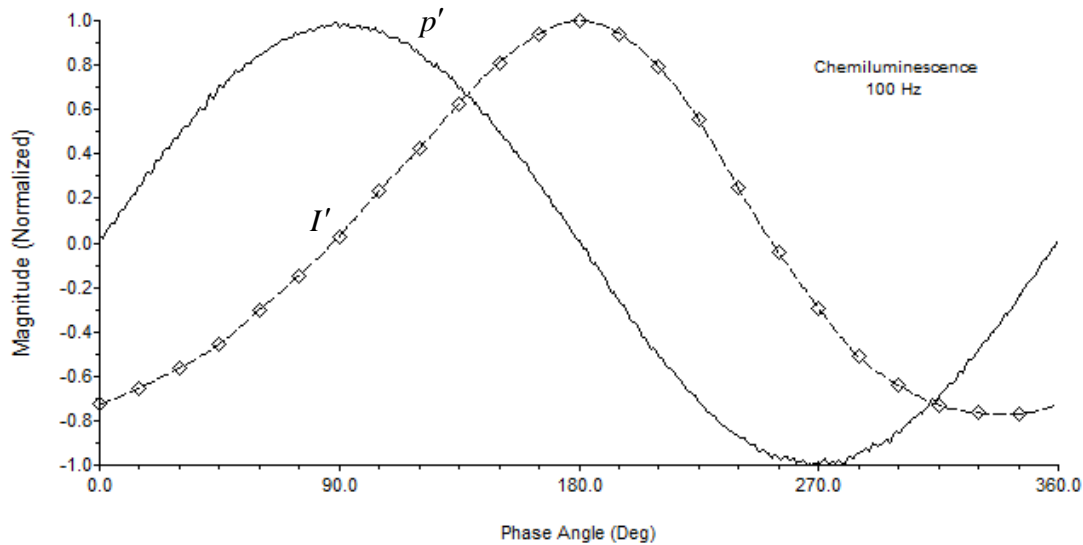


Figure H-64: Resulting waveforms from the 100 Hz chemiluminescence experiment (Experiment 669). The solid curve shows the measured acoustic waveform with the rising-edge zero crossing marking the zero-degree point. Diamonds represent total (fully integrated) intensity data points computed from the phase bins. The dashed curve is a periodic cubic spline fit to this data. Signals are normalized by their peak values.

Mode	Pressure (p')		Intensity (I')	
	Mag	Phase	Mag	Phase
1	1.0000	0.0	1.0000	80.1
2	0.0113	-147.6	0.1670	-69.4
3	0.0032	46.8	0.0277	141.5
4	0.0014	-106.7	0.0047	-8.6
5	0.0008	99.3	0.0020	-3.0
6	0.0009	-133.6	0.0010	53.7
7	0.0006	-132.6	0.0042	-6.6
8	0.0008	-74.4	0.0011	-52.7
9	0.0009	117.1	0.0048	115.1
10	0.0008	-69.3	0.0011	-30.1
11	0.0010	175.8	0.0015	-51.0

Table H-40: Harmonic content of the measured acoustic and intensity fields for the 100 Hz chemiluminescence case. The measured intensity is total (fully integrated). Magnitudes are normalized by the first mode values. All phases are in reference to the phase of the first acoustic mode. Sign convention is such that negative phases are leading while positive phases are lagging.

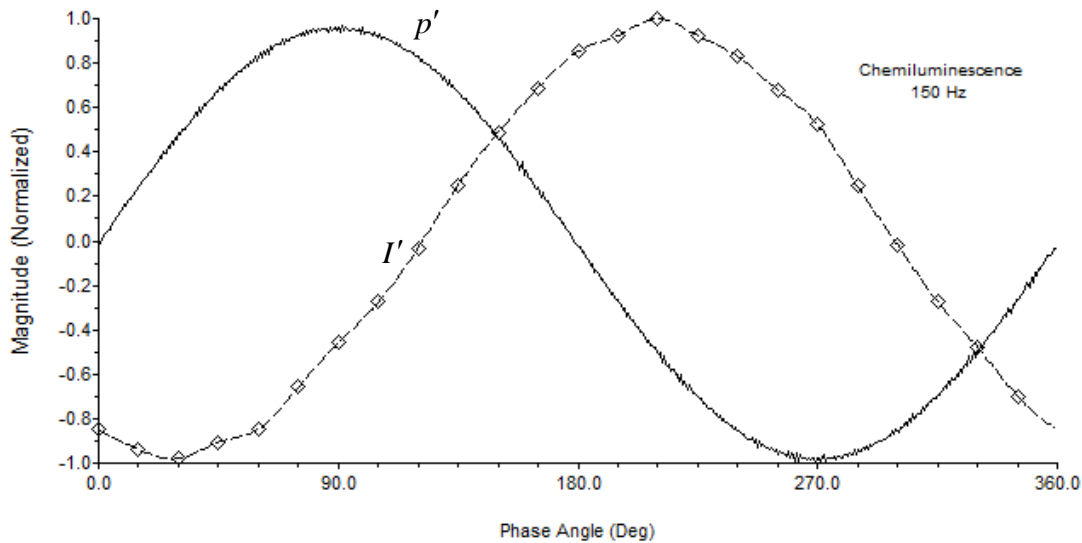


Figure H-65: Resulting waveforms from the 150 Hz chemiluminescence experiment (Experiment 670). The solid curve shows the measured acoustic waveform with the rising-edge zero crossing marking the zero-degree point. Diamonds represent total (fully integrated) intensity data points computed from the phase bins. The dashed curve is a periodic cubic spline fit to this data. Signals are normalized by their peak values.

Mode	Pressure (p')		Intensity (I')	
	Mag	Phase	Mag	Phase
1	1.0000	0.0	1.0000	119.9
2	0.0020	95.4	0.0087	14.5
3	0.0009	-26.2	0.0088	77.2
4	0.0007	70.3	0.0083	-130.6
5	0.0004	74.1	0.0055	-128.9
6	0.0005	28.0	0.0132	88.5
7	0.0005	31.8	0.0015	69.5
8	0.0003	44.1	0.0079	-106.1
9	0.0005	33.6	0.0065	-13.5
10	0.0003	-17.7	0.0017	0.9
11	0.0003	-4.2	0.0075	35.3

Table H-41: Harmonic content of the measured acoustic and intensity fields for the 150 Hz chemiluminescence case. The measured intensity is total (fully integrated). Magnitudes are normalized by the first mode values. All phases are in reference to the phase of the first acoustic mode. Sign convention is such that negative phases are leading while positive phases are lagging.

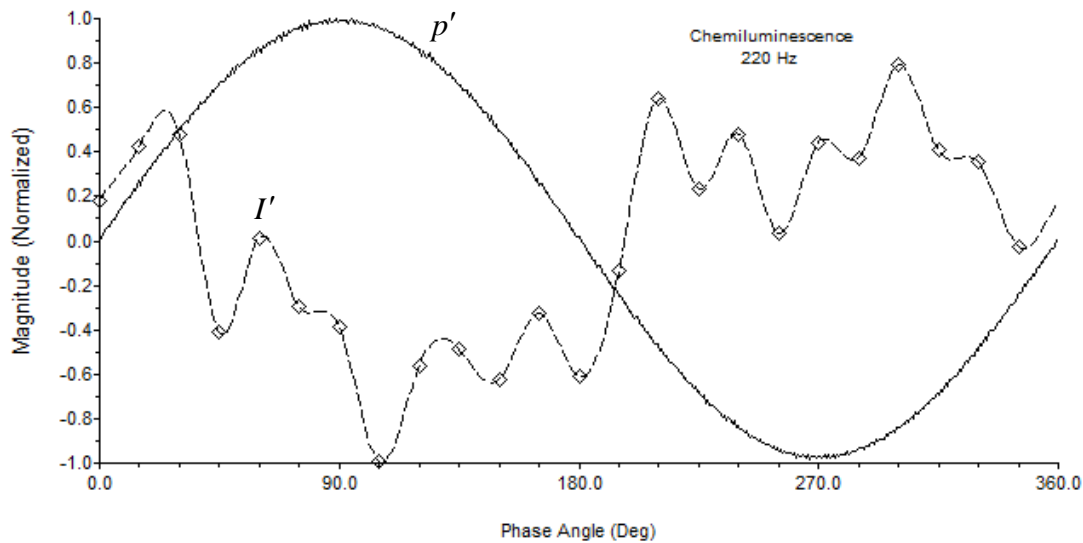


Figure H-66: Resulting waveforms from the 220 Hz chemiluminescence experiment (Experiment 671). The solid curve shows the measured acoustic waveform with the rising-edge zero crossing marking the zero-degree point. Diamonds represent total (fully integrated) intensity data points computed from the phase bins. The dashed curve is a periodic cubic spline fit to this data. Signals are normalized by their peak values.

Mode	Pressure (p')		Intensity (I')	
	Mag	Phase	Mag	Phase
1	1.0000	0.0	1.0000	-150.3
2	0.0005	-6.3	0.2871	-9.0
3	0.0005	160.1	0.0611	91.3
4	0.0002	61.0	0.2821	48.3
5	0.0001	47.7	0.2914	-55.6
6	0.0002	-175.2	0.1913	29.1
7	0.0002	147.7	0.1328	36.3
8	0.0001	47.3	0.1715	127.6
9	0.0000	-7.8	0.0852	-19.6
10	0.0000	-73.9	0.1850	131.9
11	0.0000	-24.5	0.0727	-64.6

Table H-42: Harmonic content of the measured acoustic and intensity fields for the 220 Hz chemiluminescence case. The measured intensity is total (fully integrated). Magnitudes are normalized by the first mode values. All phases are in reference to the phase of the first acoustic mode. Sign convention is such that negative phases are leading while positive phases are lagging.

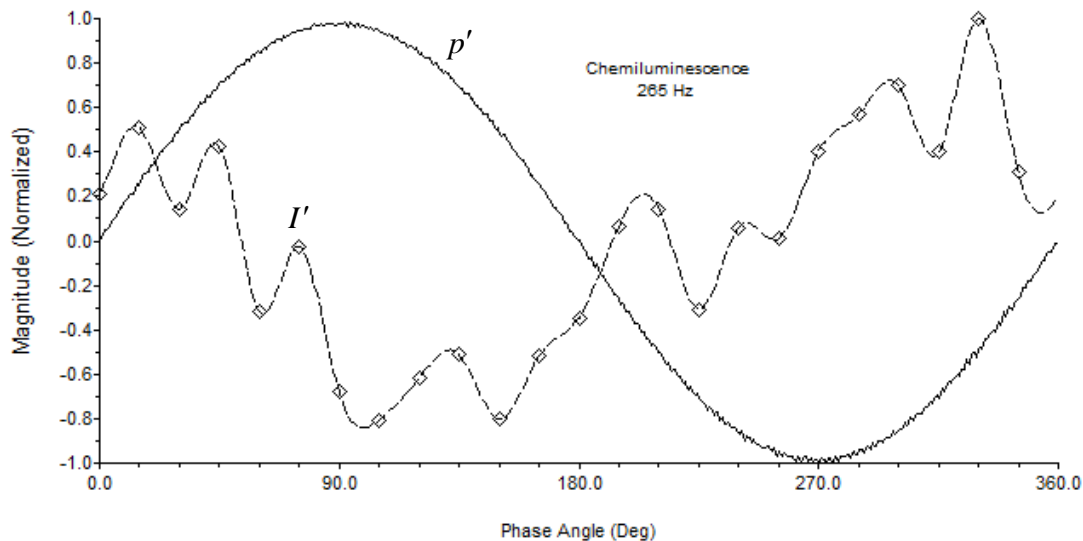


Figure H-67: Resulting waveforms from the 265 Hz chemiluminescence experiment (Experiment 673). The solid curve shows the measured acoustic waveform with the rising-edge zero crossing marking the zero-degree point. Diamonds represent total (fully integrated) intensity data points computed from the phase bins. The dashed curve is a periodic cubic spline fit to this data. Signals are normalized by their peak values.

Mode	Pressure (p')		Intensity (I')	
	Mag	Phase	Mag	Phase
1	1.0000	0.0	1.0000	-133.5
2	0.0032	-121.3	0.1560	-62.9
3	0.0041	2.3	0.2170	94.1
4	0.0005	91.2	0.1370	30.9
5	0.0004	-9.0	0.1529	176.1
6	0.0002	49.3	0.1263	33.7
7	0.0002	-93.6	0.1320	95.3
8	0.0004	29.0	0.0813	79.3
9	0.0004	-64.3	0.1864	-32.0
10	0.0002	-29.9	0.1016	3.7
11	0.0003	-158.1	0.1664	4.7

Table H-43: Harmonic content of the measured acoustic and intensity fields for the 265 Hz chemiluminescence case. The measured intensity is total (fully integrated). Magnitudes are normalized by the first mode values. All phases are in reference to the phase of the first acoustic mode. Sign convention is such that negative phases are leading while positive phases are lagging.

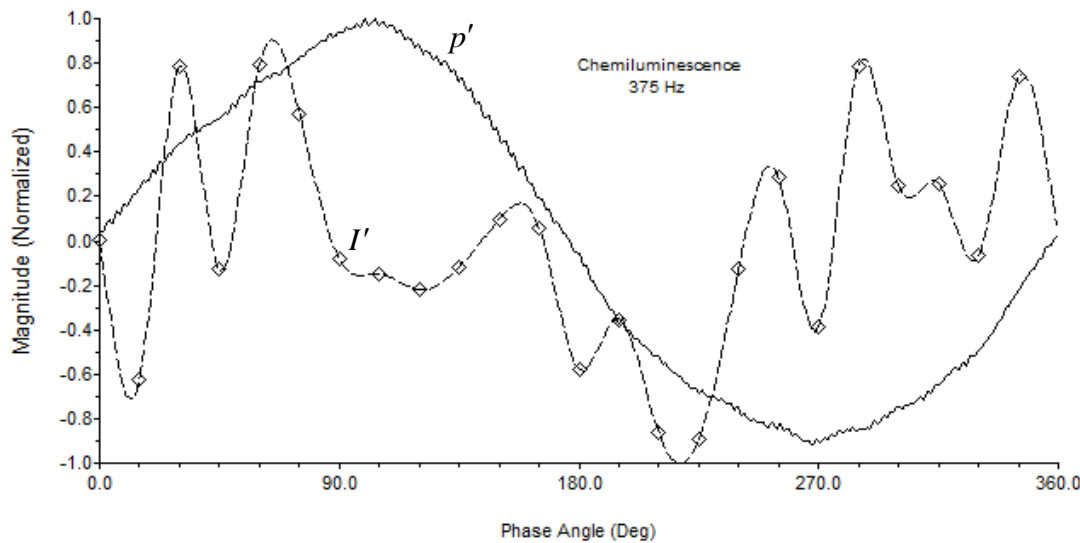


Figure H-68: Resulting waveforms from the 375 Hz chemiluminescence experiment (Experiment 674). The solid curve shows the measured acoustic waveform with the rising-edge zero crossing marking the zero-degree point. Diamonds represent total (fully integrated) intensity data points computed from the phase bins. The dashed curve is a periodic cubic spline fit to this data. Signals are normalized by their peak values.

Mode	Pressure (p')		Intensity (I')	
	Mag	Phase	Mag	Phase
1	1.0000	0.0	1.0000	-76.1
2	0.0609	143.9	0.5768	127.5
3	0.0569	-72.3	0.6420	54.5
4	0.0122	-17.4	0.5645	-175.8
5	0.0131	-6.1	0.1685	-139.1
6	0.0083	-125.0	0.1766	-121.6
7	0.0063	-161.4	0.5177	167.2
8	0.0020	-113.4	0.6909	110.4
9	0.0044	101.7	0.3240	-157.6
10	0.0090	-159.8	0.4844	-157.9
11	0.0014	-172.8	0.3770	-154.7

Table H-44: Harmonic content of the measured acoustic and intensity fields for the 375 Hz chemiluminescence case. The measured intensity is total (fully integrated). Magnitudes are normalized by the first mode values. All phases are in reference to the phase of the first acoustic mode. Sign convention is such that negative phases are leading while positive phases are lagging.

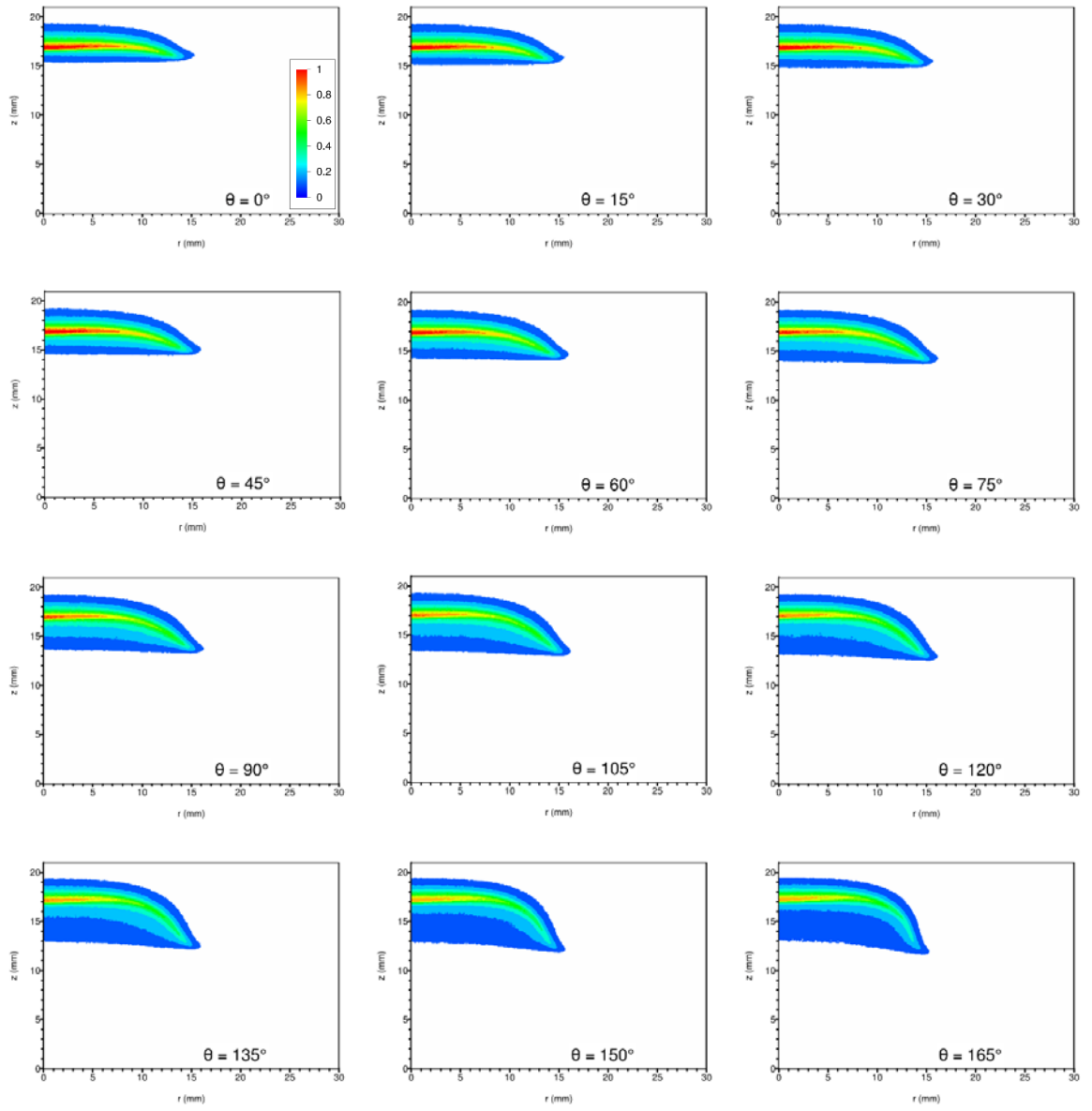


Figure H-69: Phase-resolved chemiluminescence images for acoustic forcing at 55 Hz. The horizontal axis is the radius (mm) from the centerline of the burner. The vertical axis is the distance (mm) above the nozzle exit plane. (The stagnation plane is located at $z = 21\text{mm}$.) Phase angle $\theta = 0^\circ$ corresponds to the rising-edge zero crossing of the local unsteady pressure. Data from experiment 668. A total of 24 images on 15° spacing are shown. (See next page.) The magnitude scale is normalized by the peak value over all 24 images.

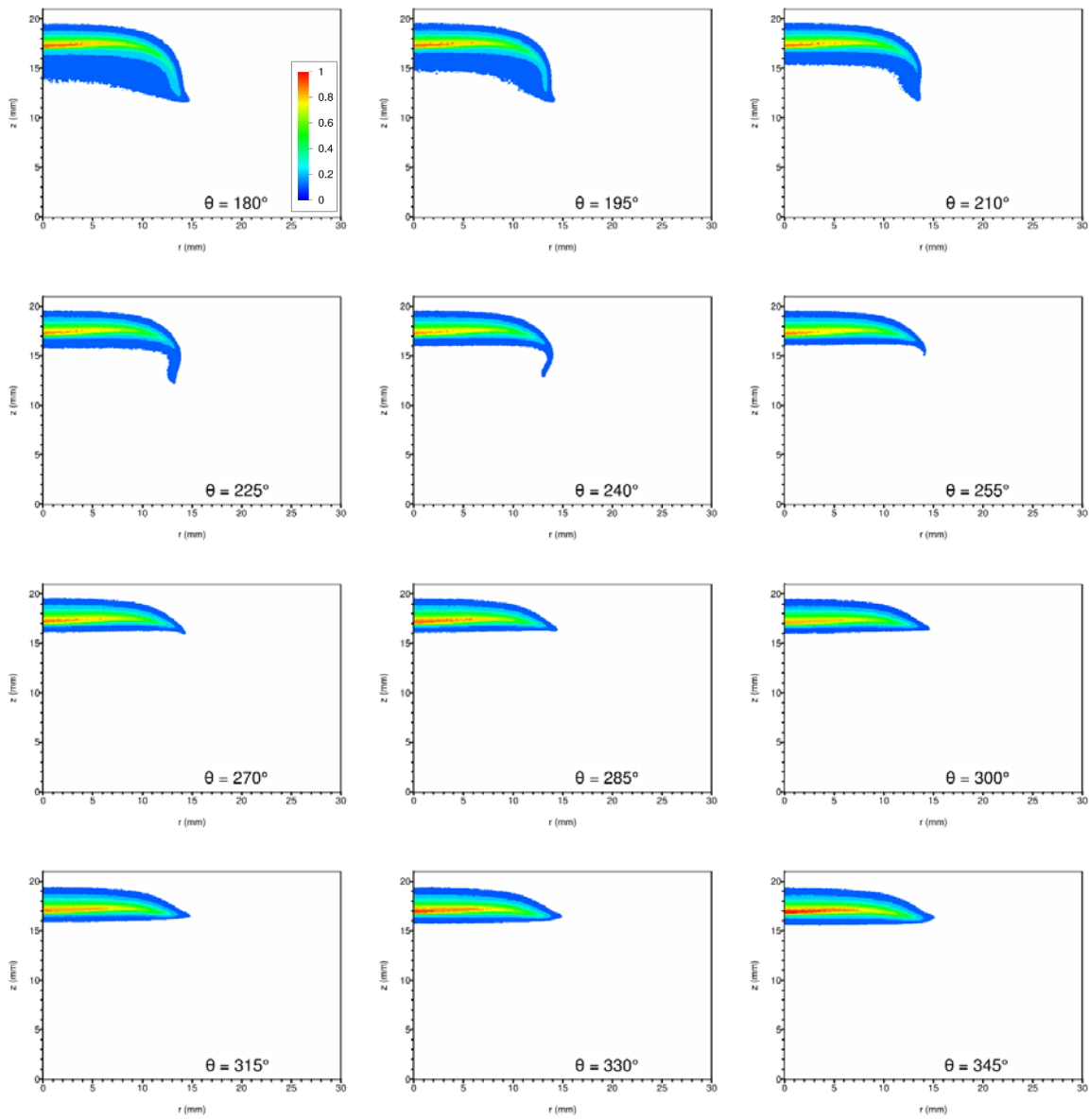


Figure H-69 (cont.): Phase-resolved chemiluminescence images for acoustic forcing at 55 Hz. The horizontal axis is the radius (mm) from the centerline of the burner. The vertical axis is the distance (mm) above the nozzle exit plane. (The stagnation plane is located at $z = 21\text{mm}$.) Phase angle $\theta = 0^\circ$ corresponds to the rising-edge zero crossing of the local unsteady pressure. Data from experiment 668. A total of 24 images on 15° spacing are shown. (See previous page.) The magnitude scale is normalized by the peak value over all 24 images.

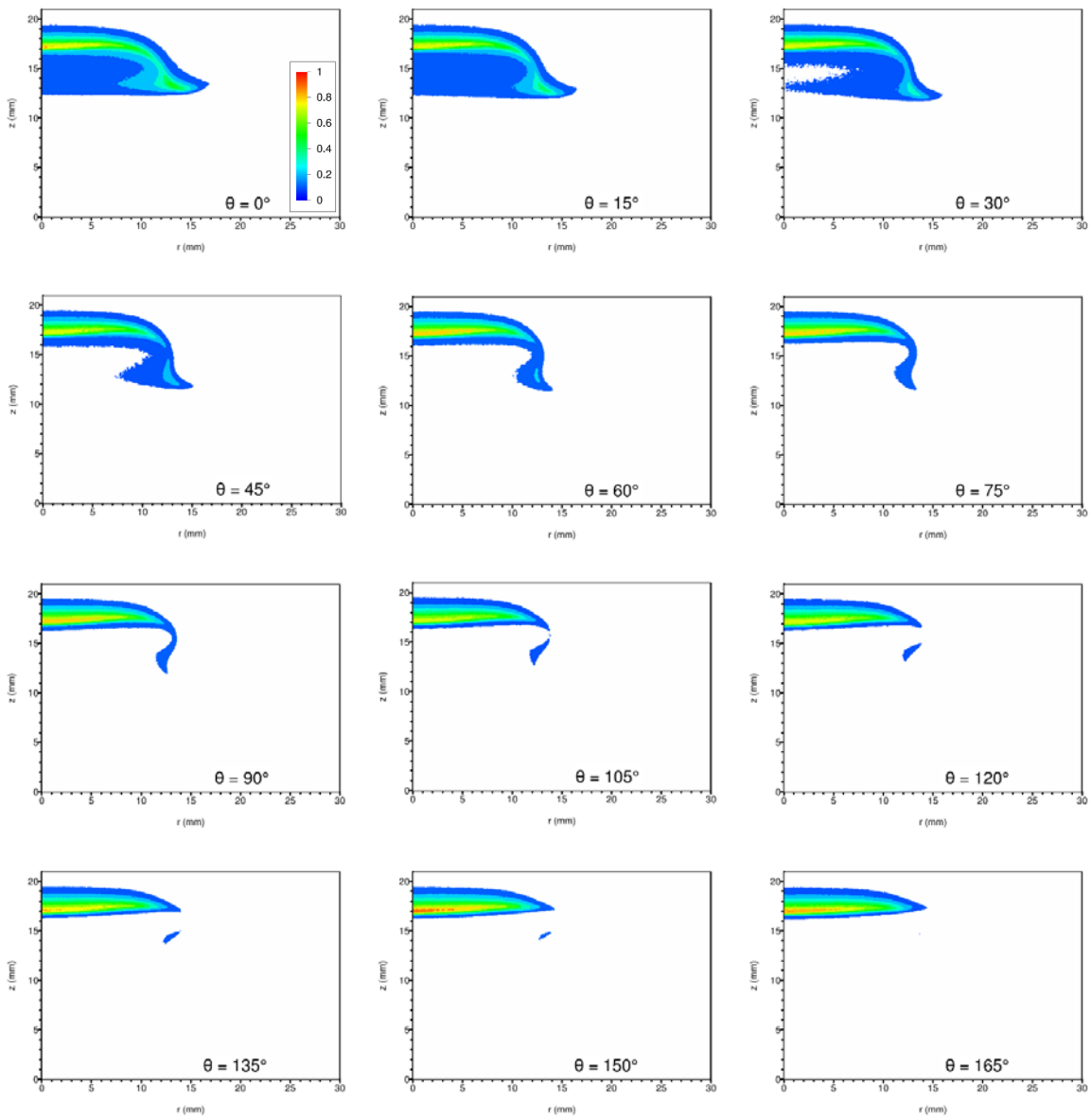


Figure H-70: Phase-resolved chemiluminescence images for acoustic forcing at 75 Hz. The horizontal axis is the radius (mm) from the centerline of the burner. The vertical axis is the distance (mm) above the nozzle exit plane. (The stagnation plane is located at $z = 21\text{mm}$.) Phase angle $\theta = 0^\circ$ corresponds to the rising-edge zero crossing of the local unsteady pressure. Data from experiment 667. A total of 24 images on 15° spacing are shown. (See next page.) The magnitude scale is normalized by the peak value over all 24 images.

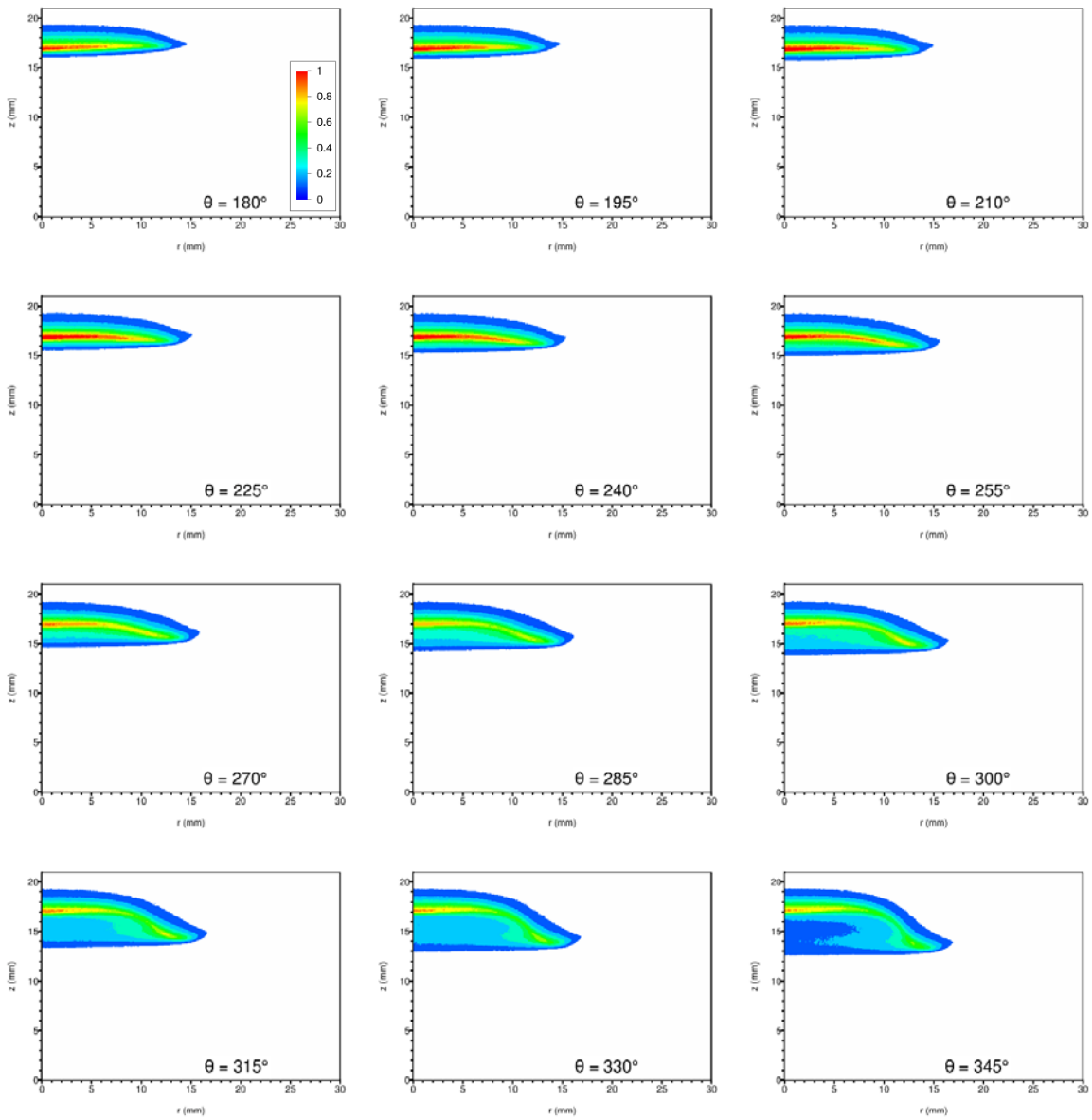


Figure H-70 (cont.): Phase-resolved chemiluminescence images for acoustic forcing at 75 Hz. The horizontal axis is the radius (mm) from the centerline of the burner. The vertical axis is the distance (mm) above the nozzle exit plane. (The stagnation plane is located at $z = 21\text{mm}$.) Phase angle $\theta = 0^\circ$ corresponds to the rising-edge zero crossing of the local unsteady pressure. Data from experiment 667. A total of 24 images on 15° spacing are shown. (See previous page.) The magnitude scale is normalized by the peak value over all 24 images.

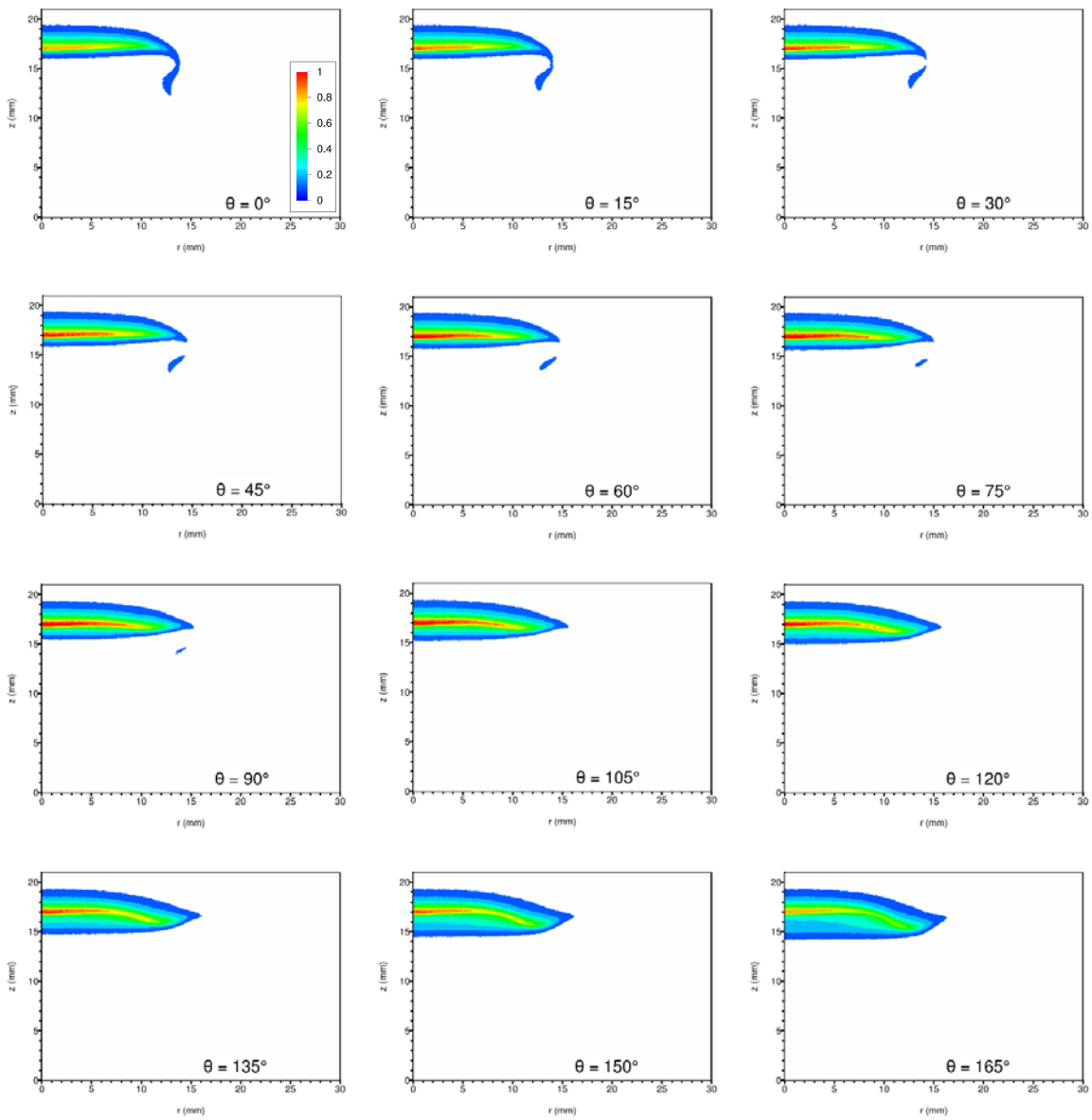


Figure H-71: Phase-resolved chemiluminescence images for acoustic forcing at 100 Hz. The horizontal axis is the radius (mm) from the centerline of the burner. The vertical axis is the distance (mm) above the nozzle exit plane. (The stagnation plane is located at $z = 21\text{mm}$.) Phase angle $\theta = 0^\circ$ corresponds to the rising-edge zero crossing of the local unsteady pressure. Data from experiment 669. A total of 24 images on 15° spacing are shown. (See next page.) The magnitude scale is normalized by the peak value over all 24 images.

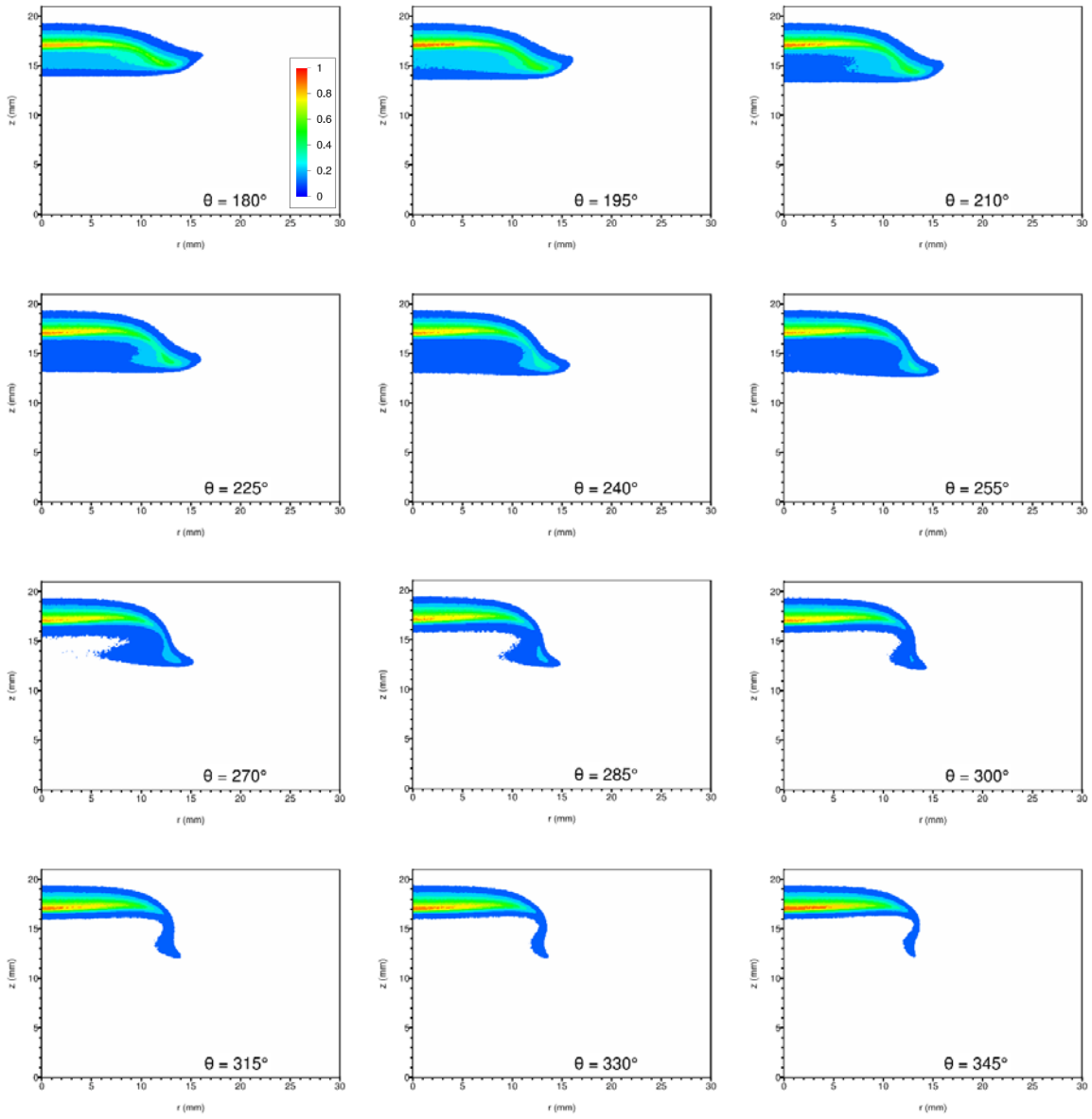


Figure H-71 (cont.): Phase-resolved chemiluminescence images for acoustic forcing at 100 Hz. The horizontal axis is the radius (mm) from the centerline of the burner. The vertical axis is the distance (mm) above the nozzle exit plane. (The stagnation plane is located at $z = 21\text{mm}$.) Phase angle $\theta = 0^\circ$ corresponds to the rising-edge zero crossing of the local unsteady pressure. Data from experiment 669. A total of 24 images on 15° spacing are shown. (See previous page.) The magnitude scale is normalized by the peak value over all 24 images.

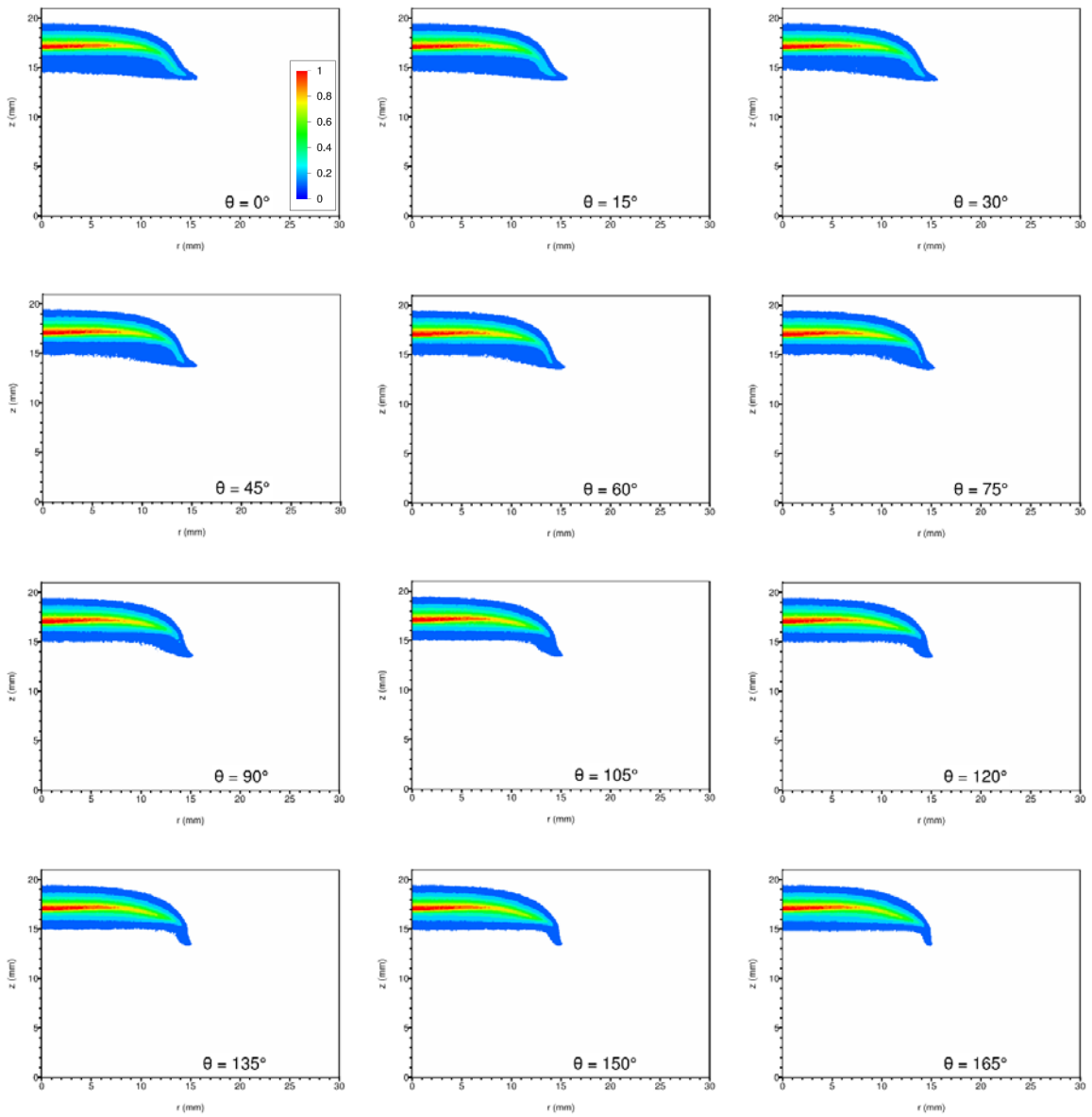


Figure H-72: Phase-resolved chemiluminescence images for acoustic forcing at 150 Hz. The horizontal axis is the radius (mm) from the centerline of the burner. The vertical axis is the distance (mm) above the nozzle exit plane. (The stagnation plane is located at $z = 21\text{mm}$.) Phase angle $\theta = 0^\circ$ corresponds to the rising-edge zero crossing of the local unsteady pressure. Data from experiment 670. A total of 24 images on 15° spacing are shown. (See next page.) The magnitude scale is normalized by the peak value over all 24 images.

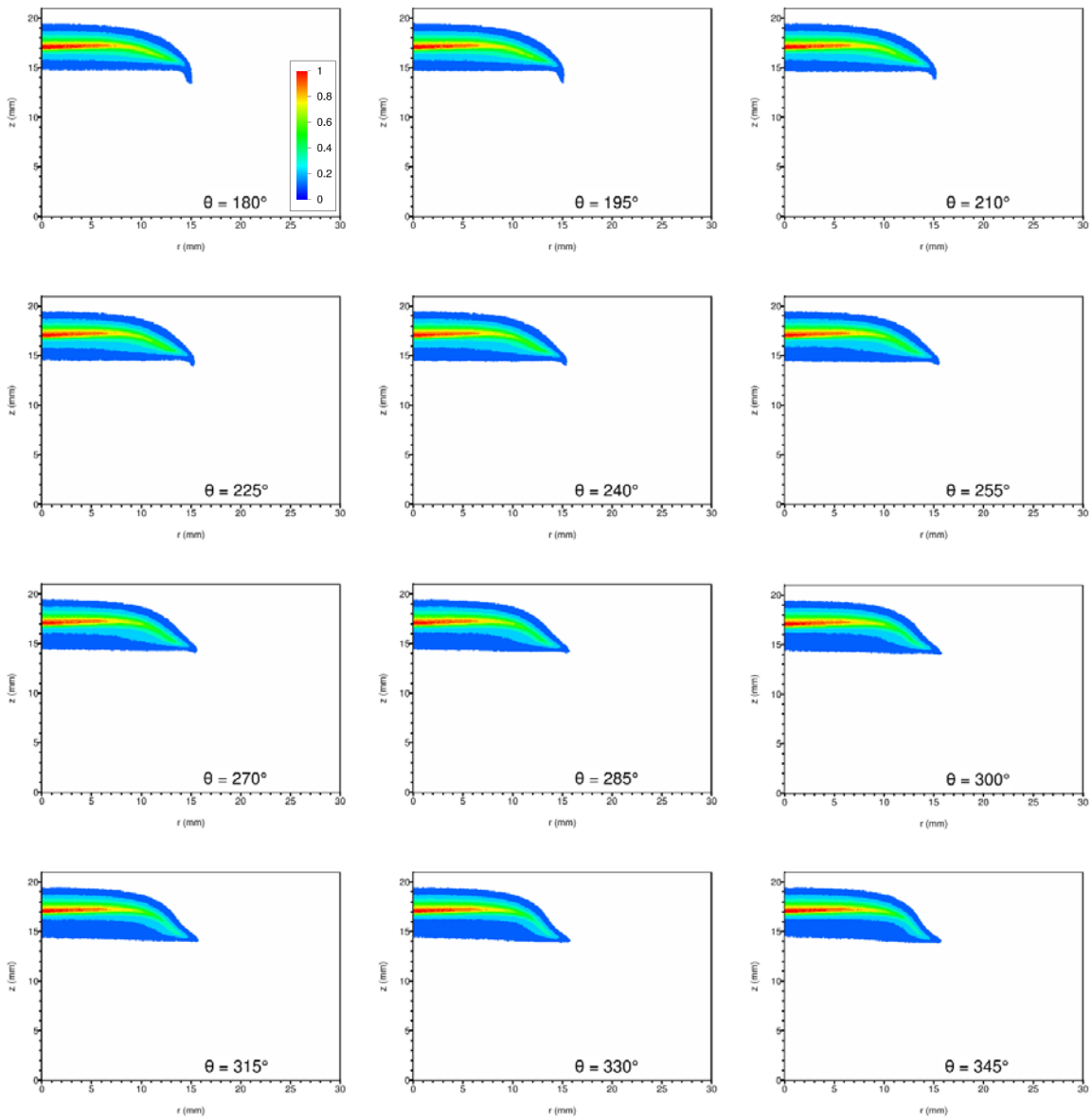


Figure H-72 (cont.): Phase-resolved chemiluminescence images for acoustic forcing at 150 Hz. The horizontal axis is the radius (mm) from the centerline of the burner. The vertical axis is the distance (mm) above the nozzle exit plane. (The stagnation plane is located at $z = 21\text{mm}$.) Phase angle $\theta = 0^\circ$ corresponds to the rising-edge zero crossing of the local unsteady pressure. Data from experiment 670. A total of 24 images on 15° spacing are shown. (See previous page.) The magnitude scale is normalized by the peak value over all 24 images.

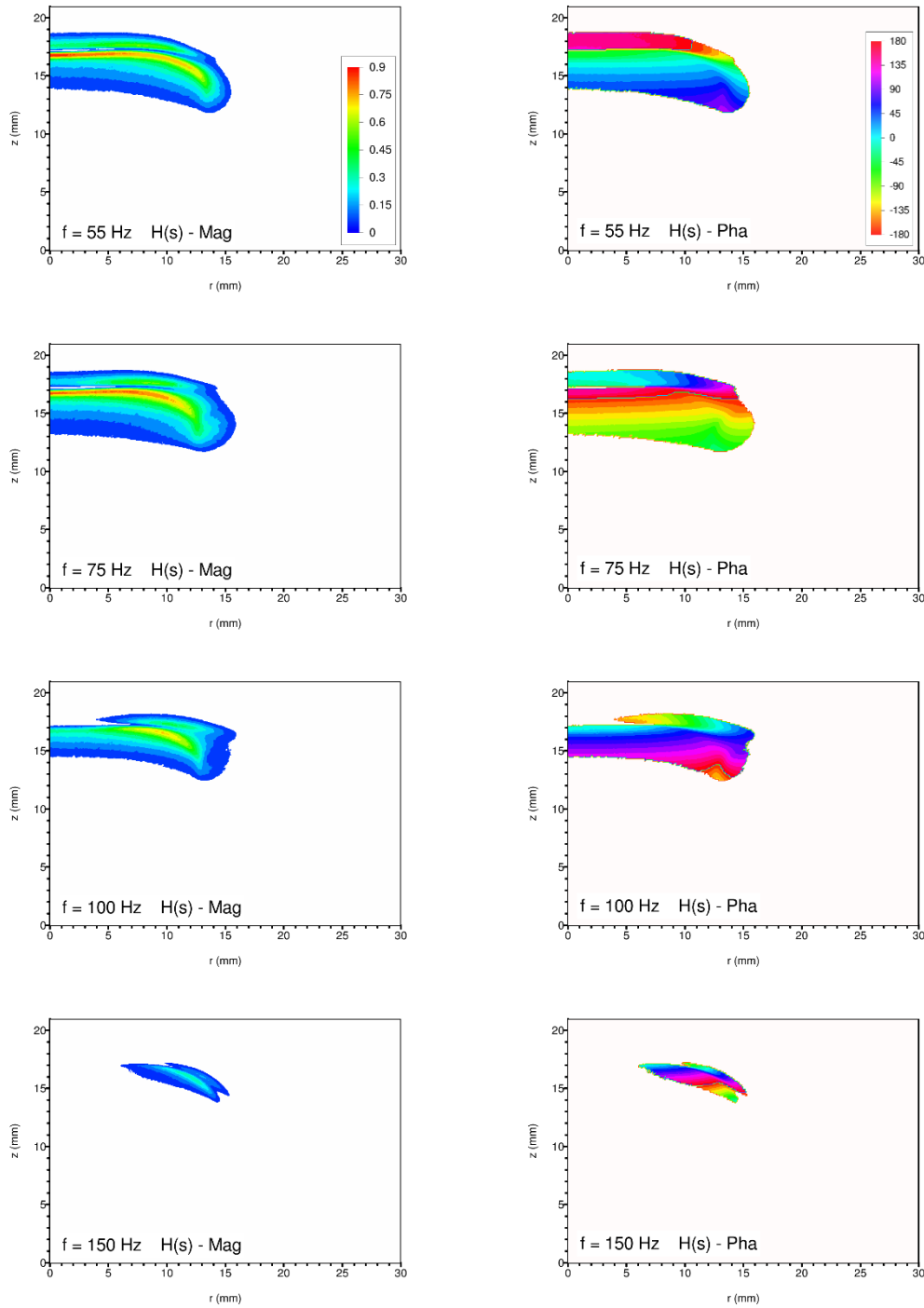


Figure H-73: Spatially resolved combustion response function produced from chemiluminescence data. Magnitude plots appear in the left column while phase plots are shown on the right. Note that positive phase values correspond to I' lagging P' . The coordinate system origin is along the burner centerline at the nozzle exit plane. Data for the seven base drive frequencies are shown. (See next page.)

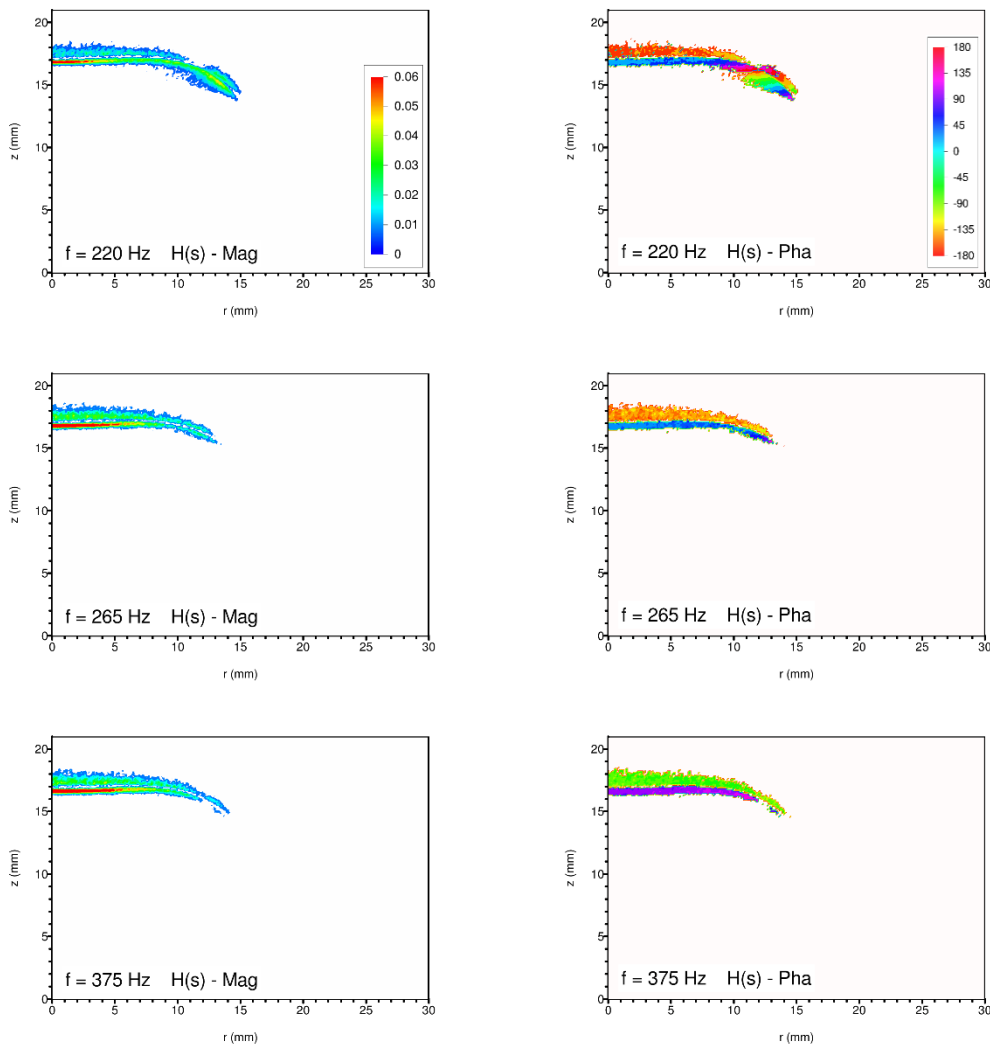


Figure H-73 (cont.): Spatially resolved combustion response function produced from chemiluminescence data. Magnitude plots appear in the left column while phase plots are shown on the right. Data for the seven base drive frequencies are shown. (See previous page.) Note the change in magnitude scale versus the plots for 150 Hz and lower frequencies.

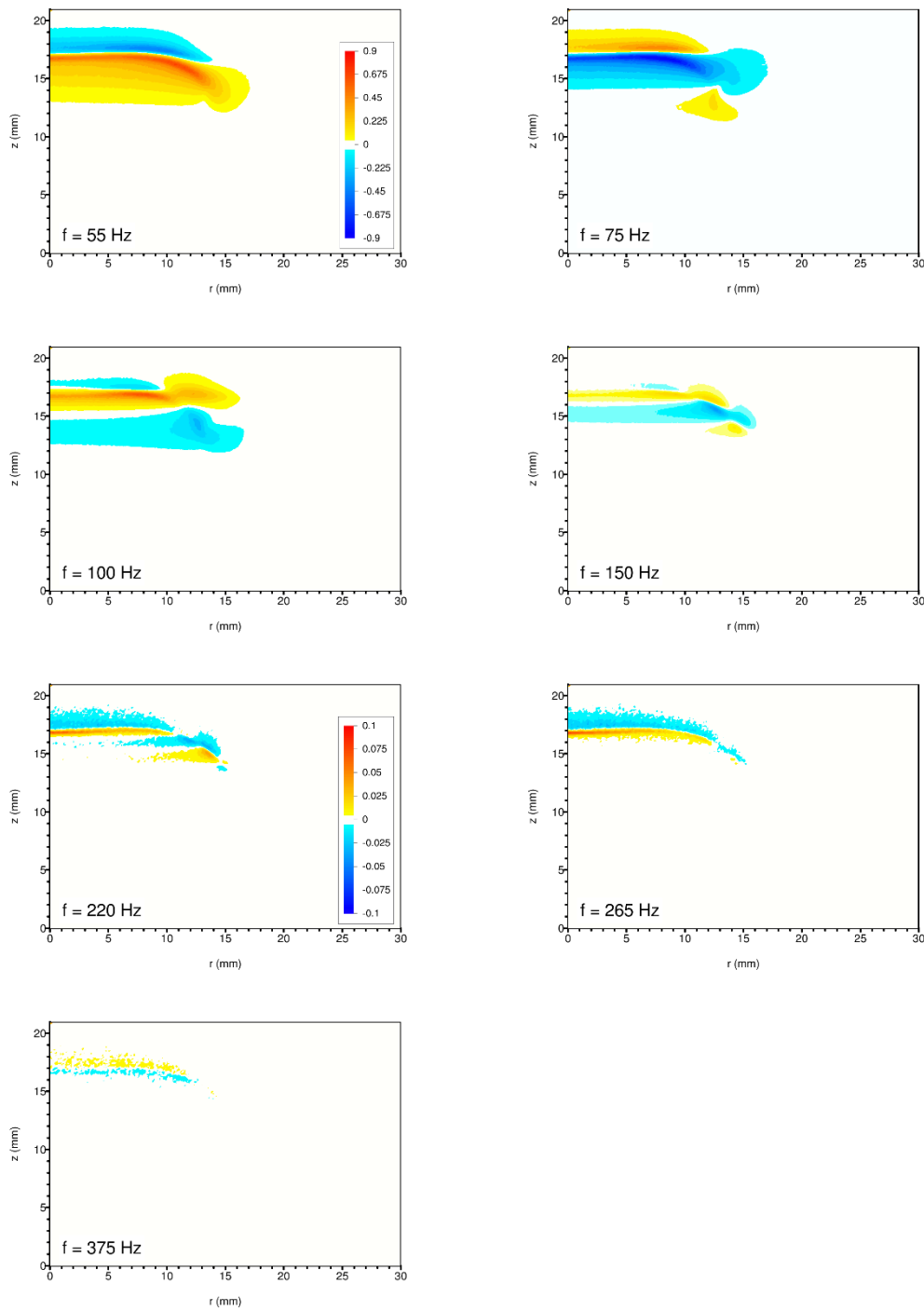


Figure H-74: Spatially resolved forced Rayleigh index produced from chemiluminescence data. Data for the seven base drive frequencies are shown. Plots for the four lower frequencies use the top magnitude legend. Plots for the three higher frequencies use the bottom magnitude legend.

H.2.6 Acetone PLIF Experimental Data

The following 15 pages present the relevant collected Acetone PLIF data. Images were collected using an Andor iStar ICCD camera coupled to a 94 mm, f/4.1, EADS-Sodern UV lens. Optical pumping of the acetone seeded flow was performed at an OPO output wavelength of ~ 277 nm. Image data was collected and processed using the techniques described in chapter 4. For the acetone PLIF data, only two of the three image correction methods were employed:

- i) Correction for the shot-to-shot variation in OPO output intensity.
- ii) Correction for the spatial variation in laser sheet intensity in the vertical direction.

Correction for laser sheet absorption was not necessary.

Further information regarding the processing of this data can be found in the beginning of this appendix as well as in chapter 4.

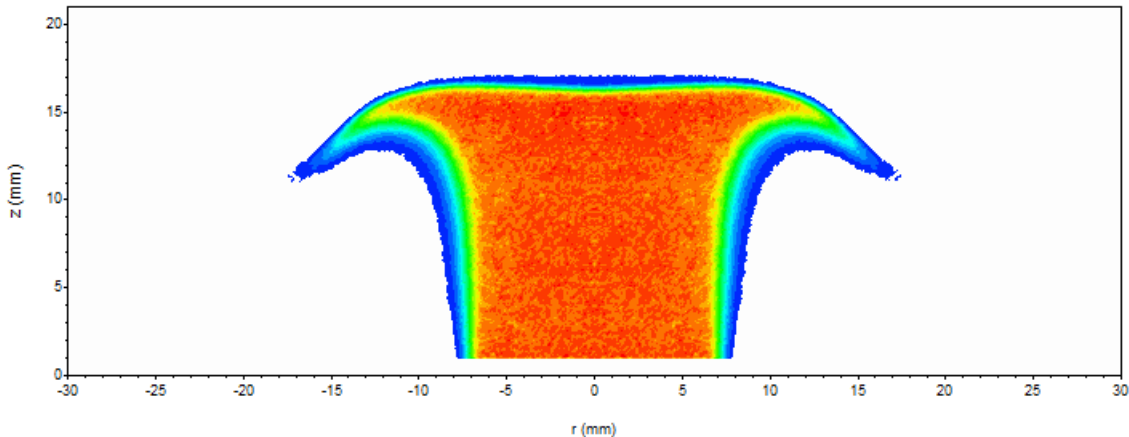


Figure H-75: Acetone PLIF image of seeded reactant flow under steady conditions (no acoustic forcing). Collected data appears on the left, and is mirrored across the centerline for a visual representation of entire flame. Burner centerline is at $r = 0$. Position $z = 0$ corresponds to the nozzle exit plane.

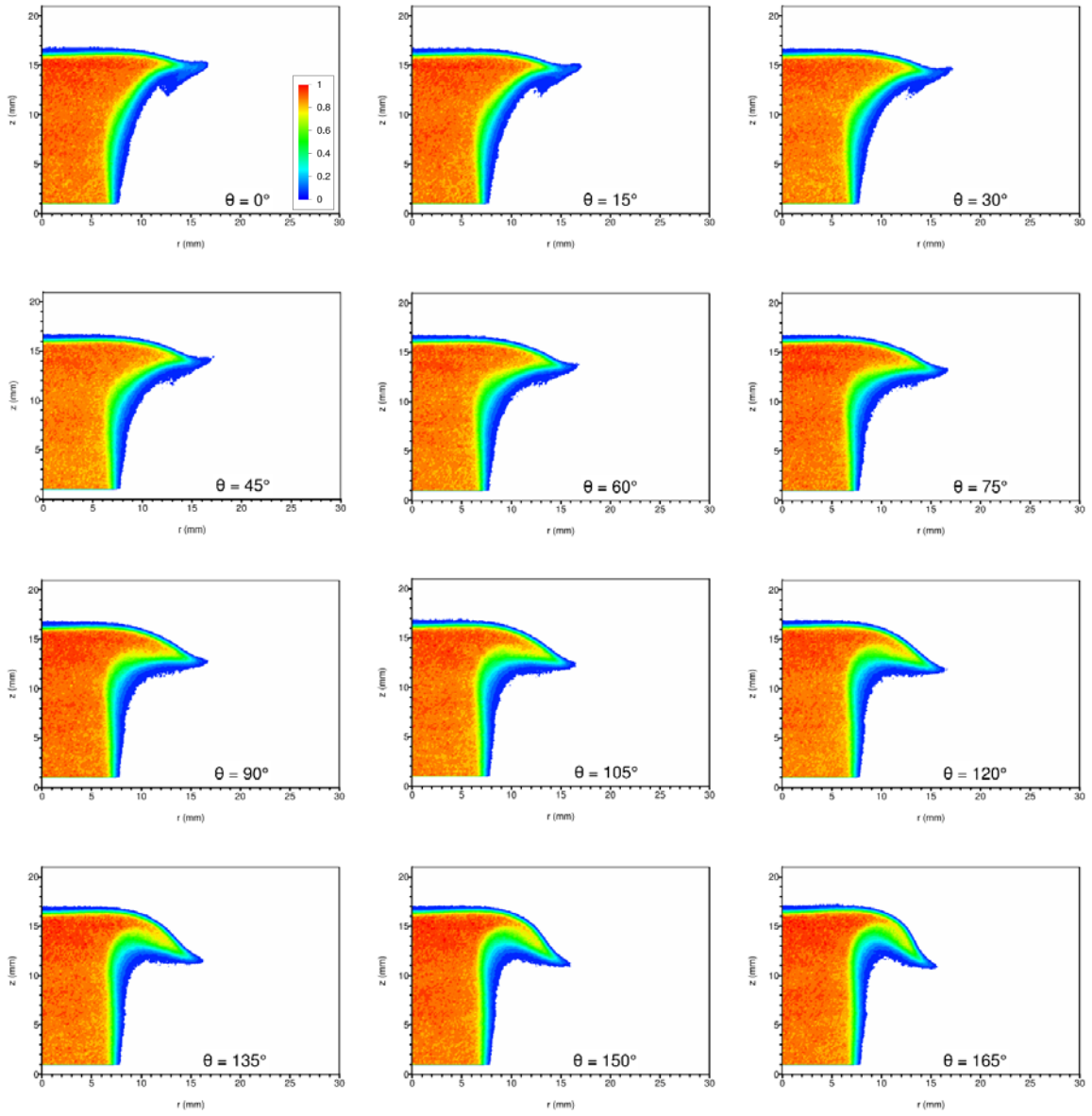


Figure H-76: Phase-resolved acetone PLIF images for acoustic forcing at 55 Hz. The horizontal axis is the radius (mm) from the centerline of the burner. The vertical axis is the distance (mm) above the nozzle exit plane. (The stagnation plane is located at $z = 21\text{mm}$.) Phase angle $\theta = 0^\circ$ corresponds to the rising-edge zero crossing of the local unsteady pressure. Data from experiment 642. A total of 24 images on 15° spacing are shown. (See next page.) The magnitude scale is normalized by the peak value over all 24 images.

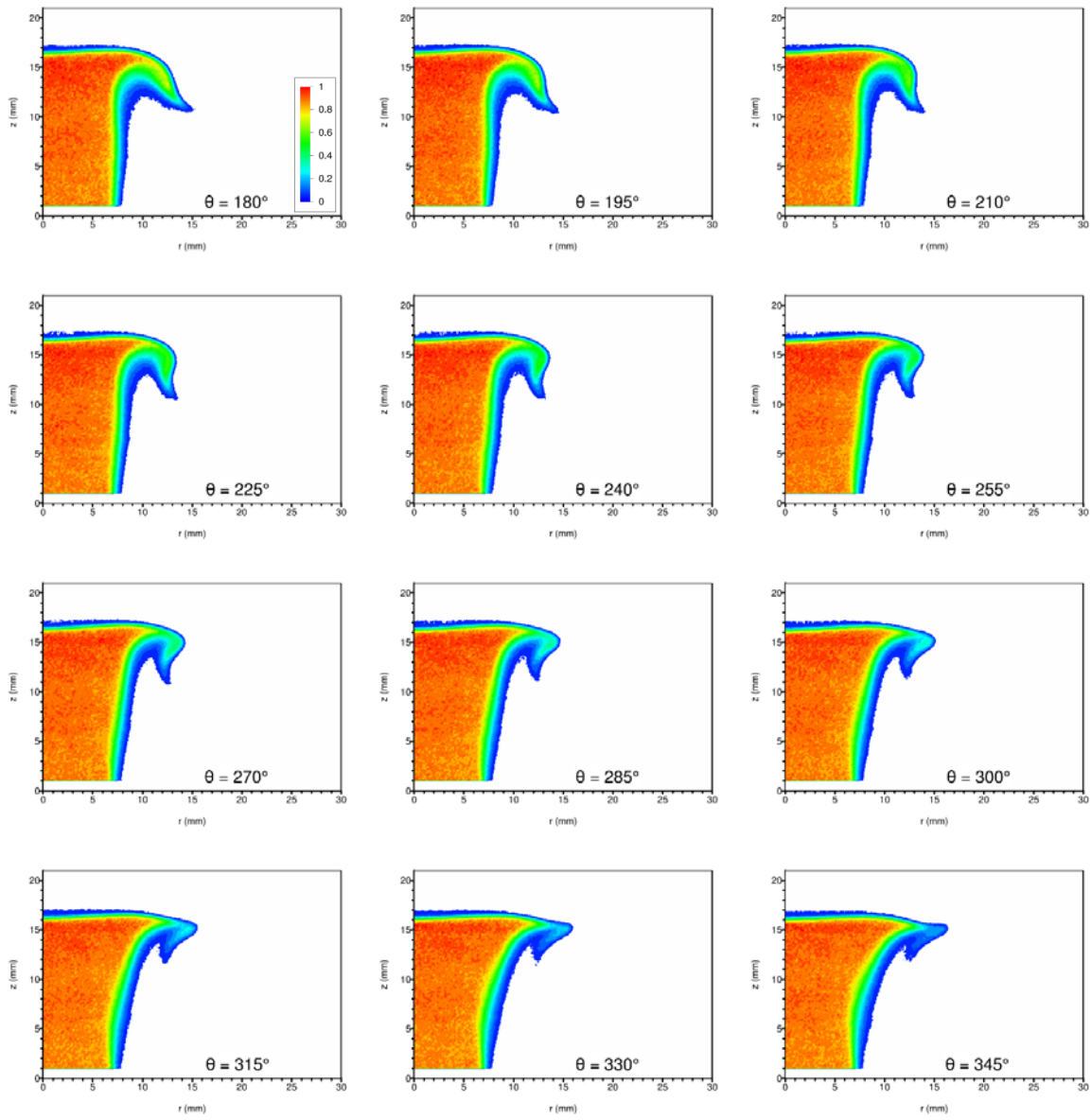


Figure H-76 (cont.): Phase-resolved acetone PLIF images for acoustic forcing at 55 Hz. The horizontal axis is the radius (mm) from the centerline of the burner. The vertical axis is the distance (mm) above the nozzle exit plane. (The stagnation plane is located at $z = 21$ mm.) Phase angle $\theta = 0^\circ$ corresponds to the rising-edge zero crossing of the local unsteady pressure. Data from experiment 642. A total of 24 images on 15° spacing are shown. (See previous page.) The magnitude scale is normalized by the peak value over all 24 images.

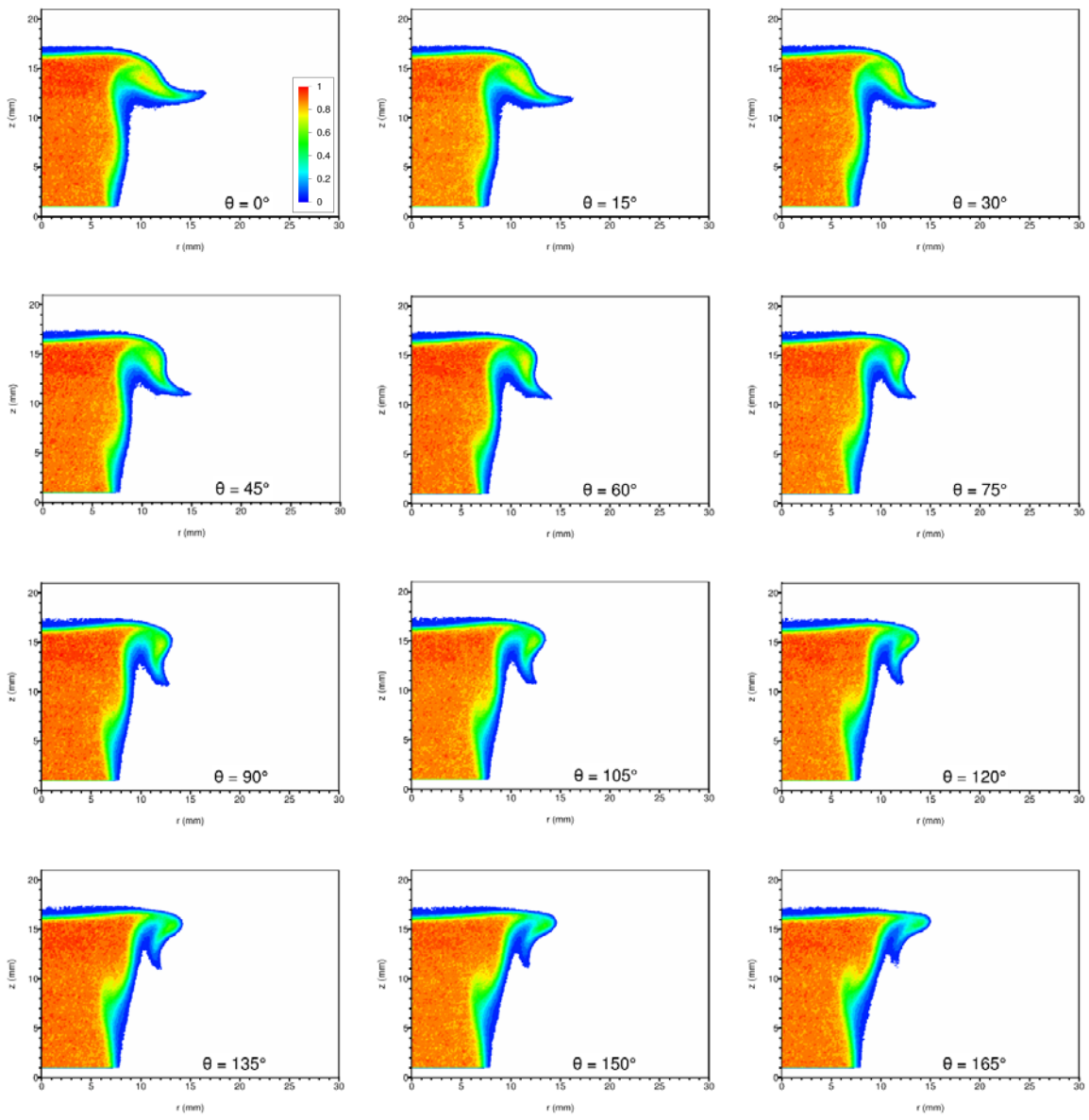


Figure H-77: Phase-resolved acetone PLIF images for acoustic forcing at 75 Hz. The horizontal axis is the radius (mm) from the centerline of the burner. The vertical axis is the distance (mm) above the nozzle exit plane. (The stagnation plane is located at $z = 21$ mm.) Phase angle $\theta = 0^\circ$ corresponds to the rising-edge zero crossing of the local unsteady pressure. Data from experiment 641. A total of 24 images on 15° spacing are shown. (See next page.) The magnitude scale is normalized by the peak value over all 24 images.

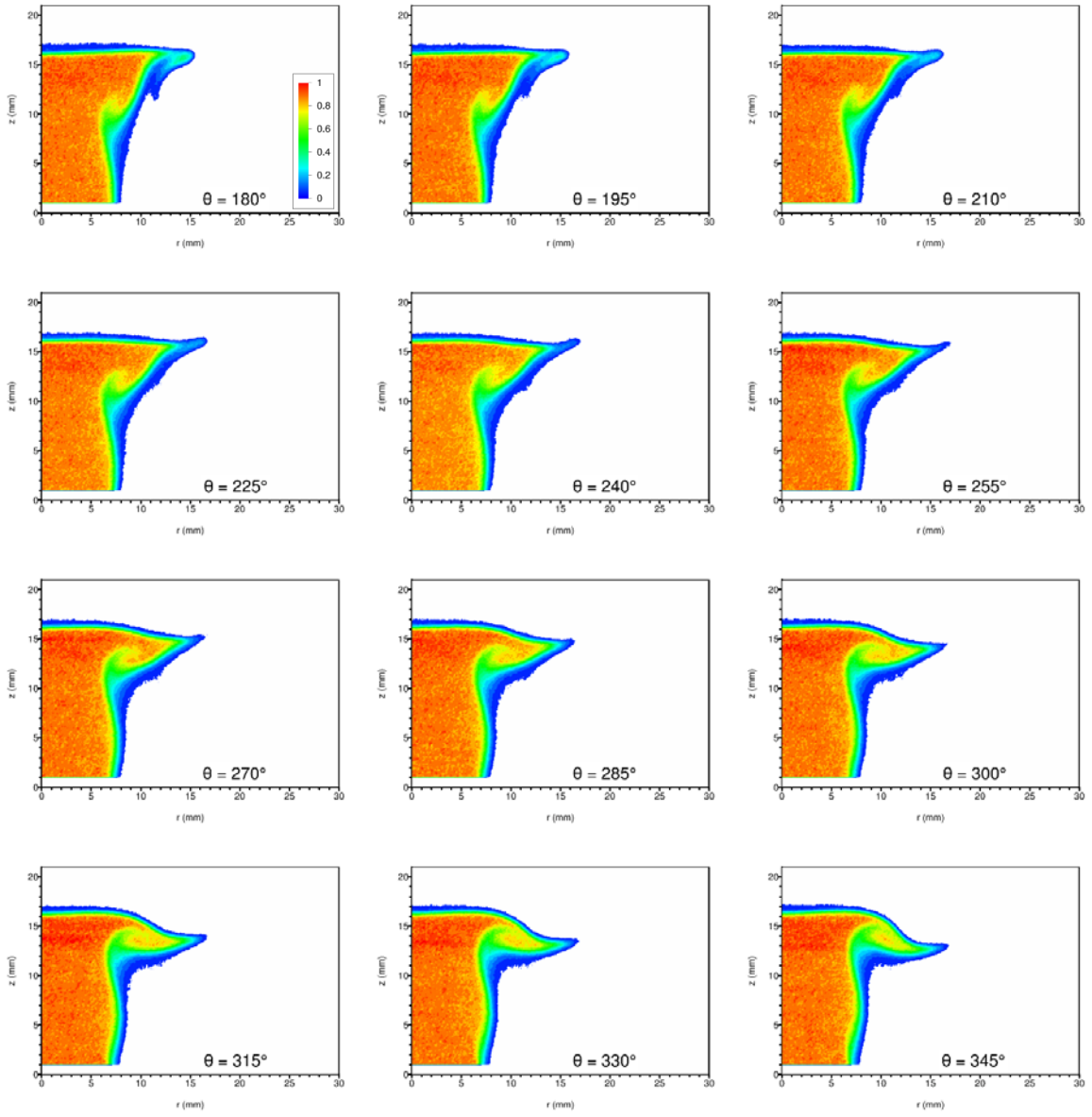


Figure H-77 (cont.): Phase-resolved acetone PLIF images for acoustic forcing at 75 Hz. The horizontal axis is the radius (mm) from the centerline of the burner. The vertical axis is the distance (mm) above the nozzle exit plane. (The stagnation plane is located at $z = 21$ mm.) Phase angle $\theta = 0^\circ$ corresponds to the rising-edge zero crossing of the local unsteady pressure. Data from experiment 641. A total of 24 images on 15° spacing are shown. (See previous page.) The magnitude scale is normalized by the peak value over all 24 images.

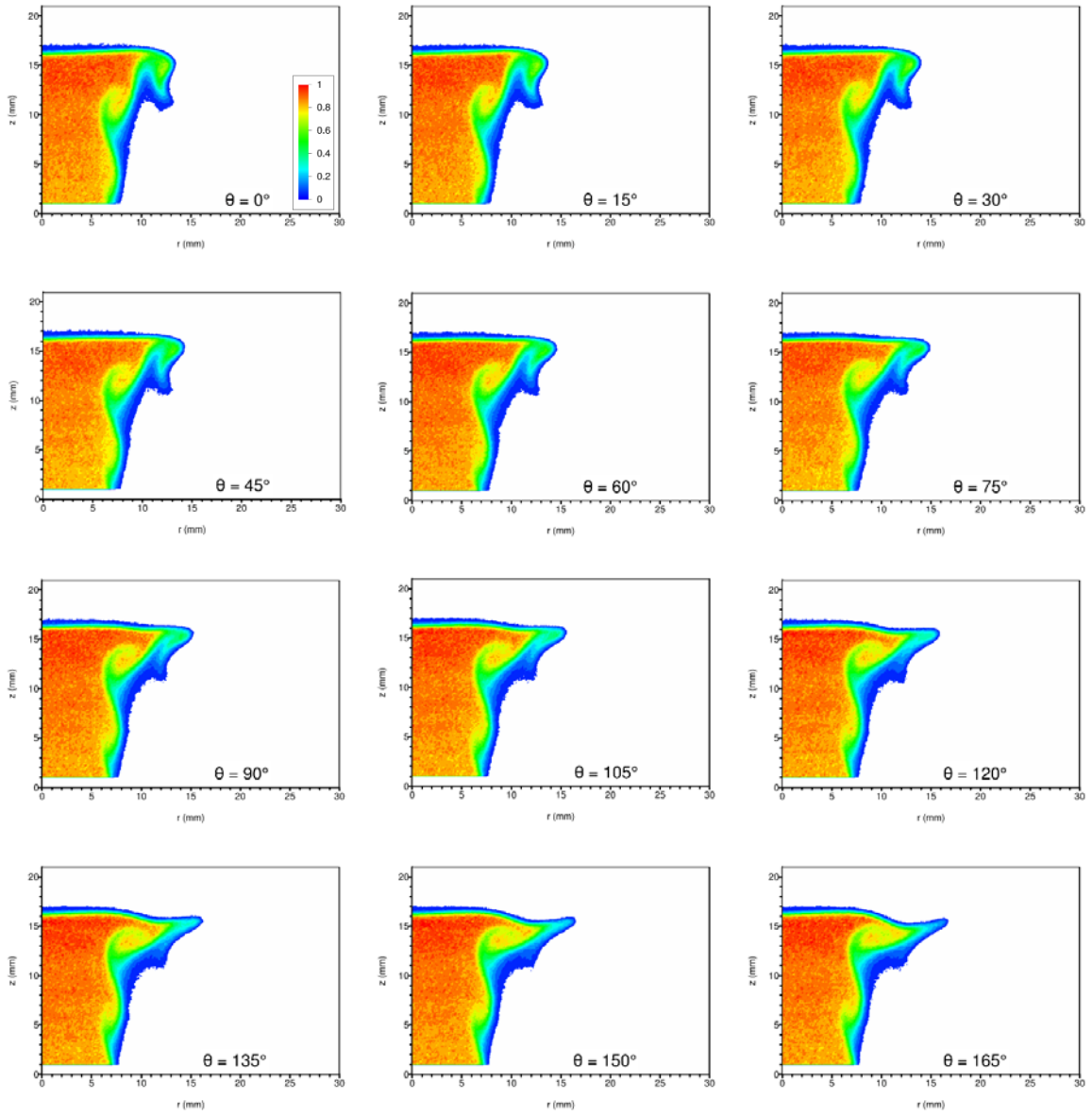


Figure H-78: Phase-resolved acetone PLIF images for acoustic forcing at 100 Hz. The horizontal axis is the radius (mm) from the centerline of the burner. The vertical axis is the distance (mm) above the nozzle exit plane. (The stagnation plane is located at $z = 21$ mm.) Phase angle $\theta = 0^\circ$ corresponds to the rising-edge zero crossing of the local unsteady pressure. Data from experiment 643. A total of 24 images on 15° spacing are shown. (See next page.) The magnitude scale is normalized by the peak value over all 24 images.

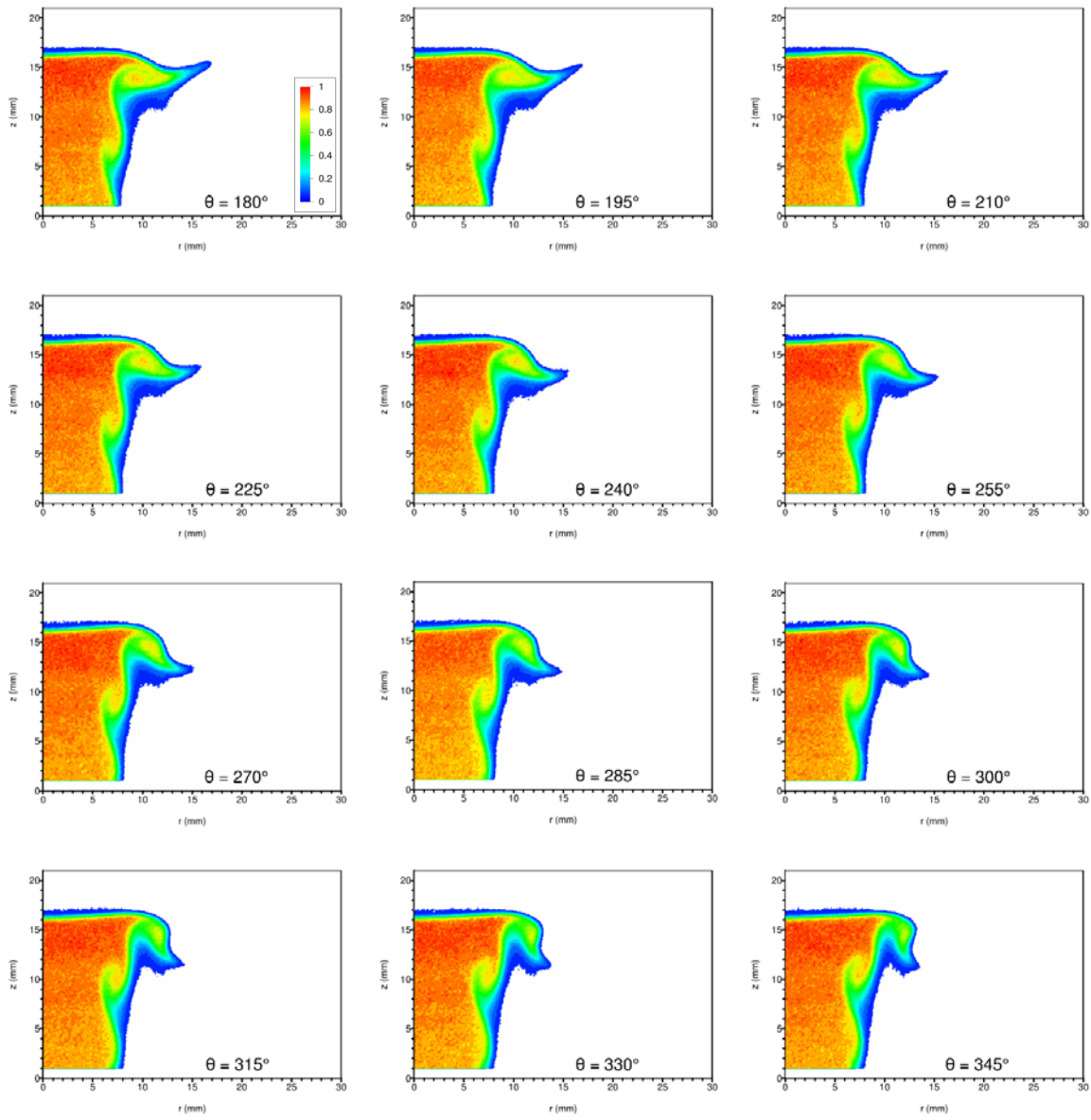


Figure H-78 (cont.): Phase-resolved acetone PLIF images for acoustic forcing at 100 Hz. The horizontal axis is the radius (mm) from the centerline of the burner. The vertical axis is the distance (mm) above the nozzle exit plane. (The stagnation plane is located at $z = 21\text{mm}$.) Phase angle $\theta = 0^\circ$ corresponds to the rising-edge zero crossing of the local unsteady pressure. Data from experiment 643. A total of 24 images on 15° spacing are shown. (See previous page.) The magnitude scale is normalized by the peak value over all 24 images.

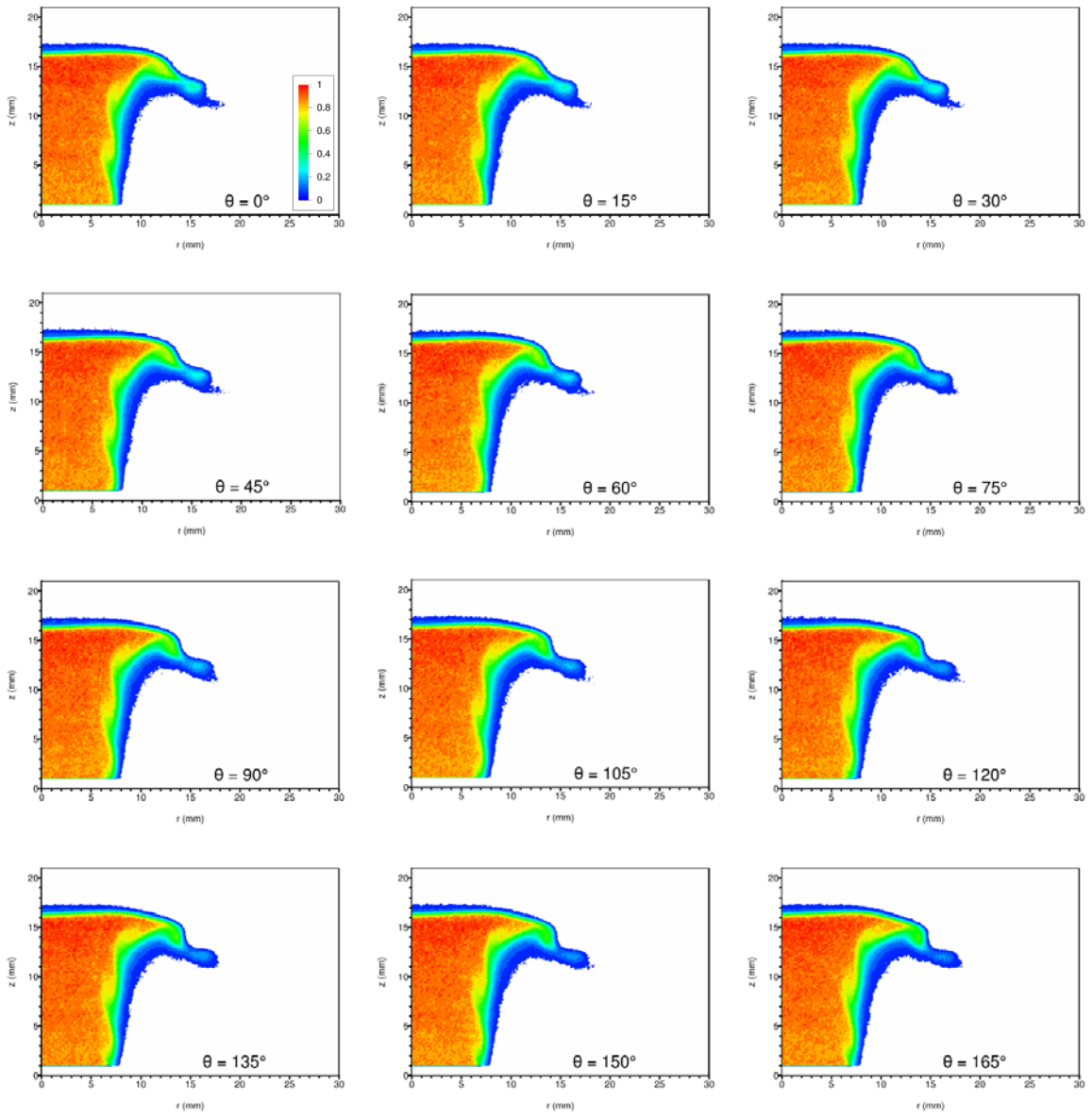


Figure H-79: Phase-resolved acetone PLIF images for acoustic forcing at 150 Hz. The horizontal axis is the radius (mm) from the centerline of the burner. The vertical axis is the distance (mm) above the nozzle exit plane. (The stagnation plane is located at $z = 21\text{mm}$.) Phase angle $\theta = 0^\circ$ corresponds to the rising-edge zero crossing of the local unsteady pressure. Data from experiment 644. A total of 24 images on 15° spacing are shown. (See next page.) The magnitude scale is normalized by the peak value over all 24 images.

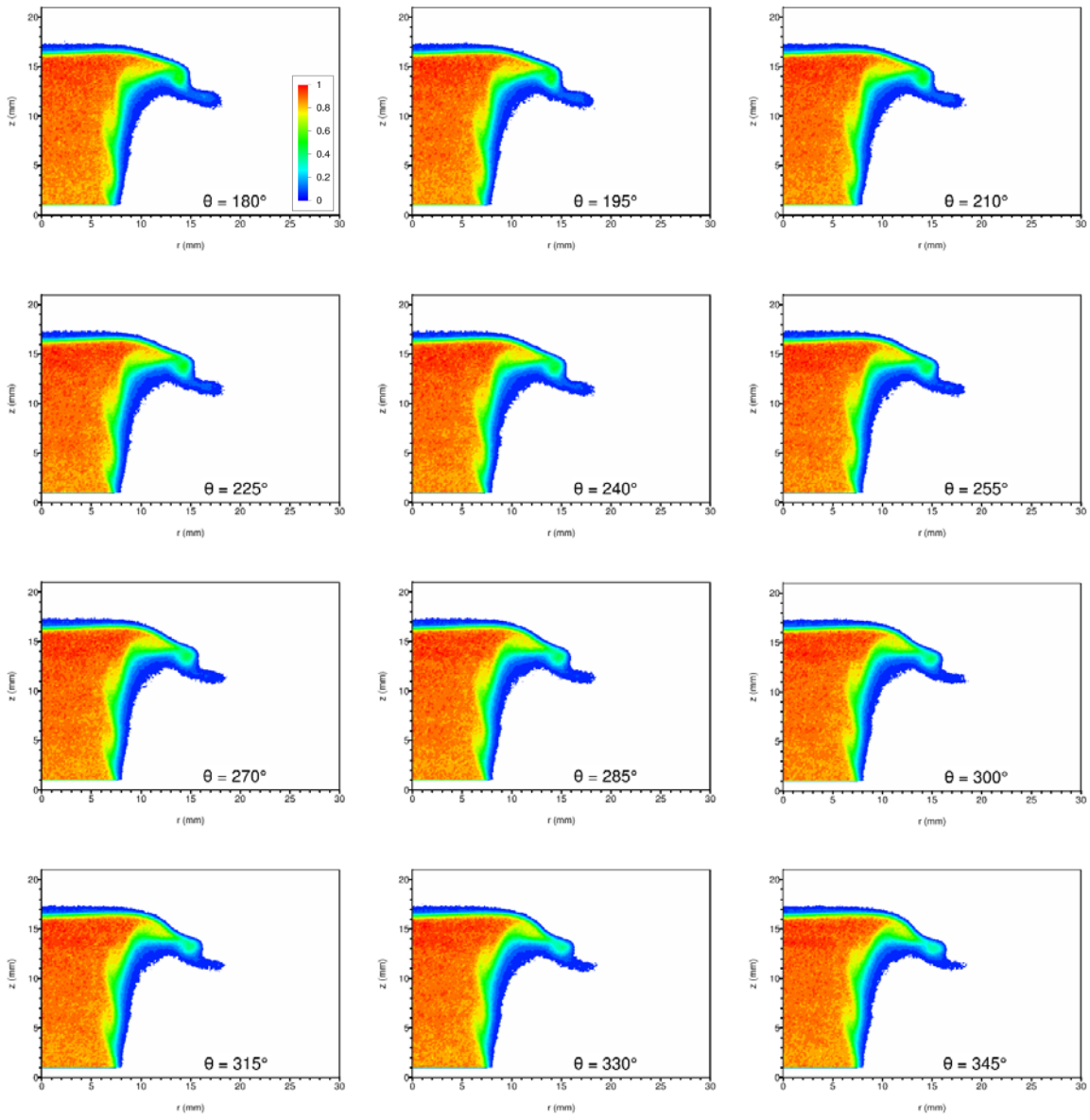


Figure H-79 (cont.): Phase-resolved acetone PLIF images for acoustic forcing at 150 Hz. The horizontal axis is the radius (mm) from the centerline of the burner. The vertical axis is the distance (mm) above the nozzle exit plane. (The stagnation plane is located at $z = 21\text{ mm}$.) Phase angle $\theta = 0^\circ$ corresponds to the rising-edge zero crossing of the local unsteady pressure. Data from experiment 644. A total of 24 images on 15° spacing are shown. (See previous page.) The magnitude scale is normalized by the peak value over all 24 images.

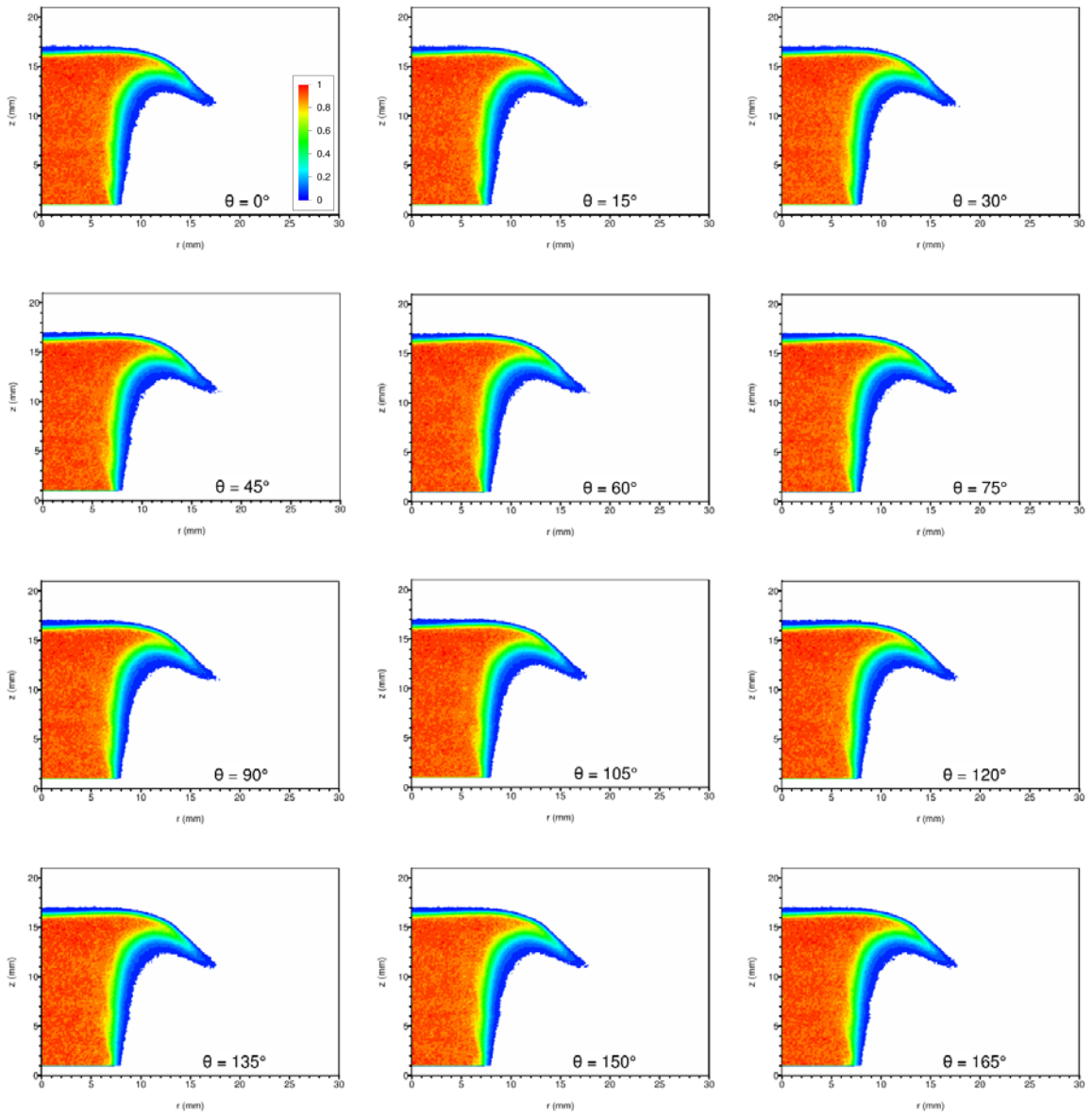


Figure H-80: Phase-resolved acetone PLIF images for acoustic forcing at 220 Hz. The horizontal axis is the radius (mm) from the centerline of the burner. The vertical axis is the distance (mm) above the nozzle exit plane. (The stagnation plane is located at $z = 21$ mm.) Phase angle $\theta = 0^\circ$ corresponds to the rising-edge zero crossing of the local unsteady pressure. Data from experiment 646. A total of 24 images on 15° spacing are shown. (See next page.) The magnitude scale is normalized by the peak value over all 24 images.

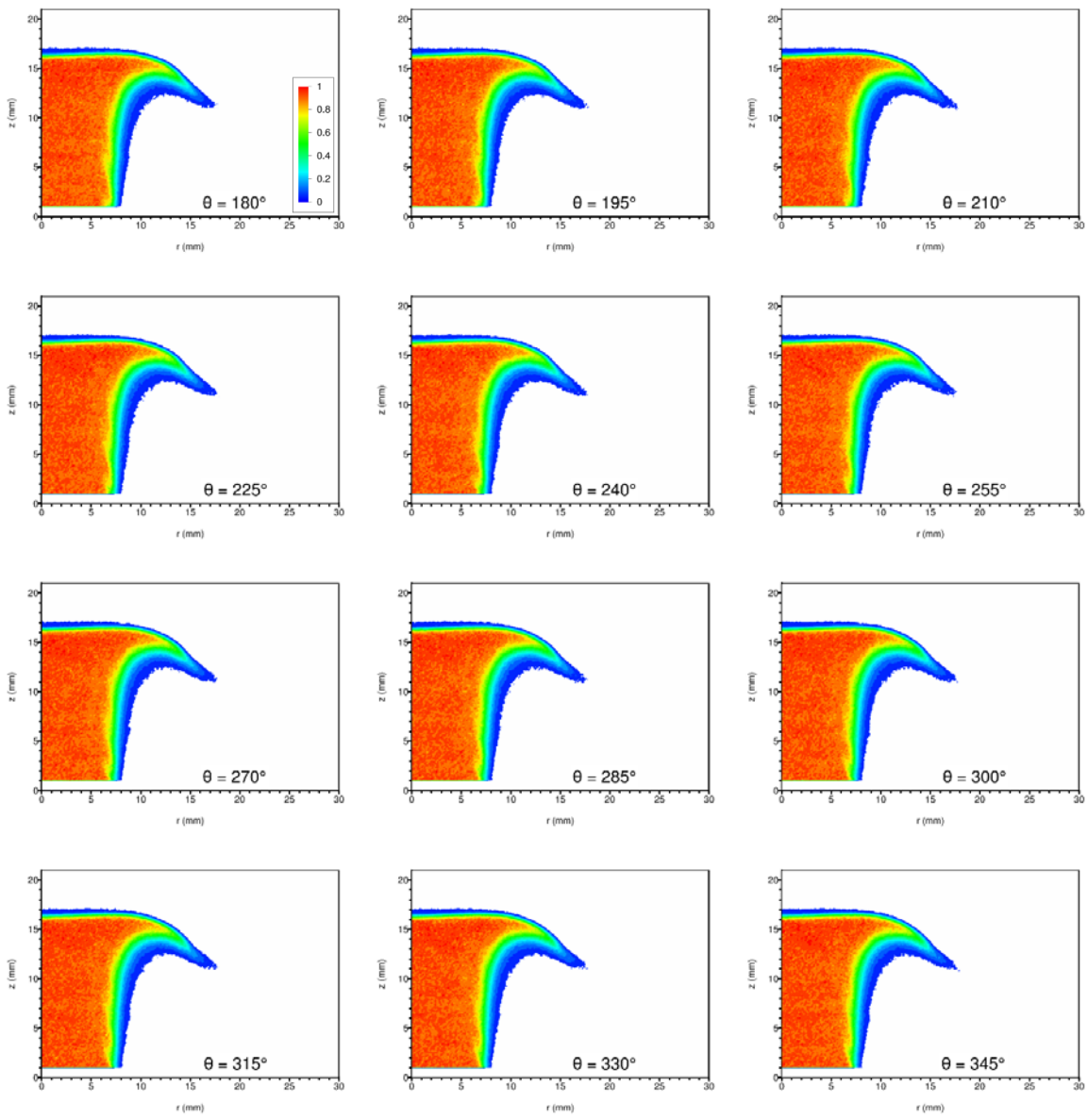


Figure H-80 (cont.): Phase-resolved acetone PLIF images for acoustic forcing at 220 Hz. The horizontal axis is the radius (mm) from the centerline of the burner. The vertical axis is the distance (mm) above the nozzle exit plane. (The stagnation plane is located at $z = 21$ mm.) Phase angle $\theta = 0^\circ$ corresponds to the rising-edge zero crossing of the local unsteady pressure. Data from experiment 646. A total of 24 images on 15° spacing are shown. (See previous page.) The magnitude scale is normalized by the peak value over all 24 images.

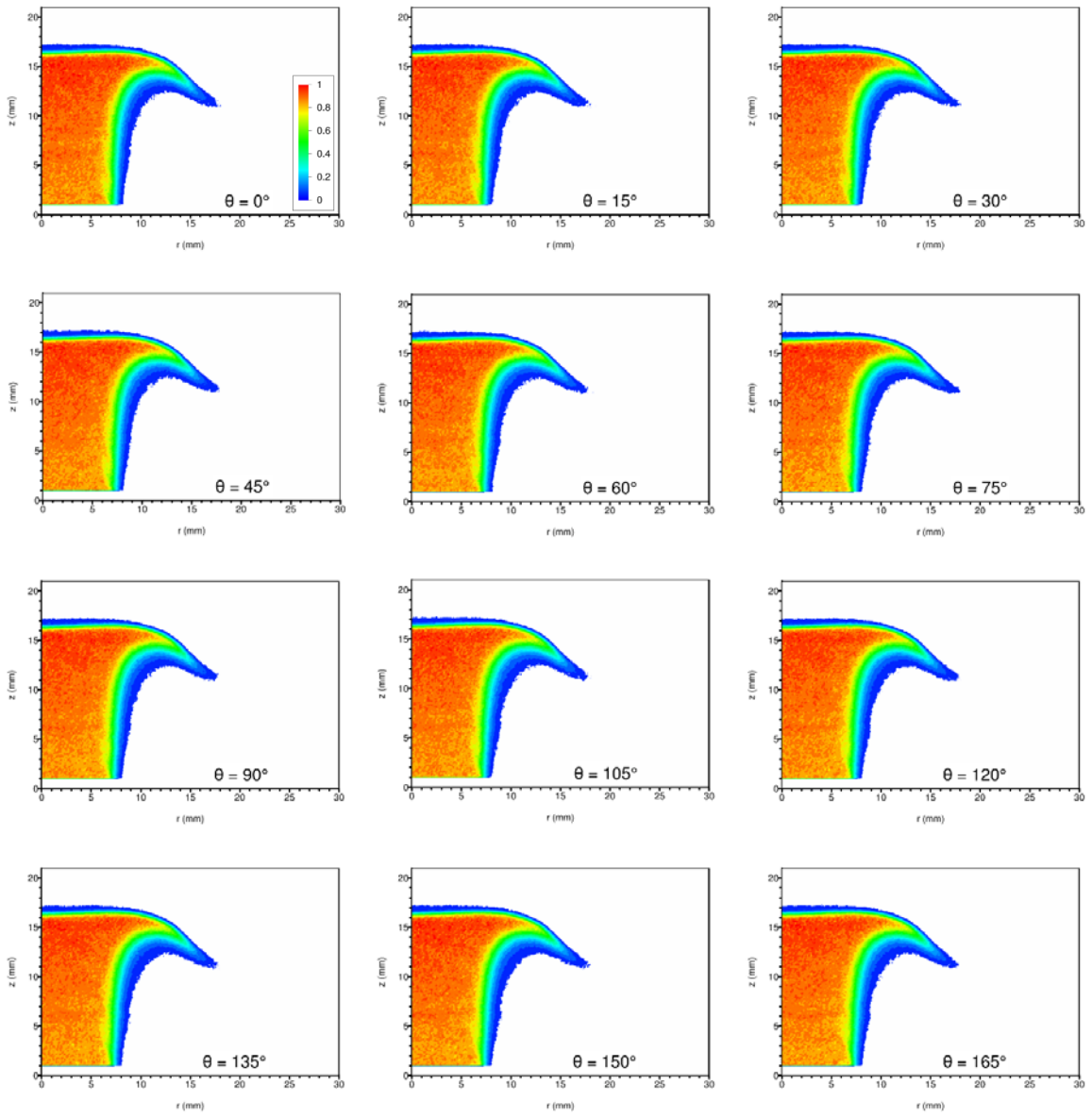


Figure H-81: Phase-resolved acetone PLIF images for acoustic forcing at 265 Hz. The horizontal axis is the radius (mm) from the centerline of the burner. The vertical axis is the distance (mm) above the nozzle exit plane. (The stagnation plane is located at $z = 21$ mm.) Phase angle $\theta = 0^\circ$ corresponds to the rising-edge zero crossing of the local unsteady pressure. Data from experiment 649. A total of 24 images on 15° spacing are shown. (See next page.) The magnitude scale is normalized by the peak value over all 24 images.

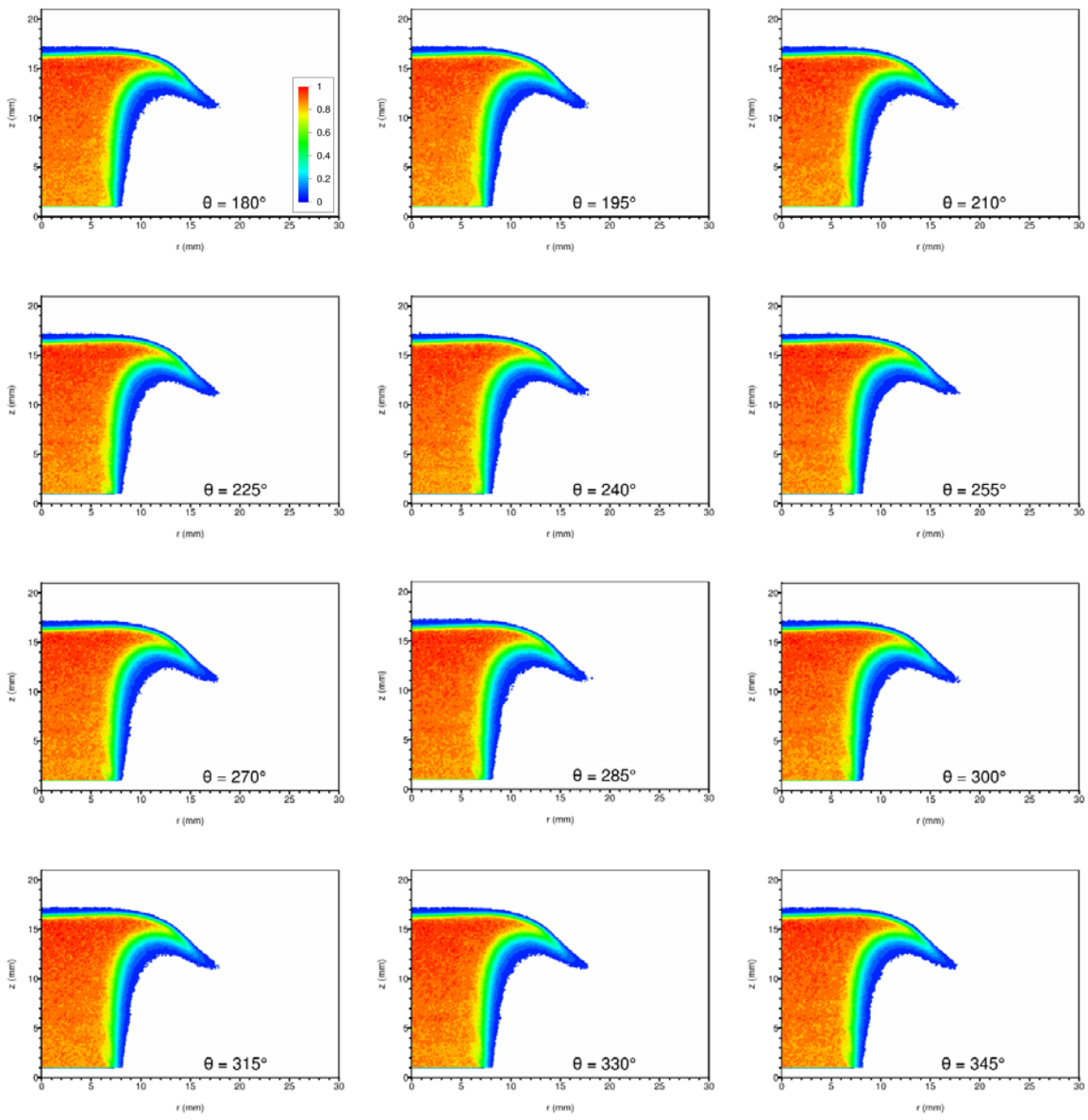


Figure H-81 (cont.): Phase-resolved acetone PLIF images for acoustic forcing at 265 Hz. The horizontal axis is the radius (mm) from the centerline of the burner. The vertical axis is the distance (mm) above the nozzle exit plane. (The stagnation plane is located at $z = 21$ mm.) Phase angle $\theta = 0^\circ$ corresponds to the rising-edge zero crossing of the local unsteady pressure. Data from experiment 649. A total of 24 images on 15° spacing are shown. (See previous page.) The magnitude scale is normalized by the peak value over all 24 images.

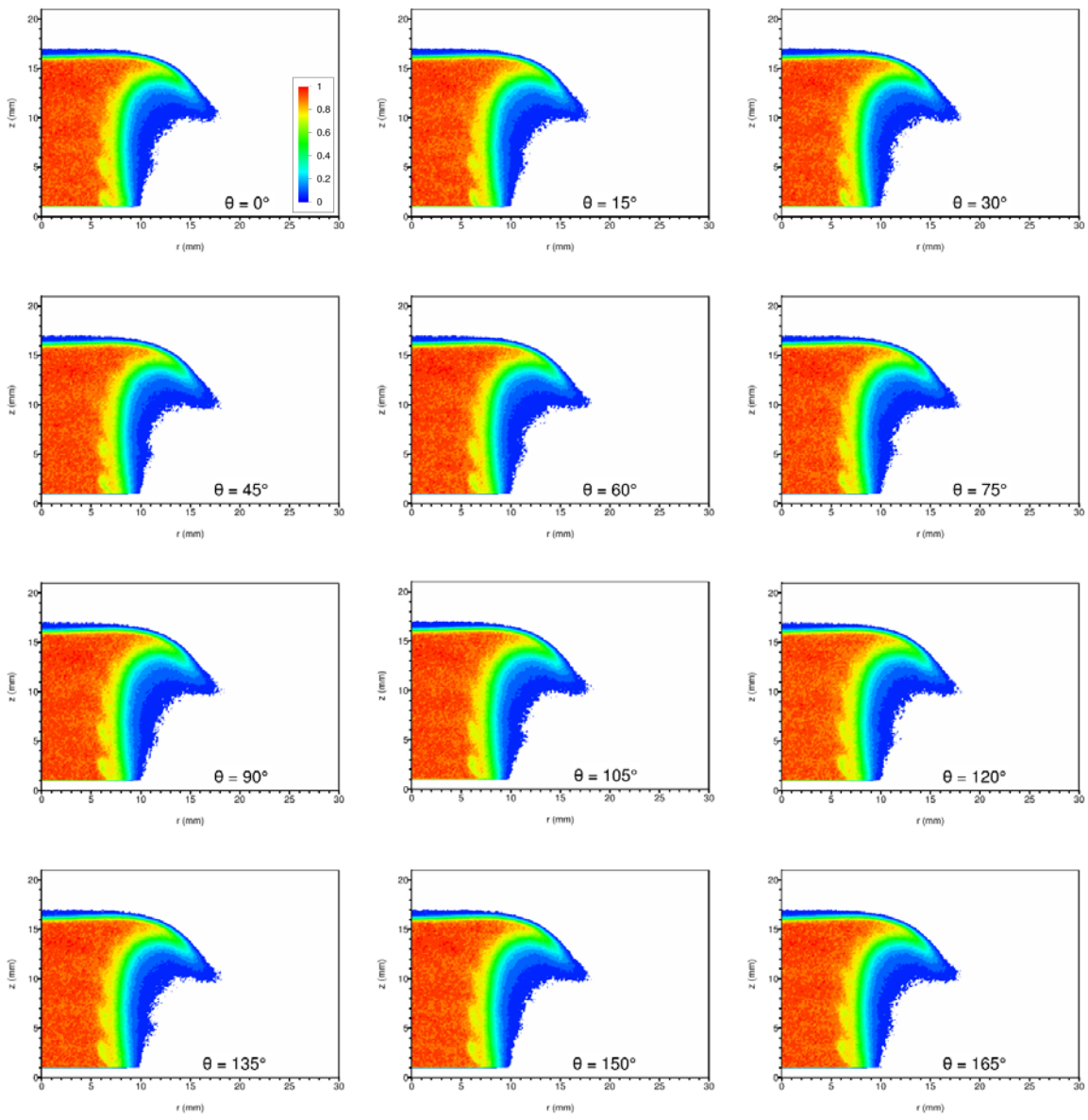


Figure H-82: Phase-resolved acetone PLIF images for acoustic forcing at 375 Hz. The horizontal axis is the radius (mm) from the centerline of the burner. The vertical axis is the distance (mm) above the nozzle exit plane. (The stagnation plane is located at $z = 21\text{mm}$.) Phase angle $\theta = 0^\circ$ corresponds to the rising-edge zero crossing of the local unsteady pressure. Data from experiment 650. A total of 24 images on 15° spacing are shown. (See next page.) The magnitude scale is normalized by the peak value over all 24 images.

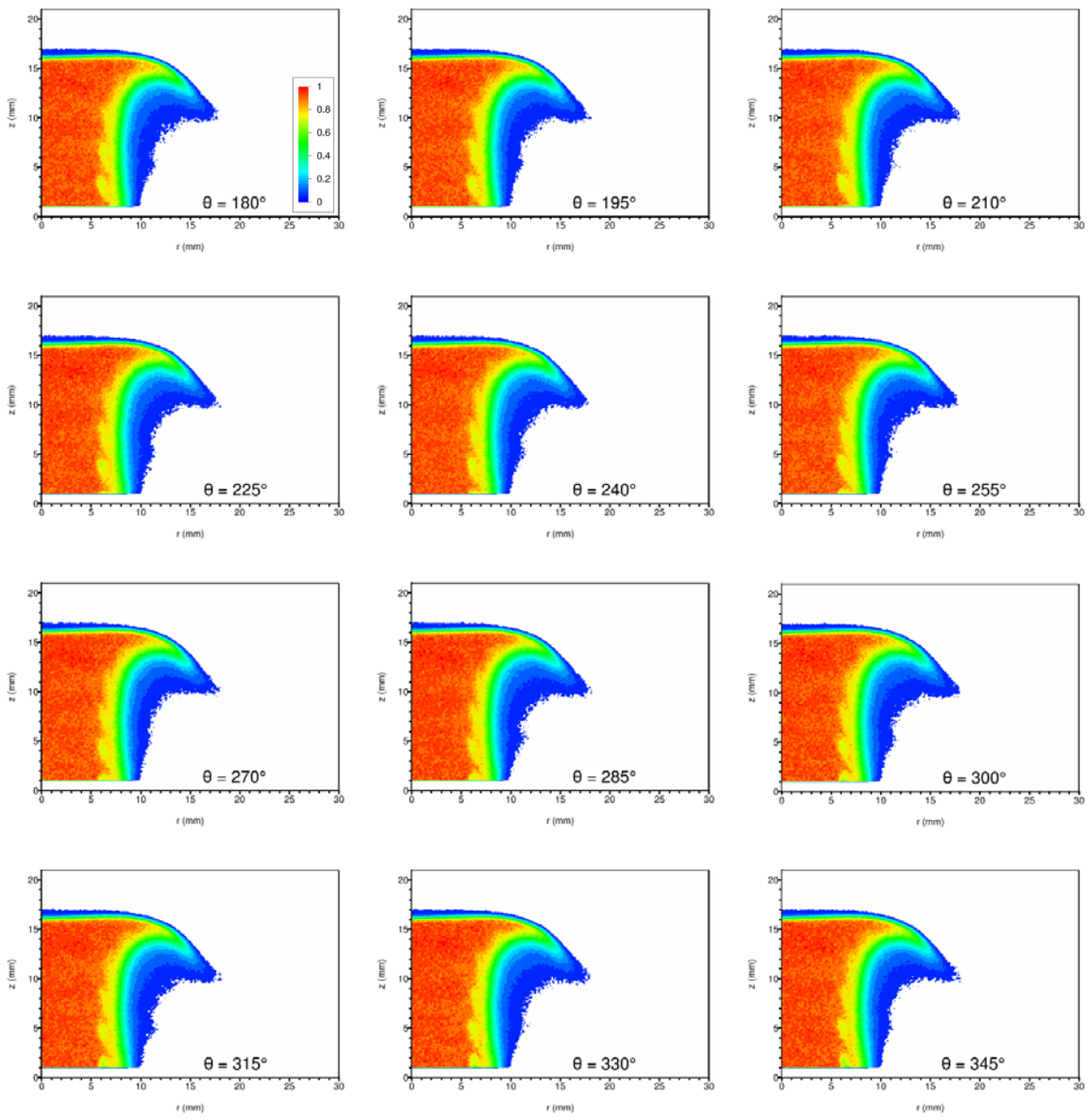


Figure H-82 (cont.): Phase-resolved acetone PLIF images for acoustic forcing at 375 Hz. The horizontal axis is the radius (mm) from the centerline of the burner. The vertical axis is the distance (mm) above the nozzle exit plane. (The stagnation plane is located at $z = 21\text{mm}$.) Phase angle $\theta = 0^\circ$ corresponds to the rising-edge zero crossing of the local unsteady pressure. Data from experiment 650. A total of 24 images on 15° spacing are shown. (See previous page.) The magnitude scale is normalized by the peak value over all 24 images.

REFERENCES

Allen, M.G., McManus, K.R., Sonnenfroh, D.M., and Paul, P.H. (1995) "Planar Laser-Induced Fluorescence Imaging Measurements of OH and Hydrocarbon Fuel Fragments in High-Pressure Spray-Flame Combustion", *Applied Optics*, Vol. 34(27).

Allen, M.G., McManus, K.R., and Sonnenfroh, D.M. (1995a) "PLIF Imaging in Spray Flame Combustors at Elevated Temperatures", *AIAA Paper 95-0172*.

Allen, M.G., Parker, T.E., Reinecke, W.G., Legner, H.H., Foutter, R.R., Rawlins, W.T., and Davis, S.J. (1993) "Fluorescence Imaging of OH and NO in a Model Supersonic Combustor", *AIAA Journal*, Vol. 31(3).

Anderson, T.J., Kendrick, D.W., and Cohen, J.M. (1998) "Measurement of Spray/Acoustic Coupling in Gas Turbine Fuel Injectors", presented at the 36th Aerospace Sciences Meeting & Exhibit, Reno, NV, *AIAA 98-0718*.

Armitage, C.A., Balachandran, R., Mastorakos, E., Cant, R.S. (2006) "Investigation of the Nonlinear Response of Turbulent Premixed Flames to Imposed Inlet Velocity Oscillations", *Combustion and Flame*, Vol. 146, pp. 419-436.

Armstrong, D.J., and Smith, A.V. (2002) "Demonstration of Improved Beam Quality in an Image-Rotating Optical Parametric Oscillator", *Optics Letters*, Vol. 27(1), pp. 40-42.

Ayache, S., Dawson, J.R., Triantafyllidis, A., Balachandran, R., Mastorakos, E. (2010) "Experiments and Large-Eddy Simulations of Acoustically Forced Bluff-Body Flows", *International Journal of Heat and Fluid Flow*, Vol. 31, pp. 754-766.

Balachandran, R., Ayoola, B.O., Kaminski, C.F., Dowling, A.P., and Mastorakos, E. (2005) "Experimental Investigation of the Nonlinear Response of Turbulent Premixed Flames to Imposed Inlet Velocity Oscillations", *Combustion and Flame*, Vol. 143, pp. 37-55.

Bellows, B.D., Bobba, M.K., Forte, A., Seitzman, J.M., and Lieuwen, T. (2007) "Flame Transfer Function Saturation Mechanisms in a Swirl-Stabilized Combustor", *Proceedings of the Combustion Institute*, Vol. 31, pp. 3181-3188.

Barlow, R.S., and Collignon, A. (1991) "Linear LIF Measurements of OH in Nonpremixed Methane-Air Flames: When are Quenching Corrections Unnecessary", *AIAA Paper 91-0179*.

Battles, B.E., and Hanson, R.K. (1995) "Laser-Induced Fluorescence Measurements of NO and OH Mole Fraction in Fuel-Lean, High-Pressure (1-10 atm) Methane Flames: Fluorescence Modeling and Experimental Validation", *J. Quant. Spectrosc. Radiat. Transfer*, Vol. 54(3), pp. 521-537.

Bergthorson, J.M. (2005) "Experiments and Modeling of Impinging Jets and Premixed Hydrocarbon Stagnation Flames", Ph.D. Thesis, California Institute of Technology, Pasadena, California.

Bernier, D., Lacas, F., and Candel, S. (2004) "Instability Mechanisms in a Premixed Prevaporized Combustor", *J. Prop. Power*, Vol. 20(4), pp. 648-656.

Birbaud, A.L., Ducruix, S., Durox, D., Candel, S. (2008) "The Nonlinear Response of Inverted 'V' Flames to Equivalence Ratio Nonuniformities", *Combustion and Flame*, Vol. 154, pp 356-367.

Bloxidge, G.J., Dowling, A.P., and Langhorne, P.J. (1988) "Reheat Buzz: An Acoustically Coupled Combustion Instability. Part 2. Theory", *J. Fluid Mech.*, Vol. 193, pp. 445-473.

Boxx, I., Stohr, M., Carter, C., and Meier, W. (2010) "Temporally Resolved Planar Measurements of Transient Phenomena in a Partially Pre-mixed Swirl Flame in a Gas Turbine Model Combustor", *Combustion and Flame*, Vol. 157, pp. 1510-1525.

Broda, J.C., Seo, S., Santoro, R.J., Shirhattikar, G., and Yang, V. (1998) "An Experimental Study of Combustion Dynamics of a Premixed Swirl Injector", 27th Symposium (International) on Combustion, The Combustion Institute, pp. 1849-1856.

Butcher, P.N., and Cotter, D. (1990) "The Elements of Nonlinear Optics", Cambridge University Press, Cambridge.

Cadou, C.P. (1996) "Two-Dimensional, Time-Resolved Temperature Measurements in a Resonant Incinerator Using Planar Laser-Induced Fluorescence", Ph.D. Thesis, University of California (Los Angeles).

Cadou, C.P., Logan, P., Karagozian, A.R., and Smith, O.I. (1991) "Laser Diagnostic Techniques in a Resonant Incinerator", *Environ. Sensing Combust. Diagn.*, SPIE, Vol. 1434, pp. 67-77.

Cadou, C.P., Smith, O.I., and Karagozian, A.R. (1998) "Transport Enhancement in Acoustically Excited Cavity Flows, Part 2: Reactive Flow Diagnostics", *AIAA Journal*, Vol. 36(9), pp. 1568-1574.

Carter, C.D., Donbar, J.M., and Driscoll, J.F. (1998) "Simultaneous CH Planar Laser-Induced Fluorescence and Particle Image Velocimetry in Turbulent Nonpremixed Flames", *Applied Physics B*, Vol. 66, pp. 129-132.

Caux-Brisebois, V., Steinberg, A.M., Arndt, C.M., and Meier, W. (2014) "Thermo-acoustic Velocity Coupling in a Swirl Stabilized Gas Turbine Model Combustor", *Combustion and Flame*, Vol. 161, pp. 3166-3180.

Cessou, A., and Stepowski, D. (1996) "Planar Laser Induced Fluorescence Measurement of [OH] in the Stabilization Stage of a Spray Jet Flame", *Combust. Sci. and Tech.*, Vol. 118, pp. 361-381.

Chao, B.H., Egolfopoulos, F.N., and Law, C.K. (1997) "Structure and Propagation of Premixed Flames in Nozzle-Generated Counterflow", *Combustion and Flame*, Vol. 109, pp. 620-638.

Chen, T. Y., Hegde, U.G., Daniel, B.R., and Zinn, B.T. (1993) "Flame Radiation and Acoustic Intensity Measurements in Acoustically Excited Diffusion Flames", *J. Propul. Power*, Vol. 9, No. 2.

Chemielewski, G.E. (1974) "Boundary-Layer Considerations in the Design of Aerodynamic Contractions", *J. Aircraft*, Vol. 11(8), pp. 435-438.

Clanet, C., Searby, G., and Clavin, C. (1999) "Primary Acoustic Instability of Flames Propagating in Tubes: Cases of Spray and Premixed Gas Combustion", *J. Fluid Mech.*, Vol. 385, pp. 157-197.

Coats, C.M., Chang, Z., and Williams, P.D. (2010) "Excitation of Thermoacoustic Oscillations by Small Premixed Flames", *Combustion and Flame*, Vol. 157, pp. 1037-1051.

Cohen, J. M., Stufflebeam, J. H., and Proscia, W. (2001) "The Effect of Fuel/Air Mixing on Actuation Authority in an Active Combustion Instability Control System", *J. Eng. Gas Turb. Power*, Vol. 123(3), pp. 537-542.

Cohen, J. M., and Banaszuk, A. (2003) "Factors Affecting the Control of Unstable Combustors", *J. of Prop. Power*, Vol. 19(5), pp. 811-821.

Correa, S.M. (1992) "A Review of NO_x Formation Under Gas-Turbine Combustion Conditions", *Combust. Sci. and Tech.*, Vol. 87, pp. 329-362.

Crosley, D. (1993) "Collisional Effects on Laser-Induced Fluorescence Flame Measurements", *Optical Engineering*, Vol. 20(7).

Culick, F.E.C. (1968) "A Review of Calculations for Unsteady Burning of a Solid Propellant", AIAA Journal, Vol. 6(12), pp. 2241-2255.

Culick, F.E.C. (1976) "Nonlinear Behavior of Acoustic Waves in Combustion Chambers", Parts I and II, Acta Astronautica, Vol. 3, pp. 714-757.

Culick, F.E.C. (1987) "A Note on Rayleigh's Criterion", Combust. Sci. and Tech., Vol. 56, pp. 159-166.

Culick, F.E.C. (1999) "Combustor Dynamics: Fundamentals, Acoustics, and Control", A Short Course of Lectures, United Technologies Research Center.

Culick, F.E.C. (2004), AFOSR final report, AFOSR_F49620-99-1-01 18.

Culick, F.E.C. (2006) "Unsteady Motions in Combustion Chambers for Propulsion Systems", AGARDograph RTO-AG-AVT-039.

Culick, F.E.C., and Jahnke, C. (1994) "An Application of Dynamical Systems Theory to Nonlinear Combustion Instabilities", J. Propul. Power, Vol. 10(4), pp. 508-517.

Daily, J.W. (1977) "Saturation Effects in Laser-Induced Fluorescence in Flames", Applied Optics, Vol. 16, pp. 568-571.

Daily, J.W. (1978) "Saturation Effects in Laser-Induced Fluorescence in Flames with a Gaussian Laser Beam", Applied Optics, Vol. 17, pp. 225-229.

Daily, J.W. (1997) "Laser-Induced Fluorescence Spectroscopy in Flames", Prog. Energ. Combust., Vol. 23, pp. 133-199.

Davies, P.O.A L., Fisher, M.J., and Barrett, M.J. (1963) "The Characteristics of the Turbulence in the Mixing Region of a Round Jet", Journal of Fluid Mechanics, Vol. 15(3), pp. 337-367.

Demare, D., and Baillot, F. (2004) "Acoustic Enhancement of Combustion in Lifted Nonpremixed Jet Flames", *Combustion and Flame*, Vol. 139(4), pp. 312-328.

Den Hartog et al. (2010) "Pulse-Burst Operation of Standard Nd:YAG Lasers", *Journal of Physics: Conference Series*, Vol. 227.

Dieke, G.H., and Crosswhite, H.M. (1962) "The Ultraviolet Bands of OH", *J. Quant. Spectrosc. Radiat. Transfer*, Vol. 2, pp. 97-199.

Dowling, A.P., and Bloxsidge, G.J. (1984) "Reheat Buzz - An Acoustically Driven Combustion Instability", *AIAA/NASA 96 Aeroacoustics Conference*, MAA-84-2321.

Dowling, A.P. (1995) "The Calculation of Thermoacoustic Oscillations", *J. Sound Vib.*, Vol 180(4), pp. 557-581.

Dowling, A.P. (2000) "The 1999 Lanchester Lecture - Vortices, Sound and Flames - A Damaging Combination", *Aeronautical Journal*, Vol. 104, No. 1033, pp. 105-116.

Duchaine, F., Boudy, F., Durox, D., Poinsot, T. (2011) "Sensitivity Analysis of Transfer Functions of Laminar Flames", *Combustion and Flame*, Vol. 158, pp. 2384-2394.

Durox, D., Schuller, T., and Candel, S. (2002) "Self-Induced Instability of a Premixed Jet Flame Impinging on a Plate", *29th Symposium (International) on Combustion*, The Combustion Institute, pp. 69-75.

Durox, D., Schuller, T., and Candel, S. (2005) "Combustion Dynamics of Inverted Conical Flames", *30th Symposium (International) on Combustion*, The Combustion Institute, pp. 1717-1724.

Dyer, M.J., and Crosley, D.R. (1982) "Two-Dimensional Imaging of OH Laser-Induced Fluorescence in a Flame", *Optics Letters*, Vol. 7(8).

Eckbreth, A.C. (1988) "Laser Diagnostics for Combustion Temperature and Species", Abacus Press, Cambridge.

Egolfopoulos, F.N. (1994) "Geometric and Radiation Effects of Steady and Unsteady Strained Laminar Flames", *P. Combust. Inst.*, Vol. 25, pp. 1375-1381

Egolfopoulos, F.N., Cho, P., and Law, C.K. (1989) "Laminar Flame Speeds of Methane-Air Mixtures Under Reduced and Elevated Pressures", *Combustion and Flame*, Vol. 76, pp. 375-391.

Egolfopoulos, F.N., Zhang, H., and Zhang, Z. (1997) "Wall Effects on the Propagation and Extinction of Steady, Strained, Laminar Premixed Flames", *Combustion and Flame*, Vol. 109, pp. 237-252.

Eteng, E., Ludford, G.S.S., and Matalon, M. (1986) "Displacement Effect of a Flame in Stagnation-Point Flow", *Physics of Fluids*, Vol. 29, pp. 2172-2180.

Fayoux, A., Zahringer, K., Gicquel, O., and Rolon, J.C. (2005) "Experimental and Numerical Determination of Heat Release in Counterflow Premixed Laminar Flames", *Proceedings of the Combustion Institute*, Vol. 30, pp. 251-257.

Fernandez, V., Ratner, A., and Culick, F.E.C. (2003) "Measured Influence of Oscillations in Fuel Mixture Fraction on Flame Behavior", *Proceedings of the Third Joint Meeting of the U.S. Sections of The Combustion Institute*, Chicago, IL, March 16-19.

Fix, A., Wirth, M., Meister A., Ehret G., Pesch, M., and Weidauer D. (2002) "Tunable Ultraviolet Optical Parametric Oscillator for Differential Absorption Lidar Measurements of Tropospheric Ozone", *Appl. Phys. B*, Vol 75, pp. 153-163.

Fric, T.F., (1993) "Effects of Fuel-Air Unmixedness on NO_x Emissions", *Journal of Propulsion and Power*, Vol. 9, No. 5, pp. 708-713.

Glassman, I. (1996) "Combustion", Third Edition, Academic Press, San Diego.

Goodwin, D., Moffat, H., Speth, R. (2016) "Cantera: An Object-Oriented Software Toolkit for Chemical Kinetics, Thermodynamics, and Transport Processes", <http://www.cantera.org>, Ver. 2.2.1.

Hall, D.R., and Jackson, P.E. (1992) "The Physics and Technology of Laser Resonators", IOP Publishing Ltd, Bristol.

Han, X., Morgans, A. (2015) "Simulation of the Flame Describing Function of a Turbulent Premixed Flame Using an Open-Source LES Solver", Combustion and Flame, Vol. 162, pp. 1778-1792.

Han, X., Yang, J., Mao, J. (2016) "LES Investigation of Two Frequency Effects on Acoustically Forced Premixed Flame", Fuel, Vol. 185, pp. 449-459.

Hanson, R.K. (1988) "Planar Laser-Induced Fluorescence Imaging", J. Quant. Spectrosc. Ra., Vol. 40, pp. 343-362.

Hanson, R.K., Seitzman, J.M., and Paul. P.H. (1990) "Planar Laser-Fluorescence Imaging of Combustion Gases", Applied Physics B, Vol. 50, pp. 441-454.

Hardalupas, Y., and Selbach, A. (2002) "Imposed Oscillations and Non-Premixed Flames", Progress in Energy and Combustion Science, pp. 75-104.

Harrington, J.E., and Smyth, K.C. (1993) "Laser-Induced Fluorescence Measurements of Formaldehyde in a Methane/Air Diffusion Flame", Chemical Physics Letters, Vol. 202, pp. 196-202.

Harrje, D.T., and Reardon, F.H. (1972) "Liquid Propellant Rocket Combustion Instability", NASA, SP-194.

Heberle, N.M., Smith, G.P., Jeffries, J.B., Crosley, D.R., and Dibble, R.W., (2000) "Simultaneous Laser-Induced Fluorescence and Rayleigh Scattering Measurements of Structure in Partially Premixed Flames", *Appl. Phys. B*, Vol. 71, pp. 733-740.

Hemchandra, S., Peters, N., and Lieuwen, T. (2011) "Heat Release Response of Acoustically Forced Turbulent Premixed Flames-Role of Kinematic Restoration", *Proceedings of the Combustion Institute*, Vol. 33, pp. 1609-1617.

Huber, A., Polifke, W. (2009) "Dynamics of Practical Premixed Flames, Part II: Identification and Interpretation of CFD Data", *International Journal of Spray and Combustion Dynamics*, Vol. 1, No. 2, pp. 229-250.

Isella, G.C. (2001) "Modeling and Simulation of Combustion Chamber and Propellant Dynamics and Issues in Active Control of Combustion Instabilities", Ph.D. Thesis, California Institute of Technology, Pasadena, California.

Isella, G., Seywert, C., Culick, F.E.C., and Zukoski, E.E. (1997) "A Further Note on Active Control of Combustion Instabilities Based on Hysteresis" *Combust. Sci. and Tech.*, Vol. 126, pp. 381-388.

Jiang, N., Webster, M., Gabet, K., and Danehy, P. (2010) "Pulse Burst Laser System for High Speed Laser and Combustion Measurements", OSU International Symposium on Molecular Spectroscopy 2010-2013.

Kang, D.M. (2006) "Measurements of Combustion Dynamics with Laser-Based Diagnostic Techniques", Ph.D. Thesis, California Institute of Technology, Pasadena, California.

Kang, D., Culick, F., and Ratner, A. (2007) "Coupling between Combustor Pressure and Fuel/Oxidizer Mixing and the Consequences in Flame Behavior", Combustion Science and Technology, Vol. 180(1), pp. 127-142.

Kappei, F., Lee, J.Y., Johnson, C.E., Lubarsky, E., Neumeier, Y., and Zinn, B.T. (2000) "Investigation of Oscillatory Combustion Processes in Actively Controlled Liquid Fuel Combustor", presented at the 36th Joint Prop. Conf., Huntsville, Al, AIAA 2000-3348.

Katto, Y., and Sajiki, A. (1977) "Onset of Oscillation of a Gas-Column in a Tube Due to the Existence of Heat-Conduction Field (A Problem of Generating Mechanical Energy from Heat)", Bulletin of the JSME, Vol. 20(147), pp. 1161-1168.

Kendrick, D.W., (1995) "An Experimental and Numerical Investigation into Reacting Vortex Structures Associated with Unstable Combustion", Ph.D. Thesis, California Institute of Technology, Pasadena, California.

Kendrick, D.W., Anderson, T.J., Sowa, W.A., and Snyder, T.S. (1999) "Acoustic Sensitivities of Lean-Premixed Fuel Injectors in a Single Nozzle Rig", J. Eng. Gas Turbines and Power, Vol. 121(3), pp. 429-436.

Kim, K.T., Lee, J.G., Quay, B.D. and, Santavicca, D.A. (2010) "Spatially Distributed Flame Transfer Functions for Predicting Combustion Dynamics in Lean Premixed Gas Turbine Combustors", Combustion and Flame, Vol. 157, pp. 1718-1730.

Kim, M., Choi, Y., Oh, J., and Yoon, Y. (2009) "Flame-Vortex Interaction and Mixing Behaviors of Turbulent Non-Premixed Jet Flames Under Acoustic Forcing", Combustion and Flame, Vol. 156, pp. 2252-2263.

Kim, T.K., Park, J., and Shin, H.D. (1993) "Mixing Mechanism Near the Nozzle Exit in a Tone Excited Non-Premixed Jet Flame", *Combust. Sci. and Tech.*, Vol. 89, No. 1-4, pp. 83-100.

Koechner, W. (1999) "Solid-State Laser Engineering", 5th ed., Springer-Verlag, New York.

Kohse-Höinghaus, K., Perc, W., and Just, T.H. (1984) "Determination of Absoluste OH and CH Concentrations in a Low Pressure Flame by Saturated Fluorescence", *P. Combust. Inst.*, Vol. 20, pp. 1177-1185.

Kollner, M., and Monkhouse, P. (1995) "Time-Resolved LIF of OH in the Flame Front of Premixed and Diffusion Flames at Atmospheric Pressure", *Appl. Phys. B*, Vol. 61, pp. 499-503.

Kopp-Vaughan, K.M., Tuttle, S.G., Renfro, M.W., and King, G.B. (2009) "Heat Release and Flame Structure Measurements of Self-Excited Acoustically Driven Premixed Methane Flames", *Combustion and Flame*, Vol. 156, pp. 1971-1982.

Kudryashov, A.V., and Weber H. (1999) "Laser Resonators: Novel Design and Development", SPIE Optical Engineering Press, Bellingham

Kulsheimer, C., and Buchner, H. (2002) "Combustion Dynamics of Turbulent Swirling Flames", *Combustion and Flame*, Vol. 131, pp. 70-84.

Kwon, Y.P., and Lee, B.H. (1985) "Stability of the Rijke Thermoacoustic Oscillation", *J. Acoust. Soc. Am.*, Vol. 74(4), pp. 1414-1420.

Laurence, J.C. (1956) "Intensity, Scale, and Spectra of Turbulence in Mixing Region of Free Subsonic Jet", NASA TR 1292.

Lawn, C.J. (2000) "The Acoustic Self-Excitation of a Bluff-Body Stabilised, Premixed Flame", *Combust. Sci. and Tech.*, Vol. 154, pp. 57-74.

Lee, S-Y., Seo, S., Broda, J.C., Pal, S., and Santoro, R.J. (2000) "An Experimental Estimation of Mean Reaction Rate and Flame Structure During Combustion Instability in a Lean Premixed Gas Turbine Combustor", Proceedings of the Combustion Institute, Vol. 28, pp. 775-782.

Lieuwen, T. (2012) "Unsteady Combustor Physics", Cambridge University Press.

Lieuwen, T., Neumeier, Y., and Zinn, B.T. (1998) "The Role of Unmixedness and Chemical Kinetics in Driving Combustion Instabilities in Lean Premixed Combustors", Combust. Sci. and Tech., Vol. 135, No. 1-6, pp. 193-211.

Lieuwen, T., and Neumeier, Y. (2002) "Nonlinear Pressure-Heat Release Transfer Function Measurements in a Premixed Combustor", 27th Symposium (International) on Combustion, The Combustion Institute, pp. 99-105.

Lozano, A., Yip, B., and Hanson, R.K. (1992) "Acetone: A Tracer for Concentration Measurements in Gaseous Flows by Planar Laser-Induced Fluorescence", Experiments in Fluids, Vol. 13, pp. 369-376.

Luque, J., and Crosley, D.R. (1999) "LIFBASE: Database and Spectral Simulation (Version 1.5)", SRI International Report MP 99-009.

Maling, G.C. (1963) "Simplified Analysis of the Rijke Phenomenon", JASA, Vol. 35(7), pp. 1058-1060.

Masayuki, T., Berg, P.A., Harrington, J.E., Luque, J., Jeffries, J.B., Smith, G.P., and Crosley, D.R. (1998) "Collisional Quenching of CH(A), OH(A), and NO(A) in Low Pressure Hydrocarbon Flames", Combustion and Flame, Vol. 114, pp. 502-514.

Masri, A.R., Dibble, R.W., and Barlow, R.S. (1996) "The Structure of Turbulent Non-premixed Flames Revealed by Raman-Rayleigh-LIF Measurements", *Prog. Energy Combust. Sci.*, Vol. 22, pp. 307-362.

Matveev, K. (2003) "Thermoacoustic Instabilities in the Rijke Tube: Experiments and Modeling", Ph.D. Thesis, California Institute of Technology, Pasadena, California.

McManus, K., Yip, B., and Candel, S., (1995) "Emission and Laser-Induced Fluorescence Imaging Methods in Experimental Combustion", *Experimental Thermal and Fluid Science*, Vol. 10, pp. 486-502.

Merk, H.J. (1957a) "Analysis of Heat-Driven Oscillations of Gas Flows I. General Considerations," *Appl. Sci. Res.*, Vol. A6, pp. 317-335.

Merk, H.J. (1957b) "Analysis of Heat-Driven Oscillations of Gas Flows II. On the Mechanisms of Rijke Tube Phenomenon," *Appl. Sci. Res.*, Vol. A6, pp. 402-420.

Moreno, I., Paez, G., and Strojnik, M. (2003) "Polarization Transforming Properties of Dove Prisms", *Optics Communications*, Vol. 220, pp. 257-268.

Nguyen, Q. (1996) "Raman-LIF Measurements of Temperature, Major Species, OH, and NO in a Methane-Air Bunsen Flame", *Combustion and Flame*, Vol. 105(4), pp. 499-510.

Paul, P.H. (1994) "A Model for Temperature Dependent Collisional Quenching of OH A2 Σ^+ ", *J. Quant. Spectrosc. Radiat. Transfer*, Vol. 51(3), pp. 511-524.

Paul, P.H. (1996) "Collisional Electronic Quenching Rates for NO A2 Σ^+ ", *Chemical Physics Letters*, Vol. 259, No. 5-6, pp. 508-514.

Paul, P.H., and Dec, J.E. (1994) "Imaging of reaction zones in hydrocarbon-air flames by use of planar laser-induced fluorescence of CH", *Optics Letters*, Vol. 19, No. 13.

Paul, P.H., Gray, J.A., Durant, J.L., and Thoman, J.W., (1993) "A Model for Temperature-Dependent Collisional Quenching of NO A2 Σ^+ ", *Appl. Phys. B*, Vol. 57, pp. 249-259.

Paul, P.H., Gray, J.A., Durant, J.L., and Thoman, J.R. (1994) "Collisional Quenching Corrections for Laser-Induced Fluorescence Measurements of NO A2 Σ^+ ", *AIAA Journal*, Vol. 32(8), pp. 1670-1675.

Paul, P.H., and Najm, H.N. (1998) "Planar Laser-Induced Fluorescence Imaging of Flame Heat Release Rate", 27th Symposium (International) on Combustion, The Combustion Institute, pp. 43-50.

Poinsot, T.J., Trouve, A.C., Veynante, D.P., Candel, S.M., and Esposito, E.J. (1987) "Vortex-Driven Acoustically Coupled Combustion Instabilities", *J. Fluid Mech.*, Vol. 177, pp. 265-292.

Poinsot, T., Bourienne, F., Candel, S., and Esposito, E. (1989) "Suppression of Combustion Instabilities by Active Control", *Journal of Propulsion and Power*, Vol. 5(1), pp. 14-20.

Preetham, Santosh, H., and Lieuwen, T. (2008) "Dynamics of Laminar Premixed Flames Forced by Harmonic Velocity Disturbances", *Journal of Propulsion and Power*, Vol. 24(6), pp. 1787-1794.

Pun, W. (2001) "Measurements of Thermoacoustic Coupling", Ph.D. Thesis, California Institute of Technology, Pasadena, California.

Pun, W., Palm, S.L., and Culick, F.E.C. (2000) "PLIF Measurements of Combustion Dynamics in a Burner under Forced Oscillatory Conditions", AIAA-2000-3123, Presented at the 36th Joint Propulsion Conference, Huntsville, Alabama.

Pun, W. Ratner, A., and Culick, F.E.C. (2002) "Phase-Resolved Chemiluminescence of an Acoustically Forced Jet Flame at Frequencies < 60 Hz", 40th AIAA Aerospace Sciences Meeting & Exhibit, AIAA-2002-0194.

Pun, W., Palm, S.L., and Culick, F.E.C. (2003) "Combustion Dynamics of an Acoustically Forced Flame", Combust. Sci. and Tech., Vol. 175(3), pp. 499-521.

Putnam, A.A., and Dennis, W.R. (1954) "Burner Oscillations of the Gauze-Tone Type", J. Acoust. Soc. Am., Vol. 26(5), pp. 716-725.

Ratner, A., Pun, W., Palm, S.L., and Culick, F.E.C. (2002) "Comparison of Chemiluminescence, OH PLIF, and NO PLIF for Determination of Flame Response to Acoustic Waves", Western States Section Meeting of the Combustion Institute.

Ratner, A., Pun, W., Palm, S.L., and Culick, F.E.C. (2003) "Phase-Resolved NO Planar Laser-Induced Fluorescence of a Jet Flame in an Acoustic Chamber with Excitation at Frequencies < 60 Hz", 29th Symposium (International) on Combustion, The Combustion Institute, pp. 85-90.

Rayleigh, J.W.S. (1945) "The Theory of Sound Vol. II", Dover Publications, New York.

Richards, G.A., Gemmen, R.S., and Yip, M.J. (1997) "A Test Device for Premixed Gas Turbine Combustion Oscillations", J. Eng. Gas Turbines and Power, Vol. 119(4), pp. 776-782.

Richards, G.A., and Janus, M.C. (1998) "Characterization of Oscillations During Premix Gas Turbine Combustion", Transactions of the ASME, Vol. 120, pp. 294-302.

Richards, G., Straub, D., and Robey, E. (2005) "Passive Control of Combustion Instabilities in Stationary Gas Turbines", Combustion Instabilities in Gas Turbine Engines, Progress in Astronautics and Aeronautics, Vol. 210.

Rosfjord, T. (1995) "Lean-Limit Combustion Instability", United Technologies Research Center.

Roux, S., Lartigue, G., Poinsot, T. et al. (2005) "Studies of Mean and Unsteady Flow in a Swirled Combustor Using Experiments, Acoustic Analysis, and Large Eddy Simulations", *Combustion and Flame*, Vol. 141, pp. 40-54.

Samieno, J.M., Yip, B., Poinsot, T., and Candel, S. (1993) "Low-Frequency Combustion Instability Mechanisms in a Side-Dump Combustor", *Combustion and Flame*, Vol. 94(4), pp. 363-380.

Sankar, S.V., Jagoda, J.I., and Zinn, B.T. (1990) "Oscillatory Velocity Response of Premixed Flat Flames Stabilized in Axial Acoustic Fields", *Combustion and Flame*, Vol. 80, pp. 371-384.

Santhanam, V., Knopf, F.C., Acharya, S., and Gutmark, E. (2002) "Fluorescence and Temperature Measurements in an Actively Forced Swirl-Stabilized Spray Combustor", *Journal of Propulsion and Power*, Vol. 18(4), pp. 855-865.

Schadow, K., Yang, V., Culick, F.E.C., Rosjford, T., Sturgess, G., and Zinn, B., (1996) "Active Combustion Control for Propulsion Systems", AGARD Workshop Report, May 6-9, 1996, Athens, Greece.

Schlimpert, S., Hemohandra, S., Meinke, M., and Schroder, W. (2015) "Hydrodynamic Instability and Shear Layer Effects on the Response of an Acoustically Excited Laminar Premixed Flame", *Combustion and Flame*, Vol. 162(2), pp. 345-367.

Schuller, T., Durox, D., and Candel, S. (2002) "Dynamics of and Noise Radiated by a Perturbed Impinging Premixed Jet Flame", *Combustion and flame*, Vol. 128, No. 1-2, pp. 88-110.

Schuller, T., Durox, D., and Candel, S. (2003) "A Unified Model for the Prediction of Laminar Flame Transfer Functions: Comparisons Between Conical and V-Flame Dynamics", *Combustion and Flame*, Vol. 134, pp. 21-34.

Schuller, T., Durox, D., and Candel, S. (2003) "Self-Induced Combustion Oscillations of Laminar Premixed Flames Stabilized on Annular Burners", *Combustion and Flame*, Vol. 135, No. 4, pp. 525-537.

Seitzman, J.M., and Hanson, R.K. (1993) "Comparison of Excitation Techniques for Quantitative Fluorescence Imaging of Reacting Flows", *AIAA Journal*, Vol. 31(3), pp. 513-519.

Selle, L., Benoit, L., Poinsot, T. et al. (2006) "Joint Use of Compressible Large-Eddy Simulation and Helmholtz Solvers for the Analysis of Rotating Modes in an Industrial Swirled Burner", *Combustion and Flame*, Vol. 145, pp. 194-205.

Seywert, C. (2001) "Combustion Instabilities: Issues in Modeling and Control", Ph.D. Thesis, California Institute of Technology, Pasadena, California.

Seywert, C., and Culick, F.E.C. (1999) "Some Influences of Noise on Combustion Instability and Combustor Dynamics", 36th JANNAF Combustion Meeting.

Shanbhogue, S., Shin, D.F., Hemchandra, S., Plaks, D., and Lieuwen, T. (2009) "Flame Sheet Dynamics of Bluff-Body Stabilized Flames During Longitudinal Acoustic Forcing", Proceedings of the Combustion Institute. Vol. 32. pp. 1787-1794.

Shih, W.P, Lee, J.G., and Santavicca, D.A., (1996) "Stability and Emissions Characteristics of a Lean Premixed Gas Turbine Combustor", Twenty-Sixth Symposium (International) on Combustion, The Combustion Institute.

Shin, D-H., Plaks, D.V., Lieuwen, T., Mondragon, U.M., Brown, C.T. and McDonell, V.G. (2011) "Dynamics of a Longitudinally Forced, Bluff Body Stabilized Flame", *Journal of Propulsion and Power*, Vol. 27(1), pp. 105-116.

Silfvast, W.T. (1996) "Laser Fundamentals", Cambridge University Press, Cambridge.

Smith, A.V. (1999) "SNLO Nonlinear Optics Code", Sandia National Laboratories

Smith, A.V., and Armstrong, D.J. (2002) "Nanosecond Optical Parametric Oscillator with 90° Image Rotation: Design and Performance", *J. Opt. Soc. Am. B*, Vol. 19(8), pp. 1801-1814.

Smith, A.V., and Bowers, M.S. (2001) "Image-Rotating Cavity Designs for Improved Beam Quality in Nanosecond Optical Parametric Oscillators", *J. Opt. Soc. Am. B*, Vol. 18(5), pp. 706-713.

Smith, L.M., Keefer, D.R., and Sudharsanan, S.I. (1988) "Abel Inversion Using Transform Techniques", *Journal of Quantum Spectroscopy and Radiation Transfer*, Vol. 39, pp. 367-373.

Smith, G.P., Luque, J., Jeffries, J.B., and Crosley, D.R. (2001) "Rate Constants for Flame Chemiluminescence", 2nd Joint Meeting of the U.S. Sections of the Combustion Institute, Oakland, CA.

Steinberg, A.M., Boxx, I., Stohr, M., Carter, C.D., and Meier, W. (2010) "Flow-Flame Interactions Causing Acoustically Coupled Heat Release Fluctuations in a Thermo-acoustically Unstable Gas Turbine Model Combustor", *Combustion and Flame*, Vol. 157, pp. 2250-2266.

Sterling, J.D. (1987) "Longitudinal Mode Combustion Instabilities in Air Breathing Engines", Ph.D. Thesis, California Institute of Technology, Pasadena, CA.

Sterling, J.D., and Zukoski, E.E., (1991) "Nonlinear Dynamics of Laboratory Combustor Pressure Oscillations", *Combust. Sci. and Tech.*, Vol. 77, pp. 225-238.

Stohr, M., Sadanandan, R., and Meier, W. (2011) "Phase-Resolved Characterization of Vortex-Flame Interaction in a Turbulent Swirl Flame", *Experimental Fluids*, Vol. 51, pp. 1153-1167.

Sutton, J.A., and Driscoll, J.F. (2003) "Optimization of CH Fluorescence Diagnostics in Flames: Range of Applicability and Improvements with Hydrogen Addition", *Applied Optics*, Vol. 42, pp. 2819-2828.

Thumuluru, S.K., and Lieuwen, T. (2009) "Characterization of Acoustically Forced Swirl Flame Dynamics", *Proceedings of the Combustion Institute*, Vol. 32, pp. 2893-2900.

Thurber, M.C., and Hanson, R.K. (2001) "Simultaneous imaging of temperature and mole fraction using acetone planar laser-induced fluorescence", *Experiments in Fluids*, Vol. 30, No. 1, pp. 93-101.

Torger, J.A., Kendrick, D.W., and Cohen, J.M. (1998) "Measurement of Spray/Acoustic Coupling in Gas Turbine Fuel Injectors", Presented at the 36th Aerospace Sciences Meeting & Exhibit, Reno, NV, AIAA 98-0718.

Truffin, K., Poinsot, T. (2005) "Comparison and Extension of Methods for Acoustic Identification of Burners", *Combustion and Flame*, Vol. 142, pp. 388-400.

Vagelopoulos, C.M., and Egolfopoulos, F.N. (1998) "Direct Experimental Determination of Laminar Flame Speeds", 27th Symposium (International) on Combustion, The Combustion Institute, pp. 513-519.

Venkataraman, K.K., Preston, L.H., Simons, D.W., Lee, B.J., Lee, J.G., and Santavicca, D.A. (1999) "Mechanism of Combustion Instability in a Lean Premixed Dump Combustor", *J. Propul. Power*, Vol 15(6), pp. 909-918.

Wang, H.Y., Law, C.K., and Lieuwen, T. (2009) "Linear Response of Stretch-Affected Premixed Flames to Flow Oscillations", *Combustion and Flame*, Vol. 156, pp. 889-895.

Wolfrum, J. (1998) "Lasers in Combustion: From Basic Theory to Practical Devices", 27th Symposium (International) on Combustion, The Combustion Institute, pp. 1-41.

Worth, N.A., and Dawson, J.R. (2012) "Cinematographic OH-PLIF Measurements of Two Interacting Turbulent Premixed Flames with and without Acoustic Forcing", Combustion and Flame, Vol. 159, pp. 1109-1126.

Wu, S., Blake, G.A., Sun, S., and Ling, J. (2000) "A Multicrystal Harmonic Generator that Compensates for Thermally Induced Phase Mismatch", Optics Communications, Vol. 173, pp. 371-376.

Xavier, P., Vandel, A., Godard, G. et al. (2016) "Investigation of Combustion Dynamics in a Cavity-Based Combustor with High-Speed Laser Diagnostics", Experiments in Fluids, Vol 57(4).

Yilmaz, I., Ratner, A., Ilbas, M., and Huang, Y. (2010) "Experimental Investigation of Thermoacoustic Coupling Using Blended Hydrogen-Methane Fuels in a Low Swirl Burner", International Journal of Hydrogen Energy, Vol. 35, pp. 329-336.

Yip, B., Miller, M.F., Lozano, A., and Hanson, R.K. (1994) "A combined OH/acetone Planar Laser-Induced Fluorescence Imaging Technique for Visualizing Combusting Flows", Experiments in Fluids, Vol. 17, pp. 330-336.

Yuan, Zeng-Guang (2003) "The Filtered Abel Transform and Its Application in Combustion Diagnostics", NASA/CR-2003-212121

Zsak, T.W. (1993) "An Investigation of the Reacting Vortex Structures Associated with Combustion", Ph.D. Thesis, California Institute of Technology, Pasadena, California.